TESIS DOCTORAL

On the variable nature of low luminosity active galactic nuclei

Lorena Hernández García

Memoria presentada para optar al grado de
Doctora en Física y Matemáticas

Directoras:

Dra. Josefa Masegosa Gallego
Dra. Isabel Márquez Pérez
Dra. Omaira González Martín

Universidad de Granada
Programa de Doctorado en Física y Matemáticas

Editor: Universidad de Granada.Tesis Doctorales
Autora: Lorena Hernández García
ISBN: 978-84-9125-218-4
URI: http://hdl.handle.net/10481/40694

A ama y aita.

Agradecimientos

No recuerdo en qué momento me entusiasmé por la astronomía. Lo que sí viene a mi memoria son las noches de verano observando el cielo en los pueblos en los que nacieron mi padre y mi madre, Valdefinjas y Antoñan del Valle.

Valdefinjas es una localidad zamorana perdida entre Toro y Venialbo – cada una a unos 10 km – donde cada medianoche apagan todas las luces del pueblo. Era entonces cuando el espectáculo nocturno acontecía sobre mi curiosa mirada. El cielo brillaba con tal intensidad que multitud de constelaciones que no acostumbraba a ver aparecían en el cielo; la Vía Láctea parecía un espectáculo frente a los ojos de la niña que entonces era. Creo firmemente que aquella oscuridad profunda en aquel lugar remoto de Castilla me hizo preguntarme por primera vez qué hay más allá de lo que nuestros ojos alcanzan a ver. De la misma forma recuerdo las noches en las que me despertaba en mitad de la noche para ver las lluvias de estrellas de agosto desde el patio de la leonesa casa de mis abuelos en Antoñan. También recuerdo ver con gran entusiasmo el famoso eclipse solar de 1999 desde Antoñan con amigos y familia. Por eso el primer agradecimiento es para quienes siempre han estado ahí, abuelos, primos, tios. Especialmente quiero agradecer a mis padres, Tere y Virgi, quienes me han apoyado en todo momento, incluso cuando no entendían lo que quería o no estaban seguros de si llegaría a alguna parte. Siempre recordaré una conversación con mi madre en la que le comentaba que quería estudiar física para poder ser astrónoma. Ella preguntó: "¿No te apetece más estudiar otra cosa, por ejemplo psicología?" Aún me da la risa al recordarlo. Agradezco enormemente la confianza que depositaron en mí para comenzar este camino desde el que ahora escribo esta memoria. También tengo que agradecer a mi hermana Sonia, de la que estoy muy orgullosa. Si bien las relaciones entre hermanas siempre son difíciles, pienso que es así porque son las personas en las que mayor confianza tienes. De hecho, Sonia siempre ha sido una de las personas con quien más he compartido.

La universidad resultó ser más divertida de lo que se suponía. Para mi significó salir de mi pueblo, Llodio, por primera vez, de forma que ligeramente expandí mis horizontes y mi mente. Nueva gente, nuevos lugares, una nueva forma de ver la vida, y además un coche. Todo esto a la vez que me hacía mayor de edad – y supuestamente más madura. Fue una época dura en Leioa, estudiar física significaba pasar por una buena etapa de suspensos que sufrí junto a compañeros como Carla, Rafa, Uri, Gemma, Lara, Elena, Nora... Llegó un punto en el que me dio igual ir por la rama de astronomía u otra, lo que quería era acabar la carrera. Como una guía apareció Itziar, quien me recordó que lo que siempre quise fue estudiar astrofísica. Por eso tengo que agradecerle a ella ese toque de atención que me dio exactamente en el momento en que lo necesitaba.

Y precisamente con ella me mudé a Tenerife. Lo cierto es que fue todo un acierto. Recuerdo los días en Tenerife como el mismo paraiso; solía ir a la playa una vez por semana, los estudios eran mucho más livianos y la gente de la isla tenía una simpatía especial. Encontrar a Tati en la isla fue una de las mayores bendiciones, a ella le debo la felicidad que irradiaba en aquella época, así como la inspiración y creatividad que aún hoy me aporta. De hecho, ella es quien ha hecho las ilustraciones de la portada y contraportada de la tesis durante la reciente visita que he hecho a la isla. En la facultad también conocí a mucha gente especial, como Eneko, Parda, Zaira, Alba, Rubén, Itziar, Lillo, Bea, Carol, Agus con quienes pasé momentos estupendos, entre fiestas, celebraciones, observaciones, y de cuando en cuando algo de estudio. Realmente las historias que contar son tantas que lo mejor es recordarlo todos juntos entre risas.

Me mudé a Granada tras acabar la carrera, porque había pedido una beca del Gobierno Vasco para hacer la tesis con Javier Gorosabel que, al final, no cuajó. A él tengo que agradecerle mis primeros pasos en la investigación y una coautoría en *Nature*. Escribí entonces a una tal Pepa, investigadora del IAA de la que una profesora tinerfeña, María Jesús, solía hablarnos mucho. Nos conocimos en el IAA tras una clase de máster en el que yo estaba matriculada. Ahora que lo pienso, no recuerdo sobre qué hablamos aquel día, pero los acontecimientos llevaron a que conociese a Isa y me ofreciesen una beca FPI. ¡Yo no podía creerlo! Así pues, primero debo agradecer a María Jesús, porque aunque nunca me lo hayan confesado, estoy segura de que sin sus recomendaciones hoy no estaría andando por este camino. Estoy muy contenta con mis directoras de tesis, no sólo como supervisoras sino también como personas. Ahora que estoy al final del trayecto se supone que debería estar cansada, asqueada. Sin embargo, debo decir que el final está siendo de lo más emocionante. Ahora que entiendo, comparto y discuto el conocimiento que hemos adquirido en este tiempo es cuando más estoy disfrutando de la ciencia. Y es gracias a Pepa, Isa y Omaira que ésta sea mi actitud en este momento. Mil millones de gracias a las tres, desde luego esta tesis que hemos hecho juntas no hubiera sido posible sin vosotras, que me habéis enseñado tanto y habéis sido tan pacientes. Debéis saber que habéis hecho realidad un sueño que llevo soñando mucho tiempo.

Han pasado casi cuatro años desde que me uní al grupo de AGN del IAA. Recuerdo las primeras reuniones en las que no entendía absolutamente nada. Con paciencia fueron compartiendo con el grupo los resultados de sus investigaciones y otras curiosidades, de forma que me hicieron ser consciente de asuntos que no están directamente relacionados con mi tesis pero que la tocan muy de cerca. A quiénes aún están y los que pasaron, Chony, Mirjana, Jaime, Jack, Ilse, César, Kasia, Israel, muchas gracias GANG.

La tesis hubiese sido mucho más dura si no hubiese contado con compañeros en la misma situación, las y los becarios del IAA. Han estado ahí para lo bueno y para lo malo, día a día compartiendo las vivencias, los sufrimientos y las alegrías. Rubén se merece una mención especial porque me ha ayudado muchísimo en la tesis, verdaderamente es el señor (ahora doctor!) que todo lo sabe. Zaira, Sol, Fran, Carol, David, Sara, gracias a todos por haber compartido tan buenos momentos, también por vuestra sabiduría. También quiero agradecer a todo el Instituto de Astrofísica de Andalucía por generar tan buen ambiente de trabajo.

El desarrollo de la tesis me ha sacado del país para abrirme a nuevas formas de investigación, nuevas culturas e idiomas. Cuando supe que tenía que ir a París durante tres meses entré en pánico. No quería ir. No sabía francés, ni siquiera sabía cómo comprar pan. De alguna forma Isa y Pepa me convencieron de que aquello no saldría tan mal. Razón tenían, París es una ciudad magnífica para pasar varios meses. Me acogió allí Florence, a quien debo agradecer por tratarme realmente como si estuviese en mi casa. Además de con la ciencia, ella me ayudó con el francés y al final fui capaz de comunicarme aunque, como digo yo, solía tener conversaciones paralelas. Las comidas las pasaba con los estudiantes, que muy amablemente me hablaban despacito entre las voces que retumbaban en la cantina; entre ellos recuerdo con especial cariño a Nico y Alba, con quienes más relación tuve. Lo que recuerdo como increíble de París es la cantidad de cultura que se respiraba en la ciudad. Museos, conciertos, charlas, no perdí ni un sólo segundo. Pasé mucho tiempo con Paulina recorriendo y conociendo París, una psiquiatra que, literalmente, me ayudó a saltar los muros del psiquiátrico. Gracias a ella llegué a muchos sitios a los que de lo contrario me hubiese dado pereza ir, y juntas abrimos nuestras mentes a una cultura que no es posible encontrar en los países que habitamos.

Como los veranos en Granada se me hacen horribles, la siguiente estancia la pasé durante dos meses de verano en Leicester (Reino Unido). Esta vez iba a trabajar con Simon, a quien agradezco mucho la ayuda prestada. Si bien es un hombre de lo más ocupado, nunca dejé de aprender y entender nuevas cosas cada día. Además me encanta cómo enseña, pintando en la pizarra de modo que es facilísimo visualizar lo que esconden las ecuaciones, de una forma realmente clara. En este caso los estudiantes no fueron demasiado hospitalarios, apenas pasé tiempo con ellos, aunque debo decir que dado que era la época de vacaciones muchos de ellos no estaban o trabajaban desde casa. Sin embargo, tampoco tuve tiempo de aburrirme y disfruté muchísimo de la estancia en Leicester. La música fue en gran parte responsable de que tenga en tan buena estima a esta pequeña ciudad inglesa. No mencionaré nombres ni historietas puesto que tendría que excederme bastante.

Ha pasado mucho tiempo desde mis primeros pensamientos en la astronomía, muchos años desde que decidí emprender este camino. Hay una persona que ha estado a mi lado gran parte de ese viaje, con quien comparto mis días y a quien agradezco de corazón que esté ahí. La universidad se hizo más amena con Igor, cuando nos distanciamos porque me fui a Tenerife aprendimos que queríamos estar juntos, y desde que vivimos en Granada se que cada día que pasa me alegra más que compartamos nuestras vidas. Tú te mereces no sólo un agradecimiento escrito en una página sino un libro completo. Pero eso lo escribimos en el viento con nuestras vivencias, para que se expanda y llegue lejos, muy lejos.

Hay mucha más gente a la que me gustaría agradecer. Vienen muchas caras a mi mente que de una u otra forma me han ayudado. Dado que he tratado de centrarme sólo en la gente que ha contribuído a esta tesis de forma directa, acabaré simplemente con un enorme GRACIAS.

Acknowledgements

I cannot remember the exact moment I get excited about astronomy. What actually comes to my mind are the summer nights observing the sky in my father and mothers hometowns, Valdefinjas and Antoñan del Valle.

Valdefinjas is a lost village in between Toro and Venialbo (Zamora) – each one located at about 10 km – where all the lights switch off at midnight. It was then that the night-show happened above my curious eyes. The sky glowed so bright that multiple constellations I was not used to see appeared in the sky; the Milky Way seemed a show in front of the eyes of the girl I was. I firmly believe that the deep darkness in that remote village of Castilla made me first ask what lies beyond what our eyes can see. I remember in the same way those nights when I woke up in the middle of the night to observe the rain of stars occurring in August from my grandparents yard in Antoñan (Leon). I also remember to observe the famous solar eclipse in 1999 with friends and family in Antoñan. That is why my first acknowledgement is for those who have always been there, grandparents, cousins, uncles and aunts. I am specially grateful to my parents, Tere and Virgi, who have always supported me, even when they did not understand what I wanted or were not sure if I would get somewhere. I will always remember a conversation with my mother. I was telling her I wanted to study physics to become an astronomer. She asked: “Do not you prefer to study a different thing, psychology for instance?” It still makes me laugh. I greatly appreciate their confidence to start this path. I also want to acknowledge my sister Sonia, of whom I am very proud. Whether is true that sisterhood is always difficult, I believe it is because they are the people who you trust most. Sonia has always been one of the persons with whom I shared more.

University resulted livelier than expected. It meant to me to get out of my hometown, Llodio, for the first time, so I slightly expanded my horizon and my mind. New people, new places, a new way to see life, and a car. All this at the same time I became an adult – and supposedly more mature. It was a hard epoch in Leioa; studying physics meant to pass through lots of failures that I suffered alongside people like Carla, Rafa, Uri, Gemma, Lara, Elena, Nora... At one point I did not mind to study astronomy or other branch of physics. As a guide appeared Itziar, who reminded me that I always wanted to study astrophysics. So I have to acknowledge her the wake-up call she gave me at the right time.

I moved with her to Tenerife. It was really a success. I remember the days in Tenerife as in paradise; I used to go to the beach once per week, studies were much easy and the people from the island had a special sympathy. Finding Tati in the island was one of the higher blessings, I own her the happiness I radiated those days, as well as the inspiration and creativity that still brings to me today. She is indeed who made the illustrations of the front and cover pages of this thesis during my recent visit to the island. I also met very special people at college; Eneko, Parda, Zaira, Alba, Rubén, Itziar, Lillo, Bea, Carol, Agus. I spend very good moments with them, between parties, celebrations, observations, and some study from time to time. The stories to tell are so many that the best is to remember them together within laughs.

I moved to Granada after finishing my career, because I asked for a fellowship from the Basque Country to make the thesis with Javier Gorosabel, but could not be. I have to acknowledge him my first steps in research and a coautorship in *Nature*. I then wrote to Pepa, a researcher from the IAA, a teacher – María Jesús – used to talk about her. We met at the IAA after a master class. Now, I cannot remember what did we talk about that particular day, but the events led to met Isa and they offered me a FPI fellow. I could not believe it! Therefore, I first have to thank María Jesús because, although they never confessed it, I am sure that without her recommendation I would not be walking through this way today. I am very happy with my supervisors, not only as supervisors but also as human beings. Now that I am at the end of the journey I am supposed to be tired, disgusted. However, I must say that the end is being the most exciting part. Now that I understand, share and discuss the knowledge we have acquired within this time is when I am enjoying science most. And it is thanks to Pepa, Isa and Omaira that this is my attitude now. Billions of thanks to you three. Of course, this thesis that we have build together would not have been possible without you, who have taught so much and have been so patient. You must know that you made a dream that I have been so long dreaming come true.

It is been almost four years since I joined the AGN group at IAA. I remember the first meetings when I did understand nothing. Patiently they shared their research and other curiosities with the group, so they made me being conscious of topics that are not directly related to my thesis but touch it very closely. To those who still are, and the ones who have left, Chony, Mirjana, Jaime, Jack, Ilse, César, Kasia, Israel, thank you so much GANG.

The thesis would have been harder without the IAA students which are in the same situation. They have been there for good and bad, day by day sharing experiences, sufferings and joys. Rubén deserves a special mention since he has greatly helped me, he is really the sir (doctor now!) who knows everything. Zaira, Sol, Fran, Carol, David, Sara, thank you all for being sharing such a good moments, also for your wisdom. I also want to acknowledge to all the IAA for generating a good work environment.

The development of the thesis has taken me out of the country to open new ways of research, new cultures and languages. When I realized I had to go to Paris for three months I entered in panic. I did not want to go. I did not know french, not even to buy bread. Somehow Isa and Pepa convinced me that it would not be so bad. They were right, Paris is an amazing city to spend a few months. Florence welcomed me, to whom I must be grateful for treating me like at home. In addition to science, she helped me with the french, and finally I was able to communicate although, as I say, I used to have parallel conversations. I spend lunch-time with the students, who kindly spoke to me slowly between the voices that reverberated in the canteen; among them I remember Nico and Alba with special affection. What I remember as incredible from Paris is the amount of culture that could be breathed in the city. Museums, concerts, talks, I did not loose a second. I spend lot of time with Paulina walking and knowing Paris, a psychiatrist who, literally, helped me jump the walls of the psychiatric. Thanks to her I met many places otherwise I would have been lazy to go, and together we opened our minds to a culture which is not possible to find in the countries we live.

As summertime in Granada is awful to me, I moved to Leicester (UK) for two months in my next short stay. I worked with Simon this time, to whom I am very grateful for his help. Whereas he is a very busy man, I never stopped learning and understanding new things each day. I love the way he teaches, drawing in the blackboard so it is super easy to visualize what is hidden in equations, in a really clear way. In this case students were not very friendly, I did not spend long time with them, although I have to say it was holidays so many of them were not at work or worked from home. Nevertheless, I did not have time to be bored either, and I fully enjoyed my stay in Leicester. Music was to a great extent responsible that I have such a good memories from this small English city. I will not mention names nor stories as I would have to extend this too much.

It is been long time since my first thoughts in astronomy, many years since I decided to undertake this way. There is a person who has been by my side most of the travel, with whom I share my days and whom I thank from my heart to be there. University became more enjoyable with Igor, when we distance ourselves because I moved to Tenerife we realized that we wanted to be together, and since we live in Granada I know that each day I am more grateful of sharing our lives. You deserve not only an acknowledge in one page but a full book. But we will write it in the wind with our experiences, so it can expand and travel far, far away.

There are much more people I would like to thank. Many faces that one way or another helped me come to my mind. Since I just wanted to focus on people who have directly contribute to this thesis, I will just finish with a huge THANKS.

La doctoranda, Lorena Hernández García, y las directoras de la tesis, Josefa Masegosa, Isabel Márquez, y Omaira González Martín, garantizamos, al firmar esta tesis doctoral, que el trabajo ha sido realizado por el doctorando bajo la dirección de los directores de la tesis y hasta donde nuestro conocimiento alcanza, en la realización del trabajo, se han respetado los derechos de otros autores a ser citados, cuando se han utilizado sus resultados o publicaciones.

En Granada, a 11 de junio de 2015

Omaira G

Josefa Masegosa
Isabel Márquez
Omaira González Martín

Lorena Hernandez

Lorena Hernández García

Resumen

Los núcleos activos de galaxias (AGN, de sus siglas en inglés) emiten energías del orden de $10^{44} erg\ s^{-1}$ en regiones muy compactas, siendo uno de los fenómenos más energéticos de todo el Universo. Hoy en día, la teoría más aceptada es que este fenómeno es consecuencia de la acreción de materia sobre un agujero negro supermasivo.

Esta tesis está centrada en el estudio de la variabilidad del extremo de los AGN de más baja luminosidad (LLAGN), los LINERs (*low ionization nuclear emission line regions*) y las conocidas galaxias Seyfert. A su vez se compara el comportamiento de ambas familias de AGN. Mientras que los núcleos Seyfert fueron descubiertos en 1943 y se caracterizan porque el núcleo produce líneas espectrales de emisión de gas altamente ionizado, hubo que esperar hasta 1980 para que Heckman descubriese los LINERs y los clasificase como una subcategoría de AGN, cuyos espectros ópticos presentan un estado de ionización más bajo que las Seyfert.

El estudio de AGN en rayos X es ideal puesto que el núcleo es accesible en este rango de frecuencias y además el efecto de oscurecimiento es mucho menor comparado con el ultravioleta (UV), óptico o infrarrojo cercano. Es por ello que los datos presentados en esta tesis son principalmente en rayos-X, aunque complementados con información simultánea en frecuencias UV.

La variabilidad es una propiedad que caracteriza a los AGN de alta potencia, que muestran variaciones en todo el espectro electromagnético, y permite inferir sobre sus propiedades físicas. Si bien esto está establecido para las galaxias Seyfert, no es algo obvio en LINERs, para los que solamente se ha estudiado una pequeña muestra de objetos tipo 1 en rayos X o una muestra algo más grande en el UV. Además, al comenzar esta tesis no se conocía cuál es el mecanismo físico que origina las variaciones en este tipo de AGN, que es uno de los principales objetivos de esta tesis.

Para analizar la variabilidad en rayos X, se ha elaborado un método que permite estudiar variaciones a corta y larga escala. Las variaciones a larga escala se analizan ajustando todos los espectros de un mismo objeto con el mismo modelo. La variabilidad a corta escala se obtiene del análisis de las curvas de luz, que se analizan de manera estándar. Esto nos permite estimar tanto las variaciones en flujo como las variaciones espectrales, lo que sirve para conocer el patrón de variabilidad y permite a su vez inferir propiedades físicas de estos objetos. Para este estudio se han utilizado datos públicos de los satélites de rayos-X *Chandra* y *XMM*–Newton en diferentes épocas. Además, con *XMM*–Newton se puede obtener de forma simultánea información sobre variabilidad en rayos X y UV. La metodología se explica en detalle en el Capítulo 2 (ver también Hernández-García et al. 2013).

Primero se aplicó la metodología a una muestra de 18 núcleos LINERs, incluyendo tipos 1 (en realidad son todos tipo 1.9) y 2 (Capítulo 2). Se clasificaron los núcleos como AGN (no-AGN) cuando mostraban una fuente puntual (o no) en la banda de energía 4.5-8.0

keV, siguiendo el trabajo de González-Martín et al. (2009b). De entre toda la muestra, tres LINERs fueron clasificados como no-AGN, todos ellos siendo candidatos a *Compton*-thick (esto es, que están oscurecidos por columnas de densidad muy altas, mayores de 10^{24} cm^{-2}), ninguno muestra variaciones en rayos-X y dos de ellos varían en el UV. Ninguno de los núcleos muestra variaciones a corta escala (entre horas y días), mientras que más de la mitad de los clasificados como AGN varían en escalas temporales largas (entre meses y años). Estas variaciones son principalmente debidas a cambios intrínsecos de las fuentes, mientras que solamente una galaxia muestra variaciones en la columna de densidad - lo que estaría directamente relacionado con cambios en la densidad del toro de polvo o la región de líneas anchas (BLR, de sus siglas en inglés). El estudio en UV muestra que este tipo de galaxias son variables a frecuencias UV. Así, se encuentra que los LINERs son objetos variables en rayos-X y UV. Además, de acuerdo a las masas de sus agujeros negros, tasas de acreción, y escalas temporales de variabilidad, encontramos que los LINERs siguen el mismo plano de variabilidad ($M_{BH} - L_{bol} - T_B$) que otros AGN más luminosos en rayos X. También hemos estudiado el mecanismo de acreción a partir de la relación entre el índice de la ley de potencias y el cociente de Eddington, donde se aprecia una anticorrelación, indicando que la acreción podría ser ineficiente (comparada con la acreción eficiente que se encuentra para objetos más luminosos). Los resultados derivados de este estudio han sido publicados en Hernández-García et al. (2014).

La misma metodología se aplicó a una muestra de 26 galaxias Seyfert tipo 2 (Capítulo 3). Ninguno de los núcleos muestra variaciones a corta escala. En este caso se realizó un estudio adicional para seleccionar candidatos a *Compton*-thick, pues, dado que estas galaxias se observan a través del toro de polvo, se espera que una fracción significativa de ellas esté altamente oscurecida. Encontramos que 12 de las galaxias son candidatas a *Compton*-thick. De entre las que son candidatas a *Compton*-thick, solamente una de ellas muestra variaciones a larga escala; la explicación más razonable es que parte del continuo es aún transmitido y por ello vemos variaciones. Entre los demás núcleos encontramos que la mayoría son variables en escalas entre meses y años, siendo el patrón de variabilidad muy similar al encontrado para los LINERs: cambios intrínsecos de la fuente de energía. Variaciones debidas a la columna de densidad se encuentran sólo en cuatro fuentes (30%). Finalmente, a diferencia de lo encontrado en LINERs, ninguna de las galaxias muestra variaciones en frecuencias UV. Los resultados de este estudio han sido publicados en Hernández-García et al. (2015).

Por tanto, el estudio de variabilidad en rayos-X en LLAGN muestra que ambas familias de AGN son variables en escalas temporales que van entre meses y años, amplitudes entre 20 y 80 % y un patrón de variabilidad común en todos ellos. En UV, al contrario, el estudio de variabilidad muestra que mientras que los LINERs son variables, las Seyfert 2 no muestran ningún cambio a estas frecuencias, detectándose la fuente UV en sólo tres galaxias. El hecho de que el núcleo varíe en este rango podría deberse a que el toro de polvo ha desaparecido en los LINERs, dejando el núcleo al descubierto, dando lugar a las variaciones observadas. El trabajo realizado en esta tesis pone de manifiesto que los LINERs y las Seyferts tipo 2 se comportan espectralmente de forma similar en el rango de frecuencias de los rayos-X. No obstante, los datos de tasas de Eddington analizados son consistentes con un mecanismo de acreción diferente, siendo eficiente para los Seyfert e ineficiente para los LINERs. Este estudio se presenta en el Capítulo 4.

La tesis se complementa con dos capítulos relacionados con la actividad nuclear y la emisión en rayos-X de objetos extragalácticos (Capítulos 5 y 6). El primero es un estudio sobre AGN en grupos y cúmulos de galaxias usando datos de *XMM*–Newton y *Chandra*, que incluye la determinación del número de AGN en cada cúmulo. Encontramos entre uno y cinco AGN por cúmulo. El segundo es un estudio de la variabilidad en objetos ultraluminosos en rayos-X (ULXs) usando datos de *XMM*–Newton y aplicando técnicas de Fourier. Estimamos la variabilidad no-lineal de las ULX, que ocurre en la misma forma que otros agujeros negros con diferentes masas, y el retardo temporal que las variaciones generan entre dos bandas de energía diferentes.

Abstract

Active Galactic Nuclei (AGN) emit energies of the order of $10^{44} erg\ s^{-1}$ in very compact regions, being one of the most energetic phenomena in the Universe. Nowadays, the most accepted theory is that this phenomena is consequence of accretion of matter onto a super massive black hole.

This thesis is centered on the variability study of the low luminosity AGN (LLAGN), including LINERs (low ionization nuclear emission line regions) and the well known Seyferts. The behaviour of the AGN families are also compared. Whereas Seyfert nuclei were discovered in 1943 and are characterized because their nuclei produce high ionized spectral emission lines, it was not until 1980 that Heckman discovered LINERs and classified them as a subclass of AGN, whose optical spectra present a lower ionization state than Seyferts.

The study of AGN in X-rays is ideal because the nucleus is accessible in this frequency range and the obscuration effect is much smaller compared to the ultraviolet (UV), optical or near-infrared. That is why the data presented in this thesis are mainly in X-rays, although complemented with simultaneous information at UV frequencies.

Variability is a property characterizing powerful AGN, which show variations in the whole electromagnetic spectrum, and allows to infer their physical properties. While this is well established for Seyfert galaxies, it is not obvious for LINERs, for which it has been studied only in a small sample of type 1s and a sample at UV frequencies. Moreover, at the beginning of this thesis the physical mechanism that originates variations in this kind of AGN was unknown, being this one of the main objectives of this thesis.

To analyze the X-ray variability, we have developed a methodology which allows the study at short- and long-term variations. The long-term variations are analyzed by fitting all the data with the same model. The short-term variations are studied from the light curves using standard procedures. This allows us to estimate not only flux variations but also spectral variations, that serves to know the variability pattern and at the same time permits to infer the physical properties of these objects. For this study archival data from *Chandra* and *XMM*–Newton satellites at different dates have been used. Moreover, *XMM*–Newton allows to simultaneously obtain variability information at X-rays and UV frequencies. The methodology is explained in detail in Chapter 2 (see also Hernández-García et al. 2013).

First, the methodology was applied to a sample of 18 LINER nuclei, including type 1 (they are actually type 1.9) and 2 (see Chapter 2). The nuclei were classified as AGN (non-AGN) when a point-like source was observed (or not) in the 4.5–8.0 keV energy band, following the work by González-Martín et al. (2009b). From the entire sample, three LINERs were classified as non-AGN, all of them being *Compton*-thick candidates (i.e., they are obscured by very high column densities, larger than $10^{24} cm^{-2}$), none show variations in X-rays and two of them vary at UV. None of the nuclei show short-term variations (between hours and

days), whereas more than a half of the AGN candidates show long-term variations (between months and years). These variations are mainly related to intrinsic changes of the sources, while only one galaxy shows column density variations – what would be directly related with changes in the density of the dusty torus or the broad line region (BLR). The study in the UV shows that this type of galaxies are variable at UV frequencies. Therefore, it is found that LINERs are variable objects both at X-rays and UV frequencies. Furthermore, according to their black hole masses, accretion rates, and variability timescales, we find that LINERs follow the same variability plane ($M_{BH} - L_{bol} - T_B$) as more powerful AGN in X-rays. We have also studied the accretion mechanism from the relation between the spectral index and the Eddington rate, where an anticorrelation is given, indicating that accretion could be inefficient (compared to the efficient accretion obtained for more powerful sources). The results derived from this study have been published in Hernández-García et al. (2014).

The same methodology was applied to a sample of 26 Seyfert 2s (Chapter 3). None of the nuclei show short-term variations. In this case, and additional analysis was performed to select *Compton*-thick candidates because, since these galaxies are observed through the dusty torus, we expect a fraction of them being highly obscured. We find that 12 sources are *Compton*-thick candidates. Among the *Compton*-thick candidates, only one shows long-term variations; the most reasonable explanation is that part of the continuum is still transmitted and thus we can observe variations. Among the remaining nuclei we find that most of them are variable in timescales between months and years, the variability pattern being very similar to that found for LINERs: intrinsic changes of the energy source. Variations related to the column density were found only in four sources (30%). Finally, in contrast to that found for LINERs, none of the galaxies show variations at UV frequencies. The results of this study have been published in Hernández-García et al. (2015).

Therefore, the X-ray variability study in LLAGN shows that both AGN families are variable in timescales ranging from months to years, with amplitudes between 20% and 80% and a common variability pattern among them. At UV, in contrast, the variability study shows that LINERs are variable, but Seyfert 2s do not show changes at these frequencies, with the nucleus detected only in three cases. The fact that the nucleus varies in this frequency range might be because the dusty torus disappeared in LINERs, leaving the core uncovered, giving place to the observed variations. The work undertaken in this thesis shows that LINERs and Seyfert 2s spectrally behave similarly at X-ray frequencies. However, the analyzed Eddington ratios are consistent with different accretion mechanisms, which is efficient for Seyferts and inefficient for LINERs. This study is presented in Chapter 4.

This thesis is complemented by two chapters related to nuclear activity and the X-ray emission in extragalactic objects (Chapters 5 and 6). The first is a study about AGN in groups and clusters of galaxies using *XMM*–Newton and *Chandra* data, which includes the determination of the number of AGN on each cluster. We find from one to five AGN per galaxy cluster. The second is a study on the variability of ultraluminous X-ray sources (ULXs) using *XMM*–Newton data and applying Fourier techniques. We estimate non-linear variability of the ULX, which occurs in the same way as in black holes of different masses, and time lags that variations generate between two different energy bands.

Contents

1

Introduction

The Universe is a violent place. As far as I know, humans have always been afraid of asteroids that may impact the Earth. The fact that this is the only concern about the processes happening outside the Earth for most people is perhaps related to the fact that the atmosphere protects us from almost all damaging radiation. We do not need to look far to be aware of the violence out there, because the Sun shows violent explosions launching large amounts of matter onto the space, releasing energies of the order of $10^{27} erg\ s^{-1}$. And do not forget that the Sun is a star that will end its life "peacefully" as a white dwarf. On the contrary, the death of massive stars ($M > 10 M_{\odot}$) gives place to strong explosions before becoming neutron stars or stellar mass black holes, releasing energies than can go from $\sim 10^{37}$ up to $\sim 10^{50} erg\ s^{-1}$ in a few seconds.

At larger scales, galaxies are composed by billions of stars of different ages. Thus, at the same time, millions of stars release their energy from inside their nuclei, others explode to give birth to new stars, while some asteroids or comets impact against planets or stars. All these violent episodes take place in part due to the gravitational force, responsible for the dance of all these bodies around the same center.

The most accepted theory nowadays is that a supermassive black hole of millions of solar masses resides in each galaxy in the Universe. Some of them are called "active" because their nuclei constantly release energies ranging from $10^{38} - 10^{48} erg\ s^{-1}$, higher than the energy released by a whole normal galaxy, as for example the Milky Way, which releases $\sim 10^{34} erg\ s^{-1}$. One of the properties characterizing active galaxies is the variability of their nuclei at different frequencies from radio to gamma-rays. This is not unexpected, because from general relativity we know that gravity affects stronger the matter located close to a black hole. Can you imagine what is happening around a supermassive black hole? Everything is movement; stars, planets, all the matter trying to escape from the inevitable drop onto the singularity, where nothing, even light, can escape. This thesis is about the observed variations taking place around different types of supermassive black holes residing in active galaxies, where one of the most violent episodes known to happen in the Universe takes place.

1.1 Active Galactic Nuclei

Early in the 20^{th} century, Fath (1909) was trying to clarify the nature of spiral nebulae. He obtained observations of different sources, most of the spectra consistent with being stars showing absorption lines. Surprisingly, one of the objects, namely NGC 1068, showed unexpected strong emission lines. During the following years, several astronomers noted the presence of nuclear emission lines in the spectra of some spiral nebulae, for example Hubble (1926), who reported a planetary nebula-like spectrum in three sources, NGC 1068, NGC 4051, and NGC 4151. These discoveries marked the beginning of the studies about active galactic nuclei (AGN).

The systematic study of galaxies with nuclear emission lines had to wait until the work by Seyfert (1943). He studied the optical spectra of six objects (NGC 1068, NGC 1275, NGC 3516, NGC 4051, NGC 4151, and NGC 7469), and found that they had similar nuclear properties, showing high-excitation nuclear emission lines superposed to a solar-type spectrum. In his honour, galaxies with high excitation nuclear emission lines are called *Seyfert galaxies*.

However, the work by Carl Seyfert was not enough to launch the study of AGN, which had to await several years. In the meanwhile, the development of radio astronomy greatly advanced in the 50s, when the first surveys of star-like objects were performed (Edge et al. 1959; Bennett 1962), and soon after optical counterparts were also detected (Zwicky 1964).

The first report of a quasi-stellar object (QSO), or quasar, as we know them today, was 3C 48 by Sandage (1964); the spectrum of 3C 48 showed broad emission lines at unfamiliar frequencies, and variability was found from its photometry, together with an excess at ultraviolet wavelengths. But it was Schmidt (1963) who first realized that the broad lines observed in the spectrum of another source he was studying, 3C 273, agreed well with being the Balmer-series and Mg II lines, so this object was located at a redshift z = 0.16. Soon after, Greenstein & Matthews (1963) were also able to obtain a redshift of 0.37 for 3C 48. Later, Greenstein & Schmidt (1964) postulated that the redshifts of these QSO may involve cosmological redshifts, what made them potential tools for the study of cosmological questions.

At this stage, a number of properties of AGN were recognized. Most astronomers accepted the cosmological redshifts of QSO, and the parallel between Seyfert galaxies and QSO suggested a common physical phenomenon (Burbidge et al. 1963).

Today, an AGN is a compact central region with luminosities between $10^{38} - 10^{48} erg\ s^{-1}$ that cannot be explained by stellar processes (Peterson 1997). While they have masses between $10^6 - 10^9 M_\odot$, it is believed that accretion onto a supermassive black hole (SMBH) is the mechanism responsible of such a high energy release (Rees 1984). Moreover, AGN emit through the whole electromagnetic spectrum, from γ-rays to sub-mm, and can be detected up to high redshifts. Indeed, the most distant AGN known is a QSO at $z \sim 7$ (Mortlock et al. 2011).

1.2 AGN subgroups

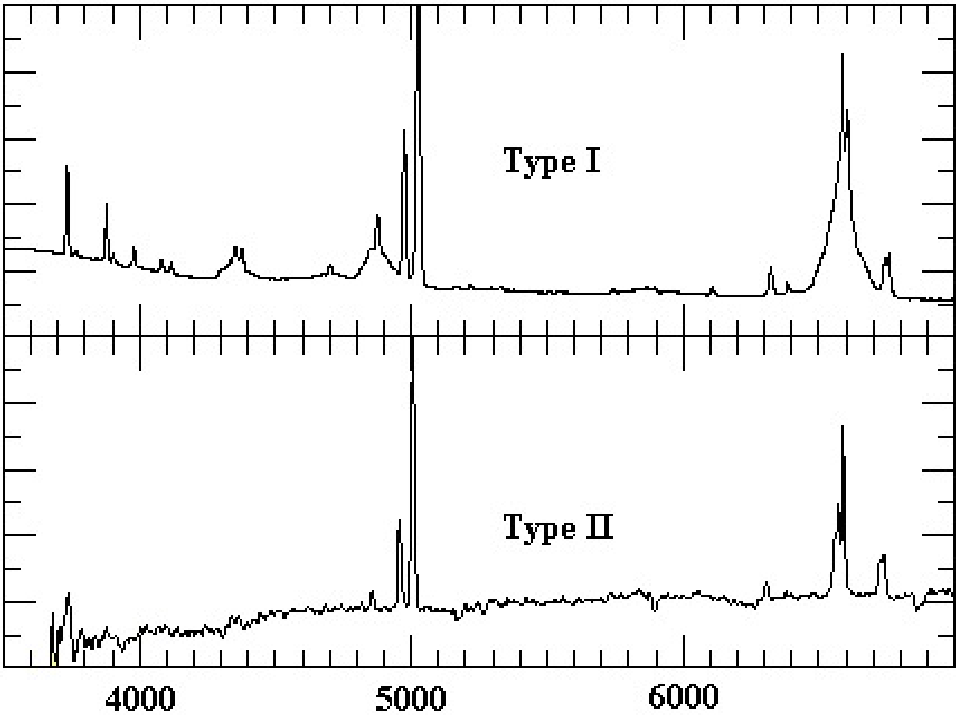

Figure 1.1: Typical spectra of type 1 and 2 AGN - Taken from Extragalactic Astronomy (http://www.uni.edu/morgans/astro/course/Notes/section3).

The classification of AGN is based on observational properties, historically from their optical spectra. Furthermore, AGN have been discovered by different physical properties. For these reasons, different tags can be given to the same object. In this section we define the main classifications of AGN.

Depending on the width of their optical Balmer permitted emission lines, they can be roughly classified as:

- Type 1 AGN: Their spectra are characterized by broad optical Balmer permitted lines with a full-width at half maximum (FWHM) of 1000-20000 $km\ s^{-1}$ superimposed to narrower lines. A non-stellar, bright nuclear source is visible at all wavelengths not contaminated by stellar light (Netzer 2015).

- Type 2 AGN: Their spectra show narrow lines with a FWHM of 300-1000 $km\ s^{-1}$ (i.e., broader than those observed in normal galaxies), with indications of photoionization by a non-stellar source (Netzer 2015). A nuclear point-like source can be observed at X-rays, but not at UV or visible (Muñoz Marín et al. 2009). They can be divided into two subgroups; those with a hidden broad line region (HBLR) that can be seen in polarized light (Tran et al. 1992), and the “true type 2 AGN” that do not show a broad line region in polarized light (i.e., NHBLR) and are characterized by narrow lines only and little absorption at X-rays (Panessa et al. 2009).

Fig. 1.1 show typical spectra of type 1 and 2 AGN, where the broad lines can be observed in the first subgroup. Using the relative intensity of the broad and narrow lines, the nuclei can also be classified as type 1.2, 1.5, 1.8 or 1.9 AGN, with type 1.2 being the sources with weaker narrow component (e.g., Osterbrock & Martel 1993).

On the other hand, different subgroups have been defined depending on multiwavelength properties, as follows:

- Quasars (QSOs): The central source is so luminous that it outshines the light from the host galaxy, and only the nucleus is visible. This is why they are observed at high redshifts. Its name comes from “quasi-stellar object” because they were first confused with star-like objects (Sandage 1964). It was later realized that radio sources are observed in a few percentage of QSO (D’Onofrio et al. 2012). They can be divided into type 1 and type 2. They show bolometric luminosities[1], $L_{bol} \sim 10^{45} - 10^{48} erg\ s^{-1}$ (Woo & Urry 2002).

- Seyferts: The emission from the central nucleus is comparable to the bolometric luminosity from the host galaxy. Their optical spectra are characterized by high ionization lines, as [O III] λ5007, [O I] λ4861, [N II] λ6583, and [S II] $\lambda\lambda$6716, 6731 (Seyfert 1943). They can be divided into type 1 and 2. They show $L_{bol} \sim 10^{42} - 10^{45} erg\ s^{-1}$ (Woo & Urry 2002; Ho 2008). Objects classified as Seyfert 2s are studied in this thesis.

- Narrow Line Seyfert 1 galaxies (NLSy1): Their appearance is similar to Seyfert 1s, but they lack the broad lines and cannot be associated to Seyfert 2s either. They show weak Balmer lines and strong Fe II emission (Véron-Cetty et al. 2001).

- Low ionization nuclear emission line regions (LINERs): Their optical spectra are characterized by low ionization lines, such as [N II] λ6584, [O I] λ6300, and [S II] λ6731 (Heckman 1980). Their luminosities are lower than those of Seyferts and QSOs ($L_{bol} \sim 10^{39} - 10^{42} erg\ s^{-1}$, Ho 2008), and can be divided as types 1 and 2, but note that type 1s refer to 1.9 classifications (Ho et al. 1997). The ionizing mechanism in these objects is still not clear (Ho 2008). Type 1 and 2 LINERs are studied in this thesis.

- Radio galaxies: They are strong radio emitters, showing a nuclear point-like radio emission, often accompanied by single or twin radio lobes. They can also be divided in radio loud (very bright at radio frequencies) and radio quiet (otherwise) AGN (Condon et al. 1980).

---

[1] The luminosity of an object measured over all wavelengths.

- Blazars: They are radio sources and consist of Optically Violent Variables and BL Lac objects. They are highly variable and do not display emission lines in their spectra. They are pure type 1 AGN (Elvis 2000).

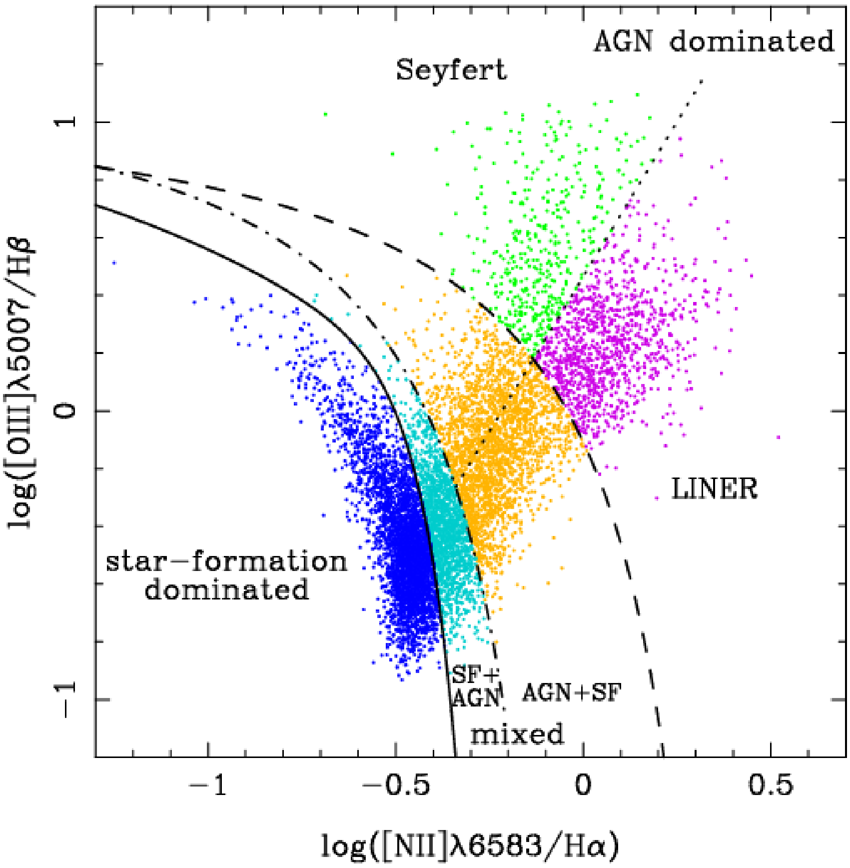

Figure 1.2: Diagnostic diagrams - Plot of log([O III]) $\lambda5007/H_\beta$ versus log([N II]) $\lambda6583/H_\alpha$. Taken from Bamford et al. (2008).

A useful way to differentiate between different kinds of AGN is using the so called "diagnostic diagrams" (also known as BPT diagrams, Baldwin et al. 1981), which can distinguish between star-forming dominated regions, Seyferts or LINERs (Baldwin et al. 1981; Veilleux & Osterbrock 1987; Kauffmann et al. 2003; Kewley et al. 2006). It is worth noting the need of removing the broad component when applying to type 1 objects. These diagrams compare various line ratios that depend on the ionizing continuum, with the most useful emission lines being [O III] λ5007, [N II] λ6583, and [O I] λ6300 combined with H_α and H_β. They assume that AGN have greater [O III] $\lambda5007/H_\beta$ ratios than those galaxies that produce stellar emission. Fig. 1.2 shows a figure from Bamford et al. (2008) that shows a diagnostic diagram. For example, a nucleus is classified as a Seyfert when log([O III]) $\lambda5007/H_\beta \gtrsim 0.5$ and log([N II]) $\lambda6583/H_\alpha \gtrsim -0.3$.

1.3 Components in AGN

In the following we specify the main components of AGN, which can be observed in Fig. 1.3:

- The supermassive black hole (SMBH): It is a relatively tiny place in space with a huge mass, affected by strong gravity (Salpeter 1964; Lynden-Bell 1969). Three parameters can define a black hole: its mass, M_{BH}, angular momentum, J, and charge, Q. The basic properties of SMBH are usually expressed using their gravitational, $r_g = GM_{BH}/c^2$, and Schwarzschild, $r_s = 2r_g$, radii, where G is the gravitational constant. As the SMBH is invisible, its mass has to be estimated by different approaches; here we summarize four common techniques:

  1. Dynamical mass measurements are based on the observed dynamics of the stars and were used to discover the correlation between the SMBH and the host galaxy (Young et al. 1978; Sargent et al. 1978).

  2. Reverberation mapping measures the delay in the appearance of the line variations over the continuum variations (Blandford & McKee 1982; Kaspi et al. 2000), so the distance from the central source to the BLR (R_{BLR}, see below) can be derived, and the mass is given by:

  $$M_{BH} = \frac{v^2 R_{BLR}}{G} \propto \frac{c\tau v^2}{G} \tag{1.1}$$

  where τ is the time delay, c the speed of light, and v the cloud velocity. However, this technique has been applied only to a few objects since long timescale coverages are required in order to measure the time delays.

  3. The BLR size-luminosity relationship uses the approach that $R_{BLR} \propto L^{\alpha}$, where L is the continuum luminosity at a given wavelength (Kaspi et al. 2005). The estimation of the mass is usually made with the optical continuum at $\lambda = 5100$ $\mathring{A}$ and the broad component of the H_β emission line:

  $$M_{BH} = 4.817\Big(\frac{\lambda L_\lambda(5100\mathring{A})}{10^{44}[erg\ s^{-1}]}\Big)^{0.7} FWHM(H_\beta)^2 \tag{1.2}$$

  where FWHM refers to the full width at half maximum of the broad component in the H_β emission line. The Mg II and C IV lines have also been used, but at high redshifts the accuracy of the measurement is lower (Sulentic et al. 2007; Netzer et al. 2007).

  4. The $M_{BH} - \sigma$ relation showed that the masses correlate with the velocity dispersions of the host bulges as $M_{BH} \propto \sigma^4$ (Ferrarese & Merritt 2000; Gebhardt et al. 2000; Gültekin et al. 2009).

- The accretion disc: It is widely accepted that accretion onto the SMBH is the mechanism responsible of the high energy in AGN (Rees 1984), where matter is transported inwards and angular momentum outwards due to dissipative processes (Shakura & Sunyaev 1973). Two fundamental quantities are related to accretion processes: the Eddington luminosity, L_{Edd}, which is the maximum luminosity a body can achieve when there is balance between the force of radiation acting outward and the gravitational force acting inward:

  $$L_{Edd} \simeq 1.5 \times 10^{38} (M/M_{\odot}) [erg\ s^{-1}] \tag{1.3}$$

  and the accretion rate, $R_{Edd} = L/L_{Edd}$, defined as the ratio between the bolometric luminosity, L_{bol}, and L_{Edd}. Through this thesis, we use the formula given by Eracleous et al. (2010):

  $$R_{Edd} = \frac{L_{bol}}{L_{Edd}} = 7.7 \times 10^{-7} \frac{(L_{bol}[erg\ s^{-1}]/10^{40})}{(M_{BH}[M_{\odot}]/10^{8})} \tag{1.4}$$

  In the following, we describe different kinds of energy emission from the different accretion discs, which are classified according to their shape into thin, slim, and thick discs:

  1. Optically thick, geometrically thin accretion discs are usually assumed to be present in AGN (Shakura & Sunyaev 1973). The fundamental parameters governing their properties are R_{Edd}, M_{BH}, and the spin, which determine the geometry of the disc, the gas temperature, the overall luminosity and the spectrum (Netzer 2013). This kind of discs are considered cooling dominated flows, where the cooling is very efficient because there is a balance between losing angular momentum and increasing kinetic energy due to local viscosity. The most accepted theory is that it may be emitting mostly ultraviolet light (UV) because their temperatures are around 10^5 K for $M_{BH} = 10^8 M_{\odot}$.

  2. Comptonization plus a disc corona can be formed by the scattering of soft photons by electrons due to the temperature gradient across the disc and the temperature increase in the atmosphere (Reynolds & Nowak 2003). The most accepted model is known as the disc-corona system (e.g., Poutanen 1998).

  3. Irradiated discs can be formed by external radiation that illuminates the disc, maybe by reflection from a material located outside the disc, or to radiation from the disc material itself (Blaes 2007; Reynolds & Nowak 2003).

  4. Slim or thick accretion discs can be formed when the accretion rate exceeds a critical value of ~0.3 (Netzer 2013). This is though to be the case of NLSy1, where the inflow timescale is shorter than the time it takes for the radiation to diffuse to the surface of the disc (Collin & Kawaguchi 2004).

5. Radiatively inefficient accretion flows occur when the accretion rate is low (of the order of one percent of R_{Edd}), and the accretion disc has low density so the cooling time may exceed the inflow time of the gas. In this case the gravitational to radiative energy conversion is inefficient because most of the energy is advected into the SMBH. These flows are generally described as advection dominated accretion flows (ADAF, Narayan & Yi 1994), or more generally as radiative inefficient accretion flows (RIAF, Quataert 2004).

- The broad line region (BLR): This region consists of gas with large column densities ($\sim 10^{23}\ cm^{-2}$) and high densities ($\sim 10^{10}\ cm^{-3}$) located at about 0.01-1 pc from the nucleus. These clouds are completely dominated by gravity, and have typical velocities of the order of 3000 $km\ s^{-1}$. This region is responsible for the broad lines observed in type 1 AGN (Netzer 2013).

- The dusty torus: This is a region of size 1-10 pc that surrounds the BH, with low densities ($\sim 10^{3-6}\ cm^{-3}$) and extreme high column densities ($\sim 10^{25}\ cm^{-2}$) located at 1-10 pc from the nucleus (Netzer 2013). The structure of the torus is not yet clear, and three generic models are explored, including a homogeneous or smooth gas distribution models (Pier & Krolik 1992), clumpy torus models (Nenkova et al. 2008), or composite models including a combination of homogeneous and clumpy structure (Stalevski et al. 2012). This is the largest structure in AGN, thus different properties are derived at different scales. The inner part of the torus is exposed to the central radiation field, where strong high-ionization X-ray lines are produced, in particular iron $K\alpha$ lines. Due to the large column densities, this part reflects and scatters the incident X-ray continuum radiation. At larger radii, the gas is optically thick and only hard X-ray radiation can penetrate - and even those photons are limited to a few Compton depths (Awaki et al. 1991). This region has large amount of dust, whose signatures are observed at infrared wavelengths (e.g., Gonzalez-Martin et al. 2015).

- The narrow line region (NLR): This region consists on gas and dust with smaller column densities than the BLR ($\sim 10^{20-21}\ cm^{-2}$) and low densities ($\sim 10^{4}\ cm^{-3}$) located at about 100-1000 pc from the nucleus. Typical velocities of the clouds are about 500 $km\ s^{-1}$. Due to the low densities, the observed spectrum of the NLR includes intense forbidden lines. This region is responsible for the narrow lines in type 1 and 2 AGN (Netzer 2013).

- Relativistic jets: Some accretion discs produce jets of twin, highly collimated, and fast outflows that emerge in opposite directions from close to the disc. They are usually divided in FRI and FRII (Fanaroff & Riley 1974), with FRII showing higher radio luminosities. FRI are kpc-scale jets, which are believed to efficiently slow from highly-relativistic to sub-relativistic flow on kpc-scales from entrainment of the external interstellar medium, while

FRII jets are low-efficiency radiators but efficient conveyors of energy to large distances of hundreds of kpc in length (Worrall 2009). They can radiate in all wavebands from the radio through to the gamma-ray range via the synchrotron and the inverse-Compton scattering processes. The jet production mechanism and indeed the jet composition on very small scales are not yet fully understood.

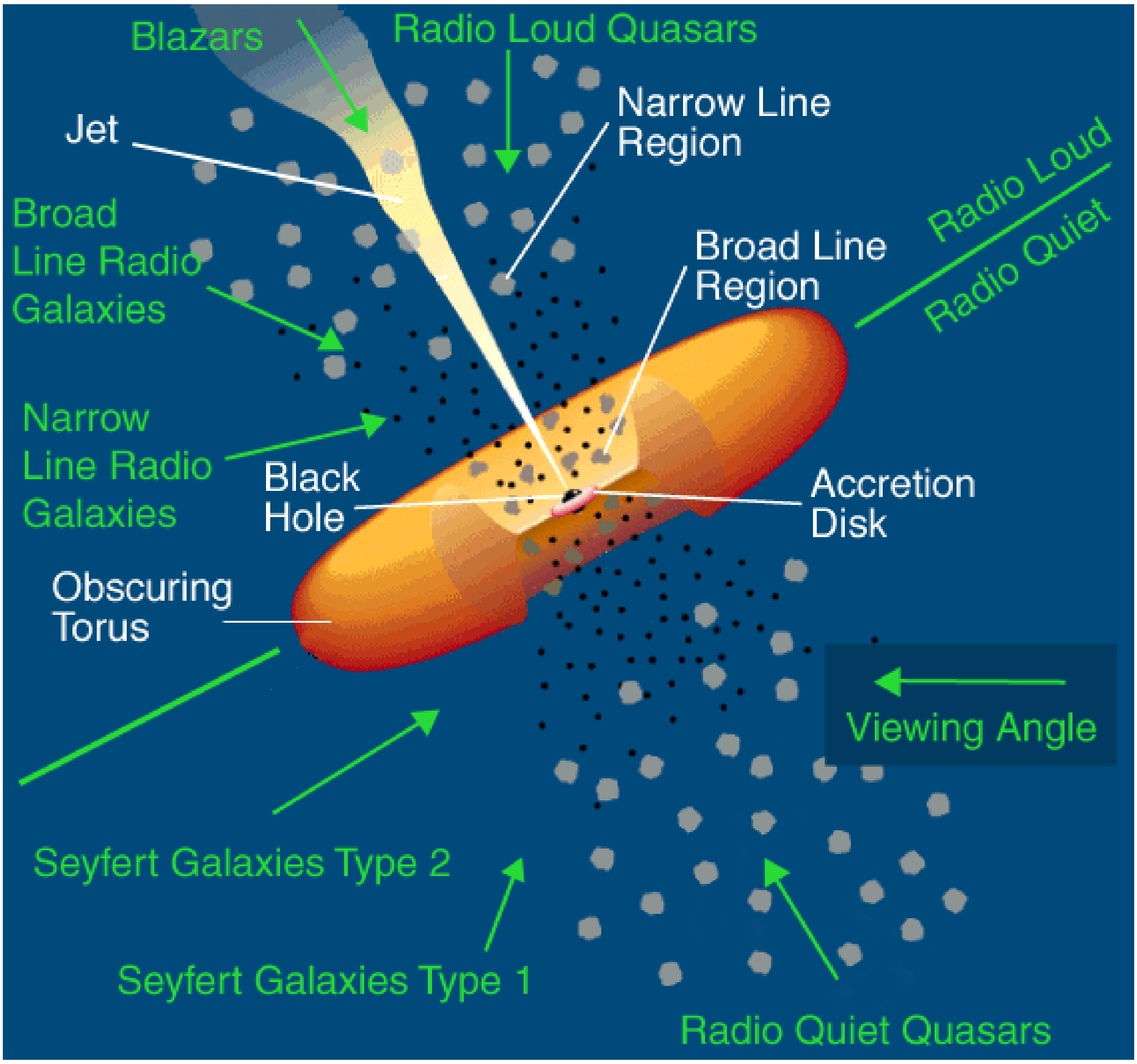

Figure 1.3: Unified Model of AGN - Taken from (Urry & Padovani 1995).

1.4 Unified Model of AGN

As different kinds of AGN have been discovered, the scientific community has been trying to explain every type of AGN within the same scenario. As stated above, it is widely accepted that every AGN are powered by accretion onto a SMBH, and therefore the structure of their nuclei should be similar in all cases. All the components explained in Sect. 1.3 appear in the most accepted theory that explains AGN, the so called *Unified Model* (UM) of AGN (Antonucci 1993; Urry & Padovani 1995). This scheme is interpreted by two parameters: the line of sight and the inclination. Within this scenario, the differences among different subclasses of AGN are only due to orientation effects. A representation of this scheme is illustrated in Fig. 1.3. If seen face on, all the components can be observed, giving place to a type 1 object. If seen edge on, the dusty torus completely obscures the UV and optical light from the accretion disc, the broad line region, and to some extent X-rays, so a type 2 is observed. Orientations in between give place to intermediate classes (i.e., types 1.2, 1.5, 1.8, and 1.9). At optical wavelengths, if face on object, and very luminous (i.e., outshines the host galaxy) it would be a QSO; if not very luminous (i.e., the nuclear luminosity is comparable to that of the host galaxy), it would be a Seyfert 1. If edge on and not very luminous, we will observe a Seyfert 2. Blazars are face on along a line of sight perpendicular to the torus.

Observational evidence supporting the UM came from spectropolarimetric data, where objects classified as Seyfert 2s showed broad polarized Balmer lines, indicating a hidden BLR (HBLR, Miller & Goodrich 1990; Tran et al. 1992). Evidence at other wavelengths are also in agreement with the UM. At X-rays, in general, Seyfert 1s have column densities $N_H < 10^{22} cm^{-2}$ (i.e., unobscured view of the SMBH), while it is higher in type 2s (i.e., obscured view of the SMBH) (e.g., Maiolino et al. 1998; Risaliti et al. 2002; Guainazzi et al. 2005), indicating that the column density is related with the obscuring material along our line of sight.

1.4.1 Problems with the UM

However, some type 2s do not show a hidden broad line region in polarized light (e.g., Tran et al. 1992). Are they truly Seyfert 2s according to the unified model? Or are they Seyfert 2s irrespective of the viewing angle, what would be against the UM? Furthermore, some subclasses of objects were not taken into account in this simple version of the UM and in fact are not well accommodated under this scheme, such as NLSy1s or LINERs. For this reason, and based on recent observations of large AGN samples that provide detailed information, several efforts have been made to modify the UM. The modifications in which the scientific community are involved right now mainly concern the nature of the torus, the dependence on the luminosity, and BH and galaxy evolution (Netzer 2015).

The first version of the UM included a homogeneous (also called smooth) torus (e.g., Pier & Krolik 1992). Nonetheless, observations did not match the models, so new models including a clumpy torus (e.g., Nenkova et al. 2008) or a two-phased medium including smooth and clumpy material (Stalevski et al. 2012) are believed to better represent the structure of the principal absorber in AGN.

As is the case of LINERs, low luminosity AGN are thought to have a different accretion mechanism compared to more powerful AGN, that could be advection dominated (e.g., Gu & Cao 2009a). In this case the accretion can be inefficient for objects accreting below a certain (unknown) percentage of L_{Edd}, the disc may be truncated and the luminosity of the AGN decreases. Moreover, it has been suggested that the torus and even the BLR may disappear at low luminosities (Elitzur & Shlosman 2006; Elitzur & Ho 2009).

Finally, new instrumentation is making possible the observations of AGN at high redshifts. Studies at z $\sim$ 2 suggest that secular processes can be predominant drivers of BH growth (Schawinski et al. 2012). This may indicate that evolutionary processes should be taken into account in the new version of the UM.

1.5 X-rays

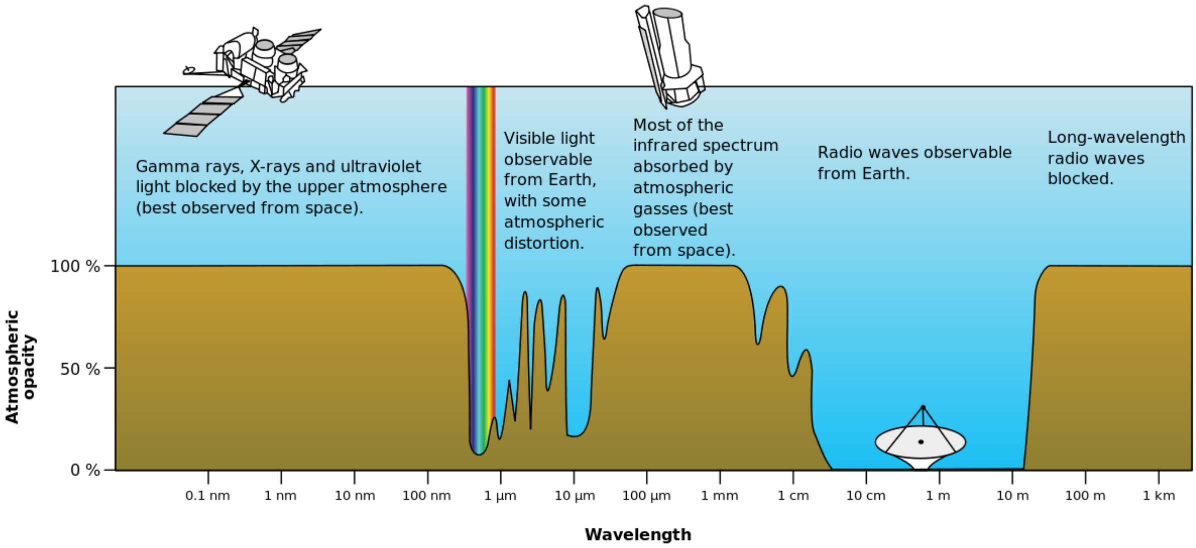

Figure 1.4: Atmospheric electromagnetic opacity - Taken from NASA (http://commons.wikimedia.org/wiki/File:Atmospheric_electromagnetic_opacity.svg).

The discovery of X-ray radiation was made by Wilhelm Röntgen in 1895, who found this new type of radiation, quite by accident, while he was experimenting with vacuum tubes. It was when he took an X-ray photograph of the hand of her wife that it clearly revealed her wedding ring and her bones. He named this new form of radiation X, as something unknown. The highly penetrating property of X-rays started to be of important application in medical and other sciences, and Röntgen was awarded the first ever Nobel Prize for Physics in 1901. Another

Nobel Prize was given to Riccardo Giacconi, also known as “the father of X-ray astronomy”, in 2002 “for his pioneering contributions to astrophysics, which have led to the discovery of cosmic X–ray sources”.

The atmosphere was a problem for astronomers, since it absorbs potentially damaging radiation before it reaches us, including of course X-rays. The atmospheric electromagnetic opacity is presented in Fig. 1.4, where it can be appreciated the impossibility of detecting X-rays from ground-based instruments. An X-ray detector must be located at least 100 km above the ground to detect X-rays coming from space, so the use of rockets or satellites was necessary.

The first rocket was launched in 1948 by the US Naval Research Laboratory, and allowed the first view of the Sun in X-rays. The X-ray astronomy was born.

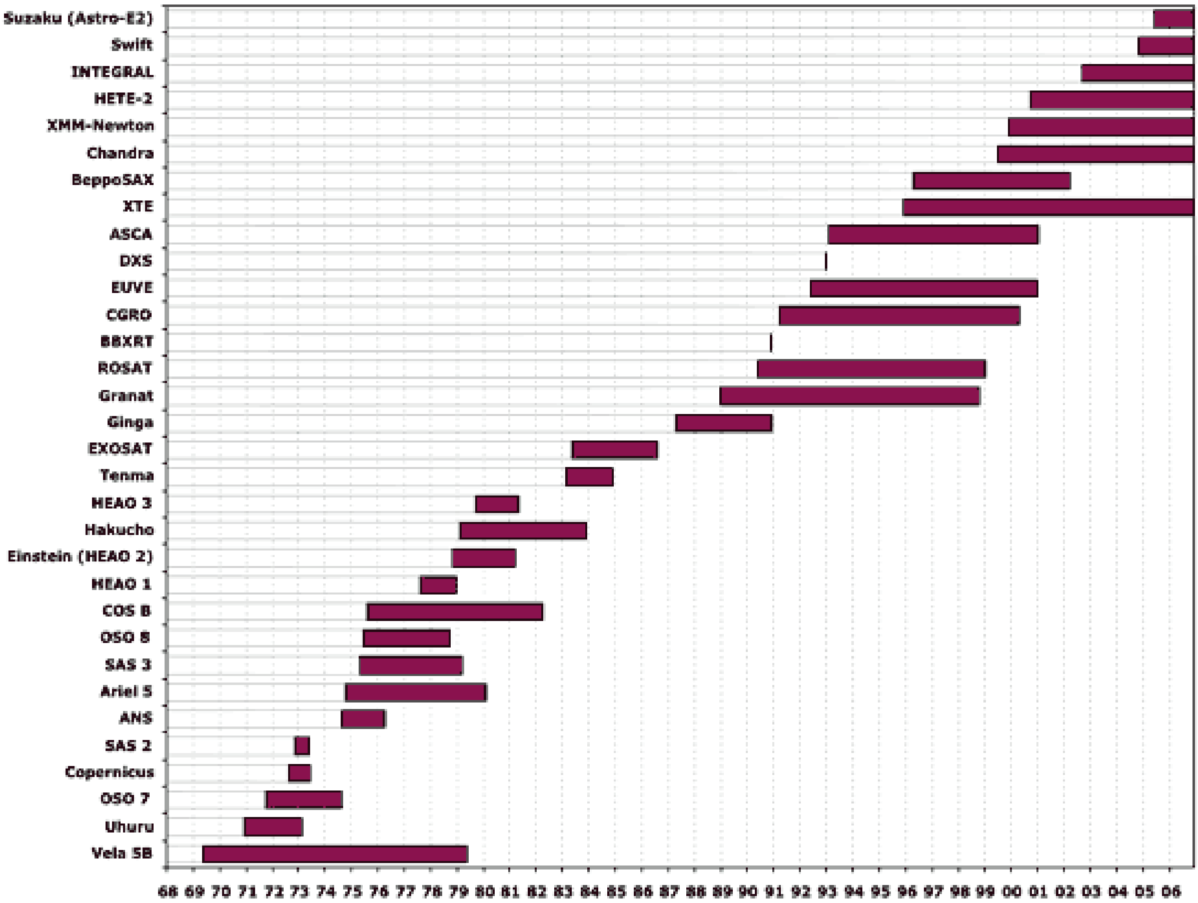

Figure 1.5: X-ray missions from 1968 to 2007 - Taken from HEASARC (https://heasarc.gsfc.nasa.gov/docs/heasarc/missions/time.html).

The first rocket that successfully detected a cosmic X-ray source was launched in 1962 by a group at the American Science and Engineering, who detected a very bright source in the Scorpius constellation (Giacconi et al. 1962). Major advances in the field came with the launch of the *UHURU* satellite (Giacconi et al. 1971) in 1970. While its mission was to provide the first

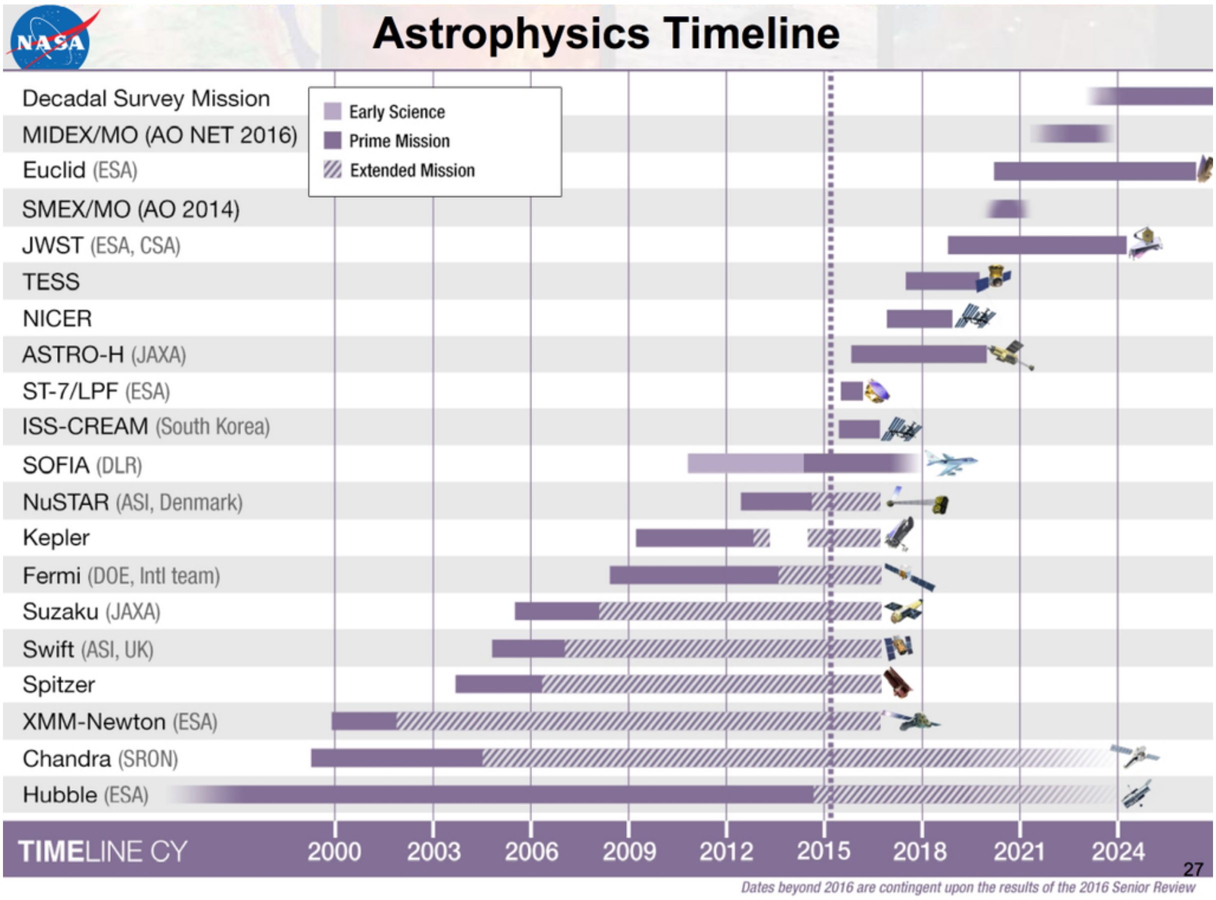

Figure 1.6: X-ray missions which are actually in use and future missions - Taken from NASA (http://science.nasa.gov/).

all-sky survey in the 2–20 keV energy range, it identified 339 objects by the end of the mission in 1973. After *UHURU*, other X-ray missions were launched, which are summarised in Fig. 1.5. In the following, I will review some of the X-ray mission which contributed to X-ray astronomy. *Copernicus* (Sanford 1974) was launched in 1972, and between its findings is the discovery of pulsars as X-ray sources. The late 70s saw a number of X-ray satellites launched monitoring the whole sky and covering the 0.1-55 keV energy range. Among them, the *High Energy Astrophysics Observatory (HEAO,* Peterson 1975) missions, and in particular *HEAO-2* (better known as the *Einstein observatory,* Giacconi et al. 1979), revolutionized the X-ray astronomy thanks to its capability to create images of extended objects and diffuse emission and to detect faint sources. Among its achievements is the discovery of ultraluminous X-ray sources (ULXs).

The next major mission launched was the *Röntgen satellite (ROSAT,* Truemper 1982) in 1990. The first six months of the mission were dedicated to an all-sky survey in X-rays (0.1–2.5 keV) and ultraviolet (62–206 eV) using an imaging telescope, resulting in a catalog containing more than 150000 sources. The first satellite to use charge-coupled device (CCD) detectors, the *Advance Satellite for Cosmology and Astrophysics (ASCA*, Tanaka et al. 1994), was launched in 1993, which was also the first X-ray mission to combine imaging capability with broad pass band, good spectral resolution, and a large effective area. The *Rossi X-ray Timing Explorer (RXTE*, Bradt et al. 1990) was launched in December 1995. It was designed to study variability in the energy output of X-ray sources with moderate spectral resolution. *BeppoSAX* (Scarsi 1997) was launched soon after in 1996, covering the largest energy range up to now, from 0.1 to 300 keV.

X-ray missions operating today are responsible of a better understanding of the X-ray Universe, such as *Chandra* (Weisskopf et al. 2003), *XMM*–Newton (Jansen et al. 2001), *Swift* (Burrows et al. 2005), *Suzaku* (Mitsuda et al. 2007), or *NuSTAR* (Harrison et al. 2013). Fig. 1.6 shows these and future missions (note that not only X-ray instruments are included). Moreover, the next generation of X-ray observatories proposed for a large mission includes the *Advanced Telescope for High ENergy Astrophysics (ATHENA+*, Barcons et al. 2012), which is expected to be launched in 2028 to give answer to e.g. how SMBH do grow and shape the Universe.

The primary data set available from X-ray astronomy are called *event files*, which consists on a 4-dimensional array including the position, time and energy (x, y, time, energy) of each photon. After removing “bad” data such as the background, cosmic rays or poor quality data, we are able to make a spatial analysis (i.e., an image), a spectral analysis (i.e., a spectrum), or temporal analysis (i.e., light curves) using tasks, scripts and libraries, specifically designed to reduce and analyze data collected by the satellites.

The development of this thesis has been carried out using data from the two major observatories that constitute the current generation of X-ray satellites, and will be described in more

Table 1.1: Comparison between *Chandra* and *XMM*–Newton instruments.

Satellite	Instrument	Energy	Spatial		Spectral resol.	Effective area
		band	FOV	Resol.	at 1 keV	at 1 keV
		(keV)		(FWHM)	(eV)	(cm^2)
Chandra	ACIS-I	0.2–10	16’×16’	1-2”	55/125[a]	410/800[a]
	ACIS-S	0.5–10	8’×48’	1-2”	55/125[a]	410/800[a]
XMM–Newton	MOS	0.2–12	30’	6”	57	850
	pn	0.1–12	30’	6”	67	1227

[a] These numbers refer to the front illuminated (FI)/back illuminated (BI) CCDs (see text).

detail in the following. *Chandra* and *XMM*–Newton were launched within five months of each other in 1999 – they are still in orbit – and are providing astronomers with unprecedented spacial and spectral resolution. A comparison between the characteristics of the instruments located in those satellites and used in this work (see below) is presented in Table 1.1.

1.5.1 *Chandra*

After being launched by the Space Shuttle Columbia in July 1999, *Chandra* was boosted into a high elliptical orbit from which it can make long duration, uninterrupted measurements of X-ray sources in the Universe. It uses the most sensitive X-ray telescope ever built, consisting of four pairs of nearly cylindrical mirrors with diameters of 0.68–1.4 m, to observe X-rays in the 0.1–10 keV energy range. These mirrors focus X-rays onto two of Chandra’s four science instruments: the High Resolution Camera (HRC, Murray & HRC Team 1999) and the Advanced Charged Couple Imaging Spectrometer (ACIS, Garmire et al. 2003). These focal plane science instruments, ACIS and HRC, are well matched to capture the sharp images formed by the mirrors and to provide information about the incoming X-rays, i.e., their number, position, energy and time of arrival. Two additional science instruments provide detailed information about the X-ray energy, the LETG (Drake 2002) and HETG (Dewey 2003) spectrometers. These are grating arrays which can be flipped into the path of the X-rays just behind the mirrors, where they redirect the X-rays according to their energy. The X-ray position is measured by HRC or ACIS, so that the exact energy can be determined. Fig. 1.7 shows an illustration of the satellite with its main devices.

All the data used in this work were retrieved from ACIS, which is composed by ten CCD chips divided in two arrays (ACIS-S and ACIS-I, see Fig. 1.8). Two CCDs are back-illuminated (BI) and eight are front-illuminated (FI). It provides imaging with a pixel size of 0.5 arcsec and spectroscopy over the 0.2–10 keV energy range, i.e., this instrument is especially useful because

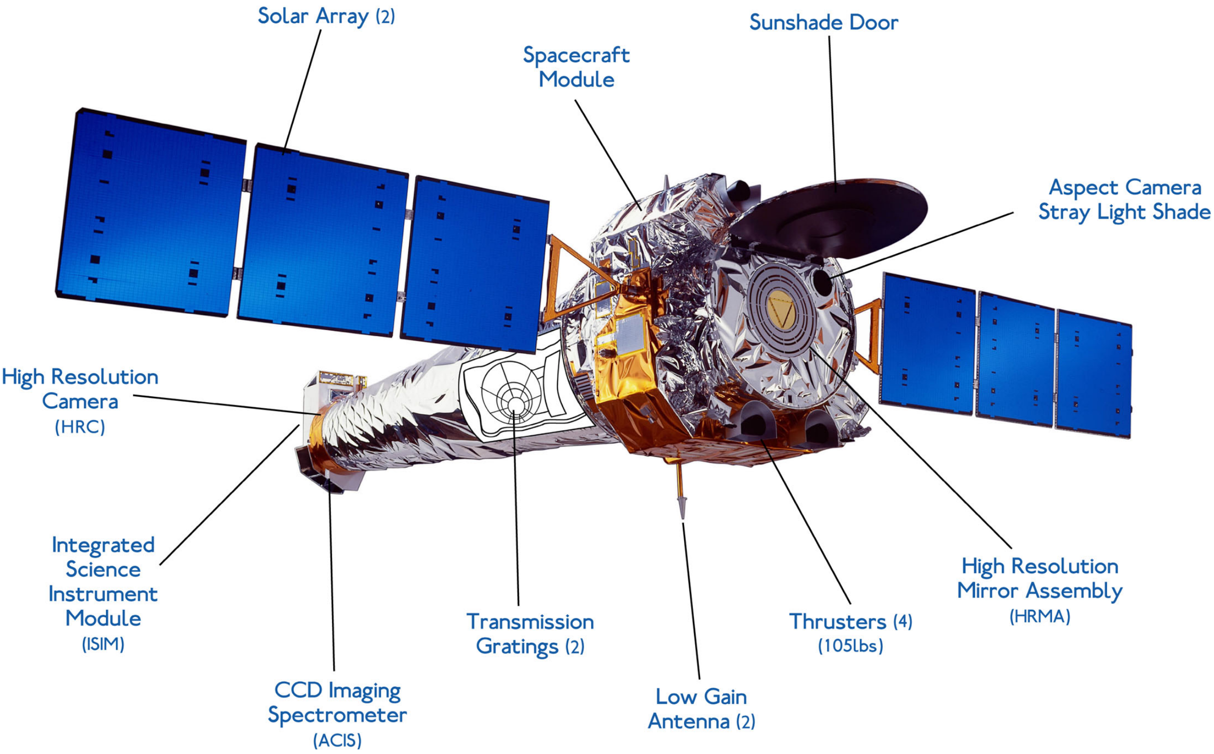

Figure 1.7: *Chandra* X-ray observatory with its main devices - Taken from Chandra (http://chandra.harvard.edu/about/spacecraft.html).

it can make X-ray images, and at the same time, measure the energy of each incoming X-ray. Indeed, the best of *Chandra* is that it has a superb spatial resolution of about 1–2 arcsec; for this reason we used data from this instrument.

1.5.2 *XMM*–Newton

This orbiting X-ray observatory was launched in December 1999 by the European Space Agency (ESA). *XMM*–Newton has three advanced X-ray telescopes, each containing 58 high-precision concentric mirrors which offer the largest possible collecting area. In addition, it carries five X-ray imaging cameras and spectrographs, including two Reflection Grating Spectrometer (RGS, den Herder et al. 2001) readout cameras, the European Photon Imaging Camera (EPIC) which includes the EPIC-pn (Turner et al. 2001) and two EPIC-MOS (Strüder et al. 2001) imaging detectors, and the data handling and power distribution units for the cameras, and an optical monitoring (OM, Mason et al. 2001) telescope. The observatory moves in a highly elliptical orbit, traveling out to nearly one third of the distance to the Moon and enabling long, uninterrupted observations of faint X-ray sources. Fig. 1.9 shows an illustration of the *XMM*–Newton satellite with its main devices.

The data used in this work were obtained from the European Photon Imaging Camera (EPIC)

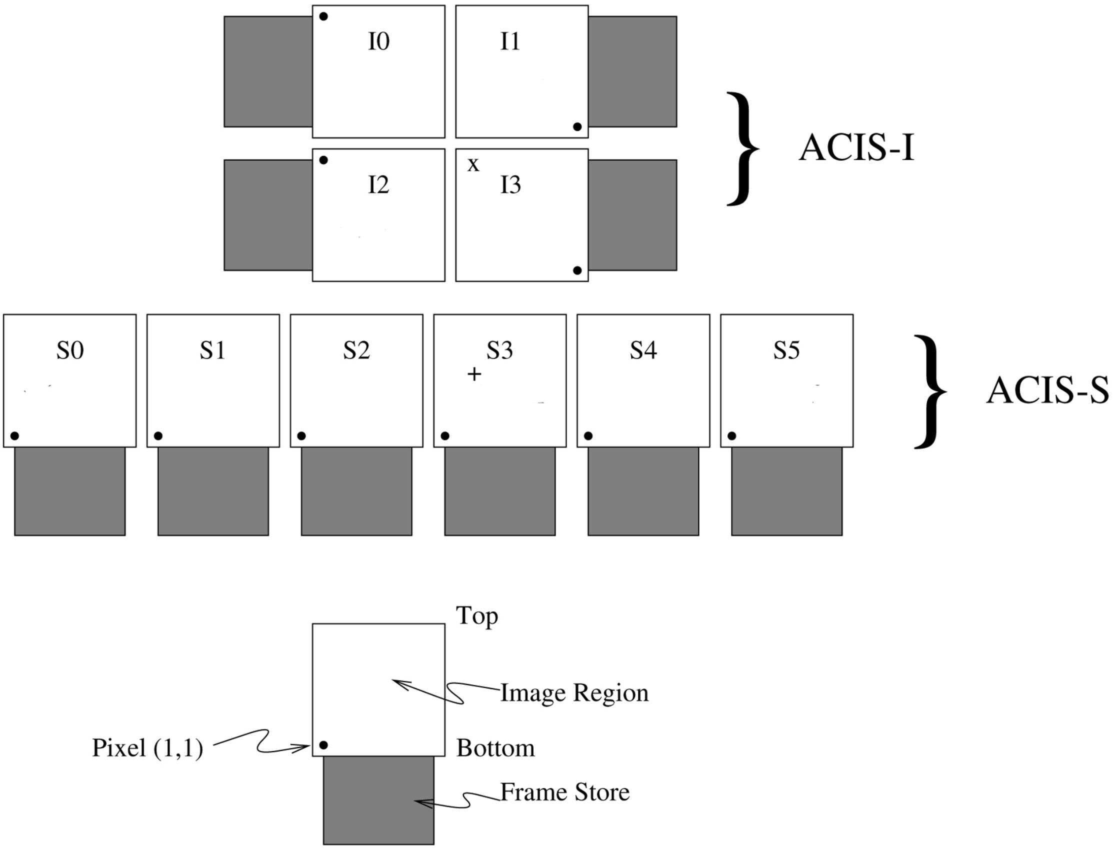

Figure 1.8: ACIS instrument on board *Chandra*, including ACIS-S and ACIS-I - Taken from Chandra (http://chandra.harvard.edu/resources/illustrations).

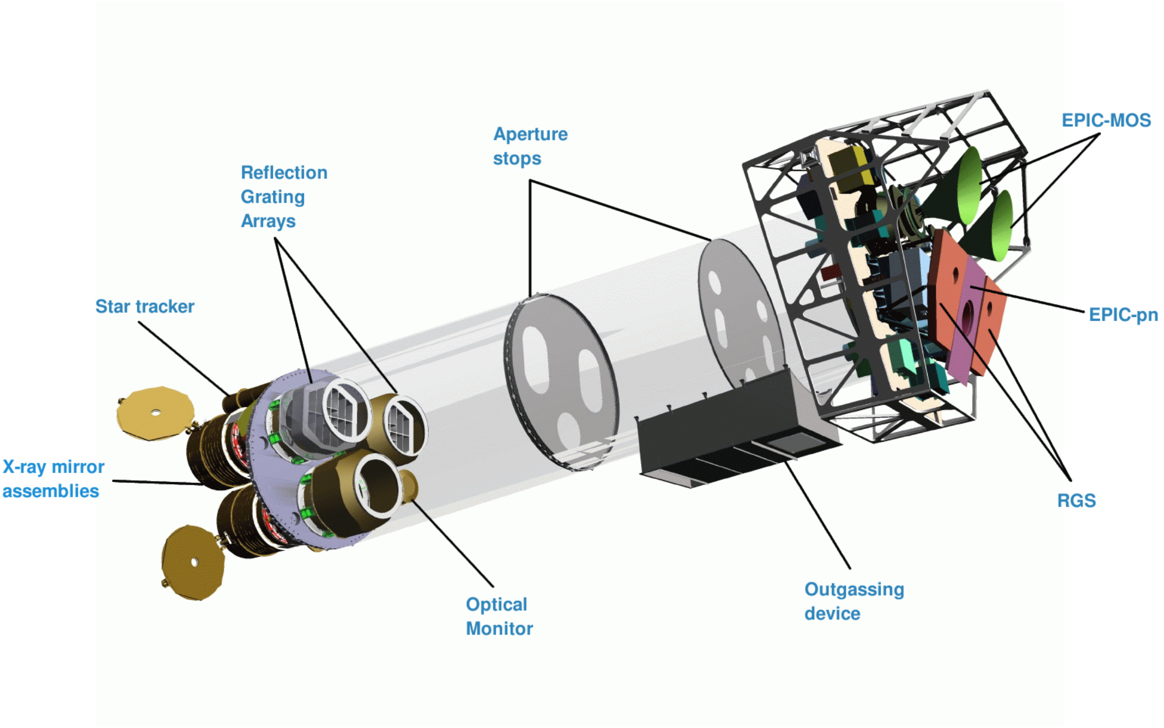

Figure 1.9: *XMM*–Newton satellite with its main devices - Taken from *XMM*-Newton Science Operations Centre (http://xmm.esac.esa.int).

detector, composed by a set of three X-ray CCD cameras. Two of the cameras are Metal Oxide Semi-conductor (MOS) CCD arrays, and the third X-ray telescope has an unobstructed beam and uses pn CCDs, thus is referred to as the pn camera. The two types of EPIC differ in some major aspects, such as their geometries or the readout times. Fig. 1.10 shows the geometry of each camera. There are seven CCDs in the focal plane of each MOS camera, with the central CCD at the focal point on the optical axis of the telescope while the outer six are stepped towards the mirror by 4.5 mm to follow approximately the focal plane curvature, and improve the focus for off-axis sources. The pn camera is composed by twelve 3 × 1 cm CCDs on a single wafer, having an imaging area of 6 × 6 cm and a pixel size of 150 × 150 microns (4.1 arcsec) with a position resolution of 120 microns, resulting in an equivalent angular resolving capability for a single photon of 3.3 arcsec. The best property of *XMM*–Newton is its high sensibility, with a good angular resolution (6 arc second FWHM); we used this instrument for this reason.

1.5.3 X-ray spectra of AGN

It is widely accepted that the accretion disc surrounding a SMBH produces an UV thermal spectrum, whereas the lower energy photons are up-scattered to higher energies by relativistic electrons in a hot corona above the accretion disc throughout inverse *Compton* scattering, producing the X-rays (Haardt & Maraschi 1993). The intrinsic spectrum has a power law shape

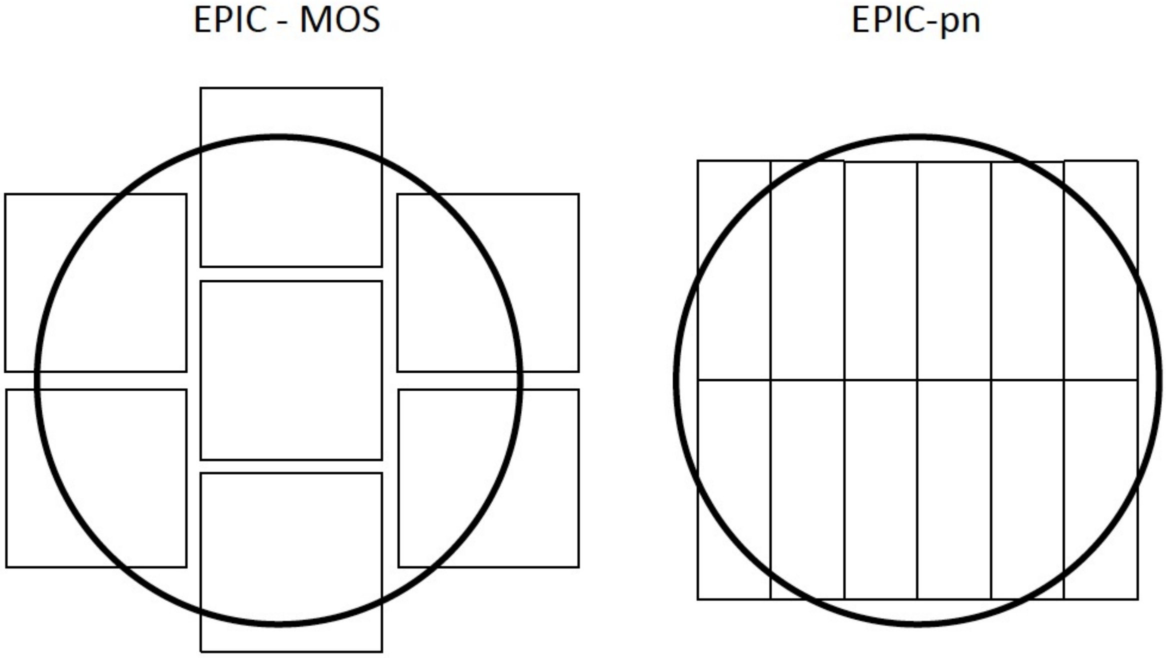

Figure 1.10: EPIC detector on board *XMM*–Newton satellite - The EPIC-MOS cameras are composed by seven CCDs each of 10.9 × 10.9 arcmin; the EPIC-pn camera is composed by 12 CCDs each of 13.6 × 4.4 arcmin. The circle diameter corresponds to 30 arcmin – Image courtesy of Dr. Toalá.

with a photon index $\Gamma \sim 2$ (e.g., Nandra & Pounds 1994; Nandra et al. 1997; Risaliti 2002; Cappi et al. 2006). Since there is a limit in the energy of the relativistic electrons, the resulting inverse *Compton* scattering will have a high-energy cut-off (Guainazzi et al. 1999; Perola et al. 2000; Nicastro et al. 2000). The origin of this component could be a two phase accretion disc, a cool thick accretion disc with kT < 50 eV, and a hot thin corona with kT $\sim$ 100 keV (Pozdnyakov et al. 1983; Mushotzky et al. 1993).

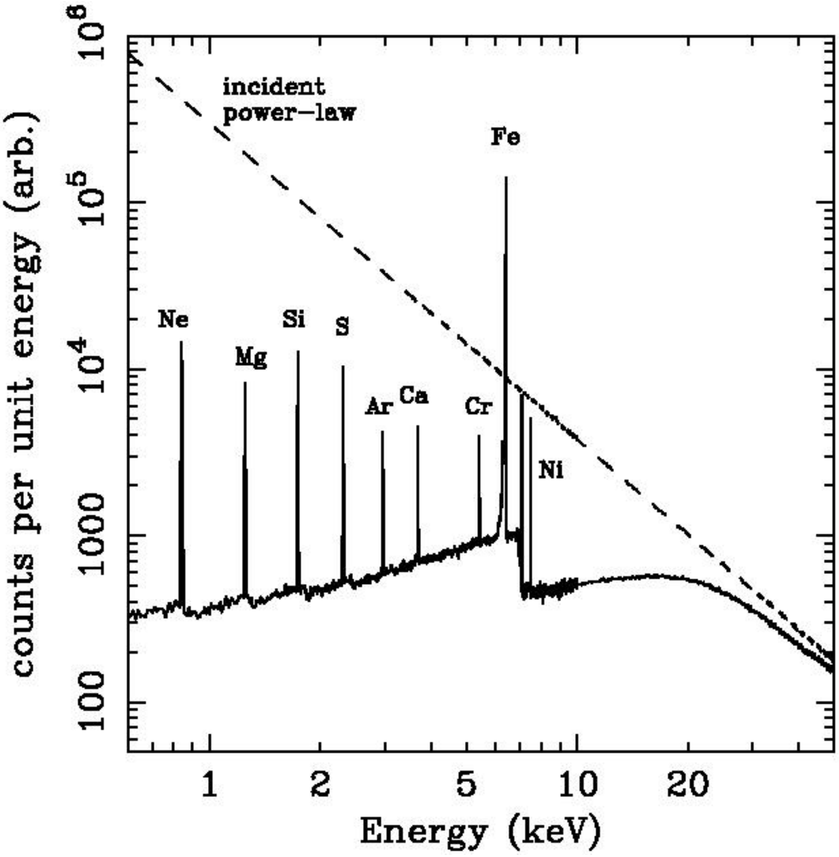

Figure 1.11: X-ray reflection spectrum from an illuminated slab - Dashed line shows the incident continuum (i.e., power law) and solid line shows the reflected spectrum (integrated over all angles). Monte Carlo simulation from Reynolds (1996).

Within this model, the hard X-ray (power-law) continuum illuminates a semi-infinite slab of cold gas, i.e., metal atoms are essentially neutral, but H and He are mostly ionised (e.g., Reynolds 1996). When a hard X-ray photon enters the slab, different possible interactions can take place: 1) *Compton* scattering by free or bound electrons, 2) photoelectric absorption followed by a fluorescent line emission, or 3) photoelectric absorption followed by de-excitation (Bearden 1967; Krolik & Kallman 1987; Matt et al. 1991; George & Fabian 1991). Due to the energy dependence of photoelectric absorption, incident soft X-rays are mostly absorbed, whereas hard photons are rarely absorbed and tend to *Compton* scatter back out of the slab,

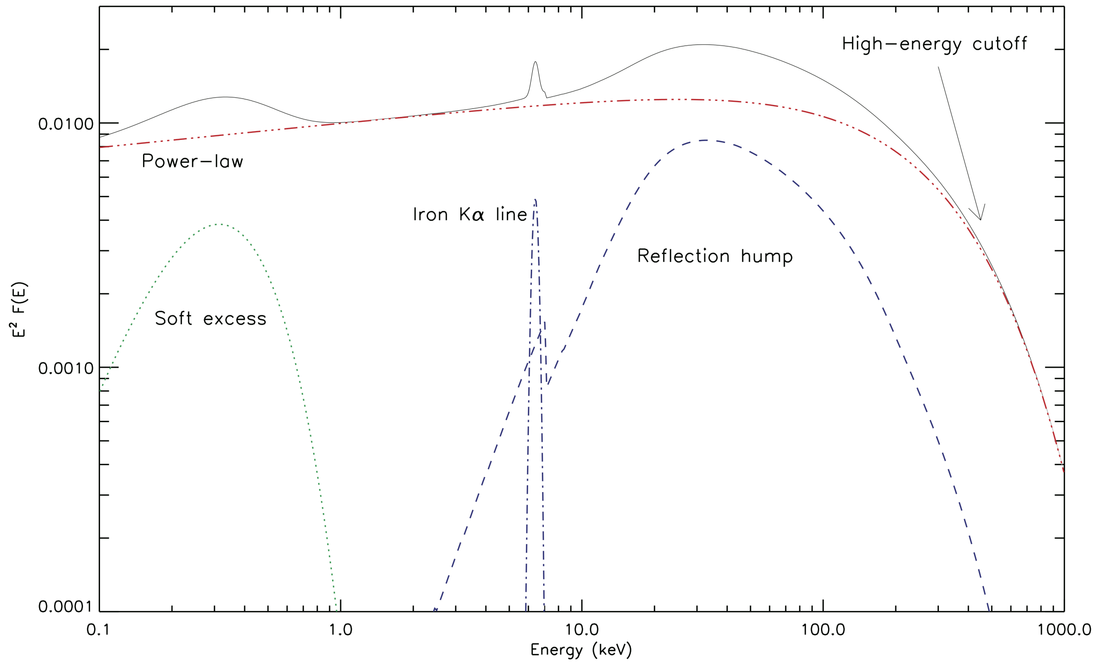

Figure 1.12: Schematic representation of the X-ray spectrum of unabsorbed AGN - The components are explained in the text – Taken from Ricci et al. (2011), PhD thesis.

i.e., they are reflected. This cold reflection gives the spectrum a broad hump-like shape, peaking at around 20–30 keV, where the reflection efficiency reaches its maximum (e.g., Piro et al. 1990). The measurement of the reflector is a difficult task because it depends on the intrinsic absorption (observed at soft energies), the spectral slope of the power-law, and the cut-off (Ueda et al. 2007; Comastri et al. 2010; Eguchi et al. 2009; Ricci et al. 2011). In addition, the spectrum shows emission lines resulting primarily from fluorescent Kα lines of the most abundant metals; the iron Kα line at 6.4 keV is the strongest of these lines (see Fig. 1.11). The line at 6.4 keV is thought to be produced when the nuclear continuum radiation is reprocessed by circumnuclear material. However, the origin of this circumnuclear material is still under debate, which may be related to the accretion disc (Tanaka et al. 1995; Miniutti et al. 2004; Miniutti & Fabian 2006), or could be distant, cold matter such as the torus (Matt et al. 1991).

Another feature observed in the X-ray spectra of AGN are the warm absorbers, i.e., highly ionised absorbers. These are usually observed in type 1 objects, with column densities up to $N_H \sim 10^{23} cm^{-2}$, and often consisting on several zones of ionized gas (e.g., Nandra et al. 1993, and references therein).

Moreover, many AGN show a ‘soft X-ray excess’ at energies below $\sim$ 2 keV, whose origin is still under debate. Three models have been proposed to explain it: 1) an additional Comptonization component (Dewangan et al. 2007), 2) ionised reflection (Crummy et al. 2006), or

3) complex or ionised absorption (Done et al. 2007). At soft energies a thermal emission can also be observed, with kT ranging from 0.1 to a few keV (Risaliti 2002; Guainazzi et al. 2005; González-Martín et al. 2009).

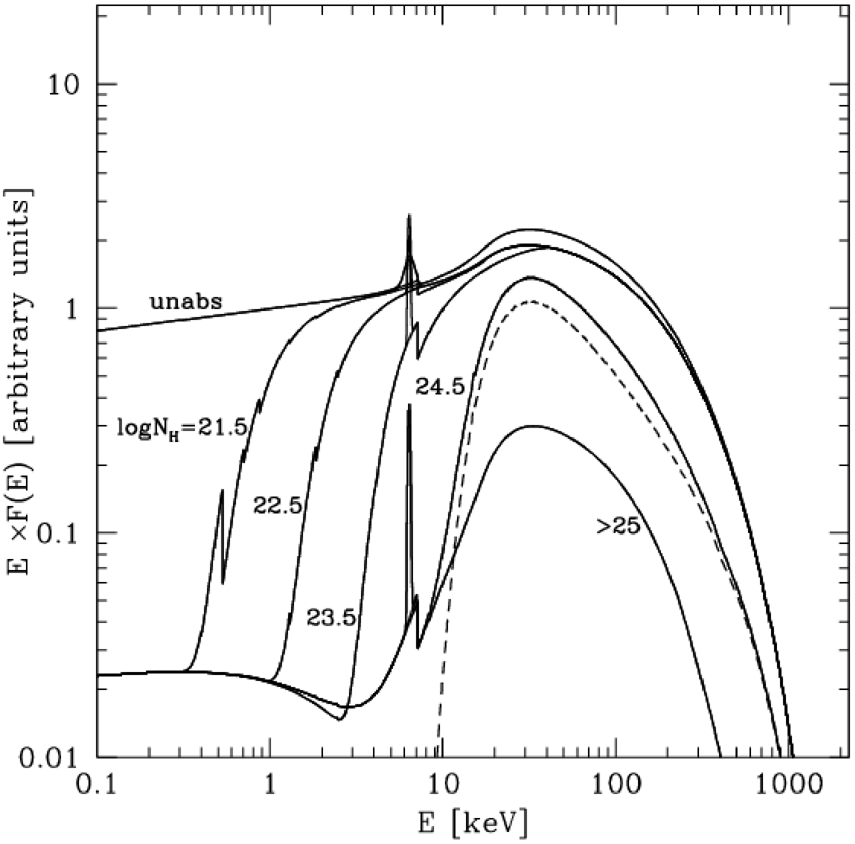

Figure 1.13: Effect of X-ray absorption in the spectra of AGN - Taken from Gilli et al. (2007).

The components explained above can be observed in Fig. 1.12, where a schematic representation of unabsorbed AGN is described as a solid line, and its components are shown.

At X-ray energies around 10 keV, absorption by material associated to the interstellar medium become noticeable. Due to this material, the primary continuum of the AGN is suppressed by photoelectric absorption, which is energy-dependent and starts being effective at column densities $N_H \sim 10^{21} cm^{-2}$. Fig. 1.13 shows the effect when there is no absorption ($N_H < 10^{18} cm^{-2}$), and when absorption becomes important (up to $N_H \sim 10^{21.5} cm^{-2}$). When the absorbing column density reaches $N_H = 1.5 \times 10^{24}$, the source is dominated by *Compton* scattering and the continuum is completely suppressed below 10 keV. The sources with such a high absorption are known as *Compton*-thick objects (Maiolino et al. 1998).

Although the components explained above are observable in AGN, in some cases not all the components are required to fit their X-ray spectra. For example, Guainazzi et al. (2005) defined two “baseline” models for *Compton*-thin (thermal emission, unabsorbed power law, absorbed power law, and Gaussian lines) and *Compton*-thick (thermal emission, power law, Compton reflection, and Gaussian lines) objects[1]. They concluded that all the components defined in the models were not required to fit their data, consisting on 25 Seyfert 2s. The best example can be seen in LINER nuclei, which have the lowest luminosities and therefore the lowest count rates. The most extensive work to characterize the spectra of LINERs was carried out by González-Martín et al. (2006, 2009), who studied samples of 51 and 82 LINERs, respectively. They defined five different models consisting on a power law, a thermal component, and/or combinations of these components; the most complex one being the “baseline” model for *Compton*-thin sources defined by Guainazzi et al. (2005). Their results showed that the spectra of most LINERs were well fitted with the “baseline” model, where 70% of the sample needed two power laws and 95% of the sample needed a thermal component at energies below 2 keV, with a mean value of kT $\sim$ 0.6 keV. Therefore, 30% of the sources in their sample were fitted with simpler models. It is interesting to introduce the way in which Brightman & Nandra (2011) fitted the spectra of different types of AGN. They started the spectral fitting only in the 2.5–10 keV energy band using a single power-law representing the underlying continuum, and then added as many components as required to each spectrum in the total 0.5-10 keV energy band, for instance representing absorptions, warm absorbers, thermal plasmas, and/or reflection.

1.6 Variability

It is well established that variability is a common characteristic of AGN (Peterson 1997). Indeed, this property was discovered before the first quasars appeared (D’Onofrio et al. 2012). Seven years before the discovery of M. Schmidt, the Russian astronomer A. Deutsch noted that the source 3C 48 showed optical variability while he was working at the Pulkovo observatory. By that time, Deutsch did not believe his own result. It was two years later that he commented the result at the IAU symposium in 1958.

Soon after the discovery of quasars by Schmidt (1963), Sharov & Efremov (1963) submitted the first paper on AGN optical variability of 3C 273, which varied by a magnitude of 0.7 over the period between 1896–1960. Therefore, variability was one of the first recognized properties of QSO (Smith & Hoffleit 1963; Matthews & Sandage 1963). After that, variability became of great interest and several scientists started to report their results (e.g., Burbidge & Burbidge 1965; Goldsmith & Kinman 1965; Ozernoi & Chertoprud 1966; Angione 1968; Kinman et al. 1968). Moreover, as the variations were found to exhibit timescales as short as days, it implied that the size of the emitting region must be of the order of light-days. Because the timescale

---

[1] Refer to Chapters 2 and 3 for details on the spectral models.

of the variability gives information about the rate at which the region varies, it provides an upper limit to the ratio between the size of the region and the velocity at which the changes propagate. This statement was in fact critical in the argument that AGN are powered by SMBH (see Peterson 1997, for details).

Variability in Seyfert galaxies was reported a few years later by Fitch et al. (1967) - although for example de Vaucouleurs et al. (1964) noted that the magnitudes of NGC 3516, NGC 4051, or NGC 4151 varied considerably, exceeding the photometric errors - but it was not as dramatic as in the case of QSOs. The reason is that the first reports on variability were those of blazars, which are remarkably different from other AGN because they are jet dominated (synchrotron emission). Furthermore, blazars are the only sources detected at TeV energies, where they can vary as much as a factor of 10 within one day.

During the next decades several monitoring programs at optical and UV wavelengths were carried out with the participation of worldwide astronomers. NGC 4151 (Antonucci & Cohen 1983) and Akn 120 (Peterson et al. 1985) were two of those monitored sources whose variability was studied.

It was in the 70s when X-ray variability was discovered from observations from the *OSO-7*, *UHURU*, and *Copernicus* satellites (Davison et al. 1975; Winkler & White 1975). The light curves of AGN fluctuate over wide range of timescales, ranging from hours to years. The variations appear to be aperiodic (Netzer 2013). The most dramatic cases of variability are observed in NLSy1s, that vary more rapidly and with larger amplitudes than other AGN (except blazars). For example, IRAS 13224-3809 was monitored by *ROSAT* during 30 days, and showed a factor of two variation in about 20 minutes, and five giant-amplitude ‘flares’, the largest with an amplitude about a factor of 60 (Boller et al. 1997).

Variability studies of Seyfert galaxies revealed that almost all type 1s are variable while there is a lower number of variable type 2s, and that variations at soft energies in type 1s are greater than those observed at hard X-rays (Nandra et al. 1997; Turner et al. 1997). The physical origin of the variations is still unknown, although it has been suggested that accretion-disc instabilities or variations in the accretion rate may be involved (Uttley et al. 2005; Breedt et al. 2010; McHardy 2010; Soldi et al. 2014). On the other hand, it has been proven that X-ray variations are in some cases related to clouds intersecting the line of sight of the observer, producing eclipses, and thus giving information about these clouds (e.g., Risaliti et al. 2002, 2007, 2011; Puccetti et al. 2007; Sanfrutos et al. 2013).

On the contrary to what is expected for AGN, LINERs were supposed to be non-variable objects (e.g., Ptak et al. 1998). In fact, the first clear evidence of variability in LINERs was reported in 2005 at UV frequencies by Maoz et al. (2005). It was a few years later that X-ray variability studies of LINERs were carried out (Pian et al. 2010; Younes et al. 2011; González-Martín et al. 2011), showing that they also share this property with other AGN.

Aside from the study of changes in the spectral shape or in the light curves of AGN, a useful way to characterize variability is in terms of the power spectral density (PSD), the product of the Fourier transform of the light curve and its complex conjugate, that describes the contribution of variability structures with a given frequency to the total light curve variance. EXOSAT data showed that X-ray variability is scale-invariant 'red noise'[1] (Lawrence et al. 1987). In AGN, the PSD is parametrized as a power law, $P(f) = f^{-\alpha}$, with $1 < \alpha < 2$ (McHardy 1988). The total power in the variations is given by integrating the PSD over all frequencies. It was noted that this PSD was very similar to those of galactic black hole X-ray binaries, although on a much longer timescale.

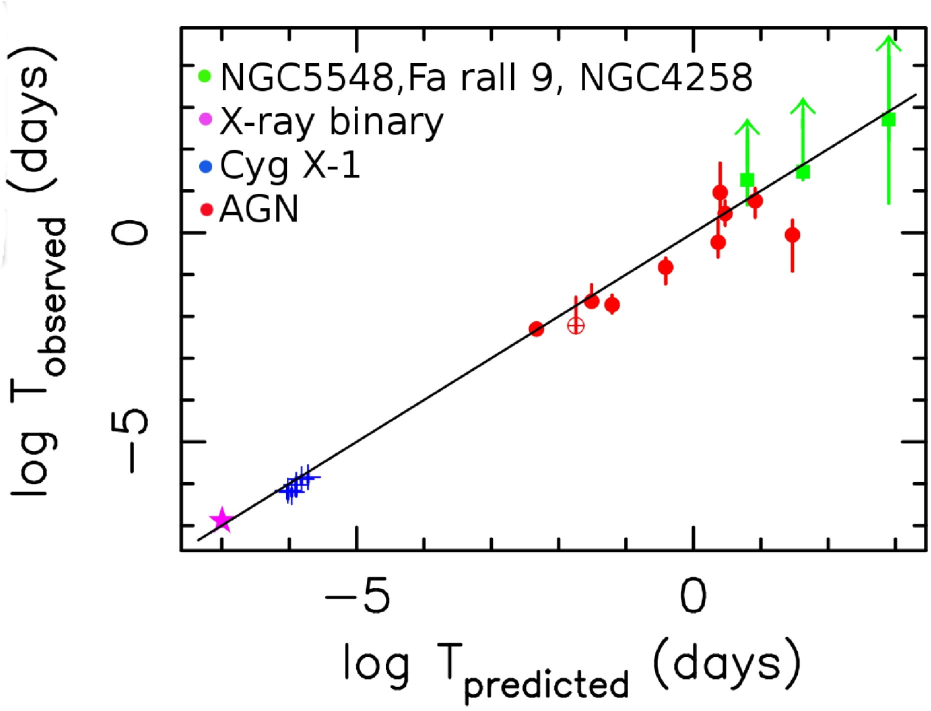

Figure 1.14: $\mathbf{T_B - M_{BH} - L_{bol}}$ plane - The predicted break timescales, $T_B = 2.1\log(M_{BH}) - 0.98\log(L_{bol}) - 2.32$ against the observed break timescales, T_{obs}. Adapted from McHardy et al. (2006).

The PSD was therefore very useful to establish a variability plane where BH of different masses spanning about eight orders of magnitude are placed. It was McHardy et al. (2006) who found that the variability time scale increases for bigger M_{BH} and/or lower L_{bol}, establishing the $T_B - M_{BH} - L_{bol}$ variability plane:

---

[1] A power density which decreases 6 dB per octave with increasing frequency (density proportional to $1/f^2$) over a frequency range which does not include direct current.

$$T_B[days] = 2.1\log(M_{BH}[10^6 M_\odot]) - 0.98\log(L_{bol}[10^{44} erg/s]) - 2.32 \tag{1.5}$$

where T_B (i.e., $T_{predicted}$) corresponds to a characteristic frequency of the PSD, ν_B, when the spectral index bends from $\alpha \sim 1$ to ~ 2. The units are written into brackets in Eq. 1.5.

This plane is represented in Fig. 1.14 as in McHardy et al. (2006). They first used a sample of 10 AGN (red circles in Fig. 1.14) with well measured variability time scales, M_{BH} and L_{bol}, and derived the $T_B - M_{BH} - L_{bol}$ plane. After, they included other AGN and X-ray binaries in the plane, concluding that they follow the same mass-scaling relationship. This relation was later reconfirmed by González-Martín & Vaughan (2012).

On the other hand, variability in different frequency bands is correlated, providing important clues about the physics of the central radiation source, and the PSD has been used to estimate time delays between different energy bands (e.g., Vaughan et al. 2003). Low frequency time lags, or hard/positive lags (i.e., hard X-ray variations lagging soft X-ray variations), can be seen in AGN and XRB, and are identified with propagation of fluctuations through the accretion flow and associated corona. Moreover, reverberation time lags, or soft/negative lags (soft X-ray variations lagging hard X-ray variations), have been detected in a few cases, and are interpreted as due to the light travel time between changes in the direct coronal emission and correspond to variations in its reflection from the accretion flow. These delays are detectable because the direct and reflected components have different spectral shapes. Based on mass-scale dependencies, De Marco et al. (2013) recently found a correlation between the BH mass and the soft time lag for AGN spanning ~ 2.5 orders of magnitude, supporting the idea that these lags originate in the innermost regions of AGN and are powerful tools for testing their physics and geometry. This is a very recent topic at X-ray frequencies whose interest is increasing among the scientific community (see Uttley et al. 2014, for a review).

1.7 Motivation of this thesis

AGN cover nine orders of magnitude in L_{bol}. It is therefore a sensitive issue to establish a luminosity limit to consider some of the nuclei being low luminosity AGN (LLAGN). Since this limit is ill defined in the literature, we would like to start by defining what LLAGN means in this thesis. Some authors have directly put a limit in their luminosity; e.g., Ptak (2001) considered LLAGN when $L(2-10keV) < 10^{42} erg\, s^{-1}$ and Gu & Cao (2009b) when $L(2-10keV) < 10^{43} erg\, s^{-1}$. The most recent review about LLAGN was written by Ho (2008). Instead of establishing a luminosity limit, he argued that its review is centered in nearby galaxies, thus by selection effects, most of the objects occupy the faintest end of the AGN luminosity function – therefore including LINERs and Seyfert galaxies. In a similar way, our selection of

LLAGN was carried out by selecting nearby objects (redshifts lower than 0.05) from their optical classifications as LINERs and Seyfert 2s. The X-ray luminosities of LLAGN in our study ranges between 10^{38} and 10^{43} $erg\ s^{-1}$.

At their most extreme manifestation, LLAGN emit a billion times less light than the most powerful known QSOs. When QSOs were first recognized, the most challenging question was to explain their huge luminosities. Ironically, fifty years later the problem has been reversed, the questions now are, why do LLAGN have such low luminosities? Are LINERs the lowest luminosity regime of the AGN family, i.e., a scaled-down version of Seyfert galaxies?

Variability has been, and still is, a powerful tool for the study of AGN, since it is capable of constraining the physics surrounding SMBH. Nonetheless, although it is well established that variability is a common property of AGN, it is under debate whether every AGN vary in the same way, or in the same timescales, or if there are differences in the variations of type 1/ type 2 objects. Furthermore, variability can give clues on the physics of AGN and help understanding the properties of the accretion disc, the physical scales at which the dusty torus is located or provide information about the existence or not of the BLR and the torus itself in these sources. For these reasons, this thesis is focused on a systematical X-ray variability study of LLAGN, including LINERs (Chapter 2, see also Hernández-García et al. 2013 and Hernández-García et al. 2014) and Seyfert 2s (Chapter 3, see also Hernández-García et al. 2015), in order to be able to obtain their variability patterns, as well as to disentangle whether the same kind of variations are observed in different types of optically selected AGN. Moreover, the spectral and variability analyses performed during this work allow us infer the physical properties of LLAGN and the comparison between these families also gives clues on the structure of AGN (Chapter 4).

AGN are not the only objects emitting at X-rays. Many AGN are indeed located in high galaxy density regions, from small galaxy groups to big galaxy clusters, whose X-ray emission originates from hot plasma. Therefore, it is important to take into account the contribution of the cluster emission when the nucleus to be studied is located within this hot plasma, because it can affect our measurements. Chapter 5 is devoted to the characterization of some galaxy groups and clusters to properly decontaminate the nuclear emission from the cluster emission. Furthermore, we use a sample of galaxy groups and clusters to determine the number of AGN located within each structure.

Extragalactic sources of special interest at X-rays are the so called ultraluminous X-ray sources (ULXs), which emit luminosities of $L(2-10keV) \sim 10^{39} erg\ s^{-1}$, very similar to those observed in LINER nuclei. We develop a variability study on these sources in Chapter 6. This is important because, although it is well established that the spectral properties of ULXs are completely different to those of AGN (Sutton et al. 2013), we might misinterpret an ULX within our line of sight as an AGN. Thus, studying spectral and variability properties of ULXs will give us the knowledge to differentiate the two kind of sources. Moreover, their origin is still unknown and different possibilities have been suggested to explain it, including stellar mass or intermediate mass BHs. Since it has been suggested that BHs of very different masses might be powered by the same emission mechanism (McHardy et al. 2006; Uttley et al. 2014), both possibilities are exciting and might relate ULX with the long-sought loose end between the lower mass objects, X-ray binaries, and the higher mass sources, AGN.

Finally, the conclusions obtained from this work are summarized in Chapter 7. Since giving answer to some questions in science always opens the door to new mysteries which researchers want to discover, future prospects derived from this work are presented in Chapter 8. Other works in which I have participated during the development of this thesis are included in Chapter 9.

References

Angione, R. J. 1968, PASP, 80, 339

Antonucci, R. 1993, ARA&A, 31, 473

Antonucci, R. R. J. & Cohen, R. D. 1983, ApJ, 271, 564

Awaki, H., Koyama, K., Inoue, H., & Halpern, J. P. 1991, PASJ, 43, 195

Baldwin, J. A., Phillips, M. M., & Terlevich, R. 1981, PASP, 93, 5

Bamford, S. P., Rojas, A. L., Nichol, R. C., et al. 2008, MNRAS, 391, 607

Barcons, X., Barret, D., Decourchelle, A., et al. 2012, ArXiv e-prints: 1207.2745

Bearden, J. A. 1967, Rev. Mod. Phys., 39, 78

Bennett, A. S. 1962, MNRAS, 68, 163

Blaes, O. 2007, in Astronomical Society of the Pacific Conference Series, Vol. 373, The Central Engine of Active Galactic Nuclei, ed. L. C. Ho & J.-W. Wang, 75

Blandford, R. D. & McKee, C. F. 1982, ApJ, 255, 419

Boller, T., Brandt, W. N., Fabian, A. C., & Fink, H. H. 1997, MNRAS, 289, 393

Bradt, H. V., Swank, J. H., & Rothschild, R. E. 1990, Advances in Space Research, 10, 297

Breedt, E., McHardy, I. M., Arévalo, P., et al. 2010, MNRAS, 403, 605

Brightman, M. & Nandra, K. 2011, MNRAS, 413, 1206

Burbidge, E. M. & Burbidge, G. R. 1965, ApJ, 142, 1351

Burbidge, G. R., Burbidge, E. M., & Sandage, A. R. 1963, Reviews of Modern Physics, 35, 947

Burrows, D. N., Hill, J. E., Nousek, J. A., et al. 2005, Space Sci. Rev., 120, 165

Cappi, M., Panessa, F., Bassani, L., et al. 2006, A&A, 446, 459

Collin, S. & Kawaguchi, T. 2004, A&A, 426, 797

Comastri, A., Iwasawa, K., Gilli, R., et al. 2010, ApJ, 717, 787

Condon, J. J., Odell, S. L., Puschell, J. J., & Stein, W. A. 1980, Nature, 283, 357

Crummy, J., Fabian, A. C., Gallo, L., & Ross, R. R. 2006, MNRAS, 365, 1067

Davison, P. J. N., Culhane, J. L., Mitchell, R. J., & Fabian, A. C. 1975, ApJ, 196, L23

De Marco, B., Ponti, G., Cappi, M., et al. 2013, MNRAS, 431, 2441

de Vaucouleurs, G. H., de Vaucouleurs, A., & Shapley, H. 1964, Reference catalogue of bright galaxies (Austin: University of Texas Press)

den Herder, J. W., Brinkman, A. C., Kahn, S. M., et al. 2001, A&A, 365, L7

Dewangan, G. C., Griffiths, R. E., Dasgupta, S., & Rao, A. R. 2007, ApJ, 671, 1284

Dewey, D. 2003, Chandra News, 10, 11

Done, C., Gierliński, M., Sobolewska, M., & Schurch, N. 2007, in Astronomical Society of the Pacific Conference Series, Vol. 373, The Central Engine of Active Galactic Nuclei, ed. L. C. Ho & J.-W. Wang, 121

D'Onofrio, M., Marziani, P., & Sulentic, J. W. 2012, Fifty Years of Quasars: Current Impressions and Future Perspectives, ed. M. D'Onofrio, P. Marziani, & J. W. Sulentic, 549

Drake, J. 2002, Chandra News, 9, 14

Edge, D. O., Shakeshaft, J. R., McAdam, W. B., Baldwin, J. E., & Archer, S. 1959, MmRAS, 68, 37

Eguchi, S., Ueda, Y., Terashima, Y., Mushotzky, R., & Tueller, J. 2009, ApJ, 696, 1657

Elitzur, M. & Ho, L. C. 2009, ApJ, 701, L91

Elitzur, M. & Shlosman, I. 2006, ApJ, 648, L101

Elvis, M. 2000, ApJ, 545, 63

Eracleous, M., Hwang, J. A., & Flohic, H. M. L. G. 2010, ApJS, 187, 135

Fanaroff, B. L. & Riley, J. M. 1974, MNRAS, 167, 31P

Fath, E. A. 1909, Lick Observatory Bulletin, 5, 71

Ferrarese, L. & Merritt, D. 2000, ApJ, 539, L9

Fitch, W. S., Pacholczyk, A. G., & Weymann, R. J. 1967, ApJ, 150, L67

Garmire, G. P., Bautz, M. W., Ford, P. G., Nousek, J. A., & Ricker, J. G. R. 2003, in Society of Photo-Optical Instrumentation Engineers (SPIE) Conference Series, Vol. 4851, Society of Photo-Optical Instrumentation Engineers (SPIE) Conference Series, ed. J. E. Truemper & H. D. Tananbaum, 28–44

Gebhardt, K., Bender, R., Bower, G., et al. 2000, ApJ, 539, L13

George, I. M. & Fabian, A. C. 1991, MNRAS, 249, 352

Giacconi, R., Branduardi, G., Briel, U., et al. 1979, ApJ, 230, 540

Giacconi, R., Gursky, H., Paolini, F. R., & Rossi, B. B. 1962, Physical Review Letters, 9, 439

Giacconi, R., Kellogg, E., Gorenstein, P., Gursky, H., & Tananbaum, H. 1971, ApJ, 165, L27

Gilli, R., Comastri, A., & Hasinger, G. 2007, A&A, 463, 79

Goldsmith, D. W. & Kinman, T. D. 1965, ApJ, 142, 1693

González-Martín, O., Masegosa, J., Márquez, I., Guainazzi, M., & Jiménez-Bailón, E. 2009, A&A, 506, 1107

González-Martín, O., Masegosa, J., Márquez, I., Guerrero, M. A., & Dultzin-Hacyan, D. 2006, A&A, 460, 45

Gonzalez-Martin, O., Masegosa, J., Marquez, I., et al. 2015, ArXiv e-prints

González-Martín, O., Papadakis, I., Braito, V., et al. 2011, A&A, 527, A142

González-Martín, O. & Vaughan, S. 2012, A&A, 544, A80

Greenstein, J. L. & Matthews, T. A. 1963, AJ, 68, 279

Greenstein, J. L. & Schmidt, M. 1964, ApJ, 140, 1

Gu, M. & Cao, X. 2009a, MNRAS, 399, 349

Gu, M. & Cao, X. 2009b, MNRAS, 399, 349

Guainazzi, M., Matt, G., & Perola, G. C. 2005, A&A, 444, 119

Guainazzi, M., Perola, G. C., Matt, G., et al. 1999, A&A, 346, 407

Gültekin, K., Richstone, D. O., Gebhardt, K., et al. 2009, ApJ, 698, 198

Haardt, F. & Maraschi, L. 1993, ApJ, 413, 507

Harrison, F. A., Craig, W. W., Christensen, F. E., et al. 2013, ApJ, 770, 103

Heckman, T. M. 1980, A&A, 87, 152

Hernández-García, L., González-Martín, O., Márquez, I., & Masegosa, J. 2013, A&A, 556, A47

Hernández-García, L., González-Martín, O., Masegosa, J., & Márquez, I. 2014, A&A, 569, A26

Hernández-García, L., Masegosa, J., González-Martín, O., & Márquez, I. 2015, ArXiv e-prints: 1505.01166

Ho, L. C. 2008, ARA&A, 46, 475

Ho, L. C., Filippenko, A. V., Sargent, W. L. W., & Peng, C. Y. 1997, ApJS, 112, 391

Hubble, E. P. 1926, ApJ, 64, 321

Jansen, F., Lumb, D., Altieri, B., et al. 2001, A&A, 365, L1

Kaspi, S., Maoz, D., Netzer, H., et al. 2005, ApJ, 629, 61

Kaspi, S., Smith, P. S., Netzer, H., et al. 2000, ApJ, 533, 631

Kauffmann, G., Heckman, T. M., Tremonti, C., et al. 2003, MNRAS, 346, 1055

Kewley, L. J., Groves, B., Kauffmann, G., & Heckman, T. 2006, MNRAS, 372, 961

Kinman, T. D., Lamla, E., Ciurla, T., Harlan, E., & Wirtanen, C. A. 1968, ApJ, 152, 357

Krolik, J. H. & Kallman, T. R. 1987, ApJ, 320, L5

Lawrence, A., Watson, M. G., Pounds, K. A., & Elvis, M. 1987, Nature, 325, 694

Lynden-Bell, D. 1969, Nature, 223, 690

Maiolino, R., Salvati, M., Bassani, L., et al. 1998, A&A, 338, 781

Maoz, D., Nagar, N. M., Falcke, H., & Wilson, A. S. 2005, ApJ, 625, 699

Mason, K. O., Breeveld, A., Much, R., et al. 2001, A&A, 365, L36

Matt, G., Perola, G. C., & Piro, L. 1991, A&A, 247, 25

Matthews, T. A. & Sandage, A. R. 1963, ApJ, 138, 30

McHardy, I. 1988, Mem. Soc. Astron. Italiana, 59, 239

McHardy, I. 2010, in Lecture Notes in Physics, Berlin Springer Verlag, Vol. 794, Lecture Notes in Physics, Berlin Springer Verlag, ed. T. Belloni, 203

McHardy, I. M., Koerding, E., Knigge, C., Uttley, P., & Fender, R. P. 2006, Nature, 444, 730

Miller, J. S. & Goodrich, R. W. 1990, ApJ, 355, 456

Miniutti, G. & Fabian, A. C. 2006, MNRAS, 366, 115

Miniutti, G., Fabian, A. C., & Miller, J. M. 2004, MNRAS, 351, 466

Mitsuda, K., Bautz, M., Inoue, H., et al. 2007, PASJ, 59, 1

Mortlock, D. J., Warren, S. J., Venemans, B. P., et al. 2011, Nature, 474, 616

Muñoz Marín, V. M., Storchi-Bergmann, T., González Delgado, R. M., et al. 2009, MNRAS, 399, 842

Murray, S. S. & HRC Team. 1999, in Bulletin of the American Astronomical Society, Vol. 31, American Astronomical Society Meeting Abstracts, 1515

Mushotzky, R. F., Done, C., & Pounds, K. A. 1993, ARA&A, 31, 717

Nandra, K., Fabian, A. C., George, I. M., et al. 1993, MNRAS, 260, 504

Nandra, K., George, I. M., Mushotzky, R. F., Turner, T. J., & Yaqoob, T. 1997, ApJ, 476, 70

Nandra, K. & Pounds, K. A. 1994, MNRAS, 268, 405

Narayan, R. & Yi, I. 1994, ApJ, 428, L13

Nenkova, M., Sirocky, M. M., Ž. Ivezić, & Elitzur, M. 2008, ApJ, 685, 147

Netzer, H. 2013, The Physics and Evolution of Active Galactic Nuclei (Cambridge University Press)

Netzer, H. 2015, ArXiv e-prints: 1505.00811

Netzer, H., Lira, P., Trakhtenbrot, B., Shemmer, O., & Cury, I. 2007, ApJ, 671, 1256

Nicastro, F., Piro, L., De Rosa, A., et al. 2000, ApJ, 536, 718

Osterbrock, D. E. & Martel, A. 1993, ApJ, 414, 552

Ozernoi, L. M. & Chertoprud, V. E. 1966, Soviet Ast., 10, 15

Panessa, F., Carrera, F. J., Bianchi, S., et al. 2009, MNRAS, 398, 1951

Perola, G. C., Matt, G., Fiore, F., et al. 2000, A&A, 358, 117

Peterson, B. M. 1997, An Introduction to Active Galactic Nuclei, ed. Peterson, B. M.

Peterson, B. M., Meyers, K. A., Carpriotti, E. R., et al. 1985, ApJ, 292, 164

Peterson, L. E. 1975, ARA&A, 13, 423

Pian, E., Romano, P., Maoz, D., et al. 2010, MNRAS, 401, 677

Pier, E. A. & Krolik, J. H. 1992, ApJ, 401, 99

Piro, L., Yamauchi, M., & Matsuoka, M. 1990, ApJ, 360, L35

Poutanen, J. 1998, in Theory of Black Hole Accretion Disks, ed. M. A. Abramowicz, G. Björnsson, & J. E. Pringle, 100–122

Pozdnyakov, L. A., Sobol, I. M., & Syunyaev, R. A. 1983, Astrophysics and Space Physics Reviews, 2, 189

Ptak, A. 2001, X-ray Astronomy: Stellar Endpoints, AGN, and the Diffuse X-ray Background, 599, 326

Ptak, A., Yaqoob, T., Mushotzky, R., Serlemitsos, P., & Griffiths, R. 1998, ApJ, 501, L37

Puccetti, S., Fiore, F., Risaliti, G., et al. 2007, MNRAS, 377, 607

Quataert, E. 2004, in Astronomical Society of the Pacific Conference Series, Vol. 311, AGN Physics with the Sloan Digital Sky Survey, ed. G. T. Richards & P. B. Hall, 131

Rees, M. J. 1984, ARA&A, 22, 471

Reynolds, C. S. 1996, PhD thesis, University of Cambridge

Reynolds, C. S. & Nowak, M. A. 2003, Phys. Rep., 377, 389

Ricci, C., Walter, R., Courvoisier, T. J.-L., & Paltani, S. 2011, A&A, 532, A102

Risaliti, G. 2002, A&A, 386, 379

Risaliti, G., Elvis, M., Fabbiano, G., et al. 2007, ApJ, 659, L111

Risaliti, G., Elvis, M., & Nicastro, F. 2002, ApJ, 571, 234

Risaliti, G., Nardini, E., Salvati, M., et al. 2011, MNRAS, 410, 1027

Salpeter, E. E. 1964, ApJ, 140, 796

Sandage, A. 1964, ApJ, 139, 416

Sanford, P. W. 1974, Royal Society of London Proceedings Series A, 340, 411

Sanfrutos, M., Miniutti, G., Agís-González, B., et al. 2013, MNRAS, 436, 1588

Sargent, W. L. W., Young, P. J., Lynds, C. R., et al. 1978, ApJ, 221, 731

Scarsi, L. 1997, in Data Analysis in Astronomy, ed. V. Di Gesu, M. J. B. Duff, A. Heck, M. C. Maccarone, L. Scarsi, & H. U. Zimmerman, 65–78

Schawinski, K., Simmons, B. D., Urry, C. M., Treister, E., & Glikman, E. 2012, MNRAS, 425, L61

Schmidt, M. 1963, Nature, 197, 1040

Seyfert, C. K. 1943, ApJ, 97, 28

Shakura, N. I. & Sunyaev, R. A. 1973, A&A, 24, 337

Sharov, A. S. & Efremov, Y. N. 1963, Information Bulletin on Variable Stars, 23, 1

Smith, H. J. & Hoffleit, D. 1963, AJ, 68, 292

Soldi, S., Beckmann, V., Baumgartner, W. H., et al. 2014, A&A, 563, A57

Stalevski, M., Fritz, J., Baes, M., Nakos, T., & Č. Popović, L. 2012, MNRAS, 420, 2756

Strüder, L., Briel, U., Dennerl, K., et al. 2001, A&A, 365, L18

Sulentic, J. W., Bachev, R., Marziani, P., Negrete, C. A., & Dultzin, D. 2007, ApJ, 666, 757

Sutton, A. D., Roberts, T. P., & Middleton, M. J. 2013, MNRAS, 435, 1758

Tanaka, Y., Inoue, H., & Holt, S. S. 1994, PASJ, 46, L37

Tanaka, Y., Nandra, K., Fabian, A. C., et al. 1995, Nature, 375, 659

Tran, H. D., Miller, J. S., & Kay, L. E. 1992, ApJ, 397, 452

Truemper, J. 1982, Advances in Space Research, 2, 241

Turner, M. J. L., Abbey, A., Arnaud, M., et al. 2001, A&A, 365, L27

Turner, T. J., George, I. M., Nandra, K., & Mushotzky, R. F. 1997, ApJS, 113, 23

Ueda, Y., Eguchi, S., Terashima, Y., et al. 2007, ApJ, 664, L79

Urry, C. M. & Padovani, P. 1995, PASP, 107, 803

Uttley, P., Cackett, E. M., Fabian, A. C., Kara, E., & Wilkins, D. R. 2014, A&A Rev., 22, 72

Uttley, P., McHardy, I. M., & Vaughan, S. 2005, MNRAS, 359, 345

Vaughan, S., Fabian, A. C., & Nandra, K. 2003, MNRAS, 339, 1237

Veilleux, S. & Osterbrock, D. E. 1987, ApJS, 63, 295

Véron-Cetty, M.-P., Véron, P., & Gonçalves, A. C. 2001, A&A, 372, 730

Weisskopf, M. C., Aldcroft, T. L., Bautz, M., et al. 2003, Experimental Astronomy, 16, 1

Winkler, J. P. F. & White, A. E. 1975, ApJ, 199, L139

Woo, J.-H. & Urry, C. M. 2002, ApJ, 579, 530

Worrall, D. M. 2009, A&A Rev., 17, 1

Younes, G., Porquet, D., Sabra, B., & Reeves, J. N. 2011, A&A, 530, A149

Young, P. J., Westphal, J. A., Kristian, J., Wilson, C. P., & Landauer, F. P. 1978, ApJ, 221, 721

Zwicky, I. F. 1964, ApJ, 140, 1467

2

LINERs

LINERs were first recognized by Heckman et al. (1980), who noticed that they might be the low luminosity end of the AGN family distribution. A long debate hold about the ionization mechanism of these sources during the following decades, which can be explained by a power-law continuum (Ho et al. 1993), shock ionization (Dopita & Sutherland 1995), or photoionization by post-AGB stars (Cid-Fernandes et al. 2011), among others. Although today it is most accepted that LINERs are LLAGN, some people still doubt the AGN origin of some LINERs (Singh et al. 2014). Thus, X-ray analyses are crucial to confirm their AGN nature.

The most extensive work made for LINERs has been carried out by González-Martín et al. (2006,2009a,2009b), which was focused in understanding the nature of the energy source observed in LINERs (see also Sambruna et al. 2003; Satyapal et al. 2004, 2005; Dudik et al. 2005). Their analysis was mainly performed at X-ray energies but is complemented by data at UV and radio frequencies. They demonstrated that 60% of the sample composed by 82 LINERs showed a compact unresolved nuclear source at high X-ray energies (4.5–8.0 keV). When taking into account multiwavelength properties, this percentage raised up to 90% of the sample showing evidence of hosting AGN.

One of the main properties characterizing AGN is the variability of their nuclei throughout the electromagnetic spectrum (Peterson 1997). Therefore, whether LINERs are truly AGN can be reinforced by studying this property. We focus our work at X-ray frequencies as they are produced close to the SMBH and have much smaller effect of obscuration than at other wavelengths, such as optical or infrared. The spectral fit of individual observations are carried out following the methodology of González-Martín et al. (2009b). The study of X-ray variability is performed by using data at different dates of the same source, so we can search for spectral variations at short and long-term timescales. We complement our work by searching for variations at UV frequencies using the OM on board *XMM*–Newton. Variations at UV frequencies in LINERs have been previously reported by Maoz et al. (2005).

This chapter is composed by two papers which are already published in Astronomy & Astrophysics. The first one was published in 2013 and is focused on the development of the methodology used to characterize the variability and its application to a few number of sources. After proving that it is worth using the methodology in a well-selected sample of LINERs, the second paper collects the results obtained for the systematic study of variability in a sample of LINERs selected at optical wavelengths. It was published in 2014.

A&A 556, A47 (2013)
DOI: 10.1051/0004-6361/201321563

Astronomy & Astrophysics

X-ray spectral variability of seven LINER nuclei with *XMM-Newton* and *Chandra* data[⋆]

L. Hernández-García[1], O. González-Martín[2,3], I. Márquez[1], and J. Masegosa[1]

[1] Instituto de Astrofísica de Andalucía, CSIC, Glorieta de la Astronomía, s/n, 18008 Granada, Spain
e-mail: `lorena@iaa.es`
[2] Instituto de Astrofísica de Canarias (IAC), C/Vía Lactea, s/n, 38205 La Laguna, Tenerife, Spain
[3] Departamento de Astrofísica, Universidad de La Laguna (ULL), 38205 La Laguna, Tenerife, Spain

Received 25 March 2013 / Accepted 9 May 2013

ABSTRACT

Context. One of the most distinctive features in active galactic nuclei (AGN) is the variability of their emission. Variability has been discovered at X-ray, UV, and radio frequencies on timescales from hours to years. Among the AGN family and according to theoretical studies, low-ionization nuclear emission line region (LINER) nuclei would be objects variable on long timescales.
Aims. Our purpose is to investigate spectral X-ray variability in LINERs and to understand the nature of these types of objects, as well as their accretion mechanism.
Methods. *Chandra* and *XMM-Newton* public archives were used to compile X-ray spectra of seven LINER nuclei at different epochs with timescales of years. To search for variability we fit all spectra from the same object with a set of models to identify the parameters responsible for the variability pattern. We also analyzed the light curves to search for short timescale (from hours to days) variability. Whenever possible, UV variability was also studied.
Results. We found spectral variability in four objects (NGC 1052, NGC 3226, NGC 4278, and NGC 4552), with variations mostly related to hard energies (2–10 keV). These variations are generated by several possible changes that act either alone or in combination: changes in the soft excess or in the absorber. Added to this can be intrinsic variations of the source, which may also be responsible by themselves for the spectral variability. These variations occurred within years, the shortest timescale being found for NGC 4278 (two months). Another two galaxies (NGC 4261 and NGC 5846) apparently do not vary. No short timescale variations during individual observations were found. Our analysis confirms the previously reported anticorrelation between the X-ray spectral index, Γ, and the Eddington ratio, $L_{\rm bol}/L_{\rm Edd}$, and also the correlation between the X-ray to UV flux ratio, $\alpha_{\rm ox}$, and the Eddington ratio, $L_{\rm bol}/L_{\rm Edd}$. These results support an advection dominated accretion flow as the accretion mechanism in LINERs.

Key words. galaxies: active – X-rays: galaxies – ultraviolet: galaxies

1. Introduction

The plethora of phenomena present in an active galactic nucleus (AGN) shows energetic processes in the nuclei of galaxies that cannot be attributed to stars (Peterson 1997). The unified model for AGN (Urry & Padovani 1995; Antonucci 1993) represents a scenario where the central, supermassive black hole (SMBH) is surrounded by a dusty torus; depending on the line of sight of the observer, the AGN appears as type 1 (pole-on view) or type 2 (edge on view). However, even if, broadly speaking, the unified model is a good representation of AGN, there are a number of objects that still cannot be fitted with this scheme. This is the case of low-ionization nuclear emission line regions (LINERs), which are the main topic of this research.

First defined by Heckman (1980), LINERs were characterized in the optical, where their spectra show strong low-ionization lines such as [OI] λ 6300 Å and [SII] $\lambda\lambda$ 6717, and 6731 Å (Veilleux & Osterbrock 1987). Different options have been proposed to explain the ionization mechanism in LINERs, such as shock-heated gas (Dopita & Sutherland 1995), photoionization by hot stars (Terlevich & Melnick 1985), by post-main-sequence stars (Cid-Fernandes et al. 2011), or a low-luminosity active galactic nuclei (LLAGN, Ho et al. 1993). Currently, the most accepted option is that they harbor AGN (see Ho 2008; Márquez 2012).

X-ray data for LLAGN offer the most reliable probe of the high-energy spectrum, providing many AGN signatures (D'Onofrio et al. 2012). It can be assessed that an AGN is present in LINERs when a point-like source is detected at hard X-ray energies (Satyapal et al. 2004, 2005; Dudik et al. 2005; Ho 2008). The most extensive work has been carried out by González-Martín et al. (2009b), who analyzed 82 LINERs with *Chandra* and/or *XMM-Newton* data for single-period observations. These authors found that 60% of the sample showed a compact nuclear source in the 4.5–8 keV band; a multiwavelength analysis found that about 80% of the sample showed evidence of AGN-related properties, which is a lower limit because Compton-thick objects were not taken into account.

It is tempting to view LINERs as a scaled-down version of Seyfert galaxies, but in fact they are qualitatively different from their neighboring class (Ho 2008). LINERs have lower luminosities ($L_{2-10\ \rm keV} \approx 10^{39}$–$10^{42}$ erg s^{-1}), lower Eddington ratios ($L_{\rm bol}/L_{\rm Edd} \approx 10^{-4}$), and more massive black holes ($M_{\rm BH} \approx 10^{8}\ M_{\odot}$, Eracleous 2010; Masegosa et al. 2011).

Variability is one of the main properties that characterizes AGN, most of which are at least mildly variable. When quasars

---

[⋆] Tables 2–11 and Appendices are available in electronic form at http://www.aanda.org were first discovered in the 1960s (Schmidt 1963), one of their key defining properties was their variability. These objects are variable over the entire wavelength range, many of them varying by 0.3–0.5 mag over timescales of a few months, and others varying significantly on timescales as short as a few days (Peterson 1997). Variability properties seem to correlate with AGN power; in quasars, variations very likely result from both accretion disk instability and microlensing, while in Seyfert galaxies the brightness of the nucleus is thought to vary, the broad-line region (BLR) responding to these changes a few weeks later (D'Onofrio et al. 2012).

At X-ray frequencies many studies have been made with the aim of understanding variability in Seyfert galaxies. Risaliti et al. (2000) studied the highly variable Seyfert 1.8 galaxy NGC 1365, which was observed for many years with different instruments; they also found variability in the Seyfert galaxy UGC 4203 using *Chandra* data (Risaliti et al. 2010). They suggested a scenario in which the variability is produced by clouds intersecting the line of sight to the observer. Evans et al. (2005) found that the 2–10 keV luminosity for NGC 6251 varied a factor of ≈ 5 from 1991 to 2003. More recently, Caballero-Garcia et al. (2012) showed that the five Seyfert galaxies studied with *Swift*/BAT showed flux variability on timescales of 1–2 days. Narrow-line Seyfert 1 galaxies (NLSy1) also show variability in X-rays (Panessa et al. 2011; Risaliti et al. 2011).

As stated by Ptak et al. (1998), "LINERs tend to show little or no significant short-term variability (i.e., with timescales less than a day)" (see also Krolik 1999). The first clear evidence of variability in LINERs was reported by Maoz et al. (2005) at UV frequencies, where all but three objects in their sample of 17 LINERs of type 1 and 2 appeared variable. Pian et al. (2010) and Younes et al. (2011) investigated type 1 LINERs at X-ray energies and also found that variability is a common property of LINERs. González-Martín et al. (2011a) studied a *Suzaku* observation of 80 ks of the Compton-thick LINER NGC 4102, and found two absorbers from the soft X-rays and the optical spectrum. They found variations of the soft-excess flux within about seven years compared whith *Chandra* data. This variation was described by a decrease in the normalization of the power-law component and the thermal component by a factor of ≈ 7. Therefore it is important to characterize the phenomenon fully, both the scale and magnitude of the variability. Taking the predictions by McHardy et al. (2006) that the timescale variations scale with black-hole masses, $M_{\rm BH}$, and bolometric luminosities, $L_{\rm bol}$, González-Martín & Vaughan (2012) estimated timescales longer than tens of days in LINERs.

This paper is organized as follows: in Sect. 2 we present the sample and the data. The reduction of the data is explained in Sect. 3. Our methodolody is described in Sect. 4, where individual and simultaneous spectral fittings, comparisons of different appertures, flux variability in X-rays and UV frequencies, and short-term variability subsections are explained. The results from this analysis are given in Sect. 5, and we discuss them in Sect. 6. Finally, our main results are summarized in Sect. 7.

2. Sample and data

For the sample of 82 LINERs of type 1 and 2 in González-Martín et al. (2009b) we searched in the current literature for hints of variability by means of differences in luminosity when different observations are considered. We used the HEASARC[1] archive to search for different observations with *Chandra* and *XMM-Newton*, with publicly available data until October 2012. This analysis provided 16 candidate variable sources. The four ultraluminous infrared galaxies (ULIRG) in this primary selection (NGC 3690, NGC 6240, IRAS 17208-0014, and UGC 08696) were discarded since our aim is to deal with typical pure LINERs (see Ho 2008), not contaminated by strong star formation where other ionization sources could be at work. NGC 4636 was also discarded because its X-ray emission is dominated by the cluster emission. We also rejected all observations affected by pile-up higher than 10% (*Chandra* data observations for objects namely NGC 4579, NGC 3998, NGC 4594, and NGC 6251 and three *Chandra* observations of NGC 4278). Finally, to guarantee a proper spectral fitting we kept only observations with at least 400 number counts. An exception was made for obs ID 11269 of NGC 4278, which met this criterion, but visual inspection revealed a very low count number in the hard band.

The final sample of LINERs contains seven objects. Table 1 shows the general properties of the target galaxies for this study and Table 2 the log of the observations. Number of counts and hardness ratios, defined as HR = (H-S)/(H+S), where H is the number of counts in the hard (2–10 keV) band and S is the number of counts in the soft (0.5–2 keV) band, are also presented. For five sources, NGC 1052, NGC 3226, NGC 4261, NGC 4278, and NGC 5846, observations at different epochs were taken with the same instrument, providing us with good examples for variability studies. In the other two sources, NGC 3627, and NGC 4552, we can estimate variability only by comparing *XMM-Newton* with *Chandra* data. These results should be viewed with caution because of the different apertures used by both instruments. A detailed study of the extended emission is made for these two objects (see Sect. 4).

3. Data reduction

Data reduction was performed following the procedure described by González-Martín et al. (2009b). We recall the methodology here.

3.1. Chandra data

Chandra observations were obtained with the ACIS instrument (Garmire et al. 2003). The data reduction and analysis were carried out in a systematic, uniform way using CXC *Chandra* Interactive Analysis of Observations (CIAO[2]), version 4.3. Level 2 event data were extracted by using the task ACIS-PROCESS-EVENTS. We first cleaned the data from background flares (i.e., periods of high background) that could affect our analysis. These "flares" are due to low-energy photons that interact with the detector. To clean them we used the task LC_CLEAN.SL[3], which removes periods of anomalously low (or high) count rates from light curves from source-free background regions of the CCD. This routine calculates a mean rate from which it deduces a minimum and maximum valid count rate, and creates a file with the periods that are considered by the algorithm to be good.

Nuclear spectra were extracted from a circular region centered on the positions given by NED[4]. We chose circular radii, aiming to include all possible photons, while excluding other sources or background effects. The radii are in the

---

[1] `http://heasarc.gsfc.nasa.gov/`

[2] `http://cxc.harvard.edu/ciao4.4/`

[3] `http://cxc.harvard.edu/ciao/ahelp/lc_clean.html`

[4] `http://ned.ipac.caltech.edu/`

Table 1. General properties of the sample galaxies.

Name (1)	Other name (2)	RA (3)	Dec (4)	Redshift (5)	Dist. (Mpc) (6)	$N_{\rm Gal}$ (cm^{-2}) (7)	m_B (8)	$E(B-V)$ (9)	Morph. type (10)
NGC 1052		02 41 04.80	+08 15 20.8	0.0049	19.41	0.0307	11.436	0.027	E
NGC 3226	UGC 5617	10 23 27.01	+19 53 54.7	0.0059	23.55	0.0214	12.339	0.023	E
NGC 3627	M 66	11 20 15.03	+12 59 29.6	0.00242	10.28	0.0243	9.735	0.033	SABb(s)
NGC 4261	UGC 7360	12 19 23.22	+05 49 30.8	0.00737	31.62	0.0155	11.35	0.018	E
NGC 4278	M 98	12 20 06.83	+29 16 50.7	0.00216	16.07	0.0177	11.042	0.029	E
NGC 4552	M 89	12 35 39.81	+12 33 22.8	0.0038	15.35	0.0257	10.67	0.041	E
NGC 5846	UGC 9705	15 06 29.29	+01 36 20.2	0.00622	24.89	0.0426	11.074	0.056	E

Notes. Names (Cols. 1 and 2), right ascension (Col. 3), declination (Col. 4), redshift (Col. 5), distance (Col. 6), galactic absorption (Col. 7), aparent magnitude in the Johnson filter B (Col. 8), reddening (Col. 9) and galaxy morphological type (Col. 10). All distances are taken from Tonry et al. (2001) except that for that NGC 3627, which was taken from Ferrarese et al. (2000).

range between 3–8″ (or 6–16 pixels, see Table 2). The background selection was made taking regions free of sources in the same chip as the target and close to the source (5″ for NGC 3627, NGC 4278, NGC 4261, and NGC 4552, and 7″ for NGC 5846 and NGC 3627) to minimize effects related to the spatial variations of the CCD response.

We used the DMEXTRACT task to extract the spectra of the source and the background regions. The response matrix file (RMF) and ancillary reference file (ARF) were generated for each source region using the MKACISRMF and MKWARF tasks, respectively. Before background subtraction, the spectra were binned to have a minimum of 20 counts per spectral bin, to be able to use the χ^2-statistics. This was made with the GRPPHA task included in FTOOLS.

3.2. XMM-Newton data

All *XMM-Newton* observations were obtained from the EPIC pn camera[5]. The data were reduced in a systematic, uniform way using the Science Analysis Software (SAS[6]), version 11.0.0. Before extracting the spectra, good-timing periods were selected (i.e., flares were excluded). The method used for this purpose maximizes the signal to noise ratio of the net source spectrum by applying a different constant count rate threshold on the single-events, $E > 10$ keV field-of-view background light curve. The nuclear positions were taken from NED, while the extraction region was determined through circles of 25″ radius and the background was determined with an algorithm that selects the best circular region around the source, that is free of other sources and as close as possible to the nucleus. This automatic selection was checked manually to ensure the best selection for the backgrounds.

We extracted the source and background regions with the EVSELECT task. RMFs were generated using the RMFGEN task, and the ARFs were generated using the ARFGEN task. We then grouped the spectra to obtain at least 20 counts per spectral bin using the GRPPHA task, as is required to use the χ^2-statistics.

3.3. Light curves

Light curves in the 0.5–10 keV band for the source and background were extracted using the DMEXTRACT task for *XMM-Newton* and EVSELECT task for *Chandra* with a 1000 s bin. The light curve from the source was manually screened for high background and flaring activity. This means that when the background light curve showed flare-like events and/or prominent decreasing/increasing trends, we did not use those intervals. After rejecting the respective time intervals, the total useful time for each observation was usually shorter than the original exposure time (see Table 2). The light curves are shown in Figs. C.1–C.7, where the solid line represents the mean value of the count rate and the dashed lines represent 1σ standard deviation.

4. Methodology

The spectral fitting process comprises two steps: (1) individual analysis of each observation to determine the best fit for each spectrum; and (2) simultaneous fitting of the set of spectra of the same object at different epochs. We used XSPEC[7] version 12.7.0 for the spectral fitting.

4.1. Individual spectral analysis

We performed an individual study of the best-fit model for each observation. For this, we followed the method used by González-Martín et al. (2009b), where five different models were used:

1. ME: a pure thermal model (MEKAL in XSPEC). The thermal emission is responsible for the bulk of the X-ray energy distribution. The free parameters in this model are the column density, $N_{\rm H}$, the temperature, kT, and the normalization, *Norm*.
2. PL: a single power law model, which corresponds to a non-thermal source representing an AGN. The column density, $N_{\rm H}$, is added as a free parameter to take the absorption by matter along our line of sight to the target into account. The free parameters in this model are the column density, $N_{\rm H}$, the slope of the power law, Γ, and the normalization, *Norm*.
3. 2PL: a model containing two power laws with the same slope, Γ. Here the bulk of the hard X-rays is due to a primary continuum described by a power law, and the soft X-rays come from a scattering component described by the other power law. The free parameters in this model are the column densities, $N_{\rm H1}$ and $N_{\rm H2}$, the slope of the power-law, Γ, and the normalizations, $Norm_1$ and $Norm_2$.

---

[5] EPIC pn is the most efficient camera because X-ray photons hit the detector from the rear side, avoiding cross-calibration problems between the pn and MOS cameras (Strüder et al. 2001).

[6] http://xmm.esa.int/sas/

[7] http://heasarc.gsfc.nasa.gov/xanadu/xspec/

4. MEPL: a composite of a thermal plus a single power law model. The AGN dominates the hard X-rays, but the soft X-rays require an additional thermal contribution. The free parameters in this model are the column densities, $N_{\rm H1}$ and $N_{\rm H2}$, the temperature, kT, the slope of the power law, Γ, and the normalizations, $Norm_1$ and $Norm_2$.
5. ME2PL: a composite of a thermal plus two power law model. This model is like MEPL, but including the contribution of the thermal emission at soft X-rays. This is the Compton-thin Seyfert 2 baseline model used by Guainazzi et al. (2005). The free parameters in this model are the column densities, $N_{\rm H1}$ and $N_{\rm H2}$, the temperature, kT, the slope of the power law, Γ, and the normalizations, $Norm_1$ and $Norm_2$.

For models 2PL, MEPL, and ME2PL we used two absorbers, $N_{\rm H1}$ and $N_{\rm H2}$. These absorbers are included in the models as abs($N_{\rm H1}$)*PL + abs($N_{\rm H2}$)*PL, abs($N_{\rm H1}$)*Mekal + abs($N_{\rm H2}$)*PL, and abs($N_{\rm H1}$)*(PL) + Mekal + abs($N_{\rm H2}$)*PL. The Galactic absoption was included in each model and was fixed to the predicted value (Col. 7 in Table 1) using the NH tool within FTOOLS (Dickey & Lockman 1990; Kalberla et al. 2005). We searched for the neutral iron fluorescence emission line, FeKα, adding a narrow Gaussian with centroid energy fixed at the observed energy corresponding to a rest frame at 6.4 keV. Two Gaussians were also included to model the recombination lines FeXXV at 6.7 keV and FeXXVI at 6.95 keV.

We imposed the following conditions to the resulting best-fit parameters to ensure a physical meaning to the best-fit solutions: $\Gamma > 0.5$, $N_{\rm H1} > N_{\rm Gal}$ and $N_{\rm H2} > N_{\rm H1}$.

We selected as the best fit the spectral fitting with χ^2/d.o.f. closer to unity and an F-test probability lower than 10^{-5} compared with a simpler model (Box 1953). Thus, the best-fit model is the simplest model that represents the data.

4.2. Simultaneous spectral analysis

The aim of this analysis is to detect variability and study the physical parameters governing its pattern for these sources. For that we simultaneously fitted the spectra for each object to the same model. The baseline model for this simultaneous fit was the best fit obtained for the individual fitting of the observations. When the best fit for individual sources did not match all observations, we used the most complex one. For each galaxy, the initial values for the parameters were set to those obtained for the spectrum with the largest number of counts.

The simultaneous fit was made in three steps. First, every spectrum was fitted with the same model and all parameters linked to the same value (SMF0). If this model was able to fit all spectra, the source is not variable. SMF0 was used as the baseline model for the next step otherwise. Second, we let the parameters $N_{\rm H1}$, $N_{\rm H2}$, Γ, $Norm1$, $Norm2$, and kT vary individually (SMF1). Among these we chose the best fit as that with $\chi^2_{\rm r} = \chi^2$/d.o.f. closest to the unity, which improved the SMF0 fit (using the F-test). The result of SMF1 was used as the baseline model for the next step. Finally, we also included the possibility that two parameters could vary together to explain the variability pattern of the sources. For that purpose we fitted each set of data, letting the parameter found as the best fit in SMF1 vary together with any of the other parameters of the fit (SMF2). Again, the $\chi^2_{\rm r}$ and F-test were used to determine whether this additional complexity of the spectral fitting resulted in a significant improvement of the final fit.

The final best fit could be (1) SMF0: the best simultaneous fit with each parameters tied together for all observations (i.e., non-variable source); (2) SMF1: in the best simultaneous fit only one parameter was allowed to vary among the observations; and (3) SMF2: the best simultaneous fit was that with two parameters allowed to vary during the observations.

A higher complexity of the spectral fitting (e.g., three parameters allowed to vary) was not required for our data set (see Sect. 5).

4.2.1. Different appertures

When data from *Chandra* and *XMM-Newton* were used together, an additional analysis was performed to ensure that the extranuclear emission did not produce the observed variability.

First, we extracted a spectrum from *Chandra* data with an aperture radius of 25″. Second, a spectrum of an annular region was extracted from *Chandra* data, whith $R_{\rm ext} = 25''$ and $R_{\rm int} = R_{\rm Chandra}$ (Col. 4 in Table 2). When the contamination by the annular region to the 25″ *Chandra* data emission was higher than 50% in the 0.5–10.0 keV energy band (see Sect. 5), we did not consider the joint analysis since the accuracy of the derived parameters could be seriously affected. For lower contamination levels, we considered that *Chandra* data could be used to estimate the contribution of the annular region to the *XMM-Newton* spectrum. We extracted the *Chandra* spectrum in that ring (from $R_{\rm int}$ to $R_{\rm ext}$) and fitted the five models explained in Sect. 4.1. Then we included the resulting model, with its corresponding parameters frozen, in the fit of the *XMM-Newton* nuclear spectrum (the circular region with $R_{\rm ext}$), and extracted the parameters for the nuclear emission. Appendix B.1 shows the images corresponding to the data used for this analysis, where the different apertures are shown. This analysis was made for all the seven objects with *Chandra* and *XMM-Newton* spectra taken on similar dates.

4.3. Flux variability

We computed X-ray luminosities for the individual and simultaneous fits. UV luminosities were also obtained when possible (see below).

4.3.1. X-ray luminosities

We computed the X-ray luminosities and sigma errors for the soft and hard bands using XSPEC. Note that distances of the sources were taken from NED. We assumed a given object as variable if the luminosity variation was stronger than 3σ and as non-variable when its variations were below 1σ.

4.3.2. UV luminosities

Simultaneous *XMM-Newton* Optical Monitor (OM)[8] data were used to compute the UV luminosities. This monitor has three different filters in the UV range, *UVW2* centered at 1894 Å (1805–2454) Å, *UVM2* centered at 2205 Å (1970–2675) Å, and *UVW1* at 2675 Å (2410–3565) Å. We used these three filters whenever possible.

We used the OM observation FITS source lists[9] to obtain the photometry. We checked that the photometry using IRAF and

---

[8] `http://xmm.esac.esa.int/external/xmm_user_support/documentation\discretionary-/technical/OM/`

[9] `ftp://xmm2.esac.esa.int/pub/odf/data/docs/XMM-SOC-GEN-ICD-0024.pdf`

the Vega magnitude system and calculating the luminosities by using SAS to estimate the count rate gave similar results. When OM data were not available, we searched for UV information in the literature (see Appendix A).

When simultaneous observations from X-rays and UV with *XMM-Newton* were available, we computed the X-ray to UV flux ratio defined as

$$\alpha_{\rm ox} = \frac{\log\left(L_x/L_{\rm UV}\right)}{\log\left(\nu_x/\nu_{\rm UV}\right)}, \tag{1}$$

where $L_{\rm UV}$ were computed from $UVM2$ and $UVW1$ filters and Lx was computed using the integral

$$F_x(0.5\text{–}2.0\ {\rm keV}) = \int_{0.5\ {\rm keV}}^{2.0\ {\rm keV}} F_\nu(2\ {\rm keV})\left(\frac{\nu}{\nu_{2\ {\rm keV}}}\right)^{(1-\Gamma)} {\rm d}\nu, \tag{2}$$

leading to

$$L(2\ {\rm keV}) = \frac{L(0.5\text{–}2.0\ {\rm keV})}{\nu_{2\ {\rm keV}}}\,\frac{2-\Gamma}{1-0.25^{2-\Gamma}}. \tag{3}$$

4.4. Short timescale variability

We analyzed the light curves for each observation to check for variability on short timescales in the sample.

Assuming a constant count rate for the whole observation, we calculated the χ^2/d.o.f. test as a first approximation to the variations. We considered the source to be variable if the count rate differed from the average above 3σ (or 99.7% probability).

To check the variability amplitude of the light curves, we calculated the normalized excess variance, $\sigma^2_{\rm NXS}$. We followed prescriptions given by Vaughan et al. (2003) to estimate $\sigma^2_{\rm NXS}$ and its error, err($\sigma^2_{\rm NXS}$) (see also González-Martín et al. 2011b):

$$\sigma^2_{\rm NXS} = \frac{S^2 - \langle\sigma^2_{\rm err}\rangle}{\langle x\rangle^2} \tag{4}$$

$${\rm err}(\sigma^2_{\rm NXS}) = \sqrt{\frac{2}{N}\left(\frac{\langle\sigma^2_{\rm err}\rangle}{\langle x\rangle^2}\right)^2 + \frac{\langle\sigma^2_{\rm err}\rangle}{N}\,\frac{4\sigma^2_{\rm NXS}}{\langle x\rangle^2}}, \tag{5}$$

where x, $\sigma_{\rm err}$ and N are the count rate, its error and the number of points in the light curve, respectively, and S^2 is the variance of the light curve,

$$S^2 = \frac{1}{N-1}\sum_{i=1}^{N}(x_i - \langle x\rangle)^2. \tag{6}$$

5. Results

5.1. Individual objects

Here we present the results of the variability of the seven sources individually. General results are given in Sect. 5.2. Each subsection describes the following: the observations used in the analysis (Table 2), variations of the hardness ratio (from Col. 8 in Table 2), individual and simultaneous best fit and the parameters varying in the model (see Tables 3–5 and Fig. 1), X-ray flux variations (see Table 6 and Fig. 2), the analysis of the annular region when data of *Chandra* and *XMM-Newton* were used together (Table 7 and Appendix B.1), and the simultaneous fittings of these observations (Table 8), short-term variability from the analysis of the light curves (see Table 9 and Appendices C.1–C.7), and UV luminosities when simultaneous data from the OM monitor was available (Table 10, Fig. 2). Moreover, a summary of the variability is given in Table 11. Notes and comparisons with previous works for individual objects are included in Appendix A.

5.1.1. NGC 1052

We used one *Chandra* and four *XMM-Newton* observations. These four *XMM-Newton* observations were taken from August 2001 to August 2009, and the *Chandra* observation was taken in August 2000 (see Table 2).

Variations of 33% (10%) in HR were obtained between the first and the last *XMM-Newton* (*Chandra*) observations (see Col. 8 in Table 2).

The individual fits gave ME2PL as the best fit. In this case SMF2 was used, because it is the best representation of the observed differences (see Fig. 1) when varying $Norm_2$ and $N_{\rm H2}$ (see Tables 3–5). Variations were 49% ($Norm_2$) and 31% ($N_{\rm H2}$) between the first and the last observations.

In Fig. 2, variations of the soft and hard intrinsic luminosities of the simultaneous fitting are presented. At soft energies we found variations at 8.3σ (20%), and at hard energies at 7.5σ (20%) over a period of eight years. The strongest variation for $Norm_2$ was found between the second and the third observation (see Table 5) with an interval of three years, where both soft and hard luminosities varied by 12% and 29% respectively (see Table 6). The strongest variation for $N_{\rm H2}$ was obtained between the first and the second observation (see Table 5) with a 32% change in four years.

We compared the *Chandra* observation from 2000 with the *XMM-Newton* observation from 2001 (see Fig. B.1), following the prescriptions given in Sect. 4.2.1. The spectral analysis of *Chandra* data was included in Tables 5 and 6, which gave ME2PL as the best fit. The annular region represented a 10% of the 25″ *Chandra* aperture luminosity in the 0.5–10 keV band. The *Chandra* data for the 25″ radius circular region provided intrinsic luminosities representing 22% (75%) for the soft (hard) energy of the emission from *XMM-Newton* data (see Table 6). After taking into account the contribution from the annular region, the analysis indicated no changes in one year period (see Tables 7 and 8) in the nuclear emission.

According to the values of $\chi^2_{\rm r}$ and σ^2 showed in Table 9, the analysis from the light curves did not show short timescale variations (see Fig. C.1), in either the *XMM-Newton* or the *Chandra* data, because variations were below 3σ.

In Fig. 2 UV luminosities (Table 10) are represented for the *UVW2* and *UVM2* filters. Variations at 7.3σ (or 16–25%) and 2σ (or 2–23%) were obtained, respectively.

5.1.2. NGC 3226

We used two *XMM-Newton* observations in November 2000 and December 2006 and one *Chandra* observation from December 1999.

Variations in the HR of 100% were obtained both from the *Chandra* and the *XMM-Newton* data (see Col. 8 in Table 2). However, Obs ID 0400270101 from *XMM-Newton* was not used for the discussion (see below).

The observation from 2000 gave as best fit the 2PL model, while that from 2006 was best fitted with the PL. The simultaneous spectral fitting was better represented by the 2PL model varying $N_{\rm H2}$ (i.e., SMF1, Fig. 1), with a 74% amplitude variation. The resulting parameters (see Tables 5 and 6) indicate

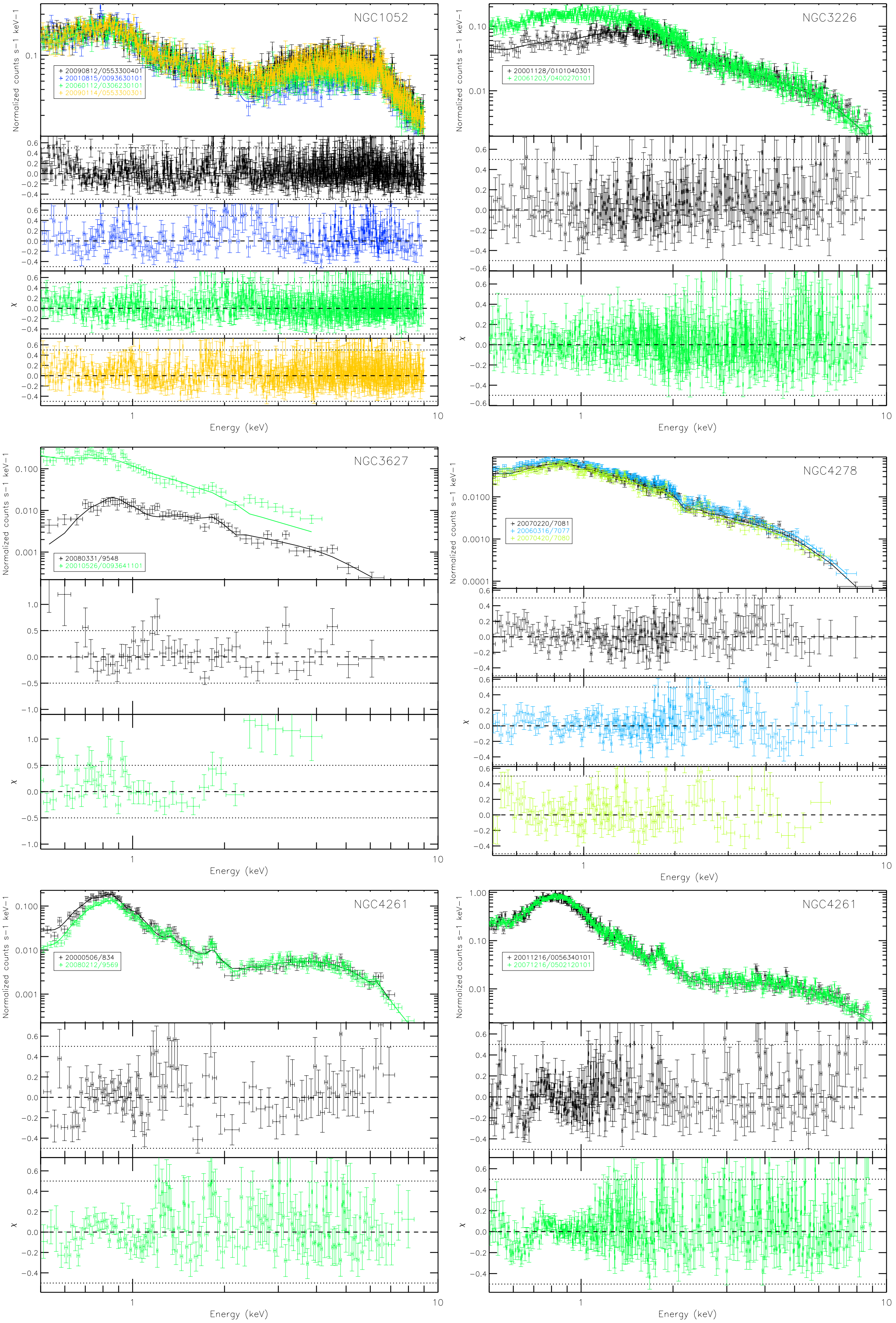

Fig. 1. For each object, all X-ray spectra are plotted together in the first row. Best fits and their residuals are also shown, one row per observation from the second row on. The legends contain the date (in the format yyyymmdd) and the obs ID. Details are given in Table 2.

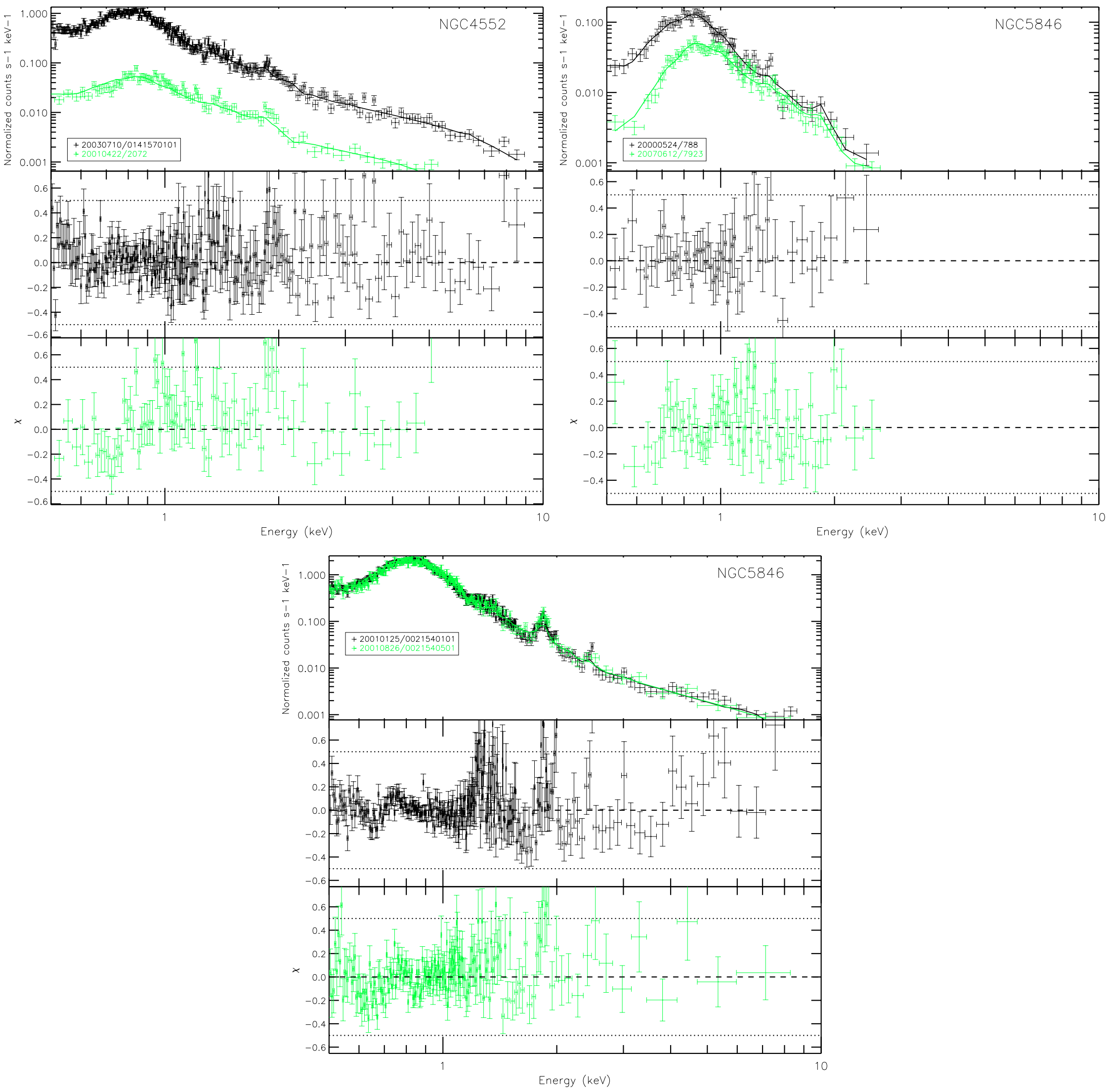

Fig. 1. continued.

that X-ray soft and hard intrinsic luminosity variations were below 1σ over a period of six years.

We compared the *Chandra* observation from 1999 with the *XMM-Newton* observation from 2000. The spectral analysis of *Chandra* data was included in Tables 5 and 6. The contribution from the annular region to the 25″ aperture *Chandra* data was 20% in the 0.5–10.0 keV band. The *Chandra* spectrum extracted with 25″ aperture represented 62% (70%) of the *XMM-Newton* soft (hard) emission (Table 7). When the contribution from the annular region was taken into account, the simultaneous fit resulted in variations of N_{H2} (93%) and $Norm_2$ (57%), with 37% (81%) variations in the soft (hard) energies in a one-year period (Table 8).

We analyzed short timescale variability from individual light curves by calculating χ^2 and σ^2 (see Table 9 and Fig. C.2 (up)). Data from 2006 showed $\chi^2_r = 4.7$ and a normalized excess variance $\sigma_{NXS} = 1.8 \pm 0.1 \times 10^{-2}$, indicating variability (see Fig. C.2, upper-right). However, NGC 3227 is a strongly variable Seyfert 1 located 2′ from NGC 3226. Thus, we analyzed the possibility that NGC 3226 was contaminated by its emission. We extracted a light curve from NGC 3227 and from a circular region between both galaxies close to NGC 3226 (background) and found the same pattern of variability. In Fig. C.2 we present the light curves for the background (middle-left) and NGC 3227 (middle-right), and the *XMM-Newton* image (down). The normalized excess variance for the background light curve was $\sigma_{NXS} = 1.5 \pm 0.5 \times 10^{-2}$. Therefore, we conclude that NGC 3226 might be contaminated by emission from NGC 3227, so its short timescale variability cannot be assessed. Only *UVW1* observations are available from OM (see Table 10 and Fig. 2), with a 10–12% variation (7.4σ).

5.1.3. NGC 3627

We used one *XMM-Newton* observation in May 2001 and another *Chandra* observation in March 2008 (see Table 2). We recall that different apertures (8″ for *Chandra* and 25″ for *XMM-Newton*) were used to extract the nuclear spectrum.

Since observations were obtained with different instruments, comparisons of HR were avoided.

According to χ^2_r, both spectra were individually best-fitted with the MEPL model. The best simultaneous fit implied variations in N_{H2} (Fig. 1), from no absorption to $N_{H2} = 1.28 \times 10^{22}$ cm^{-2} in a seven-year period (i.e., SMF1, Table 5). Even if observed fluxes vary, when computing intrinsic luminosities (see Table 6) for this model we obtained variations below 1σ in

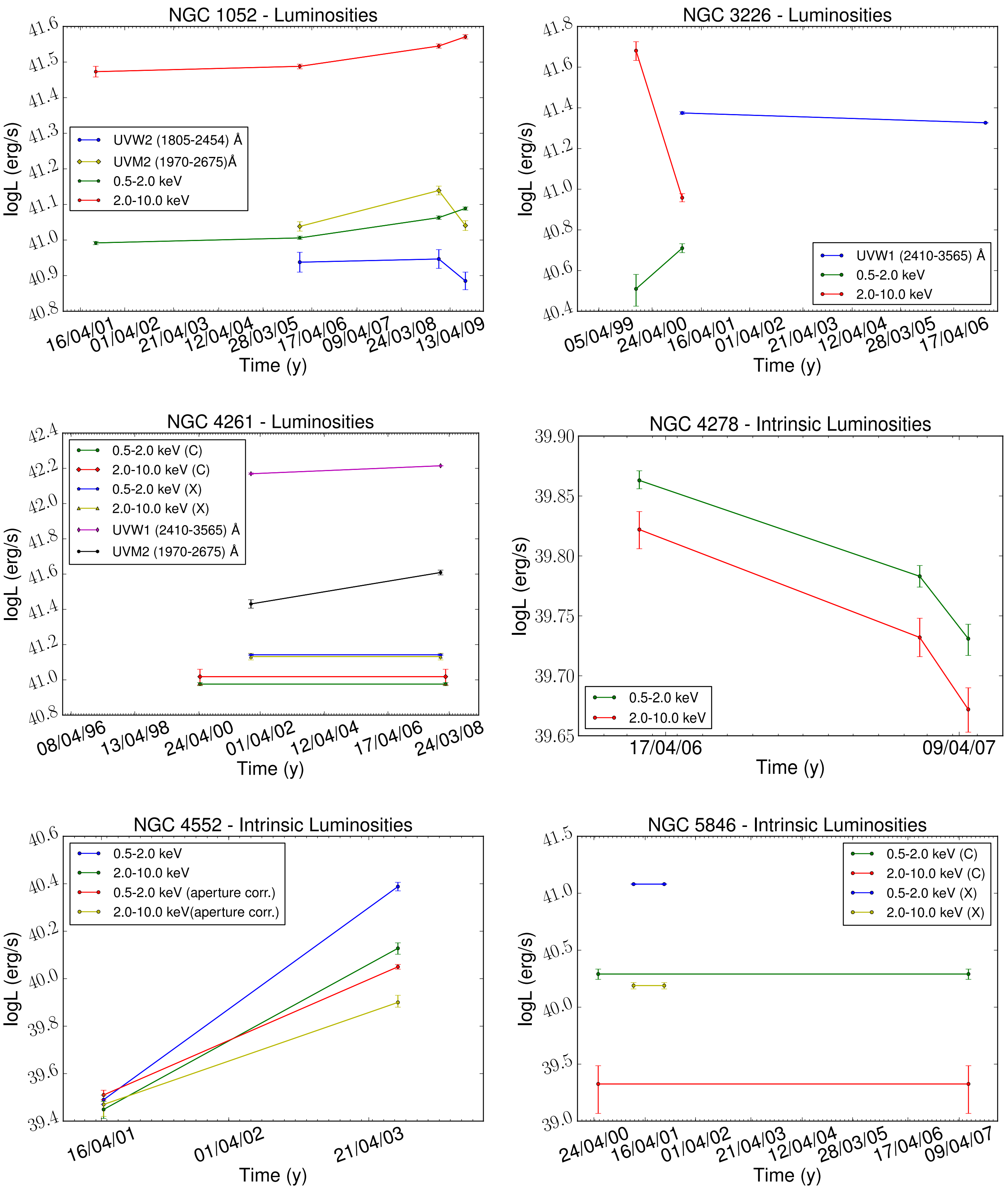

Fig. 2. Intrinsic luminosities calculated for the soft (0.5–2.0 keV) and hard (2.0–10.0 keV) energies in the simultaneous fitting and UV luminosities obtained from the data with the OM camera onboard *XMM-Newton*, when available.

the soft and hard energies, indicating no variations in seven years (Fig. 2).

To compare *Chandra* and *XMM-Newton* data, we carried out the analysis explained in Sect. 4.2.1. The contribution of the annular region to the 25″ aperture *Chandra* spectrum is ∼92% in the 0.5–10 keV band (see Table 7). Thus we assumed that *XMM-Newton* data were strongly contaminated by emission surrounding the nucleus, which avoided the joint use of *Chandra* and *XMM-Newton* data for this object (see Sect. 4.2.1).

The analysis of the light curves did not show short timescale variability (see Table 9 and Fig. C.3), since all measures were below 2σ from the average.

5.1.4. NGC 4261

We used two *Chandra* (May 2000 and February 2008) and two *XMM-Newton* observations (December 2001 and December 2007) for this object. Given the different resolutions in both sets of observations, we first performed the analysis separately (see Table 2).

Variations of 19% and 0% in HR were obtained for *Chandra* and *XMM-Newton*, respectively (from Col. 8 in Table 2).

The best fit for the *Chandra* spectra is the ME2PL model from the individual analysis. The simultaneous fit without allowing to vary any parameter (i.e., SMF0) resulted in a good fit (χ^2/d.o.f. = 1.27). Varying one parameter did not improve the final fit. Therefore, the source seemed to be non-variable (see Table 5 and Fig. 1). X-ray luminosity variations were below 1σ for the soft and the hard bands over a period of eight years (Table 6 and Fig. 2).

The individual analysis of the two observations with *XMM-Newton* again gave the ME2PL model as best fit, and variations in the parameters did not improve the fit (i.e., the best fit was SMF0). Thus, we obtained a non-variable source (Table 5 and Fig. 1). X-ray luminosity variations were below 1σ in a six-year period in this case (Table 6 and Fig. 2).

To compare data from *Chandra* and *XMM-Newton*, the procedure explained in Sect. 4.2.1 was applied to this object. We compared obs ID 9569 from *Chandra* and obs ID 0502120101 from *XMM-Newton* data (Fig. B.1) since they are the closest in time. The contribution of the emission from the annular region was 37% in the 0.5–10 keV band emission in the 25″ aperture *Chandra* data. Intrinsic luminosities of the 25″ aperture *Chandra* spectrum represented 37% (66%) of the soft (hard) emission from *XMM-Newton* data. The simultaneous fit between these data taking into account the annular contribution resulted in a non-variable object (Table 8).

To check for short timescale variability we analyzed the light curves for each observation (see Table 9 and Fig. C.4). No short time variability was detected for this object, since all measurements were below 2σ from the average.

Considering the UV range (Table 10), the variations amounted to 9–11% (10.3σ) in the *UVW1* filter and 28–39% (9.3σ) in the *UVM2* filter (see Fig. 2).

5.1.5. NGC 4278

We only used three of the nine observations taken by *Chandra* in March 2006, February 2007, and April 2007, and the *XMM-Newton* observation in May 2004 (Table 2).

HR variations amounted to 4% for the runs with useful spectroscopic *Chandra* data. Taking into account all observations from *Chandra*, 40% HR variations were found between 2000 and 2010 (from Col. 8 in Table 2).

Our best fit for *Chandra* data was the MEPL model with $Norm_2$ varying (i.e., SMF1, see Fig. 1). This parameter varied by 30% between the first and the last observation (about one year apart) (Table 5). X-ray intrinsic luminosity variations (Table 6) were within 11.2σ (9.6σ) for the soft (hard) energies. This corresponded to variation amplitudes of 26% (29%, see Fig. 2). It is remarkable that the flux varied by 11% (13%) between the second and third observations (two months apart), with a 13% variation in $Norm_2$ for the same period (Tables 5 and 6).

We compared the *XMM-Newton* observation in 2004 with the *Chandra* observation in 2006, which is the closest in time (see Fig. B.1). We applied the procedure explained in Sect. 4.2.1. The spectral analysis of *XMM-Newton* spectrum, included in Tables 5 and 6, gave the PL as the best-fit model. The contribution of the annular region is 38% in the 0.5–10.0 keV band to the emission in the 25″ aperture *Chandra* data. The *Chandra* spectrum extracted with 25″ aperture represented 25% (20%) of the soft (hard) *XMM-Newton* emission. When the contribution of the annular region was taken into account, the resulting Γ agreed with that from *XMM-Newton* data (see Table 7). The simultaneous fit shows 15% of variations in the normalization of the PL along two years (Table 8).

The analysis of the light curves (see Table 9 and Fig. C.5) did not show short timescale variability, either in *Chandra* or in *XMM-Newton* data.

5.1.6. NGC 4552

We used a *Chandra* observation taken in April 2001 and an *XMM-Newton* observation taken in July 2003. We recall that different apertures were used (3″ for *Chandra* and 25″ for *XMM-Newton* data).

Since observations were obtained with different instruments, comparisons of HR were avoided.

Both observations needed MEPL for the individual best fit. When varying parameters, the best fit was obtained when $Norm_1$ and $Norm_2$ varied (i.e., SMF2, χ^2_r = 1.21, see also Fig. 1), with 93% and 78% amplitude variations (see Table 5). We found intrinsic luminosity variations at 21.5σ (14.1σ) in the soft (hard) energies, i.e., 87% (79%) amplitude variations in a period of two years (Table 6).

The *Chandra* image of this object revealed many X-ray sources surrounding the nucleus (see Fig. B.1). The contribution of the annular region to the 0.5–10.0 keV band emission in the 25″ aperture *Chandra* data was 23%. Extraction from *Chandra* data with 25″ aperture resulted in a 72% (60%) emission of the soft (hard) *XMM-Newton* data. The simultaneous fit resulted in a variable object, where $Norm_1$ (21%) and $Norm_2$ (37%) varied, with 29% (37%) flux variations in the soft (hard) energies (see Fig. 2 and Table 8).

No short timescale variations were found (see Table 9 and Fig. C.6).

5.1.7. NGC 5846

We used two observations from *XMM-Newton* (January and August 2001) and other two observations from *Chandra* (May 2000 and June 2007). The analysis was first made separately because of the different apertures (see Table 2).

HR Variations of 1% and 6% were obtained for *XMM-Newton* and *Chandra* data, respectively (from Col. 8 in Table 2).

For the *Chandra* observations, we only made the analysis up to 3 keV because of the low count-rate at hard energies. In this case SMF0 was used, resulting in a non-variable source when fitting the MEPL model (Table 5 and Fig. 1) with flux variations below 1σ during a period of seven years (Table 6 and Fig. 2). The *XMM-Newton* data did not show variability (the best-fit model is MEPL, see Table 5 and Fig. 1), and flux variations below 1σ on the soft and hard energies for a period of seven months (Table 6).

The contribution to the 0.5–10.0 keV band emission from the 25″ aperture *Chandra* data was 73% from the annular region, which avoided the joint use of *Chandra* and *XMM-Newton* data for this object. No short timescale variability was found for this object (see Table 9 and Fig. C.7). The availability of UV data for a single epoch precludes any attempt to gain information on its variability.

5.2. Spectral variability

A rough description of the spectral shape is provided by HR. Consequently, a first approximation of the spectral variations can be obtained from the variation of HR. The use of HR allows including observations whose number of counts are not enough for a proper spectral fitting. Because the calculation of HR is based on number counts, we only used data coming from the same instrument for comparisons. We considered that variations greater than 20% (2σ error) in HR may correspond to variable objects (NGC 1052, NGC 3226, and NGC 4278). Note that variations in HR weaker than 20% can be found in variable objects, because the variations in soft and hard energies may have different signs and somewhat average each other out in the final calculation of HR.

The individual fitting of each observation revealed that composite models (2PL, MEPL or ME2PL) were needed in all cases. A thermal component was used in six objects, all of them with $kT \approx 0.60$ keV.

We fitted all available data for the same object and model, varying different parameters to obtain information on the variability pattern. Figure 1 shows the best fit (top panel) with the residuals of the individual observations (bottom panels). To analyze the data from *Chandra* and *XMM-Newton* data jointly, we estimated the influence of extra-nuclear emission on the results (see Sect. 4.2.1). For two objects (NGC 3627 and NGC 5846) the contamination by emission surrounding the nucleus in *XMM-Newton* data was so high (up to 50%) that we avoided the comparisons in these cases. For the remaining five sources (NGC 1052, NGC 3226, NGC 4261, NGC 4278, and NGC 4552), the joint analysis was attempted.

Two objects are compatible with being non-variable sources, namely NGC 4261 and NGC 5846. For these two objects the same conclusion is reached if we isolate the analysis of *Chandra* and *XMM-Newton* data, both with similar spectral parameters (see Table 5). Moreover, NGC 3627 was no longer used for the discussion, since contamination prevents any variability analysis. Four objects are variable, NGC 1052, NGC 3226, NGC 4278, and NGC 4552. NGC 1052 and NGC 3226 showed variations in N_{H2} (31% and 93%) and $Norm_2$ (49% and 57%) (in eight and one years), while NGC 4278 showed changes in $Norm_2$ (30%) (in three years). NGC 4552 showed variations in $Norm_1$ (21%) and $Norm_2$ (37%) in a two-year period. All variations occur at hard energies and are related to the absorber and/or to the nuclear power. Even if the small number of sources precludes any statistical characterization, there does not seem to exist any clear relation with either the LINER type (1 or 2) or to the Eddington ratios (see Table 11). A larger sample of LINERs is needed to search for any variability pattern to be eventually more frequently observed than others.

5.3. Flux variability

X-ray soft and hard luminosities (see Table 6) are shown in Fig. 2. Two objects are compatible with no variations of the central engine (NGC 4261, and NGC 5846). Four sources are compatible with being variable, NGC 1052 with 20% variations in both bands, NGC 3226 with 37% (81%) variations in the soft (hard) band, NGC 4278 with 26% (29%) variations in the soft (hard), and NGC 4552 with 29% (37%) variations in the soft (hard) band. Sources showing flux variability in the soft and hard bands also showed spectral variability (see Sect. 5.2).

We also studied the UV variability for the sources by studying UV and X-ray data obtained simultaneously with *XMM-Newton* (available for three galaxies). All of them are variable at UV frequencies (see Table 10 and Fig. 2). *XMM*-OM provided UV fluxes at three epochs for NGC 1052; ~20% variations were obtained with the filters $UVW2$ and $UVM2$. NGC 3226 was observed with the filter $UVW1$, showing 11% variation. NGC 4261 was observed with the filters $UVW1$ and $UVM2$, with 10% and 33% variations, respectively. Two objects, NGC 1052 and NGC 3226, showed UV and spectral variability, while another one, NGC 4261, showed UV variability but no spectral variability.

5.4. Light curves

Table 9 provides the values for χ^2_r (and the probability of variability) and the $\sigma^2_{\rm NXS}$. Objects are considered to be variable when the count rates are different 3σ from the average. No short-term variability (from hours to days) was found in our sample[10].

6. Discussion

We have performed an X-ray spectral analysis to search for variability in seven LINER nuclei, three type 1.9 (NGC 1052, NGC 3226, and NGC 4278) and four type 2 (NGC 3627, NGC 4261, NGC 4552, and NGC 5846). We used data from *Chandra* and *XMM-Newton* satellites with observations at different epochs. Whenever possible, we made the analysis separately for each instrument to avoid corrections due to different apertures. The results obtained for the long-term variability of NGC 3627 will not be used for the discussion (see Sect. 5.1.3).

Our main results are the following:

- Short-term variability: No variations were found on timescales from hours to days.
- Long-term variability: Four out of the six objects (NGC 1052, NGC 3226, NGC 4278, and NGC 4552) were variable in X-rays on timescales from months to years. The shortest variation is found for NGC 4278 on timescales of two months. Simultaneous observations in the UV for three objects (NGC 1052, NGC 3226, and NGC 4261) revealed variations on timescales of years.
- Main driver for the variability: Among the variable sources, NGC 4278 presented variations in Norm$_2$, NGC 4552 in Norm$_1$ and Norm$_2$, and NGC 1052 and NGC 3226 in N_{H2} and Norm$_2$. In all variable LINERs variations occur at hard energies.

6.1. Short and long timescale variability

In our sample of LINERs we analyzed variability from hours to days (short-term) from the analysis of the light curves for each observation (see Col. 6 in Table 2), and from months to years (long-term) from the simultaneous fitting of the different observations (see Col. 10 in Table 11).

Concerning short timescales, Pian et al. (2010) studied four type 1 LINERs and found variations of 30% in a half a day in NGC 3998, and 30% variations in the hard (1–10 keV) X-rays in ~3 h in M 81. The other two sources in their sample

---

[10] Note that we did not take into account obs ID 0400270101 from NGC 3226 (see Sect. 5.1.2).

(NGC 4203 and NGC 4579) showed no short timescale variability. The power spectral density (PSD) profiles of the 14 LINERs included in the sample of 104 AGN in González-Martín & Vaughan (2012), showed no short-term variability except for two objects (3C 218 and NGC 3031). All these studies suggest that about 20% of LINERs show short timescale variability. This percentage approaches zero in our own study, since none of our seven sources showed short timescale variability, according to the χ^2_r and the normalized excess variance, $\sigma^2_{\rm NXS}$, (see Table 9). Younes et al. (2010) found variability in ~1.5 h for NGC 4278 on the *XMM-Newton* observation, where the flux increased by 10%. Using the same observation, we found a 3% flux increase in the same period, and a null probability of being a variable source. The difference is most probably due to the different appertures used in the analysis. Adding all studied LINERs from this and previous papers, the percentage of variable LINERs at short timescales is 16%.

Long-term spectral variability is clearly found for four objects in our sample. NGC 1052 needed variations in $N_{\rm H2}$ (49%) and Norm$_2$ (31%) in a period of eight years, NGC 3226 also varied $N_{\rm H2}$ (93%) and Norm$_2$ (57%) in a period of one year, NGC 4278 varied Norm$_2$ (30%) in a period of one year, and NGC 4552 varied Norm$_1$ (21%) and Norm$_2$ (37%) in two years.

Long-term variability is common among LINERs. Younes et al. (2011) studied a sample of type 1 LINERs, where seven out of nine sources showed long-term variability (i.e., months and/or years). Two of their objects are in common with our sample, NGC 3226 and NGC 4278. We found similar spectral characteristics and the same parameters varying for both objects. For NGC 3226, they found that $N_{\rm H}$ varied by 72% and Norm varied by 48% when fitting a simple power law. This is similar to our results, although we used two absorbers instead of one. They found flux variations of 49% (46%) in the soft (hard) band between the *Chandra* and *XMM-Newton* observations, while we found 37% (81%), the differences most probably due to the different models used. For NGC 4278 they used seven public observations from the archive, while we only used three. Despite this, the same spectral variation was found (Norm$_2$). Younes et al. (2010) found for NGC 4278 a 31% (20%) variation at soft (hard) energies, where we found 26% (29%) variation for the same observations. Pian et al. (2010) found long-term variability in two of their four type 1 LINERs using *Swift* data. Therefore, long-term variability is found in ~65% of the LINERs, significantly more than that of LINERs at short timescales.

Three types of long-term X-ray variability patterns have been found in our sample: (1) variations in the soft excess (NGC 4552); (2) variations of the obscuring matter (NGC 1052 and NGC 3226); and (3) variations of the intrinsic source (NGC 1052, NGC 3226, NGC 4278, and NGC 4552). As for NGC 4552, variations at soft energies have already been reported in the literature for the type 2 LINER NGC 4102 (González-Martín et al. 2011a). This behavior is seen in type 1 Seyferts, where absorption variations are related to a partially ionized, optically thin material along the line of sight to the central source, the so-called warm absorber (Reynolds 1997; Petrucci et al. 2013). The variations due to the $N_{\rm H}$ of the X-ray absorbing gas that we see in two sources are well established for many famous type 2 Seyferts. These variations are thought to be related to the motion of clouds perpendicular to the line of sight of the observer to the AGN. These clouds produce partial eclipses of the AGN over time. In some cases, the fast movement of the clouds places them at the distance of the BLR, although in other cases the clouds seem to be located at farther distances (few parsecs) from the AGN (e.g. NGC 1365 Risaliti 2002; Risaliti et al. 2007, 2010; Braito et al. 2013). The timescale of the $N_{\rm H}$ variations in our sample are consistent with this latter scenario. The most common pattern of variability among the LINERs in our sample (four cases) is the change on the intrinsic continuum of the source. McHardy et al. (2006) found that the timescale of the intrinsic variability increases for larger masses of the black hole and/or lower bolometric luminosities for objects whose variability is related to the nuclear power[11]. According to the revised relation between the BH mass, bolometric luminosities and timescales of variations, González-Martín & Vaughan (2012) predicted that LINERs (with $M_{\rm BH} \sim 10^{8-9}\ M_{\odot}$) do not vary on timescales shorter than tens of days. Applying their formula to our four objects, predicted values for NGC 1052, NGC 3226, NGC 4278, and NGC 4552 were 13.3, 28.2, 118.0, and 449.9 days (see Table 11 for the values of $M_{\rm BH}$ and $L_{\rm bol}$), that is, timescales of days, months, and years were expected for these objects. This agrees with our results for NGC 4278 and NGC 4552. Unfortunately, we have no observations within days for NGC 1052 and NGC 3226, we were only able to search for variations on timescales from months to years. Moreover, for NGC 1052, NGC 3226, and NGC 4552 coupled variations[12] were obtained. A study of a larger sample of LINERs is required to constrain the timescale of the intrinsic variability for these sources and be able to understand whether LINERs match in the same scenario as more powerful AGN.

A first approximation of the variations can be obtained by analyzing the hardness ratios. We considered differences in HR larger than 20% as a measure of spectral variation. For NGC 1052, HR varied 33% between the first and last *XMM-Newton* observations and no variation was found for HR over the five-year period observed by *Chandra*. These results are compatible with flux variations obtained when analyzing *XMM-Newton* data. NGC 3226 presents HR differences over 100% in *Chandra* data. For NGC 4278 total HR variations amount to 40% when using all available *Chandra* data, although the results from the *Chandra* data used for spectral analysis appear to be compatible with no variations. NGC 4261 and NGC 5846 are compatible with being non-variable objects, both with *XMM-Newton* and *Chandra* data, and with both analyses, spectroscopic and HR. NGC 4261 shows HR differences of 19%, which seem to be compatible with the flux variations obtained through the individual analysis of the source.

Variability among LINERs is not restricted to X-rays. Maoz et al. (2005) was the first to show variability at UV frequencies in LINER galaxies, where all but three objects in their sample of 17 LINERs of type 1 and 2 were variable. From the literature, we found different studies for the LINERs in our sample using HST data (see Appendix A for details). Cappellari et al. (1999) studied FOC data for NGC 4552, and found a factor 4.5 brightening between 1991 and 1993 (filter $F342W$), followed by a factor ~2 dimming between 1993 and 1996 (filters $F175W$, $F275W$ and $F342W$). Maoz et al. (2005) studied both NGC 1052 and NGC 4552, concluding that both of them were variable on timescales of years. NGC 4278 was studied by Cardullo et al. (2008), who found a luminosity increase of a factor 1.6 over six months. UV data were not available for the remaining two objectsin our sample (NGC 3627 and

---

[11] Although the dependence on the bolometric luminosity does not seem to be so strong according to González-Martín & Vaughan (2012).

[12] Variations are needed for more than one parameter in the spectral fitting.

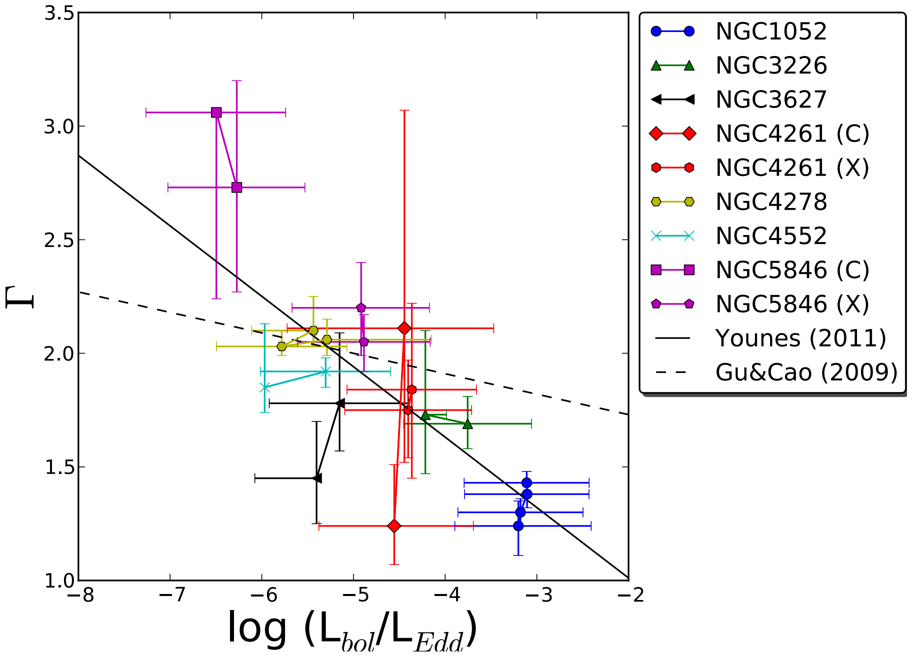

Fig. 3. Anticorrelation between the spectral index, Γ from individual fits, vs. the Eddington ratio, $\log(L_{\rm bol}/L_{\rm Edd})$, for our sample galaxies. The solid line represents the relation given by Younes et al. (2011), while the dashed line represents that by Gu & Cao (2009), both shifted to the same bolometric correction (see text).

NGC 5846). Thus, from the seven LINERs in our sample five seem to be variable at UV frequencies. Simultaneous X-rays and UV data were obtained from *XMM-Newton* data for three objects (NGC 1052, NGC 3226, and NGC 4261), all showing variability, whereas intrinsic variations in X-rays were not found for NGC 4261. A possible explanation for this source's non-simultaneous X-ray and UV variation could be time lags in both frequencies. Time lag explanations have previously been reported for the NLSy1 galaxy NGC 4051 by Alston et al. (2013). Repeated simultaneous observations at X-rays and UV frequencies are required to verify this model.

6.2. Accretion mechanism

It has been suggested in the literature that the accretion mechanism in low-luminosity active galactic nuclei (LLAGN) is different from that in more powerful AGN (e.g., Seyferts), and more similar to that in X-ray binaries (XRB) in their low/hard state (Yamaoka et al. 2005; Yuan et al. 2007; Gu & Cao 2009; Younes et al. 2011; Xu 2011). The X-ray emission is supposed to originate from the Comptonization process in advection-dominated accretion flow (ADAF), where accretion is inneficient for $L_{\rm bol}/L_{\rm Edd} < 10^{-3}$. At low accretion rates, the infalling material may never cool sufficiently to collapse into a thin disk (as is the case for efficient radiation), and an advection-dominated flow from the outermost radius down to the black hole could be formed (Narayan & Yi 1994). In powerful AGN a positive correlation between the hard X-ray photon index, Γ, and the Eddington ratio, $L_{\rm bol}/L_{\rm Edd}$ was found by Shemmer et al. (2006), who argued that the hard X-ray photon index depends primarily on the accretion rate. In contrast, according to the results provided by Mahadevan (1997), the lower the accretion rate, the less efficient is the cooling by Comptonization and the X-ray region of the spectrum becomes softer and reaches lower luminosities. In this case a negative correlation between these magnitudes has been found for LLAGN (Gu & Cao 2009; Younes et al. 2011) and also for XRB. We present these parameters for each individual observation in our sample of LINERs in Fig. 3, where the negative correlation is shown. $\log(L_{\rm bol}/L_{\rm Edd})$ were calculated following the formulation given in Eracleous et al. (2010), using $L_{\rm bol} = 33L_{2-10\ \rm keV}$. We corrected the equation given by Younes et al. (2011) by this factor (they used $L_{\rm bol} = 16L_{2-10\ \rm keV}$) and plotted it as a solid line. Our results are consistent with the correlation given by Younes et al. (2011) for their sample of type 1 LINERs. Emmanoulopoulos et al. (2012) found for the first time a "harder when brighter" (i.e., higher luminosities for harder spectra) X-ray behavior for the LLAGN NGC 7213, where they found variations in Γ. However, we did not find this behaviour for any of the sources in our sample, Fig. 3 showing the consistency of our simultaneous fittings with no variations in Γ.

We also computed the X-ray-to-UV-flux ratio, $\alpha_{\rm ox}$ (see Sect. 4.3.2). We calculated these values for all sources with simultaneous observations at X-ray and UV (see Table 10), obtaining values of $\alpha_{\rm ox}$ between [–0.81, –1.66], in good agreement with previous studies (Maoz 2007; Younes et al. 2012). Although they are similar to the $\alpha_{\rm ox}$ given for powerful AGN, these values were slightly lower (Maoz 2007). This may indicate the lack or absence of the "big blue bump".

When $\alpha_{\rm ox}$ could be calculated more than once (NGC 1052 and NGC 4261), no variations were found within the errors.

Another indication of a different emission process between powerful AGN and LINERs could be the positive correlation found by Younes et al. (2012) between $\alpha_{\rm ox}$ and $\log(L_{\rm bol}/L_{\rm Edd})$, in contrast with the anticorrelation found for powerful AGN. To compare the results from Younes et al. (2012) and ours, we recalculated $\log(L_{\rm bol}/L_{\rm Edd})$ for the sample in Younes et al. (2012) following the relation given by Eracleous et al. (2010) and using the data from Younes et al. (2011). In Fig. 4 we plot this relation (see Table 10), where the symbols used for the sources from Younes et al. (2012) are stars. The results agree well, indicating a correlation between $\alpha_{\rm ox}$ and $\log(L_{\rm bol}/L_{\rm Edd})$. Younes et al. (2012) suggested that this behavior can be understood within the framework of radiatively inefficient accretion flow models, such as ADAF.

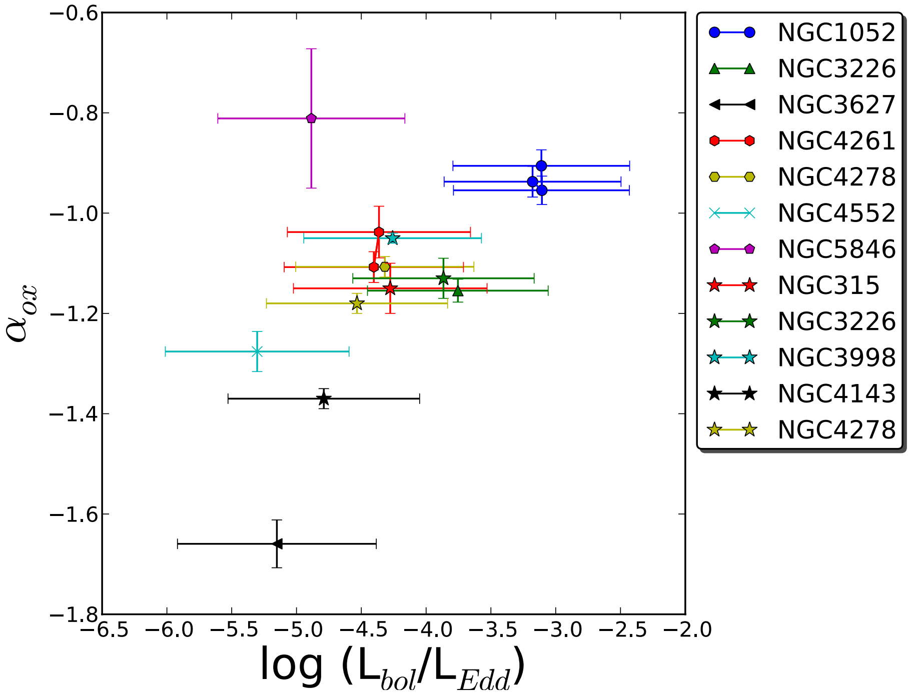

Fig. 4. Correlation between the X-ray to UV flux ratio, α_{ox}, vs. the Eddington ratio, $\log(L_{\mathrm{bol}}/L_{\mathrm{Edd}})$. Star symbols correspond to the sources in Younes et al. (2012).

7. Conclusions

A spectral variability analysis of seven LINER nuclei was performed using public data from *Chandra* and *XMM-Newton*. The main conclusions of this paper can be summarized as follows:

1. Variations greater than 20% in the hardness ratio always correspond to objects showing spectral variability.
2. Individual fits of each observation provided composite models as the best fit (2PL, MEPL, and ME2PL).
3. No short timescale variability was found, in agreement with predictions.
4. Spectral X-ray variability was found in four out of six objects. In all of them variations occurred at hard energies due to the absorber and/or the nuclear source, and variations in the soft energy were found only in NGC 4552. These variations occur on timescales of months and/or years. The shortest timescale was found for NGC 4278, with variations of two months.
5. We found an anticorrelation between the X-ray spectral index, Γ, and the Eddington ratio, $L_{\mathrm{bol}}/L_{\mathrm{Edd}}$. We also found a correlation between the X-ray to UV flux ratio, α_{ox}, and the Eddington ratio, $L_{\mathrm{bol}}/L_{\mathrm{Edd}}$. Both relations are compatible with inefficient flows being the origin of the accretion mechanism in these sources.

Acknowledgements. We thank the anonymous referee for his/her helpful comments that helped to improve the paper, T. Mahoney for reviewing the English, J. Perea for help with the statistical analysis and the AGN group at the IAA for helpful comments during this work. This work was financed by MINECO grant AYA 2010-15169, Junta de Andalucía TIC114 and Proyecto de Excelencia de la Junta de Andalucía P08-TIC-03531. L.H.G. acknowledges financial support from the Ministerio de Economía y Competitividad through the Spanish grant FPI BES-2011-043319. O.G.M. thanks Spanish MINECO through a Juan de la Cierva Fellowship. This research made use of data obtained from the *Chandra* Data Archive provided by the *Chandra* X-ray Center (CXC). This research made use of data obtained from the *XMM-Newton* Data Archive provided by the *XMM-Newton* Science Archive (XSA). This research made use of the NASA/IPAC extragalactic database (NED), which is operated by the Jet Propulsion Laboratory under contract with the National Aeronautics and Space Administration.

References

Alston, W. N., Vaughan, S., & Uttley, P. 2013, MNRAS, 429, 75
Antonucci, R. 1993, ARA&A, 31, 473
Binder, B., Markowitz, A., & Rothschild, R. E. 2009, ApJ, 691, 431
Birkinshaw, M., & Davies, R. L. 1985, ApJ, 291, 32
Boroson, B., Kim, D.-W., & Fabbiano, G. 2011, ApJ, 729, 12
Box, G. E. P. 1953, Biometrika, 40, 318
Braito, V., Ballo, L., Reeves, J. N., et al. 2013, MNRAS, 428, 2516
Brassington, N. J., Fabbiano, G., Kim, D.-W., et al. 2009, ApJS, 181, 605
Brenneman, L. W., Weaver, K. A., Kadler, M., et al. 2009, ApJ, 698, 528
Brightman, M., & Nandra, K. 2011, MNRAS, 413, 1206
Caballero-Garcia, M. D., Papadakis, I. E., Nicastro, F., & Ajello, M. 2012, A&A, 537, A87
Cappellari, M., Renzini, A., Greggio, L., et al. 1999, ApJ, 519, 117
Cardullo, A., Corsini, E. M., Beifiori, A., Pizzella, A., & Buson, L. M. 2008, in Formation and Evolution of Galaxy Disks, eds. J. G. Funes, & E. M. Corsini, ASP Conf. Ser., 396, 53
Carollo, C. M., Franx, M., Illingworth, G. D., & Forbes, D. A. 1997, ApJ, 481, 710
Dickey, J. M., & Lockman, F. J. 1990, ARA&A, 28, 215
Donato, D., Sambruna, R. M., & Gliozzi, M. 2004, ApJ, 617, 915
D'Onofrio, M., Marziani, P., & Sulentic, J. W. 2012, Fifty Years of Quasars: Current Impressions and Future Perspectives, 549
Dopita, M. A., & Sutherland, R. S. 1995, ApJ, 455, 468
Dudik, R. P., Satyapal, S., Gliozzi, M., & Sambruna, R. M. 2005, ApJ, 620, 113
Emmanoulopoulos, D., Papadakis, I. E., McHardy, I. M., et al. 2012, MNRAS, 424, 1327
Eracleous, M., Hwang, J. A., & Flohic, H. M. L. G. 2010, ApJS, 187, 135
Evans, D. A., Hardcastle, M. J., Croston, J. H., Worrall, D. M., & Birkinshaw, M. 2005, MNRAS, 359, 363
Ferrarese, L., Ford, H. C., & Jaffe, W. 1996, ApJ, 470, 444
Ferrarese, L., Ford, H. C., Huchra, J., et al. 2000, ApJS, 128, 431
Filho, M. E., Fraternali, F., Markoff, S., et al. 2004, A&A, 418, 429
Garmire, G. P., Bautz, M. W., Ford, P. G., Nousek, J. A., & Ricker, J. G. R. 2003, in SPIE Conf. Ser., eds. J. E. Truemper, & H. D. Tananbaum, 4851, 28
George, I. M., Mushotzky, R. F., Yaqoob, T., et al. 2001, ApJ, 559, 167
Gliozzi, M., Sambruna, R. M., & Brandt, W. N. 2003, A&A, 408, 949
Gondoin, P., Orr, A., & Siddiqui, H. 2004, A&A, 420, 905
González-Martín, O., & Vaughan, S. 2012, A&A, 544, A80
González-Martín, O., Masegosa, J., Márquez, I., & Guainazzi, M. 2009a, ApJ, 704, 1570
González-Martín, O., Masegosa, J., Márquez, I., Guainazzi, M., & Jiménez-Bailón, E. 2009b, A&A, 506, 1107
González-Martín, O., Papadakis, I., Braito, V., et al. 2011a, A&A, 527, A142

González-Martín, O., Papadakis, I., Reig, P., & Zezas, A. 2011b, A&A, 526, A132
Grier, C. J., Mathur, S., Ghosh, H., & Ferrarese, L. 2011, ApJ, 731, 60
Gu, M., & Cao, X. 2009, MNRAS, 399, 349
Guainazzi, M., Matt, G., & Perola, G. C. 2005, A&A, 444, 119
Heckman, T. M. 1980, A&A, 87, 152
Ho, L. C. 2008, ARA&A, 46, 475
Ho, L. C., Filippenko, A. V., & Sargent, W. L. W. 1993, ApJ, 417, 63
Ho, L. C., Filippenko, A. V., Sargent, W. L. W., & Peng, C. Y. 1997, ApJS, 112, 391
Ho, L. C., Feigelson, E. D., Townsley, L. K., et al. 2001, ApJ, 549, L51
Kalberla, P. M. W., Burton, W. B., Hartmann, D., et al. 2005, A&A, 440, 775
Krolik, J. H. 1999, Active galactic nuclei: from the central black hole to the galactic environment
Mahadevan, R. 1997, ApJ, 477, 585
Maoz, D. 2007, MNRAS, 377, 1696
Maoz, D., Nagar, N. M., Falcke, H., & Wilson, A. S. 2005, ApJ, 625, 699
Márquez, I. 2012, in Fifty Years of Quasars: From Early Observations and Ideas to Future Research, eds. M. D'Onofrio, P. Marziani, J. W. Sulentic, Astrophys. Space Sci. Lib. (Springer)
Masegosa, J., Márquez, I., Ramirez, A., & González-Martín, O. 2011, A&A, 527, A23
McHardy, I. M., Koerding, E., Knigge, C., Uttley, P., & Fender, R. P. 2006, Nature, 444, 730
Moellenhoff, C., Hummel, E., & Bender, R. 1992, A&A, 255, 35
Nagar, N. M., Falcke, H., & Wilson, A. S. 2005, A&A, 435, 521
Narayan, R., & Yi, I. 1994, ApJ, 428, L13
Panessa, F., Bassani, L., Cappi, M., et al. 2006, A&A, 455, 173
Panessa, F., de Rosa, A., Bassani, L., et al. 2011, MNRAS, 417, 2426
Pellegrini, S., Wang, J., Fabbiano, G., et al. 2012, ApJ, 758, 94
Peterson, B. M. 1997, An Introduction to Active Galactic Nuclei, ed. B. M. Peterson
Petrucci, P.-O., Paltani, S., Malzac, J., et al. 2013, A&A, 549, A73
Pian, E., Romano, P., Maoz, D., et al. 2010, MNRAS, 401, 677
Pogge, R. W., Maoz, D., Ho, L. C., & Eracleous, M. 2000, ApJ, 532, 323
Ptak, A., Yaqoob, T., Mushotzky, R., Serlemitsos, P., & Griffiths, R. 1998, ApJ, 501, L37
Reynolds, C. S. 1997, MNRAS, 286, 513
Rinn, A. S., Sambruna, R. M., & Gliozzi, M. 2005, ApJ, 621, 167
Risaliti, G. 2002, A&A, 386, 379
Risaliti, G., Maiolino, R., & Bassani, L. 2000, A&A, 356, 33
Risaliti, G., Elvis, M., Fabbiano, G., et al. 2007, ApJ, 659, L111
Risaliti, G., Elvis, M., Bianchi, S., & Matt, G. 2010, MNRAS, 406, L20
Risaliti, G., Nardini, E., Salvati, M., et al. 2011, MNRAS, 410, 1027
Sambruna, R. M., Gliozzi, M., Eracleous, M., Brandt, W. N., & Mushotzky, R. 2003, ApJ, 586, L37
Satyapal, S., Sambruna, R. M., & Dudik, R. P. 2004, A&A, 414, 825
Satyapal, S., Dudik, R. P., O'Halloran, B., & Gliozzi, M. 2005, ApJ, 633, 86
Schmidt, M. 1963, Nature, 197, 1040
Shemmer, O., Brandt, W. N., Netzer, H., Maiolino, R., & Kaspi, S. 2006, ApJ, 646, L29
Strüder, L., Briel, U., Dennerl, K., et al. 2001, A&A, 365, L18
Terashima, Y., & Wilson, A. S. 2003, ApJ, 583, 145
Terlevich, R., & Melnick, J. 1985, MNRAS, 213, 841
Tonry, J. L., Dressler, A., Blakeslee, J. P., et al. 2001, ApJ, 546, 681
Trinchieri, G., & Goudfrooij, P. 2002, A&A, 386, 472
Urry, C. M., & Padovani, P. 1995, PASP, 107, 803
Vaughan, S., Edelson, R., Warwick, R. S., & Uttley, P. 2003, MNRAS, 345, 1271
Veilleux, S., & Osterbrock, D. E. 1987, ApJS, 63, 295
Xu, Y., Xu, H., Zhang, Z., et al. 2005, ApJ, 631, 809
Xu, Y.-D. 2011, ApJ, 739, 64
Yamaoka, K., Uzawa, M., Arai, M., Yamazaki, T., & Yoshida, A. 2005, Chin. J. Astron. Astrophys. Supp., 5, 273
Younes, G., Porquet, D., Sabra, B., et al. 2010, A&A, 517, A33
Younes, G., Porquet, D., Sabra, B., & Reeves, J. N. 2011, A&A, 530, A149
Younes, G., Porquet, D., Sabra, B., Reeves, J. N., & Grosso, N. 2012, A&A, 539, A104
Yuan, F., Taam, R. E., Misra, R., Wu, X.-B., & Xue, Y. 2007, ApJ, 658, 282
Zezas, A., Birkinshaw, M., Worrall, D. M., Peters, A., & Fabbiano, G. 2005, ApJ, 627, 711

Pages 15 to 31 are available in the electronic edition of the journal at `http://www.aanda.org`

Table 2. Observational details.

Satellite (1)	Obs ID (2)	Date (3)	Radius (″) (4)	Exptime (ks) (5)	Net Exptime (ks) (6)	Counts (0.5–10 keV) (7)	HR (8)	OM (9)
				NGC 1052				
XMM-Newton[c]	093630101	2001-08-15	25	16.3	11.2	5818	0.28 ± 0.06	No
XMM-Newton	306230101	2006-01-12	25	54.9	44.8	25 565	0.34 ± 0.03	Yes
XMM-Newton	553300301	2009-01-14	25	52.3	42.4	27 367	0.39 ± 0.02	Yes
XMM-Newton[*]	553300501	2009-01-14	25	8.0	5.4	320	–	No
XMM-Newton	553300401	2009-08-12	25	59.0	46.8	30 643	0.42 ± 0.02	Yes
Chandra (ACIS-S)[*]	385	2005-09-18	3	2.4	2.3	270	0.36 ± 0.24	–
Chandra (ACIS-S)[* c]	5910	2000-08-29	3	60.0	59.2	6549	0.40 ± 0.04	–
				NGC 3226				
XMM-Newton[c]	0101040301	2000-11-28	15	40.1	30.2	6514	0.35 ± 0.04	Yes
XMM-Newton	0400270101	2006-12-03	15	107.9	93.1	28 199	–0.32 ± 0.01	Yes
Chandra (ACIS-S)[* c]	860	1999-12-30	3	47.0	46.6	476	0.53 ± 0.12	–
*Chandra (ACIS-S)**	1616	2001-03-23	3	2.5	2.2	193	–0.20 ± 0.31	–
				NGC 3627				
XMM-Newton[c]	0093641101	2001-05-26	25	11.2	5.1	1181	–0.63 ± 0.02	Yes
Chandra (ACIS-S)[*]	394	1999-11-03	8	1.8	1.8	7	–	–
Chandra (ACIS-S)[c]	9548	2008-03-31	8	50.2	49.5	964	–0.40 ± 0.05	–
				NGC 4261				
Chandra (ACIS-S)	834	2000-05-06	3	35.2	34.4	3465	–0.58 ± 0.01	–
Chandra (ACIS-S)[c]	9569	2008-02-12	3	102.2	100.9	7757	–0.47 ± 0.01	–
XMM-Newton	0056340101	2001-12-16	25	33.2	21.3	10 730	–0.68 ± 0.01	Yes
XMM-Newton[c]	0502120101	2007-12-16	25	127.0	63.0	32 156	–0.68 ± 0.01	Yes
				NGC 4278				
Chandra (ACIS-S)[*]	398	2000-04-20	3	1.4	1.4	303	–0.55 ± 0.05	–
Chandra (ACIS-S)[*]	4741	2005-02-03	3	37.9	37.5	20% pileup	–	–
Chandra (ACIS-S)[c]	7077	2006-03-16	3	111.7	110.3	9182	–0.66 ± 0.01	–
Chandra (ACIS-S)[*]	7078	2006-07-25	3	52.1	51.4	18% pileup	–	–
Chandra (ACIS-S)[*]	7079	2006-10-24	3	106.4	105.1	16% pileup	–	–
Chandra (ACIS-S)	7081	2007-02-20	3	112.1	110.7	7591	–0.66 ± 0.01	–
Chandra (ACIS-S)	7080	2007-04-20	3	56.5	55.8	3379	–0.69 ± 0.01	–
Chandra (ACIS-S)[*]	11269	2010-03-15	3	83.0	81.9	2091	–0.82 ± 0.01	–
Chandra (ACIS-S)[*]	12124	2010-03-20	3	26.2	25.8	576	–0.92 ± 0.01	–
XMM-Newton[* c]	0205010101	2004-05-23	25	35.9	20.8	34 516	–0.60 ± 0.01	Yes
				NGC 4552				
Chandra (ACIS-S)[c]	2072	2001-04-22	3	55.1	54.4	2288	–0.75 ± 0.01	–
XMM-Newton[c]	0141570101	2003-07-10	25	44.8	17.3	12180	–0.81 ± 0.01	Yes
				NGC 5846				
XMM-Newton[c]	0021540101	2001-01-25	25	30.0	25.6	25 905	–0.94 ± 0.01	Yes
XMM-Newton[d]	0021540501	2001-08-26	25	19.7	10.0	10 027	–0.95 ± 0.01	Yes
Chandra (ACIS-S)[c]	788	2000-05-24	7	30.3	29.9	1839	–0.94 ± 0.01	–
Chandra (ACIS-I)	7923	2007-06-12	7	91.2	90.0	2307	–0.88 ± 0.01	–

Notes. Instrument (Col. 1), obs ID (Col. 2), date (Col. 3), aperture radius for the nuclear extraction (Col. 4), total exposure time (Col. 5), net exposure time (Col. 6), number of counts in the 0.5–10 keV band (Col. 7), hardness ratio (Col. 8), data from the optical monitor available (Col. 9). (*) Observations were not used for the simultaneous fittings. (c) Observations used to compare *XMM-Newton* and *Chandra* data. (d) Observation with only optical OM data (UV not available).

Table 3. F-test and χ^2/d.o.f. applied to the SMF0.

Name (1)	Instrument (2)	Best fit (3)	Test (4)	vs. ($N_{\rm H1}$) (5)	vs. ($N_{\rm H2}$) (6)	vs. (kT) (7)	vs. (Γ) (8)	vs. ($Norm_1$) (9)	vs. ($Norm_2$) (10)	Var. (11)
NGC 1052	*XMM*	ME2PL	F-test	1	2.29e-113	0.07	8.5071e-114	–	5.27e-128	$Norm_2$
			χ^2/d.o.f.	1.31	1.10	1.26	1.10	–	1.07	
NGC 3226	*XMM*	2PL	F-test	3.83e-158	1.3462e-194	–	0.09	2.58e-139	2.58e-139	$N_{\rm H2}$
			χ^2/d.o.f.	1.18	0.98	–	2.57	1.30	1.30	
NGC 3627	*XMM*/*Ch*	MEPL	F-test	3.25e-20	8.24e-26	8.90e-10	0.05	2.17e-17	1.68e-25	$N_{\rm H2}$
			χ^2/d.o.f.	2.27	1.63	4.21	6.54	2.76	1.71	
NGC 4261	*Chandra*	ME2PL	F-test	0.90	0.12	0.40	0.94	0.30	0.96	None
			χ^2/d.o.f.	1.27	1.26	1.26	1.27	1.26	1.27	
	XMM	ME2PL	F-test	0.09	0.39	0.34	0.92	–	0.75	None
			χ^2/d.o.f.	1.18	1.18	1.18	1.18	–	1.18	
NGC 4278	*Chandra*	MEPL	F-test	1.75e-07	1.03e-08	1.01e-07	4.94e-06	5.27e-18	6.73e-46	$Norm_2$
			χ^2/d.o.f.	1.53	1.51	1.53	1.56	1.36	1.00	
NGC 4552	*XMM*/*Ch*	MEPL	F-test	3.22e-128	4.13e-90	1.06e-53	1.45e-03	5.70e-133	6.76e-94	$Norm_1$
			χ^2/d.o.f.	4.01	6.82	11.35	22.7	3.75	6.47	
NGC 5846	*XMM*	MEPL	F-test	1	1	4.02e-04	0.38	0.05	0.66	None
			χ^2/d.o.f.	1.29	1.29	1.26	1.29	1.28	1.29	
	Chandra	MEPL	F-test	1	0.12	0.46	0.63	0.56	0.31	None
			χ^2/d.o.f.	0.97	0.95	0.97	0.97	0.97	0.96	

Notes. When no variation in one parameter is needed, we marked it as "–". Name (Col. 1), instrument (Col. 2), best-fit model (Col. 3), statistical test (Col. 4), parameter varying with respect to SMF0 (Cols. 5–10) and the parameter that varies in SMF1 (Col. 11).

Table 4. F-test and χ^2/d.o.f. applied to the SMF1.

Name (1)	Instrument (2)	Var. (3)	Test (4)	vs. ($N_{\rm H1}$) (5)	vs. ($N_{\rm H2}$) (6)	vs. (kT) (7)	vs. (Γ) (8)	vs. ($Norm_1$) (9)	vs. ($Norm_2$) (10)	Var. (11)
NGC 1052	*XMM*	$Norm_2$	F-test	1	2.94e-10	0.03	4.12e-04	–		$N_{\rm H2}$
			χ^2/d.o.f.	1.07	1.05	1.07	1.06	–		
NGC 3226	*XMM*	$N_{\rm H2}$	F-test	1.59e-03		–	3.84e-07	1.75e-06	1.33e-06	None
			χ^2/d.o.f.	0.97		–	0.96	0.96	0.96	
NGC 3627	Both	$N_{\rm H2}$	F-test	2.46e-03		0.35	0.01	1	2.92e-03	None
			χ^2/d.o.f.	1.46		1.63	1.52	2.44	1.47	
NGC 4278	*Chandra*	$Norm_2$	F-test	1	1	0.13	0.62	0.96		None
			χ^2/d.o.f.	1.00	1.00	0.99	1.00	1.00		
NGC 4552	Both	$Norm_1$	F-test	0.93	0.94	0.02	4.17e-10		4.15e-24	$Norm_2$
			χ^2/d.o.f.	1.65	1.65	1.62	1.50		1.28	

Notes. When no variation in one parameter is needed, we marked it as "–". Name (Col. 1), instrument (Col. 2), the parameter varying in SMF1 (Col. 3), statistical test (Col. 4), parameter varying with respect to SMF1 (Cols. 5–10) and the parameter that varies in SMF2 (Col. 11).

Table 5. Final compilation of the best-fit models for the sample, including the individual best-fit model for each observation, and the simultaneous best-fit model with the varying parameters.

Instrument (1)	Obs ID (2)	Best fit (3)	N_{H1} (10^{22} cm^{-2}) (4)	N_{H2} (10^{22} cm^{-2}) (5)	kT keV (6)	Γ (7)	$Norm_1$ (10^{-4}) (8)	$Norm_2$ (10^{-4}) (9)	χ^2/d.o.f. (10)
NGC 1052									
XMM-Newton	093630101	ME2PL	–	$13.77^{15.78}_{11.95}$	$0.62^{0.69}_{0.51}$	$1.24^{1.35}_{1.11}$	$1.05^{1.13}_{0.97}$	$6.09^{4.55}_{4.79}$	269.16/234
XMM-Newton	306230101	ME2PL	–	$9.30^{9.82}_{8.79}$	$0.50^{0.55}_{0.45}$	$1.30^{1.36}_{1.24}$	$1.05^{1.09}_{1.01}$	$7.20^{8.14}_{6.34}$	799.19/822
XMM-Newton	553300301	ME2PL	–	$8.96^{9.39}_{8.54}$	$0.61^{0.64}_{0.57}$	$1.38^{1.43}_{1.32}$	$1.09^{1.14}_{1.06}$	$10.16^{11.31}_{9.10}$	923.38/869
XMM-Newton	553300401	ME2PL	–	$9.47^{9.86}_{9.09}$	$0.53^{0.61}_{0.48}$	$1.43^{1.48}_{1.38}$	$1.10^{1.14}_{1.06}$	$12.02^{13.32}_{10.82}$	1006.47/937
Chandra (3″)*	5910	ME2PL	–	$5.33^{6.86}_{3.84}$	$0.64^{0.69}_{0.58}$	$1.21^{1.46}_{1.05}$	$0.37^{0.47}_{0.37}$	$0.57^{1.06}_{0.35}$	261.04/226
Chandra (25″)*	5910	ME2PL	–	$8.13^{11.49}_{5.36}$	$0.61^{0.65}_{0.57}$	$1.25^{1.50}_{1.00}$	$0.49^{0.66}_{0.49}$	$0.61^{1.21}_{0.19}$	319.40/269
XMM-Newton	093630101	ME2PL	–	$14.14^{15.77}_{12.66}$	$0.59^{0.61}_{0.57}$	$1.36^{1.39}_{1.33}$	$1.09^{1.11}_{1.06}$	$8.06^{8.89}_{7.31}$	3043.69/2886
Simultaneous	306230101			$9.80^{10.26}_{9.36}$				$8.38^{8.97}_{7.82}$	
	553300301			$8.75^{9.11}_{8.40}$				$9.74^{10.40}_{9.11}$	
	553300401			$9.21^{9.55}_{8.88}$				$10.41^{11.11}_{9.75}$	
NGC 3226									
XMM-Newton	0101040301	2PL	$0.11^{0.15}_{0.05}$	$1.03^{1.35}_{0.76}$	–	$1.69^{1.81}_{1.58}$	$0.71^{0.92}_{0.47}$	$1.85^{2.28}_{1.50}$	245.87/252
XMM-Newton	0400270101	PL	$0.17^{0.18}_{0.16}$	–	–	$1.74^{1.77}_{1.72}$	–	–	635.19/663
Chandra (3″)*	860	PL	$0.18^{0.41}_{0.00}$	–	–	$1.73^{2.10}_{1.47}$	–	–	9.72/17
Chandra (25″)*	860	2PL	$0.29^{0.70}_{0.10}$	$15.80^{114.58}_{0.00}$	–	$1.71^{3.00}_{1.34}$	$2.03^{4.48}_{0.00}$	$1.43^{16.49}_{0.00}$	26.30/28
XMM-Newton	0101040301	2PL	$0.09^{0.12}_{0.05}$	$0.86^{0.99}_{0.76}$	–	$1.73^{1.77}_{1.71}$	$0.86^{0.98}_{0.76}$	$1.89^{2.09}_{1.68}$	905.42/920
Simultaneous	0400270101			$0.22^{0.24}_{0.19}$					
NGC 3627									
XMM-Newton	0093641101	MEPL	–	–	$0.33^{0.52}_{0.29}$	$1.78^{2.09}_{1.57}$	$0.00^{0.02}_{0.00}$	$0.68^{0.83}_{0.60}$	54.91/35
Chandra (8″)	9548	MEPL	–	$0.05^{0.15}_{0.00}$	$0.65^{0.80}_{0.46}$	$1.45^{1.70}_{1.25}$	$0.06^{0.21}_{0.05}$	$0.24^{0.31}_{0.19}$	33.63/34
Chandra (25″)*	9548	MEPL	–	–	$0.40^{0.51}_{0.35}$	$1.49^{1.63}_{1.38}$	$0.31^{0.37}_{0.24}$	$0.55^{0.61}_{0.50}$	149.42/96
Both	0093641101	MEPL	–	–	$0.63^{0.68}_{0.58}$	$2.33^{2.42}_{2.25}$	$0.14^{0.15}_{0.12}$	$0.90^{0.96}_{0.85}$	125.5/77
Simultaneous	9548			$1.28^{1.48}_{1.11}$					
NGC 4261									
Chandra	834	ME2PL	$0.18^{0.47}_{0.06}$	$11.89^{16.01}_{9.31}$	$0.58^{0.60}_{0.56}$	$2.11^{3.07}_{1.52}$	$0.29^{0.55}_{0.19}$	$4.72^{25.76}_{1.60}$	110.82/80
Chandra (3″)	9569	ME2PL	$0.18^{0.47}_{0.08}$	$8.40^{10.20}_{6.90}$	$0.57^{0.58}_{0.56}$	$1.24^{1.51}_{1.07}$	$0.26^{0.37}_{0.20}$	$2.13^{4.57}_{1.18}$	198.74/157
Chandra (25″)*	9569	ME2PL	–	$9.03^{12.90}_{6.55}$	$0.61^{0.62}_{0.60}$	$1.16^{1.39}_{0.89}$	$0.35^{0.47}_{0.35}$	$0.64^{1.11}_{0.29}$	382.42/218
Chandra	834/9569	ME2PL	$0.18^{0.31}_{0.09}$	$9.38^{10.84}_{7.96}$	$0.57^{0.58}_{0.56}$	$1.87^{2.19}_{1.55}$	$0.27^{0.34}_{0.21}$	$2.70^{4.86}_{1.49}$	312.57/247
Simultaneous									
XMM-Newton	0056340101	ME2PL	$0.08^{0.15}_{0.01}$	$11.97^{14.73}_{9.31}$	$0.63^{0.64}_{0.61}$	$1.84^{2.22}_{1.45}$	$0.72^{0.94}_{0.54}$	$2.82^{6.30}_{1.11}$	278.12/255
XMM-Newton	0502120101	ME2PL	$0.04^{0.07}_{0.00}$	$9.71^{11.14}_{8.30}$	$0.64^{0.65}_{0.64}$	$1.75^{1.97}_{1.54}$	$0.64^{0.74}_{0.55}$	$2.30^{3.65}_{1.40}$	563.80/461
XMM-Newton	0056340101	ME2PL	$0.04^{0.08}_{0.01}$	$10.28^{11.56}_{9.02}$	$0.64^{0.65}_{0.63}$	$1.76^{1.95}_{1.57}$	$0.67^{0.76}_{0.58}$	$2.36^{3.54}_{1.53}$	855.28/726
Simultaneous	0502120101								
NGC 4278									
Chandra(3″)	7077	MEPL	$0.31^{0.58}_{0.05}$	$0.01^{0.03}_{0.00}$	$0.27^{0.38}_{0.19}$	$2.06^{2.15}_{1.99}$	$0.80^{6.21}_{0.18}$	$0.98^{1.06}_{0.90}$	144.23/158
Chandra(25″)*	7077	MEPL	$0.16^{0.45}_{0.01}$	–	$0.30^{0.37}_{0.21}$	$1.88^{1.95}_{1.83}$	$0.81^{3.96}_{0.28}$	$1.32^{1.39}_{1.27}$	250.15/210
Chandra	7081	MEPL	–	–	$0.63^{0.68}_{0.57}$	$2.03^{2.10}_{1.99}$	$0.12^{0.14}_{0.09}$	$0.77^{0.82}_{0.75}$	155.54/145
Chandra	7080	MEPL	$0.22^{0.71}_{0.00}$	–	$0.47^{0.61}_{0.18}$	$2.10^{2.25}_{2.03}$	$0.24^{13.76}_{0.07}$	$0.69^{0.79}_{0.65}$	102.53/96
*XMM-Newton**	0205010101	PL	$0.02^{0.03}_{0.02}$	–	–	$2.04^{2.08}_{2.01}$	–	–	562.25/529
Chandra	7077	MEPL	–	–	$0.58^{0.62}_{0.48}$	$2.05^{2.11}_{2.03}$	$0.11^{0.12}_{0.10}$	$0.97^{1.02}_{0.82}$	414.71/415
Simultaneous	7081							$0.78^{0.82}_{0.77}$	
	7080							$0.68^{0.72}_{0.65}$	
NGC 4552									
Chandra (3″)	2072	MEPL	$0.23^{0.33}_{0.00}$	–	$0.65^{0.75}_{0.59}$	$1.85^{2.13}_{1.74}$	$0.36^{0.56}_{0.16}$	$0.29^{0.41}_{0.26}$	72.49/67
Chandra (25″)*	2072	MEPL	$0.03^{0.05}_{0.00}$	$0.00^{0.02}_{0.00}$	$0.60^{0.62}_{0.58}$	$1.89^{1.96}_{1.82}$	$1.64^{1.82}_{1.48}$	$0.91^{0.97}_{0.85}$	161.64/133
XMM-Newton	0141570101	MEPL	$0.01^{0.05}_{0.00}$	–	$0.59^{0.61}_{0.58}$	$1.92^{1.98}_{1.85}$	$2.12^{2.37}_{1.98}$	$1.46^{1.55}_{1.38}$	282.04/254
Both	2072	MEPL	–	–	$0.60^{0.62}_{0.59}$	$1.86^{1.91}_{1.81}$	$0.15^{0.17}_{0.13}$	$0.31^{0.33}_{0.29}$	397.01/328
Simultaneous	0141570101						$2.11^{2.35}_{1.96}$	$1.40^{1.48}_{1.32}$	

Notes. Satellite (Col. 1), obs ID (Col. 2), best-fit model (Col. 3), parameters in the model (Cols. 4–9) and χ^2/d.o.f. (Col. 10). $^{(*)}$ Observations not used in the simultaneous fit.

Table 5. continued.

Instrument (1)	Obs ID (2)	Best fit (3)	N_{H1} (10^{22} cm^{-2}) (4)	N_{H2} (10^{22} cm^{-2}) (5)	kT keV (6)	Γ (7)	$Norm_1$ (10^{-4}) (8)	$Norm_2$ (10^{-4}) (9)	χ^2/d.o.f. (10)
NGC 5846									
XMM-Newton	0021540101	MEPL	–	–	$0.61^{0.61}_{0.60}$	$2.05^{2.17}_{1.92}$	$5.09^{5.17}_{5.00}$	$0.61^{0.68}_{0.53}$	356.05/266
XMM-Newton	0021540501	MEPL	$0.04^{0.07}_{0.01}$	–	$0.62^{0.63}_{0.60}$	$2.20^{2.40}_{1.99}$	$5.55^{6.07}_{5.10}$	$0.69^{0.81}_{0.56}$	227.57/194
XMM-Newton Simultaneous	0021540101 0021540501	MEPL	–	–	$0.62^{0.62}_{0.61}$	$2.05^{2.14}_{1.94}$	$5.06^{5.13}_{4.98}$	$0.61^{0.67}_{0.54}$	606.06/469
Chandra(7″)	788	MEPL	–	$0.21^{0.43}_{0.00}$	$0.61^{0.64}_{0.57}$	$3.06^{0}_{2.24}$	$0.52^{0.79}_{0.48}$	$0.40^{0.76}_{0.18}$	41.72/50
Chandra(25″)*	788	MEPL	–	–	$0.62^{0.63}_{0.60}$	$1.53^{1.99}_{1.27}$	$2.83^{2.97}_{2.69}$	$0.67^{0.81}_{0.53}$	188.51/137
Chandra	7923	MEPL	$0.11^{0.18}_{0.00}$	$0.08^{0.33}_{0.00}$	$0.60^{0.64}_{0.57}$	$2.73^{3.20}_{2.27}$	$0.77^{0.98}_{0.54}$	$0.21^{0.38}_{0.12}$	63.24/59
Chandra Simultaneous	788/7923	MEPL	–	$0.21^{0.38}_{0.14}$	$0.62^{0.64}_{0.60}$	$3.11^{0}_{2.40}$	$0.52^{0.56}_{0.48}$	$0.38^{0.68}_{0.23}$	105.82/110

Table 6. Soft (0.5–2 keV) and hard (2–10 keV) intrinsic luminosities for individual (Cols. 3 and 5) and simultaneous (Cols. 4 and 6) fitting.

Satellite (1)	Obs ID (2)	log (L(0.5−2 keV)) Individual (3)	log (L(0.5−2 keV)) Simultaneous (4)	log (L(2−10 keV)) Individual (5)	log (L(2−10 keV)) Simultaneous (6)
NGC 1052					
XMM-Newton	093630101	40.955 [40.941–40.969]	40.992 [40.987–40.996]	41.460 [41.447–41.473]	41.473 [41.458–41.488]
XMM-Newton	306230101	40.960 [40.953–40.967]	41.006 [41.002–41.011]	41.483 [41.477–41.489]	41.488 [41.481–41.494]
XMM-Newton	553300301	41.104 [41.096–41.112]	41.063 [41.058–41.068]	41.555 [41.549–41.561]	41.545 [41.539– 41.551]
XMM-Newton	553300401	41.117 [41.110–41.125]	41.089 [41.084–41.093]	41.551 [41.545–41.556]	41.571 [41.565–41.577]
Chandra (3″)	5910	40.186 [40.169– 40.202]	–	41.290 [41.266– 41.292]	–
Chandra (25″)	5910	40.290 [40.274–40.306]	–	41.336 [41.299–41.370]	–
NGC 3226					
XMM-Newton	0101040301	40.762 [40.750–40.774]	40.775 [40.763–40.786]	41.057 [41.041–41.072]	41.013 [41.004 – 41.021]
XMM-Newton	0400270101	40.782 [40.777–40.787]	40.775 [40.769–40.780]	40.994 [40.986–41.003]	41.013 [41.005–41.021]
Chandra (3″)	860	40.473 [40.378–40.552]	–	40.685 [–41.311]	–
Chandra (25″)	860	40.552[40.495 – 40.602]	–	40.909[– 41.313]	–
NGC 3627					
XMM-Newton	0093641101	39.440 [39.417–39.462]	39.452 [39.429–39.474]	39.420 [39.362–39.472]	39.245 [39.197–39.288]
Chandra (8″)	9548	38.900 [38.854–38.942]	39.452 [39.421–39.481]	39.169[– 41.072]	39.224 [39.179–39.264]
Chandra (25″)	9548	39.367 [39.348–39.386]	–	39.536 [39.268–39.701]	–
NGC 4261					
Chandra	834	41.180 [41.161– 41.197]	40.976 [40.967– 40.984]	41.107 [40.857– 41.265]	41.018 [40.971– 41.060]
Chandra (3″)	9569	40.924 [40.913–40.935]	40.976 [40.967–40.984]	40.996 [41.084–40.887]	41.018 [40.971–41.060]
Chandra (25″)	9569	40.794 [40.779–40.807]	–	40.967 [40.940–40.993]	–
XMM-Newton	0056340101	41.301 [41.293–41.309]	41.142 [41.138–41.146]	41.188 [41.166–41.209]	41.132 [41.113–41.151]
XMM-Newton	0502120101	41.223 [41.219–41.227]	41.142 [41.138–41.146]	41.148 [41.136–41.160]	41.132 [41.113–41.151]
NGC 4278					
Chandra (3″)	7077	39.873 [39.865–39.881]	39.863 [39.856–39.871]	39.762 [39.319–39.977]	39.822 [39.806–39.837]
Chandra (25″)	7077	40.137 [40.102–40.169]	–	40.061 [40.035–40.084]	–
Chandra	7081	39.314 [39.303–39.324]	39.783 [39.774–39.792]	39.269 [39.244–39.293]	39.732 [39.716–39.748]
Chandra	7080	39.778 [39.741–39.813]	39.731 [39.717–39.743]	39.615 [–40.728]	39.672 [39.653–39.690]
XMM-Newton	0205010101	40.733 [40.729–40.736]	–	40.768 [40.759–40.777]	–
NGC 4552					
Chandra (3″)	2072	39.687 [39.625–39.742]	39.490 [39.471–39.509]	39.463 [39.045–40.147]	39.449 [39.411–39.483]
Chandra (25″)	2072	40.252 [40.239–40.266]	–	39.904 [39.819–39.974]	–
XMM-Newton	0141570101	40.396 [40.389–40.403]	40.388 [40.370–40.406]	40.128 [40.103–40.151]	40.128 [40.103–40.151]
NGC 5846					
XMM-Newton	0021540101	41.083 [41.079–41.088]	41.080 [41.076–41.084]	40.196 [40.163–40.227]	40.189 [40.160–40.216]
XMM-Newton	0021540501	41.122 [41.114–41.130]	41.080 [41.076–41.084]	40.165 [40.115–40.210]	40.189 [40.160–40.216]
Chandra (7″)	788	40.159 [40.118–40.195]	40.291 [40.244–40.334]	38.586 [38.528–38.637]	39.326 [39.067–39.486]
Chandra (25″)	788	40.867 [40.853–40.880]	–	40.552 [40.407 – 40.661]	–
Chandra	7923	40.490 [40.471–40.507]	40.291 [40.244–40.334]	38.809 [38.760–38.853]	39.326 [39.067–39.486]

Table 7. Results for the best fit of the annular region (ring) in *Chandra* data, and the best fit obtained for the nucleus of *XMM-Newton* data when the contribution from the annular region was removed.

Name (obs ID) (1)	Region (2)	Model (3)	$N_{\rm H1}$ (10^{22} cm^{-2}) (4)	$N_{\rm H2}$ (10^{22} cm^{-2}) (5)	kT (keV) (6)	Γ (7)	$\chi^2_{\rm r}$ (8)	log $L_{\rm soft}$ (0.5–2 keV) (9)	log $L_{\rm hard}$ (2–10 keV) (10)	Cont. % (11)
NGC 1052 (5910)	Ring	ME2PL	–	$26.10^{38.14}_{16.93}$	$0.31^{0.39}_{0.28}$	$1.98^{2.23}_{1.71}$	1.47	40.185	40.563	10
NGC 1052 (093630101)	Nucleus	ME2PL	–	$7.54^{9.98}_{5.20}$	$0.78^{0.89}_{0.68}$	$1.69^{1.86}_{1.50}$	1.13	39.875	41.235	
NGC 3226 (860)	Ring	PL	–	–	–	$1.42^{1.07}_{1.85}$	1.89	40.482	40.557	20
NGC 3226 (0101040301)	Nucleus	2PL	$0.35^{1.88}_{0.00}$	$1.02^{1.88}_{0.00}$	–	$1.72^{1.58}_{1.88}$	1.00	40.623	40.912	
NGC 3627 (9548)	Ring	MEPL	–	–	$0.41^{0.49}_{0.35}$	$1.71^{1.85}_{1.58}$	1.35	39.302	39.384	92
NGC 3627 (093641101)	Nucleus	MEPL	–	–	$0.71^{1.02}_{0.40}$	$3.37^{3.76}_{2.97}$	1.16	38.990	38.125	
NGC 4261 (9569)	Ring	MEPL	$0.06^{0.11}_{0.03}$	$0.00^{0.04}_{0.00}$	$0.61^{0.62}_{0.59}$	$1.87^{2.07}_{1.70}$	2.07	40.663	40.252	37
NGC 4261 (0502120101)	Nucleus	ME2PL	–	$8.29^{9.89}_{7.28}$	$0.67^{0.68}_{0.65}$	$1.56^{1.72}_{1.41}$	1.21	40.857	41.051	
NGC 4278 (7077)	Ring	MEPL	–	–	$0.29^{0.36}_{0.19}$	$1.61^{1.71}_{1.51}$	1.12	39.551	39.707	38
NGC 4278 (0205010101)	Nucleus	PL	$0.02^{0.03}_{0.02}$			$2.05^{2.10}_{2.03}$	1.05	40.681	40.736	
NGC 4552 (2072)	Ring	MEPL	–	–	$0.60^{0.62}_{0.57}$	$1.92^{2.06}_{1.81}$	1.47	39.648	39.304	23
NGC 4552 (0141570101)	Nucleus	MEPL	–	–	$0.58^{0.62}_{0.52}$	$1.90^{2.06}_{1.80}$	1.10	40.053	39.878	
NGC 5846 (788)	Ring	MEPL	–	–	$0.61^{0.62}_{0.59}$	$1.87^{2.46}_{1.61}$	1.63	40.815	40.217	73
NGC 5846 (0021540101)	Nucleus	MEPL	–	–	$0.63^{0.64}_{0.61}$	$4.00_{3.56}$	1.36	40.753	39.171	

Notes. Name and obs ID in parenthesis (Col. 1), extracted region (Col. 2), best-fit model (Col. 3), parameters of the best-fit model (Cols. 4–8), soft and hard intrinsic luminosities (Cols. 9 and 10), and the percentage of the contribution from the ring to the 25″ aperture *Chandra* data in the 0.5–10.0 keV band (Col. 11).

Table 8. Simultaneous fittings taking into account the contribution from the annular region given in Table 7.

Obs ID (1)	$N_{\rm H1}$ (10^{22} cm^{-2}) (2)	$N_{\rm H2}$ (10^{22} cm^{-2}) (3)	kT keV (4)	Γ (5)	$Norm_1$ (10^{-4}) (6)	$Norm_2$ (10^{-4}) (7)	χ^2/d.o.f. (8)	log $L_{\rm soft}$ (0.5–2 keV) (9)	log $L_{\rm hard}$ (2–10 keV) (10)
NGC 1052									
0093630101	–	$6.11^{7.18}_{5.07}$	$0.68^{0.73}_{0.63}$	$1.58^{1.70}_{1.47}$	$0.48^{0.53}_{0.44}$	$1.28^{1.69}_{0.95}$	577.98/477	$40.35^{40.36}_{40.34}$	$41.33^{41.35}_{41.32}$
5910								$40.35^{40.36}_{40.34}$	$41.27^{41.28}_{41.26}$
NGC 3226									
0101040301	$0.34^{0.01}_{0.54}$	$1.03^{1.42}_{0.68}$	–	$1.72^{1.86}_{1.60}$	$0.55^{0.93}_{0.03}$	$1.59^{1.23}_{2.11}$	268.434/279	$40.710^{40.732}_{40.688}$	$41.681^{41.725}_{41.633}$
860		$0.07^{0.00}_{0.32}$				$0.68^{0.92}_{0.34}$		$40.510^{40.581}_{40.425}$	$40.958^{40.978}_{40.938}$
NGC 4261									
0502120101	$0.03^{0.08}_{0.00}$	$7.64^{8.74}_{6.58}$	$0.60^{0.61}_{0.59}$	$1.55^{1.75}_{1.36}$	$0.22^{0.26}_{0.19}$	$1.53^{2.25}_{1.04}$	972.83/627	$40.84^{40.84}_{40.84}$	$41.03^{41.05}_{41.01}$
9569								$40.84^{40.85}_{40.83}$	$40.99^{41.01}_{40.97}$
NGC 4278									
0205010101	$0.03^{0.03}_{0.02}$	–	–	$2.11^{2.14}_{2.08}$	$7.74^{7.95}_{7.54}$		844.93/690	$40.71^{40.72}_{40.71}$	$40.71^{40.72}_{40.70}$
7077					$1.15^{1.18}_{1.11}$			$39.89^{39.89}_{39.88}$	$39.86^{39.87}_{39.84}$
NGC 4552									
0141570101	$0.02^{0.04}_{0.00}$	$0.01^{0.05}_{0.00}$	$0.64^{0.66}_{0.61}$	$1.85^{2.00}_{1.78}$	$0.77^{0.90}_{0.70}$	$0.84^{1.01}_{0.76}$	380.50/327	$40.05^{40.05}_{40.04}$	$39.90^{39.93}_{39.88}$
2072					$0.16^{0.18}_{0.14}$	$0.31^{0.37}_{0.28}$		$39.51^{39.53}_{39.49}$	$39.47^{39.51}_{39.42}$

Notes. Name and obs ID in parenthesis (Col. 1), parameters of the best-fit model (Cols. 2–7), χ^2/d.o.f. (Col. 8) and soft and hard intrinsic luminosities (Cols. 9 and 10).

Table 9. Statistics for the light curves. Name (Col. 1), obs ID (Col. 2), χ^2/d.o.f. and the probability of being variable (Cols. 3 and 4) and normalized excess variance with errors (Cols. 5 and 6).

Name (1)	Obs ID (2)	χ^2/d.o.f. (3)	Prob. (%) (4)	σ^2 (10^{-2}) (5)	err(σ^2) (10^{-2}) (6)
NGC 1052	0093630101	18.6/11	93	0.189	0.107
	0306230101	57.1/49	80	0.043	0.046
	0553300301	49.5/46	66	0.022	0.043
	0553300401	39.3/49	16	–0.042	0.042
	5910	48.6/59	17	–0.157	0.173
NGC 3226	860	51.2/45	76	–0.047	0.028
	0101040301	35.0/32	67	0.074	0.195
	0400270101	474.1/100	100	1.781	0.079
NGC 3627	0093641101	2.6/5	24	–0.312	0.605
	9548	63.8/49	92	0.360	0.351
NGC 4261	834	35.8/34	62	0.077	0.267
	9569	85.7/100	15	–0.243	0.195
	0056340101	25.4/19	85	0.109	0.099
	0502120101	79.6/64	91	0.075	0.057
NGC 4278	7077	124.3/111	82	0.149	0.184
	7081	91.4/107	14	–0.299	0.227
	7080	41.0/55	8	–0.445	0.354
	0205010101	2.2/11	0	–0.074	0.041
NGC 4552	2072	57.4/45	90	0.089	0.570
	0141570101	12.8/14	46	0.000	0.081
NGC 5846	0021540101	20.1/28	14	–0.034	0.037
	0021540501	7.9/8	56	0.014	0.070
	788	20.4/16	80	0.513	0.640
	7923	85.2/86	50	–0.136	0.560

Table 10. UV luminosities derived from the OM observations. Name (Col. 1), obs ID (Col. 2), filter (Col. 3) and luminosity (Col. 4).

Name (1)	Obs ID (2)	Filter (3)	log L (erg/s) (4)	$\alpha_{\rm ox}$ (5)
NGC 1052	0306230101	$UVM2$	41.038 ± 0.013	–0.94 ± 0.03
	0306230101	$UVW2$	40.938 ± 0.028	
	0553300301	$UVM2$	41.139 ± 0.012	–0.95 ± 0.03
	0553300301	$UVW2$	40.947 ± 0.026	
	0553300401	$UVM2$	41.041 ± 0.014	–0.91 ± 0.03
	0553300401	$UVW2$	40.885 ± 0.025	
NGC 3226	0101040301	$UVW1$	41.375 ± 0.006	–1.15 ± 0.70
	0400270101	$UVW1$	41.327 ± 0.001	*
NGC 3627	0093641101	$UVW1$	41.367 ± 0.007	–1.66 ± 0.05
NGC 4261	0056340101	$UVM2$	41.431 ± 0.024	–1.04 ± 0.05
	0056340101	$UVW1$	42.169 ± 0.005	
	0502120201	$UVM2$	41.609 ± 0.014	–1.11 ± 0.03
	0502120201	$UVW1$	42.214 ± 0.001	
NGC 4278	0205010101	$UVW1$	40.903 ± 0.020	–1.11 ± 0.02
NGC 4552	0141570101	$UVW2$	41.273 ± 0.033	–1.28 ± 0.04
NGC 5846	0021540101	$UVW2$	40.561 ± 0.148	–0.81 ± 0.14

Notes. (*) The observation was not used (see text).

Table 11. Summary.

Name	Type	log $L_{\rm soft}$	log $L_{\rm hard}$	log $M_{\rm BH}$	$L_{\rm bol}/L_{\rm Edd}$		Variability		T	HR
		(0.5–2 keV)	(2–10 keV)			SMF0	SMF1	SMF2	(Years)	
(1)	(2)	(3)	(4)	(5)	(6)	(7)	(8)	(9)	(10)	(11)
NGC 1052 (X)	AGN	41.04	41.52	8.07	7.2 $\times 10^{-4}$	ME2PL	$Norm_2$	$N_{\rm H2}$	8	
	1.9	20%	20%				49%	31%		33%
NGC 3226 (X,C)	AGN	40.78	41.01	8.22	1.6 $\times 10^{-4}$	2PL	$N_{\rm H2}$	$Norm_2$	1	
	1.9	37%	81%				93%	57%		
NGC 4261 (X)	AGN	40.98	41.02	8.96	2.9 $\times 10^{-5}$	ME2PL	–	–	8	
	2	0%	0%							0%
(C)						ME2PL	–	–	6	
		0%	0%							19%
NGC 4278 (C)	AGN	39.80	39.75	8.46	5.0 $\times 10^{-6}$	MEPL	$Norm_2$	–	1	
	1.9	26%	29%				30%			40%*
NGC 4552 (X,C)	AGN	39.49	39.45	8.84	1.0 $\times 10^{-6}$	MEPL	$Norm_1$	$Norm_2$	2	
	2	73%	63%				93%	78%		
NGC 5846 (X)	Non-AGN	40.29	39.33	8.49	1.8 $\times 10^{-6}$	MEPL	–	–	7	
	2	0%	0%							1%
(C)						MEPL	–	–	0.6	
		0%	0%							6%

Notes. Name, and the instrument in parenthesis (Col. 1), type (Col. 2), logarithm of the soft (0.5–2 keV) and hard (2–10 keV) X-ray luminosities, where the mean was calculated or *Chandra* luminosity was given when both instruments were used, and percentages in flux variations (Cols. 3 and 4), black-hole mass in logarithmical scale, from González-Martín et al. (2009a) (Col. 5), Eddington ratio, calculated from Eracleous (2010) using $L_{\rm bol} = 33\ L_{2-10\ \rm keV}$ (Col. 6), best fit for the SMF0 (Col. 7), parameter varying in SMF1, with the percentage of variation (Col. 8), parameter varying in SMF2, with the percentage of variation (Col. 9), the sampling timescale for variations (Col. 10), and variations in the hardness ratios (Col. 11). (*) For all *Chandra* data. With useful spectroscopic data variations are 4%.

Appendix A: Notes and comparisons with previous results for individual objects

A.1. NGC 1052

The brightest elliptical galaxy in the Cetus I group, NGC 1052, previously classed as a LINER in the pioneering work by Heckman (1980), was classified as LINER type 1.9 by Ho et al. (1997).

NGC 1052 was observed twice with *Chandra* and five times with the *XMM-Newton* satellite, which makes it a good candidate for studying variability. The general characteristics of the two *Chandra* observations Obs ID 385 (taken in 2000) and Obs ID 5910 (2005) were reported by González-Martín et al. (2009b) and Boroson et al. (2011), respectively, showing quite different spectral behavior with a flatter spectral index, lower N_H, and lower luminosity in 2005. We analyzed the observation from 2005 and found a different spectral fit than Boroson et al. (2011), since they used the PL model to fit the spectrum. However, similar luminosities were found between González-Martín et al. (2009b), Boroson et al. (2011), and this work (with $\log (L(2{-}10\text{ keV})) = 41.4^{+0.1}_{-0.8}$, 41.4 ± 0.01 and $41.3^{+0.00}_{-0.02}$, respectively).

Only one *XMM-Newton* observation (Obs ID 306230101 taken in 2006) was previously analyzed by González-Martín et al. (2009b) and Brightman & Nandra (2011), showing quite similar results as Brightman & Nandra (2011) in spite of a more absorbed spectrum in the latter. Our results agree well with those provided by González-Martín et al. (2009b). The most recent observation at X-rays reported so far is a 100 ks observation taken with *Suzaku* in 2007. The derived spectral characteristics reported by Brenneman et al. (2009) appear to be similar to those from *XMM-Newton*, which is compatible with the values in González-Martín et al. (2009b), Brightman & Nandra (2011), and this paper (intrinsic luminosity of $\log (L(2{-}10\text{ keV})) \sim 41.5$).

In the UV range, Maoz et al. (2005) studied this galaxy with HST-ACS and found a decrease in the flux of the source of a factor of 2 between the 1997 data reported by Pogge et al. (2000) and their 2002 dataset. We found UV flux variations of a factor of 1.3 from XMM-OM data in seven months.

A.2. NGC 3226

NGC 3226 is a dwarf elliptical galaxy that is strongly interacting with the Seyfert 1.5 galaxy NGC 3227, located at 2′ in projected distance (see Fig. C.19 in González-Martín et al. 2009b). NGC 3226 was classified by Ho et al. (1997) as a type 1.9 LINER.

This galaxy was observed twice with *Chandra*-ACIS in 1999 and 2001 and four times with *XMM-Newton* from 2000 to 2006.

Chandra data taken in 1999 were analyzed by George et al. (2001) and those taken in 2001 by Terashima & Wilson (2003). In both cases the X-ray spectra were fitted to a single power law, but with differing column densities, the data in 2001 being a factor 2 more absorbed; this leads to a difference in the X-ray luminosity in the hard (2–10 keV) band of 70%. The reanalysis of these data performed by Younes et al. (2011) shows spectral parameters consistent with the previous studies, although their estimated difference in luminosity is lower (40%). We did not use these data because obs ID 1616 does not match our criteria of the minimum number of counts.

The analysis by Gondoin et al. (2004) of snapshot *XMM-Newton* observations taken in 2000 also showed an X-ray spectrum consistent with a power law with $\log (L(2{-}10\text{ keV})) = 40.38 \pm 0.01$, close to the value obtained by George et al. (2001), $\log (L(2{-}10\text{ keV})) = 40.26 \pm 0.01$, for the same epoch. Binder et al. (2009) studied the *XMM-Newton* observation from 2006 and found significant short timescale flux variation, with a fractional variability amplitude of 11.7. They compared their measurements, $\log (L\,(0.4{-}2\text{ keV})) = 40.47^{+0.01}_{-0.00}$ and $\log (L(2{-}10\text{ keV})) = 40.55^{+0.02}_{-0.08}$, with those from Gondoin et al. (2004) (see above), finding variability on timescales of years. Younes et al. (2011) analyzed the longest exposure data from 2000 and 2006 and found a difference in the hard luminosity of 40%. Considering both *Chandra* and *XMM-Newton* data (obs ID. 860 and 1616, 0101040301 and 0400270101, respectively), they concluded that the source variability is due to modifications in the N_H. We find spectral parameters in agreement to those of Younes et al. (2011) for the *XMM-Newton* and *Chandra* data and obtained a $\chi^2_r = 4.7$ for obs ID 0400270101, but this observation seemed to be affected by the rapidly variable Seyfert 1.5 NGC 3227. Binder et al. (2009) and Younes et al. (2011) found similar results for this galaxy, and interpretated the variability as related to outflows or feedback processes.

A.3. NGC 3627

Together with NGC 3628 and NGC 3623, these three galaxies form the Leo Triplet (see Fig. C.27 in González-Martín et al. 2009b). Cappellari et al. (1999) classified it as a type 2.0 LINER.

This galaxy was observed twice with *Chandra*, in 1999 and 2008, and once with *XMM-Newton*, in 2001.

Ho et al. (2001) and Panessa et al. (2006) studied *Chandra* Obs ID 394 from 1999, using the PL model with $\Gamma = 1.8$, deriving similar luminosities, $\log (L(2{-}10\text{ keV})) = 37.6$ and 37.9, respectively. *Chandra* Obs ID 9548 was analyzed by Grier et al. (2011), who used the PL with $\Gamma = 2$ to obtain $\log (L(0.3{-}8\text{ keV})) = 38.51 \pm 0.03$. We used the MEPL model to fit this spectrum and obtained a higher luminosity $\log (L(2{-}10)\text{ keV})) = 39.2^{+1.9}$, the difference is most probably due to the different models used for the analysis. The *XMM-Newton* observation was analyzed by González-Martín et al. (2009b) and Brightman & Nandra (2011), who used PL and MEPL models to calculate the luminosities, and derived $\log (L(2{-}10\text{ keV})) = 39.2 \pm 0.1$ and 39.5, respectively, with which our results agree (39.4 ± 0.1).

No information on UV was found in the literature.

A.4. NGC 4261

NGC 4261 contains a pair of symmetric kpc-scale jets (Birkinshaw & Davies 1985) and a nuclear disk of dust roughly perpendicular to the radio jet (Ferrarese et al. 1996). Ho et al. (1997) classified it as a type 2.0 LINER.

It has been observed twice with *Chandra*, in 2000 and 2008, and with *XMM-Newton* in another three epochs from 2001 to 2007. However, only the analyses on *Chandra* Obs ID 834 and *XMM-Newton* Obs ID 56340101 are published.

Satyapal et al. (2005), Rinn et al. (2005), and Donato et al. (2004) reported quite consistent spectral parameters by fitting the *Chandra* spectra with a thermal and a power-law component, but with a range of variation in the reported luminosities $\log (L(2{-}10\text{ keV}))$ between 40.5 and 41.0. On the other hand, González-Martín et al. (2009b) and Zezas et al. (2005) fitted the spectra with the ME2PL, using the same value for the spectral index for the two PL in the case of González-Martín et al. (2009b) and varying the spectral index in the case of Zezas et al. (2005). The comparison of the spectral parameters is quite consistent with the largest difference being the $N_{\rm H}$, 16.45 × 10^{22} cm^{-2} for González-Martín et al. (2009b) and 8.4 × 10^{22} cm^{-2} for Zezas et al. (2005); this leads to a higher luminosity in Zezas et al. (2005), $\log{(L(2{-}10\ {\rm keV}))} = 42.0$, against $\log{(L(2{-}10\ {\rm keV}))} = 41.1^{+0.1}_{-0.7}$ in González-Martín et al. (2009b). We used the ME2PL model to fit this spectrum and found spectral parameters and luminosities in agreement with González-Martín et al. (2009b).

The *XMM-Newton* observation Obs ID 056340101 taken in 2001 was analyzed by González-Martín et al. (2009b), Sambruna et al. (2003), and Gliozzi et al. (2003). Different models were used for the three works: an absorbed PL (Gliozzi et al. 2003), an absorbed MEPL (Sambruna et al. 2003) and the ME2PL (González-Martín et al. 2009b). This could explain, in principle, the different reported luminosities. Our results ($\log L(2{-}10\ {\rm keV}) = 41.13 \pm 0.02$) agree well with the spectral parameters and luminosities ($41.2^{+0.0}_{-0.7}$) reported by González-Martín et al. (2009b), but not with those obtained by Sambruna et al. (2003) and Gliozzi et al. (2003) (41.9).

No information from the UV was found in the literature.

A.5. NGC 4278

NGC 4278 is an elliptical galaxy classified as type 1.9 LINER by Ho et al. (1997), who found a relatively weak, broad H_{α} line. The north-northwest side of the galaxy is heavily obscured by large-scale dust-lanes, whose distribution shows several dense knots interconnected by filaments (Carollo et al. 1997).

This galaxy has been observed in nine occasions with *Chandra* from 2000 to 2010 and once with *XMM-Newton* in 2004. Brassington et al. (2009) used six *Chandra* observations and found 97 variable sources within NGC 4278, in an elliptical area of 4′ centered on the nucleus. None of them are within the aperture of 3″ we used for the nuclear extraction. *Chandra* observations were taken by Fabbiano to study the plethora of sources detected in this galaxy (~250) (see Brassington et al. 2009; Boroson et al. 2011). The nuclear source was studied by González-Martín et al. (2009b) using *Chandra* obs ID 7077 taken in 2006 and *XMM-Newton* data. They found a hard X-ray luminosity difference of a factor of 10 between the two observations, which were attributed to the contamination of the numerous sources around the nucleus.

The nuclear variability of this source has been previously studied by Younes et al. (2010). They concluded that long timescale (months) variability is detected with a flux increase of a factor of ~3 on a timescale of a few months and a factor of 5 between the faintest and the brightest observation separated by about three years. We used three of these observations, our spectral fittings being in good agreement with theirs, although we found weaker variations in luminosities. Whereas the different *Chandra* observations showed no short timescale (minutes to hours) variability, during the *XMM-Newton* observation, where the highest flux level was detected, Younes et al. (2010) found a 10% flux increase on a short timescale of a few hours. With the same dataset we obtained a 3% variation in the same time range, the difference being most probably due to the different apertures used for the analysis.

Pellegrini et al. (2012) studied eight *Chandra* observations of NGC 4278. They fitted jointly the two spectra from 2010 with a thermal ($kT = 0.75 \pm 0.05$ keV) plus a power law ($\Gamma = 2.31 \pm 0.20$, $N_{\rm H} = 4.18 \pm 3.13 \times 10^{20}$ cm^{-2}) model, and compared the remaining six spectra with the results by Younes et al. (2010), which agreed well. They found an X-ray luminosity decrease by a factor of ~18 between 2005 and 2010. A direct comparison with our data cannot be done because Pellegrini et al. (2012) used different obs IDs.

In the UV, Cardullo et al. (2008) found that the luminosity increased a factor of 1.6 in about six months using data from HST WFPC2/F218W.

A.6. NGC 4552

This Virgo elliptical galaxy has been classified as a LINER 2.0 (Cappellari et al. 1999). A radio jet was detected with *VLBI* observations (Nagar et al. 2005).

It has been observed four times with *Chandra* from 2001 to 2012 and with *XMM-Newton* in a single epoch in 2003. However, three of the *Chandra* observations are not public yet, so the only reported results came from *Chandra* Obs ID 2072 (Filho et al. 2004; Xu et al. 2005; González-Martín et al. 2009b; Grier et al. 2011; Boroson et al. 2011). Filho et al. (2004) and González-Martín et al. (2009b) fitted the spectra to the MEPL, obtaining compatible results with $\log{(L(2{-}10\ {\rm keV}))} = 39.4$ and $39.2^{+0.2}_{-0.4}$, respectively. Xu et al. (2005) and Grier et al. (2011) obtained $\log{(L(0.3{-}10\ {\rm keV}))} = 39.6$ and $40.0^{+0.01}_{-0.01}$, respectively, by fitting a single PL. Our results ($\log L(2{-}10\ {\rm keV}) = 39.5^{+0.7}_{-0.4}$) agree well with all of them.

In the UV, Cappellari et al. (1999) studied this LINER with both HST imaging (FOC) and spectroscopy (FOS), with images taken in 1991, 1993, and 1996, showing long-term variability. This agrees with Maoz et al. (2005), who used HST-ACS observations with its HRC mode and found a 20% variation of the nuclear flux in both $F250W$ and $F330W$ bands.

A.7. NGC 5846

NGC 5846 is a giant elliptical galaxy at the center of a small compact group of galaxies. The inner region of the galaxy contains dust and a radio core (Moellenhoff et al. 1992). Ho et al. (1997) classified this galaxy as an ambiguous case like transient 2.0 objects but the revision made by González-Martín et al. (2009b) located this object into the LINERs 2.0 category.

Three *Chandra* observations were made for this galaxy between 2000 and 2007 and two observations with *XMM-Newton* in January and August 2001. *Chandra* Obs ID 788 was analyzed by Filho et al. (2004), Satyapal et al. (2005), and Trinchieri & Goudfrooij (2002). Three different models were fitted (PL, APEC, and MEPL), and an order-of-magnitude difference in luminosity was found between Filho et al. (2004) ($\log L(2{-}10\ {\rm keV}) = 38.4$) and the other two works (39.4 and 39.6 ± 0.4, respectively), maybe entirely due to the different models used. Our luminosity ($\log{(L(2{-}10\ {\rm keV}))} = 39.3^{+0.2}_{-0.3}$) agrees well with those from Satyapal et al. (2005) and Trinchieri & Goudfrooij (2002). González-Martín et al. (2009b) reported *Chandra* Obs ID 4009 from 2003, but we have noticed that obs ID 4009 corresponds to the galaxy NGC 5845, not to NGC 5846. The *XMM-Newton* observations reported by González-Martín et al. (2009b) based on data taken on 2001 were fitted with the ME2PL model, resulting in a $\log L(2{-}10\ {\rm keV}) = 40.8^{+0.0}_{-2.4}$, in agreement with our results (40.2 ± 0.0).

Appendix B: X-ray images

In this Appendix we present the images from *Chandra* (left) and *XMM-Newton* (right) that we used to compare data from these instruments in the 0.5–10 keV band. Big circles represent 25″ apertures. Small circles in the left figures represent the nuclear extraction aperture used with *Chandra* observations (see Table 2). In all cases, the gray levels extend from twice the value of the background dispersion to the maximum value at the center of each galaxy.

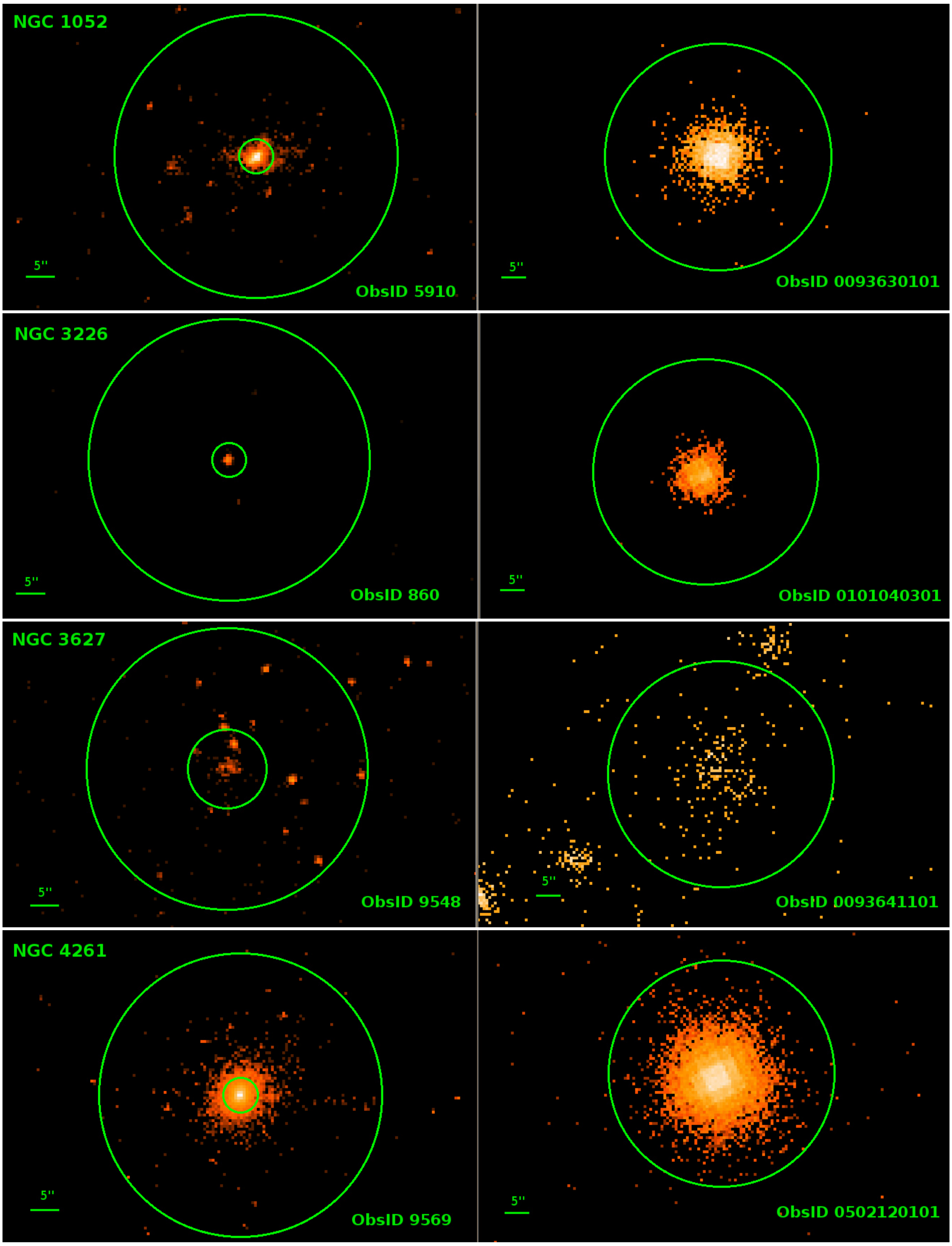

Fig. B.1. Images for *Chandra* data (*left*) and *XMM-Newton* data (*right*) for the sources in the 0.5–10 keV band. Big circles represent 25″ apertures. Small circles in the left figures represent the nuclear extraction aperture used with *Chandra* observations (see Table 2).

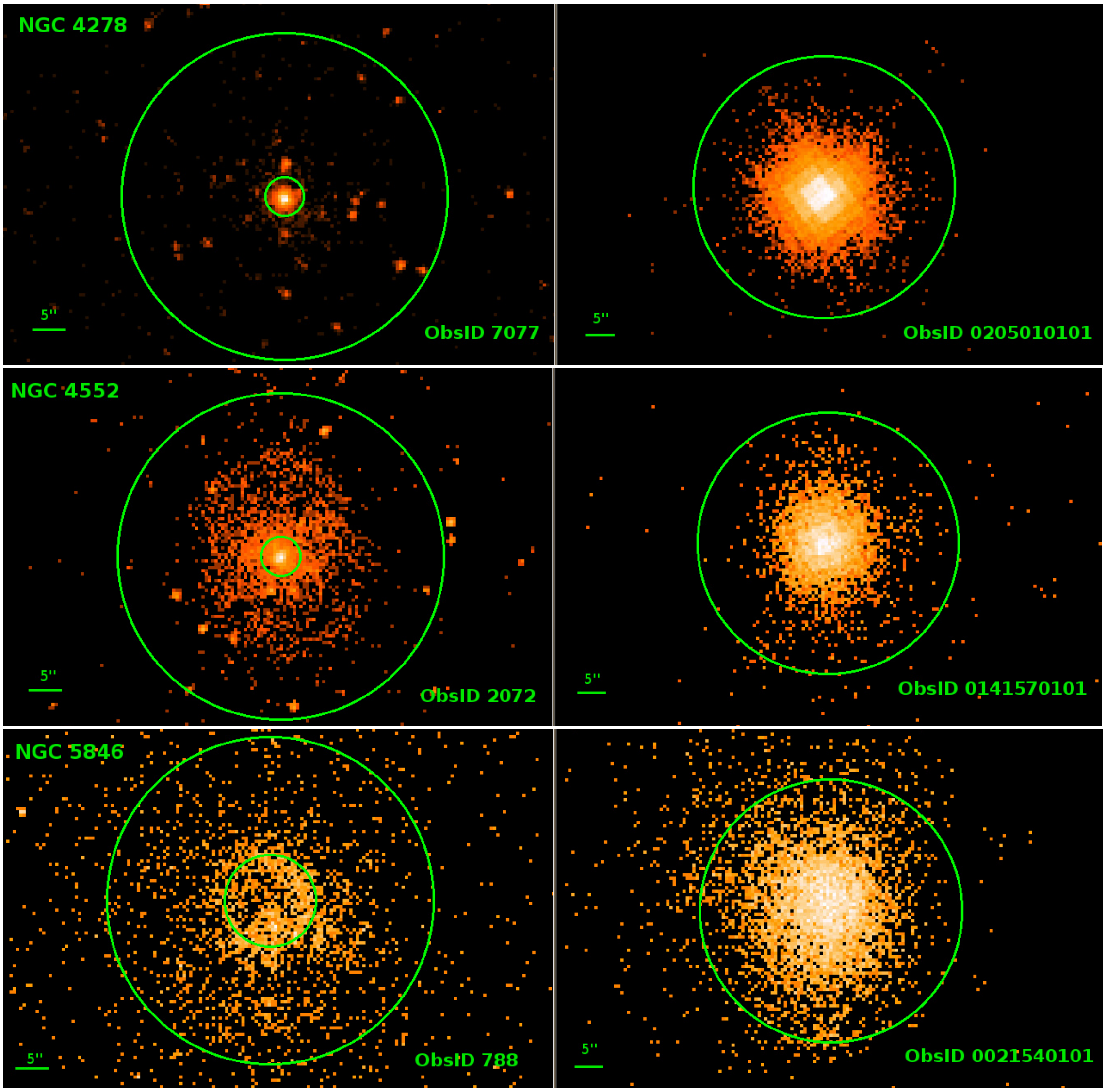

Fig. B.1. continued.

Appendix C: Light curves

The plots corresponding to the light curves are provided.

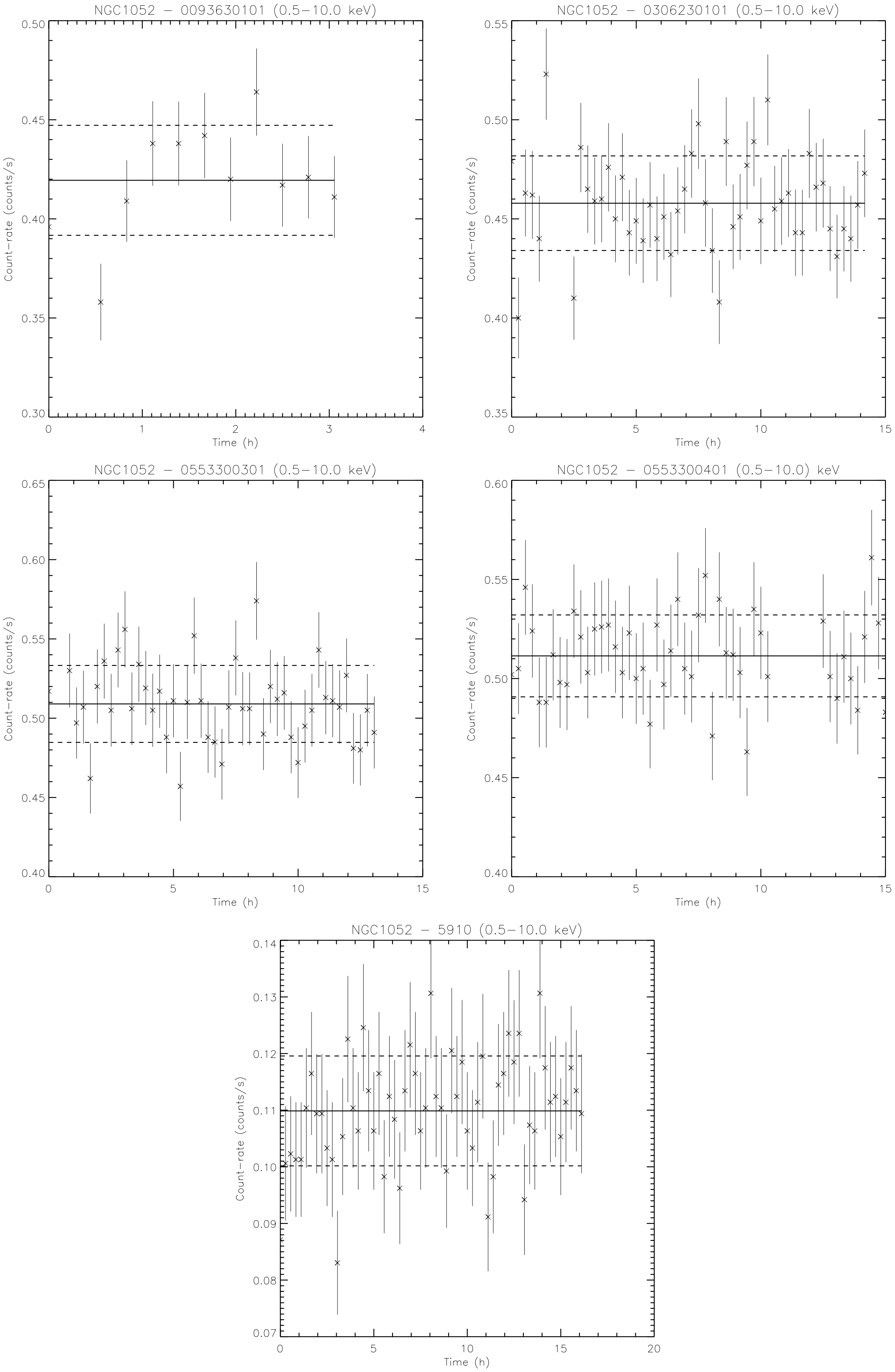

Fig. C.1. Light curves for NGC 1052.

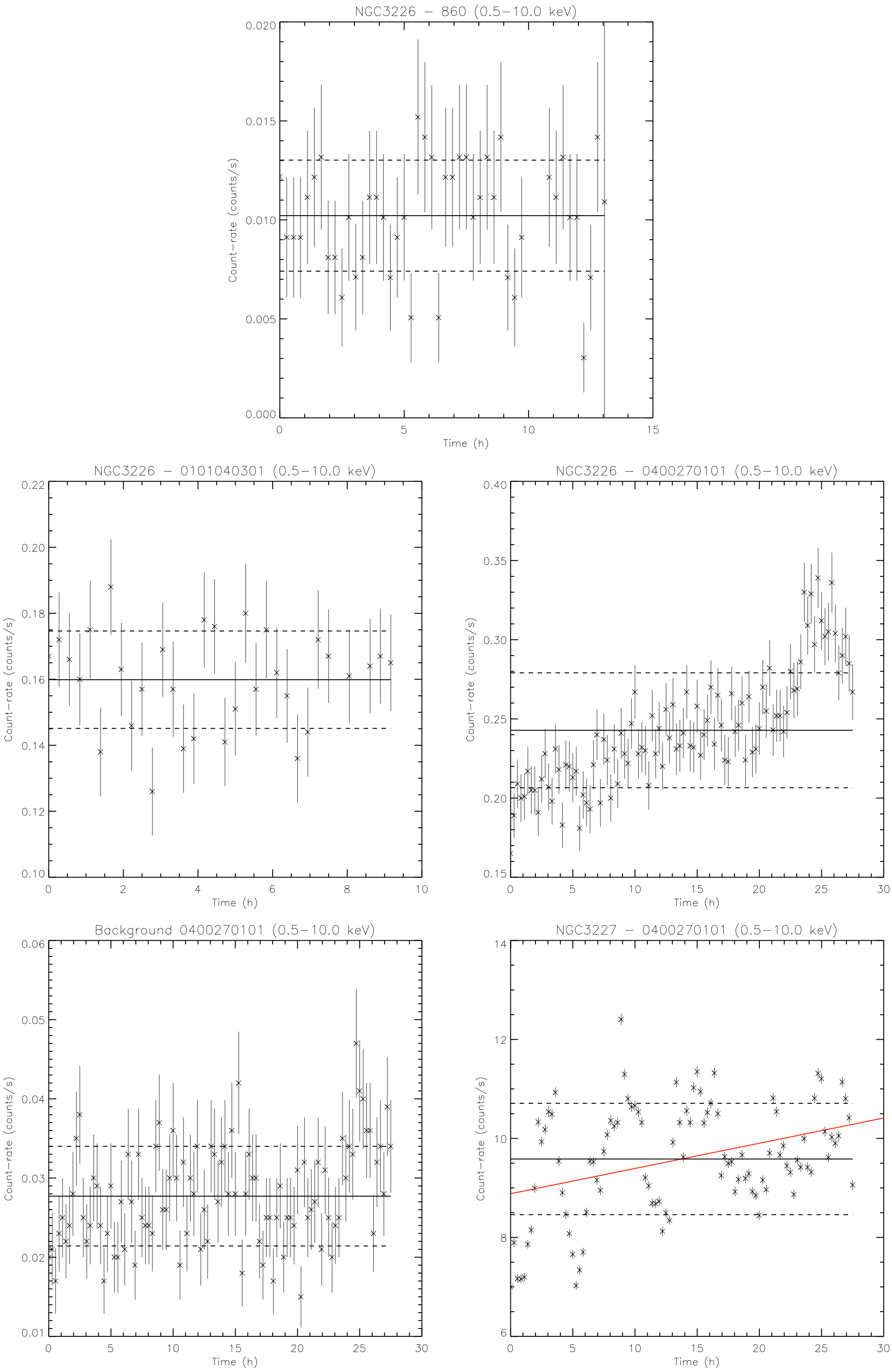

Fig. C.2. Light curves for NGC 3226 (*up*). Light curve from NGC 3227 (*middle-right*), where the red solid line represents a linear regresion, and the light curve from the background (*middle-left*). *XMM-Newton* obs ID 0400270101 image (*down*). The background follows the same behavior as NGC 3227.

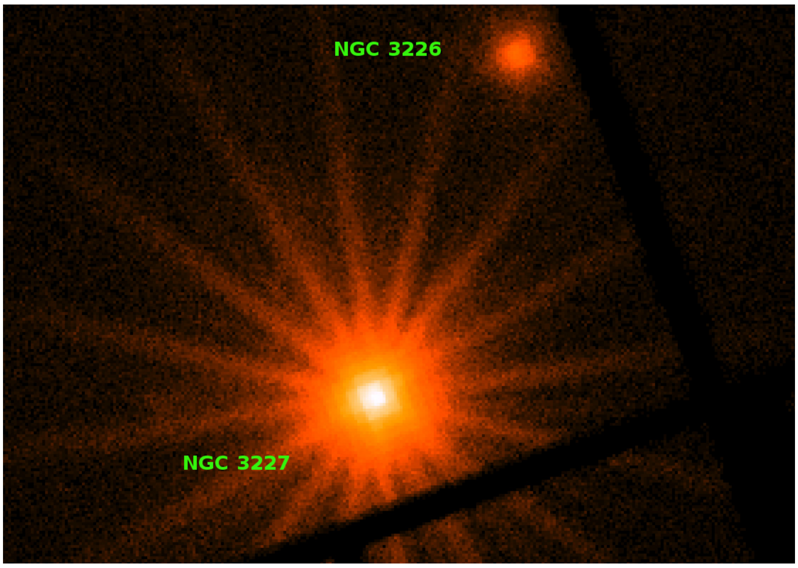

Fig. C.2. continued.

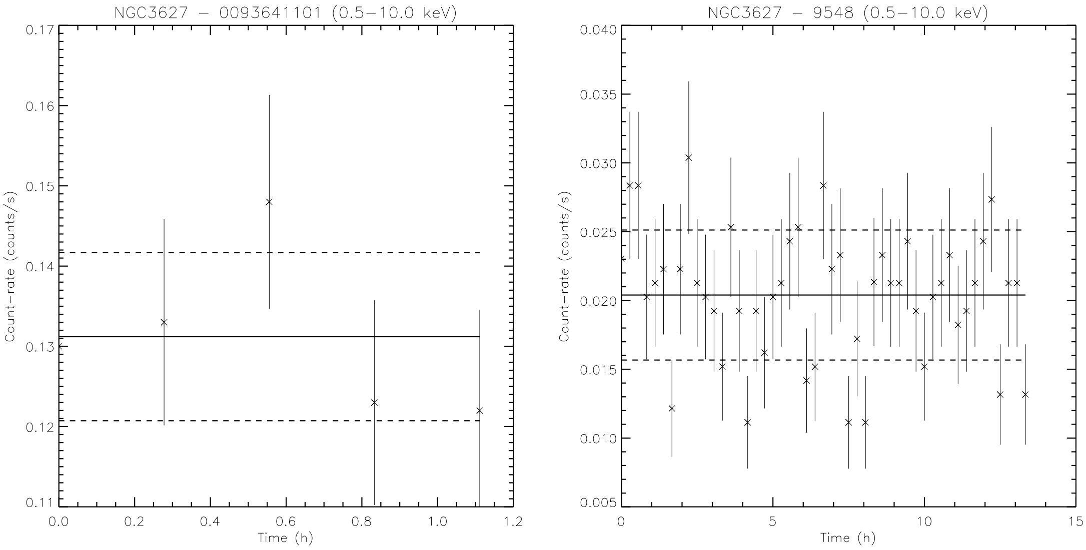

Fig. C.3. Light curves for NGC 3627.

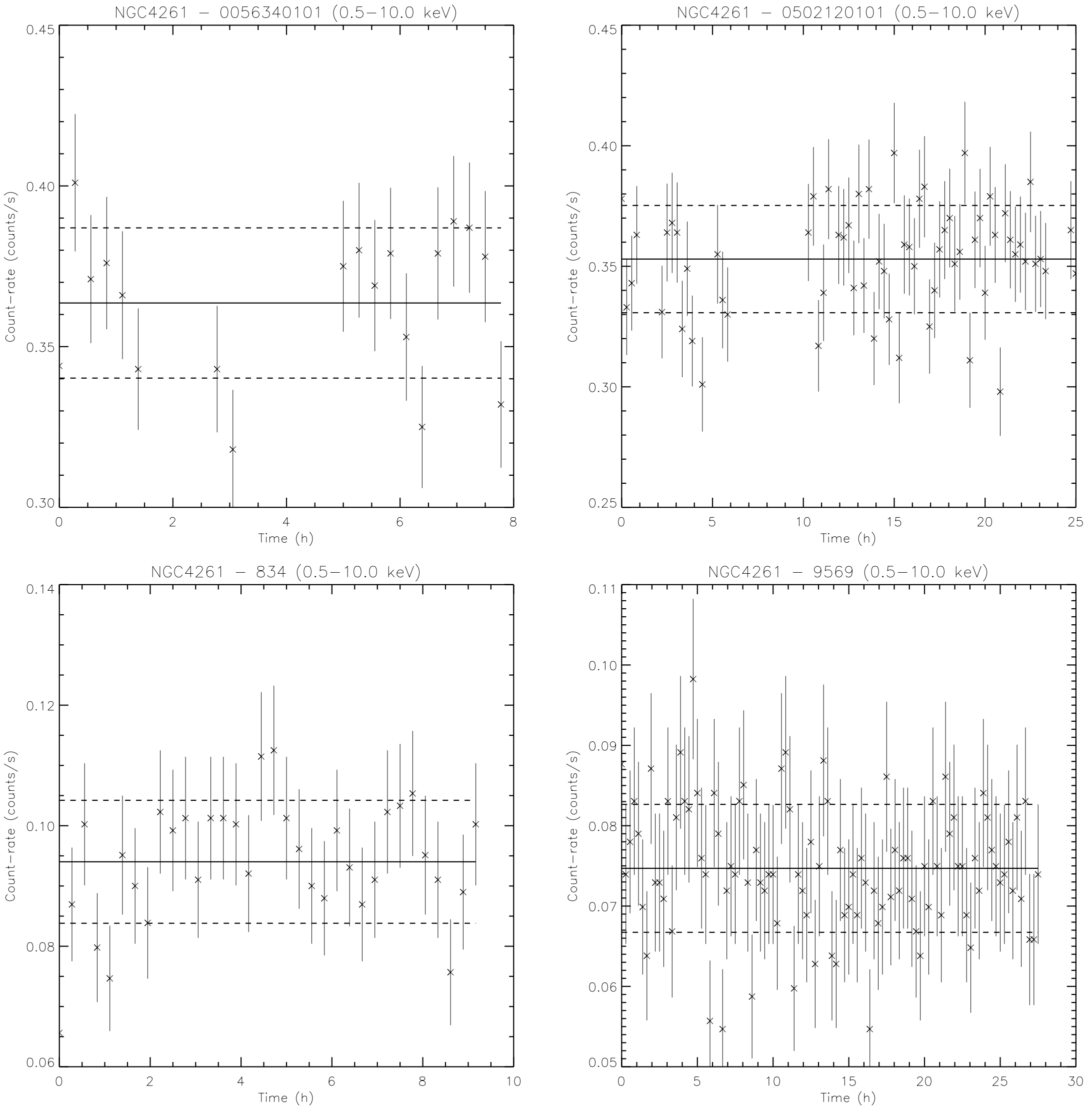

Fig. C.4. Light curves for NGC 4261.

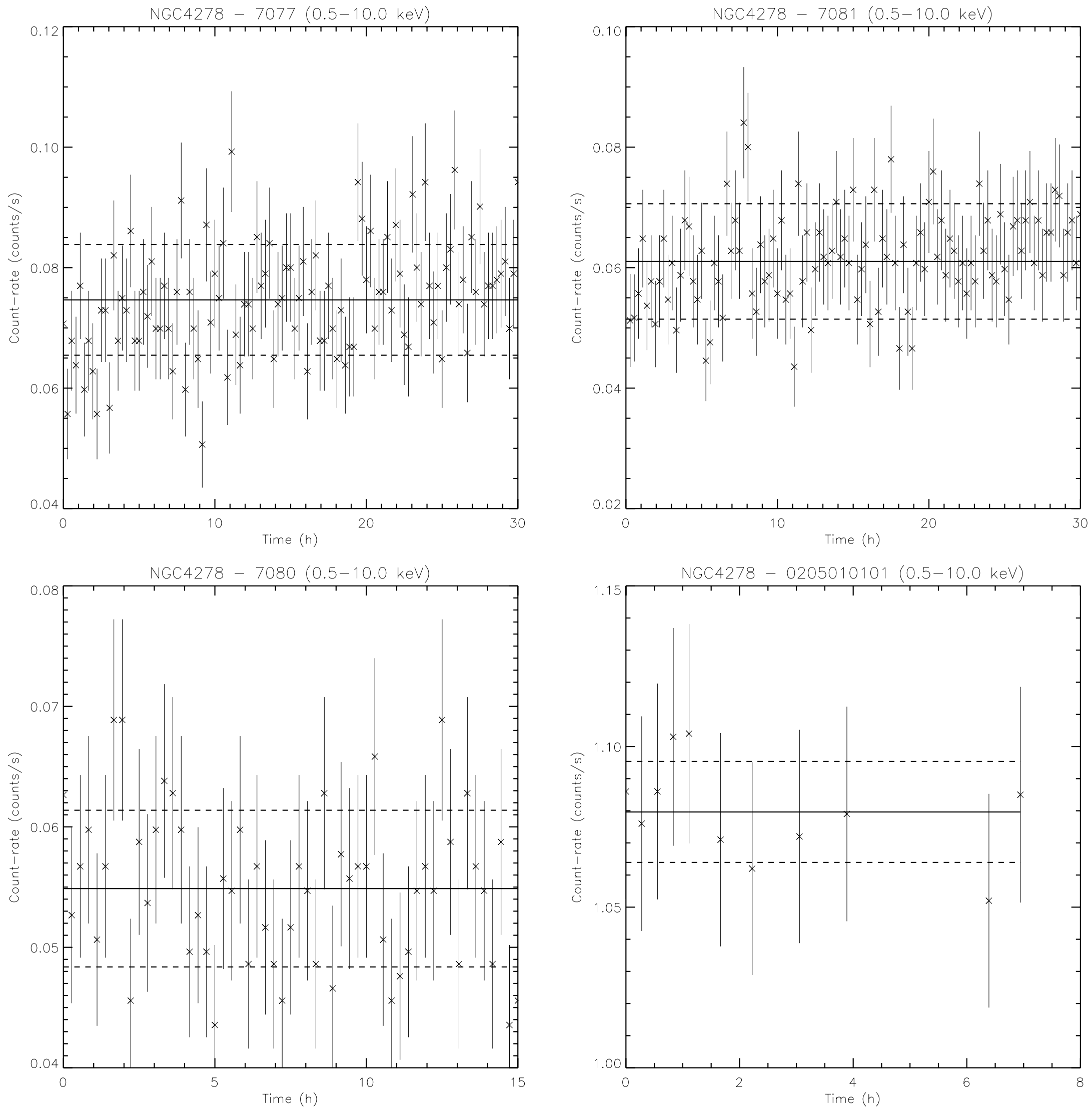

Fig. C.5. Light curves for NGC 4278.

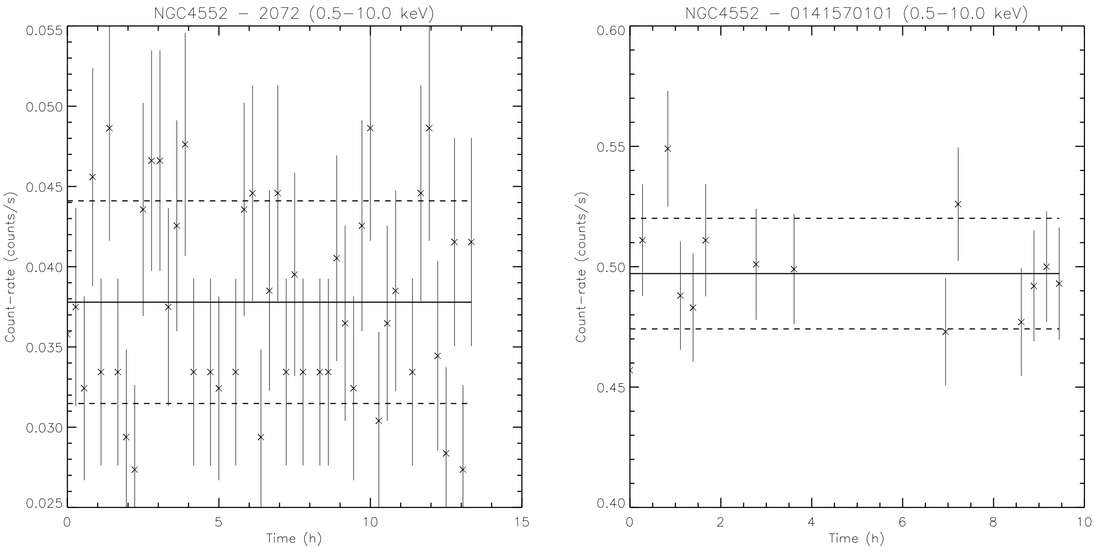

Fig. C.6. Light curves for NGC 4552.

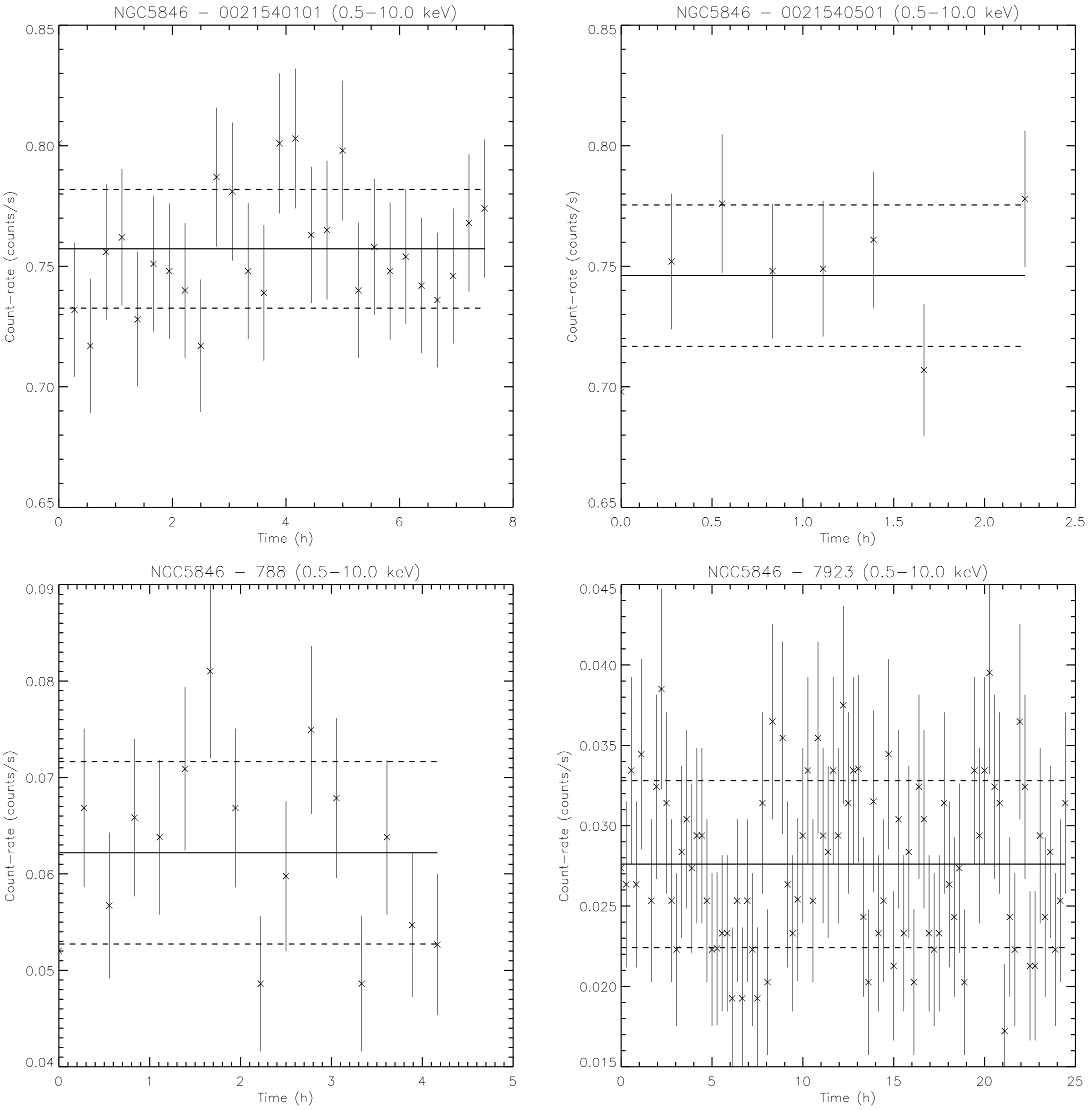

Fig. C.7. Light curves for NGC 5846.

A&A 569, A26 (2014)
DOI: 10.1051/0004-6361/201424140

Astronomy & Astrophysics

X-ray spectral variability of LINERs selected from the Palomar sample*

L. Hernández-García[1], O. González-Martín[2,3], J. Masegosa[1], and I. Márquez[1]

[1] Instituto de Astrofísica de Andalucía, CSIC, Glorieta de la Astronomía, s/n, 18008 Granada, Spain
e-mail: `lorena@iaa.es`
[2] Instituto de Astrofísica de Canarias (IAC), C/ Vía Lactea, s/n, 38205 La Laguna, Tenerife, Spain
[3] Departamento de Astrofísica, Universidad de La Laguna (ULL), 38205 La Laguna, Tenerife, Spain

Received 6 May 2014 / Accepted 30 June 2014

ABSTRACT

Context. Variability is a general property of active galactic nuclei (AGN). The way in which these changes occur at X-rays is not yet clearly understood. In the particular case of low-ionization nuclear emission line region (LINER) nuclei, variations on the timescales from months to years have been found for some objects, but the main driver of these changes is still debated.
Aims. The main purpose of this work is to investigate the X-ray variability in LINERs, including the main driver of these variations, and to search for possible differences between type 1 and 2 objects.
Methods. We examined the 18 LINERs in the Palomar sample with data retrieved from the *Chandra* and/or *XMM-Newton* archives that correspond to observations gathered at different epochs. All the spectra for the same object were fitted simultaneously to study long-term variations. The nature of the variability patterns were studied by allowing different parameters to vary during the spectral fit. Whenever possible, short-term variations from the analysis of the light curves and long-term UV variability were studied.
Results. Short-term variations are not reported in X-rays. Three LINERs are classified as non-AGN candidates in X-rays, all of them are Compton-thick candidates; none of them show variations at these frequencies, and two of them vary in the UV. Long-term X-ray variations were analyzed in 12 out of 15 AGN candidates; about half of them showed variability (7 out of the 12). At UV frequencies, most of the AGN candidates with available data are variable (five out of six). Thus, 13 AGN candidates are analyzed at UV and/or X-rays, ten of which are variable at least in one energy band. None of the three objects that do not vary in X-rays have available UV data. This means that variability on long-timescales is very common in LINERs. These X-ray variations are mainly driven by changes in the nuclear power, while changes in absorptions are found only for NGC 1052. We do not find any difference between type 1 and 2 LINERs, neither in the number of variable cases (three out of five type 1 and four out of seven type 2 LINERs), nor in the nature of the variability pattern. We find indications of an anticorrelation between the slope of the power law, Γ, and the Eddington ratio.
Conclusions. LINERs are definitely variable sources irrespective of whether they are classified as optical type 1 or 2. Their BH masses, accretion rates, and variability timescales place them in the same plane as more powerful AGN at X-rays. However, our results suggest that the accretion mechanism in LINERs may be different. UV variations of some type 2 LINERs were found, this could support the hypothesis of a torus that disappears at low luminosities.

Key words. galaxies: active – X-rays: galaxies – ultraviolet: galaxies

1. Introduction

Active galactic nuclei (AGN) are divided into two classes depending on the width of the permitted optical Balmer spectral lines, which can be broad (type 1) or narrow (type 2). From the viewpoint of the unified model (UM) of AGN (Antonucci 1993; Urry & Padovani 1995), the difference between type 1 and 2 objects is due to orientation effects relative to the obscuring medium, where a direct view into the black hole (type 1) or a view through the absorbing material (type 2) gives rise to a variety of subtypes between both classes. For low-ionization nuclear emission line regions (LINER), it is tempting to view them as a scaled-down version of Seyfert galaxies. However, different physical properties (e.g., black hole masses or luminosities) have been inferred (Eracleous et al. 2010a; Masegosa et al. 2011), and the way to introduce them into the UM is still controversial (Ho 2008). Ho et al. (1997) optically classified a variety of LINERs as 1.9 or 2.0 types, while objects resembling Seyfert 1−1.5 galaxies have not been found.

X-ray data offer the most reliable probe of the high-energy spectrum, providing many AGN signatures (D'Onofrio et al. 2012). AGN are detected as a point-like source at hard X-rays. This method was applied for LINERs in a number of publications (e.g., Satyapal et al. 2004, 2005; Dudik et al. 2005; Ho 2008). The most extensive work was carried out by González-Martín et al. (2009b). They analyzed 82 LINERs with *Chandra* and/or *XMM-Newton* data and found that 60% of the sample show a compact nuclear source in the 4.5−8 keV band; a multiwavelength analysis yielded that about 80% of the nuclei showed evidence of AGN-related properties. Moreover, their result is a lower limit since Compton-thick (CT) objects (i.e., $N_{\rm H} > 1.5 \times 10^{24}$ cm^{-2}) were not taken into account.

Variability is one of the main properties of AGN (Peterson 1997). For LINERs, the first clear evidence of variability was reported by Maoz et al. (2005) at UV frequencies. In X-rays, variability can be studied by comparing spectra at different epochs, which can account for long-term variations. This was done for

---

* Appendices are available in electronic form at http://www.aanda.org

LINERs by different authors. Pian et al. (2010) and Younes et al. (2011) showed that long-term variability is common in type 1 LINERs. González-Martín et al. (2011a) studied a type 2 LINER that also showed long-term variations. In a previous paper, we studied long-term spectral variability in six type 1 and 2 LINERs, where spectral and flux variations were found on longtimescales in four objects (Hernández-García et al. 2013, hereinafter HG13). These spectral variations may be related to the soft excess, the absorber, and/or the nuclear power.

For a one-epoch observation, when high signal-to-noise data are available, short-timescale variations can be investigated through a power spectral density (PSD) analysis of the light curve (Lawrence et al. 1987; González-Martín & Vaughan 2012). By using this analysis, González-Martín & Vaughan (2012) found 14% of variable LINERs, compared with 79% found for Seyfert galaxies.

On the other hand, the normalized excess variance, $\sigma^2_{\rm NXS}$, is the most straightforward method to search for short-term variations (Nandra et al. 1997; Vaughan et al. 2003). This quantity can be understood as a proxy of the area below the PSD shape, and can be used to search for short-term variations, with the advantage that high-quality data are not required to calculate it. In HG13 we did not find short-term variations in six LINERs.

The aim of this paper is to study the main driver of the X-ray variability in LINERs. We analyzed the X-ray variability in the largest available sample of LINERs. This paper is organized as follows: the sample and the data are presented in Sect. 2. The reduction of the data is explained in Sect. 3. A review of the methodolody is provided in Sect. 4, where individual and simultaneous spectral fittings, comparisons of different appertures, flux variability at X-ray and UV frequencies, and short-term variability are explained. The results from this analysis are given in Sect. 5, and are discussed in Sect. 6. Finally, our main results are summarized in Sect. 7.

2. Sample and data

We used the Palomar Sample (Ho et al. 1997), which is the largest sample of nearby galaxies with optical spectra, containing HII nuclei, Seyferts, LINERs, and transition objects. It includes measurements of the spectroscopic parameters for 418 emission-line nuclei. Since we are interested in LINERs, objects clasified as L1, L1:, L1::, L2, L2:, L2::, and L/S[1] were taken into account. This sample contains 89 LINERs, 22 of type 1 and 67 of type 2. Note that throughout this paper, we divide the objects into two groups, type 1 (1.9) and type 2 (2.0), in accordance with the classification by Ho et al. (1997).

We made use of all the publicly available *XMM-Newton* and *Chandra* data up to October 2013. Initially, 63 objects had either *Chandra* or *XMM-Newton* observations by the date of the sample selection. LINERs with only one available observation were rejected from the sample (28 objects). Objects affected by a pileup fraction of 10% or more were excluded (four objects, and one observation of another object). The pileup fractions were estimated using the simulation software PIMMS[2] version 4.6. We used the 0.5−2 keV and 2−10 keV fluxes, the best-fit model, and the redshift to evaluate its importance. Only two objects in the final sample are affected by a pileup fraction of 6% (obsID. 2079 of NGC 4494, and obsID. 5908 of NGC 4374). As shown later in the results (see Sect. 5.1), this does not have consequences in the variability studies. To guarantee a proper spectral fitting, observations with fewer than 400 number counts were also excluded (12 objects, and 18 observations). ObsID 011119010 of NGC 4636 and 13814 of NGC 5195 met these criteria, but a visual inspection showed low number counts in the hard band and were rejected from the sample. Finally, NGC 4486 was rejected because it is well known that this source is dominated by the jet emission (Harris et al. 2003, 2006, 2009, 2011).

The final sample of LINERs contains 18 objects, eight of type 1 and 10 of type 2. Table 1 shows the general properties of the galaxies. This sample covers the same range in total apparent blue magnitudes as all LINERs in the sample of Ho et al. (1997), with B_T from 8.7 to 12.3, included in Col. 6. The X-ray classification from González-Martín et al. (2009b) divides the objects into AGN candidates (when a point-like source is detected in the 4.5−8.0 keV energy band) and non-AGN candidates (otherwise). Evidence of jet structure at radio frequencies is provided in Col. 10. Table A.1 shows the log of the valid observations, where the observational identification (Col. 3), dates (Col. 4), extraction radius (Col. 5), and the net exposure time (Col. 6) are presented. Number of counts and hardness ratios, defined as HR = (H − S)/(H + S)[3] are also included in Cols. 7 and 8. Finally, UV luminosities from the optical monitor (OM) and its corresponding filter are given in Cols. 9 and 10.

3. Data reduction

3.1. Chandra data

Chandra observations were obtained with the ACIS instrument (Garmire et al. 2003). The data reduction and analysis were carried out in a systematic, uniform way using CXC *Chandra* Interactive Analysis of Observations (CIAO[4]), version 4.3. Level 2 event data were extracted with the task ACIS-PROCESS-EVENTS. We first cleaned the data from background flares (i.e., periods of high background) using the task LC_CLEAN.SL[5], which removes periods of anomalously low (or high) count rates from light curves from source-free background regions of the CCD. This routine calculates a mean rate from which it deduces a minimum and maximum valid count rate, and creates a file with the periods that are considered to be good by the algorithm.

Nuclear spectra were extracted from a circular region centered on the positions given by the NED[6]. These positions were visually inspected to ensure that the coordinates match the X-ray source position. We chose circular radii, aiming to include all possible photons, while excluding other sources or background effects. The radii are in the range between $r_{\rm Chandra}$ = 1.5–5.0″ (or 3−10 pixels, see Table A.1). The background selection was made taking circular regions between 5−10″ apertures free of sources in the same chip as the target and close to the source to minimize effects related to the spatial variations of the CCD response. We used the task DMEXTRACT to extract the spectra of the source and the background regions. The response matrix file (RMF) was generated for each source region using the task MKACISRMF and the ancillary reference file (ARF) with the task MKWARF. The spectra were binned to have a minimum of

---

[1] Quality ratings as described by Ho et al. (1997) are given by ":" and "::" for uncertain and highly uncertain classification, respectively.

[2] `http://heasarc.gsfc.nasa.gov/docs/software/tools/pimms.html`

[3] H is the number of counts in the hard (2−10 keV) band and S is the number of counts in the soft (0.5−2 keV) band

[4] `http://cxc.harvard.edu/ciao4.4/`

[5] `http://cxc.harvard.edu/ciao/ahelp/lc_clean.html`

[6] `http://ned.ipac.caltech.edu/`

20 counts per spectral bin so that we would be able to use the χ^2-statistics that were compiled with the task GRPPHA included in FTOOLS.

3.2. *XMM–Newton* data

All *XMM-Newton* observations were made with the EPIC pn camera (Strüder et al. 2001). The data were reduced in a systematic, uniform way using the Science Analysis Software (SAS[7]), version 11.0.0. Before extracting the spectra, good-time intervals were selected (i.e., flares were excluded). The method we used for this purpose maximizes the signal-to-noise ratio of the net source spectrum by applying a different constant count rate threshold on the single-event light curve with a field-of-view background of $E > 10$ keV. The nuclear positions were taken from the NED and were visually inspected to verify that they match the X-ray nuclear positions. As a sanity check, the task EREGIONANALYSE was used to compare whether our visual selection deviated from this selection. This task was applied to three objects with low number counts in the sample (NGC 1961, NGC 3608, and NGC 5982) and relative diferences <1% were obtained. The extraction region was determined through circles of $r_{\rm XMM} = 15{-}35''$ (i.e., 300−700 px) radius and the background with an algorithm that selects the best circular region around the source that is free of other sources and as close as possible to the nucleus. This automatic selection was checked manually to ensure the best selection for the backgrounds.

We extracted the source and background regions with the EVSELECT task. RMFs were generated using the task RMFGEN, and the ARFs were generated using the task ARFGEN. We then grouped the spectra to obtain at least 20 counts per spectral bin using the task GRPPHA, as is required to be able to use the χ^2-statistics.

3.3. Light curves

Light curves in the 0.5−10 keV, 0.5−2.0 keV and 2.0−10.0 keV energy bands of the source and background were extracted using the task DMEXTRACT for *XMM-Newton* and the task EVSELECT for *Chandra* with a 1000 s bin. We studied only light curves with exposure times longer than 30 ks. Light curves with longer exposure times were divided into segments of 40 ks. Thus, in some cases more than one segment was obtained from the same light curve. The light curve from the source was manually screened for high background and flaring activity, i.e., when the background light curve showed flare-like events and/or prominent decreasing/increasing trends. After this process the total useful observation time is usually lower, therefore only light curves with more than a total of 30 ks were used for the analysis. The light curves are shown in Appendix D. Note that the values of the means and standard deviations were not used for the variability analysis, but for a visual inspection of the data.

4. Methodology

The methodology is explained in HG13, but differs in the treatment of the short-term variability (see Sect. 4.4). For clarity, we recall the procedure below.

4.1. Individual spectral analysis

An individual spectral analysis allowed us to select the best-fit model for each data set. We used XSPEC[8] version 12.7.0 to fit the data with five different models:

- ME: $e^{N_{\rm Gal}\sigma(E)} \cdot e^{N_{\rm H}\sigma(E(1+z))}[N_{\rm H}] \cdot MEKAL[kT, {\rm Norm}]$
- PL : $e^{N_{\rm Gal}\sigma(E)} \cdot e^{N_{\rm H}\sigma(E(1+z))}[N_{\rm H}] \cdot {\rm Norm}e^{-\Gamma}[\Gamma, {\rm Norm}]$
- 2PL: $e^{N_{\rm Gal}\sigma(E)}(e^{N_{\rm H1}\sigma(E(1+z))}[N_{\rm H1}] \cdot {\rm Norm}_1e^{-\Gamma}[\Gamma, {\rm Norm}_1] + e^{N_{\rm H2}\sigma(E(1+z))}[N_{\rm H2}] \cdot {\rm Norm}_2e^{-\Gamma}[\Gamma, {\rm Norm}_2])$
- MEPL: $e^{N_{\rm Gal}\sigma(E)}(e^{N_{\rm H1}\sigma(E(1+z))}[N_{\rm H1}] \cdot MEKAL[kT, {\rm Norm}_1] + e^{N_{\rm H2}\sigma(E(1+z))}[N_{\rm H2}] \cdot {\rm Norm}_2e^{-\Gamma}[\Gamma, {\rm Norm}_2])$
- ME2PL: $e^{N_{\rm Gal}\sigma(E)}(e^{N_{\rm H1}\sigma(E(1+z))}[N_{\rm H1}] \cdot {\rm Norm}_1e^{-\Gamma}[\Gamma, {\rm Norm}_1] + MEKAL[kT] + e^{N_{\rm H2}\sigma(E(1+z))}[N_{\rm H2}] \cdot {\rm Norm}_2e^{-\Gamma}[\Gamma, {\rm Norm}_2])$.

Here $\sigma(E)$ is the photo-electric cross-section, z is the redshift, and $Norm_i$ are the normalizations of the power law or the thermal component (i.e., ${\rm Norm}_1$ and ${\rm Norm}_2$). For each model, the parameters that vary are written in brackets. The Galactic absoption, $N_{\rm Gal}$, is included in each model and fixed to the predicted value (Col. 5 in Table 1) using the tool NH within FTOOLS (Dickey & Lockman 1990; Kalberla et al. 2005).

The χ^2/d.o.f. and F-test were used to select the simplest model that best represents the data.

4.2. Simultaneous spectral analysis

We simultaneously fitted the spectra for each object with the same model. The baseline model was obtained from the individual fittings. For each galaxy, the initial values for the parameters were set to those obtained for the spectrum with the largest number counts.

The simultaneous fit was made in three steps:

0. SMF0 (Simultaneous fit 0): The same model was used with all parameters linked to the same value to fit every spectra of the same object, i.e., the non-variable case.
1. SMF1: using SMF0 as the baseline for this step, we let the parameters $N_{\rm H1}$, $N_{\rm H2}$, Γ, ${\rm Norm}_1$, ${\rm Norm}_2$, and kT vary individually. The best fit was selected for the $\chi^2_{\rm r}$ closest to unity that improved SMF0 (using the F-test).
2. SMF2: using SMF1 as the baseline for this step (when SMF1 did not fit the data well), we let two parameters vary, the one that varied in SMF1 along with any of the other parameters of the fit. The $\chi^2_{\rm r}$ and F-test were again used to confirm an improvement of the fit.

Whenever possible, this method was separately applied to the data from the two instruments. When data from *Chandra* and *XMM-Newton* were used together, an additional analysis was performed to make sure the sources included in the larger aperture did not produce the observed variability. A spectrum of an annular region was then extracted from *Chandra* data, with $r_{\rm ext} = r_{\rm XMM}$ and $r_{\rm int} = r_{\rm Chandra}$. We recall that the PSF of *Chandra* is energy dependent and therefore the annular region might be affected by contamination from the source photons at high energies. We have estimated this contribution by simulating the PSF of the sources in our sample using ChaRT[9] and MARX[10]. A monochromatic energy of 8 keV was used and the ray density was obtained individually for each observation. We find that

---

[7] http://xmm.esa.int/sas/

[8] http://heasarc.nasa.gov/xanadu/xspec/

[9] http://cxc.harvard.edu/chart/

[10] http://space.mit.edu/ASC/MARX/

Table 1. General properties of the sample galaxies.

Name (1)	RA (J2000) (2)	Dec (J2000) (3)	Dist.[1] (Mpc) (4)	N_{Gal} (10^{20} cm^{-2}) (5)	m_{B} (6)	Morph. type (7)	Optical class. (8)	X-ray class. (9)	Jet (10)	Ref.[2] (11)
NGC 315	00 57 48.88	+00 21 08.8	59.60	5.88	12.20	E	L1.9	AGN	Y	(1)
NGC 1052	02 41 04.80	+08 15 20.8	19.48	3.07	11.44	E	L1.9	AGN	Y	(2)
NGC 1961	05 42 04.6	+69 22 42	56.20	8.28	11.01	SAB(rs)c	L2	AGN	Y	(3)
NGC 2681	08 53 32.73	+51 18 49.3	15.25	2.45	11.15	S0-a(s)	L1.9	AGN*	N	(1)
NGC 2787	09 19 18.56	+69 12 12.0	10.24	4.32	11.60	S0-a(sr)	L1.9	AGN	N	(1)
NGC 2841	09 22 02.63	+50 58 35.5	16.62	1.45	10.06	Sb(r)	L2	AGN	N	(1)
NGC 3226[3]	10 23 27.01	+19 53 54.7	29.84	2.14	12.34	E	L1.9	AGN	N	(1)
NGC 3608	11 16 58.96	+18 08 54.9	24.27	1.49	11.57	E	L2/S2:	Non-AGN*	N	(1)
NGC 3718	11 32 34.8	+53 04 05	17.00	1.08	11.19	SB(s)a	L1.9	AGN	Y	(1)
NGC 4261	12 19 23.22	+05 49 30.8	31.32	1.55	11.35	E	L2	AGN	Y	(4)
NGC 4278	12 20 06.83	+29 16 50.7	15.83	1.77	11.04	E	L1.9	AGN	Y	(5)
NGC 4374	12 25 03.74	+12 53 13.1	17.18	2.60	10.11	E	L2	AGN*	Y	(6)
NGC 4494	12 31 24.03	+25 46 29.9	13.84	1.52	10.68	E	L2::	AGN	N	(1)
NGC 4636	12 42 49.87	+02 41 16.0	16.24	1.81	10.43	E	L1.9	Non-AGN*	Y	(7)
NGC 4736	12 50 53.06	+41 07 13.6	5.02	1.44	8.71	Sab(r)	L2	AGN	N	(1)
NGC 5195	13 29 59.6	+47 15 58	7.91	1.56	10.38	IA	L2:	AGN	N	(8)
NGC 5813	15 01 11.26	+01 42 07.1	30.15	4.21	11.48	E	L2:	Non-AGN*	Y	(9)
NGC 5982	15 38 39.8	+59 21 21	41.22	1.82	12.05	E	L2::	AGN	N	(10)

Notes. (Col. 1) Name, (Col. 2) right ascension, (Col. 3) declination, (Col. 4) distance, (Col. 5) galactic absorption, (Col. 6) aparent magnitude in the Johnson filter *B* from Ho et al. (1997), (Col. 7) galaxy morphological type from González-Martín et al. (2009a), (Col. 8) optical classification from Ho et al. (1997), (Col. 9) X-ray classification from González-Martín et al. (2009b), where the * represent Compton-thick candidates from González-Martín et al. (2009a), (Col. 10) evidence of radio jet, and (Col. 11) references for radio data. (1) All distances are taken from the NED and correspond to the average redshift-independent distance estimates. (2) References: (1) Nagar et al. (2005); (2) Vermeulen et al. (2003); (3) Krips et al. (2007); (4) Birkinshaw & Davies (1985); (5) Giroletti et al. (2005); (6) Xu et al. (2000); (7) Giacintucci et al. (2011); (8) Ho & Ulvestad (2001); (9) Randall et al. (2011); (10) Vrtilek et al. (2013). (3) We rejected the long-term variability analysis (i.e., comparison of spectra at different epochs) of NGC 3226 because *XMM-Newton* data may be contaminated by emission from NGC 3227 (see HG13), while we have mantained the UV and short-term analyses (i.e., light curves).

the highest contribution from the source photons at 8 keV is 7%. Note that this contribution is at high energies (i.e., the contribution is lower at lower energies) and does not affect our results (see Sect. 5.1). The data used for comparisons are marked with *c* in Table A.1. When the contamination by the annular region to the *Chandra* data with the r_{XMM} aperture emission was higher than 50% in the 0.5−10.0 keV energy band, we did not consider the joint analysis since the accuracy of the derived parameters could be seriously affected. For lower contamination levels, we considered that *Chandra* data can be used to estimate the contribution of the annular region to the *XMM-Newton* spectrum. The ring from *Chandra* data was fitted with the five models explained above. The resulting model was incorporated (with its parameters frozen) in the fit of the *XMM-Newton* nuclear spectrum, which enabled us to extract the parameters of the nuclear emission. When multiple observations of the same object and instrument were available, we compared the data with similar dates (see Table A.1).

4.3. Flux variability

X-ray luminosities for the individual and simultaneous fits were computed using XSPEC for the soft and hard bands. Distances were taken from NED and correspond to the average redshift-independent distance estimate for each object when available (or to the redshift-estimated distance otherwise) and are listed in Table 1.

UV luminosities were obtained (when available) from the optical monitor (OM) onboard *XMM-Newton* simultaneously to X-ray data. Whenever possible, measurements from different filters were retrieved. We recall that *UVW*2 is centered at 1894 Å (1805−2454) Å, UVM2 at 2205 Å (1970−2675) Å, and *UVW*1 at 2675 Å (2410−3565) Å. For NGC 4736 we used data from the *U* filter (centered at 3275 Å (3030−3890) Å) because measures from other filters were not available. We used the OM observation FITS source lists (OBSMLI)[11] to obtain the photometry. When OM data were not available, we searched for UV information in the literature. We note that in this case the X-ray and UV data might not be simultaneous (see Appendix B).

We assumed an object to be variable when

$$L_{\max} - L_{\min} > 3 \times \sqrt{(\mathrm{err}L_{\max})^2 + (\mathrm{err}L_{\min})^2} \qquad (1)$$

where $L_{\max}$ and $L_{\min}$ are the highest and lowest luminosities of an object, and err$L_{\max}$ and err$L_{\min}$ are the measurement errors. We note that this relation was used to determine whether an object was variable, not as an error estimate.

4.4. Short-term variability

We assumed a constant count rate for the whole observation in the 0.5−10 keV energy band, and we calculated χ^2/d.o.f. as a proxy to the variations. We considered the source to be variable if the count rate differed from the average by more than 3σ (or 99.7% probability).

To compare the variability amplitude of the light curves between observations, we calculated the normalized excess variance, σ^2_{NXS}, for each light curve segment with 30−40 ks. This

---

[11] `ftp://xmm2.esac.esa.int/pub/odf/data/docs/XMM-SOC-GEN-ICD-0024.pdf`

magnitude is related to the area below the PSD shape. We followed the prescriptions given by Vaughan et al. (2003) to estimate $\sigma^2_{\rm NXS}$ and its error, err($\sigma^2_{\rm NXS}$) (see also González-Martín et al. 2011b)

$$\sigma^2_{\rm NXS} = \frac{S^2 - \langle\sigma^2_{\rm err}\rangle}{\langle x\rangle^2} \tag{2}$$

$$\mathrm{err}(\sigma^2_{\rm NXS}) = \sqrt{\frac{2}{N}\left(\frac{\langle\sigma^2_{\rm err}\rangle}{\langle x\rangle^2}\right)^2 + \frac{\langle\sigma^2_{\rm err}\rangle}{N}\frac{4\sigma^2_{\rm NXS}}{\langle x\rangle^2}}, \tag{3}$$

where x, $\sigma^2_{\rm err}$ and N are the count rate, its error, and the number of points in the light curve, respectively, and S^2 is the variance of the light curve,

$$S^2 = \frac{1}{N-1}\sum_{i=1}^{N}(x_i - \langle x\rangle)^2, \tag{4}$$

when $\sigma^2_{\rm NXS}$ was negative or compatible with zero within the errors, we estimated the 90% upper limits using Table 1 in Vaughan et al. (2003). We assumed a PSD slope of −1, the upper limit from Vaughan et al. (2003), and we added the value of 1.282err($\sigma^2_{\rm NXS}$) to the limit (to take into account the uncertainty due to the experimental Poisson fluctuations). For a number of segments, N, obtained from an individual light curve, an upper limit for the normalized excess variance was calculated as

$$\sigma^2_{\rm NXS} = \frac{\sqrt{\sum_{i=1}^{N}\sigma^2_{\rm NXS_i}}}{N}, \tag{5}$$

when N segments were obtained for the same light curve and at least one was consistent with being variable, we calculated the normalized weighted mean and its error as the weighted variance.

5. Results

In this section we present the individual results on the variability in LINERs of all the sources (Sect. 5.1) as well as the general results (Sects. 5.2, 5.3, and 5.4). This includes short- and long-term variations in X-rays and long-term variations at UV frequencies. The summary of the results obtained for the variability is given in Table 2. Notes and comparisons with previous works for individual objects are included in Appendix B.

5.1. Individual objects

To be concise, we list the peculiarities of each source. For details on the data and results, we refer to the following tables and figures: the observations used in the analysis (Table A.1), variations of the hardness ratio, HR, only compared for data from the same instrument (Col. 8 in Table A.1), UV luminosities when simultaneous data from the OM monitor were available for more than one date (Col. 9 in Table A.1 and Fig. 2), individual and simultaneous best fit and the parameters that varied in the model (Table A.2 and Fig. 1), X-ray flux variations (Table A.3 and Fig. 3), the analysis of the annular region when data from *Chandra* and *XMM-Newton* were used together (Table A.4), the simultaneous fittings of these observations (Table A.5), and short-term variability from the analysis of the light curves (Table A.6 and Appendix D). When short-term variations were not detected, upper limits of $\sigma^2_{\rm NXS}$ were calculated.

- NGC 315: from the simultaneous analysis of *Chandra* data, variations are not found in a three-year period (i.e., SMF0). The annular region contributes with 3% in *Chandra* data. When they are compared with *XMM-Newton* data, variations of the parameters do not improve the fit within the five-year period. The analysis of one of the *Chandra* light curves shows variations in the hard band at 1.6σ confidence level.
- NGC 1052: SMF2 was used to fit its *XMM-Newton* data, with variations of Norm$_2$ (49%) and $N_{\rm H2}$ (31%) over a period of eight years. Flux variations of 20% are obtained for soft and hard energies in the same period. Since the annular region contributes with 10% in *Chandra* data, *Chandra* and *XMM-Newton* data were compared, without changes in a one-year period. Short-term variations are not detected. UV variations from the *UVW*2 (13%) and UVM2 (21%) are found.
- NGC 1961: *XMM-Newton* data do not show variations in a one-month period (i.e., SMF0). UV data are available, but the nucleus of the galaxy is not detected.
- NGC 2681: the SMF0 results for *Chandra* data did not improve for varying parameters. Consequently, the object does not vary in a period of four months. Short-term variations are not detected.
- NGC 2787: one observation per instrument is available. When they are compared, the emission from the annular region contributes with 53% in *Chandra* data. Therefore we did not perform a simultaneous fit and did not use this object to discuss long-term variations. Short-term variations are not detected.
- NGC 2841: one observation per instrument is available. When they are compared, the emission from the annular region contributes with 60% in *Chandra* data. Therefore we did not perform a simultaneous fit and did not use this object to discuss long-term variations. In this case the *Chandra* image reveals at least three X-ray sources within the annular region (see Appendix C).
- NGC 3226: long-term X-ray variations from this source are not taken into account because of possible contamination from NGC 3227. We refer to HG13 for details. The analysis from the *Chandra* light curve shows variations in the soft and total bands below the 2σ confidence level. UV variations amount to 11% in the *UVW*1 filter.
- NGC 3608: SMF0 was used to fit the *XMM-Newton* data, with no variations in a 12 year period.
- NGC 3718: we jointly fit *Chandra* and *XMM-Newton* data since emission from the annular region is negligible. The best representation of the data need Norm$_2$ to vary (37%), i.e., SMF1 was used. This implies a change in luminosity of 35% (29%) at soft (hard) energy in a one-year period. The nucleus of the galaxy is not detected in the UV data.
- NGC 4261: the simultaneous fit with constant parameters (i.e., SMF0) results in a good fit both in *Chandra* and *XMM-Newton* data over a period of eight and six years, respectively. A simultaneous fit of *Chandra* and *XMM-Newton* (the annular region contributes with 37% in *Chandra* data) did not show changes. Short-term variations are not detected. Considering the UV range, variations amount to 9% in the *UVW*1 filter and 34% in the UVM2 filter.
- NGC 4278: the best fit for *Chandra* data is SMF1, with Norm$_2$ varying (30%) in a one-year period. An X-ray intrinsic luminosity variation at soft (hard) energy of 26% (29%) is found. The contribution of the annular region in *Chandra* data amounts to 38%. When comparing *XMM-Newton* and *Chandra* data, a variation in the normalization of the

Table 2. Results of the variability analysis.

Name	Type	log ($L_{\rm soft}$)	log ($L_{\rm hard}$)	log ($M_{\rm BH}$)	log ($R_{\rm Edd}$)	Variability			T	HR
		(0.5−2 keV)	(2−10 keV)			SMF0	SMF1	SMF2	(Years)	
(1)	(2)	(3)	(4)	(5)	(6)	(7)	(8)	(9)	(10)	(11)
NGC 315 (C)	AGN	41.38	41.58	8.65	−3.67	MEPL	–	–	3	
	L1.9	0%	0%							8%
NGC 1052 (X)	AGN	41.04	41.52	8.07	−3.14	ME2PL	Norm$_2$	$N_{\rm H2}$	8	
	L1.9	20%	20%				49%	31%		33%
NGC 1961 (X)	AGN	41.20	41.23	8.67	−4.03	ME2PL	–	–	0.08	
	L2	0%	0%							0%
NGC 2681* (C)	AGN	39.02	38.93	7.07	−4.73	MEPL	–	–	0.4	
	L1.9	0%	0%							4%
NGC 3608* (X)	Non-AGN	40.32	40.24	8.06	−4.41	ME2PL	–	–	12	
	L2/S2:	0%	0%							4%
NGC 3718 (C+X)	AGN	40.76	40.99	7.85	−3.60	2PL	Norm$_2$	–	1	
	L1.9	35%	29%				37%			14%
NGC 4261 (X)	AGN	40.98	41.02	8.96	−4.54	ME2PL	–	–	8	
	L2	0%	0%							0%
(C)						ME2PL	–	–	6	
		0%	0%							19%
NGC 4278 (C)	AGN	39.80	39.75	8.46	−5.30	MEPL	Norm$_2$	–	1	
	L1.9	26%	29%				30%			4%
NGC 4374* (C)	AGN	39.64	39.59	8.74	−5.79	MEPL	Norm$_2$	–	5	
	L2	64%	71%				73%			12%
NGC 4494 (X,C)	AGN	39.13	39.37	7.64	−4.84	PL	Norm	–	0.3	
	L2::	31%	35%				33%			
NGC 4636* (X)	Non-AGN	40.86	39.81	8.16	−5.00	MEPL	–	–	0.5	
	L1.9	0%	0%							14%
NGC 4736 (X)	AGN	39.61	39.73	6.98	−3.84	MEPL	–	–	4	
	L2	0%	0%							5%
NGC 5195 (X)	AGN	39.24	39.25	7.59	−4.86	MEPL	Norm$_2$	–	8	
	L2:	9%	19%				20%			3%
(C)		38.56	38.61			MEPL	–	–	0	
		0%	0%							2%
NGC 5813* (X)	Non-AGN	41.33	40.30	8.42	−4.72	MEPL	–	–	4	
	L2:	0%	0%							1%
(C)		39.68	39.07	8.42	−5.95	MEPL	–	–	6	
		0%	0%							5%
NGC 5982 (X)	AGN	40.70	40.49	8.44	−4.71	MEPL	Norm$_2$	–	1	
	L2::	11%	49%				50%			10%

Notes. (Col. 1) Name (the asterisks represent Compton−thick objects), and the instrument (C: *Chandra* and/or X: *XMM-Newton*) in parenthesis, (Col. 2) X-ray and optical types, (Cols. 3 and 4) logarithm of the soft (0.5−2 keV) and hard (2−10 keV) X-ray luminosities, where the mean was calculated for objects with variability, and percentages in flux variations, (Col. 5) black-hole mass in logarithmical scale, determined using the correlation between stellar velocity dispersion (from HyperLeda) and black-hole mass (Tremaine et al. 2002), (Col. 6) Eddington ratio, $L_{\rm bol}/L_{\rm Edd}$, calculated from Eracleous et al. (2010a) using $L_{\rm bol} = 33 L_{2-10 \ \rm keV}$, (Col. 7) best fit for SMF0, (Col. 8) parameter varying in SMF1, with the percentage of variation, (Col. 9) parameter varying in SMF2, with the percentage of variation, (Col. 10) the sampling timescale, and (Col. 11) variations in the hardness ratios.

PL (15%) during two years is found. Short-term variations are not detected.

- NGC 4374: SMF1 was used for the simultaneous fit with *Chandra* data, with variations of Norm$_2$ (73%) in a period of five years. Flux variation of 64% (71%) in the soft (hard) band during the same period are found. Data from different instruments were not compared because the annular region contributes 84% in *Chandra* data. Short-term variations in the soft and total bands are found from one *Chandra* observation below 2σ confidence level.
- NGC 4494: the simultaneous fit was jointly performed for *Chandra* and *XMM-Newton* data (the contribution of the annular region is 21% in *Chandra* data) up to 4.5 keV, because *Chandra* data show a low count-rate at harder energies. We used SMF1 and obtained the best representation of the data set when Norm varied (33%). Flux variation of 31% (35%) is obtained for the soft (hard) energy in a four-month period.
- NGC 4636: SMF0 was used to fit *XMM-Newton* data, i.e., variations were not found over a six-month period. Note that $\chi^2_{\rm r} \sim 2$. Unfortunately, none of the proposed models are good enough to improve the final fit. From the analysis of the light curves, short-term variations in the hard band are obtained from one *XMM-Newton* observation at 1.4σ confidence level. Variations of 28% are obtained from the *UVW*1 filter in the UV.
- NGC 4736: variations are not found from *XMM-Newton* data, i.e., SMF0 was used in a period of four years. *Chandra* and *XMM-Newton* data were not compared since the emission from the annular region contributes with 84% in *Chandra* data. From the analysis of the light curves, variations in the soft, hard, and total bands are obtained below 2σ

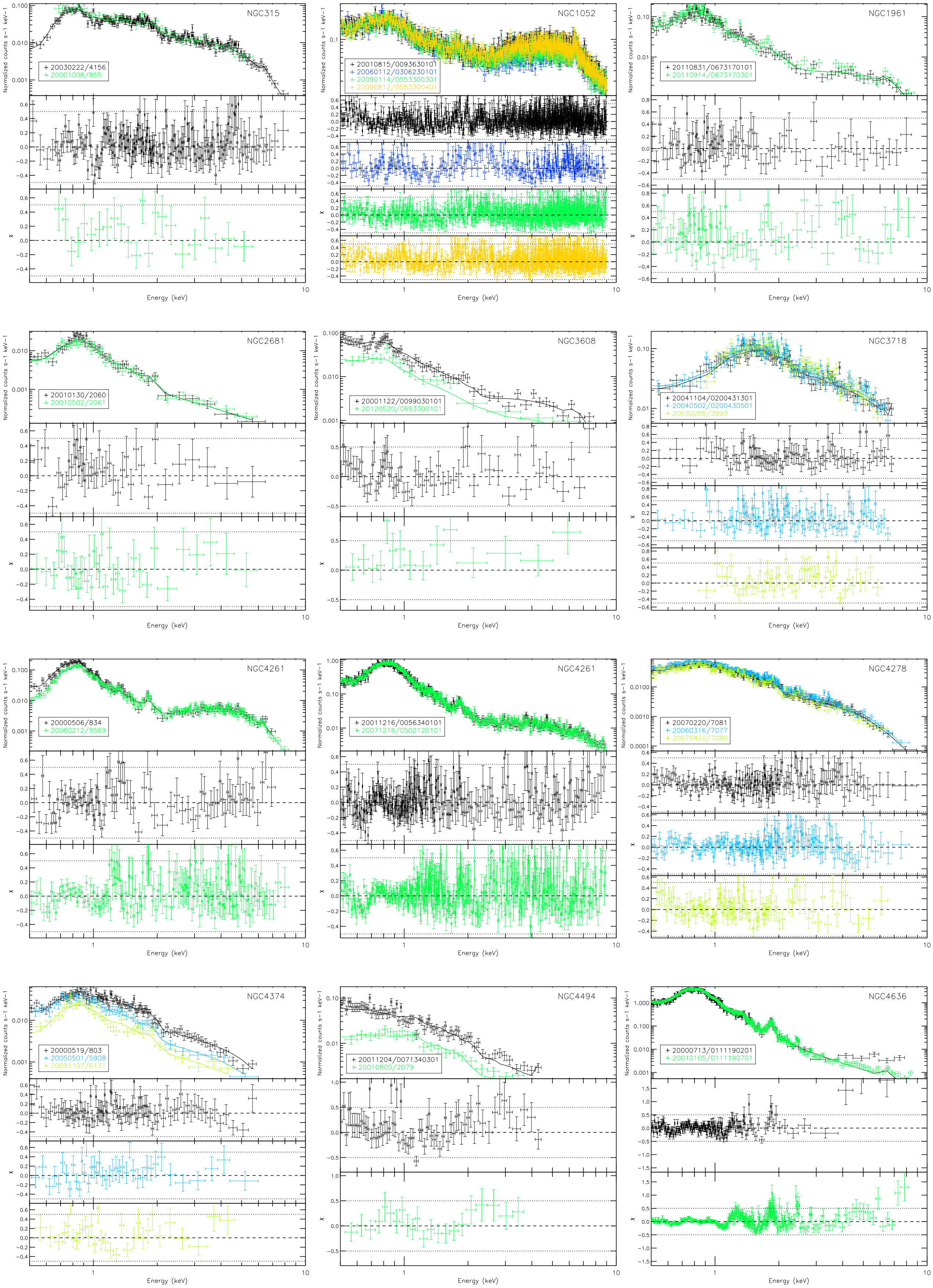

Fig. 1. For each object and instrument we plot (*top*): a simultaneous fit of X-ray spectra; (*from second row on*): the residuals. The legends contain the date (in the format yyyymmdd), and the obsID. Details are given in Table A.1.

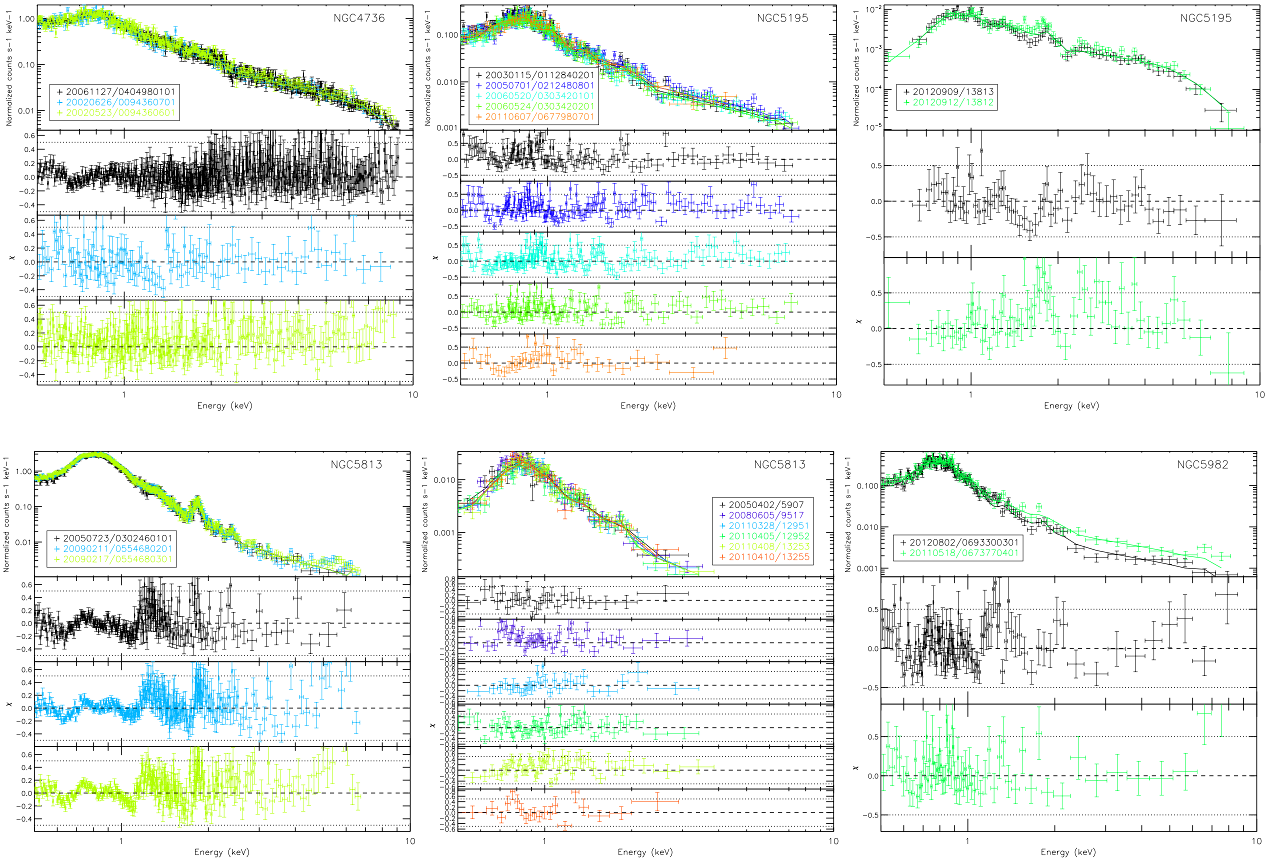

Fig. 1. continued.

confidence level in all cases. At UV frequencies, a variation of 66% is obtained from the *U* filter.

- NGC 5195: SMF1 was used for *XMM-Newton* data, where the best representation was achieved for Norm$_2$ varying (20%). A flux variation of 9% (19%) in the soft (hard) energy band was found in a period of eight years. For *Chandra* data, no variations are found from the simultaneous fit (i.e., SMF0) in a three-day period. The annular region contributes with 74% in *Chandra* data, so the data from the two instruments were not compared. The analysis of one *Chandra* light curve reveals short-term variations in the soft and total bands below 2σ confidence level. At UV frequencies, variation of 16% are found with the *UVW*1 filter.
- NGC 5813: for *Chandra* data we made the simultaneous analysis up to 4 keV because of the low count rate at harder energies. For both *Chandra* and *XMM-Newton* data SMF0 was used, with no improvement of the fit when we varied the parameters in a period of six and four years, respectively. Note that $\chi^2_{\rm r} \sim 2$ in *XMM-Newton* data. Unfortunately, none of the proposed models are good enough to improve the final fit. The data from the two instruments were not compared since the annular region contributes with 100% in *Chandra* data. Short-term variations are not detected. In the UV, OM observations with the *UVW*1 filter were used, which show variations of 8% in a period of four years.
- NGC 5982: SMF1 was used to fit *XMM-Newton* data, with the best representation achieved by varying Norm$_2$ (50%). Flux variations of 11% (49%) in the soft (hard) band were obtained in a period of one year. UV variations are not found.

5.2. Long-term X-ray spectral variability

A first approximation to the spectral variations can be made from the hardness ratios (HR). Following the results in HG13, an object can be considered to be variable when HR varies by more than 20%. One out of the 14 objects in our sample is variable according to this criterion, using the HR measurements with the same instrument (NGC 1052). Since we mainly doubled the sample number, we conclude that the result obtained in HG13 is a consequence of low number statistics. However, no clear relation can be invoked between variable objects and a minimum in HR variations (see Table 2).

Chandra and *XMM-Newton* data are available together for the same object in 12 cases. We recall that we only compared the data from the two instruments when the emission from the annular region with $r_{\rm ext} = r_{XMM}$ and $r_{\rm int} = r_{Chandra}$ contributed less than 50% in *Chandra* data with the r_{XMM} aperture. For NGC 3718 there is no extranuclear contamination, therefore we performed the simultaneous analysis without any prior analysis of the extended emission. In six cases we made no simultaneous fit with data from the two instruments. In five objects (NGC 315, NGC 1052, NGC 4261, NGC 4278, and NGC 4494) the extranuclear contamination was taken into account for the simultaneous fit following the methodology described in Sect. 4.2.

None of the three non-AGN candidates show variations (one type 1 and two type 2). Seven out of the 12 AGN candidates (three out of five type 1, and four out of seven type 2) show spectral variations. We find no variations in the spectral index, Γ, in any of the objects in the sample. In all cases Norm$_2$ is responsible for these variations (between 20−73%). In one case (NGC 1052, type 1) variation in $N_{\rm H2}$ (31%) is required along

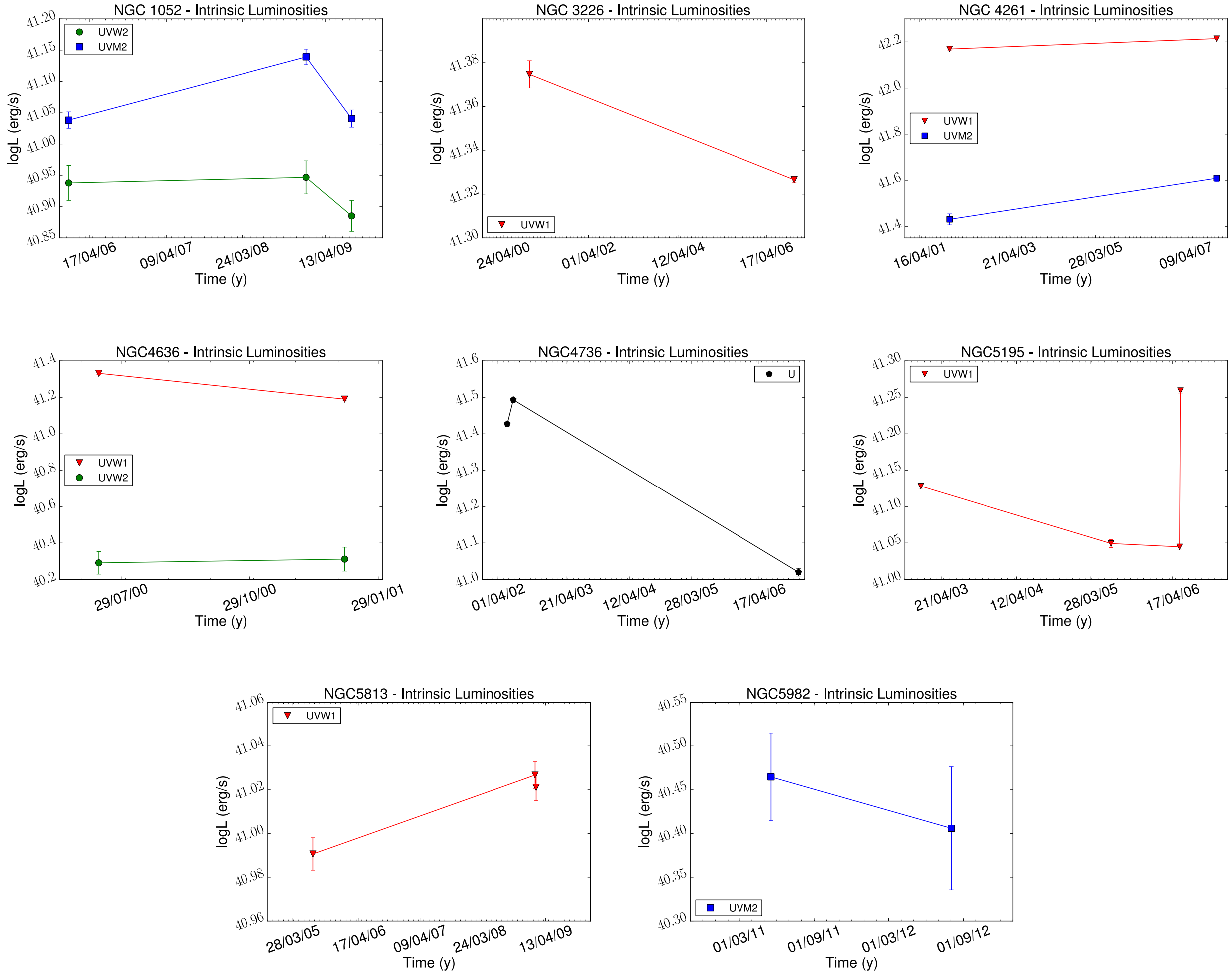

Fig. 2. UV luminosities obtained from the data with the OM camera onboard *XMM-Newton*, when available. Different filters have been used; *UVW*1 (red triangles), *UVW*2 (green circles), UVM2 (blue squares), *U* (black pentagons).

with variations in Norm$_2$. These variations were found irrespective of the LINER type (see Table 2).

5.3. UV and X-ray long-term flux variability

Since variations in Norm$_2$ naturally imply changes in the flux, all the objects that show spectral variations at X-ray frequencies also show flux variability (see Sect. 5.2). This means that none of the non-AGN candidates show flux variations, while seven out of the 12 AGN candidates do. Variations from 9 to 64% (19 to 71%) are obtained in the soft (hard) band (see Table 2). Soft and hard X-ray luminosities are listed in Table A.3 and are presented in Fig. 3 for objects with flux variations.

In eight out of the 18 cases, data at UV frequencies are provided by the OM onboard *XMM-Newton* at different epochs (simultaneously with X-ray data). Two of them are non-AGN candidates (the type 1 NGC 4636 and the type 2 NGC 5813). Both show variations in the *UVW*1 filter, while NGC 4636 does not vary in the *UVW*2 filter. Five out of the six AGN candidates show UV variability in at least one filter (except for NGC 5982, type 2). Two variable objects are type 1 (NGC 1052 varies about 20% in the UVM2 and *UVW*2 filters, and NGC 3226[12] shows 11% variation in the *UVW*1 filter), and three are type 2 (NGC 4261 shows 10% (33%) variations in the *UVW*1 (*UVM*2) filter, NGC 4736 varies 66% in the *U* filter, and NGC 5195 varies 51% in the *UVW*1 filter). In summary, three out of four type 1 and the two type 2 AGN candidates are variable objects at UV frequencies. Their UV luminosities are presented in Table A.1 and Fig. 2.

A comparison of X-ray and UV flux variations shows two non-AGN candidates have UV variations but no X-ray variations (one type 1 and one type 2). Of the AGN candidates, three show X-ray and UV flux variations (two type 1 and one type 2), and three type 2 LINERs show variations only in one of the frequencies (two in the UV, one in X-rays).

Taking into account UV and/or X-ray variations, ten out of 13 AGN candidates are variable (four out of six type 1, and six out of seven type 2). We note that the three objects without variations at X-ray frequencies (NGC 315, NGC 2681, and NGC 1961) do not have UV data in more than one epoch.

5.4. Short-term variability

According to the values of $\sigma^2_{\rm NXS}$, four objects show positive values within the errors in the soft and total bands, one type 1 (NGC 3226), and three type 2 (NGC 4374, NGC 4736, NGC 5195). We obtain $\sigma^2_{\rm NXS}$ values above zero for three objects in the hard band, two type 1 (NGC 315, and NGC 4636), and one

---

[12] We recall that NGC 3226 varies at UV frequencies, but long-term variations in X-rays were rejected for the analysis.

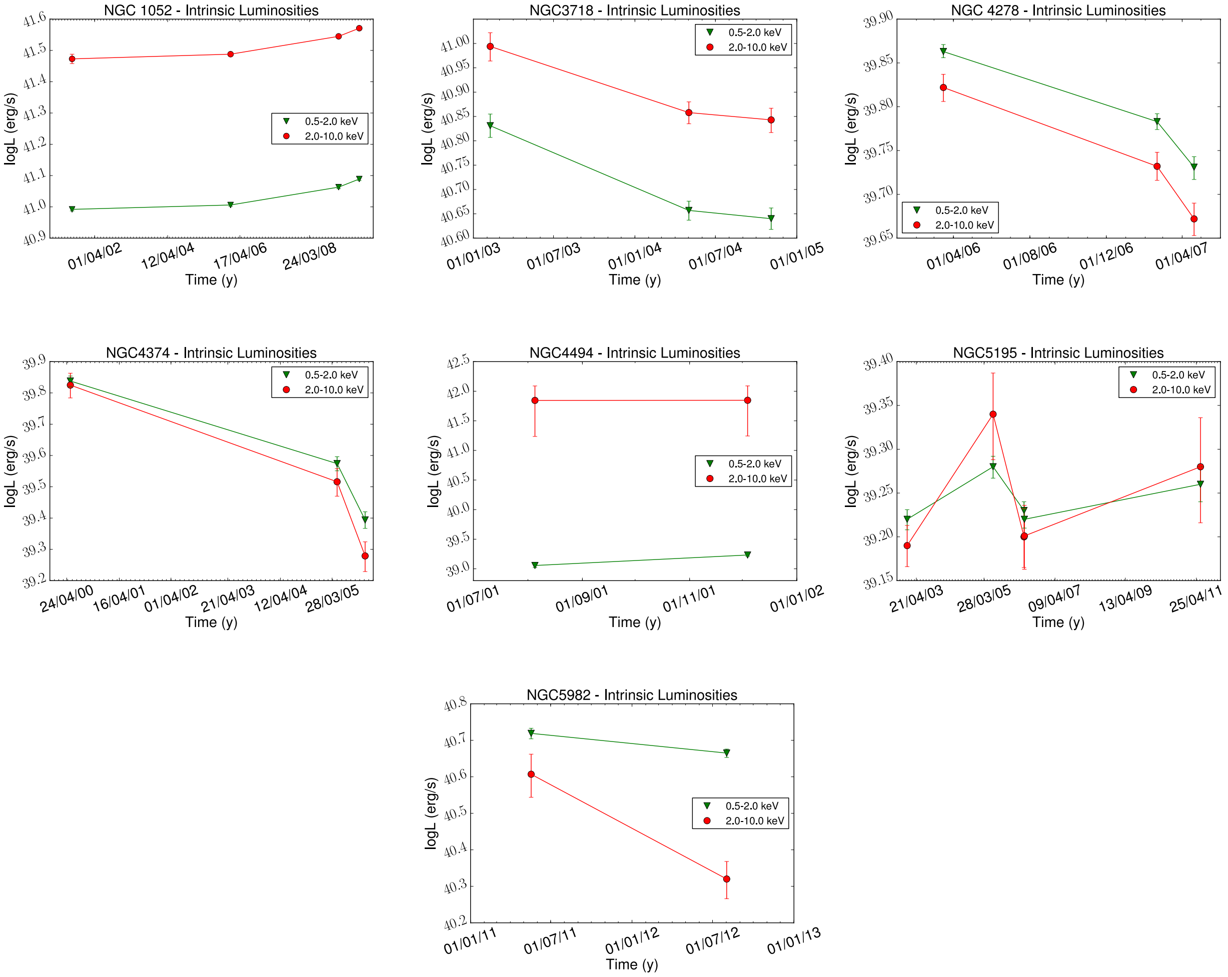

Fig. 3. Intrinsic luminosities calculated for the soft (0.5−2.0 keV, green triangles) and hard (2.0−10.0 keV, red circles) energies in the simultaneous fitting, only for the variable objects.

type 2 (NGC 4736). However, all the measurements are consistent with zero at 2σ level. For the remaining light curves we estimate upper limits for the normalized excess variance. Therefore, we cannot confirm short-term variability in our sample. The light curves are presented in Appendix D, their statistics in Table A.6.

6. Discussion

6.1. Long-term variations

We analyzed three non-AGN candidates (one type 1 and two type 2), but none of them showed X-ray spectral or flux variations. An additional source, NGC 5846 (type 2), was studied in HG13, but did not show variations either. All of them were classified as CT candidates by González-Martín et al. (2009a). In these objects, the nuclear obscuration is such that X-ray emission cannot be observed directly, i.e., the view of their nuclear emission is suppressed below ~10 keV (Maiolino et al. 1998). If this is the case, spectral variations might not be detected, in accordance with our results. Indications for classifying objects as an AGN candidate can be found at other frequencies, for example, with radio data. At these frequencies, a compact, flat-spectrum nuclear source can be considered as an AGN signature (Nagar et al. 2002, 2005). González-Martín et al. (2009b) collected multiwavelength properties of 82 LINERs. In their sample, 18 objects are classified in X-rays as non-AGN candidates and have detected nuclear radio cores. From these, 14 are classified as CT candidates. Thus, it might be possible that the AGN in CT objects are not seen at X-ray frequencies (and therefore their X-ray classification is non-AGN), whereas at radio frequencies the AGN can be detected. Of the four non-AGN candidates studied in HG13 and this work, radio cores are detected in three objects and, in fact, evidence of jet structures are reported in the literature (NGC 4636, Giacintucci et al. 2011; NGC 5813, Randall et al. 2011; NGC 5846, Filho et al. 2004), which suggests that they are AGN. Moreover, in this work UV variability is found for NGC 4636 and NGC 5813, while UV data are not available to study long-term variations in the other two cases. A nuclear counterpart was not detected for NGC 3608 with VLA by Nagar et al. (2005). Therefore, an X-ray variable nature of CT objects cannot be excluded, but variability analyses at higher energies need to be performed.

Of the 12 AGN candidates in our sample, two objects are proposed to be CT candidates (NGC 2681 and NGC 4374, González-Martín et al. 2009a). In these objects a point-like source at hard energies is detected, which might indicate that part of the AGN continuum is still contributing below 10 keV. Hence, variations in the nuclear continuum may be observed, as is the case of NGC 4374. An example of a confirmed CT type 2 Seyfert that shows spectral variations with *XMM-Newton* data is Mrk 3 (Guainazzi et al. 2012).

Only in one case (NGC 1052) were variations in N_{H2} needed along with those in Norm$_2$ (see below). Variations in the column density have been extensively observed in type 1 Seyferts (e.g., NGC 1365, Risaliti et al. 2007; NGC 4151, Puccetti et al. 2007; Mrk 766, Risaliti et al. 2011; Swift J2127.4+5654, Sanfrutos et al. 2013). Brenneman et al. (2009) studied a 101 ks observation of NGC 1052 from *Suzaku* data and did not find short-term variations. NGC 1052 also shows variations at UV frequencies, as shown by Maoz et al. (2005), and we confirm this here. However, the LINER nature of this source has been discussed in the literature; Pogge et al. (2000) studied 14 LINERs with *HST* data and only NGC 1052 shows clear evidence for an ionization cone, analogously to those seen in Seyferts. From a study that used artificial neural networks (ANN) to classify X-ray spectra, NGC 1052 seems to be associated to type 1 Seyfert galaxies in X-rays (Gonzalez-Martin et al. 2014). The fact that the observed variations in NGC 1052 are similar to those seen in type 1 Seyfert galaxies agrees well with the observation that this galaxy resembles Seyferts at X-ray frequencies.

Spectral variations do not necessarily imply flux variations. For example, if variations in the column density, N_H, alone were found, flux variations would not be present. However, all the results reported in the literature for LINERs show spectral variations that are related to flux variability. Variations in the normalization of the power law, that is, in Norm$_2$, are found in all the variable sources in our sample. Variations of other components, such as the soft emission (NGC 4102, González-Martín et al. 2011a; NGC 4552, HG13) or the slope of the power law (NGC 7213, Emmanoulopoulos et al. 2012) are reported in the literature. The variations in Γ found by Emmanoulopoulos et al. (2012) are small and were obtained on average every two days from 2006 to 2009. In contrast, the observations we used here were obtained with separations of months, and therefore it might be that if these variations occurred in LINERs we are unable to detect them. The most natural explanation for the variations in Norm$_2$ is that the AGN continuum changes with time. The first conclusion derived from this result is that the X-ray emission in these variable LINERs is AGN-like. Moreover, these types of variation are common in other AGN (e.g., Turner et al. 1997). Thus, even if the sample is not large enough to be conclusive, from the point of view of the X-ray variability, LINERs are similar to more powerful AGN. This is confirmed by the characteristic timescales derived from our analysis (see Sect. 6.2).

Our results show that UV and X-ray variations are not simultaneous (see Sect. 5.3). This means that some X-ray variable sources are not UV variable, and vice versa. The most illustrative case is NGC 5195, which changes 39% at UV frequencies but does not vary in X-rays in the same period (see Tables A.1 and A.3, and Figs. 2 and 3). The most widely accepted scenario assumes that the X-ray emission is produced by a disk-corona system, where UV photons from the inner parts of the accretion disk are thermally Comptonized and scattered into the X-rays by a hot corona that surrounds the accretion disk (Haardt & Maraschi 1991). In this case we expect that X-ray and UV emissions reach us at different times, because of the time that light takes to travel from one place to another. These time lags will depend on the sizes of the BH, the disk and the corona, so that the larger the sizes, the longer the time lags we expect. For example, Degenaar et al. (2014) conducted a multiwavelength study of the X-ray binary (XRB) Swift J1910.2-0546 and found time lags between X-ray and UV frequencies of about eight days. They argued that the changes may be related to the accretion morphology, perhaps due to a jet or a hot flow. LINERs have larger sizes than XRBs and, therefore, longer time lags are expected. Thus, the mismatch between UV and X-ray variabilities might be due to these time lags. Simultaneous X-ray and UV studies monitoring the sources would be useful for measuring these time lags, and also for calculating the sizes of the variable regions.

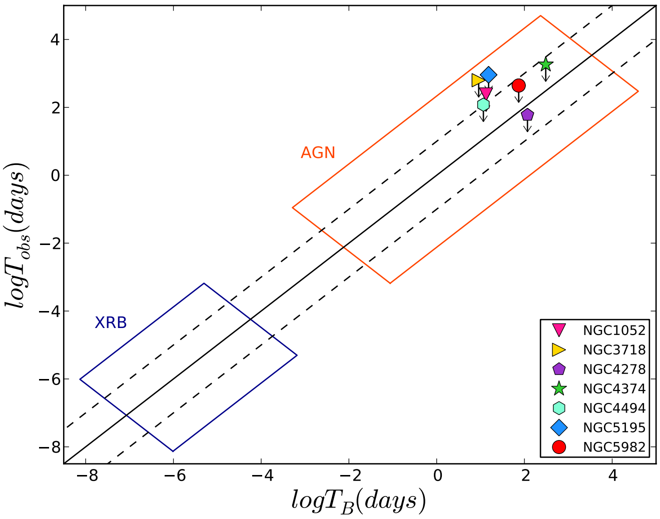

Fig. 4. Observed variability timescale, $T_{\rm obs}$, against the predicted value, $T_{\rm B}$, from González-Martín & Vaughan (2012). The solid line represents the 1:1 relationship, the dashed lines the errors. Only variable objects are represented. The big orange rectangle represents the location of AGN, the small blue rectangle the location of XRB as in McHardy et al. (2006).

6.2. Variability timescales

Short-term variability (~few days) is found in the literature. Pian et al. (2010) and Younes et al. (2011) found short-term variations in two objects in their analyses of type 1 LINERs, i.e., four in total. Two objects are in common with our sample (NGC 3226 and NGC 4278). However, in HG13 we did not find short-term variations, neither in these two nor in the other objects in the sample. González-Martín & Vaughan (2012) reported two out of 14 variable LINERs, one of them in common with those reported by Pian et al. (2010). In the present paper, we studied short-term variability from the analysis of the light curves for a total of 12 objects in three energy bands (soft, hard, total). Six objects show $\sigma^2_{\rm NXS} > 0$ in at least one of the three bands. However, we note that these variations are below the 2σ confidence level. None of the objects show a value that is higher than zero above 3σ, and therefore we cannot confirm short-term variations.

McHardy et al. (2006) reported a relation between the bend timescale for variations (i.e., the predicted timescale, $T_{\rm B}$), black-hole mass, and bolometric luminosity. This $T_{\rm B}$ corresponds to a characteristic frequency, $\nu_{\rm B}$, of the PSD, which occurs when the spectral index of the power law bends from ~1 to ~2. González-Martín & Vaughan (2012) updated this relation as

$$\log(T_{\rm B}) = A \log(M_{\rm BH}) + B \log(L_{\rm bol}) + C, \tag{6}$$

where $A = 1.34^{+}_{-}0.36$, $B = -0.24^{+}_{-}0.28$, $C = -1.88^{+}_{-}0.36$, and $T_{\rm B}$, $M_{\rm BH}$, and $L_{\rm bol}$ are in units of *days*, 10^6 $M_\odot$, and 10^{44} erg/s, respectively. By using Eq. (6), we plot the observed timescales of the variability, $T_{\rm obs}$, against the predicted timescales, $T_{\rm B}$, for the sources with variations in our sample (Fig. 4). The observed timescales were computed from the shortest periods in which variations were observed, and are represented as upper limits.

It is important to note that the timescales between the observations probably differ from the predicted timescales. This is obvious since the observations were obtained randomly at different epochs. All the variable objects are compatible with the 1:1 relation (represented by a solid line, and dashed lines are the errors), although most of them have longer $T_{\rm obs}$ than predicted. In Fig. 4, we also plot the location of AGN and X-ray binaries (XRB) as reported in McHardy et al. (2006). It can be observed that LINERs are located in the upper part of the relation together with the most massive AGN because of the strong dependence of $T_{\rm B}$ on the $M_{\rm BH}$. Note here that while $T_{\rm B}$ represents the bending frequency of the PSD, $T_{\rm obs}$ is a direct measure of changes in the spectral shape. This implies that the variability timescales are often shorter than the timescales between the observations (except for NGC 4278) for our sample. All the variable objects are then consistent with the relation reported by González-Martín & Vaughan (2012).

On the other hand, five objects in our sample do not show variations (and are not represented in Fig. 4). For these (NGC 315, NGC 1961, NGC 2681, NGC 4261, and NGC 4494), we obtain $T_{\rm B}$ ($T_{\rm obs}$) ~ 77 (873), 100 (14), 3 (92), 273 (2830), and 12 (120) days, respectively. In the case of NGC 1961, $T_{\rm B} > T_{\rm obs}$, so variations between the observations are not expected. From Eq. (6), we would expect variations from the other sources. It could be possible that we do not detect variations because observations were taken at random. However, it could also be possible that these objects do not follow Eq. (6).

Our results are consistent with the scaling relation found by McHardy et al. (2006) and González-Martín & Vaughan (2012) because, according to the BH mass and accretion rates of LINERs, variations of the intrinsic continuum are expected to be of large scales. This means that LINERs would follow the same relation as other AGN and XRBs (see Fig. 4). We recall that $T_{\rm B}$ has a strong dependence on $M_{\rm BH}$, while the dependence with $L_{\rm bol}$ (and with the accretion rate) is much lower (McHardy 2010), and hence it prevents us from obtaining useful information related to accretion physics.

Although LINERs and more powerful AGN are located in the same plane, different authors have pointed out that the accretion mechanism in LINERs could be different from that in more powerful AGN (e.g., Gu & Cao 2009; Younes et al. 2011). When a source accretes at a very low Eddington rate ($R_{\rm Edd} < 10^{-3}$), the accretion is dominated by radiatively inefficient accretion flows (RIAF, Narayan & Yi 1994; Quataert 2004). Such flows are thought to be present in XRB, since they are closer accreting black holes that can be easily studied. It is well known that XRB show different X-ray emission states that are separated by their spectral properties (e.g., Remillard & McClintock 2006). In comparison with XRB, LINERs should be in the "low/hard" state or, if the Eddington ratio is too low, in the "quiescent" state, while more powerful AGN should be in the "high/soft" state.

An anticorrelation between the slope of the power law, Γ, and the Eddington ratio, $R_{\rm Edd}$, is expected from RIAF models. Qiao & Liu (2013) theoretically investigated this correlation for XRB and found that advection-dominated accretion flow (ADAF)[13] models can reproduce it well. In these models the X-ray emission is produced by Comptonization of the synchrotron and bremsstrahlung photons. Later, they studied low-luminosity AGN (LLAGN) in the framework of a disk evaporation model (inner ADAF plus an outer truncated accretion disk) and found that it can also reproduce the anticorrelation (Qiao et al. 2013).

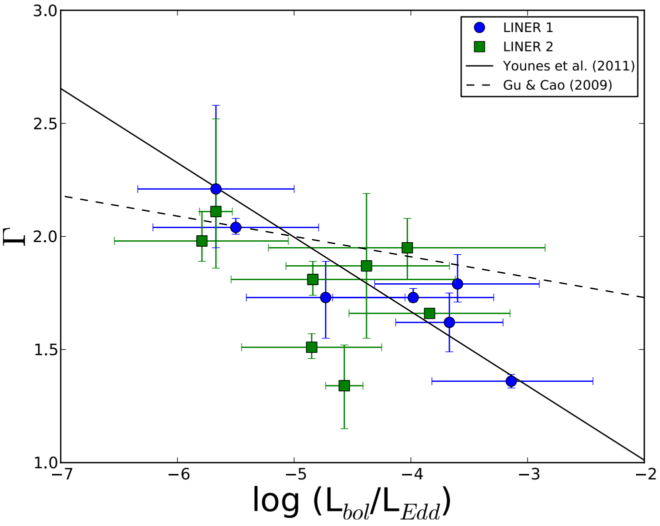

Fig. 5. Spectral index, Γ, versus the Eddington ratio, $R_{\rm Edd}$ = log ($L_{\rm bol}/L_{\rm Edd}$). Type 1 (blue circles) and type 2 (green squares) LINERs are distinguished. The solid and dashed lines represent the relations given by Younes et al. (2011) and Gu & Cao (2009), respectively, shifted to the same bolometric correction (see text).

Some efforts have been made to observationally investigate that relationship for LLAGN. Gu & Cao (2009) used a sample of 55 LLAGN (including 27 LINERs and 28 Seyferts) and found a regular anticorrelation between Γ and $R_{\rm Edd}$. However, when LINERs were considered alone, they did not find a strong correlation. Later, Younes et al. (2011) studied a sample of type 1 LINERs and found a statistically significant anticorrelation. In HG13 we found that the seven LINERs studied in the sample fitted the relation given by Younes et al. (2011) well. Here we plot the same relation in Fig. 5, where the values of Γ and $L_{2-10\ \rm keV}$ were obtained from the simultaneous fittings, since Γ did not vary in any of the objects (see Table 2). For NGC 2787 and NGC 2841 the individual fit from *Chandra* data was used because a simultaneous fit cannot be performed (see Sect. 5.1). $R_{\rm Edd}$ were calculated following the formulation given in Eracleous et al. (2010b), assuming $L_{\rm bol} = 33 L_{2-10\ \rm keV}$. The solid and dashed lines in Fig. 5 are the relations given by Younes et al. (2011) and Gu & Cao (2009), respectively, corrected to our $L_{\rm bol}$. The coefficient of the Pearson correlation is $r = -0.66$, with a coefficient of determination of $p = 0.008$. This might suggest that RIAF models apply to LINERs, indicating an inefficient accretion disk, in contrast to the efficient accretion disk found for more powerful AGN. A larger sample of LINERs would be useful to be conclusive.

6.3. Type 1 and type 2 variable AGN candidates

Some studies at X-ray frequencies have shown the variable nature of LINERs. Type 1 LINERs were studied by Pian et al. (2010), Younes et al. (2011), Emmanoulopoulos et al. (2012), and HG13. Pian et al. (2010) studied four sources with *Swift* and found variations in two of them. Younes et al. (2011) detected long-term variations in seven out of the nine sources in their sample from *XMM-Newton* and *Chandra* data. Emmanoulopoulos et al. (2012) studied one object with the Rossi X-ray Timing Explorer (RXTE) and found a "harder when brighter" behavior. In HG13 we analyzed three AGN candidates using *Chandra* and/or *XMM-Newton* data and found variations in all the three.

---

[13] The RIAF model is an updated version of the ADAF model.

In the present analysis our sample contains five type 1 AGN candidates, three of them variable. From the sample by Younes et al. (2011), five objects are in common with our sample, four of them with similar results, and differs only for NGC 315 (see Appendix B for notes and comparisons).

Type 2 objects were studied by González-Martín et al. (2011a) and HG13. González-Martín et al. (2011a) used *Suzaku*, *Chandra*, and *Swift* data to study one object and found variations in the thermal component. In HG13 we reported long-term variations in one of the two AGN candidates.

In the present analysis our sample contains seven type 2 AGN candidates, four of them variable.

Taking into account the present analysis and the studies listed above from the literature, 14 out of 22 LINERs are X-ray variable objects (eight out of 13 type 1, and six out of nine type 2). Therefore, there is no significant difference in the proportion of variable objects in X-rays in terms of the classification into optical type 1 or type 2. Given that the observed variations are intrinsic to the sources, similar proportions were expected in view of the UM, in good agreement with our results.

A similar behavior is found at UV frequencies. Maoz et al. (2005) were the first authors to show that UV variability is common in LINERs, and to demostrate the presence of a non-stellar component at these frequencies. From their sample of 17 LINERs, only three do not show either short-term (<1 yr) or long-term (>1 yr) variability. From these, all the seven type 1 LINERs and seven out of ten type 2 objects show variations.

When data from the OM onboard *XMM-Newton* were available, we searched for UV variability. Taking into account only AGN candidates, five out of six objects show variations (two type 1 and three type 2). This supports the hypothesis of a variable nature of LINERs. In common with our sample, Maoz et al. (2005) already showed the variable nature of NGC 1052 and NGC 4736. Thus, taking into account the present analysis and the study by Maoz et al. (2005), 17 out of 21 LINERs are variable at UV frequencies (eight type 1, and nine out of 13 type 2). As previously noted by Maoz et al. (2005), the fact that type 2 LINERs show variations at UV frequencies suggests that the UM may not always apply to LINERs. It has been suggested that the broad-line region (BLR) and the torus, responsible for obscuring the continuum that is visible in type 1 AGN, dissapear at low luminosities (Elitzur & Shlosman 2006; Elitzur & Ho 2009). The dissapearence of the torus could in principle explain why type 2 LINERs do vary in the UV, because the naked AGN is directly seen at these frequencies.

We find that some objects show variations in X-rays but do not vary at UV frequencies, or vice versa. This means that the percentage of variable objects is higher if we take into account different frequencies. From all the 34 LINERs studied at UV and X-ray frequencies in this and other works, 27 LINERs show variations in at least one energy band (13 out of 16 type 1, and 14 out of 18 type 2). Thus, the percentage of type 1 and 2 variable objects is similar. Consequently, variability is very common in LINER nuclei, a property they share with other AGN.

7. Conclusions

Using *Chandra* and *XMM-Newton* public archives, we performed a spectral and flux, short and long-term variability analysis of 18 LINERs in the Palomar sample. The main results of this study can be summarized as follows:

1. Seven out of the 12 AGN candidate LINERs show long-term spectral variability, while the three non-AGN candidates do not. In two cases the simultaneous fit was not possible because of strong external contamination, and in one case the long-term analysis was rejected because of possible contamination of a companion galaxy.
2. No significant difference in the proportion of X-ray variable nuclei (type 1 or 2) was found.
3. The main driver of the spectral variations is the change in the normalization of the power law, Norm_2; only for NGC 1052 is this accompained by variations in the column density, N_{H2}.
4. UV variations are found in five out of six AGN candidates. The two non-AGN candidates also show variations.
5. Short-term variations are not found.

From X-ray and UV data, we find that ten out of 13 LINERs in our sample show evidence of long-term variability in at least one energy band. Hence, variability is very common in LINERs.

X-ray variations are caused by changes in the continuum of the AGN. These results agree well with the expected variations according to their BH masses and accretion rates. In this sense, LINERs are in the same plane as more powerful AGN and XRB. However, we found an anticorrelation between the slope of the power law, Γ, and the Eddington ratio, which might suggest that a different accretion mechanism is active in LINERs, that is more similar to the hard state of XRB.

On the other hand, the result that some type 2 LINERs possibly vary at UV frequencies may suggest that a naked AGN can be observed at these wavelengths, which could be explained within the scenario where the torus dissapears at low luminosities.

Acknowledgements. We thank the anonymous referee for his/her helpful comments that helped us to improve the paper, and the AGN group at the IAA for helpful comments during this work. This work was financed by MINECO grant AYA 2010-15169, Junta de Andalucía TIC114 and Proyecto de Excelencia de la Junta de Andalucía P08-TIC-03531. L.H.G. acknowledges financial support from the Ministerio de Economía y Competitividad through the Spanish grant FPI BES-2011-043319. OGM thanks Spanish MINECO through a Juan de la Cierva Fellowship. This research made use of data obtained from the *Chandra* Data Archive provided by the *Chandra* X-ray Center (CXC). This research made use of data obtained from the *XMM-Newton* Data Archive provided by the *XMM-Newton* Science Archive (XSA). This research made use of the NASA/IPAC extragalactic database (NED), which is operated by the Jet Propulsion Laboratory under contract with the National Aeronautics and Space Administration. We acknowledge the usage of the HyperLeda database (`http://leda.univ-lyon1.fr`).

References

Antonucci, R. 1993, ARA&A, 31, 473
Birkinshaw, M., & Davies, R. L. 1985, ApJ, 291, 32
Brassington, N. J., Fabbiano, G., Kim, D.-W., et al. 2009, ApJS, 181, 605
Brenneman, L. W., Weaver, K. A., Kadler, M., et al. 2009, ApJ, 698, 528
Brightman, M., & Nandra, K. 2011, MNRAS, 413, 1206
Cappellari, M., Renzini, A., Greggio, L., et al. 1999, ApJ, 519, 117
Cardullo, A., Corsini, E. M., Beifiori, A., Pizzella, A., & Buson, L. M. 2008, in Formation and Evolution of Galaxy Disks, eds. J. G. Funes, & E. M. Corsini, ASP Conf. Ser., 396, 53
Carollo, C. M., Franx, M., Illingworth, G. D., & Forbes, D. A. 1997, ApJ, 481, 710
de Vaucouleurs, G. 1975, Soc. Stud. Sci., 9, 557
Degenaar, N., Maitra, D., Cackett, E. M., et al. 2014, ApJ, 784, 122
Dickey, J. M., & Lockman, F. J. 1990, ARA&A, 28, 215
D'Onofrio, M., Marziani, P., & Sulentic, J. W. 2012, Fifty Years of Quasars: Current Impressions and Future Perspectives, eds. M. D'Onofrio, P. Marziani, & J. W. Sulentic, 549
Dudik, R. P., Satyapal, S., Gliozzi, M., & Sambruna, R. M. 2005, ApJ, 620, 113
Elitzur, M., & Ho, L. C. 2009, ApJ, 701, L91
Elitzur, M., & Shlosman, I. 2006, ApJ, 648, L101
Emmanoulopoulos, D., Papadakis, I. E., McHardy, I. M., et al. 2012, MNRAS, 424, 1327

Eracleous, M., Shields, J. C., Chartas, G., & Moran, E. C. 2002, ApJ, 565, 108
Eracleous, M., Hwang, J. A., & Flohic, H. M. L. G. 2010a, ApJ, 711, 796
Eracleous, M., Hwang, J. A., & Flohic, H. M. L. G. 2010b, ApJS, 187, 135
Ferrarese, L., Ford, H. C., & Jaffe, W. 1996, ApJ, 470, 444
Filho, M. E., Fraternali, F., Markoff, S., et al. 2004, A&A, 418, 429
Garcia, A. M. 1993, A&AS, 100, 47
Garmire, G. P., Bautz, M. W., Ford, P. G., Nousek, J. A., & Ricker, J. G. R. 2003, in SPIE Conf. Ser. 4851, eds. J. E. Truemper, & H. D. Tananbaum, 28
Giacintucci, S., O'Sullivan, E., Vrtilek, J., et al. 2011, ApJ, 732, 95
Giroletti, M., Taylor, G. B., & Giovannini, G. 2005, ApJ, 622, 178
González-Martín, O., & Vaughan, S. 2012, A&A, 544, A80
González-Martín, O., Masegosa, J., Márquez, I., & Guainazzi, M. 2009a, ApJ, 704, 1570
González-Martín, O., Masegosa, J., Márquez, I., Guainazzi, M., & Jiménez-Bailón, E. 2009b, A&A, 506, 1107
González-Martín, O., Papadakis, I., Braito, V., et al. 2011a, A&A, 527, A142
González-Martín, O., Papadakis, I., Reig, P., & Zezas, A. 2011b, A&A, 526, A132
Gonzalez-Martin, O., Diaz-Gonzalez, D., Acosta-Pulido, J. A., et al. 2014, A&A, 567, A92
Gu, M., & Cao, X. 2009, MNRAS, 399, 349
Guainazzi, M., Oosterbroek, T., Antonelli, L. A., & Matt, G. 2000, A&A, 364, L80
Guainazzi, M., La Parola, V., Miniutti, G., Segreto, A., & Longinotti, A. L. 2012, A&A, 547, A31
Haardt, F., & Maraschi, L. 1991, ApJ, 380, L51
Harris, D. E., Biretta, J. A., Junor, W., et al. 2003, ApJ, 586, L41
Harris, D. E., Cheung, C. C., Biretta, J. A., et al. 2006, ApJ, 640, 211
Harris, D. E., Cheung, C. C., Stawarz, Ł., Biretta, J. A., & Perlman, E. S. 2009, ApJ, 699, 305
Harris, D. E., Massaro, F., Cheung, C. C., et al. 2011, ApJ, 743, 177
Heckman, T. M. 1980, A&A, 87, 152
Hernández-García, L., González-Martín, O., Márquez, I., & Masegosa, J. 2013, A&A, 556, A47
Ho, L. C. 2008, ARA&A, 46, 475
Ho, L. C., & Ulvestad, J. S. 2001, ApJS, 133, 77
Ho, L. C., Filippenko, A. V., Sargent, W. L. W., & Peng, C. Y. 1997, ApJS, 112, 391
Ishwara-Chandra, C. H., & Saikia, D. J. 1999, MNRAS, 309, 100
Kalberla, P. M. W., Burton, W. B., Hartmann, D., et al. 2005, A&A, 440, 775
Krips, M., Eckart, A., Krichbaum, T. P., et al. 2007, A&A, 464, 553
Lawrence, A., Watson, M. G., Pounds, K. A., & Elvis, M. 1987, Nature, 325, 694
Maiolino, R., Salvati, M., Bassani, L., et al. 1998, A&A, 338, 781
Maoz, D., Nagar, N. M., Falcke, H., & Wilson, A. S. 2005, ApJ, 625, 699
Masegosa, J., Márquez, I., Ramirez, A., & González-Martín, O. 2011, A&A, 527, A23
McHardy, I. 2010, in Lect. Notes Phys. 794 (Berlin: Springer Verlag), ed. T. Belloni, 203
McHardy, I. M., Koerding, E., Knigge, C., Uttley, P., & Fender, R. P. 2006, Nature, 444, 730
Nagar, N. M., Falcke, H., Wilson, A. S., & Ulvestad, J. S. 2002, A&A, 392, 53
Nagar, N. M., Falcke, H., & Wilson, A. S. 2005, A&A, 435, 521
Nandra, K., George, I. M., Mushotzky, R. F., Turner, T. J., & Yaqoob, T. 1997, ApJ, 476, 70
Narayan, R., & Yi, I. 1994, ApJ, 428, L13
O'Sullivan, E., Vrtilek, J. M., & Kempner, J. C. 2005, ApJ, 624, L77
Pellegrini, S., Fabbiano, G., Fiore, F., Trinchieri, G., & Antonelli, A. 2002, A&A, 383, 1
Pellegrini, S., Wang, J., Fabbiano, G., et al. 2012, ApJ, 758, 94
Peterson, B. M. 1997, An Introduction to Active Galactic Nuclei, ed. B. M. Peterson (Cambridge: New York: Cambridge University Press)
Pian, E., Romano, P., Maoz, D., et al. 2010, MNRAS, 401, 677
Pogge, R. W., Maoz, D., Ho, L. C., & Eracleous, M. 2000, ApJ, 532, 323
Puccetti, S., Fiore, F., Risaliti, G., et al. 2007, MNRAS, 377, 607
Qiao, E., & Liu, B. F. 2013, ApJ, 764, 2
Qiao, E., Liu, B. F., Panessa, F., & Liu, J. Y. 2013, ApJ, 777, 102
Quataert, E. 2004, in AGN Physics with the Sloan Digital Sky Survey, eds. G. T. Richards, & P. B. Hall, ASP Conf Ser., 311, 131
Randall, S. W., Forman, W. R., Giacintucci, S., et al. 2011, ApJ, 726, 86
Remillard, R. A., & McClintock, J. E. 2006, ARA&A, 44, 49
Risaliti, G., Elvis, M., Fabbiano, G., et al. 2007, ApJ, 659, L111
Risaliti, G., Nardini, E., Salvati, M., et al. 2011, MNRAS, 410, 1027
Rubin, V. C., Ford, W. K. J., & Roberts, M. S. 1979, ApJ, 230, 35
Sambruna, R. M., Gliozzi, M., Eracleous, M., Brandt, W. N., & Mushotzky, R. 2003, ApJ, 586, L37
Sanfrutos, M., Miniutti, G., Agís-González, B., et al. 2013, MNRAS, 436, 1588
Satyapal, S., Sambruna, R. M., & Dudik, R. P. 2004, A&A, 414, 825
Satyapal, S., Dudik, R. P., O'Halloran, B., & Gliozzi, M. 2005, ApJ, 633, 86
Strüder, L., Briel, U., Dennerl, K., et al. 2001, A&A, 365, L18
Terashima, Y., & Wilson, A. S. 2003, ApJ, 583, 145
Terashima, Y., & Wilson, A. S. 2004, ApJ, 601, 735
Tremaine, S., Gebhardt, K., Bender, R., et al. 2002, ApJ, 574, 740
Turner, T. J., George, I. M., Nandra, K., & Mushotzky, R. F. 1997, ApJS, 113, 23
Urry, C. M., & Padovani, P. 1995, PASP, 107, 803
Vaughan, S., Edelson, R., Warwick, R. S., & Uttley, P. 2003, MNRAS, 345, 1271
Venturi, T., Giovannini, G., Feretti, L., Comoretto, G., & Wehrle, A. E. 1993, ApJ, 408, 81
Vermeulen, R. C., Ros, E., Kellermann, K. I., et al. 2003, A&A, 401, 113
Vrtilek, J. M., O'Sullivan, E., David, L. P., et al. 2013, in AAS/High Energy Astrophysics Division, 13, #116.06
Xu, C., Baum, S. A., O'Dea, C. P., Wrobel, J. M., & Condon, J. J. 2000, AJ, 120, 2950
Younes, G., Porquet, D., Sabra, B., et al. 2010, A&A, 517, A33
Younes, G., Porquet, D., Sabra, B., & Reeves, J. N. 2011, A&A, 530, A149
Younes, G., Porquet, D., Sabra, B., Reeves, J. N., & Grosso, N. 2012, A&A, 539, A104

Pages 15 to 46 are available in the electronic edition of the journal at http://www.aanda.org

Appendix A: Tables

Table A.1. Observational details.

Name	Instrument	ObsID	Date	*R* ($''$)	Net Exptime (ks)	Counts	HR	log (L_{UV}) (erg/s)	Filter
(1)	(2)	(3)	(4)	(5)	(6)	(7)	(8)	(9)	(10)
NGC 315	*XMM-Newton*^{c}	0305290201	2005-07-02	25	14	5799	−0.55±0.01	41.75 ± 0.05	*UVM*2
	Chandra	855	2000-10-08	3	5	501	−0.27±0.13	–	
	Chandra^c	4156	2003-02-22	3	55	5550	−0.23±0.05	–	
NGC 1052	*XMM-Newton*^{c}	0093630101	2001-08-15	25	11.2	5818	0.28 ± 0.06	–	
	XMM-Newton	0306230101	2006-01-12	25	44.8	25 565	0.34 ± 0.03	41.04 ± 0.01	*UVM*2
								40.94 ± 0.03	*UVW*2
	XMM-Newton	0553300301	2009-01-14	25	42.4	27 367	0.39 ± 0.02	41.14 ± 0.01	*UVM*2
								40.95 ± 0.03	*UVW*2
	XMM-Newton	0553300401	2009-08-12	25	46.8	30 643	0.42 ± 0.02	41.04 ± 0.01	*UVM*2
								40.89 ± 0.03	*UVW*2
	Chandra^c	5910	2000-08-29	3	59.2	6549	0.40 ± 0.04	–	
NGC 1961	*XMM-Newton*	0673170101	2011-08-31	35	17	1934	−0.54 ± 0.02	Not detected	
	XMM-Newton	0673170301	2011-09-14	35	14	1680	−0.54 ± 0.02	Not detected	
NGC 2681	*Chandra*	2060	2001-01-30	3	81	1126	−0.76 ± 0.01	–	
	Chandra	2061	2001-05-02	3	79	1018	−0.73 ± 0.01	–	
NGC 2787	*XMM-Newton*^{c}	0200250101	2004-10-10	25	25	2557	−0.37 ± 0.04	–	
	Chandra^c	4689	2004-05-18	3	31	527	−0.59 ± 0.03	–	
NGC 2841	*XMM-Newton*^{c}	0201440101	2004-11-09	30	9	1712	−0.57 ± 0.02	41.28 ± 0.03	*UVW*2
	Chandra^c	6096	2004-12-18	5	28	486	−0.81 ± 0.01	–	
NGC 3226	*XMM-Newton*	0101040301	2000-11-28	–	–	–	–	41.38 ± 0.01	*UVW*1
	XMM-Newton	0400270101	2006-12-03	–	–	–	–	41.33 ± 0.01	*UVW*1
	Chandra	860	1999-12-30	3	46.6	476	0.53 ± 0.12	–	
NGC 3608	*XMM-Newton*	0099030101	2000-11-22	20	12	454	−0.48 ± 0.06	–	
	XMM-Newton	0693300101	2012-05-20	20	23	1749	−0.46 ± 0.03	41.01 ± 0.07	*UVM*2
NGC 3718	*XMM-Newton*^{c}	0200430501	2004-05-02	25	10	2473	0.12±0.19	Not detected	
	XMM-Newton^c	0200431301	2004-11-04	25	8	1734	0.14±0.20	Not detected	
	Chandra^c	3993	2003-02-08	3	5	1143	0.11±0.29	–	
NGC 4261	*Chandra*	834	2000-05-06	3	34.4	3465	−0.58 ± 0.01	–	
	Chandra^c	9569	2008-02-12	3	100.9	7757	−0.47 ± 0.01	–	
	XMM-Newton	0056340101	2001-12-16	25	21.3	10 730	−0.68 ± 0.01	41.43 ± 0.02	*UVM*2
								42.17 ± 0.01	*UVW*1
	XMM-Newton^c	0502120101	2007-12-16	25	63.0	32 156	−0.68 ± 0.01	41.61 ± 0.01	*UVM*2
								42.21 ± 0.01	*UVW*1
NGC 4278	*Chandra*^{c}	7077	2006-03-16	3	110.3	9182	−0.66 ± 0.01	–	
	Chandra	7081	2007-02-20	3	110.7	7591	−0.66 ± 0.01	–	
	Chandra	7080	2007-04-20	3	55.8	3379	−0.69 ± 0.01	–	
	XMM-Newton^c	0205010101	2004-05-23	25	20.8	34 516	−0.60 ± 0.01	40.90 ± 0.02	*UVW*1
NGC 4374	*XMM-Newton*^{c}	0673310101	2011-06-01	25	25	19 788	−0.87 ± 0.01	41.48 ± 0.01	*UVM*2
	Chandra	803	2000-05-19	2	28	1010	−0.67 ± 0.02	–	
	Chandra	5908	2005-05-01	2	46	2401	−0.60 ± 0.01	–	
	Chandra^c	6131	2005-11-07	2	41	812	−0.68 ± 0.02	–	
NGC 4494	*XMM-Newton*^{c}	0071340301	2001-12-04	20	24	2116	−0.46 ± 0.04	41.99 ± 0.01	*UVW*1
	Chandra^c	2079	2001-08-05	3	25	580	−0.57 ± 0.03	–	
NGC 4636	*XMM-Newton*	0111190201	2000-07-13	25	6	9889	−0.95 ± 0.01	40.62 ± 0.06	*UVW*2
								41.66 ± 0.01	*UVW*1
	XMM-Newton	0111190701	2001-01-05	25	51	91 789	−0.97 ± 0.01	40.64 ± 0.07	*UVW*2
								41.52 ± 0.01	*UVW*1
NGC 4736	*XMM-Newton*^{c}	0094360601	2002-05-23	20	8	11 041	−0.59 ± 0.01	40.69 ± 0.01	*U*
	XMM-Newton	0094360701	2002-06-26	20	3	3010	−0.62 ± 0.01	40.76 ± 0.01	*U*
	XMM-Newton	0404980101	2006-11-27	20	33	42 048	−0.60 ± 0.01	40.29 ± 0.01	*U*
	Chandra^c	808	2000-05-13	1.5	47	2986	−0.73 ± 0.01	–	

Notes. (Col. 1) name, (Col. 2) instrument, (Col. 3) obsID, (Col. 4) date, (Col. 5) aperture radius for the nuclear extraction, (Col. 6) net exposure time, (Col. 7) number of counts in the 0.5-10 keV band, (Col. 8) hardness ratio, (Cols. 9 and 10) UV luminosity from the optical monitor and filter. The *c* represents data from different instruments that were compared as explained in Sect. 4.2.

Table A.1. continued.

Name (1)	Instrument (2)	ObsID (3)	Date (4)	R ($''$) (5)	Net Exptime (ks) (6)	Counts (7)	HR (8)	$\log(L_{\rm UV})$ (erg/s) (9)	Filter (10)
NGC 5195	*XMM-Newton*	0112840201	2003-01-15	20	17	2976	−0.77 ± 0.01	40.98 ± 0.01	*UVW*1
	XMM-Newton	0212480801	2005-07-01	20	22	3756	−0.68 ± 0.01	40.80 ± 0.01	*UVW*1
	XMM-Newton	0303420101	2006-05-20	20	27	4297	−0.69 ± 0.01	40.89 ± 0.01	*UVW*1
	XMM-Newton	0303420201	2006-05-24	20	21	3312	−0.70 ± 0.01	41.11 ± 0.01	*UVW*1
	XMM-Newton[c]	0677980701	2011-06-07	20	5	888	−0.79 ± 0.01	–	
	Chandra[c]	13813	2012-09-09	3	179	1340	−0.43 ± 0.04	–	
	Chandra	13812	2012-09-12	3	157	1359	−0.42 ± 0.04	–	
NGC 5813	*XMM-Newton*	0302460101	2005-07-23	30	20	25 419	−0.96±0.01	42.01 ± 0.01	*UVW*1
	XMM-Newton	0554680201	2009-02-11	30	43	58 821	−0.95±0.01	42.04 ± 0.01	*UVW*1
	XMM-Newton[c]	0554680301	2009-02-17	30	43	58 175	−0.95±0.01	42.04 ± 0.01	*UVW*1
	Chandra	5907	2005-04-02	3	48	518	−0.92±0.01	–	
	Chandra[c]	9517	2008-06-05	3	99	1181	−0.90±0.01	–	
	Chandra	12951	2011-03-28	3	74	714	−0.95±0.01	–	
	Chandra	12952	2011-04-05	3	143	1451	−0.90±0.01	–	
	Chandra	13253	2011-04-08	3	118	1295	−0.91±0.01	–	
	Chandra	13255	2011-04-10	3	43	465	−0.92±0.01	–	
NGC 5982	*XMM-Newton*	0673770401	2011-05-18	25	9	1932	−0.78 ± 0.01	41.71 ± 0.05	*UVM*2
	XMM-Newton	0693300301	2012-08-02	25	21	4235	−0.87 ± 0.01	41.65 ± 0.07	*UVM*2

Table A.2. Final compilation of the best-fit models for the sample, including the individual best-fit model for each observation, and the simultaneous best-fit model with the varying parameters.

Analysis (1)	ObsID (2)	Model (3)	N_{H1} (4)	N_{H2} (5)	kT keV (6)	Γ (7)	Norm$_1$ (10^{-4}) (8)	Norm$_2$ (10^{-4}) (9)	χ^2/d.o.f. F-test (10)
NGC 315									
Ind	0305290201	MEPL	–	$0.17^{0.25}_{0.11}$	$0.56^{0.58}_{0.54}$	$1.59^{1.69}_{1.50}$	$1.20^{1.29}_{1.11}$	$1.58^{1.77}_{1.41}$	197.97/198
Ind	855	MEPL	–	$0.35^{0.87}_{0.00}$	$0.33^{0.55}_{0.17}$	$1.53^{2.01}_{1.10}$	$0.52^{0.87}_{0.25}$	$1.66^{3.27}_{1.01}$	15.16/17
Ind (3″)	4156*	MEPL	$0.00^{0.02}_{0.00}$	$0.77^{0.92}_{0.62}$	$0.52^{0.55}_{0.49}$	$1.61^{1.76}_{1.49}$	$0.40^{0.43}_{0.37}$	$2.04^{2.44}_{1.71}$	190.43/172
Ind (25″)	4156	MEPL	–	$0.16^{0.23}_{0.12}$	$0.56^{0.57}_{0.55}$	$1.30^{1.38}_{1.22}$	$1.17^{1.25}_{1.11}$	$1.51^{1.67}_{1.39}$	258.47/206
SMF0	All	MEPL	–	$0.75^{0.90}_{0.61}$	$0.52^{0.55}_{0.49}$	$1.62^{1.75}_{1.49}$	$0.40^{0.43}_{0.39}$	$2.02^{2.40}_{1.70}$	209.89/195
NGC 1052									
Ind	093630101	ME2PL	–	$13.77^{15.78}_{11.95}$	$0.62^{0.69}_{0.51}$	$1.24^{1.35}_{1.11}$	$1.05^{1.13}_{0.97}$	$6.09^{4.55}_{4.79}$	269.16/234
Ind	306230101	ME2PL	–	$9.30^{9.82}_{8.79}$	$0.50^{0.55}_{0.45}$	$1.30^{1.36}_{1.24}$	$1.05^{1.09}_{1.01}$	$7.20^{8.14}_{6.34}$	799.19/822
Ind	553300301	ME2PL	–	$8.96^{9.39}_{8.54}$	$0.61^{0.64}_{0.57}$	$1.38^{1.43}_{1.32}$	$1.09^{1.14}_{1.06}$	$10.16^{11.31}_{9.10}$	923.38/869
Ind	553300401*	ME2PL	–	$9.47^{9.86}_{9.09}$	$0.53^{0.61}_{0.48}$	$1.43^{1.48}_{1.38}$	$1.10^{1.14}_{1.06}$	$12.02^{13.32}_{10.82}$	1006.47/937
Ind (3″)	5910	ME2PL	–	$5.33^{6.86}_{3.84}$	$0.64^{0.69}_{0.58}$	$1.21^{1.46}_{1.05}$	$0.37^{0.47}_{0.37}$	$0.57^{1.06}_{0.35}$	261.04/226
Ind (25″)	5910	ME2PL	–	$8.13^{11.49}_{5.36}$	$0.61^{0.65}_{0.57}$	$1.25^{1.50}_{1.00}$	$0.49^{0.66}_{0.49}$	$0.61^{1.21}_{0.19}$	319.40/269
SMF2	093630101	ME2PL	–	$14.14^{15.77}_{12.66}$	$0.59^{0.61}_{0.57}$	$1.36^{1.39}_{1.33}$	$1.09^{1.11}_{1.06}$	$8.06^{8.89}_{7.31}$	3043.69/2886
	306230101			$9.80^{10.26}_{9.36}$				$8.38^{8.97}_{7.82}$	1.0e-24
	553300301			$8.75^{9.11}_{8.40}$				$9.74^{10.40}_{9.11}$	
	553300401			$9.21^{9.55}_{8.88}$				$10.41^{11.11}_{9.75}$	
NGC 1961									
Ind	0673170101*	ME2PL	$0.00^{0.08}_{0.00}$	$20.83^{33.49}_{13.41}$	$0.63^{0.67}_{0.58}$	$2.00^{2.50}_{1.89}$	$0.34^{0.52}_{0.34}$	$1.44^{3.96}_{0.84}$	69.32/70
Ind	0673170301	ME2PL	$0.00^{0.05}_{0.00}$	$9.88^{18.23}_{5.67}$	$0.56^{0.61}_{0.49}$	$1.84^{2.27}_{1.60}$	$0.31^{0.41}_{0.31}$	$0.80^{1.43}_{0.35}$	85.39/62
SMF0	All	ME2PL	–	$15.60^{22.74}_{10.82}$	$0.60^{0.63}_{0.56}$	$1.95^{2.08}_{1.81}$	$0.37^{0.40}_{0.34}$	$1.07^{1.55}_{0.71}$	165.72/142
NGC 2681									
Ind	2060*	MEPL	$0.11^{0.26}_{0.00}$	–	$0.64^{0.71}_{0.56}$	$1.67^{1.86}_{1.45}$	$0.12^{0.18}_{0.07}$	$0.07^{0.08}_{0.06}$	43.34/36
Ind	2061	MEPL	$0.00^{0.16}_{0.00}$	–	$0.63^{0.68}_{0.56}$	$1.61^{1.78}_{1.41}$	$0.06^{0.07}_{0.06}$	$0.07^{0.08}_{0.06}$	29.71/33
SMF0	All	MEPL	$0.07^{0.19}_{0.00}$	–	$0.64^{0.69}_{0.58}$	$1.73^{1.89}_{1.55}$	$0.09^{0.12}_{0.06}$	$0.07^{0.08}_{0.06}$	81.23/72
NGC 2787									
Ind (25″)	0200250101	PL	–	–	–	$1.61^{1.66}_{1.55}$	–	–	146.28/98
Ind (3″)	4689	PL	$0.09^{0.18}_{0.03}$	–	–	$2.21^{2.58}_{1.95}$	–	–	20.72/21
Ind (25″)	4689	PL	$0.01^{0.07}_{0.00}$	–	–	$1.70^{1.98}_{1.59}$	–	–	42.31/48
NGC 2841									
Ind	0201440101	MEPL	$0.82^{0.95}_{0.68}$		$0.29^{0.34}_{0.25}$	$1.76^{1.97}_{1.60}$	$3327.57^{7082.60}_{368.14}$	$0.49^{0.57}_{0.43}$	71.15/50
Ind (5″)	6096	MEPL	$0.00^{0.68}_{0.00}$	–	$0.63^{0.74}_{0.44}$	$2.09^{2.52}_{1.86}$	$0.08^{7.27}_{0.06}$	$0.13^{0.16}_{0.11}$	3.52/13
Ind (30″)	6096	MEPL	$0.00^{0.45}_{0.00}$	–	$0.48^{0.61}_{0.25}$	$1.57^{1.75}_{1.43}$	$0.16^{0.21}_{0.12}$	$0.49^{0.55}_{0.43}$	54.51/57
NGC 3608									
Ind	0099030101	ME2PL	–	$9.69^{36.25}_{2.76}$	$0.60^{0.80}_{0.36}$	$2.13^{2.56}_{1.79}$	$0.21^{0.33}_{0.21}$	$0.92^{2.90}_{0.23}$	6.30/8
Ind	0693300101*	ME2PL	–	$13.77^{23.33}_{8.17}$	$0.40^{0.59}_{0.28}$	$2.11^{2.32}_{1.79}$	$0.21^{0.26}_{0.21}$	$0.95^{1.60}_{0.32}$	89.32/55
SMF0	All	ME2PL	–	$10.02^{15.64}_{6.26}$	$0.51^{0.60}_{0.35}$	$2.21^{2.38}_{2.03}$	$0.24^{0.26}_{0.22}$	$0.95^{1.40}_{0.62}$	88.67/70
NGC 3718									
Ind	0200430501	2PL	$1.02^{1.35}_{0.91}$	$0.01^{0.22}_{0.00}$	–	$1.76^{1.97}_{1.71}$	$0.21^{0.62}_{0.13}$	$5.56^{6.78}_{4.60}$	129.94/104
Ind	0200431301*	2PL	$0.08^{0.36}_{0.00}$	$0.96^{1.59}_{0.77}$	–	$1.67^{1.93}_{1.49}$	$0.31^{1.46}_{0.12}$	$4.23^{5.67}_{3.25}$	56.16/71
Ind	3993	PL	$0.95^{1.12}_{0.79}$	–	–	$1.73^{1.92}_{1.54}$	–	–	51.98/48
Ind		2PL	$3.08^{5.04}_{0.00}$	$0.87^{1.19}_{0.00}$	–	$2.15^{3.01}_{1.69}$	$8.74^{44.58}_{0.61}$	$6.77^{13.37}_{0.08}$	49.04/43

Notes. (Col. 1) kind of analysis performed, where Ind refers to the individual fitting of the observation, SMF0 is the simultaneous fit without varying parametes, SMF1 is the simultaneous fit varying one parameter and SMF2 is the simultaneous fit varying two parameters, (Col. 2) obsID, where the * represents the data that are used as a reference model for the simultaneous fit, (Col. 3) best-fit model, (Cols. 4−9) parameters in the model, where N_H are in units of 10^{22} cm^{-2}, and (Col. 10) χ^2/d.o.f. and in SMFx (where $x = 1, 2$) the result of the F-test is presented in the second line.

Table A.2. continued.

Analysis	ObsID	Model	N_{H1}	N_{H2}	kT keV	Γ	Norm$_1$ (10^{-4})	Norm$_2$ (10^{-4})	χ^2/d.o.f. F-test
(1)	(2)	(3)	(4)	(5)	(6)	(7)	(8)	(9)	(10)
NGC 4261									
SMF1	0200431301	2PL	$0.09^{0.22}_{0.00}$	$1.10^{1.32}_{0.97}$	–	$1.79^{1.92}_{1.71}$	$0.32^{0.67}_{0.17}$	$5.11^{6.24}_{4.45}$	237.70/224
	0200430501							$5.31^{6.48}_{4.61}$	1.0e-17
	3993							$8.06^{9.92}_{7.02}$	
Ind	834	ME2PL	$0.18^{0.47}_{0.06}$	$11.89^{16.01}_{9.31}$	$0.58^{0.60}_{0.56}$	$2.11^{3.07}_{1.52}$	$0.29^{0.55}_{0.19}$	$4.72^{25.76}_{1.60}$	110.82/80
Ind (3″)	9569*	ME2PL	$0.18^{0.47}_{0.08}$	$8.40^{10.20}_{6.90}$	$0.57^{0.58}_{0.56}$	$1.24^{1.51}_{1.07}$	$0.26^{0.37}_{0.20}$	$2.13^{4.57}_{1.18}$	198.74/157
Ind (25″)	9569	ME2PL	–	$9.03^{12.90}_{6.55}$	$0.61^{0.62}_{0.60}$	$1.16^{1.39}_{0.89}$	$0.35^{0.47}_{0.35}$	$0.64^{1.11}_{0.29}$	382.42/218
SMF0	All	ME2PL	$0.18^{0.31}_{0.09}$	$9.38^{10.84}_{7.96}$	$0.57^{0.58}_{0.56}$	$1.87^{2.19}_{1.55}$	$0.27^{0.34}_{0.21}$	$2.70^{4.86}_{1.49}$	312.57/247
Ind	0056340101	ME2PL	$0.08^{0.15}_{0.01}$	$11.97^{14.73}_{9.31}$	$0.63^{0.64}_{0.61}$	$1.84^{2.22}_{1.45}$	$0.72^{0.94}_{0.54}$	$2.82^{6.30}_{1.11}$	278.12/255
Ind	0502120101*	ME2PL	$0.04^{0.07}_{0.00}$	$9.71^{11.14}_{8.30}$	$0.64^{0.65}_{0.64}$	$1.75^{1.97}_{1.54}$	$0.64^{0.74}_{0.55}$	$2.30^{3.65}_{1.40}$	563.80/461
SMF0	All	ME2PL	$0.04^{0.08}_{0.01}$	$10.28^{11.56}_{9.02}$	$0.64^{0.65}_{0.63}$	$1.76^{1.95}_{1.57}$	$0.67^{0.76}_{0.58}$	$2.36^{3.54}_{1.53}$	855.28/726
NGC 4278									
Ind (3″)	7077*	MEPL	$0.31^{0.58}_{0.05}$	$0.01^{0.03}_{0.00}$	$0.27^{0.38}_{0.19}$	$2.06^{2.15}_{1.99}$	$0.80^{6.21}_{0.18}$	$0.98^{1.06}_{0.90}$	144.23/158
Ind (25″)	7077	MEPL	$0.16^{0.45}_{0.01}$	–	$0.30^{0.37}_{0.21}$	$1.88^{1.95}_{1.83}$	$0.81^{3.96}_{0.28}$	$1.32^{1.39}_{1.27}$	250.15/210
Ind	7081	MEPL	–	–	$0.63^{0.68}_{0.57}$	$2.03^{2.10}_{1.99}$	$0.12^{0.14}_{0.09}$	$0.77^{0.82}_{0.75}$	155.54/145
Ind	7080	MEPL	$0.22^{0.71}_{0.00}$	–	$0.47^{0.61}_{0.18}$	$2.10^{2.25}_{2.03}$	$0.24^{13.76}_{0.07}$	$0.69^{0.79}_{0.65}$	102.53/96
Ind	0205010101	PL	$0.02^{0.03}_{0.02}$	–	–	$2.04^{2.08}_{2.01}$	–	–	562.25/529
SMF1	7077	MEPL	–	–	$0.58^{0.62}_{0.48}$	$2.05^{2.11}_{2.03}$	$0.11^{0.12}_{0.10}$	$0.97^{1.02}_{0.82}$	414.71/415
	7081							$0.78^{0.82}_{0.77}$	6.7e-46
	7080							$0.68^{0.72}_{0.65}$	
NGC 4374									
Ind	0673310101	ME2PL	$0.01^{0.02}_{0.00}$	$269.73^{462.21}_{79.23}$	$0.62^{0.63}_{0.61}$	$2.02^{2.08}_{1.93}$	$1.06^{1.23}_{1.06}$	$20.74^{1161.27}_{1.99}$	283.99/282
Ind	803	MEPL	$0.45^{0.79}_{0.00}$	$0.17^{0.28}_{0.10}$	$0.30^{0.60}_{0.18}$	$2.06^{2.42}_{1.79}$	$0.87^{10.78}_{0.06}$	$0.45^{0.61}_{0.34}$	35.48/36
Ind	5908*	PL	$0.10^{0.13}_{0.07}$	–	–	$2.18^{2.32}_{2.13}$	–	–	78.73/87
		MEPL	$0.00^{0.39}_{0.00}$	$0.10^{0.13}_{0.06}$	$0.54^{0.71}_{0.21}$	$2.07^{2.22}_{1.93}$	$0.06^{0.53}_{0.03}$	$0.83^{0.95}_{0.72}$	67.73/81
Ind (2″)	6131	MEPL	$0.00^{0.20}_{0.00}$	$0.00^{0.09}_{0.00}$	$0.60^{0.66}_{0.54}$	$1.48^{1.81}_{1.32}$	$0.11^{0.13}_{0.09}$	$0.14^{0.18}_{0.12}$	33.27/28
Ind (25″)	6131	MEPL	–	–	$0.55^{0.57}_{0.53}$	$1.95^{2.09}_{1.856}$	$2.07^{2.16}_{1.97}$	$0.90^{0.98}_{0.81}$	160.27/114
SMF1	5908	MEPL	$0.02^{0.14}_{0.00}$	$0.09^{0.15}_{0.08}$	$0.59^{0.64}_{0.51}$	$1.98\,^{2.11}_{1.89}$	$0.10^{0.13}_{0.07}$	$0.80^{0.88}_{0.73}$	161.08/154
	803							$0.39^{0.44}_{0.35}$	3.02e-55
	6131							$0.22^{0.25}_{0.20}$	
NGC 4494									
Ind	0071340301*	PL	–	–	–	$1.76^{1.83}_{1.68}$	–	–	115.04/74
Ind (3″)	2079	PL	–	–	–	$1.66^{1.94}_{1.51}$	–	–	19.32/21
Ind (20″)	2079	PL	$0.00^{0.03}_{0.00}$	–	–	$1.49^{1.68}_{1.38}$	–	–	69.38/43
SMF1		0071340301	–			$1.81^{1.89}_{1.74}$	$0.36^{0.38}_{0.35}$		117.35/86
		2079					$0.24^{0.27}_{0.23}$		6.9e-09
NGC 4636									
Ind	0111190201*	MEPL	–	–	$0.53^{0.55}_{0.52}$	$2.47^{2.74}_{2.27}$	$7.93^{8.13}_{7.64}$	$1.01^{1.20}_{0.88}$	280.73/176
Ind	0111190701	MEPL	–	–	$0.55^{0.55}_{0.54}$	$2.58^{2.64}_{2.52}$	$8.07^{8.15}_{7.99}$	$1.01^{1.06}_{0.96}$	958.65/344
SMF0	All	MEPL	–	–	$0.55^{0.55}_{0.54}$	$2.58^{2.64}_{2.52}$	$8.05^{8.13}_{7.98}$	$1.02^{1.07}_{0.97}$	1260.17/529
NGC 4736									
Ind	0094360601	MEPL	$0.00^{0.04}_{0.00}$	–	$0.48^{0.51}_{0.45}$	$1.66^{1.70}_{1.64}$	$1.59^{1.73}_{1.47}$	$4.27^{4.43}_{4.10}$	337.72/297
Ind	0094360701	MEPL	$0.01^{0.09}_{0.00}$	$0.00^{0.01}_{0.00}$	$0.43^{0.52}_{0.31}$	$1.70^{1.80}_{1.60}$	$1.51^{1.74}_{10.23}$	$4.00^{4.31}_{3.67}$	100.34/100
Ind	0404980101*	MEPL	$0.00^{0.01}_{0.00}$	–	$0.55^{0.57}_{0.54}$	$1.66^{1.68}_{1.64}$	$1.61^{1.68}_{1.55}$	$3.87^{3.95}_{3.79}$	562.21/587
Ind (1.5″)	808	MEPL	$0.33^{0.49}_{0.27}$	$0.04^{0.09}_{0.02}$	$0.55^{0.61}_{0.47}$	$2.00^{2.25}_{1.88}$	$0.32^{0.80}_{0.23}$	$0.53^{0.67}_{0.51}$	66.80/86
Ind (20″)	808	MEPL	–	–	$0.51^{0.53}_{0.49}$	$1.57^{1.60}_{1.55}$	$1.28^{1.34}_{1.21}$	$3.07^{3.14}_{2.99}$	232.63/232
SMF0	All	MEPL	–	–	$0.54\,^{0.55}_{0.52}$	$1.66\,^{1.68}_{1.65}$	$1.60^{1.66}_{1.55}$	$3.95^{4.01}_{3.88}$	1051.57/1002

Table A.2. continued.

Analysis (1)	ObsID (2)	Model (3)	$N_{\rm H1}$ (4)	$N_{\rm H2}$ (5)	kT keV (6)	Γ (7)	Norm$_1$ (10^{-4}) (8)	Norm$_2$ (10^{-4}) (9)	χ^2/d.o.f. F-test (10)
					NGC 5195				
Ind	0112840201	MEPL	$0.42^{0.51}_{0.31}$	–	$0.29^{0.34}_{0.25}$	$1.58^{1.70}_{1.45}$	$4.74^{8.95}_{2.34}$	$0.37^{0.42}_{0.32}$	131.59/102
Ind	0212480801*	MEPL	$0.03^{0.10}_{0.00}$	$0.00^{0.04}_{0.00}$	$0.58^{0.63}_{0.50}$	$1.49^{1.60}_{1.41}$	$0.57^{0.73}_{0.50}$	$0.53^{0.58}_{0.48}$	174.79/126
Ind	0303420101	MEPL	$0.48^{0.53}_{0.37}$	–	$0.28^{0.32}_{0.26}$	$1.41^{1.54}_{1.30}$	$6.17^{8.69}_{3.08}$	$0.35^{0.39}_{0.31}$	249.19/143
Ind	0303420201	MEPL	$0.39^{0.52}_{0.29}$	–	$0.31^{0.38}_{0.26}$	$1.39^{1.53}_{1.26}$	$3.70^{8.21}_{1.93}$	$0.34^{0.39}_{0.29}$	177.87/111
Ind	0677980701	MEPL	$0.63^{0.79}_{0.45}$	$0.00^{0.06}_{0.00}$	$0.25^{0.35}_{0.18}$	$1.68^{2.08}_{1.51}$	$12.14^{57.71}_{3.71}$	$0.46^{0.55}_{0.37}$	34.82/30
SMF1	0112840201	MEPL	–	–	$0.61^{0.63}_{0.60}$	$1.51^{1.57}_{1.46}$	$0.55^{0.61}_{0.53}$	$0.36^{0.39}_{0.33}$	639.89/533
	0212480801							$0.51^{0.55}_{0.48}$	6.8e-12
	0303420101							$0.38^{0.40}_{0.35}$	
	0303420201							$0.37^{0.40}_{0.34}$	
	0677980701							$0.45^{0.51}_{0.40}$	
Ind (3″)	13813	MEPL	$0.40^{0.65}_{0.16}$	$0.95^{2.83}_{0.00}$	$0.61^{0.67}_{0.53}$	$1.53^{2.95}_{1.01}$	$0.22^{0.36}_{0.08}$	$0.10^{0.95}_{0.04}$	47.08/50
Ind (20″)	13813	MEPL	$0.23^{0.31}_{0.14}$	$0.04^{0.17}_{0.00}$	$0.57^{0.60}_{0.52}$	$1.73^{2.09}_{1.47}$	$0.42^{0.57}_{0.31}$	$0.12^{0.17}_{0.09}$	129.49/107
Ind	13812	MEPL	$0.41^{0.63}_{0.00}$	$0.18^{0.73}_{0.08}$	$0.62^{0.83}_{0.48}$	$1.37^{1.79}_{1.19}$	$0.11^{0.25}_{0.03}$	$0.11^{0.21}_{0.08}$	59.03/50
SFM0	All	MEPL	$0.37^{0.49}_{0.19}$	$0.15^{0.69}_{0.06}$	$0.62^{0.67}_{0.57}$	$1.27^{1.61}_{1.11}$	$0.14^{0.21}_{0.08}$	$0.07^{0.12}_{0.06}$	134.19/106
					NGC 5813				
Ind	5907	MEPL	$0.42^{0.63}_{0.26}$	$0.00^{2.33}_{0.00}$	$0.27^{0.35}_{0.21}$	3.98^{0}_{0}	$0.52^{2.26}_{0.11}$	$0.04^{0.19}_{0.01}$	19.61/20
Ind (3″)	9517	MEPL	$0.00^{0.11}_{0.00}$	–	$0.56^{0.60}_{0.48}$	$2.05^{2.32}_{1.72}$	$0.13^{0.20}_{0.12}$	$0.05^{0.07}_{0.04}$	50.12/39
Ind (25″)	9517	MEPL	$0.09^{0.22}_{0.00}$	$0.00^{0.93}_{0.00}$	$0.54^{0.63}_{0.45}$	$2.04^{3.61}_{1.34}$	$0.10^{0.17}_{0.07}$	$0.03^{0.08}_{0.02}$	27.74/16
Ind	12951	MEPL	$0.08^{0.18}_{0.00}$	$0.00^{0.28}_{0.00}$	$0.64^{0.69}_{0.60}$	3.92^{0}_{0}	$0.12^{0.21}_{0.10}$	$0.05^{0.17}_{0.04}$	49.45/24
Ind	12952*	MEPL	$0.10^{0.19}_{0.00}$	–	$0.60^{0.65}_{0.53}$	$2.35^{2.60}_{2.09}$	$0.14^{0.19}_{0.10}$	$0.06^{0.07}_{0.05}$	53.22/48
Ind	13253	MEPL	$0.00^{0.12}_{0.00}$	$0.18^{0.48}_{0.00}$	$0.62^{0.65}_{0.58}$	$2.44^{3.00}_{1.59}$	$0.13^{0.18}_{0.11}$	$0.08^{0.18}_{0.04}$	59.76/43
Ind	13255	MEPL	$0.29^{0.49}_{0.15}$	$1.71^{4.86}_{0.58}$	$0.33^{0.59}_{0.25}$	$2.60^{0}_{1.10}$	$0.63^{1.78}_{0.13}$	$0.20^{1.10}_{0.09}$	21.43/15
SMF0	All	MEPL	$0.01^{0.07}_{0.00}$	$0.06^{0.17}_{0.00}$	$0.60^{0.62}_{0.57}$	$2.40^{2.87}_{2.01}$	$0.12^{0.13}_{0.11}$	$0.07^{0.09}_{0.05}$	260.993/213
Ind	0302460101	MEPL	$0.01^{0.02}_{0.00}$	$0^{0.03}_{0.00}$	$0.58^{0.59}_{0.57}$	$2.10^{2.33}_{2.00}$	$7.12^{7.30}_{6.77}$	$0.53^{0.65}_{0.48}$	436.83/251
Ind	0554680201	MEPL	$0.01^{0.01}_{0.00}$	$0.00^{0.01}_{0.00}$	$0.60^{0.60}_{0.61}$	$1.88^{2.04}_{1.74}$	$7.28^{7.49}_{7.15}$	$0.47^{0.56}_{0.40}$	687.18/329
Ind	0554680301*	MEPL	$0.00^{0.01}_{0.00}$	–	$0.59^{0.60}_{0.59}$	$1.66^{1.77}_{1.48}$	$7.19^{7.31}_{7.11}$	$0.44^{0.50}_{0.35}$	849.57/334
SMF0	All	MEPL	$0.01^{0.01}_{0.00}$	$0.01^{0.01}_{0.00}$	$0.59^{0.60}_{0.59}$	$1.95^{2.01}_{1.91}$	$7.17^{7.28}_{7.07}$	$0.51^{0.58}_{0.49}$	1937.02/918
					NGC 5982				
Ind	0673770401	MEPL	–	–	$0.53^{0.56}_{0.49}$	$1.28^{1.50}_{0.99}$	$0.81^{0.93}_{0.76}$	$0.23^{0.29}_{0.17}$	65.24/64
Ind	0693300301*	MEPL	–	–	$0.52^{0.54}_{0.50}$	$1.52^{1.78}_{1.21}$	$0.76^{0.80}_{0.72}$	$0.16^{0.20}_{0.11}$	186.37/117
SMF1	0693300301	MEPL	–	–	$0.52^{0.54}_{0.50}$	$1.34^{1.52}_{1.15}$	$0.79^{0.82}_{0.75}$	$0.13^{0.16}_{0.10}$	260.60/189
	0673770401							$0.26^{0.31}_{0.21}$	3.3e-9

Table A.3. X-ray luminosities.

			Individual		Simultaneous	
Name	Satellite	ObsID	log (L(0.5−2 keV))	log (L(2−10 keV))	log (L(0.5−2 keV))	log (L(2−10 keV))
(1)	(2)	(3)	(4)	(5)	(6)	(7)
NGC 315	*XMM-Newton*	0305290201	$41.46^{41.47}_{41.44}$	$41.55^{41.57}_{41.52}$		
	Chandra	855	$41.31^{41.43}_{41.15}$	$41.55^{41.63}_{41.47}$	$41.38^{41.40}_{41.37}$	$41.58^{41.61}_{41.55}$
	Chandra (3″)	4156	$41.38^{41.39}_{41.37}$	$41.58^{41.61}_{41.56}$	$41.38^{41.40}_{41.37}$	$41.58^{41.61}_{41.55}$
	Chandra (25″)	4156	$41.44^{41.45}_{41.44}$	$41.68^{41.700}_{41.66}$		
NGC 1052	*XMM-Newton*	093630101	$40.96^{40.97}_{40.94}$	$41.46^{41.47}_{41.45}$	$40.99^{41.00}_{40.99}$	$41.47^{41.49}_{41.46}$
	XMM-Newton	306230101	$40.96^{40.97}_{40.95}$	$41.48^{41.49}_{41.48}$	$41.01^{41.01}_{41.00}$	$41.49^{41.49}_{41.48}$
	XMM-Newton	553300301	$41.10^{41.11}_{41.10}$	$41.56^{41.56}_{41.55}$	$41.06^{41.07}_{41.06}$	$41.55^{41.55}_{41.54}$
	XMM-Newton	553300401	$41.12^{41.13}_{41.11}$	$41.55^{41.56}_{41.55}$	$41.09^{41.09}_{41.08}$	$41.57^{41.58}_{41.57}$
	Chandra (3″)	5910	$40.19^{40.20}_{40.17}$	$41.29^{41.29}_{41.27}$	–	–
	Chandra (25″)	5910	$40.29^{40.31}_{40.27}$	$41.34^{41.37}_{41.30}$	–	–
NGC 1961	*XMM-Newton*	0673170101	$41.20^{41.22}_{41.18}$	$41.27^{41.31}_{41.22}$	$41.20^{41.21}_{41.18}$	$41.23^{41.27}_{41.20}$
	XMM-Newton	0673170301	$41.42^{41.44}_{41.40}$	$41.01^{41.06}_{40.97}$	$41.20^{41.21}_{41.18}$	$41.23^{41.27}_{41.20}$
NGC 2681	*Chandra*	2060	$39.11^{39.13}_{39.08}$	$38.89^{38.97}_{38.80}$	$39.02^{39.04}_{38.99}$	$38.93^{38.99}_{38.87}$
	Chandra	2061	$38.95^{38.97}_{38.92}$	$38.95^{39.02}_{38.86}$	$39.02^{39.04}_{38.99}$	$38.93^{38.99}_{38.87}$
NGC 2787	*XMM-Newton*	0200250101	$39.13^{39.15}_{39.12}$	$39.49^{39.52}_{39.47}$		
	Chandra (3″)	4689	$38.95^{38.99}_{38.90}$	$38.86^{38.94}_{38.76}$		
	Chandra (25″)	4689	$39.15^{39.18}_{39.11}$	$39.34^{39.41}_{39.26}$		
NGC 2841	*XMM-Newton*	0201440101	$39.74^{39.76}_{39.72}$	$39.75^{39.79}_{39.71}$		
	Chandra (5″)	6096	$39.22^{39.27}_{39.17}$	$39.16^{39.29}_{38.98}$		
	Chandra (30″)	6096	$39.71^{39.73}_{39.68}$	$39.86^{39.92}_{39.78}$		
NGC 3608	*XMM-Newton*	0099030101	$39.65^{39.69}_{39.62}$	$40.37^{40.41}_{40.33}$	$40.32^{40.34}_{40.30}$	$40.24^{40.28}_{40.19}$
	XMM-Newton	0693300101	$40.33^{40.35}_{40.31}$	$40.31^{40.35}_{40.26}$	$40.32^{40.34}_{40.30}$	$40.24^{40.28}_{40.19}$
NGC 3718	*XMM-Newton*	0200430501	$40.65^{40.67}_{40.63}$	$40.84^{40.86}_{40.82}$	$40.66^{40.68}_{40.64}$	$40.86^{40.88}_{40.83}$
	XMM-Newton	0200431301	$40.42^{40.44}_{40.39}$	$40.85^{40.87}_{40.82}$	$40.64^{40.66}_{40.62}$	$40.84^{40.87}_{40.82}$
	Chandra (3″)	3993	$40.76^{40.79}_{40.72}$	$41.01^{41.14}_{40.84}$	$40.83^{40.86}_{40.81}$	$40.99^{41.02}_{40.97}$
	Chandra (25″)	3993	$40.75^{40.78}_{40.72}$	$41.02^{41.15}_{40.24}$		
NGC 4261	*Chandra*	834	$41.18^{41.20}_{41.16}$	$41.11^{41.27}_{40.86}$	$40.98^{40.98}_{40.97}$	$41.02^{41.06}_{40.97}$
	Chandra (3″)	9569	$40.92^{40.94}_{40.91}$	$41.00^{40.89}_{41.08}$	$40.98^{40.98}_{40.97}$	$41.02^{41.06}_{40.97}$
	Chandra (25″)	9569	$40.79^{40.81}_{40.78}$	$40.97^{40.99}_{40.94}$		
	XMM-Newton	0056340101	$41.30^{41.31}_{41.29}$	$41.19^{41.21}_{41.17}$	$41.14^{41.15}_{41.14}$	$41.13^{41.15}_{41.11}$
	XMM-Newton	0502120101	$41.22^{41.23}_{41.22}$	$41.15^{41.16}_{41.14}$	$41.14^{41.15}_{41.14}$	$41.13^{41.15}_{41.11}$
NGC 4278	*Chandra* (3″)	7077	$39.87^{39.88}_{39.87}$	$39.76^{39.98}_{39.32}$	$39.86^{39.87}_{39.86}$	$39.82^{39.84}_{39.81}$
	Chandra (25″)	7077	$40.14^{40.17}_{40.10}$	$40.06^{40.08}_{40.04}$	–	–
	Chandra	7081	$39.31^{39.32}_{39.30}$	$39.27^{39.29}_{39.24}$	$39.78^{39.79}_{39.77}$	$39.73^{39.75}_{39.72}$
	Chandra	7080	$39.78^{39.81}_{39.74}$	$39.62^{40.73}$	$39.73^{39.74}_{39.72}$	$39.67^{39.69}_{39.65}$
	XMM-Newton	0205010101	$40.73^{40.74}_{40.73}$	$40.77^{40.78}_{40.76}$	–	–
NGC 4374	*Chandra*	803	$39.95^{40.02}_{39.86}$	$39.53^{39.60}_{39.44}$	$39.83^{39.85}_{39.82}$	$39.82^{39.86}_{39.78}$
	Chandra	5908	$39.83^{39.86}_{39.80}$	$39.80^{39.84}_{39.75}$	$39.57^{39.59}_{39.55}$	$39.51^{39.55}_{39.47}$
	Chandra	6131	$39.30^{39.35}_{39.24}$	$39.39^{39.46}_{39.30}$	$39.39^{39.42}_{39.36}$	$39.28^{39.32}_{39.23}$
	Chandra(25″)	6131	$40.39^{40.40}_{40.38}$	$39.98^{40.09}_{39.83}$		
	XMM-Newton	0673310101	$41.30^{41.30}_{41.29}$	$41.31^{41.33}_{41.28}$		
NGC 4494	*XMM-Newton*	0071340301	$39.29^{39.31}_{39.27}$	$39.50^{39.54}_{39.46}$	$39.26^{39.28}_{39.25}$	$39.48^{39.57}_{39.36}$
	Chandra (3″)	2079	$39.13^{39.19}_{39.06}$	$39.37^{39.46}_{39.25}$	$39.10^{39.14}_{39.07}$	$39.29^{39.41}_{39.13}$
	Chandra (20″)	2079	$39.29^{39.34}_{39.23}$	$39.65^{39.73}_{39.54}$		
NGC 4636	*XMM-Newton*	0111190201	$40.85^{40.86}_{40.84}$	$39.89^{39.94}_{39.85}$	$40.86^{40.86}_{40.86}$	$39.81^{39.83}_{39.80}$
	XMM-Newton	0111190701	$40.87^{40.87}_{40.86}$	$39.05^{39.05}_{39.04}$	$40.86^{40.86}_{40.86}$	$39.81^{39.83}_{39.80}$
NGC 4736	*XMM-Newton*	0094360601	$39.63^{39.64}_{39.63}$	$39.75^{39.77}_{39.73}$	$39.61^{39.61}_{39.61}$	$39.73^{39.74}_{39.72}$
	XMM-Newton	0094360701	$39.59^{39.61}_{39.58}$	$39.73^{39.76}_{39.69}$	$39.61^{39.61}_{39.61}$	$39.73^{39.74}_{39.72}$
	XMM-Newton	0404980101	$39.74^{39.75}_{39.74}$	$39.77^{39.78}_{39.76}$	$39.61^{39.61}_{39.61}$	$39.73^{39.74}_{39.72}$
	Chandra	808	$38.80^{38.84}_{38.76}$	$38.60^{38.64}_{38.54}$		
	Chandra (20″)	808	$39.50^{39.51}_{39.50}$	$39.66^{39.67}_{39.64}$		

Notes. (Cols. 4 and 5) soft and hard intrinsic luminosities for individual fits, and (Cols. 6 and 7) soft and hard intrinsic luminosities for simultaneous fitting. Blanks mean observations that are not used for the simultaneous fittings.

Table A.3. continued.

			Individual		Simultaneous	
Name (1)	Satellite (2)	ObsID (3)	log (L(0.5−2 keV)) (4)	log (L(2−10 keV)) (5)	log (L(0.5−2 keV)) (6)	log (L(2−10 keV)) (7)
NGC 5195	*XMM-Newton*	0112840201	$39.86^{39.88}_{39.85}$	$39.17^{39.21}_{39.12}$	$39.22^{39.24}_{39.20}$	$39.19^{39.22}_{39.15}$
	XMM-Newton	0212480801	$39.29^{39.31}_{39.28}$	$39.39^{39.42}_{39.35}$	$39.28^{39.30}_{39.26}$	$39.34^{39.37}_{39.31}$
	XMM-Newton	0303420101	$39.44^{39.45}_{39.43}$	$39.39^{39.43}_{39.35}$	$39.23^{39.24}_{39.21}$	$39.20^{39.23}_{39.17}$
	XMM-Newton	0303420201	$39.76^{39.77}_{39.74}$	$39.23^{39.26}_{39.18}$	$39.22^{39.24}_{39.20}$	$39.20^{39.23}_{39.16}$
	XMM-Newton	0677980701	$40.19^{40.23}_{40.15}$	$39.19^{39.26}_{39.10}$	$39.26^{39.28}_{39.23}$	$39.28^{39.33}_{39.23}$
	Chandra (3″)	13813	$38.77^{38.83}_{38.71}$	$38.59^{38.66}_{38.49}$	$38.59^{38.61}_{38.56}$	$38.61^{38.64}_{38.57}$
	Chandra (20″)	13813	$39.00^{39.03}_{38.97}$	$38.55^{38.65}_{38.44}$		
	Chandra	13812	$38.60^{38.66}_{38.52}$	$38.66^{38.72}_{38.57}$	$38.59^{38.61}_{38.56}$	$38.61^{38.64}_{38.57}$
NGC 5813	*Chandra*	5907	$40.09^{40.25}_{39.83}$	$39.32^{39.58}_{38.65}$	$39.68^{39.72}_{39.63}$	$39.07^{39.15}_{38.95}$
	Chandra (3″)	9517	$39.69^{39.72}_{39.66}$	$39.15^{39.24}_{39.02}$	$39.68^{39.72}_{39.63}$	$39.07^{39.16}_{38.95}$
	Chandra (30″)	9517	$39.53^{39.56}_{39.49}$	$39.03^{39.16}_{38.83}$		
	Chandra	12951	$39.67^{39.80}_{39.48}$	$39.02^{39.16}_{38.78}$	$39.68^{39.72}_{39.63}$	$39.07^{39.16}_{38.95}$
	Chandra	12952	$39.73^{39.76}_{39.69}$	$39.00^{39.10}_{38.88}$	$39.68^{39.72}_{39.63}$	$39.07^{39.16}_{38.95}$
	Chandra	13253	$39.74^{39.81}_{39.66}$	$39.09^{39.22}_{38.91}$	$39.68^{39.72}_{39.63}$	$39.07^{39.16}_{38.95}$
	Chandra	13255	$39.36^{39.43}_{39.29}$	$39.30^{39.42}_{39.14}$	$39.68^{39.72}_{39.63}$	$39.07^{39.16}_{38.95}$
	XMM-Newton	0302460101	$41.32^{41.33}_{41.32}$	$40.23^{40.26}_{40.19}$	$41.33^{41.33}_{41.32}$	$40.30^{40.32}_{40.28}$
	XMM-Newton	0554680201	$41.52^{41.52}_{41.51}$	$40.84^{40.87}_{40.82}$	$41.33^{41.33}_{41.32}$	$40.30^{40.32}_{40.28}$
	XMM-Newton	0554680301	$41.32^{41.33}_{41.32}$	$40.38^{40.40}_{40.35}$	$41.33^{41.33}_{41.32}$	$40.30^{40.32}_{40.28}$
NGC 5892	*XMM-Newton*	0673770401	$40.73^{40.75}_{40.71}$	$40.68^{40.73}_{40.61}$	$40.72^{40.73}_{40.70}$	$40.61^{40.66}_{40.54}$
	XMM-Newton	0693300301	$40.67^{40.68}_{40.66}$	$40.11^{40.17}_{40.05}$	$40.67^{40.68}_{40.65}$	$40.32^{40.37}_{40.27}$

Table A.4. Results for the best fit of the annular region (ring) in *Chandra* data, and the best fit obtained for the nucleus of *XMM-Newton* data when the contribution from the annular region was removed.

Name (obsID) (1)	Region (2)	Model (3)	$N_{\rm H1}$ (10^{22} cm^{-2}) (4)	$N_{\rm H2}$ (10^{22} cm^{-2}) (5)	kT (keV) (6)	Γ (7)	$\chi^2_{\rm r}$ (8)	log($L_{\rm soft}$) (0.5−2 keV) (9)	log($L_{\rm hard}$) (2−10 keV) (10)	Cont. % (11)
NGC 315 (4156)	Ring*	MEPL	–	–	$0.59_{0.57}^{0.61}$	$1.47_{1.31}^{1.63}$	1.49	41.13	40.88	3
NGC 315 (0305290201)	Nucleus**	MEPL	–	$0.77_{0.47}^{1.08}$	$0.53_{0.45}^{0.59}$	$1.96_{1.74}^{2.20}$	0.97	41.41	41.43	–
NGC 1052 (5910)	Ring*	ME2PL	–	$26.10_{16.93}^{38.14}$	$0.31_{0.28}^{0.39}$	$1.98_{1.71}^{2.23}$	1.47	40.185	40.563	10
NGC 1052 (093630101)	Nucleus**	ME2PL	–	$7.54_{5.20}^{9.98}$	$0.78_{0.68}^{0.89}$	$1.69_{1.50}^{1.86}$	1.13	39.875	41.235	–
NGC 2787 (4689)	Ring*	PL	$0.00_{0.00}^{0.05}$	–	–	$1.59_{1.43}^{1.92}$	1.05	38.82	39.23	53
NGC 2787 (0200250101)	Nucleus**	PL	–	–	–	$1.65_{1.54}^{1.77}$	1.49	39.12	39.47	–
NGC 2841 (6096)	Ring*	PL	$0.02_{0.00}^{0.11}$	–	–	$1.96_{1.72}^{2.45}$	1.09	39.54	39.60	60
NGC 2841 (0201440101)	Nucleus**	MEPL	$0.43_{0.00}^{0.51}$	–	$0.31_{0.19}^{0.60}$	$2.19_{1.93}^{2.34}$	1.41	39.73	39.77	–
NGC 4261 (9569)	Ring*	MEPL	$0.06_{0.03}^{0.11}$	$0.00_{0.00}^{0.04}$	$0.61_{0.59}^{0.62}$	$1.87_{1.70}^{2.07}$	2.07	40.663	40.252	37
NGC 4261 (0502120101)	Nucleus**	ME2PL	–	$8.29_{7.28}^{9.89}$	$0.67_{0.65}^{0.68}$	$1.56_{1.41}^{1.72}$	1.21	40.857	41.051	–
NGC 4278 (7077)	Ring*	MEPL	–	–	$0.29_{0.19}^{0.36}$	$1.61_{1.51}^{1.71}$	1.12	39.551	39.707	38
NGC 4278 (0205010101)	Nucleus**	PL	$0.02_{0.02}^{0.03}$			$2.05_{2.03}^{2.10}$	1.05	40.681	40.736	–
NGC 4374 (6131)	Ring*	MEPL	–	–	$0.54_{0.52}^{0.56}$	$2.11_{1.98}^{2.23}$	1.41	40.36	39.78	84
NGC 4374 (0673310101)	Nucleus**	MEPL	–	–	$0.71_{0.68}^{0.74}$	$1.57_{1.33}^{1.80}$	1.06	40.00	39.76	–
NGC 4494 (2079)	Ring*	ME	–	–	$4.00_{3.34}$		3.23	38.76	38.88	21
NGC 4494 (0071340301)	Nucleus**	PL	–	–		$1.76_{1.68}^{1.83}$	1.54	39.25	39.54	–
NGC 4736 (808)	Ring*	MEPL	–	–	$0.52_{0.49}^{0.54}$	$1.50_{1.47}^{1.54}$	1.12	39.41	39.60	84
NGC 4736 (0404980101)	Nucleus**	MEPL	–	–	$0.62_{0.59}^{0.65}$	$2.03_{1.97}^{2.10}$	0.93	39.15	39.04	–
NGC 5195 (13813)	Ring*	ME	$0.32_{0.27}^{0.37}$	–	$0.54_{0.50}^{0.58}$		1.35	39.00	37.18	74
NGC 5195 (0677980701)	Nucleus**	MEPL	$0.66_{0.41}^{0.90}$	–	$0.23_{0.14}^{0.36}$	$1.71_{1.46}^{1.95}$	1.11	39.17	39.14	–
NGC 5813 (9517)	Ring*	MEPL	–	–	$0.59_{0.58}^{0.60}$	$2.29_{2.10}^{2.47}$	1.55	41.08	40.22	100
NGC 5813 (0554680301)	Nucleus**	MEPL	–	–	$0.71_{0.70}^{0.72}$	$0.54_{0.00}^{2.15}$	1.78	40.85	40.05	–

Notes. (Col. 1) name and obsID in parenthesis, (Col. 2) extracted region, (Col. 3) best-fit model, (Cols. 4−8) parameters of the best-fit model, (Cols. 9 and 10) soft and hard intrinsic luminosities, and (Col. 11) the percentage of the contribution from the ring to the $r_{\rm ext}$ aperture *Chandra* data in the 0.5−10.0 keV band. $^{(*)}$ Spectral parameters of the annular region in *Chandra* data. $^{(**)}$ Spectral parameters of the nuclear region in *XMM-Newton* data when the spectral parameters of the ring from *Chandra* data are included in the fit.

Table A.5. Simultaneous fittings taking into account the contribution from the annular region given in Table A.4.

ObsID (1)	$N_{\rm H1}$ (10^{22} cm^{-2}) (2)	$N_{\rm H2}$ (10^{22} cm^{-2}) (3)	kT (keV) (4)	Γ (5)	Norm$_1$ (10^{-4}) (6)	Norm$_2$ (10^{-4}) (7)	χ^2/d.o.f. (8)	log ($L_{\rm soft}$) (0.5−2 keV) (9)	log ($L_{\rm hard}$) (2−10 keV) (10)
NGC 315									
0305290201	–	$0.86_{0.73}^{1.00}$	$0.52_{0.50}^{0.55}$	$1.85_{1.74}^{1.96}$	$0.42_{0.39}^{0.44}$	$2.38_{2.05}^{2.77}$	467.58/379	$41.44_{41.43}^{41.55}$	$41.54_{41.52}^{41.56}$
4156								$41.44_{41.43}^{41.55}$	$41.51_{41.49}^{41.53}$
NGC 1052									
0093630101	–	$6.11_{5.07}^{7.18}$	$0.68_{0.63}^{0.73}$	$1.58_{1.47}^{1.70}$	$0.48_{0.44}^{0.53}$	$1.28_{0.95}^{1.69}$	577.98/477	$40.35_{40.34}^{40.36}$	$41.33_{41.32}^{41.35}$
5910								$40.35_{40.34}^{40.36}$	$41.27_{41.26}^{41.28}$
NGC 4261									
0502120101	$0.03_{0.00}^{0.08}$	$7.64_{6.58}^{8.74}$	$0.60_{0.59}^{0.61}$	$1.55_{1.36}^{1.75}$	$0.22_{0.19}^{0.26}$	$1.53_{1.04}^{2.25}$	972.83/627	$40.84_{40.84}^{40.84}$	$41.03_{41.01}^{41.05}$
9569								$40.84_{40.83}^{40.85}$	$40.99_{40.97}^{41.01}$
NGC 4278									
0205010101	$0.03_{0.02}^{0.03}$	–	–	$2.11_{2.08}^{2.14}$	$7.74_{7.54}^{7.95}$		844.93/690	$40.71_{40.71}^{40.72}$	$40.71_{40.70}^{40.72}$
7077					$1.15_{1.11}^{1.18}$			$39.89_{39.88}^{39.89}$	$39.86_{39.84}^{39.87}$
NGC 4494									
0071340301	$0.00_{0.00}^{0.01}$			$1.81_{1.74}^{1.89}$	$0.36_{0.35}^{0.38}$		117.35/86	$39.26_{39.25}^{39.28}$	$41.85_{41.29}^{42.08}$
2079					$0.24_{0.23}^{0.27}$		$39.10_{39.07}^{39.14}$	$41.85_{41.28}^{42.08}$	

Notes. (Col. 1) name and obsID in parenthesis, (Col. 2−7) parameters of the best-fit model, (Col. 8) χ^2/d.o.f., and (Cols. 9 and 10) soft and hard intrinsic luminosities.

Table A.6. Statistics of the light curves.

Name (1)	ObsID (2)	Energy (3)	χ^2/d.o.f. (4)	Prob.(%) (5)	$\sigma^2_{\rm NXS}$ (6)	$\langle\sigma^2_{\rm NXS}\rangle$ (7)
NGC 315	4156	0.5–10	50.2/55	34	<0.0046	
		0.5–2			<0.0086	
		2–10			0.0096 ± 0.0059	
NGC 1052	0306230101	0.5–10	57.1/49	80	<0.0012	
		0.5–2			<0.0039	
		2–10			<0.0018	
	0553300301	0.5–10	49.5/46	66	<0.0012	
		0.5–2			<0.0037	
		2–10			<0.0016	
	0553300401	0.5–10	39.3/49	16	<0.0011	
		0.5–2			<0.0037	
		2–10			<0.0016	
	5910	0.5–10	48.6/59	17	<0.0046	
		0.5–2			<0.0160	
		2–10			<0.0070	
NGC 2681	2060	0.5–10 (1)	109.8/80	98	<0.0450	<0.0302
		0.5–10 (2)			<0.0403	
		0.5–2 (1)			<0.0517	<0.0344
		0.5–2 (2)			<0.0454	
		2–10 (1)			<0.3848	<0.2995
		2–10 (2)			<0.4590	
	2061	0.5–10	133.0/78	100	<0.0447	
		0.5–2			<0.0510	
		2–10			<0.5007	
NGC 2787	4689	0.5–10	33.4/30	70	<0.0357	
		0.5–2			<0.0464	
		2–10			<0.1732	
NGC 3226	860	0.5–10	51.2/45	76	0.0367 ± 0.0227	
		0.5–2			0.0838 ± 0.0649	
		2–10			<0.0784	
NGC 4261	834	0.5–10	35.8/34	62	<0.0063	
		0.5–2			<0.0079	
		2–10			<0.0306	
	9569	0.5–10 (1)	85.7/100	15	<0.0072	<0.0051
		0.5–10 (2)			<0.0072	
		0.5–2 (1)			<0.0095	<0.0068
		0.5–2 (2)			<0.0097	
		2–10 (1)			<0.0285	<0.0198
		2–10 (2)			<0.0274	
NGC 4278	7077	0.5–10 (1)	124.3/111	82	<0.0076	<0.0052
		0.5–10 (2)			<0.0070	
		0.5–2 (1)			<0.0093	<0.0062
		0.5–2 (2)			<0.0083	
		2–10 (1)			<0.0461	<0.0307
		2–10 (2)			<0.0406	
	7081	0.5–10 (1)	91.4/107	14	<0.0090	<0.0062
		0.5–10 (2)			<0.0086	
		0.5–2 (1)			<0.0109	<0.0075
		0.5–2 (2)			<0.0104	
		2–10 (1)			<0.0538	<0.0361
		2–10 (2)			<0.0482	
	7080	0.5–10	41.0/55	8	<0.0095	
		0.5–2			<0.0116	
		2–10			<0.0573	
NGC 4374	5908	0.5–10	77.8/46	97	0.0089 ± 0.0048	
		0.5–2			0.0094 ± 0.0061	
		2–10			<0.0540	
	6131	0.5–10	38.1/39	49	<0.0278	
		0.5–2			<0.0325	
		2–10			<0.1785	

Notes. (Col. 1) name, (Col. 2) obsID, (Col. 3) energy band in keV, (Cols. 4 and 5) χ^2/d.o.f. and the probability of being variable in the 0.5−10.0 keV energy band of the total light curve, (Col. 6) normalized excess variance, $\sigma^2_{\rm NXS}$, and (Col. 8) the mean value of the normalized excess variance, $\langle\sigma^2_{\rm NXS}\rangle$, for each light curve and energy band.

Table A.6. continued.

Name (1)	ObsID (2)	Energy (3)	χ^2/d.o.f. (4)	Prob.(%) (5)	$\sigma^2_{\rm NXS}$ (6)	$\langle\sigma^2_{\rm NXS}\rangle$ (7)
NGC 4636	0111190701	0.5–10	40.9/56	7	<0.0005	
		0.5–2			<0.0005	
		2–10			0.0278 ± 0.0201	
NGC 4736	0404980101	0.5–10	50.5/39	94	0.0005 ± 0.0003	
		0.5–2			0.0005 ± 0.0004	
		2–10			0.0030 ± 0.0015	
	808	0.5–10	89.64/35	100	0.0082 ± 0.0063	
		0.5–2			0.0137 ± 0.0078	
		2–10			<0.0788	
NGC 5195	13813	0.5–10(1)	247.4/179	100	<0.1059	<0.0393
		0.5–10 (2)			<0.0672	
		0.5–10 (3)			<0.0631	
		0.5–10 (4)			<0.0709	
		0.5–2 (1)			<0.1544	<0.0557
		0.5–2 (2)			<0.0957	
		0.5–2 (3)			<0.0876	
		0.5–2 (4)			<0.0950	
		2–10 (1)			<0.4636	<0.1640
		2–10 (2)			<0.2457	
		2–10 (3)			<0.2805	
		2–10 (4)			<0.2758	
	13812	0.5–10 (1)	231.4/157	100	<0.0626	0.0116±0.0004
		0.5–10 (2)			0.0437 ± 0.0285	
		0.5–10 (3)			<0.0512	
		0.5–2 (1)			<0.0890	0.0189±0.0011
		0.5–2 (2)			0.0764 ± 0.0434	
		0.5–2 (3)			<0.0756	
		2–10 (1)			<0.2172	<0.1203
		2–10 (2)			<0.2260	
		2–10 (3)			<0.1787	
NGC 5813	5907	0.5–10	31.6/48	4	<0.0417	
		0.5–2			<0.0447	
		2–10			<1.1984	
	9517	0.5–10 (1)	100.4/97	61	<0.0415	<0.0294
		0.5–10 (2)			<0.0417	
		0.5–2 (1)			<0.0440	<0.0320
		0.5–2 (2)			<0.0464	
		2–10 (1)			<0.7487	<0.6505
		2–10 (2)			<1.0640	
	12951	0.5–10	73.8/73	55	<0.0487	
		0.5–2			<0.0538	
		2–10			<1.6736	
	12952	0.5–10 (1)	165.7/142	91	<0.0445	<0.0264
		0.5–10 (2)			<0.0464	
		0.5–10 (3)			<0.0464	
		0.5–2 (1)			<0.0480	<0.0284
		0.5–2 (2)			<0.0494	
		0.5–2 (3)			<0.0498	
		2–10 (1)			<1.0246	<0.7446
		2–10 (2)			<1.5137	
		2–10 (3)			<1.2842	
	13253	0.5–10 (1)	129.8/117	80	<0.0482	<0.0321
		0.5–10 (2)			<0.0424	
		0.5–2 (1)			<0.0533	<0.0347
		0.5–2 (2)			<0.0445	
		2–10 (1)			<0.6305	<0.7111
		2–10 (2)			<1.2749	
	13255	0.5–10	46.5/42	71	<0.0487	
		0.5–2			<0.0556	
		2–10			<0.7024	

Appendix B: Notes and comparisons with previous results for individual objects

B.1. NGC 315

NGC 315 is a radio galaxy located in the Zwicky cluster 0107.5+3212. It was classified optically as a type 1.9 LINER by Ho et al. (1997) and as an AGN candidate at X-ray frequencies (González-Martín et al. 2009b).

At radio frequencies (*VLBI* and VLA) the galaxy shows an asymmetric morphology, with a compact nuclear emission and a one-sided jet (Venturi et al. 1993). The jet can also be observed in X-rays (see Appendix C). Using VLA data, Ishwara-Chandra & Saikia (1999) did not find significant variability over a timescale of ~12 years.

In X-rays, it was observed twice with *Chandra* in 2000 and 2003 and once with *XMM-Newton* in 2005. Younes et al. (2011) found variations in Γ (from $1.5^{+}_{-}0.1$ to $2.1^{+0.1}_{-0.2}$), and a decreasing in the hard luminosity of 53% between 2003 and 2005. They included the emission of the jet in *XMM-Newton* data to derive the nuclear spectral parameters. With the same data set, we obtained very similar individual spectral fittings and luminosities (see Tables A.2 and A.3 for *Chandra* data and Table A.4 for the nuclear region in *XMM-Newton* data). However, we do not find spectral variations, since SMF0 was used both for *Chandra* data and when comparing *Chandra* and *XMM-Newton*. The difference found with the results reported by Younes et al. (2011) might be due to the different errors. A large set of X-ray observations would be desirable to obtain conclusive results.

XMM-Newton data were used to study short-term variations. From its PSD analysis, González-Martín & Vaughan (2012) did not find them in any of the energy bands (soft, hard, total). From the light curve in the 0.5−10 keV energy band, Younes et al. (2011) reported no variations. We found $\sigma^2_{\rm NXS} > 0$ at 1.6σ confidence level in the 2−10 keV energy band, consistent with no variability.

At UV frequencies, Younes et al. (2012) derived the luminosities from the OM onboard *XMM-Newton* with *UVW*2 and UVM2 filters that agree with our results. Variability cannot be studied since OM data are only available at one epoch.

B.2. NGC 1052

This is the brightest elliptical galaxy in the Cetus I group. Previously classed as a LINER in the pioneering work by Heckman (1980), it was classified optically as a type 1.9 LINER (Ho et al. 1997) and as an AGN candidate at X-ray frequencies (González-Martín et al. 2009b). VLA data show a core-dominated and a two-sided jet structure at radio frequencies (Vermeulen et al. 2003).

NGC 1052 was observed twice with *Chandra* and five times with *XMM-Newton*. Long-term variability studies are not found in the literature. We find variations caused by the nuclear power, Norm$_2$ (49%) and the column density, $N_{\rm H2}$ (31%), both at hard energies, in an eight-year period.

González-Martín & Vaughan (2012) studied short term variations from the PSD with *XMM-Newton* data and did not find variations in any of the energy bands. We analyzed *Chandra* and *XMM-Newton* light curves and found no variations. Short-term variations were previously studied with other instruments; Guainazzi et al. (2000) studied *Beppo*SAX data and did not find short-term variations. The most recent observation in X-rays reported so far is a 100 ks observation taken with *Suzaku* in 2007, the derived spectral characteristics reported by Brenneman et al. (2009) appear to be similar to those from *XMM-Newton*, which are compatible with the values in González-Martín et al. (2009b), Brightman & Nandra (2011), and this paper (intrinsic luminosity of $\log(L(2{-}10\ \rm keV)) \sim 41.5$), and no variations along the observation.

In the UV range, Maoz et al. (2005) studied this galaxy with HST ACS and found a decrease by factor of 2 in the flux of the source between the 1997 data reported by Pogge et al. (2000) and their 2002 dataset. We found UV flux variations of a factor of 1.3 using XMM-OM data in a seven-month period.

B.3. NGC 1961

NGC 1961 is one of the most massive spiral galaxies known (Rubin et al. 1979). It was classified as a type 2 LINER by Ho et al. (1997). MERLIN and EVN data show a core plus two-sided jet structure for this source at radio frequencies (Krips et al. 2007), which makes it a suitable AGN candidate.

This galaxy was observed once with *Chandra* in 2010 and twice with *XMM-Newton* in 2011. X-ray variability from these data was not studied before. We did not find variations in a one-month period.

No information in the UV is found for this object in the literature.

B.4. NGC 2681

The nucleus of this galaxy was optically classified as a type 1.9 LINER (Ho et al. 1997). Classified as an AGN and as a Compton-thick candidate in X-rays (González-Martín et al. 2009b,a), a nuclear counterpart at radio frequencies has not been detected (Nagar et al. 2005).

The source was observed twice with *Chandra* in January and May 2001. Younes et al. (2011) did not find short-term variations from the analysis of the light curves or long-term variations from the spectral analysis. These results agree with our variability analysis.

At UV frequencies, no variations were found (Cappellari et al. 1999).

B.5. NGC 2787

The nucleus of NGC 2787 is surrounded by diffuse emission extending up to ~30″ (Terashima & Wilson 2003). It was optically classified as a type 1.9 LINER (Ho et al. 1997) and as an AGN candidate at X-ray frequencies (González-Martín et al. 2009b).

Nagar et al. (2005) detected a radio core with VLA, while evidence of a jet structure has not been found in the literature. Flux variations were obtained at 2 and 3.6 cm on timescales of months (Nagar et al. 2002).

In X-rays, this galaxy was observed twice with *Chandra* in 2000 (snapshot) and 2004 and once with *XMM-Newton* in 2004. Younes et al. (2011) found this to be a non-variable object at long-timescales after correcting *XMM-Newton* data from contamination of X-ray sources. Because of the high contamination from the extranuclear emission in *XMM-Newton* data, we did not perform a simultaneous fit for this object.

From one *Chandra* light curve, Younes et al. (2011) calculated an upper limit of $\sigma^2_{\rm NXS}$, with which our value agrees.

No UV data are found in the literature.

B.6. NGC 2841

Ho et al. (1997) optically classified NGC 2841 as a type 2 LINER. It was classified as an AGN candidate at X-ray frequencies by González-Martín et al. (2009b). This galaxy shows some X-ray sources in the surroundings (González-Martín et al. 2009b). A core structure was found with VLA by Nagar et al. (2005), without evidence of any jet structure.

NGC 2841 was observed twice with *Chandra* in 1999 (snapshot) and 2004 and once with *XMM-Newton* in 2004. We did not use in the analysis the snapshot *Chandra* data because it does not have a high enough count rate for the spectral analysis. Moreover, since the extranuclear emission in *Chandra* data contributed with 60% in the 0.5−10.0 keV energy band, we cannot analyze the spectral variations in this source. No information on variability is reported in the literature for this source.

B.7. NGC 3226

NGC 3226 is a dwarf elliptical galaxy that is strongly interacting with the type 1.5 Seyfert NGC 3227, located at 2′ in projected distance (see Fig. C.19 in González-Martín et al. 2009b). NGC 3226 was optically classified by Ho et al. (1997) as a type 1.9 LINER, and as an AGN candidate at X-ray frequencies by González-Martín et al. (2009b). A compact source is detected with VLA (Nagar et al. 2005), without evidence of any jet structure.

This galaxy was observed twice with *Chandra* in 1999 and 2001 and four times with *XMM-Newton* from 2000 to 2006. The possible contamination of NGC 3227 prevents an analysis of long-term variations. We refer to HG13 for details on this subject.

We analyzed one *Chandra* light curve and obtained $\sigma^2_{\rm NXS} > 0$ below 2σ, consistent with no short-term variations.

UV variations are not found in the literature. We found 11% variations in the *UVW*1 filter from OM data.

B.8. NGC 3608

NGC 3608 is a member of the Leo II group, which forms a non-interacting pair with NGC 3607. It was optically classified as a type 2 LINER (Ho et al. 1997). No hard nuclear point source was detected in *Chandra* images (González-Martín et al. 2009b), thus it was classified in X-rays as a non-AGN candidate, and also it appears to be a Compton-thick candidate (González-Martín et al. 2009a). A compact nuclear source at radio frequencies has not been detected (Nagar et al. 2005).

This galaxy was observed once with *Chandra* and twice with *XMM-Newton* in 2000 and 2012. Variability studies are not found at any frequency in the literature. We did not find variations in the 12-year period analyzed.

B.9. NGC 3718

NGC 3718 has a distorted gas and a dusty disk, maybe caused by the interaction with a close companion (Krips et al. 2007). It was optically classified as a type 1.9 LINER (Ho et al. 1997). It shows a point-like source in the 4.5−8.0 keV energy band (see Fig. B.1), and therefore we can classify it as an AGN candidate following González-Martín et al. (2009b).

At radio frequencies, NGC 3718 was observed with the VLA by Nagar et al. (2005), and with *MERLIN* at 18 cm by Krips et al. (2007), where it shows a core and a compact jet. Nagar et al. (2002) reported radio variability at 2 cm with VLA data, although the result "is not totally reliable".

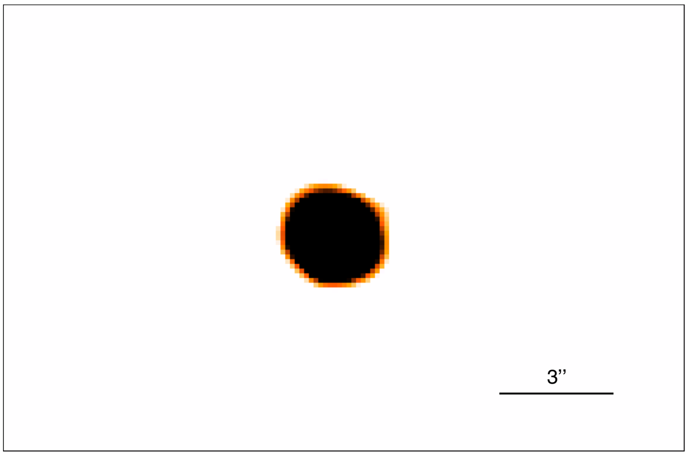

Fig. B.1. *Chandra* image in the 4.5−8.0 keV energy band of NGC 3718, where a point-like source can be distinguished.

In X-rays, this galaxy was observed once with *Chandra* in 1999 and twice with *XMM-Newton* in 2004. Younes et al. (2011) studied all the available data for this object and reported it as variable. When jointly fit *Chandra* and *XMM-Newton* data, we found spectral variations in $\rm Norm_2$ (37%).

Younes et al. (2011) did not find short-term variations from the analysis of the light curves. We did not analyze short-term variations because the length of the observations is <30 ks.

At UV frequencies, Younes et al. (2012) studied this galaxy with *XMM-Newton*, but the nucleus was not detected, so they estimated upper limits for the flux in one epoch.

B.10. NGC 4261

Ho et al. (1997) optically classified this galaxy as a type 2 LINER. González-Martín et al. (2009b) classified it as an AGN candidate at X-ray frequencies. NGC 4261 contains a pair of symmetric kpc-scale jets (Birkinshaw & Davies 1985) and a nuclear disk of dust roughly perpendicular to the radio jet (Ferrarese et al. 1996).

It was observed twice with *Chandra*, in 2000 and 2008, and with *XMM-Newton* in another three epochs from 2001 to 2007. Long-term variability studies are not found in the literature. We did not find variations in six years period.

Sambruna et al. (2003) found variations of 3−5 ks in the 2−10 keV and 0.3−8.0 keV energy bands in the light curve from 2001, and argued in favor of these variations being more closely related to the inner X-ray jet than to an advection-dominated accretion flow (ADAF), since the expected timescale for the light-crossing time of an ADAF was ~2 orders of magnitude longer than the observed variability timescale. In HG13 we analyzed the same observation in the 0.5−10 keV band and reported it as non-variable. However, we notice that $\sigma^2_{\rm NXS} = 0.109 \pm 0.099$ at 1σ confidence level. In the present paper we did not analyze this light curve since the net exposure time is shorter than 30 ks. Other light curves were studied. González-Martín & Vaughan (2012) did not find short-term variations from the PSD analysis of *XMM-Newton* data. In the present study we analyzed two *Chandra* observations and cannot confirm rapid variations in this source, since upper limits for the $\sigma^2_{\rm NXS}$ were obtained in both cases.

No information from the UV is found in the literature. We found variation of a 10% (33%) in the *UVW*1(*UVW*2) filter.

B.11. NGC 4278

The north-northwest side of NGC 4278 is heavily obscured by large-scale dustlanes, whose distribution shows several dense knots interconnected by filaments (Carollo et al. 1997). It is an elliptical galaxy with a relatively weak, broad H_α line, which caused Ho et al. (1997) to classify it optically as a type 1.9 LINER. It was classified at X-ray frequencies as an AGN candidate (González-Martín et al. 2009b).

A two-sided jet is observed at radio frequencies wih VLBA and VLA (Giroletti et al. 2005). Nagar et al. (2002) reported radio variability at 2 and 3.6 cm with VLA data. However, these results "are not totally reliable".

In X-rays this galaxy was observed on nine occasions with *Chandra* from 2000 to 2010 and once with *XMM-Newton* in 2004. Brassington et al. (2009) used six *Chandra* observations and found 97 variable sources within NGC 4278, in a 4′ elliptical area centered on the nucleus, none of them within the aperture we used for the nuclear extraction. Pellegrini et al. (2012) studied *Chandra* observations of NGC 4278 and found an X-ray luminosity decrease by a factor of ~18 between 2005 and 2010. Younes et al. (2010) detected a factor of ~3 flux increase on a timescale of a few months and a variation of a factor of 5 between the faintest and brightest observations (separated by about three years). We used three of these observations (others were affected by pileup or did not meet the minimum count number), and found that our spectral fittings agreed well with theirs, although we found weaker variations in luminosities.

While the different *Chandra* observations did not show short-term variability, during the *XMM-Newton* observation Younes et al. (2010) found a flux increase of a 10% in few hours. With the same dataset, HG13 obtained a 3% variation in the same time range, the difference being most probably due to the different apertures used for the analysis (10″ vs. 25″).

In the UV, Cardullo et al. (2008) found that the luminosity increased by a factor of 1.6 in about six months using data from *HST* WFPC2/F218W.

B.12. NGC 4374

NGC 4374 is one of the brightest giant elliptical galaxies in the center of the Virgo cluster. Optically classified as a type type 2 LINER (Ho et al. 1997), at X-ray frequencies it is a Compton-thick AGN candidate (González-Martín et al. 2009a,b).

It shows a core-jet structure at radio frecuencies, with two-sided jets emerging from its compact core (Xu et al. 2000). Nagar et al. (2002) reported flux variations at 3.6 cm with VLA, and variations at 2 cm that "are not fully reliable".

This galaxy was observed four times with *Chandra*, twice in 2000 (ObsID 401 is a snapshot) and twice in 2005, and once with *XMM-Newton* in 2011. No information about variability in X-ray or UV is found in the literature. Here we report strong variations at hard energies (73% in Norm_2).

We analyzed two *Chandra* light curves, one of them with $\sigma^2_{\text{NXS}} > 0$ below 2σ confidence level, which is compatible with no variations.

B.13. NGC 4494

NGC 4494 is an elliptical galaxy located in the Coma I cloud. It was optically classified as a type 2 LINER (Ho et al. 1997), and at X-rays as an AGN candidate (González-Martín et al. 2009b). The nucleus of this galaxy was not detected in radio with VLA data (Nagar et al. 2005).

This galaxy was observed twice with *Chandra* in 1999 (snapshot) and 2001 and once with *XMM-Newton* in 2001. Variability analyses are not found in the literature. We report the source as variable at X-ray frequencies.

B.14. NGC 4636

NGC 4636 was optically classified as a type 1.9 LINER by Ho et al. (1997). At X-rays it does not show emission at hard energies and therefore was classified as a non-AGN candidate (González-Martín et al. 2009b). It was also classified as a Compton-thick candidate (González-Martín et al. 2009a).

At radio frequencies, it shows a compact core with VLA data (Nagar et al. 2005). Recently, Giacintucci et al. (2011) found bright jets at radio frequencies. No variations were found at 2 cm with VLA data (Nagar et al. 2002).

This galaxy was observed four times with *Chandra* data between 1999 and 2003, and three times with *XMM-Newton* between 2000 and 2001. O'Sullivan et al. (2005) studied the X-ray morphology of the galaxy and suggest that it can be the result of a past AGN that is actually quiescent. Long-term variations were not found in the present analysis.

González-Martín & Vaughan (2012) did not find short-term variations from the analysis of *XMM-Newton* light curves. From one *XMM-Newton* light curve, we found $\sigma^2_{\text{NXS}} > 0$ at 1.4σ confidence level. We did not find long term variations.

No UV variability studies are found in the literature. Our analysis lets us conclude that it is variable at UV frequencies.

B.15. NGC 4736

NGC 4736 is a Sab spiral galaxy, member of the Canes Venatici I cloud (CVn I) (de Vaucouleurs 1975). Optically classified as a type 2 LINER (Ho et al. 1997), it is an AGN candidate at X-ray frequencies (González-Martín et al. 2009b). Nagar et al. (2005) reported an unresolved nuclear source at its nucleus, using 0.15″ resolution VLA data, without evidence of any jet structure.

This galaxy was observed three times with *Chandra* between 2000 and 2008 and three times with *XMM-Newton* between 2002 and 2006. No long-term variability information is found in the literature. In the present work we did not find any variation in a four-year period.

It harbors a plethora of discrete X-ray sources in and around its nucleus (see Appendix C). Eracleous et al. (2002) studied *Chandra* data from 2000. They found a very dense cluster of ten discrete sources in the innermost 400 × 400 pc of the galaxy. They studied the brightest four sources (namely X-1 to X-4) and found that spectra are well described by a single power-law with photon indices in the range 1.1–1.8, and 2–10 keV luminosities between $4–9 \times 10^{39}$ erg s^{-1}. They also studied short-term variability from the analysis of the light curves. They estimated the normalized excess variance ($\sigma^2 = 0.06 \pm 0.04$) of the nucleus of NGC 4736 (X-2), and reported it as variable. The other sources also showed short-term variations (see Table 5 in Eracleous et al. 2002). They argued that there is no evidence for the presence of an AGN and concluded that this LINER spectrum could be the result either of a current or recent starburst or of an AGN.

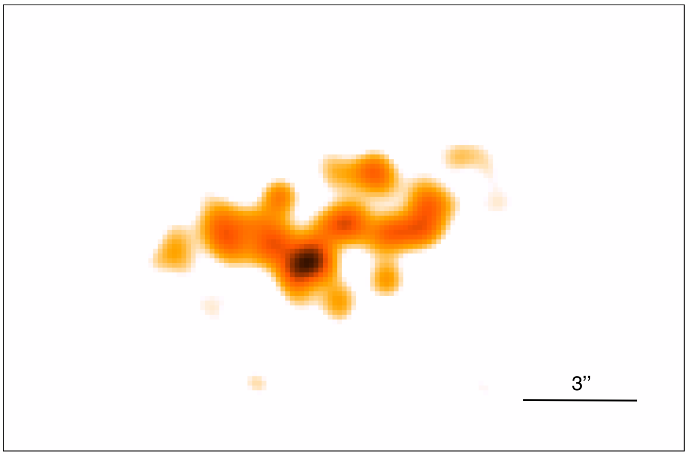

Fig. B.2. *Chandra* image of NGC 5195 in the 4.5−8.0 keV energy band, where a point-like source can be distinguished.

However, they noted that X-2 is the only source with an UV counterpart detected by HST. González-Martín et al. (2009b) assigned X-2 to the nucleus of the galaxy, since it coincides with the 2MASS near-IR nucleus within 0.82″.

By studying *Beppo*SAX and *ROSAT* data, Pellegrini et al. (2002) excluded variations of the 2−10 keV flux higher than ∼50% on timescales on the order of one day. Comparing data from both instruments, they did not find variations between 1995 and 2000. They concluded that the X-ray emission is caused by a recent starburst in NGC 4736. However, they mentioned that an extremely low-luminosity AGN could still be present, because of a compact nonthermal radio source that is coincident with an X-ray faint central point source.

González-Martín & Vaughan (2012) studied the PSD of the *XMM-Newton* data from 2006 and found no short-term variations.

We analyzed *Chandra* and *XMM-Newton* light curves. Variations were found, but were throughout below the 2σ confidence level, in agreement with Eracleous et al. (2002).

At UV frequencies, Maoz et al. (2005) found long-term variations between 1993 and 2003, the nucleus being 2.5 times brighter in 2003. From the OM data, we found variations of 66% in the *U* filter between 2002 and 2006.

B.16. NGC 5195

NGC 5195 is tidally interacting with a companion SB0 galaxy NGC 5194 (M51). It was optically classified as a type 2 LINER by Ho et al. (1997). It shows a point-like source in the 4.5−8.0 keV energy band (see Fig. B.2), and therefore we can classify it as an AGN candidate following González-Martín et al. (2009b). A radio counterpart was found by Ho & Ulvestad (2001) with VLA data at 6 and 20 cm, without any jet indications.

This source was observed eight times with *Chandra* between 2000 and 2012 and five times with *XMM-Newton* between 2003 and 2011. Terashima & Wilson (2004) studied *Chandra* data from 2000 and 2001 and found neither long term, nor short-term variability in the full, soft, or hard energy bands. Since the *Chandra* observations from 2000 and 2001 were rejected from our sample because of the low number counts, we cannot compare our spectral fittings with theirs. However, our estimate of the luminosity in *Chandra* data agrees with their results. We found this object to be variable on long-timescales, while short-term variations were not detected.

At UV frequencies, no references are found in the literature. We found variations in the *UVW*1 filter.

B.17. NGC 5813

NGC 5813 is one of the galaxies in the group catalog compiled by de Vaucouleurs (1975), with NGC 5846 being the brightest member of the group. It was classified as a type 2 LINER by Ho et al. (1997). The X-ray morphology is extremely diffuse, with very extended emission at softer energies and without emission above 4 keV, which caused González-Martín et al. (2009b) to classify it as a non-AGN candidate. It was also classified as Compton-thick candidate (González-Martín et al. 2009a). At radio frequencies, it shows a compact core (Nagar et al. 2005) and a jet-like structure (Randall et al. 2011).

This source was observed nine times with *Chandra* between 2005 and 2011 and three times with *XMM-Newton* between 2005 and 2009. Variability studies at X-ray and UV frequencies are not reported in the literature. We did not find either long-term or short-term variations in X-rays. UV variations were found in the *UVW*1 filter.

B.18. NGC 5982

NGC 5982 is the brightest galaxy in the LGG 402 group, which is composed of four members (Garcia 1993). Recently, Vrtilek et al. (2013) found a compact radio core in the position of the source using *GMRT* 610 MHz observations, which indicates that this is an AGN-like object; jets were not detected.

This galaxy was observed twice with *XMM-Newton* in 2011 and 2012. Variability studies are not reported in the literature. We found variations in the nuclear power (50%) in a one-year period, while UV variations were not found.

Appendix C: Images

In this appendix we present the images from *Chandra* (left) and *XMM-Newton* (right) that were used to compare the spectra from these two instruments in the 0.5−10 keV band. In all cases, the gray levels extend from twice the value of the background dispersion to the maximum value at the center of each galaxy.

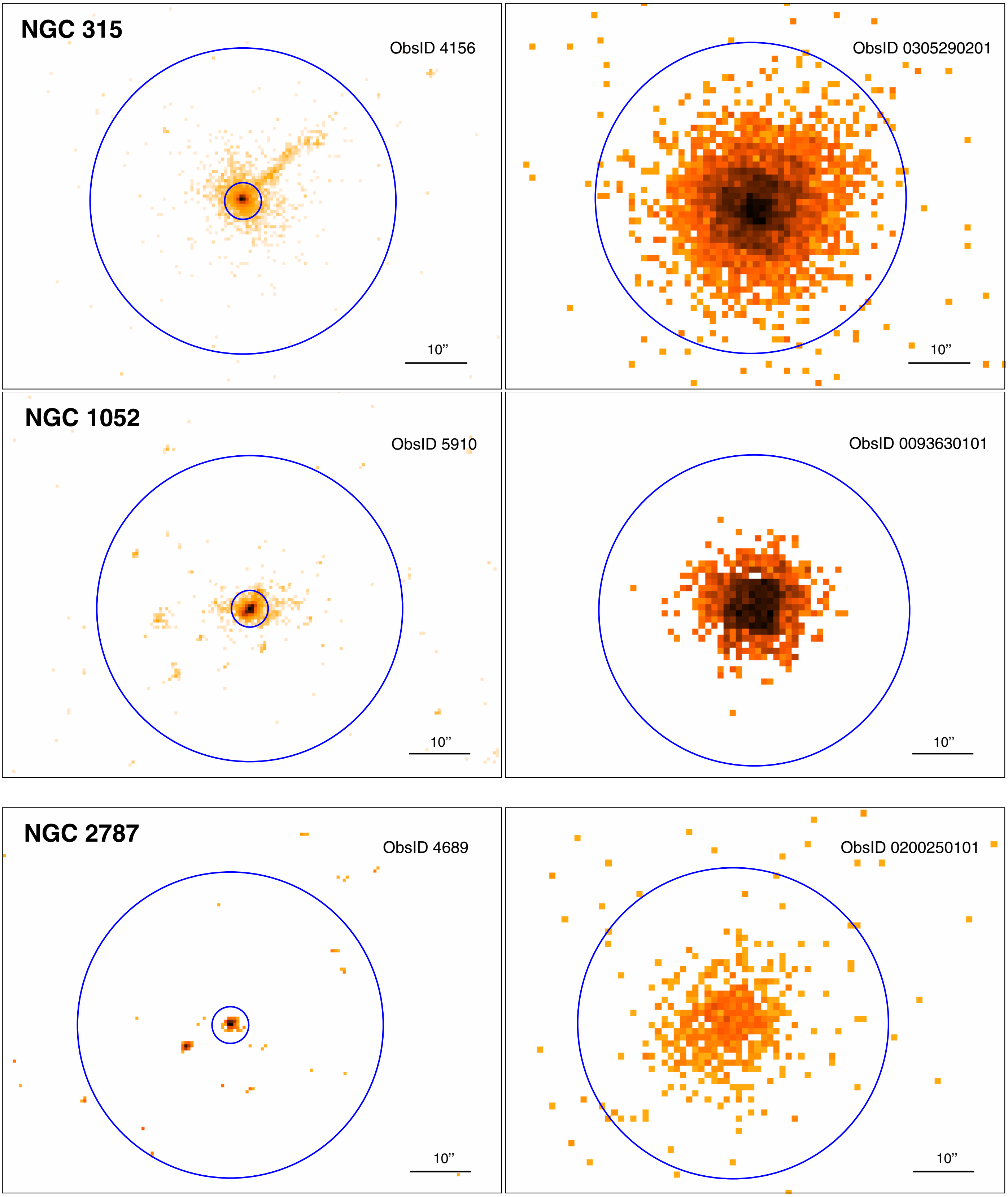

Fig. C.1. Images for *Chandra* data (*left*) and *XMM-Newton* data (*right*) for the sources in the 0.5−10 keV band. Big circles represent *XMM-Newton* data apertures. Small circles in the figures to the left represent the nuclear extraction aperture used with *Chandra* observations (see Table A.1).

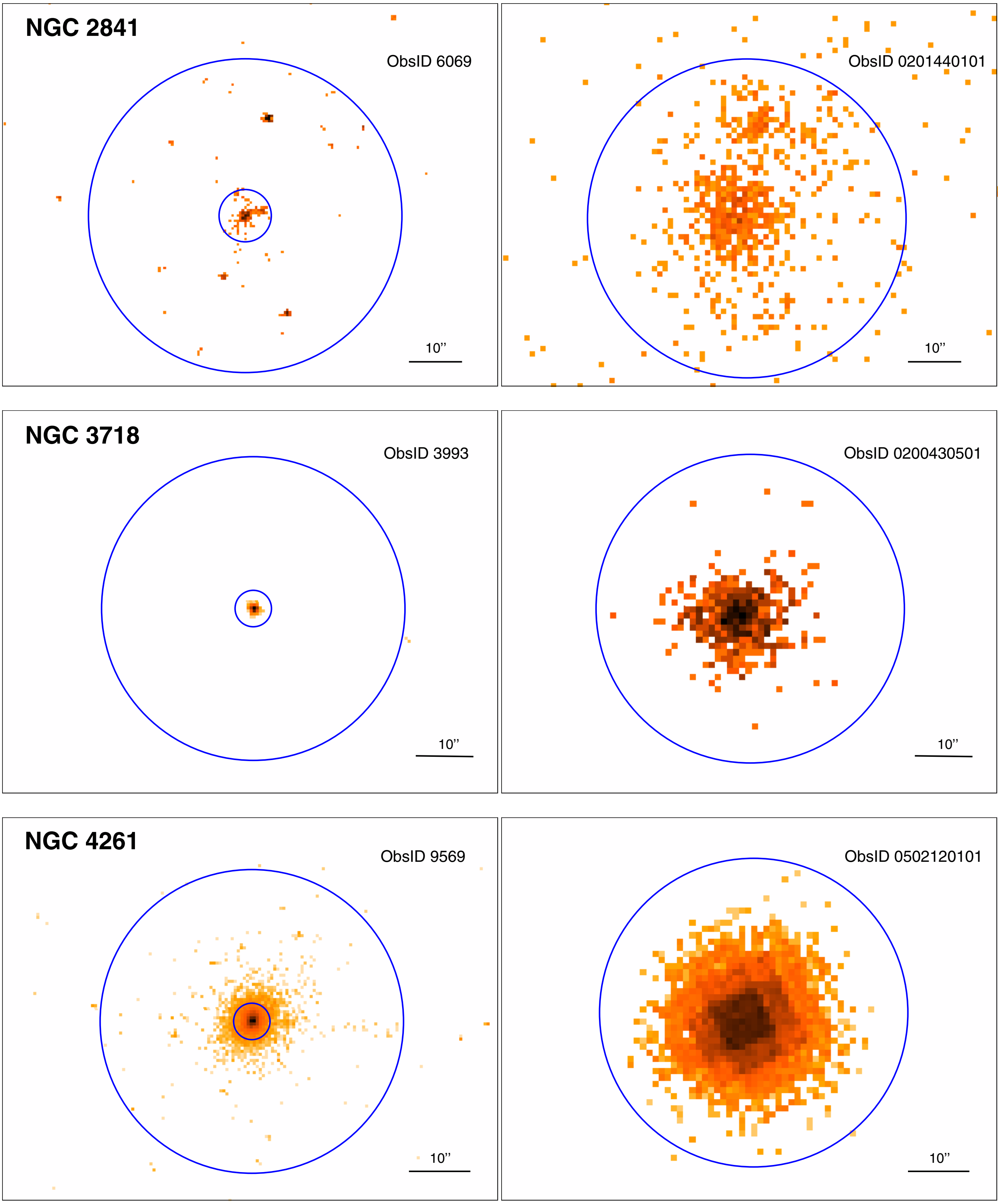

Fig. C.1. continued.

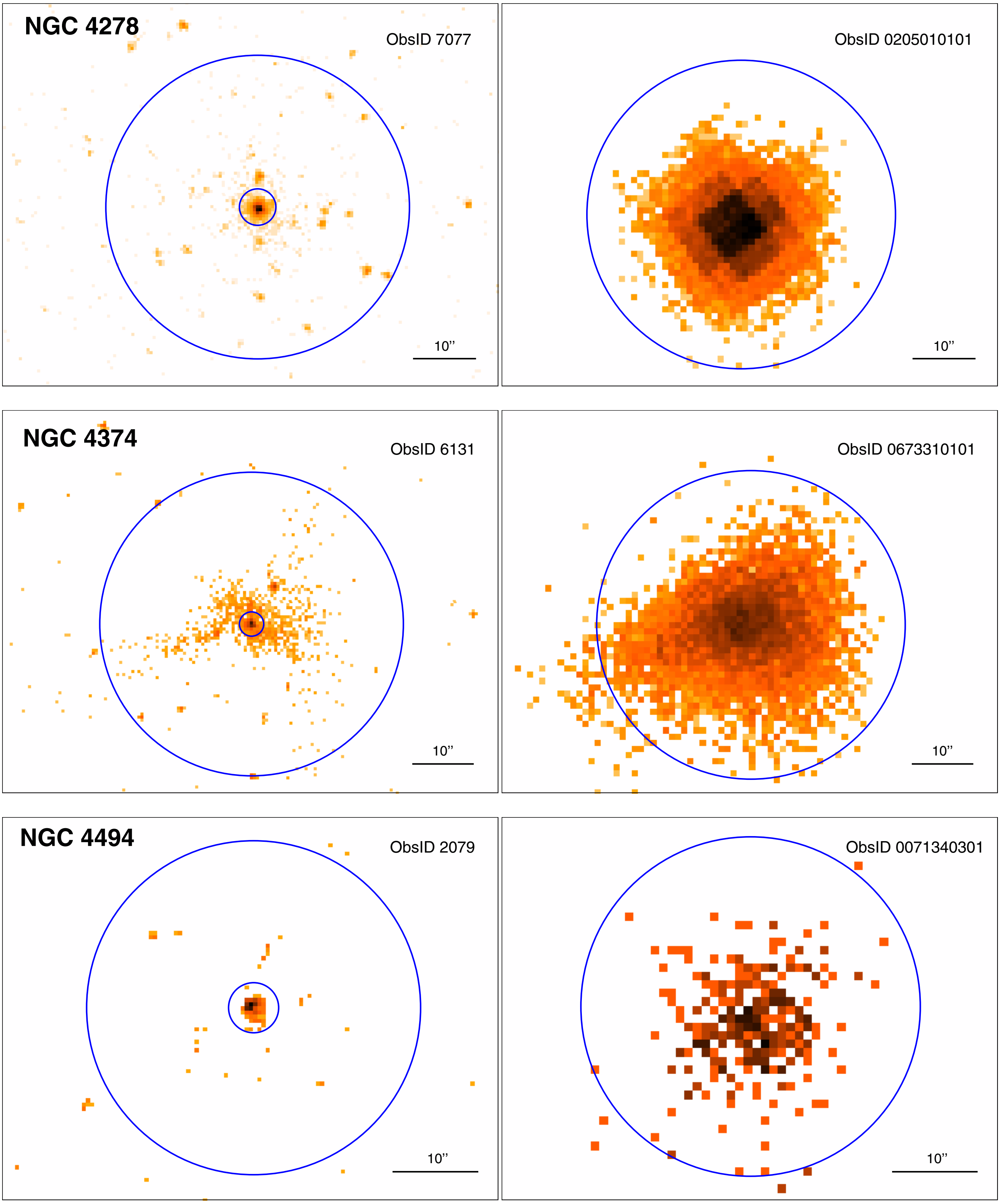

Fig. C.1. continued.

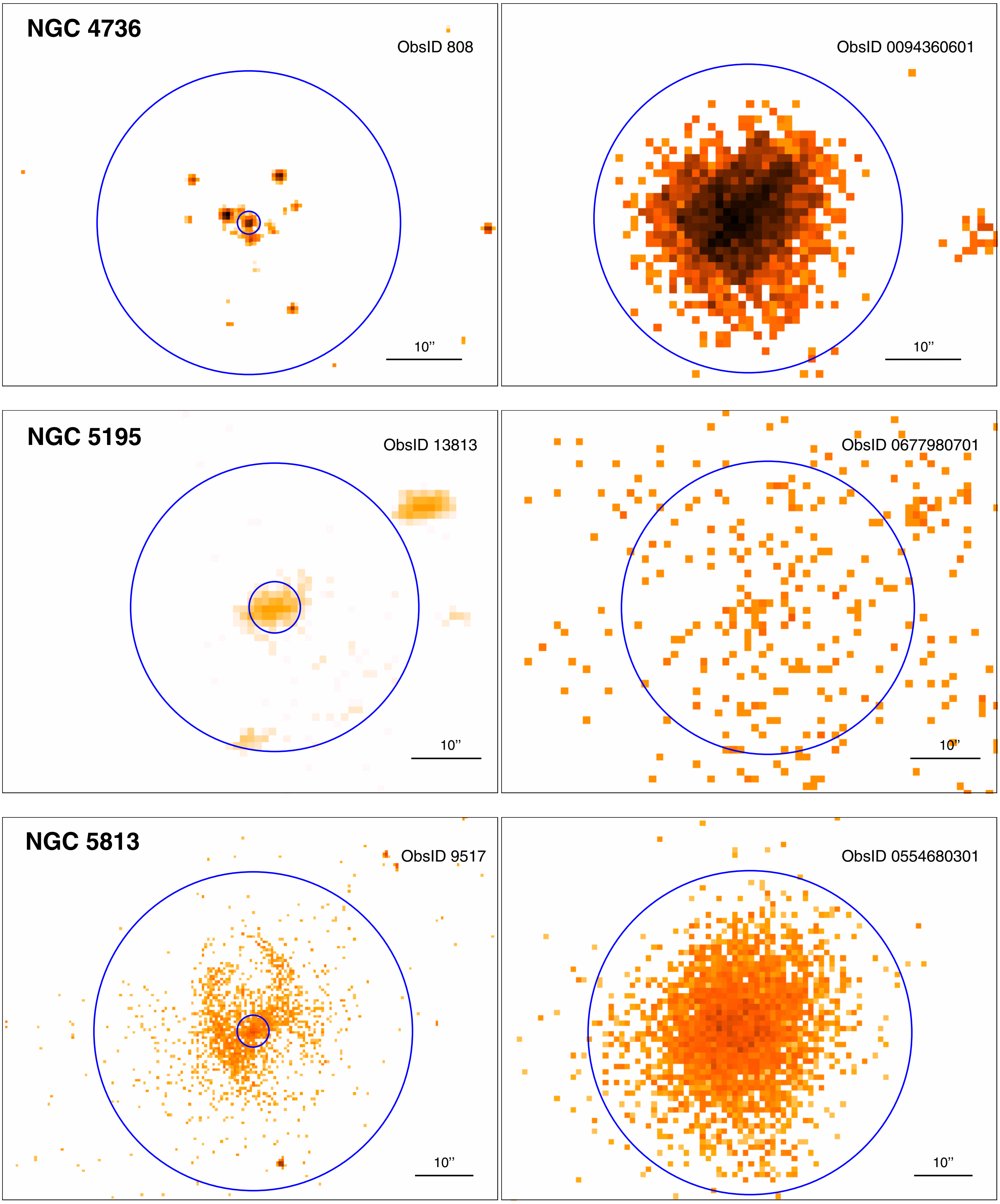

Fig. C.1. continued.

Appendix D: Light curves

In this appendix the plots corresponding to the light curves are provided. Three plots per observation are presented, corresponding to soft (left), hard (middle), and total (right) energy bands. Each light curve has a minimum of 30 ks (i.e., 8 h) exposure time, while long light curves are divided into segments of 40 ks (i.e., 11 h). Each segment is enumerated in the title of the light curve. Count rates versus time continua are represented. The solid line represents the mean value, dashed lines the $\pm 1\sigma$ from the average.

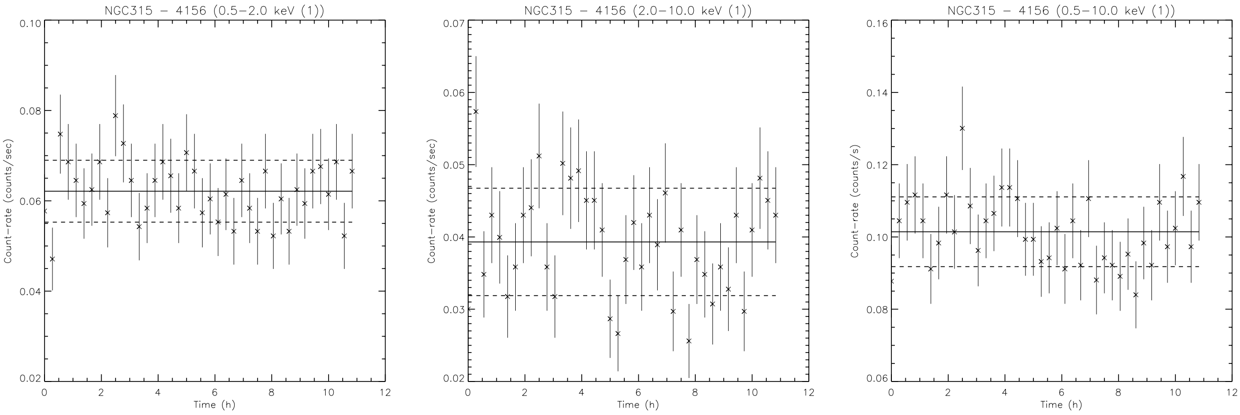

Fig. D.1. Light curves of NGC 315 from *Chandra* data.

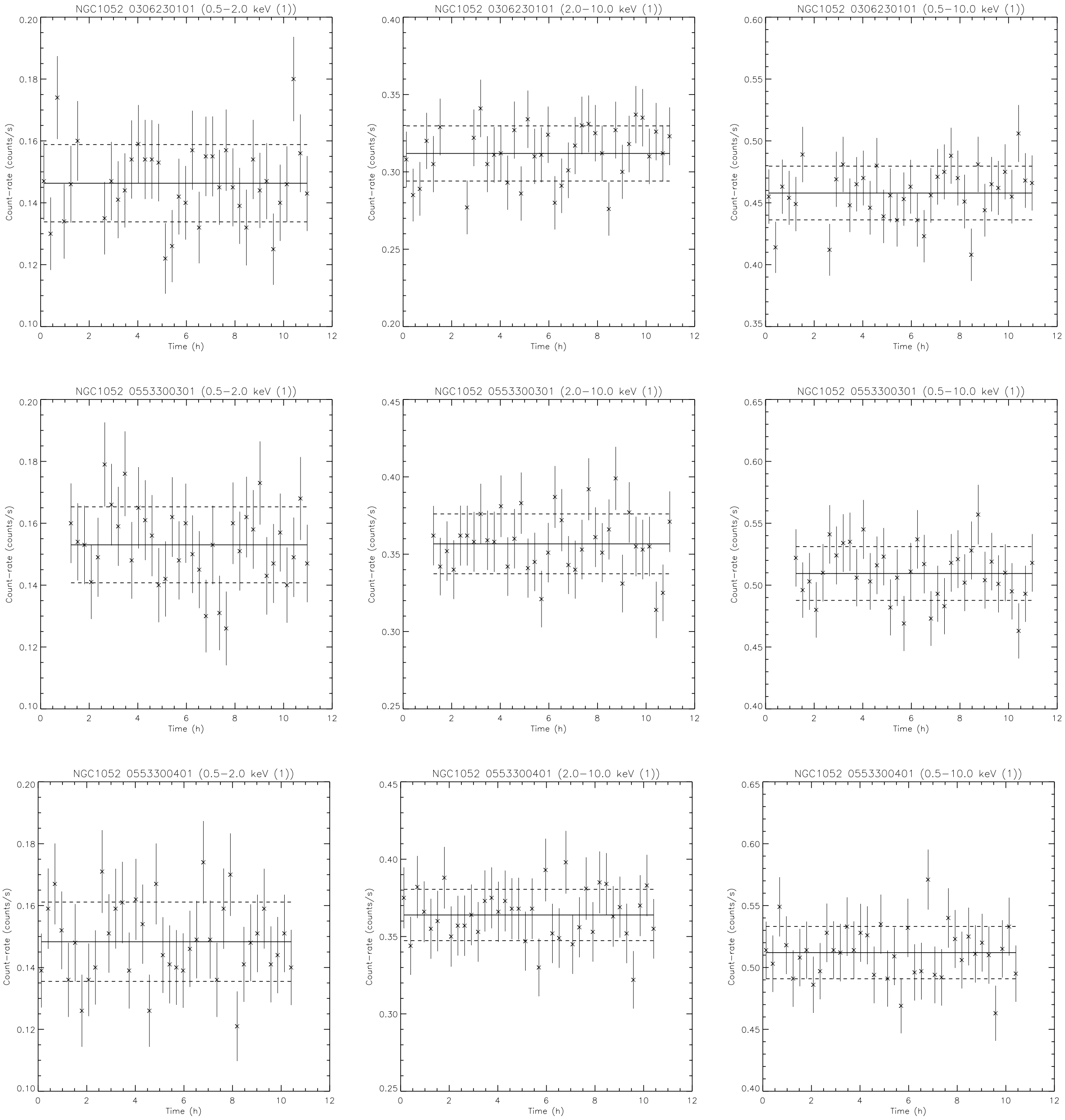

Fig. D.2. Light curves of NGC 1052 from *XMM-Newton* data.

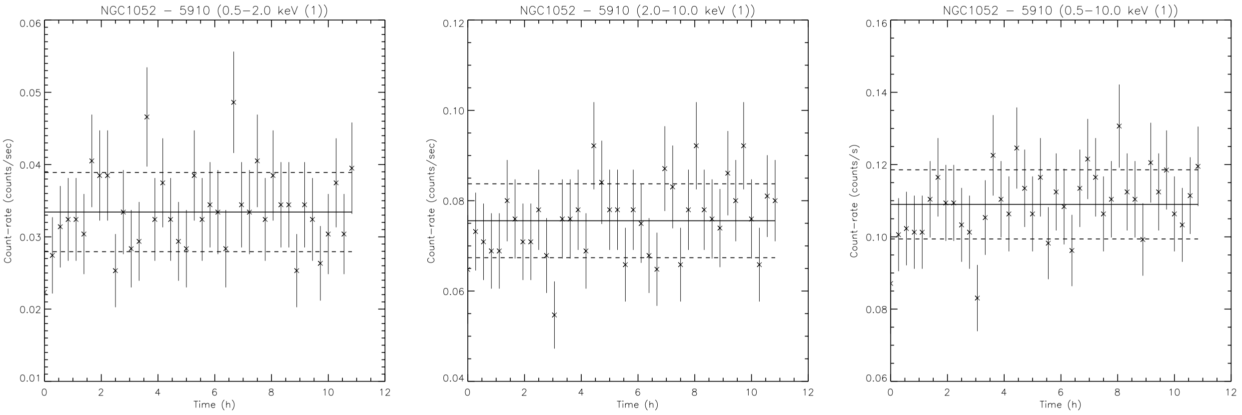

Fig. D.3. Light curves of NGC 1052 from *Chandra* data.

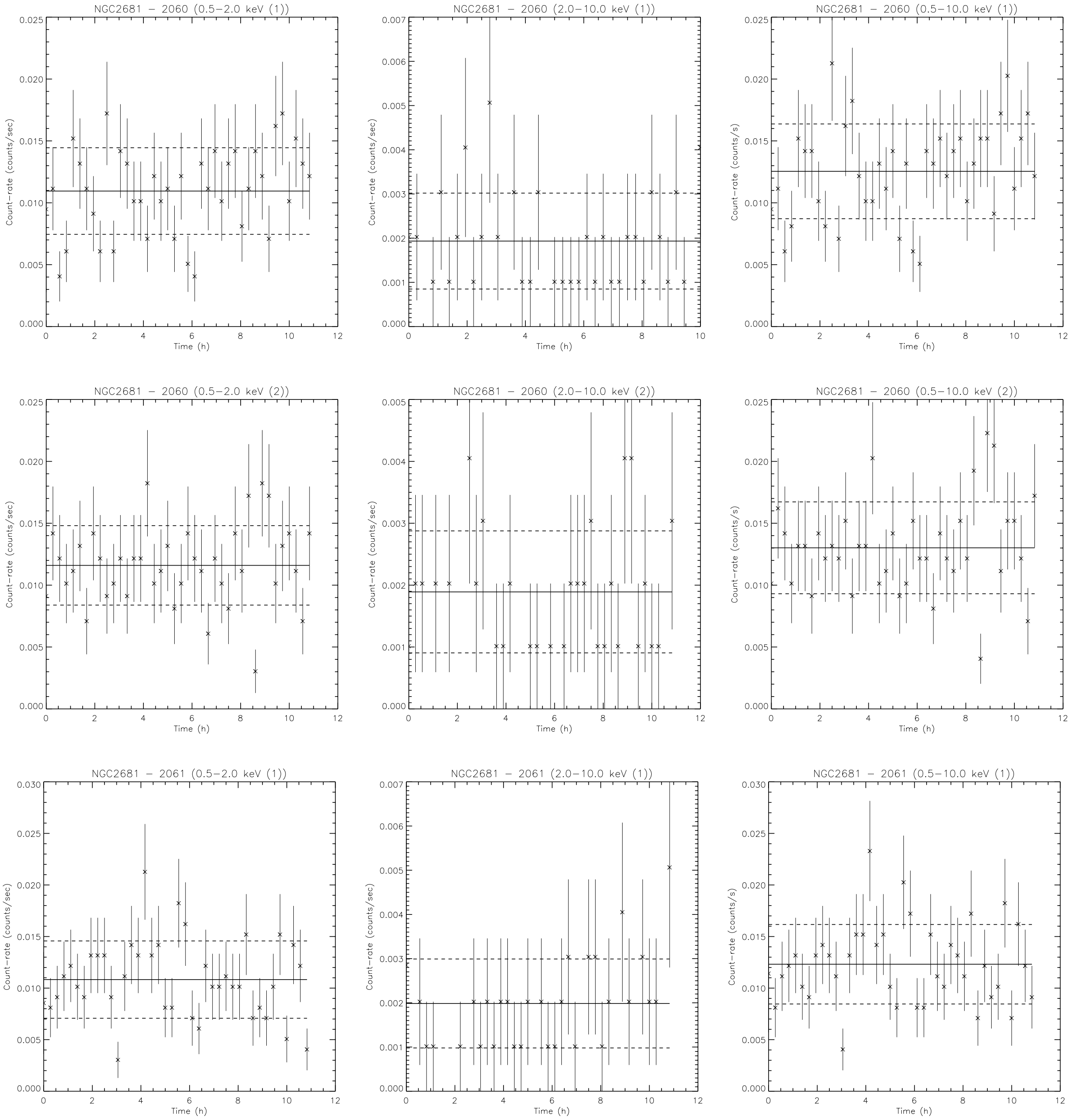

Fig. D.4. Light curves of NGC 2681 from *Chandra* data. Note that ObsID. 2060 is divided into two segments.

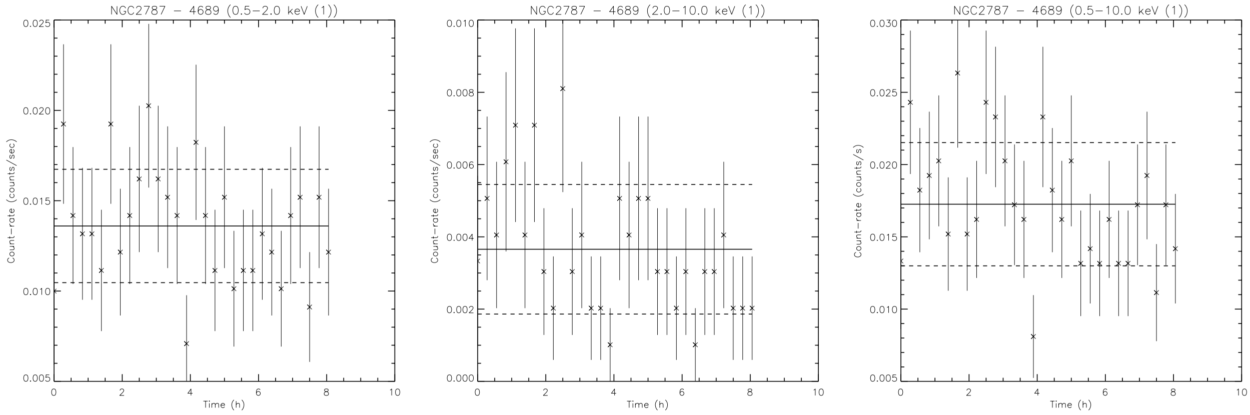

Fig. D.5. Light curves of NGC 2787 from *Chandra* data.

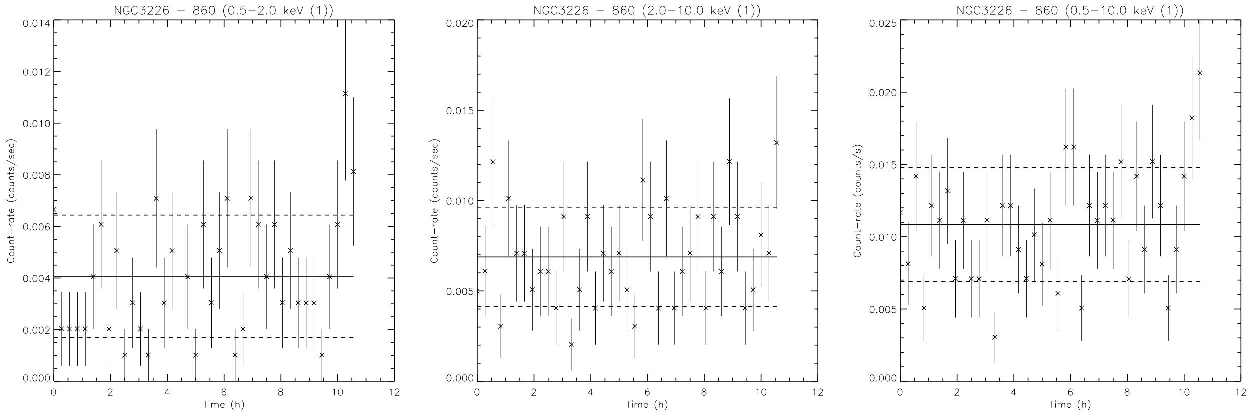

Fig. D.6. Light curves of NGC 3226 from *Chandra* data.

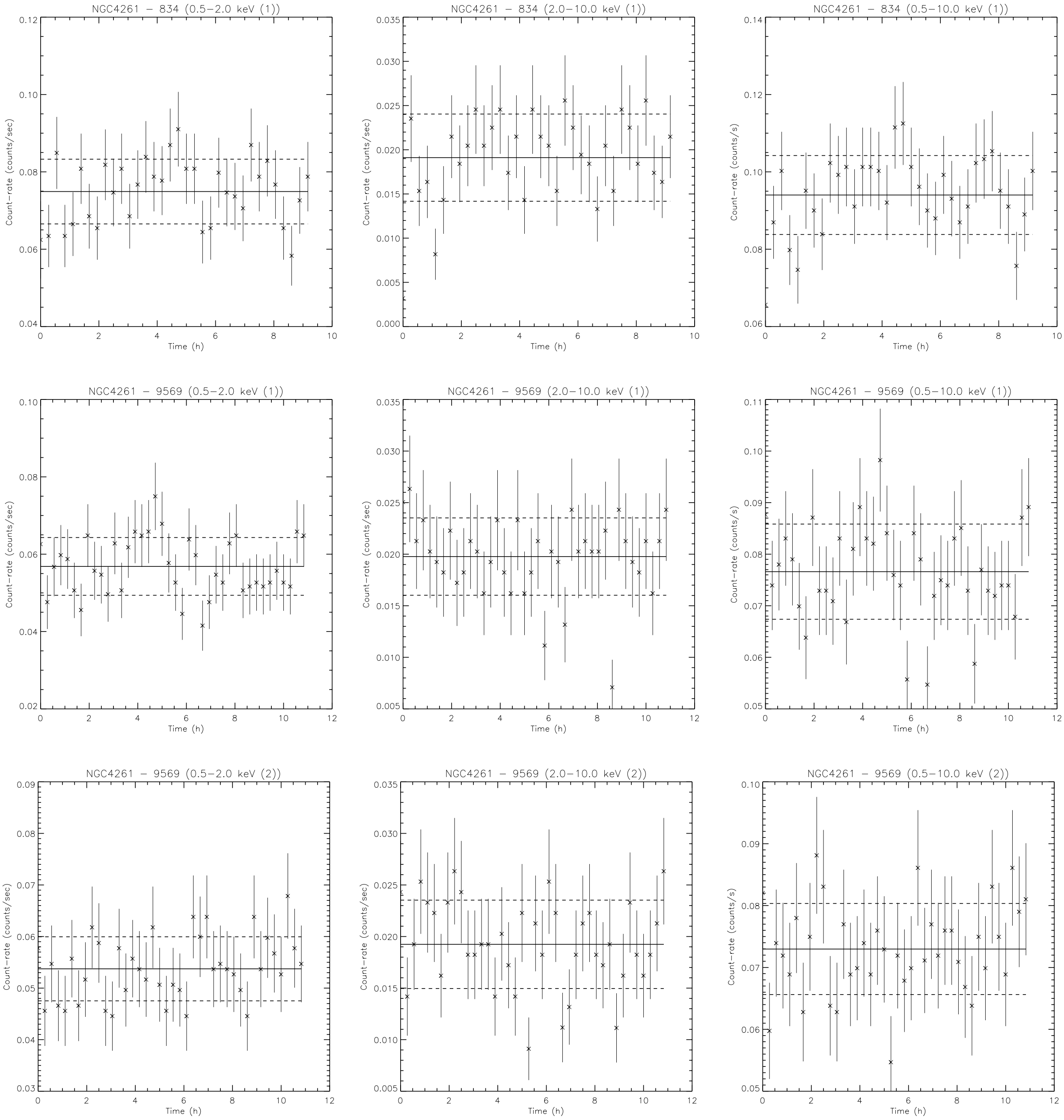

Fig. D.7. Light curves of NGC 4261 from *Chandra* data. Note that ObsID. 9569 is divided into two segments.

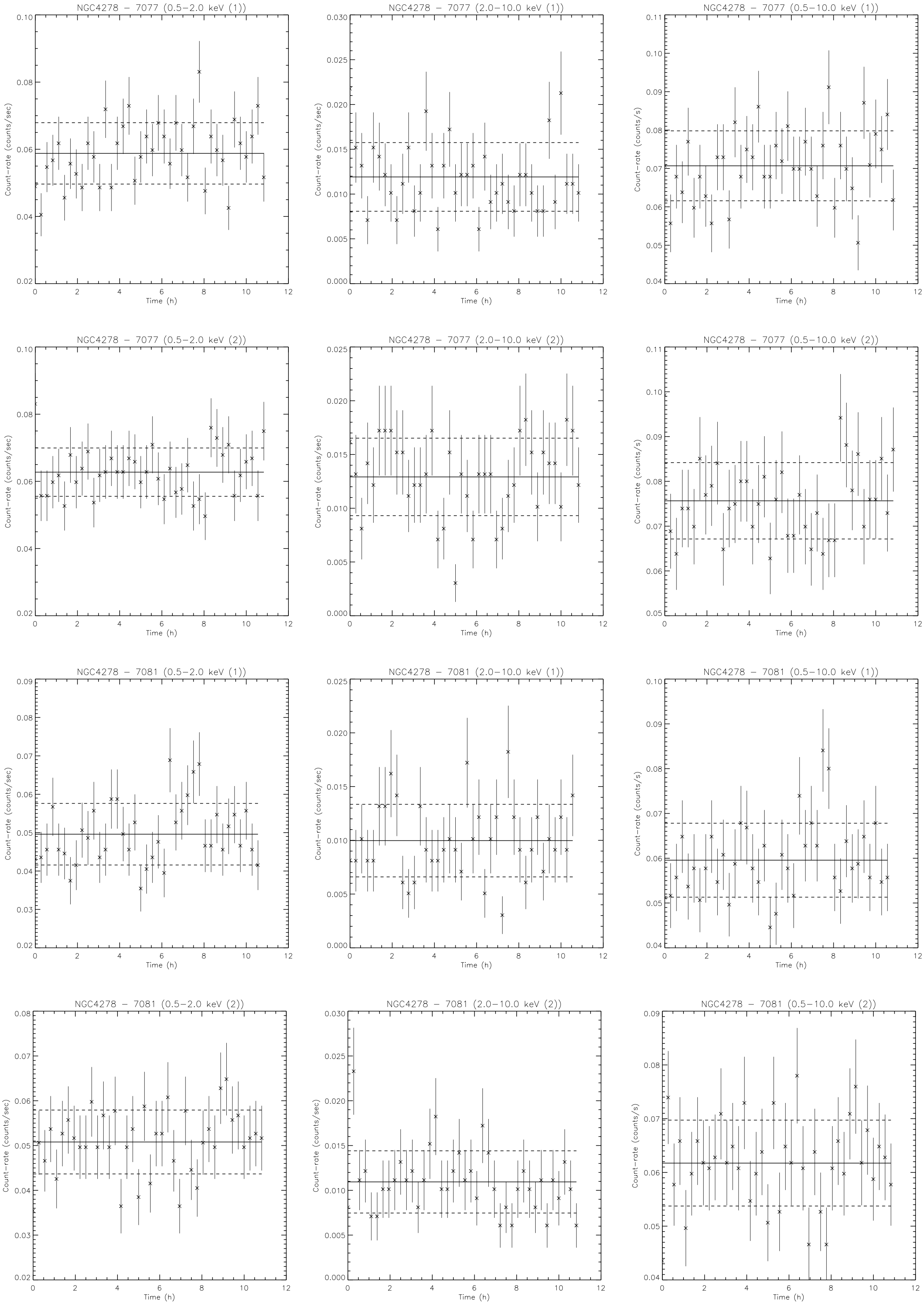

Fig. D.8. Light curves of NGC 4278 from *Chandra* data. Note that ObsID. 7077 and 7081 are divided into two segments.

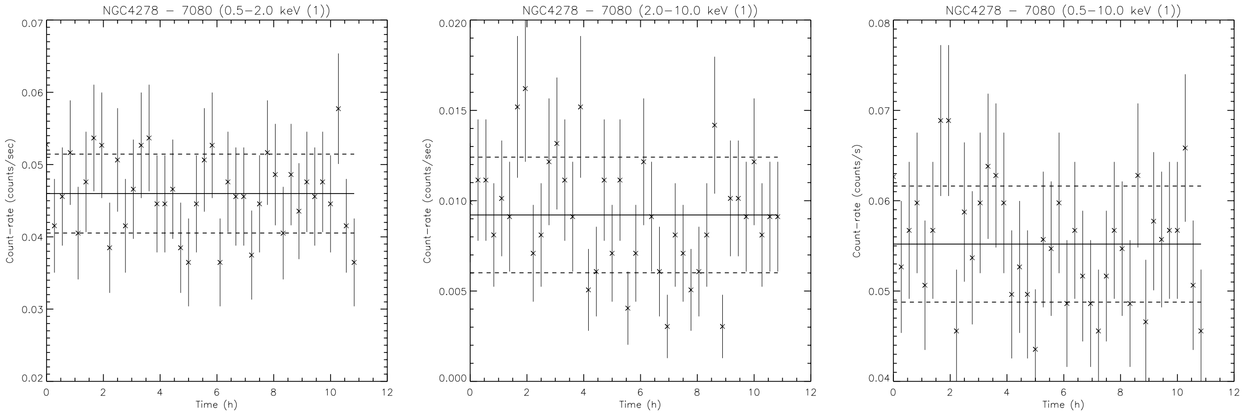

Fig. D.8. continued.

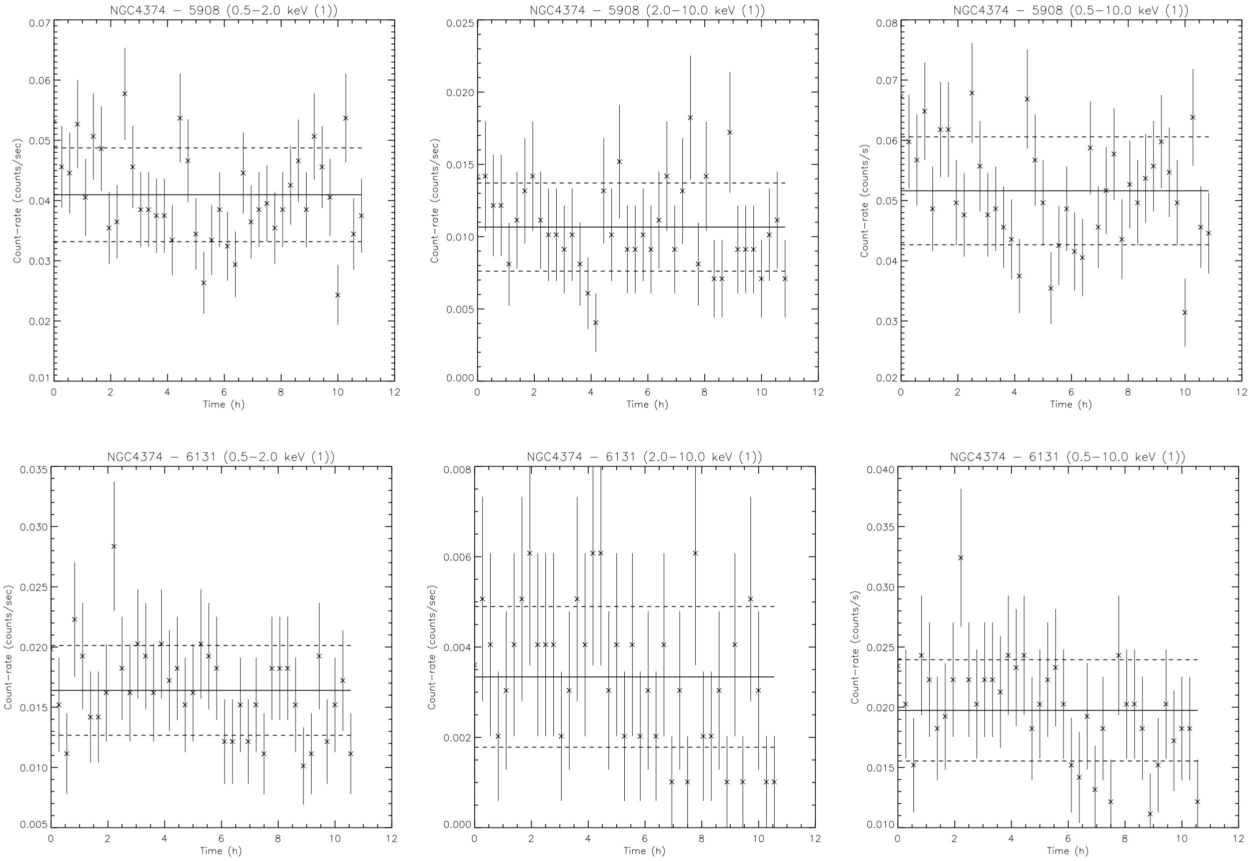

Fig. D.9. Light curves of NGC 4374 from *Chandra* data.

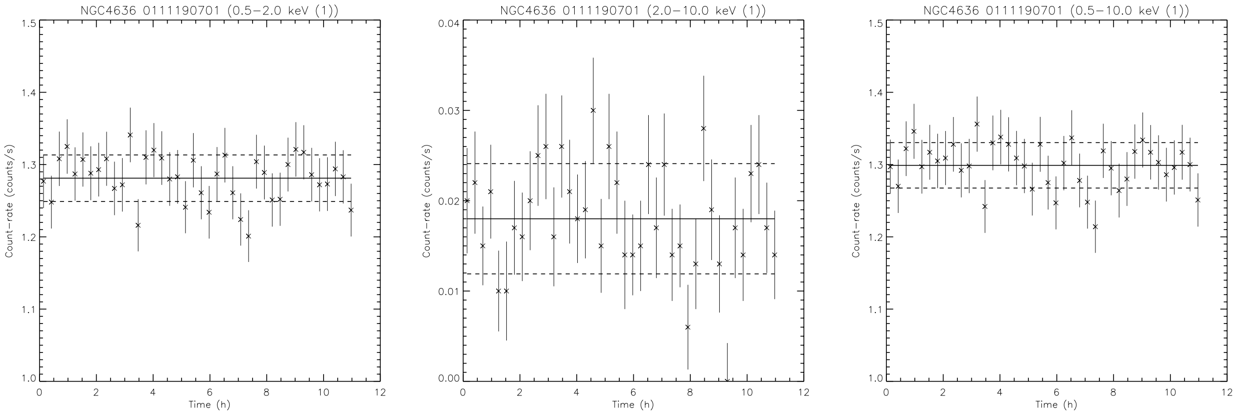

Fig. D.10. Light curves of NGC 4636 from *XMM-Newton* data.

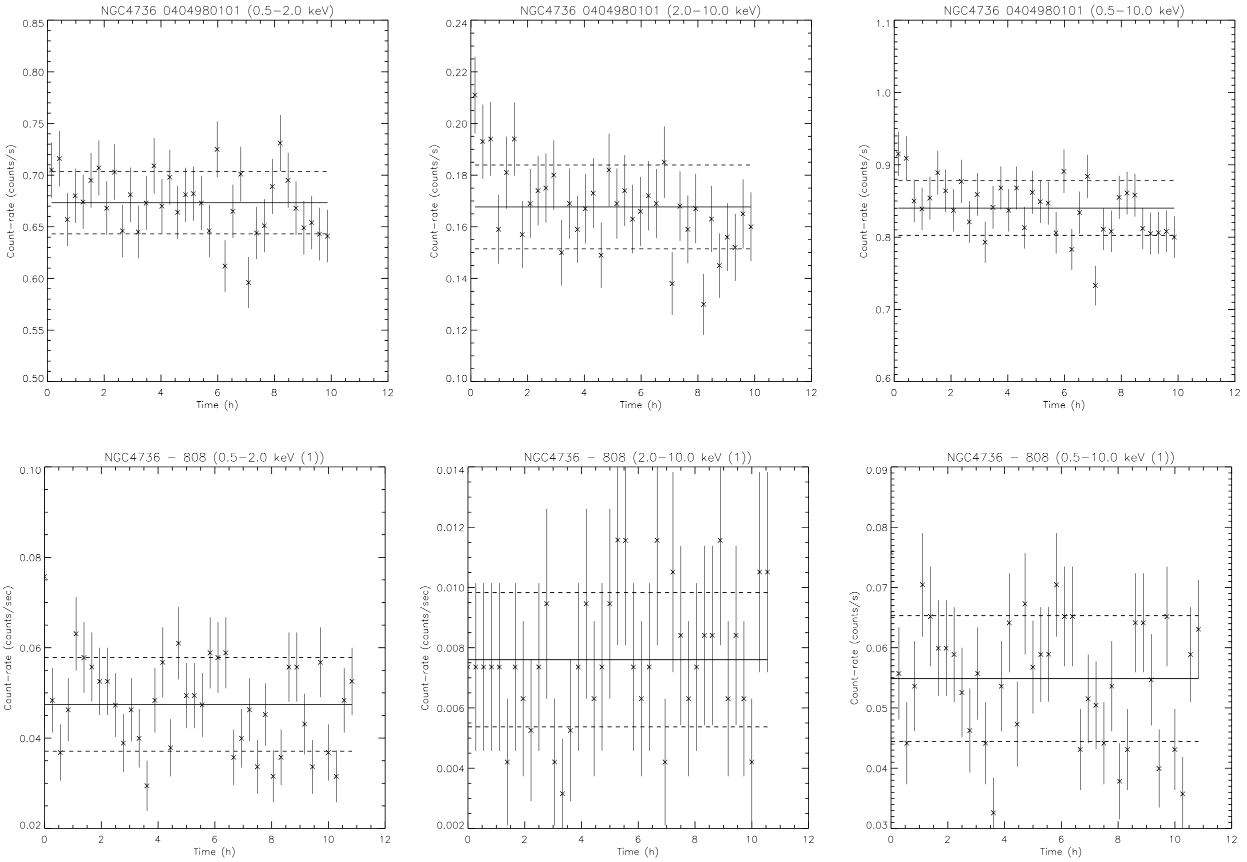

Fig. D.11. Light curves of NGC 4736 from *XMM-Newton* (*top*) and *Chandra* (*bottom*) data.

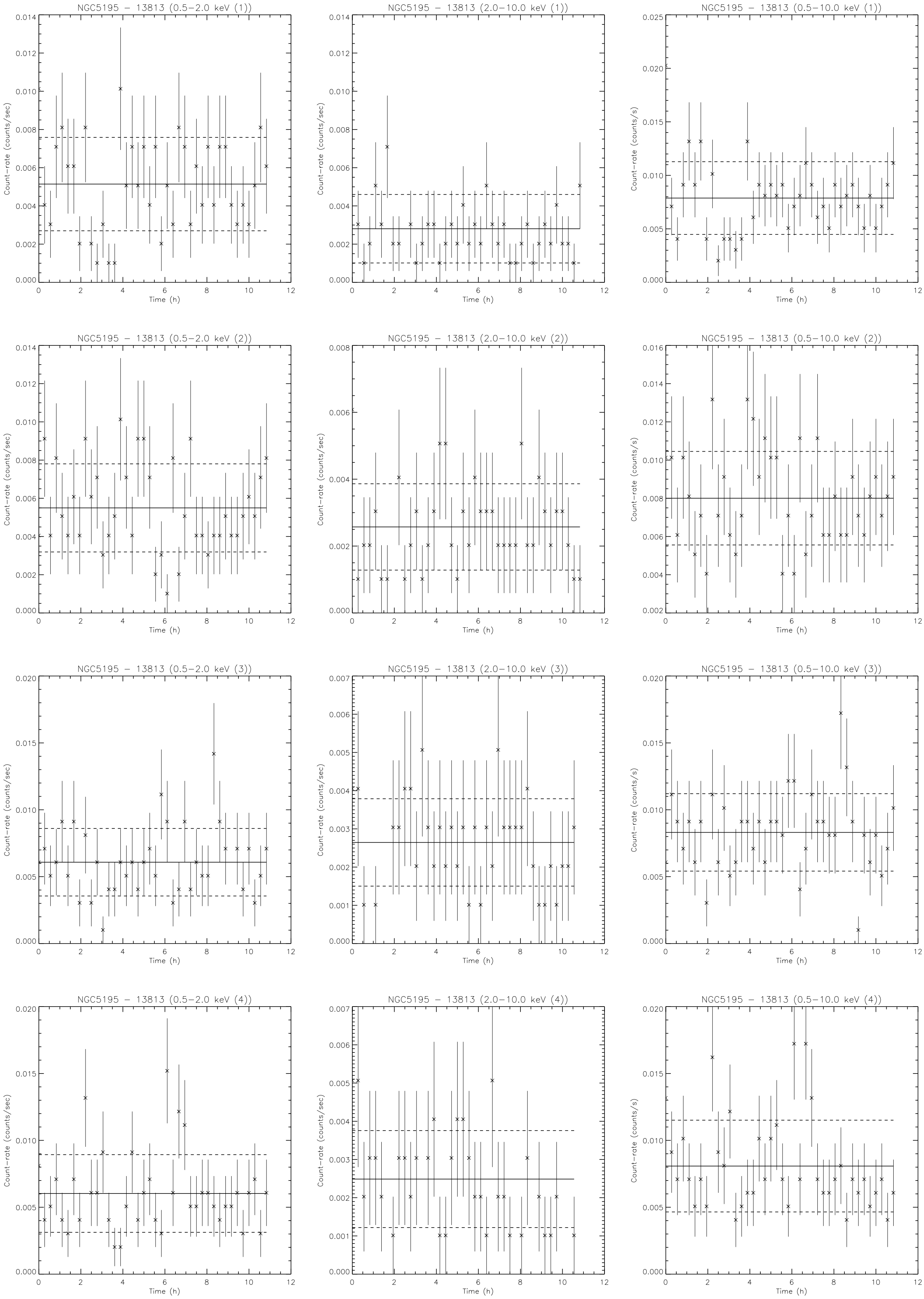

Fig. D.12. Light curves of NGC 5195 from *Chandra* data. Note that ObsID. 13813 is divided into four segments and ObsID. 13812 into three segments.

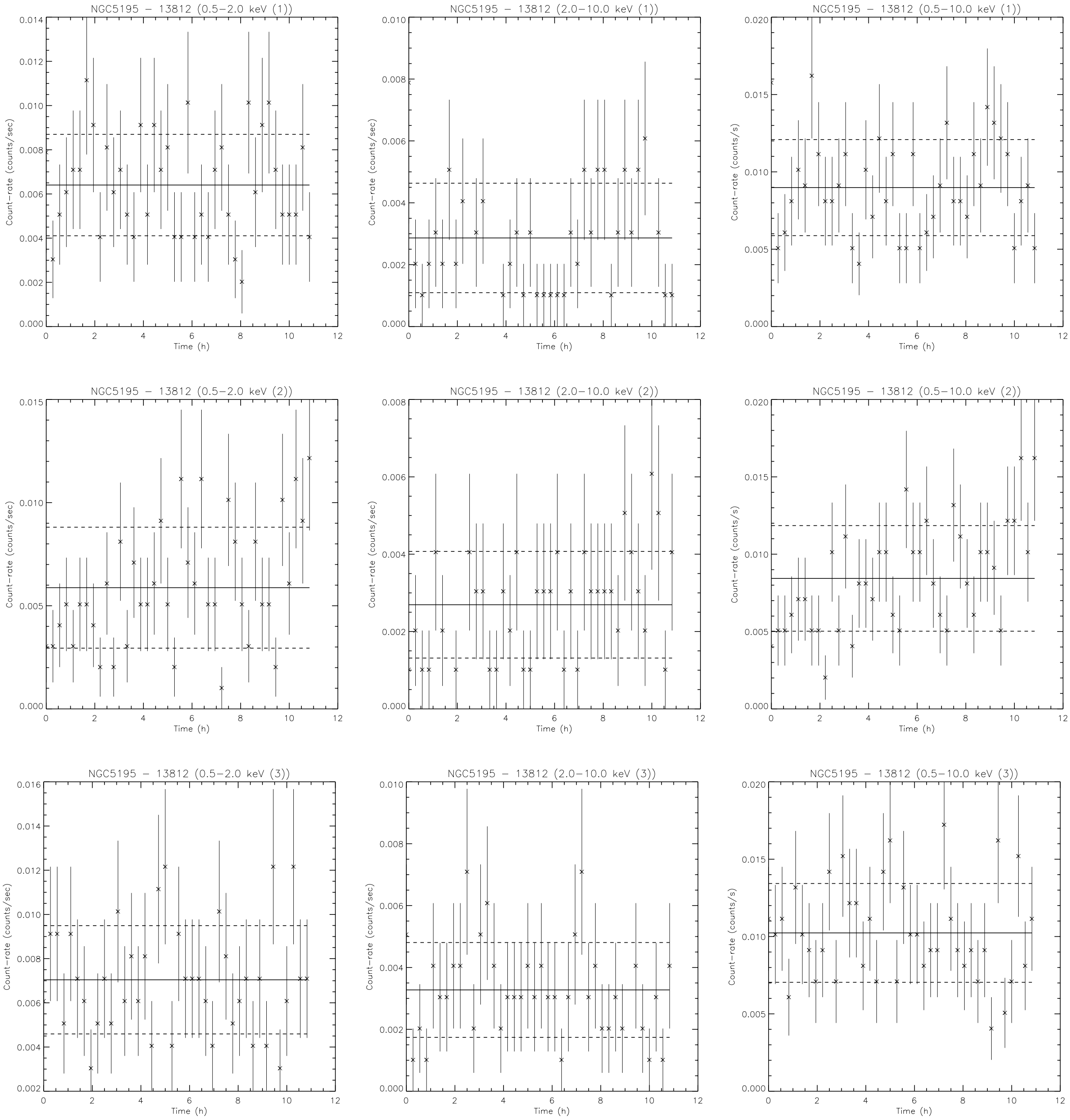

Fig. D.12. continued.

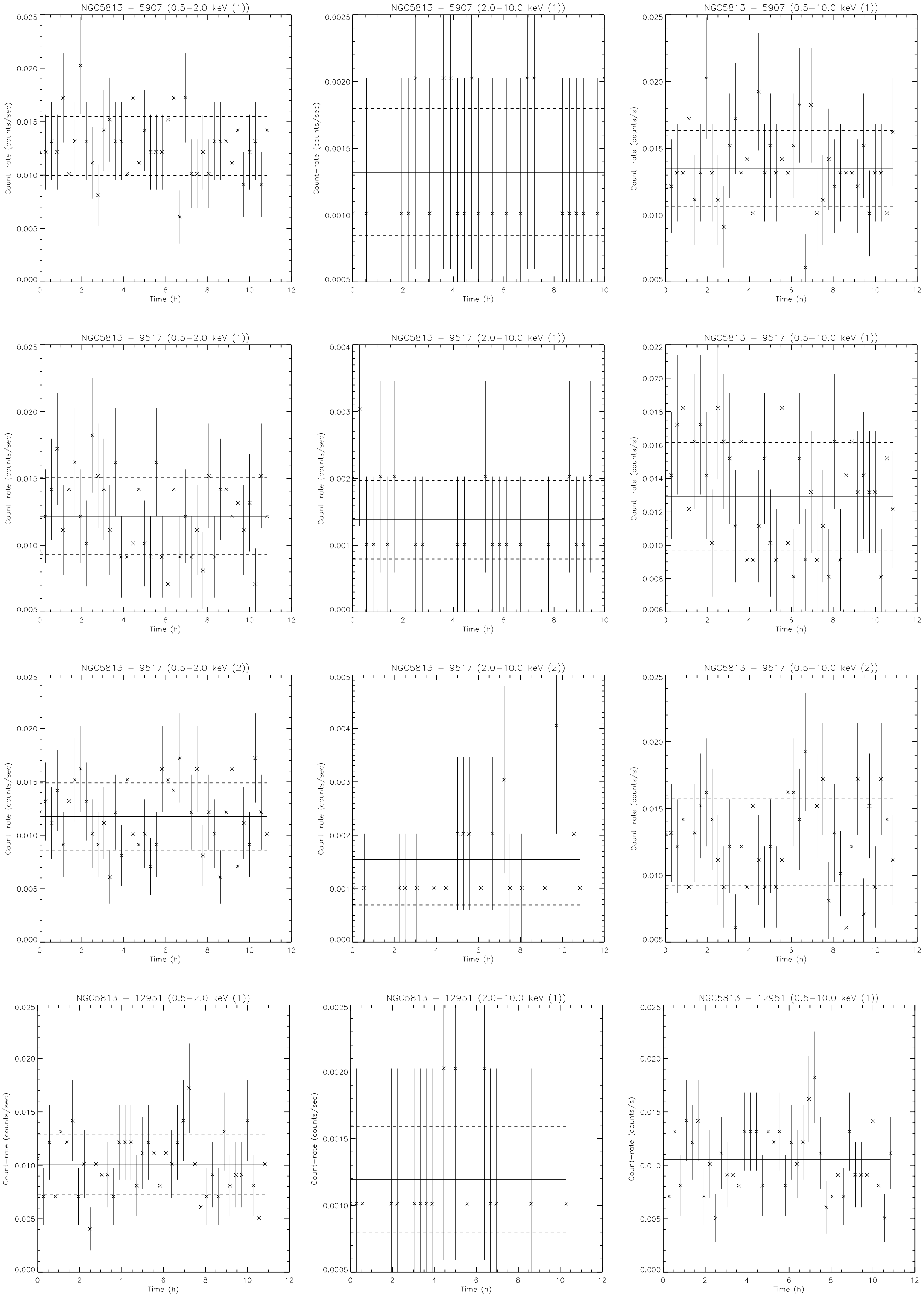

Fig. D.13. Light curves of NGC 5813 from *Chandra* data. Note that ObsID. 9517 and 13253 are divided into two segments.

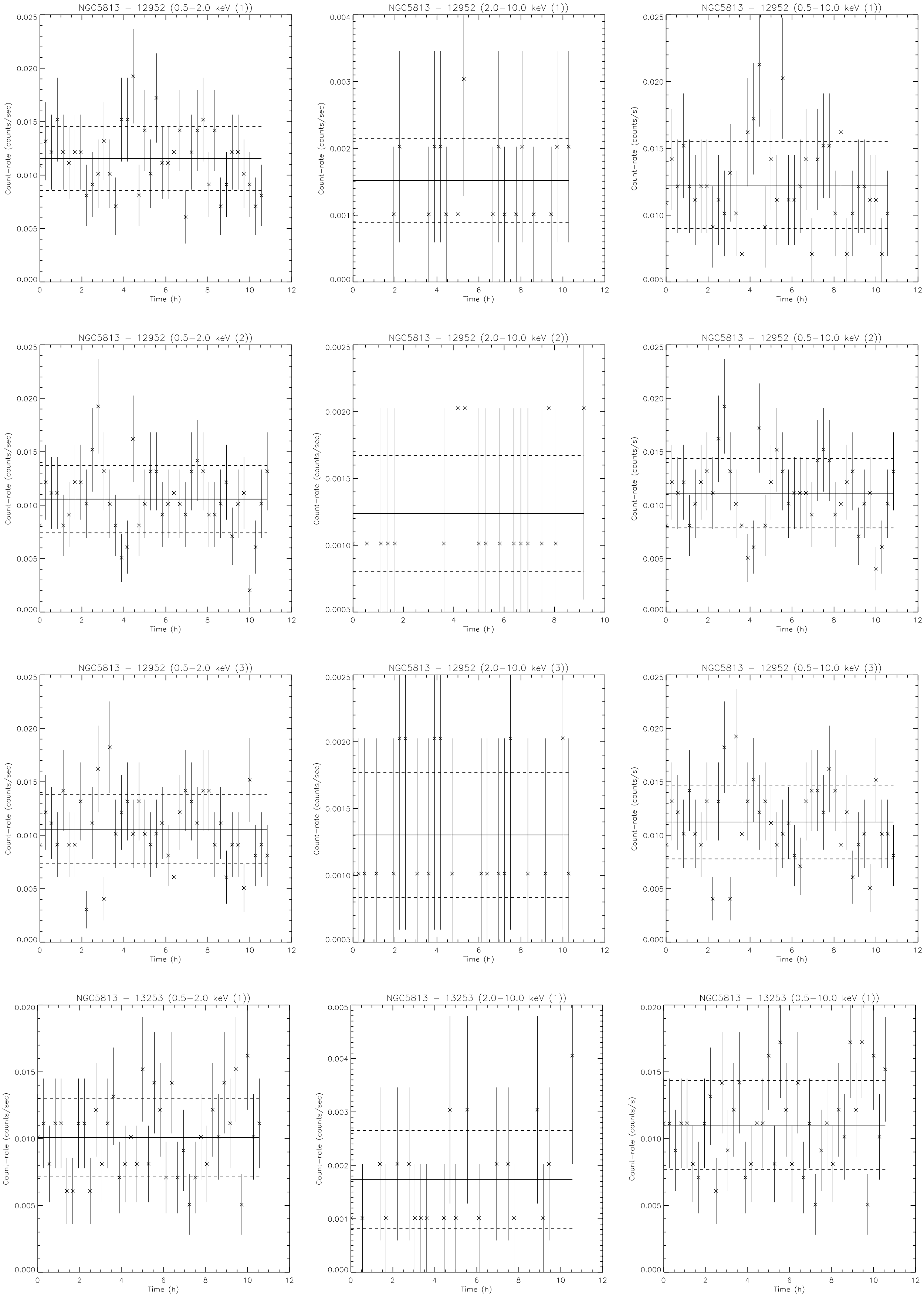

Fig. D.13. continued.

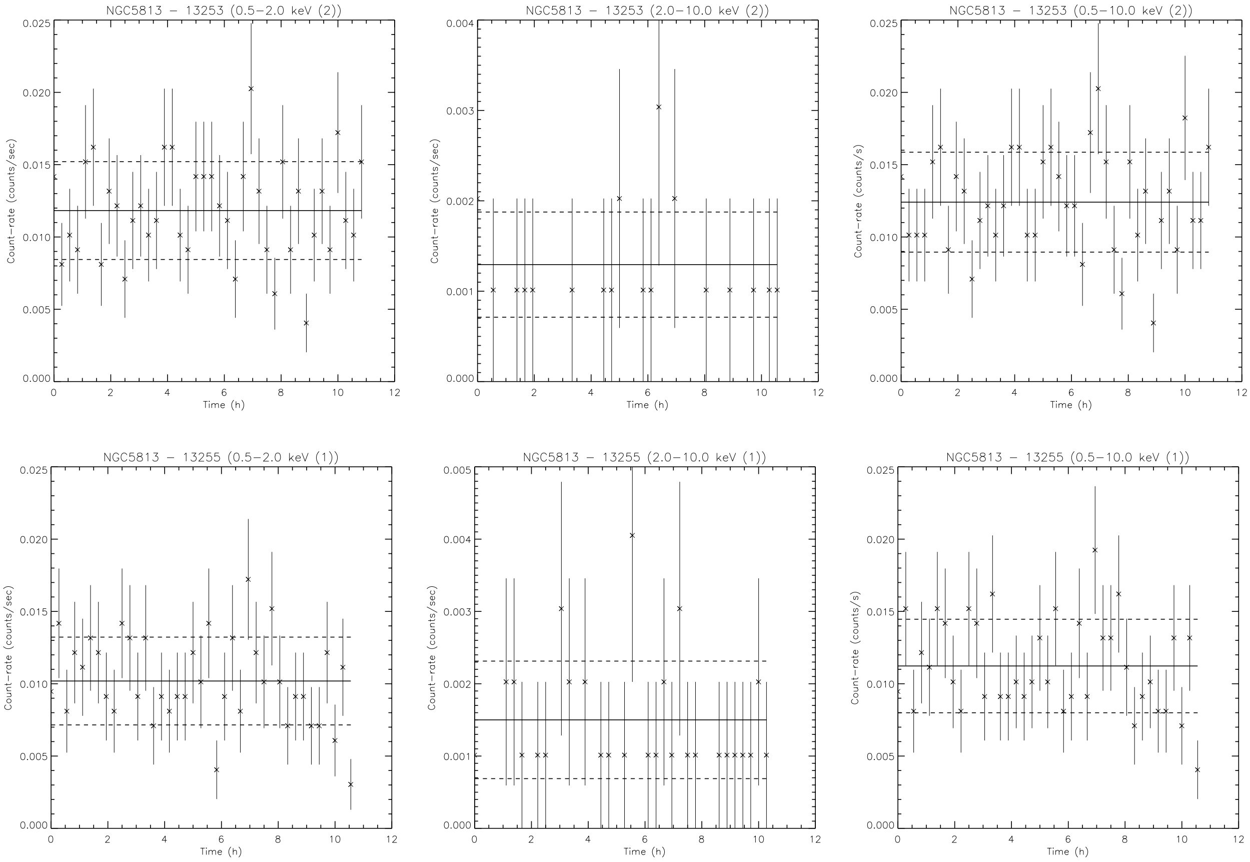

Fig. D.13. continued.

3

Seyfert 2

We find that LINERs are variable sources both at X-ray and UV frequencies, confirming the AGN nature of these sources. The next natural step was to compare the variability patterns observed in LINERs with those of more powerful AGN: the Seyfert family. We then applied the same methodology used for LINERs to a sample of Seyfert galaxies.

Although the same method was applied for the study, a few differences are to be noted in the analysis. On one hand, we needed to add two new models to fit the spectra of Seyferts, which appeared to be more complex than those of LINERs. On the other hand, we made a study of the *Compton*-thickness of the galaxies in the sample. Since the spectra of *Compton*-thin and *Compton*-thick sources might be dominated by different components, it is important to differentiate between them, also because the variability properties of these sources could be different. Note that the study of *Compton*-thickness in LINERs was made by González-Martín et al. (2009a).

This chapter is centered on the systematic study of the variability in a sample of Seyfert 2s selected at optical wavelengths. It is constituted by a paper that has recently been accepted for publication in Astronomy & Astrophysics (date: 02/05/2015).

Astronomy & Astrophysics manuscript no. Seyfert ©ESO 2015
June 10, 2015

X-ray spectral variability of Seyfert 2 galaxies

Hernández-García, L.[1]; Masegosa, J.[1]; González-Martín, O.[2]; Márquez, I.[1]

[1] Instituto de Astrofísica de Andalucía, CSIC, Glorieta de la Astronomía, s/n, 18008 Granada, Spain
e-mail: `lorena@iaa.es`
[2] Centro de radioastronomía y Astrofísica (CRyA-UNAM), 3-72 (Xangari), 8701, Morelia, Mexico

Received 18 March 2015 / Accepted 2 May 2015

ABSTRACT

Context. Variability across the electromagnetic spectrum is a property of active galactic nuclei (AGN) that can help constrain the physical properties of these galaxies. Nonetheless, the way in which the changes happen and whether they occur in the same way in every AGN are still open questions.
Aims. This is the third in a series of papers with the aim of studying the X-ray variability of different families of AGN. The main purpose of this work is to investigate the variability pattern(s) in a sample of optically selected Seyfert 2 galaxies.
Methods. We use the 26 Seyfert 2s in the Véron-Cetty and Véron catalog with data available from *Chandra* and/or *XMM*–Newton public archives at different epochs, with timescales ranging from a few hours to years. All the spectra of the same source were simultaneously fitted, and we let different parameters vary in the model. Whenever possible, short-term variations from the analysis of the light curves and/or long-term UV flux variations were studied. We divided the sample into Compton-thick and Compton-thin candidates to account for the degree of obscuration. When transitions between Compton-thick and thin were obtained for different observations of the same source, we classified it as a changing-look candidate.
Results. Short-term variability at X-rays was studied in ten cases, but variations are not found. From the 25 analyzed sources, 11 show long-term variations. Eight (out of 11) are Compton-thin, one (out of 12) is Compton-thick, and the two changing-look candidates are also variable. The main driver for the X-ray changes is related to the nuclear power (nine cases), while variations at soft energies or related to absorbers at hard X-rays are less common, and in many cases these variations are accompanied by variations in the nuclear continuum. At UV frequencies, only NGC 5194 (out of six sources) is variable, but the changes are not related to the nucleus. We report two changing-look candidates, MARK 273 and NGC 7319.
Conclusions. A constant reflection component located far away from the nucleus plus a variable nuclear continuum are able to explain most of our results. Within this scenario, the Compton-thick candidates are dominated by reflection, which suppresses their continuum, making them seem fainter, and they do not show variations (except MARK 3), while the Compton-thin and changing-look candidates do.

Key words. Galaxies: active – X-rays: galaxies – Ultraviolet: galaxies

1. Introduction

It is widely accepted that active galactic nuclei (AGN) are powered by accretion onto a supermassive black hole (SMBH, Rees 1984). Among them, the different classes of Seyfert galaxies (type 1/type 2) have led to postulating a unified model (UM) for all AGN (Antonucci 1993; Urry & Padovani 1995). Under this scheme, the SMBH is fed by the accretion disk that is surrounded by a dusty torus. This structure is responsible for obscuring the region where the broad lines are produced (known as broad line region, BLR) in type 2 objects, while the region where the narrow lines are produced (narrow line region, NLR) is still observed at optical frequencies. The difference between type 1 and 2 objects is therefore due to orientation effects.

In agreement with the UM, the type 1/type 2 classifications at X-ray frequencies are based on the absorption column density, N_H, because it is related with the obscuring material along our line of sight (Maiolino et al. 1998); therefore, we observe a Seyfert 1 if $N_H < 10^{22} cm^{-2}$, i.e., unobscured view of the inner parts of the AGN, and a type 2 if the column density is higher, i.e., obscured view through the torus (e.g., Risaliti et al. 2002). When $N_H > 1.5 \times 10^{24} cm^{-2}$, the absorbing column density is higher than the inverse of the Compton-scattering cross-section, and the sources are known as Compton-thick (Maiolino et al. 1998).

In fact, X-rays are a suitable tool for studying AGN because they are produced very close to the SMBH and because of the much smaller effect of obscuration at these frequencies than at UV, optical, or near-IR. Numerous studies have been made at X-ray frequencies to characterize the spectra of Seyfert galaxies (e.g., Turner et al. 1997; Risaliti 2002; Guainazzi et al. 2005b,a; Panessa et al. 2006; Cappi et al. 2006; Noguchi et al. 2009; LaMassa et al. 2011; Brightman & Nandra 2011a). The present work is focused on Seyfert 2 galaxies, which represent ~ 80% of all AGN (Maiolino & Rieke 1995). The works mentioned above have shown that the spectra of these objects are characterized by a primary power-law continuum with a photoelectric cut-off, a thermal component, a reflected component, and an iron emission line at 6.4 keV. It is important to appropiately account for the physical parameters of their spectra in order to constrain physical properties of the nuclei.

Given that variability across the electromagnetic spectrum is a property of all AGN, understanding these variations offers an exceptional opportunity to constrain the physical characteristics of AGN, which are known to show variations on timescales

Table 1: General properties of the sample galaxies.

Name (1)	RA (J2000) (2)	DEC (J2000) (3)	Dist.[1] (Mpc) (4)	N_{Gal} (10^{20} cm^{-2}) (5)	m_V (6)	Morph. type (7)	HBLR (8)	Ref. (9)
MARK 348	0 48 47.2	31 57 25	63.90	5.79	14.59	S0-a	✓	1
NGC 424	1 11 27.7	-38 5 1	47.60	1.52	14.12	S0-a	✓	1
MARK 573	1 43 57.8	2 20 59	71.30	2.52	14.07	S0-a	✓	1
NGC 788	2 1 6.5	- 6 48 56	56.10	2.11	12.76	S0-a	✓	1
ESO 417-G06	2 56 21.5	-32 11 6	65.60	2.06	14.30	S0-a	-	
MARK 1066	2 59 58.6	36 49 14	51.70	9.77	13.96	S0-a	✗	2
3C 98.0	3 58 54.5	10 26 2	124.90	10.20	15.41	E	-	
MARK 3	6 15 36.3	71 2 15	63.20	9.67	13.34	S0	✓	1
MARK 1210	8 4 5.9	5 6 50	53.60	3.45	13.70	-	✓	2
NGC 3079	10 1 58.5	55 40 50	19.10	0.89	12.18	SBcd	✗	2
IC 2560	10 16 19.3	-33 33 59	34.80	6.40	13.31	SBb	-	
NGC 3393	10 48 23.4	-25 9 44	48.70	6.03	13.95	SBa	-	
NGC 4507	12 35 36.5	-39 54 33	46.00	5.88	13.54	Sab	✓	1
NGC 4698	12 48 22.9	8 29 14	23.40	1.79	12.27	Sab	-	
NGC 5194	13 29 52.4	47 11 41	7.85	1.81	13.47	Sbc	✗	2
MARK 268	13 41 11.1	30 22 41	161.50	1.37	14.66	S0-a	-	
MARK 273	13 44 42.1	55 53 13	156.70	0.89	14.91	Sab	-	
Circinus	14 13 9.8	-65 20 17	4.21	74.40	12.1	Sb	✓	1
NGC 5643	14 32 40.7	-44 10 28	16.90	7.86	13.60	Sc	✗	2
MARK 477	14 40 38.1	53 30 15	156.70	1.05	15.03	E?	✓	2
IC 4518A	14 57 41.2	-43 7 56	65.20	8.21	15.	Sc	-	
ESO 138-G01	16 51 20.5	-59 14 11	36.00	13.10	13.63	E-S0	-	
NGC 6300	17 16 59.2	-62 49 5	14.43	7.76	13.08	SBb	-	
NGC 7172	22 2 1.9	-31 52 8	33.90	1.48	13.61	Sa	✗	2
NGC 7212	22 7 2.0	10 14 0	111.80	5.12	14.8	Sb	✓	1
NGC 7319	22 36 3.5	33 58 33	77.25	6.15	13.53	Sbc	-	

(Col. 1) Name, (Col. 2) right ascension, (Col. 3) declination, (Col. 4) distance, (Col. 5) galactic absorption, (Col. 6) aparent magnitude in the Johnson filter V from Véron-Cetty & Véron (2010), (Col. 7) galaxy morphological type from Hyperleda, (Col. 8) hidden broad polarized lines detected, and (Col. 9) its refs.: (1) Véron-Cetty & Véron (2010); and (2) Gu & Huang (2002).

[1] All distances are taken from the NED and correspond to the average redshift-independent distance estimates.

ranging from a few days to years (Peterson 1997). The first systematic variability study of Seyfert 2 galaxies was performed by Turner et al. (1997) using *ASCA* data. Their results show that short-term variability (from hours to days) is not common in Seyfert 2s, in contrast to what is observed in Seyfert 1 (e.g., Nandra et al. 1997). Because these galaxies are obscured by the torus, the lack of variations could come from these sources being reflection-dominated, as shown by some authors that studied Compton-thick sources (Awaki et al. 1991; LaMassa et al. 2011; Matt et al. 2013; Arévalo et al. 2014). However, a number of Seyfert 2s actually do show variations. The study of the variability has been approached in different ways from the analysis of the light curves to study of short-term variations (Awaki et al. 2006), through count-rate or flux variations (Isobe et al. 2005; Trippe et al. 2011), or comparisons of spectra of the same source at different epochs (LaMassa et al. 2011; Marinucci et al. 2013; Marchese et al. 2014). The observed variations may be related with absorbing material that crosses our line of sight (Risaliti et al. 2002, 2010) and/or can be intrinsic to the sources (Evans et al. 2005; Sobolewska & Papadakis 2009; Braito et al. 2013). A few Seyfert 2s also showed changes from being reflection-dominated to transmission-dominated objects, so were called changing-look objects (Guainazzi et al. 2002; Guainazzi 2002; Matt et al. 2003; Risaliti et al. 2010).

Although it is well established that a number of Seyfert 2s are variable, it is unknown whether the same kind of variation is common for all the nuclei or, more important, what drives those variations. It is the purpose of this paper to systematically study the variability pattern at X-rays in Seyfert 2 nuclei. This is the third in a series of papers aimed at studying the X-ray variability in different families of AGN. In Hernández-García et al. (2013, 2014), this study was made for LINERs, while the study of Seyfert 1 and the comparison between different families of AGN will be presented in forthcoming papers.

This paper is organized as follows. In Sec. 2 the sample and the data are presented, and data reduction is explained in Sect. 3. The methodology used for the analysis is described in Sect. 4, including individual and simultaneous spectral fittings, comparisons using data with different instruments, long-term X-ray and UV variations, short-term X-ray variations, and Compton-thickness analysis. The results derived from this work are explained in Sect. 5 and are discussed in Sect. 6. Finally, the main conclusions are summarized in Sect. 7.

2. Sample and data

We used the 13th edition of the Véron-Cetty and Véron catalogue (Véron-Cetty & Véron 2010), which contains quasars and active galactic nuclei. We selected galaxies located at redshift below 0.05 and classified as Seyfert 2 (S2) or objects with broad polarized Balmer lines detected (S1h). Indeed, S1h objects are those optically classified as Seyfert 2 that show broad lines in polarized light, which is the reason for their selection. This subsample includes 730 S2 and 27 S1h.

We searched for all the publicly available data for sources with observations in more than one epoch with *Chandra* and/or *XMM*–Newton using the HEASARC[2] browser up to May 2014. This first selection includes 73 nuclei. To be able to properly fit and compare spectra at different epochs, we selected sources with a minimum of 400 number counts in the 0.5-10.0 keV energy band, as required to use the χ^2-statistics. Thirty-four galaxies and nine observations did not met this criterium and were excluded from the sample. Objects affected by a pileup fraction higher than 10% were also removed, which made us exclude three objects and 14 observations.

For the remaining 36 nuclei we searched for their optical classifications in the literature with the aim of including only pure Seyfert 2 objects in the sample. Nine galaxies were excluded following this condition: NGC 4258, and NGC 4374 (S1.9 and L2 in Ho et al. 1997), 3C 317.0 and 3C 353.0 (LINERs in NED[3]), NGC 7314 (S1.9 in Liu & Bregman 2005), MCG-03.34.064 (S1.8 in Aguero et al. 1994), NGC 5252 (S1.9 in Osterbrock & Martel 1993), and NGC 835 and NGC 6251 (LINERs in González-Martín et al. 2009b). NGC 4472 was also excluded because its classification is based on the upper limits of line intensity ratios (Ho et al. 1997), and other classifications have been found in the literature (e.g., Boisson et al. 2004).

The final sample of Seyfert 2 galaxies contains 26 objects, 18 classified as S2 and 8 classified as S1h in Véron-Cetty & Véron (2010). However, we revisited the literature to search for hidden broad-line-region (HBLR, an usual name for S1h) and non-hidden broad-line-region (NHBLR) objects (e.g., Tran et al. 1992; Tran 1995; Moran et al. 2000; Lumsden et al. 2001; Gu & Huang 2002). We found two additional HBLR (MARK 1210 and MARK 477) and five NHBLR (MARK 1066, NGC 3079, NGC 5194, NGC 5643, and NGC 7172) sources. We did not find information about the remaining 11 nuclei, so we assumed they are most probably not observed in polarized light.

The final sample of Seyfert 2s in our work thus contains 26 objects (including 10 HBLR and five NHBLR). The target galaxies and their properties are presented in Table 1. Tables are in Appendix A, and notes on the individual nuclei in Appendix B and images at different wavelenths in Appendix C.1.

3. Data reduction

3.1. Chandra data

Chandra observations were obtained from the ACIS instrument (Garmire et al. 2003). Data reduction and analysis were carried out in a systematic, uniform way using CXC Chandra Interactive Analysis of Observations (CIAO[4]), version 4.3. Level 2 event data were extracted by using the task ACIS-PROCESS-EVENTS. Background flares were cleaned using the task LC_CLEAN.SL[5], which calculates a mean rate from which it deduces a minimum and maximum valid count rate and creates a file with the periods that are considered by the algorithm to be good.

Nuclear spectra were extracted from a circular region centered on the positions given by NED[6]. We chose circular radii, aiming to include all possible photons, while excluding other sources or background effects. The radii are in the range between 2-5″ (or 4-10 pixels, see Table A.1). The background was extracted from circular regions in the same chip that are free of sources and close to the object.

For the source and background spectral extractions, the DMEXTRACT task was used. The response matrix file (RMF) and ancillary reference file (ARF) were generated for each source region using the MKACISRMF and MKWARF tasks, respectively. Finally, the spectra were binned to have a minimum of 20 counts per spectral bin using the GRPPHA task (included in FTOOLS), to be able to use the χ^2 statistics.

3.2. XMM-Newton data

XMM-Newton observations were obtained with the EPIC pn camera (Strüder et al. 2001). The data were reduced in a systematic, uniform way using the Science Analysis Software (SAS [7]), version 11.0.0. First, good-timing periods were selected using a method that maximizes the signal-to-noise ratio of the net source spectrum by applying a different constant count rate threshold on the single events, E > 10 keV field-of-view background light curve. We extracted the spectra of the nuclei from circles of 15–30″ (or 300-600 px) radius centered on the positions given by NED, while the backgrounds were extracted from circular regions using an algorithm that automatically selects the best area - and closest to the source - that is free of sources. This selection was manually checked to ensure the best selection for the backgrounds.

The source and background regions were extracted with the EVSELECT task. The response matrix files (RMF) and the ancillary response files (ARF) were generated using the RMFGEN and ARFGEN tasks, respectively. To be able to use the χ^2 statistics, the spectra were binned to obtain at least 20 counts per spectral bin using the GRPPHA task.

3.3. Light curves

Light curves in three energy bands (0.5–2.0 keV, 2.0–10.0 keV, and 0.5–10 keV) for the source and background regions as defined above were extracted using the DMEXTRACT task (for *XMM*-Newton) and EVSELECT task (for *Chandra*) with a 1000 s bin. To be able to compare the variability amplitudes in different light curves of the same object, only those observations with a net exposure time longer than 30 ksec were taken into account. For longer observations, the light curves were divided into segments of 40 ksec, so in some cases more than one segment of the same light curve can be extracted. Intervals with "flare"-like events and/or prominent decreasing/increasing trends were manually rejected from the source light curves. We notice that after excluding these events, the exposure time of the light curve could be shorter, thus we recall that only observations with a net exposure time longer than 30 ksec were used for the analysis. The light curves are shown in Appendix D. We recall that these values are used only for visual inspection of the data and not as estimators of the variability (as in Hernández-García et al. 2014).

4. Methodology

The methodology is explained in Hernández-García et al. (2013) and Hernández-García et al. (2014). In contrast to the study of LINER nuclei, we added a new model (namely 2ME2PL), and a cold reflection component for the individual spectral fittings and

---

[2] http://heasarc.gsfc.nasa.gov/

[3] http://ned.ipac.caltech.edu/

[4] http://cxc.harvard.edu/ciao4.4/

[5] http://cxc.harvard.edu/ciao/ahelp/lc_clean. html

[6] http://ned.ipac.caltech.edu/

[7] http://xmm.esa.int/sas/

an analysis of the Compton-thickness for the Seyfert galaxies. Additionally, we changed the way we estimate the nuclear contribution in *XMM*–Newton spectra to perform the simultaneous fit using different instruments (see Sect. 4.2). A comparison with a sample of LINERs will be performed in a forthcoming paper. For clarity, we recall the procedure below.

4.1. Individual spectral analysis

An individual spectral analysis allowed us to select the best-fit model for each data set. We added a new model with respect to previous works (2ME2PL), including an additional thermal component to the more complex model, ME2PL, to explain the two ionized zones observed in some Seyfert galaxies (e.g., Netzer & Turner 1997; Bianchi et al. 2010). Then, we also added a cold reflection component (PEXRAV in XSPEC, Magdziarz & Zdziarski 1995) to the best-fit model to check whether this component improves the fit. We used XSPEC[8] version 12.7.0 to fit the data with six different models:

- PL: A single power law representing the continuum of a non-stellar source. The empirical model is $e^{N_{Gal}\sigma(E)} \cdot e^{N_H\sigma(E(1+z))}[N_H] \cdot Norm e^{-\Gamma}[\Gamma, Norm]$.
- ME: The emission is dominated by hot diffuse gas, i.e., a thermal plasma. A MEKAL (in XSPEC) model is used to fit the spectrum. The model is $e^{N_{Gal}\sigma(E)} \cdot e^{N_H\sigma(E(1+z))}[N_H] \cdot MEKAL[kT, Norm]$.
- 2PL: In this model the primary continuum is an absorbed power law representing the non stellar source, while the soft energies are due to a scattering component that is represented by another power law. Mathematically the model is explained as $e^{N_{Gal}\sigma(E)}(e^{N_{H1}\sigma(E(1+z))}[N_{H1}] \cdot Norm_1 e^{-\Gamma}[\Gamma, Norm_1] + e^{N_{H2}\sigma(E(1+z))}[N_{H2}] \cdot Norm_2 e^{-\Gamma}[\Gamma, Norm_2])$.
- MEPL: The primary continuum is represented by an absorbed power law, but at soft energies a thermal plasma dominates the spectrum. Empirically it can be described as $e^{N_{Gal}\sigma(E)}(e^{N_{H1}\sigma(E(1+z))}[N_{H1}] \cdot MEKAL[kT, Norm_1] + e^{N_{H2}\sigma(E(1+z))}[N_{H2}] \cdot Norm_2 e^{-\Gamma}[\Gamma, Norm_2])$.
- ME2PL: This is same model as MEPL, but an additional power law is required to explain the scattered component at soft energies, so mathematically it is $e^{N_{Gal}\sigma(E)}(e^{N_{H1}\sigma(E(1+z))}[N_{H1}] \cdot Norm_1 e^{-\Gamma}[\Gamma, Norm_1] + MEKAL[kT] + e^{N_{H2}\sigma(E(1+z))}[N_{H2}] \cdot Norm_2 e^{-\Gamma}[\Gamma, Norm_2])$.
- 2ME2PL: The hard X-ray energies are represented by an absorbed power law, while the spectrum shows a complex structure at soft energies, where a composite of two thermal plasmas plus a power law are required. In Seyfert galaxies, at least two ionized phases (a warm and a hot) are required to properly fit their spectra (Netzer & Turner 1997), which is confirmed by high resolution data (e.g., Bianchi et al. 2010; Marinucci et al. 2011). Ideally, the spectral fit should be made by using photoionization models to fit high quality data (e.g., RGS) and then use the obtained spectral parameters to fit lower quality data, as in Bianchi et al. (2010) or González-Martín et al. (2010). We tried to use photoionized models using Cloudy to fit the soft emission. We found that, due to the low resolution of our data, these models fit the data similarly to MEKAL models. Therefore, for simplicity, in this work we represent the photoionized gas by two thermal plasmas plus Gaussian lines when required (see below). The power law at soft energies represents the scattering component. Although this is probably a simple model for fitting the complexity of the spectra, the data analyzed in this work do not have enough spectral resolution to properly fit the data with more realistic models, and therefore this model is enough for our purposes. It is represented as $e^{N_{Gal}\sigma(E)}(e^{N_{H1}\sigma(E(1+z))}[N_{H1}] \cdot Norm_1 e^{-\Gamma}[\Gamma, Norm_1] + MEKAL[kT_1] + MEKAL[kT_2] + e^{N_{H2}\sigma(E(1+z))}[N_{H2}] \cdot Norm_2 e^{-\Gamma}[\Gamma, Norm_2])$.
- (Best-fit model) + PEXRAV: From the six models described above, we selected the one that provided the best fit to the data and added a reflection component (we have chosen PEXRAV within XSPEC) to account for a plausible contribution of this component in highly obscured Seyfert 2s. The parameters of the MEKAL component(s) were frozen to the best-fit values. In this model the absorbed power law at hard energies represents the transmitted component, while the PEXRAV is indicative of the reflected fraction from the primary continuum alone, by setting the reflection scaling factor to 1. The spectral index was set to be that of the power law(s), the exponential cutoff was fixed to 200 keV, and the inclination angle to 45°. These parameters are based on typical values obtained from X-ray analyses at harder energies (e.g., Guainazzi et al. 2005b; Matt et al. 2004; Akylas & Georgantopoulos 2009; Noguchi et al. 2009). The free parameters in this model are therefore $N_{H1}, N_{H2}, \Gamma, Norm_1, Norm_2$, and $Norm_{pex}$. It is worth noting that we tried similar models to fit the data, such as exchanging the hard PL by PEXRAV or by an absorbed PEXRAV, and obtained very similar results, but the model explained above allowed the use of the F test to check for eventual improvements in the fits.

In the equations above, $\sigma(E)$ is the photo-electric cross-section, z is the redshift, and $Norm_i$ are the normalizations of the power law, the thermal component or the reflected component (i.e., $Norm_1$, $Norm_2$, and $Norm_{pex}$). For each model, the parameters that vary are written in brackets. The Galactic absoption, N_{Gal}, is included in each model and fixed to the predicted value (Col. 5 in Table 1) using the tool NH within FTOOLS (Dickey & Lockman 1990; Kalberla et al. 2005). Even if not included in the mathematical form above, all the models include three narrow Gaussian lines to take the iron lines at 6.4 keV (FeKα), 6.7 keV (FeXXV), and 6.95 keV (FeXXVI) into account. In a few cases, additional Gaussian lines were required at soft energies from a visual inspection, including Ne X at 1.2 keV, Mg XI at 1.36 keV, Si XIII at 1.85 keV, and S XIV at 2.4 keV.

The $\chi^2/d.o.f$ and F test were used to select the simplest model that represents the data best.

4.2. Simultaneous spectral analysis

Once the individual best-fit model is selected for each observation, and if the models are different for the individual observations, then the most complex model that fits each object was chosen. This model was used to simultaneously fit spectra obtained at different dates of the same nuclei. Initially, the values of the spectral parameters were set to those obtained for the spectrum with the largest number counts for each galaxy. To determine whether spectral variations are observed in the data, this simultaneous fit was made in three steps:

0. SMF0 (Simultaneous fit 0): The same model was used with all parameters linked to the same value to fit every spectra of the same object, i.e., the non-variable case.

---

[8] http://heasarc.nasa.gov/xanadu/xspec/

1. SMF1: Using SMF0 as the baseline for this step, we let the parameters N_{H1}, N_{H2}, Γ, $Norm_1$, $Norm_2$, $Norm_{pex}$, kT_1, and kT_2 vary individually. The best fit was selected for the χ_r^2 closest to unity that improved SMF0 (using the F test).
2. SMF2: Using SMF1 as the baseline for this step (when SMF1 did not fit the data well), we let two parameters vary, the one that varied in SMF1 along with any of the other parameters of the fit. The χ_r^2 and F test were again used to confirm an improvement in the fit.

When data from the same instrument were available at different epochs, this method was applied separately for *Chandra* and/or *XMM*–Newton. However, in some cases only one observation was available per instrument. Instead of directly comparing the spectra from different instruments, we tried to decontaminate the extranuclear emission in *XMM*–Newton data, to make sure that the emission included in the larger aperture did not produce the observed variability. This additional analysis was performed by extracting an annular region from *Chandra* data, fitting the models explained above to its spectrum, and selecting the one that best fits the annular region. This model was later incorporated into the *XMM*–Newton spectrum (with its parameters frozen), so the parameters of the nuclear emission can be estimated. We determined the contribution by the annular region to the *Chandra* data from the number counts (i.e., model-independent) in the 0.5-10.0 keV energy band, and this percentage was used to estimate the number counts in the nuclear region of *XMM*–Newton data. Following the same criteria as we used to select the data (see Sect. 2), data from different instruments were compared when the number counts in the nuclear *XMM*–Newton spectrum was more than 400 counts. We note that this procedure differs from the one used in Hernández-García et al. (2013, 2014). When multiple observations of the same object and instrument were available, we compared the data with the closest dates (marked with *c* in Table A.1).

4.3. Flux variability

The luminosities in the soft and hard X-ray energy bands were computed using XSPEC for both the individual and the simultaneous fits. For their calculation, we took the distances from NED, corresponding to the average redshift-independent distance estimate for each object, when available, or to the redshift-estimated distance otherwise; distances are listed in Table 1.

When data from the optical monitor (OM) onboard *XMM*–Newton were available, UV luminosities (simultaneously to X-ray data) were estimated in the available filters. We recall that UVW2 is centered at 1894Å (1805-2454) Å, UVM2 at 2205Å (1970-2675) Å, and UVW1 at 2675Å (2410-3565) Å. We used the OM observation FITS source lists (OBSMLI)[9] to obtain the photometry. When OM data were not available, we searched for UV information in the literature. We note that in this case, the X-ray and UV data might not be simultaneous (see Appendix B).

We assumed an object to be variable when the square root of the squared errors was at least three times smaller than the difference between the luminosities (see Hernández-García et al. 2014, for details).

4.4. Short-term variability

Firstly, we assumed a constant count rate for segments of 30-40 ksec of the observation in each energy band and calculated χ^2/d.o.f as a proxy to the variations. We considered the source as a candidate for variability if the count rate differed from the average by more than 3σ (or 99.7% probability).

Secondly, and to be able to compare the variability amplitude of the light curves between observations, we calculated the normalized excess variance, $\sigma^2_{\rm NXS}$, for each light curve segment with 30-40 ksec following prescriptions in Vaughan et al. (2003) (see also González-Martín et al. 2011b; Hernández-García et al. 2014). We recall that $\sigma^2_{\rm NXS}$ is related to the area below the power spectral density (PSD) shape.

When $\sigma^2_{\rm NXS}$ was negative or compatible with zero within the errors, we estimated the 90% upper limits using Table 1 in Vaughan et al. (2003). We assumed a PSD slope of -1, the upper limit from Vaughan et al. (2003), and we added the value of 1.282err($\sigma^2_{\rm NXS}$) to the limit to account for Poisson noise. For a number of segments, N, obtained from an individual light curve, an upper limit for the normalized excess variance was calculated. When N segments were obtained for the same light curve and at least one was consistent with being variable, we calculated the normalized weighted mean and its error as the weighted variance.

We considered short-term variations for $\sigma^2_{\rm NXS}$ detections above 3σ of the confidence level.

4.5. Compton *thickness*

Highly obscured AGN are observed through the dusty torus, in some cases with column densities higher than $1.5\times10^{24}cm^{-2}$ (the so-called Compton-thick). In these cases the primary emission can be reflected at energies ~ 10 keV. Since the primary continuum cannot be directly observed, some indicators using X-rays and [O III] data have been used to select candidates (Ghisellini et al. 1994; Bassani et al. 1999; Panessa & Bassani 2002; Cappi et al. 2006).

To properly account for the slope of the power law, Γ, and the equivalent width of the iron line, EW(FeKα), an additional analysis was performed. We fit the 3-10 keV energy band of each spectrum individually with a PL model (see Sect. 4.1) to obtain the values of Γ and EW(FeKα). Compton-thick candidates can be selected by using three different criteria:

- $\underline{\Gamma < 1}$: since the transmitted component is suppressed below 10 keV, a flattening of the observed spectrum is expected (Cappi et al. 2006; González-Martín et al. 2009a).
- $\underline{\rm EW(FeK\alpha) > 500\ eV}$: if the nuclear emission is obscured by a Compton-thick column density, the primary continuum underneath the FeKα line is strongly suppressed, and the equivalent width of the line enhanced to ~keV (Krolik et al. 1994; Ghisellini et al. 1994).
- $\underline{F(2-10keV)/F_{[OIII]} < 1}$: since the primary continuum is suppressed, the X-ray luminosity is underestimated, so when comparing with an isotropic indicator of the AGN power (as is the case for the [O III] emission line), the ratio between the two values decreases (Bassani et al. 1999; Guainazzi et al. 2005b; Cappi et al. 2006; González-Martín et al. 2009a). Thus, we have used this ratio to select Compton-thick candidates, where the extinction-corrected [O III] fluxes were obtained from the literature (and corrected when needed following Bassani et al. 1999), and the hard X-ray luminosities, $L(2-10keV)$, from the individual fits were used (see Table A.3) for the calculation.

---

[9] ftp://xmm2.esac.esa.int/pub/odf/data/docs/XMM-SOC-GEN-ICD-0024.pdf

We considered that a source is a Compton-thick candidate when at least two of the three criteria above were met. Otherwise, the source is considered to be a Compton-thin candidate. When different observations of the same source result in different classifications, the object was considered to be a changing-look candidate.

The spectral fits reported in Sects. 4.1 and 4.2 are performed with the spectral indices of the soft, Γ_{soft}, and the hard, Γ_{hard}, power laws tied to the same value. When a source is Compton-thick, its spectrum is characterized by a flat power law at hard energies (see above), whereas the slope of the power law is dominated by the scattered component if we tied $\Gamma_{soft} = \Gamma_{hard}$, giving an unrealistic steep power-law index. Thus, the simultaneous analysis was repeated by leaving Γ_{soft} and Γ_{hard} free for the objects classified as Compton-thick candidates. We first made the SMF1 with Γ_{hard} vary and found that this component does not vary in any case. The values of Γ_{hard} obtained for the Compton-thick candidates following this procedure are reported in Table A.7 (Col. 9). We checked that the rest of the parameters in the model are consistent with those reported in Table A.2 within the uncertainties. The same procedure was applied to Compton-thin candidates, and compatible values of Γ_{soft} and Γ_{hard} were found. It is worth pointing out that it is not within the scope of this work to obtain the best spectral parameters for each source, but to obtain their variability patterns. Thus, we have kept the same general analysis for all the objects (i.e., with $\Gamma_{soft} = \Gamma_{hard}$, although we notice that this is not the case for Compton-thick candidates), but this procedure does not affect the main results presented in this paper.

5. Results

In this section we present the results for the variability analysis of the Seyfert 2 galaxies individually (see Sect. 5.1), as well as the general results, including the characterization of the spectra of Seyfert 2s (Sect. 5.2), the long-term variability (Sect. 5.3), first for the whole sample in general and later divided into subsamples, X-ray short-term variations (Sect. 5.4), and flux variations at UV frequencies (Sect. 5.5). The main results of the analysis are summarized in Table 2. Individual notes on each galaxy and comparisons with previous works can be found in Appendix B.

5.1. Individual objects

For details on the data and results, we refer the reader to the following tables and figures: the observations used in the analysis (Table A.1); UV luminosities with simultaneous OM data (Col. 9 of Table A.1 and Fig. 1); individual and simultaneous best fit, and the parameters varying in the model (Table A.2 and Fig. 2); X-ray flux variations (Table A.3 and Fig. 3); comparison of *Chandra* and *XMM*–Newton data using the annular region (Table A.4); the simultaneous fit between these observations (Table A.5 and Figs. A.1 and A.2); short-term variability from the analysis of the light curves (Table A.6 and Appendix D); and the *Compton*-thickness analysis, where an object was classified on the basis that at least two of the three criteria presented in Sect 4.5 were met (Table A.7). We notice that the addition of a cold reflection component is not statistically required by the data, so we do not mention the analysis except in one case (3C 98.0) where the simultaneous fit was performed.

- MARK 348: SMF1 with variations in $Norm_2$ (69%) represents the data best. These variations were found within a nine-year period, which implies intrinsic flux variations of 69% (68%) in the soft (hard) energy band. We classify it as a Compton-thin candidate.
- NGC 424: Two *XMM*–Newton data sets are available. SMF0 results in χ^2_r=2.20, and SMF1 does not improve the fit; this is most probably because the spectra from 2008 shows a more complex structure compared to 2000, preventing a proper simultaneous spectral fitting. Thus, we do not perform the simultaneous spectral fit between the two *XMM*–Newton data sets. The contribution from the annular region is negligible, thus the spectral analysis can be jointly performed using *XMM*–Newton and *Chandra* data together. SMF0 is the best representation of the data. Short-term variations from the *XMM*–Newton light curve are not found. We classify it as a Compton-thick candidate.
- MARK 573: The *Chandra* data do not show variations (SMF0 was used) within a four-year period. When compared with *XMM*–Newton data, the annular region contributes with 24% to the *Chandra* data. Again, SMF0 results in the best representation of the data. Three additional Gaussian lines are needed to fit the data at 1.20 keV (Ne X), 1.36 keV (Mg XI), and 2.4 keV (S XIV). Two *Chandra* light curves are analyzed, and variations are not detected. We classify it as a Compton-thick candidate.
- NGC 788: One observation per instrument is available. The emission from the annular region is negligible so we jointly fit *Chandra* and *XMM*–Newton data. SMF0 was used, thus no variations are found in a two years period. We classify it as a Compton-thin candidate.
- ESO 417-G06: SMF1 with N_{H2} (21%) because the parameter varying represents the data best. These variations were obtained within about a one-month period, corresponding to no flux intrinsic variations. We classify it as a Compton-thin candidate.
- MARK 1066: Only one observation per instrument is available. The annular region contributes with 8% to *Chandra* data. The simultaneous fit without allowing any parameter to vary (i.e., SMF0) results in a good fit of the data. We classify it as a Compton-thick candidate.
- 3C 98.0: This is the only object where the unabsorbed PEXRAV component improves the fit. The values of the spectral parameters in this fit are $Norm_1 = 70.22^{81.21}_{58.82} \times 10^{-4} Photons\ keV^{-1} cm^{-2} s^{-1}$, $N_{H2} = 9.68^{11.31}_{8.20} \times 10^{22} cm^{-2}$, $\Gamma = 1.30^{1.54}_{1.07}$, $Norm_{pex} = 0.10^{0.15}_{0.07} \times 10^{-4} Photons\ keV^{-1} cm^{-2} s^{-1}$, $Norm_2 = 5.51^{8.72}_{3.55} \times 10^{-4} Photons\ keV^{-1} cm^{-2} s^{-1}$ (*XMM*–Newton obsID. 0064600101), $3.03^{4.86}_{1.93} \times 10^{-4} Photons\ keV^{-1} cm^{-2} s^{-1}$ (*XMM*–Newton obsID. 0064600301), and $\chi/d.o.f = 109.30/126$. Thus, the best representation of the data requires $Norm_2$ to vary between the two *XMM*–Newton data sets, while the reflection component remains constant. This spectral fit with $Norm_2$ varying agrees with the one using the MEPL model (Table A.2). The percentages of the variations are compatible between the two SMF1 and also the luminosities. For simplicity, we report the results of the MEPL model in the following. The simultaneous fit of the *XMM*–Newton data needs SMF1 with $Norm_2$ (43%) varing over a period of about half a year. This implies an intrinsic flux variation of 5% (42%) at soft (hard) energies. The annular region contributes with 8% to the *Chandra*

Table 2: Results of the variability analysis.

Name	Type	log (L_{soft})	log (L_{hard})	log (M_{BH})	log (R_{Edd})	Variability			ΔT$_{max}$
		(0.5-2 keV)	(2-10 keV)			SMF0	SMF1	SMF2	(Years)
(1)	(2)	(3)	(4)	(5)	(6)	(7)	(8)	(9)	(10)
MARK 348 (X)	HBLR	42.76 $69^{+}_{-}5\%$	43.15 $68^{+}_{-}3\%$	7.58	-1.02	ME2PL	$Norm_2$ $69^{+17}_{-14}\%$	-	10
NGC 424 (C,X)*	HBLR	41.74 0%	41.85 0%	7.78	-2.53	2ME2PL	-	-	0.16
MARK 573 (C)*	HBLR	41.65 0%	41.54 0%	7.37	-2.42	2ME2PL (+3gauss)	-	-	4
(X,C)		41.73 0%	41.41 0%			2ME2PL	-	-	2
NGC 788 (X,C)	HBLR	42.11 0%	42.60 0%	7.43	-1.43	2ME2PL	-	-	0.33
ESO 417-G06 (X)	-	42.46 0%	42.50 0%	7.44	-1.53	MEPL	N_{H2} $21^{+5}_{-5}\%$	-	0.08
MARK 1066 (X,C)*	NHBLR	41.40 0%	41.43 0%	7.23	-2.38	ME2PL	-	-	2
3C 98.0 (X)	-	43.13 $5^{+}_{-}4\%$	42.80 $42^{+}_{-}7\%$	7.75	-1.73	MEPL	$Norm_2$ $43^{+41}_{-26}\%$	-	0.41
(X,C)		42.40 0%	42.60 0%			MEPL	-	-	5
MARK 3 (X)*	HBLR	42.24 $29^{+}_{-}7\%$	42.74 $32^{+}_{-}4\%$	8.74	-2.58	2ME2PL	$Norm_2$ $37^{+16}_{-14}\%$	-	1
MARK 1210 (C)	HBLR	42.31 $7^{+}_{-}5\%$	42.79 $7^{+}_{-}1\%$	7.70	-1.50	2ME2PL	$Norm_2$ $11^{+10}_{-6}\%$	N_{H2} $20^{+5}_{-4}\%$	4
IC 2560 (X,C)*	-	40.57 0%	41.03 0%	6.46	-2.02	2ME2PL (+1gauss)	-	-	0.16
NGC 3393 (C)*	-	41.64 0%	41.29 0%	8.10	-3.41	2ME2PL	-	-	7
(X,C)		41.44 0%	41.26 0%			2ME2PL	-	-	0.66
NGC 4507 (X)	HBLR	42.04 $96^{+}_{-}4\%$	42.67 $81^{+}_{-}10\%$	8.26	-2.28	2ME2PL (+2gauss)	$Norm_2$ $51^{+26}_{-20}\%$	N_{H2} $4^{+12}_{-9}\%$	9
(X,C)		41.96 $45^{+}_{-}3\%$	42.85 $38^{+}_{-}3\%$				$Norm_2$ $53^{+36}_{-27}\%$	-	0.41
NGC 4698 (X)	-	40.14 0%	40.08 0%	7.53	-4.04	2PL	-	-	9
NGC 5194 (C)*	NHBLR	39.53 0%	39.51 0%	6.73	-3.82	ME2PL	-	-	11
(X,C)		39.94 0%	39.39 0%			2ME2PL	-	-	0.6
MARK 268 (X)	-	41.34 0%	42.92 0%	7.95	-1.62	ME2PL	-	-	0.01
MARK 273 (X,C)$^{CL?}$	-	41.34 $24^{+}_{-}2\%$	42.29 $32^{+}_{-}6\%$	7.74	-2.05	2ME2PL	N_{H2} $51^{+15}_{-14}\%$	-	2
Circinus (C)*	HBLR	39.80 0%	40.60 0%	7.71	-3.71	2ME2PL (+4gauss)	-	-	9
NGC 5643 (X)*	NHBLR	40.44 0%	40.87 0%	6.30	-2.02	2ME2PL	-	-	6
MARK 477 (X)*	HBLR	42.60 0%	43.11 0%	7.20	-0.68	2ME2PL	-	-	0.01
IC 4518A (X)	-	42.06 $40^{+}_{-}2\%$	42.45 $41^{+}_{-}6\%$	7.48	-1.63	2ME2PL	$Norm_2$ $42^{+45}_{-30}\%$	-	0.02
ESO 138-G01 (X)*	-	42.23 0%	42.11 0%	5.50	0.01	ME2PL	-	-	6
NGC 6300 (C)	-	41.32 0%	41.95 0%	7.18	-2.68	2PL	-	-	0.01
(X,C)		41.06 $98^{+}_{-}50\%$	41.68 $98^{+}_{-}16\%$			2PL	$Norm_2$ $98^{+12}_{-77}\%$	$Norm_1$ $93^{+25}_{-25}\%$	8

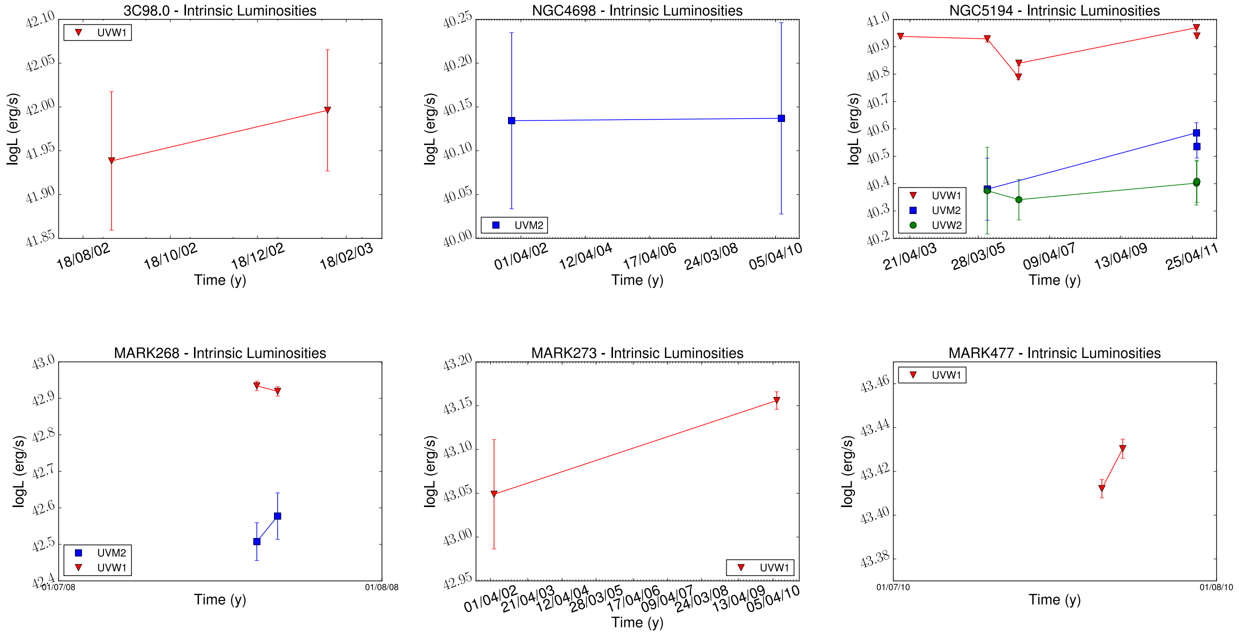

Fig. 1: UV luminosities obtained from the data with the OM camera onboard *XMM*–Newton, when available. Different filters have been used; UVW1 (red triangles), UVW2 (green circles), and UVM2 (blue squares).

Table 2: Cont.

Name	Type	log (L_{soft}) (0.5-2 keV)	log (L_{hard}) (2-10 keV)	log (M_{BH})	log (R_{Edd})	Variability			ΔT$_{max}$ (Years)
						SMF0	SMF1	SMF2	
(1)	(2)	(3)	(4)	(5)	(6)	(7)	(8)	(9)	(10)
NGC 7172 (X)	NHBLR	42.50	42.82	8.20	-1.98	ME2PL	*Norm*$_2$	-	5
		51$^{+}_{-}$2%	51$^{+}_{-}$1%				51$^{+5}_{-5}$%		
NGC 7212 (X,C)*	HBLR	41.81	42.60	7.54	-1.55	2ME2PL	-	-	1
		0%	0%						
NGC 7319 (C)$^{CL?}$	-	42.99	42.98	7.43	-1.26	ME2PL	*Norm*$_2$	N_{H1}	7
		38$^{+}_{-}$8%	38$^{+}_{-}$5%				39$^{+53}_{-22}$%	100$^{+27}_{-23}$%	
(X,C)		42.58	42.84			ME2PL	*Norm*$_2$	-	6
		71$^{+}_{-}$8%	69$^{+}_{-}$7%				72$^{+64}_{-46}$%		

Notes. (Col. 1) Name (the asterisks represent Compton–thick or changing look candidates), and the instrument (C: *Chandra* and/or X: *XMM*–Newton) in parenthesis; (Col. 2) (non) hidden broad line region objects only in the cases where there are available observations; (Cols. 3 and 4) logarithm of the soft (0.5–2 keV) and hard (2–10 keV) X-ray luminosities, where the mean was calculated for variable objects, and percentages in flux variations; (Col. 5) black-hole mass on logarithmical scale, determined using the correlation between stellar velocity dispersion (from HyperLeda) and black-hole mass (Tremaine et al. 2002), or obtained from the literature otherwise (MARK 1210 and NGC 4507 from Nicastro et al. (2003); IC 4518A from Alonso-Herrero et al. (2013); NGC 6300 and NGC 5643 from Davis et al. (2014); IC 2560 from Baloković et al. (2014); MARK 268 from Khorunzhev et al. (2012); and MARK 477 from Singh et al. (2011)); (Col. 6) Eddington ratio, $L_{bol}/!L_{Edd}$, calculated from Eracleous et al. (2010) using $L_{bol} = 33L_{2-10keV}$; (Col. 7) best fit for SMF0; (Col. 8) parameter varying in SMF1, with the percentage of variation; (Col. 9) parameter varying in SMF2, with the percentage of variation; (Col. 10) and the sampling timescale, corresponding to the difference between the first and the last observation. The percentages correspond to this ΔT$_{max}$.

data, and SMF0 was used when comparing *Chandra* and *XMM*–Newton data, i.e., variations were not found within a five-year period. Short-term variations are not detected from the *Chandra* data. UV data from the UVW1 filter did not show any variability. We classify it as a Compton-thin candidate.

- MARK 3: The *XMM*–Newton data need SMF1 with *Norm*$_2$ (37%) as the parameter responsible for the variations. This corresponds to flux variations of 29% (32%) in the soft (hard) energy band in a one-year period. We classify it as a Compton-thick candidate.

- MARK 1210: X-rays observations with *Chandra* covering a period of about four years are simultaneously fitted, resulting in SMF2 with N_{H2} (20%) and *Norm*$_2$ (43%) as the parameters varying in this model. This corresponds to intrinsic flux

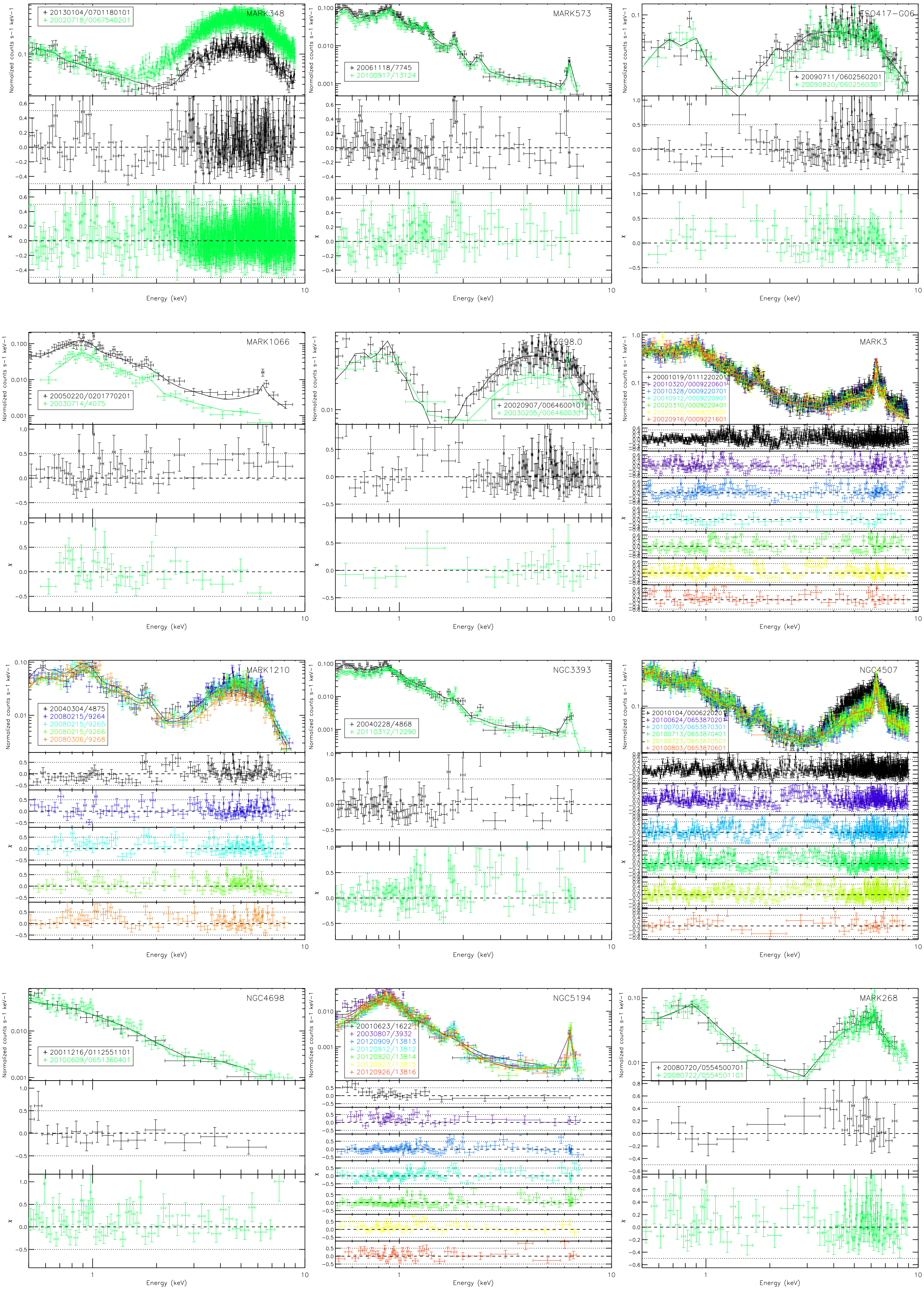

Fig. 2: For each object, (top): simultaneous fit of X-ray spectra; (from second row on): residuals in units of σ. The legends contain the date (in the format yyyymmdd) and the obsID. Details are given in Table 1.

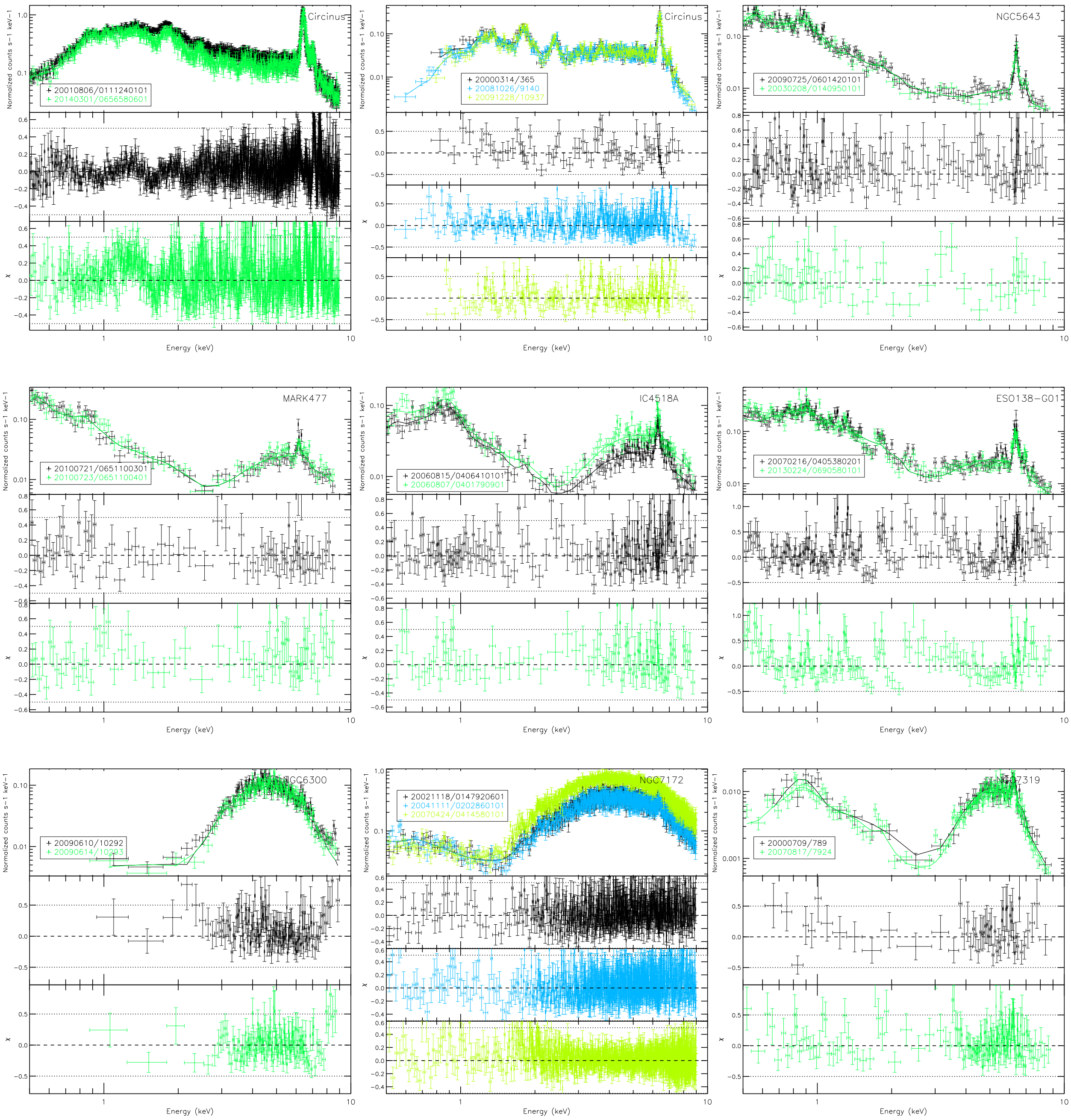

Fig. 2: Cont.

variations of 40% (41%) at soft (hard) energies. We classify the object as a Compton-thin candidate.

- NGC 3079: One observation per instrument is available. The annular region contributes with 79% to *Chandra* data. The estimated number counts in the nuclear component of the *XMM*–Newton spectrum is 235 counts, so we do not perform a simultaneous fitting. This object will not be used to discuss long-term variations. We classify it as a Compton-thin candidate. We refer the reader to Appendix B for the discussion of this source.

- IC 2560: Only one observation per instrument is available. When comparing the data, the annular region contributes with 11% to the *Chandra* data. No variations were observed within two months, i.e., SMF0 was used for the simultaneous fit. An additional Gaussian line was needed in the fit at 1.85 keV (Si XIII). A *XMM*–Newton and a *Chandra* light curve were analyzed. We notice that the *XMM*–Newton light curve showed a positive value of σ^2_{NXS} at 2.5σ of confidence level, close to our limit (see Sect. 4.4). We classify it as a Compton-thick candidate.

- NGC 3393: *Chandra* data are fitted with SMF0, resulting in no variations in a seven years period. When comparing with *XMM*–Newton data, the annular region contributes with 17%, and SMF0 is needed to fit the data within a one-year period. Short-term variations are not found from one *Chandra* light curve. We classify it as a Compton-thick candidate.

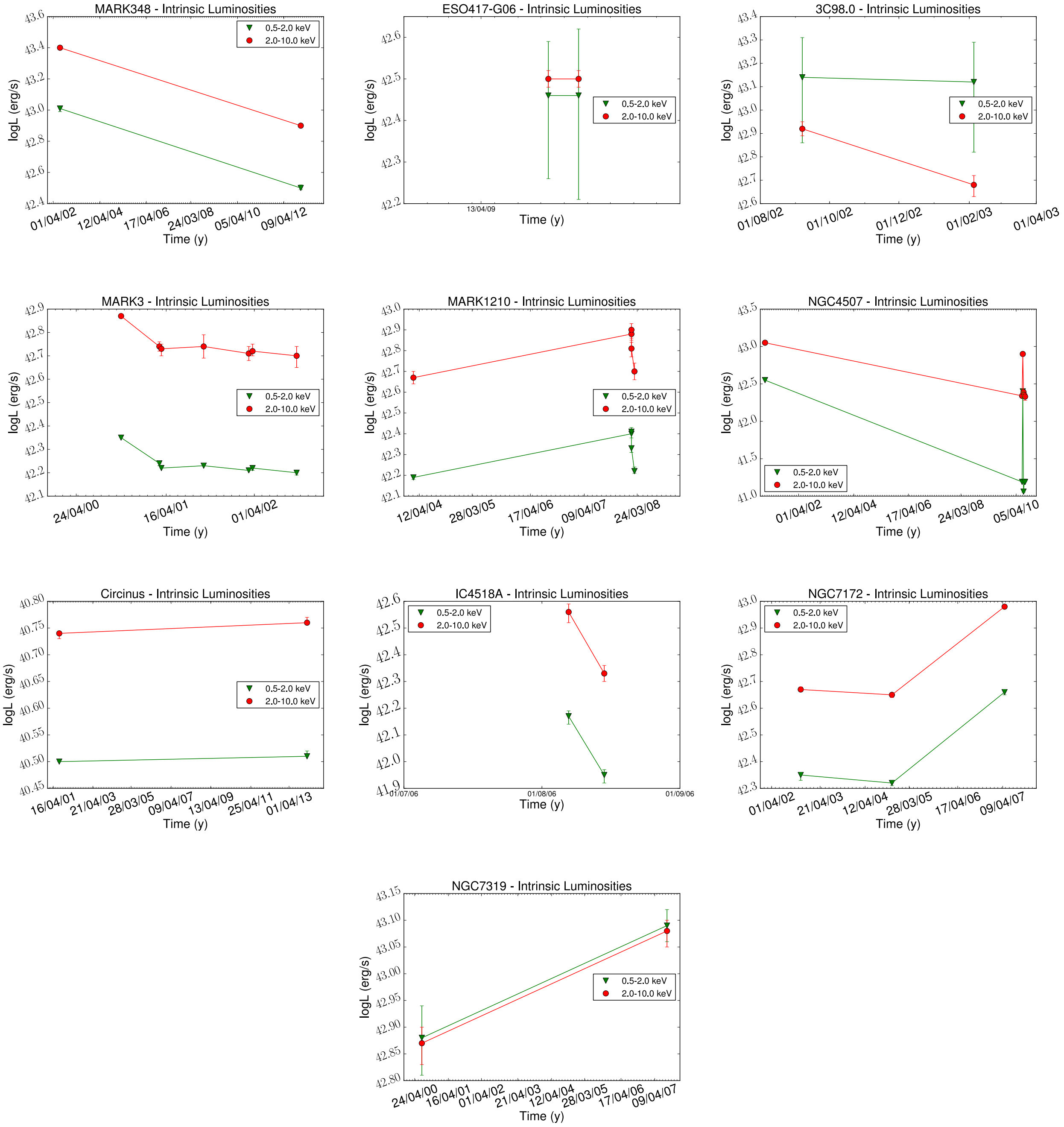

Fig. 3: X-ray intrinsic luminosities calculated for the soft (0.5–2.0 keV, green triangles) and hard (2.0–10.0 keV, red circles) energies in the simultaneous fits, only for the variable objects.

- NGC 4507: SMF2 was used to fit the *XMM*–Newton data, with $Norm_2$ (36%) and N_{H2} (21%) varying in a nine-year period. This corresponds to a flux variation of 96% (81%) in the soft (hard) energy band. Two additional Gaussian lines at 1.36 (Mg XI) and 1.85 (Si XIII) keV are needed to fit the data. The annular region contributes with 13% to the *Chandra* data. When comparing *Chandra* and *XMM*–Newton data, the best fit resulted in SMF1 with $Norm_2$ (53%) varying over nine years. Short-term variations are found from neither *Chandra* nor *XMM*–Newton light curves. We classify it as a Compton-thin candidate.
- NGC 4698: SMF0 was used in the simultaneous fit, resulting in no variations in a nine-year period. UV data in the UVM2 filter is available, where the object does not show changes. We classify it as a Compton-thin candidate.
- NGC 5194: The simultaneous fit results in no variations (i.e., SMF0 was used) within an 11-year period. The annular region contributes with 91% to the *Chandra* data. When comparing data from *XMM*–Newton and *Chandra*, SMF0 results in the best representation of the data. Six *Chandra* light curves were analyzed in three energy bands, but variations are not reported. UV data are available in three filters, one showing variations (UVW1) and the remaining two not

(UVW2, UVM2). We classify it as a Compton-thick candidate.

- MARK 268: The *XMM*–Newton observations are separated by two days. SMF0 was used to fit the data. UV data are available in two filters (UVW1 and UVM2); none of them show variability. We classify it as a Compton-thin candidate.
- MARK 273: Only one observation per instrument can be used for the variability analysis. The annular region contributes with 31% to the *Chandra* data. Variations in N_{H2} (51%) were needed in the SMF1. This corresponds to a luminosity variation of 24% (32%) in the soft (hard) energy band over a two-year period. UV data are available in two epochs, with no variations observed. The analysis of the *Chandra* light curve results in no short-term variations. Compton-thick and Compton-thin classifications were obtained for different observations, so we classify it as a changing-look candidate (see Table A.7).
- Circinus: *Chandra* and *XMM*–Newton data are available at different epochs. The *Chandra* data analysis results in SMF0 (i.e., no variations) in a nine-year period, while the *XMM*–Newton data set needs SMF2 with $Norm_1$ (34%) and $Norm_2$ (31%) varying within a 13-year period. However, the *XMM*–Newton data did not show any flux variations. The spectra are quite complex, so two (at 1.85 (Si XIII) and 2.4 (S XIV) keV) and four (at 1.2 (Ne X), 1.36 (Mg XI), 1.85 (Si XIII), and 2.4 (S XIV) keV) additional Gaussian lines are required for the *XMM*–Newton and *Chandra* fits, respectively. The annular region contributes with 28% to the *Chandra* data. However, the comparison between the data sets was not carried out owing to the complexity of the spectra. Short-term variations are not found from a *Chandra* light curve. We classify it as a *Compton*-thick candidate. We notice that the variations obtained from *XMM*–Newton data will not be used for further discussion, because this variability seems to be caused by extranuclear sources (see B.18 for details), and therefore this nucleus is considered as non-variable.
- NGC 5643: The *XMM*–Newton data were fitted with the SMF0; i.e., variations were not observed within a six-year period. We classify it as a Compton-thick candidate.
- MARK 477: The two observations are separated by two days. SMF0 was used, so no variations are reported. At UV frequencies variations are not found. We classify the source as a Compton-thick candidate.
- IC 4518A: The *XMM*–Newton data need SMF1 with $Norm_2$ (42%) varying. The variations are found in an eight-day period, and correspond to a flux variation of 40% (41%) in the soft (hard) energy band. We classify it as a Compton-thin candidate.
- ESO 138-G01: No variations are found (i.e., SMF0 was used) within a five-year period. We classify it as a Compton-thick candidate.
- NGC 6300: The *Chandra* observations are separated by four days. SMF0 results in the best fit; i.e., variations are not found. The annular region contributes with 5% to the *Chandra* data. When comparing *Chandra* and *XMM*–Newton data, SMF2 was used, with $Norm_1$ (98%) and $Norm_2$ (98%) varying over an eight-year period. We classify it as a Compton-thin candidate.
- NGC 7172: SMF1 is the best representation of the *XMM*–Newton data, with $Norm_2$ (54%) varying over a three-year period. This implies an intrinsic flux variation of 54% (53%) at soft (hard) energies. We classify it as a Compton-thin candidate.
- NGC 7212: One observation per instrument is available. The annular region contributes with 16% to the *Chandra* data. When comparing both data sets, SMF0 is needed; i.e., variations are not found. We classify this source as a Compton-thick candidate.
- NGC 7319: The best representation of the data used SMF2 with N_{H1} (passed from $N_{H1} = 6.5 \times 10^{21} cm^{-2}$ to $N_{H1} = N_{Gal}$) and $Norm_2$ (39%) varying in a seven-year period. Intrinsic flux variations of 38% in both the soft and hard energy bands are obtained. The annular region contributes with 17% to the *Chandra* data. When comparing *XMM*–Newton and *Chandra* data, SMF1 with $Norm_2$ (54%) varying is required, implying flux variations of 71% (69%) at soft (hard) energies over six years. Short-term variations were not detected. We classify it as a changing-look candidate because Compton-thick and Compton-thin classifications were obtained for different observations (see Table A.7).

5.2. Spectral characteristics

The sample of 26 optically classified Seyfert 2 galaxies presented in this work show a variety of spectral shapes. None of them are well-fitted with the ME or the PL models alone. Composite models are required in all cases.

The models we used in previous works (to represent the spectra of LINERs, González-Martín et al. 2009b; Hernández-García et al. 2013, 2014) describe the spectra of 12 galaxies well (MARK 348, ESO 417-G06, MARK 1066, 3C 98.0, NGC 3079, NGC 4698, NGC 5194, MARK 268, ESO 138-G01, NGC 6300, NGC 7172, and NGC 7319). Three models are required (2PL, MEPL, and ME2PL) for the spectral fits. Among the 15 objects in our sample observed in polarized light (see Table 1), one galaxy in this group has a HBLR and four a NHBLR.

On the other hand, 14 objects (NGC 424, MARK 573, NGC 788, MARK 3, MARK 1210, IC 2560, NGC 3393, NGC 4507, MARK 273, Circinus, NGC 5643, MARK 477, IC 4518A, and NGC 7212) show a more complex structure at energies below and around 2 keV, which cannot be fitted with a single thermal component. These nuclei need the 2ME2PL model to fit the data. Besides, four of the objects need additional Gaussian lines to properly fit the data. Nine galaxies in this group have a HBLR and one a NHBLR.

The addition of a cold reflection component to the best-fit model is not statistically required by the data, except in obsID 0064600101 (*XMM*–Newton) of 3C98.0. It is worth noting that even if a model including this component is physically more meaningful, the lack of data at harder energies prevents us from setting the best values required by the model, and therefore a single power law is enough for studying nuclear variations. On the other hand, we find that the cold reflection component remains constant for 3C 98.0 in SMF1. If this is the general scenario (see Sect. 6.2), the lack of this component in the models will not introduce biases into the variability analysis.

A thermal component at soft energies is needed to fit the data in 24 out of the 26 sources; in 14 cases, two MEKAL are needed. It is worth recalling that even if a MEKAL model fits the data well, because of its spectral resolution, photoion-

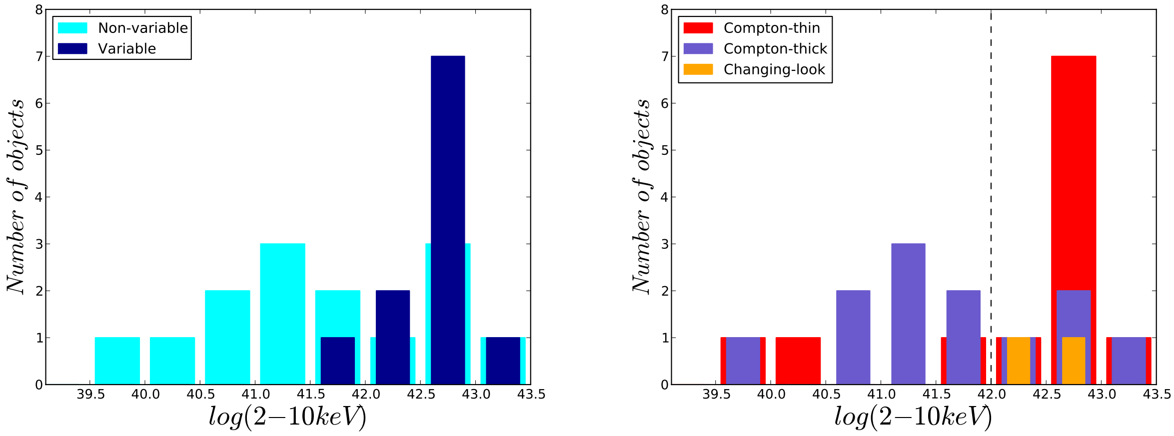

Fig. 4: Histograms of: (Left): the luminosities for the variable (dark blue) and non-variable (light blue) galaxies in the sample; and (Right): the luminosities for the galaxies in the sample divided into Compton-thick (purple), Compton-thin (red), and changing-look (orange) candidates. The dashed line represents the value for the selection of faint (below) and bright (above) Seyfert 2s.

ized models would be required to properly describe the data (see Sect. 4.1). The values of the temperatures are in the range kT_1 = [0.04–0.26] keV (only when the 2ME2PL model is fitted) with a mean value of 0.12±0.03 keV, and kT_2 = [0.13-1.00] keV with a mean value of 0.60±0.14 keV. The values of the spectral index (which is the same at soft and hard energies, when two are required) is in the range Γ = [0.61–3.23], with a mean value of 1.56±0.40, and the absorbing column densities at hard energies N_{H2} = [5.15–152.21] $\times 10^{22} cm^{-2}$, with a mean value of 34.69±15.30 $\times 10^{22} cm^{-2}$.

5.3. Long-term X-ray spectral variability

>From the 26 galaxies in our sample, we compared data at different epochs from the same instrument in 19 cases. Among these, seven objects were observed with *Chandra*, 13 with *XMM*–Newton, and in one case (namely Circinus) observations at different epochs with both instruments were available.

Chandra and *XMM*–Newton data are available for the same object in 15 cases (see Table A.1). We did not compare these data sets for NGC 3079 because the number counts of the nuclear contribution of *XMM*–Newton spectrum (after decontaminating from the annular region) is not enough for a reliable spectral fit. Given that NGC 3079 has one observation per instrument that cannot be compared, this object will not be used to discuss long-term variations. Additionally, the *Chandra* and *XMM*–Newton spectra of Circinus are very different, most probably because extranuclear sources are included in the *XMM*–Newton aperture radius, thus preventing us from properly comparing both. For the remaining 13 objects, the simultaneous analysis was carried out (Table A.5), where the extranuclear emission were negligible in two cases (NGC 424 and NGC 788). Four of these sources showed spectral variations.

In total, 25 (out of 26) nuclei have been analyzed to study long-term X-ray spectral variations, with 11 of them (excluding Circinus[10]) showing variability. In Fig. 4 (left) we present a histogram of the luminosities of the variable and non-variable sources. A K-S test results in p=0.006, so we can reject the hypothesis that the sample came from the same normal distribution. The spectral changes are mainly due to variations in the nuclear power (i.e., $Norm_2$), which is observed in nine nuclei (MARK 348, 3C 98.0, MARK 3, MARK 1210, NGC 4507, IC 4518A, NGC 6300, NGC 7172, and NGC 7319). Changes in the column density (i.e., N_{H2}) are also present in four cases (ESO 417-G06, MARK 273, MARK 1210, and NGC 4507 – in the last two accompained by changes in $Norm_2$). Changes at soft energies are found in two objects: NGC 7319 (N_{H1} together with $Norm_2$) and NGC 6300 ($Norm_1$ together with $Norm_2$). This means that from the 11 sources showing variations, most of them (nine out of 11) show variations in the nuclear continuum (i.e., $Norm_2$), while variations due to absorptions are less common (four in total, in two objects accompained by variations in $Norm_2$).

5.3.1. HBLR vs. NHBLR

>From the 15 objects in the sample with available observations in polarized light (see Table 1), ten are HBLR objects and five NHBLR. Nine out of the ten HBLR objects need the 2ME2PL model for the spectral fits (except MARK 348). The mean values of the parameters in the simultaneous fits are reported in Table 3. From the ten HBLR, four (MARK 348, MARK 3, MARK 1210, and NGC 4507) show variations in $Norm_2$, in two sources accompained by variations in N_{H2}. One (NGC 7172) out of the four NHBLR sources shows variations in $Norm_2$.

Therefore, although the number of objects in this subsample is not enough to be conclusive, it seems that there is no difference in either the proportion of variable objects or in the pattern of the variations.

5.3.2. Compton-thick vs. Compton-thin

We select Compton-thick candidates when at least two out of the three indicators were met (see Sect. 4.5). These indicators are obtained from X-ray (EW(FeKα) and Γ) and the [O III] line ($F_x/F_{[OIII]}$) data. In Fig. 5 we represent the histogram of these values for the whole sample, where the mean was calculated when multiple observations were available (from Table A.7). One Compton-thin candidate has $\Gamma < 1$ (NGC 4698), one Comp-

---

[10] We exclude the variations found with *XMM*–Newton data because they are most probably due to extranuclear sources, while variations with *Chandra* data are not reported.

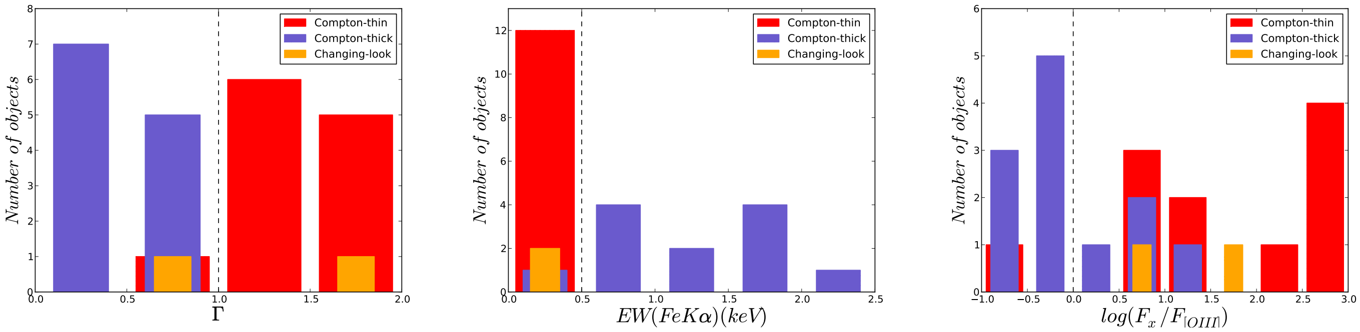

Fig. 5: Histograms of (Left): the slope of the power law, Γ from Table A.7; (Middle): equivalent width of the iron line, EW(FeKα); and (Right): the X-ray to [O III] flux ratios. In all cases the sample is divided into Compton-thick (purple), Compton-thin (red), and changing-look (orange) candidates. The dashed lines represents the values for the selection of Compton-thick (below) and Compton-thin (above) candidates.

ton-thick candidate has EW(FeKα)<0.5 keV (MARK 477), one Compton-thin candidate has log($F_x/F_{[OIII]}$)$<$ 0 (NGC 3079), and four Compton-thick candidates have log($F_x/F_{[OIII]}$)$>$ 0 (NGC 424, IC 2560, ESO 138-G01, and NGC 7212; see discussion in Sect. 6.2).

>From the 26 nuclei, 12 are classified as Compton-thick candidates (NGC 424, MARK 573, MARK 3, MARK 1066, IC 2560, NGC 3393, NGC 5194, Circinus, NGC 5643, MARK 477, ESO 138-G01, and NGC 7212), 12 as Compton-thin candidates (MARK 348, NGC 788, ESO 417-G06, 3C 98.0, MARK 1210, NGC 3079, NGC 4507, NGC 4698, MARK 268, IC 4518A, NGC 6300, and NGC 7172), and two as changing-look candidates (MARK 273, and NGC 7319). The mean values of the spectral parameters in these subgroups are reported in Table 3, where Compton-thin candidates are more luminous and less obscured and have steeper spectral indices than Compton-thick candidates. The spectral index of Compton-thick candidates was estimated using $\Gamma_{soft} \neq \Gamma_{hard}$ (see details in Sect. 4.5) and the values are reported in Table A.7.

Only one (out of the 12) Compton-thick candidates shows variations (MARK 3), in $Norm_2$. Eight (out of 11) Compton-thin candidates show changes, with these variations related mainly to $Norm_2$ (seven cases, in three sources accompained by variations in N_{H2} or $Norm_1$) and only in one case to N_{H2} alone. The two changing-look candidates show X-ray long-term variations, MARK 273 varies N_{H2}, and NGC 7319 needs variations in N_{H1} plus $Norm_2$.

Therefore, the number of variable Compton-thin and changing look candidates is notably higher than that of Compton-thick candidates.

Table 3: Mean values of the spectral parameters for the subgroups.

Group	Γ	N_{H2}	log(L(2–10 keV))
All	1.56±0.40	34.69±15.30	42.56±0.89
HBLR	1.34±0.43	39.22±18.62	42.72±0.80
NHBLR	1.58±0.48	40.17±20.23	41.40±1.04
Compton-thick	0.57±0.29[1]	43.95±19.53	42.33±1.01
Compton-thin	1.43±0.32	20.31±14.39	42.73±1.12
Changing-look	1.68±0.49	45.99±1.24	42.76±0.49
Bright	1.44±0.40	32.11±20.12	42.78±0.29
Faint	1.69±0.61	34.53±21.20	41.38±0.82

(Col. 1) Group, (Col. 2) values of Γ, (Col. 3) column density in units of $10^{22} cm^{-2}$, and (Col. 4) intrinsic luminosity in the 2–10 keV energy band.

[1] This value is calculated from the simultaneous values reported in Table A.7.

5.3.3. Bright vs. faint nuclei

In Fig. 4 (right), we present the histogram of the luminosities of the AGN in the sample as reported in Table 2, for Compton-thick (purple), Compton-thin (red), and changing-look (orange) candidates. A bimodal distribution can be appreciatted (K-S test, p=0.030), with the difference around log(L(2–10 keV))~42. Based on this histogram we separate the objects into faint (with log(L(2–10 keV))<42) and bright (log(L(2–10 keV))>42) Seyfert 2s.

>From these, 15 sources are bright, including four Compton-thick (one variable, MARK 3), two changing-look (both variable, MARK 273, and NGC 7319), and nine Compton-thin (seven variable, MARK 348, ESO 417-G06, 3C 98.0, MARK 1210, NGC 4507, IC 4518A, and NGC 7172). The remaining 11 objects are faint Seyfert 2s, including three Compton-thin (one shows variations, NGC 6300) and eight Compton-thick (none varies).

In total, 10 (out of 15) bright nuclei, and one (out of 10) faint nuclei show variations. Therefore, brighter sources include more variable sources and less Compton-thick candidates, a trend that can be derived by comparing left- and righthand panels in Fig. 4. Moreover, we note that NGC 6300 (i.e., the only faint source that varies) has log(L(2–10 keV))=41.95, very close to the established luminosity limit. The mean values of the spectral parameters of these subgroups are reported in Table 3, where faint objects show a steeper power law index than bright objects.

5.4. Short-term X-ray variability

Observations with a net exposure time > 30 ksec are used to study short-term variations. This requirement leaves us with ten sources for the analysis (see Table A.6). Three of them (IC 2560, NGC 5194, and MARK 573) show positive values of σ^2_{NXS}, but below 3σ of confidence level in all cases. Therefore we cannot claim short-term variations in any of the objects in our sample. Upper limits of σ^2_{NXS} have been estimated for all the other cases.

5.5. Long-term UV flux variability

XMM–Newton data at different epochs were used to study long-term X-ray spectral variations in 13 sources. In nine of them data from the OM cannot be used because the source is outside the detector or because the same filter is not available at different epochs. In contrast, two objects (MARK 273 and NGC 5194) have OM data while the sources were out of the pn detector, so these data were also used to search for variations at UV frequencies. Thus, UV data for variability studies are available for six galaxies (3C 98.0, NGC 4698, NGC 5194, MARK 268, MARK 273, and MARK 477). Only NGC 5194 shows variations above 3σ of the confidence level in one filter (UVW1).

We also searched in the literature for UV variations for the sources in the sample, but this information was available only for MARK 477 (see Appendix B). Comparing the analyses at X-rays and UV, two out of the six sources do vary at X-rays but not at UV frequencies (3C98.0 and MARK 273), and one (NGC 5194) does not show variations in X-rays but it does at UV. The remaining three objects do not vary neither in X-rays nor at UV frequencies.

6. Discussion

6.1. X-ray spectral variability

A long-term X-ray variability analysis was performed for 25 out of the 26 nuclei in our sample of Seyfert 2 galaxies[11]. From these, 11 sources are variable at X-rays. Among the remaining 14 nuclei where variations are not detected, 11 are Compton-thick candidates, and therefore variations are not expected (e.g., Matt et al. 2013, and references therein). This agrees well with our results, where only one out of the 12 Compton-thick candidates shows variations. We refer the reader to Sect. 6.2 for a complete discussion about Compton-thick candidates. The other three nuclei where variations are not detected are Compton-thin candidates (NGC 788, NGC 4698, and MARK 268). The lack of variations may be due to the short timescale between observations for MARK 268 (two days). The timescales between observations for the other two sources are on the order of years, so, in principle, variations could be detected. New data would therefore be required before confirming the non-variable nature of these sources.

In this section the discussion is focused on the different patterns of variability obtained for the 11 variable nuclei, including eight Compton-thin, two changing-look, and one Compton-thick candidates. We notice that this is the first time that transitions from a Compton-thin to a Compton-thick (or vice versa) appearance have been reported for MARK 273 and NGC 7319, which should be added to the short list of known changing-look Seyfert 2s, such as NGC 2992 (Gilli et al. 2000), MARK 1210 (Guainazzi et al. 2002), NGC 6300 (Guainazzi 2002), NGC 7674 (Bianchi et al. 2005a), and NGC 7582 (Bianchi et al. 2009).

6.1.1. Variations at soft energies

We found that most of the objects in our sample do not vary at soft X-ray energies, indicating that the mechanism responsible for the soft emission should be located far from the nucleus. Indeed, using artificial neural networks, González-Martín et al. (2014) compared the spectra of different classes of AGN and starburst galaxies and find that Seyferts 2 have a high contribution from processes that are related star formation, which may be related to emission coming from the host galaxy.

Notwithstanding, two sources show variations at soft energies (<2 keV), each showing a different variability pattern, but in both cases these variations are accompanied by variations in the normalization of the hard power law; NGC 6300 shows variations in the normalization at soft energies, $Norm_1$, when comparing data from *XMM*–Newton and *Chandra*; and NGC 7319 showed variations in the absorber at soft energies, N_{H1}, when comparing two *Chandra* observations. It is worth noting that the soft X-ray fluxes are on the order of $10^{-13} erg\ cm^{-2} s^{-1}$ in the two nuclei, which is typical of Seyfert galaxies (Guainazzi et al. 2005b), so these variations are not related to low-count number statistics. However, variations at soft energies in these sources have not been reported before. Up to now, such variations have only been found for two Seyfert 2s. Paggi et al. (2012) found variations at soft X-rays in the Seyfert 2 MARK 573 when comparing four *Chandra* observations. This nucleus is also included in the present sample, but variations are not found here, mainly because we did not use two of the observations included in the work of Paggi et al. (2012) since they were affected by a pileup fraction higher than 10%. Guainazzi et al. (2012) speculate that variations at soft X-ray energies in MARK 3 may be present when comparing *XMM*–Newton and *Swift* data, but confirmation is still required. They argue that these variations are most probably due to cross-calibration uncertainties between the instruments, but if true, soft X-ray variations could be related to the innermost part of the narrow-line region.

On the other hand, the variability patterns found in this work have also been reported for other types of AGN. Variations in the absorbers, as seen in NGC 7319, were found by González-Martín et al. (2011a), who used *Suzaku* data to study the LINER 2 NGC 4102. They argue that the variations at soft energies are due to an absorbing material located within the torus and perpendicular to the plane of the disk. Variability timescales can be used to estimate the lower limits of the cloud velocity (e.g., Risaliti et al. 2007). However, the timescales between our observations were obtained randomly, so the variability timescale of the eclipse can be shorter. In the case of NGC 7319, variations are obtained within a timescale of seven years, which is too long to estimate the distance at which the cloud is located. It is worth noting that we classified this object as a changing-look candidate. Besides, we found that NGC 6300 varied the normalizations at soft and hard energies. Using the same method as explained in this work, Hernández-García et al. (2013) find the same variability pattern in the LINER 2 NGC 4552, indicating that these variations may be intrinsic to the emitting material.

6.1.2. Absorber variations

Variations in the circumnuclear absorbers are thought to be very common in Seyfert galaxies. In fact, these variations are usually observed in Seyferts 1-1.9 (e.g., NGC 1365, Risaliti et al. 2007; NGC 4151, Puccetti et al. 2007; MARK 766, Risaliti et al. 2011), where it has been shown that the changes are most probably related to the broad line region (BLR), although it has been suggested that multiple absorbers may be present in an AGN, located at different scales (Braito et al. 2013). However, it is not so clear whether variations due to absorbers are common for optically classified Seyfert 2s, for which this kind of variation has only been reported in a few cases (e.g., MARK 348, Marchese et al. 2014; NGC 4507, Braito et al. 2013 and Marinucci et al. 2013; MARK 1210, Risaliti et al. 2010).

---

[11] We recall that NGC 3079 will not be used for the discussion of variability, see Sect. 5.1.

>From the 11 variable sources in our sample, variations due to absorbers at hard energies are detected in four nuclei. In two of them, MARK 1210 and NGC 4507, variations in N_{H2} are accompained by variations in the nuclear continuum, $Norm_2$. The variability pattern reported for these objects agrees with previous results presented by Risaliti et al. (2010) and Braito et al. (2013), who argue that the physical properties of the absorber are consistent with these variations occurring in the BLR. Following prescriptions in Risaliti et al. (2010) and using the BH masses (Table 2) and variability timescales of one and ten days for MARK 1210 and NGC 4507, respectively, we estimate the cloud velocities to be higher than $10^3 km\ s^{-1}$ in both cases, thus also locating the absorbers at the BLR.

On the other hand, ESO 417-G06 and MARK 273 showed variations only in N_{H2}. Trippe et al. (2011) report variations of a factor about two in the count rate of ESO 417-G06 from the 22-month survey of *Swift*, and Balestra et al. (2005) fit the *XMM*–Newton and *Chandra* spectra of MARK 273 studied in this work and note that different column densities were required to fit the data well (its values in good agreement with ours), indicating variations due to absorption. The timescale between observations for ESO 417-G06 is 40 days and two years for MARK 273. Therefore, we cannot estimate the cloud velocity for MARK 273 because the timescale is too large. Assuming the variability timescale of ESO 417-G06 (40 days) and following prescriptions in Risaliti et al. (2010), we estimate a cloud velocity $> 60\ km\ s^{-1}$, so too low to restrict the location of the cloud. Since this estimate is a lower limit of the cloud velocity, a monitoring campaign of these sources would be needed to constrain their variability timescales, in order to properly constrain the locus of the absorbers.

6.1.3. Flux variations

The most frequently varying parameter in our sample is $Norm_2$, which is related to the nuclear continuum. These kinds of variations are observed in nine out of the 11 X-ray variable sources – sometimes accompanied by variations in other parameters (see Sects. 6.1.1 and 6.1.2). Therefore the most natural explanation for the observed variations in Seyfert 2 galaxies is that the nuclear power is changing with time. We recall that variations are not due to changes in the power law index, Γ, but related to its normalization. It has been shown that hard X-ray variability is usual in Seyfert 2 galaxies (e.g., Turner et al. 1997; Trippe et al. 2011; Marchese et al. 2014). In fact, this kind of variation has already been reported in the literature for objects included in the present work from intrinsic flux variations indicating changes in the nuclear continuum (Isobe et al. 2005) or because they needed to set free the normalization of the power law for a proper fit to the data (LaMassa et al. 2011). Also at higher energies, Soldi et al. (2014) studied the long-term variability of 110 AGN selected from the BAT 58-month survey and argue in favor of a variable nuclear continuum plus a constant reflection component. Their result is independent of the classification of the objects, which includes Seyferts, NLSy1s, radio galaxies, and quasars.

Flux variations are indeed a property of AGN, and they have been reported at different frequencies for Seyfert 2s, such as in radio (Nagar et al. 2002; Neff & de Bruyn 1983) or infrared (Sharples et al. 1984; Hönig et al. 2012). In the present work we used data from the OM onboard *XMM*–Newton to study UV variability. These data are available at different epochs for six objects in our sample, but only NGC 5194 shows variations in the UVW1 filter. This is a Compton-thick candidate that does not vary in X-rays, so variations at UV frequencies from the nuclear component are not expected. It has been shown that the UV/optical spectra of Seyferts 2 include scattered AGN light, and it can sometimes be produced by young starbursts, including supernovae explosions (e.g., González Delgado et al. 2004). In fact, supernovae explosions in NGC 5194 have been reported in 1945, 1994, 2005, and 2011 (Van Dyk et al. 2011), which could account for the observed variations in the UV.

None of the remaining five nuclei show variations at UV frequencies, although there are two nuclei that are variable in X-rays (3C 98.0 and MARK 273). The lack of UV variations could be explained because X-ray and UV variations might not happen simultaneously (e.g., Hernández-García et al. 2014) or because we are not directly observing the nucleus. Muñoz Marín et al. (2009) studied 15 Seyfert galaxies with *HST* data (including types 1 and 2) and found that most type 2 nuclei appear resolved or absent at UV frequencies, concluding that the UV emission in Seyfert 2s does not come from the nucleus. Thus, the lack of UV variations in Seyfert 2s is most probably because we are not directly observing the nucleus at UV.

6.2. Compton-*thickness*

Brightman & Nandra (2011a) show that at column densities $\sim 4{\times}10^{24} cm^{-2}$, the observed flux below 10 keV is half that of the intrinsic flux at harder energies (see also Ghisellini et al. 1994). This indicates that in Compton-thick objects, the primary continuum is so absorbed in the 2-10 keV energy band that the emission is optically thick to Compton scattering, and the spectrum is reflection-dominated. For this reason, we have distinguished between Compton-thin and Compton-thick candidates (see Sects. 4.5 and 5.3).

However, the task of classifying Compton-thick objects with X-ray data comprising energies up to ∼ 10 keV is hard because the peak of the primary emission is above 10 keV. Instead, three different indicators involving X-ray and [O III] emission line data are used for their selection (see Sect. 4.5, for details). While the three criteria are met in most cases, our results have shown that the X-ray to [O III] line flux ratio, $\log(F_x/F_{[OIII]})$ is the most unsuitable indicator (see Fig. 5). This agrees with Brightman & Nandra (2011b), who argue that this parameter can be inaccurate for classifying Compton-thick sources because of the uncertainty in the reddening correction of the [O III] line flux. Moreover, in Fig. 5 (right) there are four objects with $\log(F_x/F_{[OIII]}) > 2.5$, which is higher than the values found by other authors (Bassani et al. 1999; Cappi et al. 2006; Panessa et al. 2006), what may be due to a underestimation of the [O III] line flux. Although the [O III] line is a good luminosity indicator, the reddening correction might depend on the geometry of the narrow line region, leading to an underestimation of its flux if we do not take it into account and leading to very high values of F_x/F_{OIII}.

In the present work, 12 nuclei are classified as Compton-thick candidates. Among them, variations are found only in MARK 3, which was previously classified as a Compton-thick candidate (Bassani et al. 1999; Goulding et al. 2012), with a column density of $1.1 \times 10^{24} cm^{-2}$ measured by *BeppoSAX* (Cappi et al. 1999). In fact, variations in MARK 3 have already been reported by Guainazzi et al. (2012), who studied its variability using *XMM*–Newton, *Suzaku*, and *Swift* data, and found variations on timescales of months. We found that the changes in MARK 3 are related to $Norm_2$, i.e., intrinsic to the source. The most likely explanation for these variations could therefore be that part of the emission is still transmitted below 10 keV, so variations can be observed.

Interestingly, we found that most of the Compton-thick candidates are non-variable and tend to be fainter than Compton-thin and changing-look candidates, which show X-ray variations (see Fig. 4). This can be explained because the intrinsic luminosity is underestimated if the primary continuum is suppressed at energies below 10 keV, in agreement with the results of Brightman & Nandra (2011a). In fact, the only Compton-thick candidate that shows variations in X-rays is included as a bright Seyfert 2. It could be that variations are not observed because the spectra of Compton-thick sources are dominated by the reflection component. If so, this component might be located farther away from the central source, so it remains constant. This scenario agrees with the results we have obtained for the only source where a reflection component was statistically required by the data (namely 3C 98.0). These results are also in good agreement with those found by other authors, who did not find X-ray variability for objects classified as Compton-thick (e.g., NGC 424 and NGC 5194, LaMassa et al. 2011; Circinus, Arévalo et al. 2014; NGC 5643, Matt et al. 2013).

As noted above, if the reflection component does not vary, it might indicate that the reflection of the primary continuum occurs at large distances from the SMBH. The same result was obtained by Risaliti (2002), who studied Seyfert 2s with *BeppoSAX* and found that the cold reflection component is compatible with being non-variable. They argue that if the reflection originates in the accretion disk, the reflection and the transmitted components must be closely related, but if the distance of the reflector to the SMBH is greater than the light crossing time of the intrinsic variations, the reflected component must remain constant. Therefore a reflector located far away from the SMBH is supported by our results, maybe in the torus or in the host galaxy.

6.3. Caveats and limitations of the analysis

The models used in this work to characterize the spectra of Seyfert 2 galaxies are a simplification of the true physical scenario occurring in these nuclei. In particular, the 2–10 keV energy band – where variations are mostly found – is represented by an absorbed power law continuum, which could be an over-simplification of the real scenario.

Spectral variability analyses of seven sources studied in this work have been reported previously. Since at least some of these works study individual sources, the models used in their analyses might be more complex than ours (see Appendix B, for details). This comparison shows that our results are almost always compatible with those reported in the literature (MARK 1210, Matt et al. 2009 and Risaliti et al. 2010; NGC 4507, Matt et al. 2004, Marinucci et al. 2013, and Braito et al. 2013; MARK 273, Balestra et al. 2005; Circinus, Arévalo et al. 2014; NGC 6300, Guainazzi 2002; and NGC 7172, LaMassa et al. 2011). However, we cannot discard variations due to components that we did not fit in the models. For instance, Marchese et al. (2014) analyzed the *XMM*–Newton and *Suzaku* data of MARK 348 (also included in the present work), and report variations due to a neutral plus an ionized absorbers, together with a change in the ionization parameter of the ionized absorber. Their analysis is based on the residuals of the spectral fitting, where they include as many components as required, and the variability analysis is performed by testing different scenarios, including a variable continuum plus a constant reflection component ($\chi^2/d.o.f$=567.7/407), a variable continuum plus a variable reflection component ($\chi^2/d.o.f$=551.1/406, but variations are not observed), variations due to absorptions, and changes in the ionization state ($\chi^2/d.o.f$=551.6/407). We notice that our spectral fit of MARK 348 with $Norm_2$ varies results in a very good fit ($\chi^2/d.o.f$=1520.5/1368) when comparing the two *XMM*–Newton data sets, and residuals are mostly at energies below ~ 2.5 keV (see Fig. 2). Therefore, the presence of complex variations like these in at least some sources in our sample cannot be completely discarded.

7. Conclusions

Using *Chandra* and *XMM*–Newton public archives we performed a spectral, flux, short-, and long-term variability analysis of 26 optically selected Seyfert 2 galaxies. The main results of this study can be summarized as follows:

1. Long-term variability was found in 11 out of the 25 analyzed nuclei, which are more frequent among the brightest sources (log(L(2-10 keV)) > $10^{42} erg\ s^{-1}$). From the 11 variable sources, eight are Compton-thin candidates, two are changing-look, and only one (namely MARK 3) is a Compton-thick candidate. No difference in the variability is found among the HBLR and NHBLR objects. We report two changing-look candidates for the first time: MARK 273 and NGC 7319.

2. Short-term variability has not been detected in any of the sources. Nor UV variability.

3. The main driver of the observed variations is due to the power of the central engine manifested through variations in the normalization of the power law at high energies. At soft energies variations are rare, and column density variations have only been observed in four cases.

Our results are compatible with a scenario where a constant reflection component located far away from the nucleus and a variable nuclear continuum take place. Within this scenario, Compton-thick objects are dominated by reflection and do not show any X-ray spectral or flux variations. This implies that their luminosities are suppressed at hard X-rays, making them fainter sources than Compton-thin objects. In contrast, most of the Compton-thin or changing-look candidates are variable, showing different patterns of variability. These changes are mainly due to variations in the nuclear continuum. However, variations of the absorber or at soft energies are also found in some cases, with many of them accompanied by variations of the nuclear continuum. These variations are mainly due to clouds intersecting our line of sight.

Acknowledgements. We acknowledge the referee, M. Guainazzi, for his comments and suggestions that helped to improve the paper, and the AGN group at the IAA for helpful comments during this work. This work was financed by MINECO grant AYA 2010-15169, AYA 2013-42227-P, Junta de Andalucía TIC114 and Proyecto de Excelencia de la Junta de Andalucía P08-TIC-03531. LHG acknowledges financial support from the Ministerio de Economía y Competitividad through the Spanish grant FPI BES-2011-043319. This research made use of data obtained from the *Chandra* Data Archive provided by the *Chandra* X-ray Center (CXC). This research made use of data obtained from the *XMM*-Newton Data Archive provided by the *XMM*-Newton Science Archive (XSA). This research made use of the NASA/IPAC extragalactic database (NED), which is operated by the Jet Propulsion Laboratory under contract with the National Aeronautics and Space Administration. We acknowledge the usage of the HyperLeda data base (http://leda.univ-lyon1.fr).

References

Afanas'ev, V. L., Lipovetskii, V. A., & Shapovalova, A. I. 1981, Astrophysics, 17, 342

Aguero, E. L., Calderon, J. H., Paolantonio, S., & Suarez Boedo, E. 1994, PASP, 106, 978

Akylas, A. & Georgantopoulos, I. 2009, A&A, 500, 999

Akylas, A., Georgantopoulos, I., Griffiths, R. G., et al. 2002, MNRAS, 332, L23

Alloin, D., Bica, E., Bonatto, C., & Prugniel, P. 1992, A&A, 266, 117

Alonso-Herrero, A., Pereira-Santaella, M., Rieke, G. H., et al. 2013, ApJ, 765, 78

Antonucci, R. 1993, ARA&A, 31, 473

Aoki, K., Kosugi, G., Wilson, A. S., & Yoshida, M. 1999, ApJ, 521, 565

Arévalo, P., Bauer, F. E., Puccetti, S., et al. 2014, ApJ, 791, 81

Awaki, H., Koyama, K., Inoue, H., & Halpern, J. P. 1991, PASJ, 43, 195

Awaki, H., Murakami, H., Leighly, K. M., et al. 2005, ApJ, 632, 793

Awaki, H., Murakami, H., Ogawa, Y., & Leighly, K. M. 2006, ApJ, 645, 928

Balestra, I., Boller, T., Gallo, L., Lutz, D., & Hess, S. 2005, A&A, 442, 469

Baloković, M., Comastri, A., Harrison, F. A., et al. 2014, ApJ, 794, 111

Bassani, L., Dadina, M., Maiolino, R., et al. 1999, ApJS, 121, 473

Beckmann, V., Barthelmy, S. D., Courvoisier, T. J.-L., et al. 2007, A&A, 475, 827

Bian, W. & Gu, Q. 2007, ApJ, 657, 159

Bianchi, S., Chiaberge, M., Evans, D. A., et al. 2010, MNRAS, 405, 553

Bianchi, S., Guainazzi, M., & Chiaberge, M. 2006, A&A, 448, 499

Bianchi, S., Guainazzi, M., Matt, G., et al. 2005a, A&A, 442, 185

Bianchi, S., Miniutti, G., Fabian, A. C., & Iwasawa, K. 2005b, MNRAS, 360, 380

Bianchi, S., Panessa, F., Barcons, X., et al. 2012, MNRAS, 426, 3225

Bianchi, S., Piconcelli, E., Chiaberge, M., et al. 2009, ApJ, 695, 781

Boisson, C., Joly, M., Pelat, D., & Ward, M. J. 2004, A&A, 428, 373

Braito, V., Ballo, L., Reeves, J. N., et al. 2013, MNRAS, 428, 2516

Brightman, M. & Nandra, K. 2011a, MNRAS, 413, 1206

Brightman, M. & Nandra, K. 2011b, MNRAS, 414, 3084

Cappi, M., Bassani, L., Comastri, A., et al. 1999, A&A, 344, 857

Cappi, M., Panessa, F., Bassani, L., et al. 2006, A&A, 446, 459

Carilli, C. L. & Taylor, G. B. 2000, ApJ, 532, L95

Collinge, M. J. & Brandt, W. N. 2000, MNRAS, 317, L35

Comastri, A. 2004, in Astrophysics and Space Science Library, Vol. 308, Supermassive Black Holes in the Distant Universe, ed. A. J. Barger, 245

Corbett, E. A., Norris, R. P., Heisler, C. A., et al. 2002, ApJ, 564, 650

Costero, R. & Osterbrock, D. E. 1977, ApJ, 211, 675

Davis, B. L., Berrier, J. C., Johns, L., et al. 2014, ApJ, 789, 124

de Rosa, A., Bassani, L., Ubertini, P., et al. 2008, A&A, 483, 749

de Rosa, A., Panessa, F., Bassani, L., et al. 2012, MNRAS, 420, 2087

Dessauges-Zavadsky, M., Pindao, M., Maeder, A., & Kunth, D. 2000, A&A, 355, 89

Dewangan, G. C., Griffiths, R. E., Choudhury, M., Miyaji, T., & Schurch, N. J. 2005, ApJ, 635, 198

Diaz, A. I., Prieto, M. A., & Wamsteker, W. 1988, A&A, 195, 53

Dickey, J. M. & Lockman, F. J. 1990, ARA&A, 28, 215

Elmouttie, M., Haynes, R. F., Jones, K. L., Sadler, E. M., & Ehle, M. 1998, MNRAS, 297, 1202

Eracleous, M., Hwang, J. A., & Flohic, H. M. L. G. 2010, ApJ, 711, 796

Evans, D. A., Hardcastle, M. J., Croston, J. H., Worrall, D. M., & Birkinshaw, M. 2005, MNRAS, 359, 363

Fairall, A. P. 1986, MNRAS, 218, 453

Falcke, H., Wilson, A. S., & Simpson, C. 1998, ApJ, 502, 199

Ford, H. C., Crane, P. C., Jacoby, G. H., Lawrie, D. G., & van der Hulst, J. M. 1985, ApJ, 293, 132

Fukazawa, Y., Iyomoto, N., Kubota, A., Matsumoto, Y., & Makishima, K. 2001, A&A, 374, 73

Garmire, G. P., Bautz, M. W., Ford, P. G., Nousek, J. A., & Ricker, J. G. R. 2003, in Society of Photo-Optical Instrumentation Engineers (SPIE) Conference Series, Vol. 4851, Society of Photo-Optical Instrumentation Engineers (SPIE) Conference Series, ed. J. E. Truemper & H. D. Tananbaum, 28–44

Georgantopoulos, I. & Zezas, A. 2003, ApJ, 594, 704

Ghisellini, G., Haardt, F., & Matt, G. 1994, MNRAS, 267, 743

Gilli, R., Maiolino, R., Marconi, A., et al. 2000, A&A, 355, 485

Gimeno, G. N., Díaz, R. J., & Carranza, G. J. 2004, AJ, 128, 62

González Delgado, R. M., Cid Fernandes, R., Pérez, E., et al. 2004, ApJ, 605, 127

González-Martín, O., Acosta-Pulido, J. A., Perez Garcia, A. M., & Ramos Almeida, C. 2010, ApJ, 723, 1748

González-Martín, O., Díaz-González, D., Acosta-Pulido, J. A., et al. 2014, A&A, 567, A92

González-Martín, O., Masegosa, J., Márquez, I., & Guainazzi, M. 2009a, ApJ, 704, 1570

González-Martín, O., Masegosa, J., Márquez, I., Guainazzi, M., & Jiménez-Bailón, E. 2009b, A&A, 506, 1107

González-Martín, O., Papadakis, I., Braito, V., et al. 2011a, A&A, 527, A142

González-Martín, O., Papadakis, I., Reig, P., & Zezas, A. 2011b, A&A, 526, A132

González-Martín, O. & Vaughan, S. 2012, A&A, 544, A80

Goodrich, R. W. & Osterbrock, D. E. 1983, ApJ, 269, 416

Goulding, A. D., Alexander, D. M., Bauer, F. E., et al. 2012, ApJ, 755, 5

Gu, Q. & Huang, J. 2002, ApJ, 579, 205

Gu, Q., Melnick, J., Cid Fernandes, R., et al. 2006, MNRAS, 366, 480

Guainazzi, M. 2002, MNRAS, 329, L13

Guainazzi, M., Fabian, A. C., Iwasawa, K., Matt, G., & Fiore, F. 2005a, MNRAS, 356, 295

Guainazzi, M., La Parola, V., Miniutti, G., Segreto, A., & Longinotti, A. L. 2012, A&A, 547, A31

Guainazzi, M., Matt, G., Antonelli, L. A., et al. 1998, MNRAS, 298, 824

Guainazzi, M., Matt, G., Fiore, F., & Perola, G. C. 2002, A&A, 388, 787

Guainazzi, M., Matt, G., & Perola, G. C. 2005b, A&A, 444, 119

Hernández-García, L., González-Martín, O., Márquez, I., & Masegosa, J. 2013, A&A, 556, A47

Hernández-García, L., González-Martín, O., Masegosa, J., & Márquez, I. 2014, A&A, 569, A26

Ho, L. C., Filippenko, A. V., Sargent, W. L. W., & Peng, C. Y. 1997, ApJS, 112, 391

Ho, L. C. & Ulvestad, J. S. 2001, ApJS, 133, 77

Hönig, S. F., Kishimoto, M., Antonucci, R., et al. 2012, ApJ, 755, 149

Huchra, J. P., Wyatt, W. F., & Davis, M. 1982, AJ, 87, 1628

Ishida, M., Tsujimoto, M., Kohmura, T., et al. 2011, PASJ, 63, 657

Isobe, N., Makishima, K., Tashiro, M., & Hong, S. 2005, ApJ, 632, 781

Kalberla, P. M. W., Burton, W. B., Hartmann, D., et al. 2005, A&A, 440, 775

Khachikian, E. Y. & Weedman, D. W. 1974, ApJ, 192, 581

Khorunzhev, G. A., Sazonov, S. Y., Burenin, R. A., & Tkachenko, A. Y. 2012, Astronomy Letters, 38, 475

Kim, D.-C., Veilleux, S., & Sanders, D. B. 1998, ApJ, 508, 627

Kinney, A. L., Antonucci, R. R. J., Ward, M. J., Wilson, A. S., & Whittle, M. 1991, ApJ, 377, 100

Kirsch, M. G. F., Altieri, B., Chen, B., et al. 2004, in Society of Photo-Optical Instrumentation Engineers (SPIE) Conference Series, Vol. 5488, UV and Gamma-Ray Space Telescope Systems, ed. G. Hasinger & M. J. L. Turner, 103–114

Komossa, S. & Schulz, H. 1997, A&A, 323, 31

Koski, A. T. 1978, ApJ, 223, 56

Kraemer, S. B., Schmitt, H. R., Crenshaw, D. M., et al. 2011, ApJ, 727, 130

Krolik, J. H., Madau, P., & Zycki, P. T. 1994, ApJ, 420, L57

LaMassa, S. M., Heckman, T. M., Ptak, A., et al. 2011, ApJ, 729, 52

Leahy, J. P., Black, A. R. S., Dennett-Thorpe, J., et al. 1997, MNRAS, 291, 20

Levenson, N. A., Weaver, K. A., & Heckman, T. M. 2001, ApJS, 133, 269

Liu, J.-F. & Bregman, J. N. 2005, ApJS, 157, 59

Lumsden, S. L., Heisler, C. A., Bailey, J. A., Hough, J. H., & Young, S. 2001, MNRAS, 327, 459

Magdziarz, P. & Zdziarski, A. A. 1995, MNRAS, 273, 837

Maia, M. A. G., Machado, R. S., & Willmer, C. N. A. 2003, AJ, 126, 1750

Maiolino, R. & Rieke, G. H. 1995, ApJ, 454, 95

Maiolino, R., Salvati, M., Bassani, L., et al. 1998, A&A, 338, 781

Marchese, E., Braito, V., Reeves, J. N., et al. 2014, MNRAS, 437, 2806

Marinucci, A., Bianchi, S., Matt, G., et al. 2011, A&A, 526, A36

Marinucci, A., Risaliti, G., Wang, J., et al. 2013, MNRAS, 429, 2581

Marquez, I. & Moles, M. 1996, A&AS, 120, 1

Martini, P., Pogge, R. W., Ravindranath, S., & An, J. H. 2001, ApJ, 562, 139

Matsumoto, C., Nava, A., Maddox, L. A., et al. 2004, ApJ, 617, 930

Matt, G., Bianchi, S., Awaki, H., et al. 2009, A&A, 496, 653

Matt, G., Bianchi, S., D'Ammando, F., & Martocchia, A. 2004, A&A, 421, 473

Matt, G., Bianchi, S., Guainazzi, M., et al. 2003, A&A, 399, 519

Matt, G., Bianchi, S., Marinucci, A., et al. 2013, A&A, 556, A91

Matt, G., Guainazzi, M., Maiolino, R., et al. 1999, A&A, 341, L39

Miller, J. S. & Goodrich, R. W. 1990, ApJ, 355, 456

Moran, E. C., Barth, A. J., Kay, L. E., & Filippenko, A. V. 2000, ApJ, 540, L73

Morganti, R., Tsvetanov, Z. I., Gallimore, J., & Allen, M. G. 1999, A&AS, 137, 457

Morris, S., Ward, M., Whittle, M., Wilson, A. S., & Taylor, K. 1985, MNRAS, 216, 193

Muñoz Marín, V. M., Storchi-Bergmann, T., González Delgado, R. M., et al. 2009, MNRAS, 399, 842

Nagar, N. M., Falcke, H., Wilson, A. S., & Ulvestad, J. S. 2002, A&A, 392, 53

Nagar, N. M., Wilson, A. S., Mulchaey, J. S., & Gallimore, J. F. 1999, ApJS, 120, 209

Nandra, K., George, I. M., Mushotzky, R. F., Turner, T. J., & Yaqoob, T. 1997, ApJ, 476, 70

Neff, S. G. & de Bruyn, A. G. 1983, A&A, 128, 318

Netzer, H. & Turner, T. J. 1997, ApJ, 488, 694

Nicastro, F., Martocchia, A., & Matt, G. 2003, ApJ, 589, L13

Noguchi, K., Terashima, Y., & Awaki, H. 2009, ApJ, 705, 454

Oliva, E., Marconi, A., Cimatti, A., & di Serego Alighieri, S. 1998, A&A, 329, L21

Oliva, E., Salvati, M., Moorwood, A. F. M., & Marconi, A. 1994, A&A, 288, 457

Osterbrock, D. E. & Martel, A. 1993, ApJ, 414, 552

Paggi, A., Wang, J., Fabbiano, G., Elvis, M., & Karovska, M. 2012, ApJ, 756, 39

Panessa, F. & Bassani, L. 2002, A&A, 394, 435

Panessa, F., Bassani, L., Cappi, M., et al. 2006, A&A, 455, 173

Pereira-Santaella, M., Alonso-Herrero, A., Santos-Lleo, M., et al. 2011, A&A, 535, A93

Peterson, B. M. 1997, An Introduction to Active Galactic Nuclei (Cambridge University Press)

Phillips, M. M., Charles, P. A., & Baldwin, J. A. 1983, ApJ, 266, 485

Pogge, R. W. & Eskridge, P. B. 1993, AJ, 106, 1405

Puccetti, S., Fiore, F., Risaliti, G., et al. 2007, MNRAS, 377, 607

Ramos Almeida, C., Pérez García, A. M., Acosta-Pulido, J. A., & González-Martín, O. 2008, ApJ, 680, L17

Rees, M. J. 1984, ARA&A, 22, 471

Risaliti, G. 2002, A&A, 386, 379

Risaliti, G., Elvis, M., Bianchi, S., & Matt, G. 2010, MNRAS, 406, L20

Risaliti, G., Elvis, M., Fabbiano, G., et al. 2007, ApJ, 659, L111

Risaliti, G., Elvis, M., & Nicastro, F. 2002, ApJ, 571, 234

Risaliti, G., Nardini, E., Salvati, M., et al. 2011, MNRAS, 410, 1027

Rodríguez-Baras, M., Rosales-Ortega, F. F., Díaz, A. I., Sánchez, S. F., & Pasquali, A. 2014, MNRAS, 442, 495

Ryder, S. D., Buta, R. J., Toledo, H., et al. 1996, ApJ, 460, 665

Severgnini, P., Caccianiga, A., & Della Ceca, R. 2012, A&A, 542, A46

Sharples, R. M., Longmore, A. J., Hawarden, T. G., & Carter, D. 1984, MNRAS, 208, 15

Singh, V., Shastri, P., & Risaliti, G. 2011, A&A, 532, A84

Smith, D. A., Georgantopoulos, I., & Warwick, R. S. 2001, ApJ, 550, 635

Smith, M. G. 1975, ApJ, 202, 591

Sobolewska, M. A. & Papadakis, I. E. 2009, MNRAS, 399, 1597

Soldi, S., Beckmann, V., Baumgartner, W. H., et al. 2014, A&A, 563, A57

Strüder, L., Briel, U., Dennerl, K., et al. 2001, A&A, 365, L18

Teng, S. H., Veilleux, S., Anabuki, N., et al. 2009, ApJ, 691, 261

Terashima, Y. & Wilson, A. S. 2001, ApJ, 560, 139

Tran, H. D. 1995, ApJ, 440, 578

Tran, H. D., Miller, J. S., & Kay, L. E. 1992, ApJ, 397, 452

Tremaine, S., Gebhardt, K., Bender, R., et al. 2002, ApJ, 574, 740

Trinchieri, G., Sulentic, J., Breitschwerdt, D., & Pietsch, W. 2003, A&A, 401, 173

Trippe, M. L., Reynolds, C. S., Koss, M., Mushotzky, R. F., & Winter, L. M. 2011, ApJ, 736, 81

Trotter, A. S., Greenhill, L. J., Moran, J. M., et al. 1998, ApJ, 495, 740

Tsujimoto, M., Guainazzi, M., Plucinsky, P. P., et al. 2011, A&A, 525, A25

Turner, T. J., George, I. M., Nandra, K., & Mushotzky, R. F. 1997, ApJS, 113, 23

Ulvestad, J. S. & Wilson, A. S. 1984, ApJ, 278, 544

Ulvestad, J. S. & Wilson, A. S. 1989, ApJ, 343, 659

Unger, S. W., Lawrence, A., Wilson, A. S., Elvis, M., & Wright, A. E. 1987, MNRAS, 228, 521

Urry, C. M. & Padovani, P. 1995, PASP, 107, 803

Van Dyk, S. D., Li, W., Cenko, S. B., et al. 2011, ApJ, 741, L28

Vaughan, S., Edelson, R., Warwick, R. S., & Uttley, P. 2003, MNRAS, 345, 1271

Veilleux, S., Kim, D.-C., Sanders, D. B., Mazzarella, J. M., & Soifer, B. T. 1995, ApJS, 98, 171

Veilleux, S. & Osterbrock, D. E. 1987, ApJS, 63, 295

Veron, P., Goncalves, A. C., & Veron-Cetty, M.-P. 1997, A&A, 319, 52

Véron-Cetty, M.-P. & Véron, P. 2010, A&A, 518, A10

Xanthopoulos, E., Muxlow, T. W. B., Thomasson, P., & Garrington, S. T. 2004, MNRAS, 353, 1117

Zaw, I., Farrar, G. R., & Greene, J. E. 2009, ApJ, 696, 1218

Appendix A: Tables

Table A.1: Observational details.

Name	Instrument	ObsID	Date	R ($''$)	Net Exptime (ksec)	Counts	$\log(L_{UV})$ (erg/s)	Filter
(1)	(2)	(3)	(4)	(5)	(6)	(7)	(8)	(9)
MARK 348	*XMM*–Newton	0067540201	2002-07-18	25	18.5	39552	-	
	XMM–Newton	0701180101	2013-01-04	25	7.2	5681	-	
NGC 424	*XMM*–Newton	0002942301[c]	2001-12-10	20	4.5	1777	-	
	XMM–Newton	0550950101	2008-12-07	20	127.5	33452	-	
	Chandra	3146[c]	2002-02-04	2	9.2	1266	-	
MARK 573	*Chandra*	7745[c]	2006-11-18	2	38.1	3181	-	
	Chandra	13124	2010-09-17	2	52.4	3456	-	
	XMM–Newton	0200430701[c]	2004-01-15	20	9.0	3605	42.75±0.01	UVW1
							42.50±0.05	UVW2
NGC 788	*XMM*–Newton	0601740201[c]	2010-01-15	20	12.0	4464	-	
	Chandra	11680[c]	2009-09-06	3	13.6	1155	-	
ESO 417-G06	*XMM*–Newton	0602560201	2009-07-11	20	5.9	2273	-	
	XMM–Newton	0602560301	2009-08-20	20	6.1	2031	-	
MARK 1066	*Chandra*	4075[c]	2003-07-14	3	19.9	807	-	
	XMM–Newton	0201770201	2005-02-20	20	7.6	974	-	
3C 98.0	*XMM*–Newton	0064600101	2002-09-07	20	9.5	2453	41.94±0.08	UVW1
	XMM–Newton	0064600301[c]	2003-02-05	20	2.9	422	41.99±0.07	UVW1
	Chandra	10234[c]	2008-12-24	2	31.7	1353	-	
MARK 3	*XMM*–Newton	0111220201	2000-10-19	30	35.2	30700	-	
	XMM–Newton	0009220601	2001-03-20	30	4.3	3471	-	
	XMM–Newton	0009220701	2001-03-28	30	3.1	2465	-	
	XMM–Newton	0009220901	2001-09-12	30	0.9	708	-	
	XMM–Newton	0009220401	2002-03-10	30	2.7	2215	-	
	XMM–Newton	0009220501	2002-03-25	30	4.3	3512	-	
	XMM–Newton	0009221601	2002-09-16	30	1.3	1042	-	
MARK 1210	*Chandra*	4875	2004-03-04	2	10.4	1998	-	
	Chandra	9264	2008-02-15	2	9.8	2052	-	
	Chandra	9265	2008-02-15	2	9.4	1873	-	
	Chandra	9266	2008-02-15	2	9.4	1752	-	
	Chandra	9268	2008-03-06	2	9.8	1608	-	
NGC 3079	*Chandra*	2038[c]	2001-03-07	4	27	414	-	
	XMM–Newton	0110930201[c]	2001-04-13	25	5	1112	-	
IC 2560	*XMM*–Newton	0203890101[c]	2003-12-26	20	70.7	7694	-	
	Chandra	4908[c]	2004-02-16	3	55.4	1583	-	
NGC 3393	*Chandra*	4868[c]	2004-02-28	5	29.3	1971	-	
	Chandra	12290	2011-03-12	5	69.2	3716	-	
	XMM–Newton	0140950601[c]	2003-07-05	20	10.1	2759	-	
NGC 4507	*XMM*–Newton	0006220201	2001-01-04	30	32.3	35004	-	
	XMM–Newton	0653870201	2010-06-24	30	15.1	11977	-	
	XMM–Newton	0653870301	2010-07-03	30	12.1	9574	-	
	XMM–Newton	0653870401[c]	2010-07-13	30	12.2	10023	-	
	XMM–Newton	0653870501	2010-07-23	30	10.3	8247	-	
	XMM–Newton	0653870601	2010-08-03	30	1.0	752	-	
	Chandra	12292[c]	2010-12-02	2	39.6	9048		
NGC 4698	*XMM*–Newton	0112551101	2001-12-16	25	8	411	40.14±0.10	UVM2
	XMM–Newton	0651360401	2010-06-09	25	28	1647	40.14±0.11	UVM2
NGC 5194	*Chandra*	1622	2001-06-23	2	27	451	-	
	Chandra	3932[c]	2003-08-07	2	48	940	-	

Table A.1: (Cont.)

Name (1)	Instrument (2)	ObsID (3)	Date (4)	R (″) (5)	Net Exptime (ksec) (6)	Counts (7)	log(L_{UV}) (erg/s) (8)	Filter (9)
	Chandra	13813	2012-09-09	2	179.2	2238	-	
	Chandra	13812	2012-09-12	2	157.5	2516	-	
	Chandra	13814	2012-09-20	2	189.9	2574	-	
	Chandra	13815	2012-09-23	2	67.2	1022	-	
	Chandra	13816	2012-09-26	2	73.1	1033	-	
	XMM–Newton	0112840201^c	2003-01-15	25	17	11641	40.94±0.01	UVW1
	XMM–Newton	0212480801	2005-07-01	-	-	-	40.93±0.01	UVW1
							40.38±0.11	UVM2
							40.37±0.16	UVW2
	XMM–Newton	0303420101	2006-05-20	-	-	-	40.79±0.01	UVW1
	XMM–Newton	0303420201	2006-05-24	-	-	-	40.84±0.01	UVW1
							40.34±0.07	UVW2
	XMM–Newton	0677980701	2011-06-07	-	-	-	40.97±0.01	UVW1
							40.59±0.04	UVM2
							40.40±0.08	UVW2
	XMM–Newton	0677980801	2011-06-11	-	-	-	40.94±0.01	UVW1
							40.53±0.04	UVM2
							40.41±0.08	UVW2
MARK 268	*XMM*–Newton	0554500701	2008-07-20	20	2.3	547	42.59±0.05	UVM2
							42.93±0.01	UVW1
	XMM–Newton	0554501101	2008-07-22	20	10.5	2469	42.66±0.064	UVM2
							42.92±0.01	UVW1
MARK 273	*XMM*–Newton	0101640401^c	2002-05-07	20	17.8	1796	43.05±0.06	UVW1
	XMM–Newton	0651360301	2010-05-13	-	-	-	43.16±0.01	UVW1
	Chandra	809^c	2000-04-19	4	44.2	1633	-	
Circinus	*Chandra*	365	2000-03-14	2	5.0	1638	-	
	Chandra	9140	2008-10-26	2	48.8	15594	-	
	Chandra	10937^c	2009-12-28	2	18.3	5929	-	
	XMM–Newton	0111240101	2001-08-06	15	63.8	139614	-	
	XMM–Newton	0656580601^c	2014-03-01	15	24.1	43031	-	
NGC 5643	*XMM*–Newton	0140950101	2003-02-08	25	5.9	1419	-	
	XMM–Newton	0601420101	2009-07-25	25	16.1	4142	-	
MARK 477	*XMM*–Newton	0651100301	2010-07-21	20	7.2	1898	43.41±0.01	UVW1
	XMM–Newton	0651100401	2010-07-23	20	6.5	1761	43.43±0.01	UVW1
IC 4518A	*XMM*–Newton	0401790901	2006-08-07	20	7.5	2082	-	
	XMM–Newton	0406410101	2006-08-15	20	21.1	4003	-	
ESO 138-G01	*XMM*–Newton	0405380201	2007-02-16	20	10.5	4454	-	
	XMM–Newton	0690580101	2013-02-24	20	7.7	3179	-	
NGC 6300	*Chandra*	10292^c	2009-06-10	2	9.8	3686	-	
	Chandra	10293	2009-06-14	2	9.8	3331	-	
	XMM–Newton	0059770101^c	2001-03-02	20	34.9	919	-	
NGC 7172	*XMM*–Newton	0147920601	2002-11-18	25	10.9	19949	-	
	XMM–Newton	0202860101	2004-11-11	25	18.1	31517	-	
	XMM–Newton	0414580101	2007-04-24	25	26.9	92998	-	
NGC 7212	*XMM*–Newton	0200430201^c	2004-05-20	20	9.6	1365	Not detected	
	Chandra	4078^c	2003-07-22	3	19.9	682	-	
NGC 7319	*Chandra*	789	2000-07-09	3	19.7	880	-	
	Chandra	7924^c	2007-08-17	3	93.2	3796	-	
	XMM–Newton	0021140201^c	2001-12-07	20	32.3	5839	Not detected	

Table A.1: (Cont.)

Name	Instrument	ObsID	Date	R	Net Exptime	Counts	log(L_{UV})	Filter
				($''$)	(ksec)		(erg/s)	
(1)	(2)	(3)	(4)	(5)	(6)	(7)	(8)	(9)

Notes. (Col. 1) name, (Col. 2) instrument, (Col. 3) obsID, (Col. 4) date, (Col. 5) aperture radius for the nuclear extraction, (Col. 6) net exposure time, (Col. 7) number of counts in the 0.5-10 keV band, (Cols. 8 and 9) UV luminosity from the optical monitor and filter. The *c* represents data from different instruments that were compared as explained in Sect. 4.2.

Table A.2: Final compilation of the best-fit models for the sample, including the individual best-fit model for each observation, and the simultaneous best-fit model with the varying parameters.

Analysis	ObsID	Model	N_{H1}	N_{H2}	kT	Γ	$Norm_1$	$Norm_2$	$\chi^2/d.o.f$
					keV		(10^{-4})	(10^{-4})	F-test
(1)	(2)	(3)	(4)	(5)	(6)	(7)	(8)	(9)	(10)
MARK 348									
Ind	0067540201*	ME2PL	$0.00^{0.03}_{0.00}$	$13.40^{13.61}_{12.94}$	$0.18^{0.20}_{0.14}$	$1.50^{1.56}_{1.44}$	$0.59^{0.63}_{0.55}$	$80.76^{101.65}_{80.76}$	1281.96/1132
Ind	0701180101	ME2PL	-	$12.89^{14.12}_{11.74}$	$0.20^{0.23}_{0.18}$	$1.42^{1.58}_{1.26}$	$0.37^{0.49}_{0.37}$	$23.81^{32.79}_{17.39}$	219.05/227
SMF1	0067540201	ME2PL	-	$13.29^{13.70}_{12.90}$	$0.19^{0.21}_{0.18}$	$1.50^{1.56}_{1.44}$	$0.54^{0.57}_{0.50}$	$88.49^{98.95}_{79.91}$	1520.54/1368
	0701180101							$27.17^{30.49}_{24.37}$	0
NGC 424									
Ind	0002942301*	2ME2PL	-	$34.89^{51.68}_{23.92}$	$0.07^{0.09}_{0.06}(0.65^{0.72}_{0.58})$	$1.49^{1.91}_{1.07}$	$0.48^{0.85}_{0.48}$	$4.21^{10.69}_{1.44}$	66.80/54
Ind	0550950101	2ME2PL	-	$45.55^{51.01}_{41.29}$	$0.10^{0.11}_{0.09}$ $(0.71^{0.72}_{0.70})$	$2.03^{2.10}_{1.93}$	$0.74^{0.83}_{0.74}$	$11.47^{13.75}_{9.26}$	1165.90/532
Ind	3146	2ME2PL	-	$17.12^{22.84}_{13.14}$	$0.10^{0.15}_{0.08}$ $(0.71^{0.84}_{0.60})$	$2.35^{2.63}_{1.94}$	$0.68^{1.01}_{0.68}$	$13.76^{23.77}_{6.62}$	48.02/37
SMF0	0002942301/3146	2ME2PL	-	$24.49^{31.94}_{18.65}$	$0.09\,^{0.10}_{0.07}$ $(0.67\,^{0.73}_{0.61})$	$1.82^{2.15}_{1.46}$ †	$0.72\,^{0.88}_{0.58}$	$6.70^{13.11}_{3.11}$	138.97/103
MARK 573									
Ind	7745	2ME2PL	-	$33.28^{98.24}_{15.65}$	$0.13^{0.15}_{0.11}$ $(0.71^{0.76}_{0.66})$	$2.50^{2.78}_{2.02}$	$0.48^{0.55}_{0.36}$	$3.97^{16.71}_{1.51}$	71.22/67
Ind	13124*	2ME2PL	-	$38.48^{68.89}_{29.40}$	$0.09^{0.13}_{0.07}$ $(0.67^{0.72}_{0.62})$	$1.92^{2.27}_{1.61}$	$0.57^{0.87}_{0.57}$	$5.18^{11.29}_{2.49}$	92.51/78
Ind	0200430701	2ME2PL	-	$17.12^{28.98}_{10.02}$	$0.14^{0.18}_{0.11}(0.73^{0.82}_{0.68})$	$3.23^{3.45}_{3.03}$	$0.66^{0.87}_{0.66}$	$9.85^{18.62}_{5.19}$	78.04/88
SMF0	All	2ME2PL	-	$45.83^{103.01}_{25.56}$	$0.10\,^{0.12}_{0.09}(0.67^{0.69}_{0.64})$	$2.12\,^{2.45}_{1.85}$ †	$0.41\,^{0.51}_{0.38}$	$2.74\,^{5.16}_{1.37}$	198.73/161
NGC 788									
Ind	0601740201*	2ME2PL	-	$50.32^{56.40}_{44.62}$	$0.11^{0.12}_{0.09}$ $(0.71^{0.76}_{0.64})$	$1.41^{1.67}_{1.15}$	$0.31^{0.47}_{0.31}$	$16.84^{30.52}_{9.18}$	199.77/154
Ind	11680	2ME2PL	-	$44.35^{53.07}_{36.55}$	$0.14^{0.17}_{0.09}$ $(0.76^{0.87}_{0.67})$	$0.61^{1.06}_{0.15}$	$0.15^{0.31}_{0.15}$	$4.10^{10.51}_{1.53}$	34.4566/39
SMF0	All(+ring)	2ME2PL	-	$46.61\,^{51.35}_{42.14}$	$0.11\,^{0.12}_{0.09}$ $(0.71^{0.75}_{0.67})$	$1.28\,^{1.51}_{1.06}$	$0.35\,^{0.41}_{0.29}$	$12.43\,^{20.51}_{7.55}$	262.36/205
ESO 417-G06									
Ind	0602560201*	MEPL	$0.77^{0.91}_{0.57}$	$5.15^{6.10}_{4.41}$	$0.13^{0.18}_{0.10}$	$1.03^{1.25}_{0.85}$	$59.98^{571.31}_{10.32}$	$4.52^{6.40}_{3.22}$	129.13/96
Ind	0602560301	MEPL	$0.72^{0.87}_{0.50}$	$7.85^{9.19}_{6.70}$	$0.19^{0.26}_{0.14}$	$1.44^{1.70}_{1.20}$	$16.28^{102.57}_{2.52}$	$8.56^{13.80}_{5.48}$	108.13/85
SMF1	0602560201	MEPL	$0.76^{0.84}_{0.62}$	$5.64\,^{6.38}_{5.01}$	$0.15^{0.19}_{0.14}$	$1.21^{1.37}_{1.07}$	$46.28^{110.75}_{9.33}$	$5.91^{7.95}_{4.57}$	249.86/189
	0602560301			$7.16^{8.02}_{6.42}$					2.6e-5
MARK 1066									
Ind	4075	ME2PL	$0.25^{0.47}_{0.13}$	$70.47^{186.87}_{18.90}$	$0.65^{0.71}_{0.59}$	$2.17^{2.40}_{1.85}$	$0.40^{1.20}_{0.40}$	$5.66^{20.92}_{0.22}$	41.68/24
Ind	0201770201*	ME2PL	$0.09^{0.19}_{0.00}$	$54.30^{106.19}_{30.42}$	$0.76^{0.86}_{0.61}$	$2.17^{2.68}_{1.57}$	$0.45^{1.05}_{0.45}$	$6.23^{19.76}_{1.74}$	27.86/35
SMF0	All	ME2PL	$0.12^{0.24}_{0.03}$	$82.29^{175.04}_{45.83}$	$0.68^{0.79}_{0.62}$	$2.02^{2.36}_{1.71}$ †	$0.53^{0.71}_{0.40}$	$7.11^{25.58}_{2.23}$	96.11/69
3C 98.0									
Ind	0064600101*	MEPL	$0.67^{0.76}_{0.57}$	$7.08^{8.28}_{6.03}$	$0.15^{0.17}_{0.12}$	$1.04^{1.27}_{0.81}$	$91.66^{337.94}_{37.02}$	$3.27^{4.95}_{2.21}$	117.19/102
Ind	0064600301	MEPL	$0.69^{1.00}_{0.52}$	$7.15^{10.52}_{4.61}$	$0.17^{0.21}_{0.11}$	$0.99^{1.64}_{0.48}$	$40.52^{138.52}_{9.40}$	$1.75^{5.60}_{0.70}$	7.30/12
Ind	10234	MEPL	$1.34^{2.02}_{0.00}$	$7.07^{9.09}_{5.56}$	$0.21^{0.25}_{0.10}$	$1.04^{1.48}_{0.66}$	$13.04^{662.07}_{0.25}$	$1.73^{4.18}_{0.90}$	64.69/53
SMF1	0064600101	MEPL	$0.69^{0.77}_{0.61}$	$7.08^{8.20}_{6.11}$	$0.14^{0.17}_{0.13}$	$1.02^{1.23}_{0.83}$	$92.50^{231.65}_{36.51}$	$3.22^{4.75}_{2.24}$	127.89/122
	0064600301							$1.85^{2.74}_{1.27}$	6.1e-19
MARK 3									
Ind	0111220201*	2ME2PL	-	$44.07^{47.24}_{41.14}$	$0.16^{0.17}_{0.14}$ $(0.69^{0.71}_{0.67})$	$1.25^{1.33}_{1.17}$	$1.54^{1.74}_{1.54}$	$15.89^{19.10}_{13.17}$	934.21/789
Ind	0009220601	2ME2PL	-	$43.05^{53.76}_{34.88}$	$0.12^{0.18}_{0.09}$ $(0.67^{0.73}_{0.63})$	$1.37^{1.62}_{1.12}$	$1.38^{2.01}_{1.38}$	$14.55^{25.44}_{8.03}$	162.96/134
Ind	0009220701	2ME2PL	-	$38.53^{53.89}_{28.53}$	$0.11^{0.18}_{0.06}$ $(0.79^{0.86}_{0.73})$	$1.54^{1.84}_{1.21}$	$1.43^{2.30}_{1.42}$	$18.14^{34.58}_{8.68}$	93.31/93
Ind	0009220901	2ME2PL	-	$24.25^{92.09}_{10.54}$	$0.12^{0.19}_{0.07}$ $(0.59^{0.69}_{0.46})$	$0.97^{1.61}_{0.31}$	$0.78^{2.03}_{0.78}$	$3.48^{14.84}_{0.31}$	10.50/21

Table A.2: (Cont.)

Analysis	ObsID	Model	N_{H1}	N_{H2}	kT	Γ	$Norm_1$	$Norm_2$	$\chi^2/d.o.f$
					keV		(10^{-4})	(10^{-4})	F-test
(1)	(2)	(3)	(4)	(5)	(6)	(7)	(8)	(9)	(10)
Ind	0009220401	2ME2PL	-	$45.36^{67.96}_{30.98}$	$0.12^{0.17}_{0.08}$ $(0.67^{0.77}_{0.61})$	$1.30^{1.60}_{0.99}$	$1.38^{2.18}_{1.38}$	$11.89^{23.91}_{5.51}$	119.22/81
Ind	0009220501	2ME2PL	-	$34.51^{44.58}_{26.80}$	$0.18^{0.21}_{0.14}$ $(0.68^{0.79}_{0.63})$	$1.31^{1.58}_{1.04}$	$1.32^{1.95}_{1.32}$	$10.36^{18.73}_{5.36}$	141.61/135
Ind	0009221601	2ME2PL	-	$53.09^{97.46}_{30.30}$	$0.13^{0.18}_{0.07}$ $(0.73^{0.82}_{0.65})$	$1.17^{1.59}_{0.75}$	$1.11^{2.21}_{1.11}$	$9.95^{27.66}_{2.93}$	41.96/35
SMF1	0111220201	2ME2PL	-	$43.26^{45.99}_{40.72}$	$0.15^{0.17}_{0.15}$ $(0.69^{0.71}_{0.68})$	$1.28^{1.34}_{1.21}$ †	$1.66^{1.74}_{1.57}$	$16.47^{19.22}_{14.07}$	1560.36/1354
	0009220601							$11.75^{14.10}_{9.73}$	5.6e-28
	0009220701							$11.29^{13.68}_{9.23}$	
	0009220901							$11.68^{14.87}_{8.90}$	
	0009220401							$10.86^{13.21}_{8.82}$	
	0009220501							$11.16^{13.42}_{9.21}$	
	0009221601							$10.42^{13.15}_{8.06}$	
					MARK 1210				
Ind	4875	2ME2PL	$1.29^{2.76}_{0.00}$	$22.72^{28.05}_{17.72}$	$0.20^{0.23}_{0.18}$ $(1.00^{1.09}_{0.84})$	$1.01^{1.41}_{0.78}$	$0.62^{2.60}_{0.62}$	$17.54^{64.50}_{5.36}$	97.40/75
Ind	9264*	2ME2PL	-	$19.71^{21.03}_{16.00}$	$0.21^{0.25}_{0.18}$ $(0.83^{3.37}_{0.00})$	$0.98^{1.14}_{0.63}$	$0.43^{0.96}_{0.00}$	$6.72^{21.94}_{6.72}$	110.80/78
Ind	9265	2ME2PL	$1.18^{1.98}_{0.10}$	$33.39^{38.54}_{25.79}$	$0.20^{0.24}_{0.15}$ $(0.82^{0.94}_{0.72})$	$1.94^{2.44}_{1.14}$	$1.61^{3.44}_{0.63}$	$29.30^{255.59}_{29.30}$	71.09/69
Ind	9266	2ME2PL	$0.65^{1.42}_{0.00}$	$29.43^{35.07}_{24.21}$	$0.14^{0.19}_{0.05}$ $(0.66^{0.79}_{0.59})$	$2.00^{2.61}_{1.46}$	$1.31^{2.81}_{0.62}$	$32.02^{295.37}_{32.02}$	66.41/64
Ind	9268	2ME2PL	-	$29.13^{33.38}_{25.21}$	$0.07^{0.20}_{0.02}$ $(0.77^{0.87}_{0.63})$	$1.62^{2.24}_{1.25}$	$0.61^{1.10}_{0.61}$	$39.88^{89.44}_{15.67}$	82.76/58
SMF2	4875	2ME2PL	-	$21.16^{23.64}_{18.87}$	$0.18^{0.20}_{0.15}(0.81^{0.87}_{0.75})$	$1.29^{1.48}_{1.11}$	$0.57^{0.65}_{0.50}$	$14.93^{22.44}_{10.71}$	496.50/384
	9264			$22.74^{25.15}_{20.53}$				$24.72^{37.28}_{17.72}$	8.2e-19
	9265			$26.40^{29.05}_{23.93}$				$26.67^{18.37}_{38.79}$	1.6e-8
	9266			$23.33^{25.83}_{21.00}$				$21.58^{14.81}_{31.47}$	
	9268			$26.31^{29.62}_{23.30}$				$16.73^{24.45}_{11.44}$	
					NGC 3079				
Ind	2038	MEPL	$1.76^{2.06}_{1.47}$	$8.74^{30.63}_{0.00}$	$0.91^{1.16}_{0.73}$	<1.41	$2.22^{3.26}_{1.72}$	$0.24^{28.65}_{0.07}$	21.02/20
Ind	0110930201	MEPL	$0.65^{0.88}_{0.44}$	$0.00^{0.03}_{0.00}$	$0.25^{0.38}_{0.18}$	$1.52^{1.72}_{1.36}$	$11.26^{89.45}_{2.54}$	$0.61^{0.70}_{0.51}$	43.91/54
					IC 2560				
Ind	0203890101*	2ME2PL	-	$34.00^{44.64}_{26.38}$	$0.09^{0.09}_{0.07}$ $(0.58^{0.61}_{0.50})$	$1.32^{1.55}_{1.09}$	$0.13^{0.19}_{0.13}$	$0.83^{1.38}_{0.47}$	298.27/247
Ind	4908	2ME2PL	-	$26.99^{43.33}_{17.12}$	$0.11^{0.15}_{0.09}$ $(0.59^{0.65}_{0.35})$	$1.28^{1.78}_{0.85}$	$0.10^{0.17}_{0.09}$	$0.53^{1.45}_{0.17}$	87.87/51
SMF0	All(+ring)	2ME2PL	-	$31.42^{39.74}_{25.13}$	$0.09^{0.09}_{0.07}$ $(0.60^{0.62}_{0.57})$	$1.28^{1.52}_{1.03}$	$0.12^{0.15}_{0.10}$	$0.67^{1.14}_{0.38}$	387.65/309
					NGC 3393				
Ind	4868	2ME2PL	$0.00^{0.05}_{0.00}$	$32.57^{120.39}_{13.65}$	$0.14^{0.16}_{0.10}$ $(0.59^{0.65}_{0.52})$	$2.67^{3.04}_{2.24}$	$0.36^{0.55}_{0.36}$	$4.19^{20.08}_{0.78}$	68.66/53
Ind	12290*	2ME2PL	$0.00^{0.02}_{0.00}$	$24.25^{40.24}_{13.95}$	$0.15^{0.18}_{0.12}$ $(0.69^{0.72}_{0.64})$	$2.72^{2.99}_{2.37}$	$0.43^{0.60}_{0.43}$	$4.33^{7.97}_{2.21}$	144.84/88
Ind	0140950601	2ME2PL	$0.00^{0.24}_{0.00}$	$21.30^{775.71}_{8.06}$	$0.11^{0.12}_{0.09}$ $(0.58^{0.62}_{0.52})$	$2.20^{2.89}_{1.35}$	$0.20^{0.59}_{0.19}$	$1.26^{4.35}_{0.20}$	85.17/76
SMF0	All	2ME2PL	-	$27.77^{42.19}_{18.92}$	$0.15^{0.16}_{0.12}$ $(0.65^{0.69}_{0.61})$	$2.68^{2.89}_{2.43}$ †	$0.50^{0.56}_{0.43}$	$4.26^{7.18}_{2.43}$	232.76/153
					NGC 4507				
Ind	0006220201*	2ME2PL	-	$41.77^{43.11}_{40.45}$	$0.12^{0.14}_{0.11}$ $(0.62^{0.64}_{0.59})$	$1.62^{1.70}_{1.53}$	$1.07^{1.14}_{1.00}$	$75.80^{108.71}_{75.80}$	1117.20/987
Ind	0653870201	2ME2PL	-	$47.09^{50.49}_{43.84}$	$0.12^{0.15}_{0.11}$ $(0.64^{0.67}_{0.60})$	$1.24^{1.39}_{1.09}$	$0.83^{1.04}_{0.82}$	$23.56^{33.00}_{16.75}$	438.97/420
Ind	0653870301	2ME2PL	-	$50.08^{54.24}_{46.11}$	$0.11^{0.13}_{0.10}$ $(0.65^{0.68}_{0.61})$	$1.09^{1.26}_{0.93}$	$0.76^{0.98}_{0.75}$	$20.61^{29.98}_{14.10}$	440.94/344
Ind	0653870401	2ME2PL	-	$43.00^{46.80}_{39.40}$	$0.15^{0.17}_{0.13}$ $(0.69^{0.75}_{0.65})$	$0.96^{1.18}_{0.79}$	$0.68^{0.88}_{0.68}$	$13.90^{20.19}_{9.51}$	398.38/363
Ind	0653870501	2ME2PL	-	$46.19^{50.42}_{42.22}$	$0.12^{0.16}_{0.11}$ $(0.61^{0.65}_{0.57})$	$1.18^{1.35}_{1.00}$	$0.79^{1.05}_{0.79}$	$22.03^{32.92}_{14.62}$	346.92/299
Ind	0653870601	2ME2PL	-	$27.56^{40.28}_{15.78}$	$0.14^{0.20}_{0.08}$ $(0.75^{0.89}_{0.63})$	$0.77^{1.63}_{-0.07}$	$0.22^{0.94}_{0.22}$	$6.47^{37.34}_{0.85}$	20.13/21
Ind	12292	2ME2PL	-	$44.68^{47.46}_{42.02}$	$0.15^{0.17}_{0.14}$ $(0.73^{0.78}_{0.66})$	$0.84^{1.00}_{0.69}$	$0.63^{0.80}_{0.62}$	$19.74^{27.37}_{14.19}$	393.04/287
SMF2	0006220201	2ME2PL	-	$38.51^{39.63}_{37.42}$	$0.12^{0.13}_{0.12}$ $(0.63^{0.65}_{0.62})$	$1.34^{1.40}_{1.27}$	$0.93^{0.98}_{0.88}$	$48.16^{55.11}_{42.04}$	2891.79/2482
	0653870201			$48.45^{51.45}_{45.63}$				$30.92^{36.10}_{26.47}$	0
	0653870301			$49.56^{52.97}_{46.37}$				$33.06^{38.77}_{28.18}$	1.1e-13
	0653870401			$46.23^{49.45}_{43.23}$				$33.16^{38.82}_{28.32}$	
	0653870501			$46.52^{50.03}_{43.26}$				$30.99^{36.41}_{26.38}$	
	0653870601			$37.01^{47.70}_{28.95}$				$23.42^{31.84}_{17.47}$	
					NGC 4698				
Ind	0112551101	PL	$0.00^{0.03}_{0.00}$	-	-	$2.16^{2.41}_{1.98}$	-	-	16.12/11
		2PL	-	$7.45^{17.35}_{2.20}$	-	$2.44^{2.80}_{2.21}$	$0.20^{0.23}_{0.17}$	$0.75^{1.25}_{0.21}$	8.01/9

Table A.2: (Cont.)

Analysis (1)	ObsID (2)	Model (3)	N_{H1} (4)	N_{H2} (5)	kT keV (6)	Γ (7)	$Norm_1$ (10^{-4}) (8)	$Norm_2$ (10^{-4}) (9)	$\chi^2/d.o.f$ F-test (10)
Ind	0651360401*	2PL	-	$11.11^{16.21}_{6.99}$	-	$2.13^{2.27}_{2.00}$	$0.22^{0.23}_{0.21}$	$0.74^{1.02}_{0.48}$	75.70/53
SMF0	All	2PL	-	$9.84^{14.24}_{6.69}$		$2.19^{2.33}_{2.08}$	$0.22^{0.23}_{0.21}$	$0.70^{0.97}_{0.50}$	92.73/70
NGC 5194									
Ind	1622	ME2PL	$0.01^{0.26}_{0.00}$	$10.42^{100.05}_{0.00}$	$0.64^{0.70}_{0.57}$	$2.68^{3.01}_{2.23}$	$0.00^{0.23}_{0.00}$	$0.22^{493.63}_{0.00}$	10.38/8
Ind	3932	ME2PL	$0.00^{0.10}_{0.00}$	$36.13^{152.06}_{24.54}$	$0.66^{0.70}_{0.61}$	$2.32^{2.96}_{2.12}$	$0.08^{0.12}_{0.08}$	$0.97^{3.67}_{0.22}$	35.93/27
Ind	13813	ME2PL	-	$60.36^{98.94}_{27.81}$	$0.64^{0.66}_{0.61}$	$1.92^{2.10}_{1.72}$	$0.06^{0.08}_{0.06}$	$0.90^{2.12}_{0.37}$	62.16/70
Ind	13812	ME2PL	$0.14^{0.28}_{0.00}$	$24.53^{123.81}_{15.73}$	$0.65^{0.68}_{0.61}$	$3.04^{3.87}_{2.05}$	$0.08^{0.24}_{0.08}$	$1.91^{6.69}_{0.53}$	83.06/65
Ind	13814*	ME2PL	$0.06^{0.16}_{0.00}$	$41.09^{56.65}_{30.76}$	$0.62^{0.64}_{0.59}$	$2.52^{3.10}_{2.07}$	$0.06^{0.13}_{0.06}$	$1.91^{5.31}_{0.71}$	87.12/68
Ind	13815	ME2PL	$0.01^{0.11}_{0.00}$	$70.97^{96.19}_{35.84}$	$0.67^{0.72}_{0.63}$	$2.40^{3.10}_{2.23}$	$0.09^{0.18}_{0.09}$	$3.40^{17.48}_{0.06}$	20.00/31
Ind	13816	ME2PL	$0.00^{0.20}_{0.00}$	$152.21^{201.29}_{67.83}$	$0.60^{0.64}_{0.56}$	$2.06^{3.36}_{1.39}$	$0.06^{0.09}_{0.06}$	$11.58^{96.47}_{1.16}$	55.55/29
Ind	0112840201	2ME2PL	$0.00^{0.04}_{0.00}$	$12.01^{14.77}_{9.82}$	$0.15^{0.19}_{0.12}$ $(0.60^{0.61}_{0.59})$	$2.81^{3.08}_{2.59}$	$0.70^{0.94}_{0.70}$	$8.69^{14.93}_{5.82}$	177.67/207
SMF0	All	ME2PL	$0.00^{0.05}_{0.00}$	$48.69^{68.60}_{35.14}$	$0.64^{0.65}_{0.63}$	$2.14^{2.43}_{2.08}$ †	$0.08^{0.09}_{0.07}$	$1.03^{1.81}_{0.70}$	448.67/358
MARK 268									
Ind	0554500701	2PL	$0.10^{0.24}_{0.00}$	$35.25^{43.55}_{28.41}$	-	$2.49^{3.26}_{1.83}$	$0.47^{0.74}_{0.31}$	$91.33^{409.21}_{26.18}$	12.07/17
		ME2PL	$0.13^{1.76}_{0.00}$	$31.86^{45.21}_{24.47}$	$0.57^{0.88}_{0.32}$	$2.11^{3.07}_{1.35}$	$0.15^{1.70}_{0.15}$	$42.96^{311.67}_{10.25}$	6.52/15
Ind	0554501101*	ME2PL	$0.01^{0.09}_{0.00}$	$34.27^{39.16}_{30.47}$	$0.81^{0.89}_{0.69}$	$1.70^{2.05}_{1.48}$	$0.22^{0.30}_{0.18}$	$11.84^{39.96}_{11.83}$	104.44/99
SMF0	All	ME2PL	$0.02^{0.09}_{0.00}$	$33.65^{37.93}_{30.26}$	$0.78^{0.86}_{0.64}$	$1.75^{2.06}_{1.51}$	$0.24^{0.31}_{0.19}$	$20.82^{40.42}_{12.52}$	124.87/124
MARK 273									
Ind	0101640401*	ME2PL	-	$58.46^{75.12}_{43.97}$	$0.67^{0.74}_{0.61}$	$1.91^{2.07}_{1.74}$	$0.27^{0.34}_{0.27}$	$6.19^{9.71}_{3.73}$	81.61/64
		2ME2PL	-	$59.94^{78.44}_{43.57}$	$0.26^{0.40}_{0.16}$ $(0.74^{0.88}_{0.64})$	$1.66^{1.93}_{1.32}$	$0.19^{0.31}_{0.19}$	$3.78^{7.18}_{1.63}$	77.53/62
Ind	809	2ME2PL	$0.42^{1.10}_{0.17}$	$45.11^{52.33}_{39.00}$	$0.04^{0.16}_{0.02}$ $(0.81^{0.94}_{0.73})$	$2.30^{3.07}_{1.76}$	$0.26^{0.70}_{0.26}$	$20.70^{107.25}_{8.06}$	56.07/58
SMF1	0101640401	2ME2PL	-	$78.85^{90.96}_{67.72}$	$0.01^{0.15}_{0.01}$ $(0.88^{0.99}_{0.82})$	$1.33^{1.46}_{1.17}$	$0.17^{0.19}_{0.15}$	$2.86^{3.85}_{2.09}$	193.34/131
	809			$38.43^{43.94}_{33.42}$					
Circinus									
Ind	365	2ME2PL	-	$60.04^{81.16}_{33.78}$	1.05^{0}_{0} (0.44^{0}_{0})	$0.98^{1.23}_{0.75}$	$2.45^{3.51}_{2.45}$	$14.15^{25.59}_{5.09}$	130.43/58
Ind	9140*	2ME2PL	-	$41.33^{46.73}_{36.55}$	$0.07^{0.34}_{0.03}$ $(0.71^{0.77}_{0.64})$	$1.00^{1.10}_{0.91}$	$2.76^{3.20}_{2.76}$	$13.34^{16.57}_{10.80}$	965.62/397
Ind	10937	2ME2PL	-	$54.02^{67.25}_{43.53}$	0.07^{0}_{0} $(0.75^{0.94}_{0.63})$	$0.88^{1.01}_{0.70}$	$2.29^{2.93}_{2.29}$	$15.15^{21.23}_{10.62}$	476.34/198
Ind	0111240101*	2ME2PL	-	$39.33^{44.20}_{35.06}$	$0.11^{0.13}_{0.10}$ $(0.59^{0.61}_{0.57})$	$1.35^{1.38}_{1.33}$	$14.69^{15.40}_{14.69}$	$14.52^{16.47}_{12.72}$	2661.99/1584
Ind	0656580601	2ME2PL	-	$46.28^{49.26}_{44.78}$	$0.02^{0.40}_{0.01}$ $(0.61^{0.63}_{0.59})$	$1.31^{1.33}_{1.30}$	$9.43^{9.69}_{9.43}$	$40.08^{46.79}_{34.17}$	2193.02/1090
SMF0	All (*Chandra*)	2ME2PL	-	$39.70^{46.17}_{34.50}$	$0.14^{0.227}_{0.04}$ $(0.72^{0.84}_{0.65})$	$0.63^{0.73}_{0.53}$ †	$1.86^{2.03}_{1.69}$	$5.70^{7.20}_{4.42}$	1114.28/673
SMF2	0111240101	2ME2PL	-	$42.56^{46.27}_{39.17}$	$0.11^{0.12}_{0.08}$ $(0.62^{0.63}_{0.60})$	$1.34^{1.37}_{1.31}$	$14.35^{14.68}_{14.03}$	$15.79^{17.63}_{14.06}$	4410.83/2682
	0656580601						$9.48^{9.75}_{9.23}$	$22.93^{25.11}_{20.90}$	1.2e-255
									1.8e-13
NGC 5643									
Ind	0140950101	2ME2PL	-	$87.04^{221.48}_{37.68}$	$0.16^{0.19}_{0.14}$ $(0.68^{0.77}_{0.62})$	$0.99^{1.42}_{0.60}$	$0.20^{0.41}_{0.20}$	$1.90^{11.03}_{0.37}$	35.98/46
Ind	0601420101*	2ME2PL	-	$35.23^{51.46}_{25.63}$	$0.09^{0.11}_{0.08}$ $(0.59^{0.63}_{0.51})$	$1.51^{1.82}_{1.21}$	$0.41^{0.63}_{0.41}$	$2.81^{5.35}_{1.40}$	184.91/139
SMF0	All	2ME2PL	-	$44.65^{68.03}_{30.74}$	$0.11^{0.14}_{0.09}$ $(0.61^{0.64}_{0.58})$	$1.32^{1.59}_{1.08}$ †	$0.43^{0.52}_{0.36}$	$2.26^{4.01}_{1.21}$	245.69/197
MARK 477									
Ind	0651100301*	2ME2PL	-	$25.58^{31.53}_{20.04}$	$0.15^{0.19}_{0.11}$ $(0.59^{0.74}_{0.36})$	$1.10^{1.48}_{0.71}$	$0.21^{0.36}_{0.21}$	$2.89^{6.60}_{1.17}$	55.96/63
Ind	0651100401	2ME2PL	-	$29.72^{35.63}_{24.41}$	$0.11^{0.17}_{0.07}$ $(0.50^{0.69}_{0.30})$	$1.54^{1.94}_{1.12}$	$0.28^{0.49}_{0.28}$	$8.42^{18.78}_{3.64}$	50.90/60
SMF0	All	2ME2PL	-	$27.76^{31.89}_{23.92}$	$0.15^{0.17}_{0.09}$ $(0.60^{0.69}_{0.33})$	$1.30^{1.58}_{1.02}$ †	$0.32^{0.38}_{0.26}$	$4.89^{8.84}_{2.63}$	122.47/135
IC 4518A									
Ind	0401790901	ME2PL	-	$22.85^{25.65}_{19.99}$	$0.68^{0.75}_{0.61}$	$1.94^{2.19}_{1.66}$	$0.28^{0.42}_{0.28}$	$23.18^{38.48}_{13.11}$	84.82/84
		2ME2PL	$0.58^{1.42}_{0.01}$	$21.92^{26.44}_{19.79}$	$0.18^{0.22}_{0.12}$ $(0.71^{0.79}_{0.65})$	$1.72^{2.21}_{1.29}$	$0.23^{0.76}_{0.23}$	$15.05^{36.19}_{6.64}$	69.71/82
Ind	0406410101*	2ME2PL	-	$24.65^{27.85}_{21.58}$	$0.09^{0.21}_{0.05}$ $(0.65^{0.69}_{0.60})$	$1.47^{1.72}_{1.21}$	$0.22^{0.33}_{0.22}$	$6.05^{10.42}_{3.46}$	169.18/161
SMF1	0401790901	2ME2PL	-	$22.22^{24.52}_{19.98}$	$0.16^{0.22}_{0.09}$ $(0.68^{0.76}_{0.64})$	$1.50^{1.70}_{1.29}$	$0.27^{0.31}_{0.22}$	$10.29^{15.68}_{6.70}$	258.87/254
	0406410101							$5.92^{9.08}_{3.83}$	5.2e-26
ESO 138-G01									
Ind	0405380201*	ME2PL	-	$31.43^{35.98}_{27.61}$	$0.71^{0.78}_{0.65}$	$2.31^{2.40}_{2.21}$	$1.70^{1.94}_{1.70}$	$38.74^{48.57}_{30.65}$	287.95/174
Ind	0690580101	ME2PL	-	$25.88^{30.83}_{22.91}$	$0.71^{0.84}_{0.66}$	$2.60^{2.71}_{2.49}$	$1.76^{2.04}_{1.76}$	$49.99^{66.24}_{39.89}$	211.76/126

Table A.2: (Cont.)

Analysis	ObsID	Model	N_{H1}	N_{H2}	kT keV	Γ	$Norm_1$ (10^{-4})	$Norm_2$ (10^{-4})	$\chi^2/d.o.f$ F-test
(1)	(2)	(3)	(4)	(5)	(6)	(7)	(8)	(9)	(10)
SMF0	All	ME2PL	-	$29.82^{32.26}_{26.29}$	$0.71^{0.77}_{0.68}$	$2.42^{2.50}_{2.35}$ †	$1.85^{1.94}_{1.75}$	$43.38^{51.19}_{36.05}$	521.97/310
					NGC 6300				
Ind	10292*	2PL	$0.00^{0.42}_{0.00}$	$14.06^{15.37}_{12.14}$	-	$0.77^{0.99}_{0.42}$	$0.12^{0.16}_{0.08}$	$17.51^{29.15}_{10.86}$	145.61/131
Ind	10293	2PL	-	$19.83^{21.17}_{17.11}$	-	$1.48^{1.69}_{1.07}$	$0.13^{0.17}_{0.10}$	$76.69^{113.25}_{35.41}$	130.28/121
Ind	0059770101	2PL	-	$25.41^{29.69}_{21.70}$	-	$2.19^{2.65}_{1.78}$	$0.02^{0.02}_{0.01}$	$5.64^{13.89}_{2.52}$	29.26/35
SMF0	All	2PL	-	$16.46^{17.85}_{15.32}$	-	$1.02^{1.26}_{0.86}$	$0.12^{0.15}_{0.10}$	$32.70^{51.16}_{24.19}$	304.19/260
					NGC 7172				
Ind	0147920601	ME2PL	$0.00^{0.05}_{0.00}$	$8.45^{8.81}_{8.12}$	$0.35^{0.57}_{0.27}$	$1.52^{1.58}_{1.44}$	$0.23^{0.33}_{0.23}$	$61.18^{69.78}_{53.78}$	655.26/682
Ind	0202860101	ME2PL	-	$8.75^{9.02}_{8.48}$	$0.20^{0.25}_{0.17}$	$1.56^{1.62}_{1.50}$	$0.30^{0.34}_{0.27}$	$57.43^{70.75}_{57.43}$	943.47/1046
Ind	0414580101*	ME2PL	-	$8.34^{8.50}_{8.19}$	$0.28^{0.51}_{0.19}$	$1.65^{1.68}_{1.61}$	$0.31^{0.39}_{0.31}$	$152.90^{162.22}_{143.87}$	1482.81/1454
SMF1	0147920601	ME2PL	-	$8.43^{8.56}_{8.31}$	$0.26^{0.31}_{0.24}$	$1.61^{1.63}_{1.58}$	$0.30^{0.32}_{0.28}$	$70.73^{74.30}_{67.35}$	3198.23/3200
	0202860101							$66.95^{70.30}_{63.78}$	0
	0414580101							$145.45^{152.64}_{138.64}$	
					NGC 7212				
Ind	0200430201*	2ME2PL	-	$118.96^{264.77}_{54.65}$	$0.16^{0.20}_{0.11}$ $(0.66^{0.78}_{0.58})$	$0.64^{0.91}_{0.39}$	$0.15^{0.25}_{0.15}$	$1.42^{8.63}_{0.28}$	57.77/46
Ind	4078	2ME2PL	-	$34.50^{46.59}_{28.60}$	$0.01^{0.83}_{0.00}$ $(0.49^{0.65}_{0.26})$	$1.22^{1.36}_{1.14}$	$0.19^{0.24}_{0.19}$	$2.66^{7.05}_{0.94}$	45.19/19
SMF0	All(+ring)	2ME2PL	-	$81.67^{124.96}_{51.53}$	$0.12^{0.17}_{0.08}$ $(0.59^{0.66}_{0.52})$	$0.80\,^{1.04}_{0.57}$ †	$0.17^{0.21}_{0.14}$	$1.43\,^{2.92}_{0.62}$	106.34/77
					NGC 7319				
Ind	789	ME2PL	-	$39.11^{48.43}_{33.65}$	$0.85^{0.99}_{0.73}$	$1.29^{2.20}_{0.79}$	$0.08^{0.14}_{0.05}$	$4.42^{52.91}_{4.42}$	47.441/31
Ind	7924*	ME2PL	-	$46.06^{49.01}_{43.15}$	$0.65^{0.75}_{0.57}$	$2.03^{2.25}_{1.79}$	$0.19^{0.22}_{0.16}$	$40.65^{10.32}_{40.65}$	187.45/141
Ind	0021140201	2ME2PL	-	$51.88^{57.69}_{46.20}$	$0.18^{0.24}_{0.08}$ $(0.63^{0.67}_{0.60})$	$1.35^{1.63}_{1.07}$	$0.12^{0.18}_{0.11}$	$7.17^{13.38}_{3.79}$	263.86/213
SMF2	789	ME2PL	$0.65\,^{0.99}_{0.36}$	$46.87^{49.70}_{44.36}$	$0.67^{0.81}_{0.60}$	$2.03^{2.29}_{1.88}$	$0.19^{0.22}_{0.17}$	$41.72\,^{70.42}_{29.64}$	240.07/193
	7924		-					$67.87\,^{113.69}_{49.42}$	1.5e-18
									1.3e-9

Notes. (Col. 1) kind of analysis performed, where Ind refers to the individual fitting of the observation, SMF0 is the simultaneous fit without varying parametes, SMF1 the simultaneous fit varying one parameter, and SMF2 the simultaneous fit varying two parameters, (Col. 2) obsID, where the * represents the data that are used as a reference model for the simultaneous fit, (Col. 3) best-fit model, (Col. 4, 5, 6, 7, 8, and 9) parameters in the model, where N_H are in units of $10^{22} cm^{-2}$, and (Col. 10) $\chi^2/d.o.f$, and in SMFx (where x = 1,2), the result of the F-test is presented in the second line.
† The spectral index at hard energies is reported in Table A.7 for Compton-thick candidates.

Table A.3: X-ray luminosities.

			Individual		Simultaneous	
Name	Satellite	ObsID	log(L(0.5-2 keV))	log(L(2-10 keV))	log(L(0.5-2 keV))	log(L(2-10 keV))
(1)	(2)	(3)	(4)	(5)	(6)	(7)
MARK 348	*XMM*–Newton	0067540201	$43.01^{43.03}_{42.98}$	$43.41^{43.41}_{43.40}$	$43.01^{43.02}_{42.99}$	$43.40^{43.41}_{43.40}$
	XMM–Newton	0701180101	$42.47^{42.50}_{42.44}$	$42.89^{42.91}_{42.88}$	$42.50^{42.52}_{42.49}$	$42.90^{42.91}_{42.89}$
NGC 424	*XMM*–Newton	0002942301	$41.70^{41.72}_{41.68}$	$42.01^{42.07}_{41.93}$	$41.74^{41.76}_{41.72}$	$41.87^{41.92}_{41.81}$
	XMM–Newton	0550950101	$41.95^{41.95}_{41.94}$	$42.00^{42.01}_{41.99}$		
	Chandra (2″)	3146	$42.02^{42.06}_{41.97}$	$41.91^{41.97}_{41.83}$	$41.74^{41.76}_{41.72}$	$41.84^{41.89}_{41.79}$
	Chandra (20″)	3146	$42.00^{42.04}_{41.95}$	$41.94^{42.01}_{41.86}$		
MARK 573	*Chandra* (2″)	7745	$42.02^{42.06}_{41.98}$	$41.69^{41.77}_{41.59}$	$41.65^{41.72}_{41.56}$	$41.54^{41.59}_{41.48}$
	Chandra (20″)	7745	$42.19^{42.21}_{42.17}$	$41.87^{41.96}_{41.76}$		
	Chandra	13124	$41.94^{41.98}_{41.89}$	$41.73^{41.80}_{41.66}$	$41.64^{41.71}_{41.55}$	$41.54^{41.59}_{41.49}$
	XMM–Newton	0200430701	$42.23^{42.25}_{42.21}$	$41.61^{41.66}_{41.55}$		
NGC 788	*XMM*–Newton	0601740201	$42.23^{42.25}_{42.21}$	$42.67^{42.70}_{42.64}$	$42.11\,^{42.17}_{42.04}$	$42.63\,^{42.66}_{42.60}$
	Chandra (3″)	11680	$41.70^{41.74}_{41.66}$	$42.59^{42.71}_{42.42}$	$42.11\,^{42.17}_{42.04}$	$42.59\,^{42.62}_{42.56}$
	Chandra (20″)	11680	$41.81^{41.85}_{41.76}$	$42.70^{42.82}_{42.55}$		

Table A.3: (Cont.)

			Individual		Simultaneous	
Name (1)	Satellite (2)	ObsID (3)	log(L(0.5-2 keV)) (4)	log(L(2-10 keV)) (5)	log(L(0.5-2 keV)) (6)	log(L(2-10 keV)) (7)
ESO 417-G06	*XMM*–Newton	0602560201	$42.59^{42.66}_{42.51}$	$42.50^{42.52}_{42.48}$	$42.46^{42.59}_{42.26}$	$42.50^{42.52}_{42.48}$
	XMM–Newton	0602560301	$42.39^{42.44}_{42.33}$	$42.51^{42.53}_{42.49}$	$42.46^{42.62}_{42.21}$	$42.50^{42.52}_{42.48}$
MARK 1066	*XMM*–Newton	0201770201	$41.79^{41.82}_{41.77}$	$41.75^{41.80}_{41.70}$	$41.40^{41.42}_{41.38}$	$41.44^{41.53}_{41.33}$
	Chandra (3″)	4075	$41.68^{41.75}_{41.60}$	$41.55^{41.73}_{41.21}$	$41.39^{41.41}_{41.37}$	$41.42^{41.49}_{41.32}$
	Chandra (20″)	4075	$41.90^{41.97}_{41.81}$	$41.02^{41.19}_{40.72}$		
3C 98.0	*XMM*–Newton	0064600101	$43.28^{43.39}_{43.15}$	$42.91^{42.92}_{42.89}$	$43.14^{43.30}_{42.87}$	$42.92^{42.95}_{42.89}$
	XMM–Newton	0064600301	$43.15^{43.29}_{42.96}$	$42.68^{42.74}_{42.61}$	$43.12^{43.29}_{42.83}$	$42.68^{42.72}_{42.63}$
	Chandra (2″)	10234	$42.67^{42.80}_{42.47}$	$42.61^{42.70}_{42.48}$		
	Chandra (20″)	10234	$42.81^{42.97}_{42.56}$	$42.64^{42.74}_{42.50}$		
MARK 3	*XMM*–Newton	0111220201	$42.29^{42.30}_{42.29}$	$42.86^{42.87}_{42.86}$	$42.35^{42.36}_{42.35}$	$42.87^{42.88}_{42.86}$
	XMM–Newton	0009220601	$42.16^{42.17}_{42.14}$	$42.73^{42.77}_{42.70}$	$42.24^{42.24}_{42.23}$	$42.74^{42.76}_{42.72}$
	XMM–Newton	0009220701	$42.03^{42.05}_{42.01}$	$42.66^{42.71}_{42.61}$	$42.22^{42.23}_{42.22}$	$42.73^{42.75}_{42.70}$
	XMM–Newton	0009220901	$41.76^{41.79}_{41.72}$	$42.52^{42.59}_{42.43}$	$42.23^{42.24}_{42.23}$	$42.74^{42.79}_{42.69}$
	XMM–Newton	0009220401	$42.09^{42.11}_{42.07}$	$42.72^{42.76}_{42.67}$	$42.21^{42.22}_{42.21}$	$42.71^{42.74}_{42.68}$
	XMM–Newton	0009220501	$42.11^{42.12}_{42.09}$	$42.65^{42.68}_{42.62}$	$42.22^{42.22}_{42.21}$	$42.72^{42.75}_{42.70}$
	XMM–Newton	0009221601	$42.04^{42.07}_{42.01}$	$42.72^{42.79}_{42.63}$	$42.20^{42.20}_{42.19}$	$42.70^{42.74}_{42.65}$
MARK 1210	*Chandra*	4875	$42.25^{42.29}_{42.21}$	$42.69^{42.85}_{42.42}$	$42.19^{42.20}_{42.18}$	$42.67^{42.70}_{42.64}$
	Chandra	9264	$42.36^{42.45}_{42.24}$	$42.87^{42.99}_{42.73}$	$42.40^{42.41}_{42.38}$	$42.88^{42.91}_{42.85}$
	Chandra	9265	$42.89^{42.94}_{42.84}$	$43.02^{43.19}_{42.74}$	$42.41^{42.43}_{42.40}$	$42.90^{42.93}_{42.86}$
	Chandra	9266	$41.43^{41.52}_{41.33}$	$42.60^{42.62}_{42.58}$	$42.33^{42.34}_{42.31}$	$42.81^{42.84}_{42.77}$
	Chandra	9268	$42.57^{42.64}_{42.49}$	$42.77^{42.93}_{42.53}$	$42.22^{42.24}_{42.21}$	$42.70^{42.74}_{42.66}$
NGC 3079	*Chandra* (4″)	2038	$39.58^{39.67}_{39.46}$	$39.82^{39.90}_{39.72}$		
	Chandra (25″)	2038	$40.02^{40.10}_{39.93}$	$40.07^{40.14}_{39.99}$		
	XMM–Newton	0110930201	$39.88^{39.90}_{39.86}$	$40.08^{40.10}_{40.05}$		
IC 2560	*XMM*–Newton	0203890101	$40.72^{40.73}_{40.71}$	$41.12^{41.14}_{41.09}$	$40.57^{40.58}_{40.56}$	$41.05^{41.08}_{41.03}$
	Chandra (3″)	4908	$40.48^{40.53}_{40.44}$	$40.95^{41.02}_{40.87}$	$40.56^{40.57}_{40.55}$	$41.01^{41.04}_{40.99}$
	Chandra (20″)	4908	$40.61^{40.64}_{40.57}$	$41.01^{41.08}_{40.93}$		
NGC 3393	*Chandra* (5″)	4868	$41.63^{41.65}_{41.61}$	$41.29^{41.40}_{41.14}$	$41.64^{41.65}_{41.63}$	$41.29^{41.32}_{41.25}$
	Chandra (20″)	4868	$41.59^{41.61}_{41.57}$	$41.28^{41.36}_{41.17}$		
	Chandra	12290	$41.65^{41.67}_{41.64}$	$41.29^{41.33}_{41.24}$	$41.64^{41.65}_{41.63}$	$41.29^{41.32}_{41.25}$
	XMM–Newton	0140950601	$41.38^{41.39}_{41.36}$	$41.21^{41.37}_{40.97}$		
NGC 4507	*XMM*–Newton	0006220201	$42.79^{42.79}_{42.78}$	$43.12^{43.13}_{43.12}$	$42.55^{42.56}_{42.55}$	$43.05^{43.06}_{43.05}$
	XMM–Newton	0653870201	$42.16^{42.17}_{42.15}$	$42.82^{42.83}_{42.81}$	$41.19^{41.20}_{41.19}$	$42.34^{42.35}_{42.33}$
	XMM–Newton	0653870301	$42.20^{42.21}_{42.19}$	$42.87^{42.88}_{42.85}$	$42.40^{42.40}_{42.39}$	$42.90^{42.91}_{42.88}$
	XMM–Newton	0653870401	$42.04^{42.05}_{42.03}$	$42.81^{42.82}_{42.80}$	$41.06^{41.06}_{41.05}$	$42.39^{42.40}_{42.37}$
	XMM–Newton	0653870501	$42.20^{42.21}_{42.18}$	$42.84^{42.85}_{42.82}$	$41.19^{41.20}_{41.19}$	$42.35^{42.37}_{42.34}$
	XMM–Newton	0653870601	$41.65^{41.69}_{41.61}$	$42.61^{42.72}_{42.45}$	$41.19^{41.20}_{41.19}$	$42.33^{42.37}_{42.28}$
	Chandra (2″)	12292	$42.21^{42.23}_{42.20}$	$42.99^{43.01}_{42.97}$		
	Chandra (30″)	12292	$42.24^{42.25}_{42.22}$	$43.07^{43.09}_{43.05}$		
NGC 4698	*XMM*–Newton	0112551101	$40.00^{40.05}_{39.95}$	$39.97^{42.91}_{39.78}$	$40.14^{40.17}_{40.12}$	$40.08^{40.12}_{40.04}$
	XMM–Newton	0651360401	$40.22^{40.24}_{40.19}$	$40.16^{41.22}_{39.73}$	$40.14^{40.17}_{40.12}$	$40.08^{40.12}_{40.04}$
NGC 5194	*Chandra*	1622	$39.25^{39.34}_{39.15}$	$38.88^{39.12}_{38.33}$	$39.53^{39.54}_{39.52}$	$39.51^{39.54}_{39.48}$
	Chandra (2″)	3932	$39.30^{39.35}_{39.25}$	$39.21^{39.32}_{39.07}$	$39.53^{39.54}_{39.52}$	$39.51^{39.54}_{39.48}$
	Chandra (25″)	3932	$40.26^{40.28}_{40.24}$	$39.64^{39.74}_{39.50}$		
	Chandra	13813	$39.26^{39.27}_{39.24}$	$39.34^{39.41}_{39.26}$	$39.53^{39.54}_{39.52}$	$39.51^{39.54}_{39.48}$
	Chandra	13812	$40.33^{40.36}_{40.29}$	$40.39^{40.51}_{40.23}$	$39.53^{39.54}_{39.52}$	$39.51^{39.54}_{39.48}$
	Chandra	13814	$39.57^{39.60}_{39.55}$	$39.46^{39.56}_{39.34}$	$39.53^{39.54}_{39.52}$	$39.51^{39.54}_{39.48}$
	Chandra	13815	$39.79^{39.84}_{39.75}$	$39.58^{39.70}_{39.41}$	$39.53^{39.54}_{39.52}$	$39.51^{39.54}_{39.48}$
	Chandra	13816	$40.32^{40.35}_{40.30}$	$40.41^{40.55}_{40.21}$	$39.53^{39.54}_{39.52}$	$39.51^{39.54}_{39.48}$
	XMM–Newton	0112840201	$39.46^{39.47}_{39.45}$	$39.66^{39.67}_{39.65}$		

Table A.3: (Cont.)

			Individual		Simultaneous	
Name	Satellite	ObsID	log(L(0.5-2 keV))	log(L(2-10 keV))	log(L(0.5-2 keV))	log(L(2-10 keV))
(1)	(2)	(3)	(4)	(5)	(6)	(7)
MARK 268	*XMM*–Newton	0554500701	$41.29^{41.34}_{41.22}$	$43.54^{43.60}_{43.48}$	$41.45^{41.48}_{41.41}$	$42.92^{42.98}_{42.84}$
	XMM–Newton	0554501101	$41.39^{41.42}_{41.37}$	$43.42^{43.44}_{43.40}$	$41.27^{41.30}_{41.24}$	$42.92^{42.98}_{42.84}$
MARK 273	*XMM*–Newton	0101640401	$42.71^{42.73}_{42.68}$	$42.83^{42.87}_{42.80}$	$41.40^{41.41}_{41.39}$	$42.20^{42.24}_{42.16}$
	Chandra (4″)	809	$43.20^{43.24}_{43.16}$	$43.06^{43.21}_{42.83}$	$41.28^{41.30}_{41.26}$	$42.37^{42.41}_{42.33}$
	Chandra (20″)	809	$42.97^{43.00}_{42.95}$	$43.03^{43.12}_{42.93}$		
Circinus	*Chandra*	365	$39.98^{40.06}_{39.88}$	$40.76^{40.81}_{40.70}$	$39.80^{39.82}_{39.78}$	$40.60^{40.61}_{40.59}$
	Chandra	9140	$40.03^{40.05}_{40.02}$	$40.66^{40.67}_{40.65}$	$39.80^{39.82}_{39.78}$	$40.60^{40.61}_{40.59}$
	Chandra (2″)	10937	$39.98^{40.00}_{39.96}$	$40.76^{40.78}_{40.74}$	$39.80^{39.82}_{39.78}$	$40.60^{40.61}_{40.59}$
	Chandra (15″)	10937	$40.39^{40.40}_{40.38}$	$40.96^{40.98}_{40.94}$		
	XMM–Newton	0111240101	$40.49^{40.49}_{40.48}$	$40.71^{40.72}_{40.71}$	$40.50^{40.50}_{40.50}$	$40.74^{40.74}_{40.73}$
	XMM–Newton	0656580601	$40.66^{40.66}_{40.65}$	$40.83^{40.84}_{40.83}$	$40.51^{40.52}_{40.51}$	$40.76^{40.77}_{40.76}$
NGC 5643	*XMM*–Newton	0601420101	$40.51^{40.53}_{40.49}$	$40.84^{40.88}_{40.80}$	$40.44^{40.47}_{40.42}$	$40.87^{40.90}_{40.84}$
	XMM–Newton	0140950101	$40.38^{40.41}_{40.36}$	$40.98^{41.04}_{40.91}$	$40.44^{40.47}_{40.42}$	$40.87^{40.90}_{40.84}$
MARK 477	*XMM*–Newton	0651100301	$42.54^{42.56}_{42.51}$	$43.06^{43.11}_{43.01}$	$42.60^{42.62}_{42.58}$	$43.11^{43.16}_{43.06}$
	XMM–Newton	0651100401	$42.94^{42.97}_{42.91}$	$43.21^{43.2}_{43.16}$	$42.60^{42.62}_{42.58}$	$43.11^{43.16}_{43.06}$
IC 4518A	*XMM*–Newton	0401790901	$42.33^{42.35}_{42.30}$	$42.57^{42.59}_{42.54}$	$42.17^{42.19}_{42.14}$	$42.56^{42.59}_{42.52}$
	XMM–Newton	0406410101	$41.92^{41.95}_{41.89}$	$42.36^{42.38}_{42.33}$	$41.95^{41.97}_{41.92}$	$42.33^{42.36}_{42.30}$
ESO 138-G01	*XMM*–Newton	0405380201	$42.23^{42.24}_{42.22}$	$42.12^{42.14}_{42.10}$	$42.23^{42.25}_{42.22}$	$42.11^{42.13}_{42.09}$
	XMM–Newton	0690580101	$42.29^{42.30}_{42.27}$	$42.05^{42.07}_{42.02}$	$42.23^{42.25}_{42.22}$	$42.11^{42.13}_{42.09}$
NGC 6300	*Chandra* (2″)	10292	$41.05^{41.15}_{40.91}$	$41.92^{41.96}_{41.88}$	$41.32^{41.40}_{41.23}$	$41.95^{41.98}_{41.93}$
	Chandra (20″)	10292	$41.17^{41.30}_{40.98}$	$41.96^{42.01}_{41.91}$		
	Chandra	10293	$41.64^{41.75}_{41.48}$	$42.01^{42.06}_{41.95}$	$41.32^{41.40}_{41.23}$	$41.95^{41.98}_{41.93}$
	XMM–Newton	0059770101	$40.44^{40.52}_{40.35}$	$40.45^{40.48}_{40.41}$		
NGC 7172	*XMM*–Newton	0147920601	$42.30^{42.32}_{42.28}$	$42.67^{42.68}_{42.67}$	$42.35^{42.36}_{42.33}$	$42.67^{42.68}_{42.67}$
	XMM–Newton	0202860101	$42.30^{42.32}_{42.28}$	$42.66^{42.66}_{42.65}$	$42.32^{42.33}_{42.31}$	$42.65^{42.65}_{42.64}$
	XMM–Newton	0414580101	$42.68^{42.69}_{42.67}$	$42.98^{42.98}_{42.98}$	$42.66^{42.67}_{42.65}$	$42.98^{42.98}_{42.98}$
NGC 7212	*XMM*–Newton	0200430201	$41.65^{41.68}_{41.62}$	$42.58^{42.62}_{42.54}$	$41.81^{41.84}_{41.76}$	$42.63^{42.69}_{42.56}$
	Chandra (3″)	4078	$42.04^{42.08}_{42.00}$	$42.48^{43.38}_{42.45}$	$41.80^{41.84}_{41.74}$	$42.58^{42.64}_{42.52}$
	Chandra (20″)	4078	$42.06^{42.09}_{42.03}$	$42.48^{42.57}_{42.35}$		
NGC 7319	*Chandra*	789	$42.68^{42.74}_{42.62}$	$42.82^{42.96}_{42.61}$	$42.88^{42.94}_{42.81}$	$42.87^{42.90}_{42.83}$
	Chandra (3″)	7924	$43.03^{43.07}_{42.99}$	$43.06^{43.12}_{42.99}$	$43.09^{43.12}_{43.06}$	$43.08^{43.10}_{43.05}$
	Chandra (20″)	7924	$43.31^{43.33}_{43.28}$	$43.15^{43.18}_{43.12}$		
	XMM–Newton	0021140201	$42.10^{42.12}_{42.09}$	$42.58^{42.60}_{42.56}$		

Notes. (Cols. 4 and 5) soft and hard intrinsic luminosities for individual fits; (Cols. 6 and 7) soft and hard intrinsic luminosities for simultaneous fitting. Blanks mean observations that are not used for the simultaneous fittings.

Table A.4: Results for the best fit of the annular region (ring) in *Chandra* data, and the best fit obtained for the nucleus of *XMM*–Newton data when the contribution from the annular region was removed.

Name (obsID)	Region	Model	N_{H1}^{a}	N_{H2}^{a}	kT (keV)	Γ	χ_r^2	$log(L_{soft})$ (0.5-2 keV)	$log(L_{hard})$ (2-10 keV)	Cont. %
(1)	(2)	(3)	(4)	(5)	(6)	(7)	(8)	(9)	(10)	(11)
MARK 573 (7745)	Ring*	ME2PL	-	$75.90^{160.34}_{26.64}$	$0.67^{0.75}_{0.57}$	$3.86^{-}_{3.64}$	1.97	43.12	42.01	24
MARK 573 (0200430701)	Nucleus**	2ME2PL	-	$9.82^{18.25}_{5.83}$	$0.15^{0.18}_{0.14}$ $(0.76^{0.86}_{0.68})$	$3.01^{3.37}_{2.61}$	0.86	41.88	41.34	-
MARK 1066 (4075)	Ring*	PL	$0.21^{0.35}_{0.00}$	-	-	$3.99^{4.00}_{2.68}$	1.40	39.65	39.26	8
MARK 1066 (0201770201)	Nucleus**	ME2PL	$0.08^{0.16}_{0.00}$	$53.37^{110.46}_{28.95}$	$0.76^{0.87}_{0.61}$	$2.00^{2.56}_{1.50}$	0.78	41.61	41.67	-
3C 98.0 (10234)	Ring*	ME	$15.78^{27.17}_{8.21}$	-	$3.99^{0}_{1.24}$	-	4.30	41.58	41.65	8
3C 98.0 (0064600301)	Nucleus**	MEPL	$0.72^{0.94}_{0.52}$	$6.98^{9.76}_{4.45}$	$0.17^{0.21}_{0.11}$	$0.99^{1.61}_{0.43}$	0.72	42.93	42.67	-

Table A.4: (Cont.)

Name (obsID) (1)	Region (2)	Model (3)	N_{H1}^{a} (4)	N_{H2}^{a} (5)	kT (keV) (6)	Γ (7)	χ_r^2 (8)	$log(L_{soft})$ (0.5-2 keV) (9)	$log(L_{hard})$ (2-10 keV) (10)	Cont. % (11)
NGC 3079 (2038)	Ring*	MEPL	$0.01_{0.00}^{0.24}$	$0.07_{0.00}^{0.16}$	$0.65_{0.61}^{0.69}$	$2.16_{1.76}^{2.75}$	0.91	39.92	39.63	78
NGC 3079 (0110930201)	Nucleus**	MEPL	$0.59_{0.00}^{1.82}$	-	$0.23_{0.20}^{0.28}$	$1.24_{0.57}^{4.96}$	1.04	40.36	41.92	-
IC 2560 (4908)	Ring*	MEPL	-	$0.00_{0.00}^{2.18}$	$0.29_{0.21}^{0.41}$	$0.82_{0.28}^{2.92}$	1.56	39.22	39.62	11
IC 2560 (0203890101)	Nucleus**	2ME2PL	-	$33.94_{26.02}^{44.73}$	$0.09_{0.07}^{0.09}$ $(0.60_{0.57}^{0.63})$	$1.32_{1.03}^{1.60}$	1.14	40.61	41.08	-
NGC 3393 (4868)	Ring*	MEPL	$0.15_{0.00}^{0.54}$	$0.03_{0.00}^{0.39}$	$0.19_{0.08}^{0.31}$	$2.92_{2.32}^{3.70}$	1.35	41.02	39.85	17
NGC 3393 (0140950601)	Nucleus**	2ME2PL	-	$21.98_{8.83}^{64.98}$	$0.09_{0.08}^{0.11}$ $(0.59_{0.54}^{0.62})$	$1.19_{0.72}^{1.69}$	1.08	41.10	41.11	-
NGC 4507 (12292)	Ring*	ME2PL	-	$66.35_{51.97}^{82.45}$	$0.77_{0.64}^{0.87}$	$2.40_{1.97}^{2.77}$	1.40	40.48	41.44	13
NGC 4507 (0653870401)	Nucleus**	2ME2PL	-	$37.50_{32.87}^{42.42}$	$0.15_{0.14}^{0.17}$ $(0.69_{0.64}^{0.77})$	$0.58_{0.36}^{0.78}$	1.06	41.71	42.66	-
NGC 5194 (3932)	Ring*	ME2PL	$0.11_{0.031}^{0.15}$	$11.18_{9.18}^{13.61}$	$0.57_{0.54}^{0.59}$	$3.78_{3.24}^{4.00}$	1.34	40.74	39.69	91
NGC 5194 (0112840201)	Nucleus**	2ME2PL	$3.43_{0.06}^{10.37}$	$106.33_{53.17}^{190.36}$	$0.15_{0.12}^{0.19}(0.69_{0.63}^{0.76})$	$3.44_{3.37}^{3.51}$	0.92	41.70	40.75	-
MARK 273 (809)	Ring*	MEPL	$0.00_{0.00}^{0.11}$	$0.00_{0.00}^{0.11}$	$0.63_{0.54}^{0.69}$	$2.65_{2.40}^{3.44}$	1.27	41.05	40.78	31
MARK 273 (0101640401)	Nucleus**	2ME2PL	-	$55.97_{40.39}^{78.04}$	$0.26_{0.00}^{0.53}$ $(0.80_{0.65}^{1.00})$	$1.39_{0.98}^{1.74}$	1.25	42.23	42.68	-
Circinus (10937)	Ring*	ME2PL	-	$123.38_{48.72}^{150.24}$	$0.75_{0.64}^{0.83}$	$1.81_{1.74}^{2.08}$	1.05	40.18	40.30	28
Circinus (0656580601)	Nucleus**	2ME2PL	-	$39.57_{35.25}^{44.55}$	$0.03_{0.02}^{0.03}$ $(0.58_{0.50}^{0.61})$	$1.41_{1.34}^{1.49}$	1.68	40.49	40.72	-
NGC 6300 (10292)	Ring*	ME	$56.21_{42.23}^{83.99}$	-	$0.70_{0.59}^{1.09}$	-	2.00	40.00	40.74	5
NGC 6300 (0059770101)	Nucleus**	2PL	-	$32.45_{27.67}^{37.86}$	-	$2.52_{2.07}^{2.98}$	0.85	40.84	40.58	-
NGC 7212 (4078)	Ring*	PL	$0.00_{0.00}^{0.12}$	-	-	$2.11_{1.75}^{2.88}$	3.08	40.57	40.91	16
NGC 7212 (0200430201)	Nucleus**	2ME2PL	-	$121.46_{49.26}^{391.31}$	$0.17_{0.11}^{0.22}$ $(0.67_{0.58}^{0.80})$	$0.37_{0.10}^{0.66}$	1.25	41.66	42.72	-
NGC 7319 (7924)	Ring*	ME2PL	-	$53.32_{30.39}^{93.89}$	$0.61_{0.52}^{0.69}$	$3.34_{2.94}^{3.78}$	0.68	42.72	41.93	17
NGC 7319 (0021140201)	Nucleus**	2ME2PL	-	$49.09_{56.28}^{42.28}$	$0.33_{0.41}^{0.16}(0.73_{0.84}^{0.62})$	$0.93_{1.23}^{0.61}$	1.23	41.75	42.78	-

Notes (Col. 1) name and obsID in parenthesis, (Col. 2) extracted region, (Col. 3) best-fit model, (Cols. 4, 5, 6, 7, and 8) parameters of the best-fit model (^{a} n units of $10^{22} cm^{-2}$.), (Cols. 9 and 10) soft and hard intrinsic luminosities, and (Col. 11) the percentage of the number counts contribution from the ring to the r_{ext} aperture *Chandra* data in the 0.5-10.0 keV band.

*Spectral parameters of the annular region in *Chandra* data.

**Spectral parameters of the nuclear region in *XMM*-Newton data when the spectral parameters of the ring from *Chandra* data are included in the fit.

Table A.5: Simultaneous fittings taking the contribution from the annular region given in Table A.4 into account.

ObsID (1)	N_{H1} ($10^{22} cm^{-2}$) (2)	N_{H2} ($10^{22} cm^{-2}$) (3)	kT (keV) (4)	Γ (5)	$Norm_1$ (10^{-4}) (6)	$Norm_2$ (10^{-4}) (7)	$\chi^2/d.o.f$ (8)	$log(L_{soft})$ (0.5-2 keV) (9)	$log(L_{hard})$ (2-10 keV) (10)
				NGC 424					
0002942301	-	$24.49^{31.94}_{18.65}$	$0.09^{0.10}_{0.07}$ $(0.67^{0.73}_{0.61})$	$1.82^{2.15}_{1.46}$	$0.72^{0.88}_{0.58}$	$6.70^{13.11}_{3.11}$	138.97/103	$41.74^{41.76}_{41.72}$	$41.87^{41.92}_{41.81}$
3146								$41.74^{41.76}_{41.72}$	$41.84^{41.89}_{41.79}$
				NGC 788					
0601740201	-	$46.61^{51.35}_{42.14}$	$0.11^{0.12}_{0.09}$ $(0.71^{0.75}_{0.67})$	$1.28^{1.51}_{1.06}$	$0.35^{0.41}_{0.29}$	$12.43^{20.51}_{7.55}$	262.36/205	$42.11^{42.17}_{42.04}$	$42.63^{42.66}_{42.60}$
11680								$42.11^{42.17}_{42.04}$	$42.59^{42.62}_{42.56}$
				MARK 573					
0200430701	-	$11.40^{53.26}_{0.00}$	$0.12^{0.15}_{0.11}$ $(0.71^{0.76}_{0.67})$	$2.67^{2.91}_{2.32}$	$0.02^{0.02}_{0.01}$	$0.51^{0.59}_{0.43}$	198.75/171	$41.75^{41.76}_{41.74}$	$41.41^{41.48}_{41.31}$
7745								$41.71^{41.73}_{41.70}$	$41.40^{41.49}_{41.30}$
				MARK 1066					
0201770201	$0.12^{0.24}_{0.03}$	$82.29^{175.04}_{45.83}$	$0.68^{0.79}_{0.62}$	$2.02^{2.36}_{1.71}$	$0.53^{0.71}_{0.40}$	$7.11^{25.58}_{2.23}$	96.11/69	$41.40^{41.42}_{41.38}$	$41.44^{41.53}_{41.33}$
4075								$41.39^{41.41}_{41.37}$	$41.42^{41.49}_{41.32}$
				3C 98.0					
0064600301	$0.45^{0.61}_{0.09}$	$6.14^{7.46}_{4.99}$	$0.17^{0.28}_{0.12}$	$0.85^{1.16}_{0.59}$	$9.85^{13.56}_{0.51}$	$1.25^{2.02}_{0.76}$	94.67/73	$42.41^{42.58}_{42.11}$	$42.64^{42.69}_{42.58}$
10234								$42.40^{42.58}_{42.10}$	$42.59^{42.64}_{42.54}$
				IC 2560					
0203890101	-	$31.42^{39.74}_{25.13}$	$0.09^{0.09}_{0.07}$ $(0.60^{0.62}_{0.57})$	$1.28^{1.52}_{1.03}$	$0.12^{0.15}_{0.10}$	$0.67^{1.14}_{0.38}$	387.65/309	$40.57^{40.58}_{40.56}$	$41.05^{41.08}_{41.03}$
4908								$40.56^{40.57}_{40.55}$	$41.01^{41.04}_{40.99}$
				NGC 3393					
0140950601	-	$32.83^{96.98}_{18.88}$	$0.10^{0.12}_{0.09}$ $(0.58^{0.61}_{0.54})$	$2.29^{2.72}_{1.86}$	$0.35^{0.45}_{0.26}$	$2.34^{5.61}_{1.04}$	167.03/141	$41.44^{41.48}_{41.39}$	$41.26^{41.32}_{41.19}$
4868								$41.53^{41.57}_{41.47}$	$42.76^{42.82}_{42.69}$
				NGC 4507					
0653870401	-	$41.19^{43.59}_{38.85}$	$0.15^{0.17}_{0.14}$ $(0.70^{0.76}_{0.67})$	$0.66^{0.79}_{0.53}$	$0.56^{0.62}_{0.50}$	$6.25^{8.45}_{4.58}$	784.58/659	$41.81^{41.82}_{41.80}$	$42.73^{42.74}_{42.71}$
12292						$13.35^{17.61}_{10.07}$		$42.07^{42.08}_{42.06}$	$42.94^{42.96}_{42.92}$
				NGC 5194					
0112840201	$0.10^{0.17}_{0.04}$	$197.20^{255.61}_{81.98}$	$0.02^{0.02}_{0.01}$ $(0.65^{0.68}_{0.62})$	$3.46^{3.60}_{3.26}$	$0.16^{0.20}_{0.14}$	$41.71^{114.02}_{30.51}$	322.54/202	$40.03^{40.03}_{40.02}$	$39.59^{39.62}_{39.55}$
3932								$39.84^{39.75}_{39.92}$	$39.18^{39.24}_{39.11}$
				MARK 273					
0101640401	-	$78.85^{90.96}_{67.72}$	$0.01^{0.15}_{0.01}$ $(0.88^{0.99}_{0.82})$	$1.33^{1.46}_{1.17}$	$0.17^{0.19}_{0.15}$	$2.86^{3.85}_{2.09}$	193.34/131	$41.40^{41.41}_{41.39}$	$42.20^{42.24}_{42.16}$
809		$38.43^{43.94}_{33.42}$						$41.28^{41.30}_{41.26}$	$42.37^{42.41}_{42.33}$
				NGC 6300					
0059770101	-	$16.56^{18.30}_{14.86}$		$1.07^{1.33}_{0.82}$	$0.01^{0.01}_{0.01}$	$0.57^{0.94}_{0.34}$	221.55/172	$39.55^{39.66}_{39.41}$	$40.23^{40.27}_{40.19}$
10292					$0.15^{0.19}_{0.11}$	$37.75^{61.02}_{23.34}$		$41.35^{41.44}_{41.23}$	$41.97^{42.00}_{41.93}$
				NGC 7212					
0200430201	-	$81.67^{124.96}_{51.53}$	$0.12^{0.17}_{0.08}$ $(0.59^{0.66}_{0.52})$	$0.80^{1.04}_{0.57}$	$0.17^{0.21}_{0.14}$	$1.43^{2.92}_{0.62}$	106.34/77	$41.81^{41.84}_{41.76}$	$42.63^{42.69}_{42.56}$
4078								$41.80^{41.84}_{41.74}$	$42.58^{42.64}_{42.52}$
				NGC 7319					
0021140201		$45.98^{48.72}_{43.31}$	$0.62^{0.65}_{0.58}$	$1.68^{1.85}_{1.49}$	$0.15^{0.17}_{0.13}$	$10.15^{14.84}_{6.83}$	613.13/364	$42.23^{42.25}_{42.22}$	$42.51^{42.53}_{42.49}$
7924						$35.67^{51.54}_{24.35}$		$42.77^{42.80}_{42.74}$	$43.02^{43.04}_{42.99}$

Notes. (Col. 1) name and obsID in parenthesis, (Cols. 2, 3, 4, 5, 6, and 7) parameters of the best-fit model, (Col. 8) $\chi^2/d.o.f$, and (Cols. 9 and 10) soft and hard intrinsic luminosities.

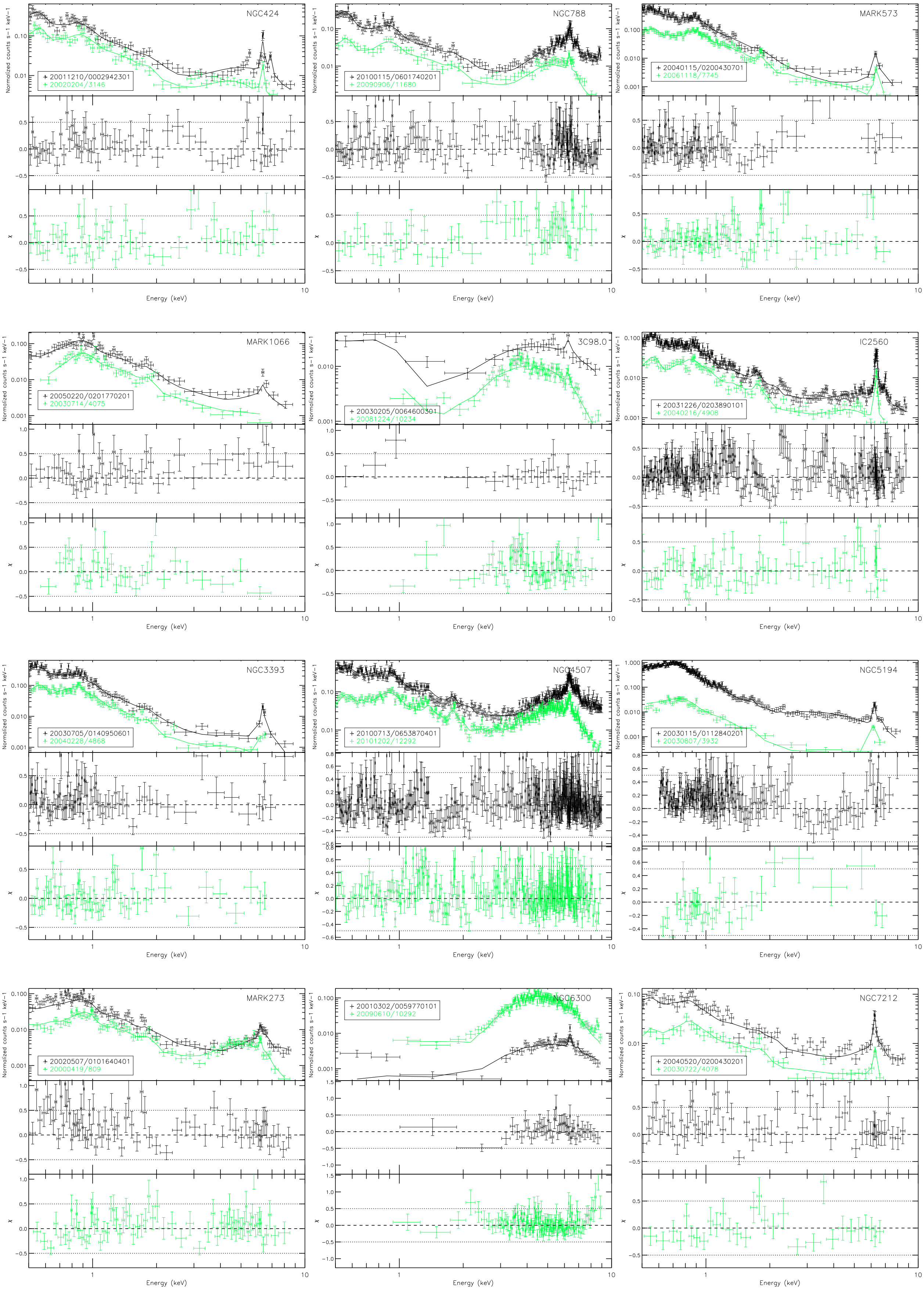

Fig. A.1: For each object, (top): simultaneous fit comparing *Chandra* and *XMM*–Newton spectra; (from second row on): residuals in units of σ. The legends contain the date (in the format yyyymmdd) and the obsID. The observations used for comparisons are marked with *c* in Table A.1.

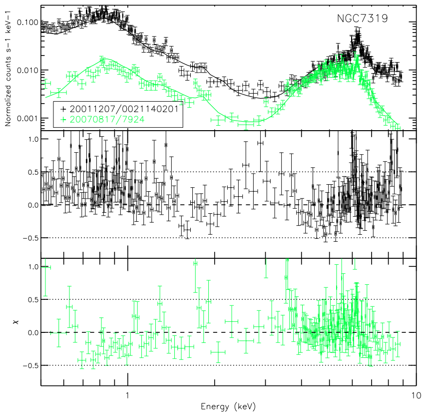

Fig. A.1: Cont.

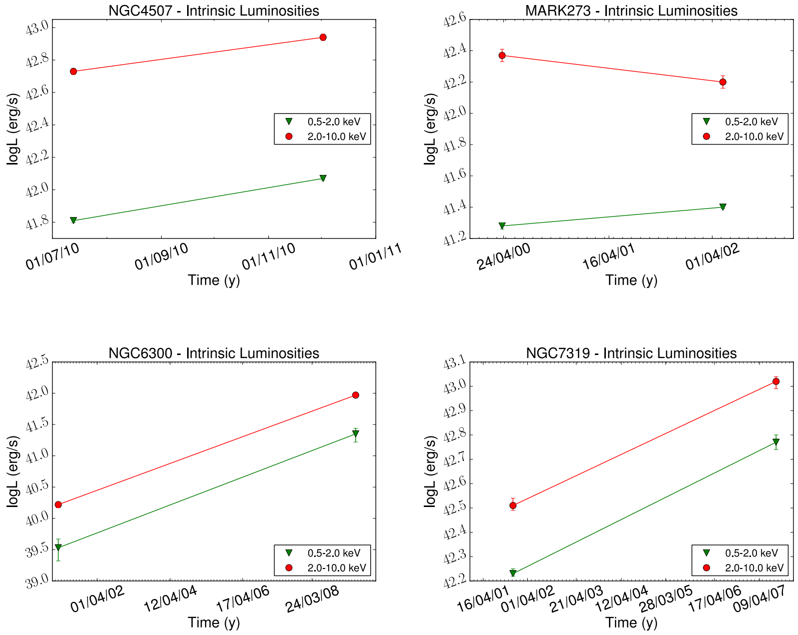

Fig. A.2: X-ray intrinsic luminosities calculated for the soft (0.5–2.0 keV, green triangles) and hard (2.0–10.0 keV, red circles) energies in the simultaneous fitting, only for the variable objects, when *Chandra* and *XMM*–Newton data are compared.

Table A.6: Statistics of the light curves.

Name (1)	ObsID (2)	Energy (3)	$\chi^2/d.o.f$ (4)	Prob.(%) (5)	σ^2_{NXS} (6)	$<\sigma^2_{NXS}>$ (7)
NGC 424	0550950101	0.5-10 (1)	48.7/40	84	<0.0026	<0.0020
		0.5-10 (2)	13.0/30	1	<0.0031	
		0.5-2 (1)	38.8/40	48	<0.0034	<0.0027
		0.5-2 (2)	17.3/30	3	<0.0041	
		2-10 (1)	33.0/40	22	<0.0102	<0.0077
		2-10 (2)	31.8/30	62	<0.0116	
MARK 573	7745	0.5-10	44.4/38	88	0.0041 ± 0.0037	
		0.5-2	34.9/38	39	<0.0096	
		2-10	76.0/38	100	<0.0710	
	13124	0.5-10	56.0/40	95	<0.0108	
		0.5-2	46.9/40	79	<0.0122	
		2-10	50.7/40	88	<0.0900	

Table A.6: (Cont.)

Name (1)	ObsID (2)	Energy (3)	$\chi^2/d.o.f$ (4)	Prob.(%) (5)	σ^2_{NXS} (6)	$<\sigma^2_{NXS}>$ (7)
3C 98.0	10234	0.5-10	17.2/31	2	<0.0157	
		0.5-2	32.3/31	60	<0.2035	
		2-10	17.9/31	3	<0.0169	
IC 2560	0203890101	0.5-10	62.0/40	99	0.0108 ± 0.0043	
		0.5-2	44.5/40	71	<0.0156	
		2-10	49.1/40	85	<0.0268	
	4908	0.5-10	48.1/40	82	<0.0204	
		0.5-2	60.7/40	99	0.0172± 0.0140	
		2-10	29.3/40	11	<0.0581	
NGC 3393	12290	0.5-10	30.2/40	13	<0.0109	
		0.5-2	31.3/40	16	<0.0127	
		2-10	42.2/40	62	<0.0724	
NGC 4507	0006220201	0.5-10	35.4/30	77	<0.0007	
		0.5-2	25.7/30	31	<0.0031	
		2-10	36.4/30	81	<0.0009	
	12292	0.5-10	39.2/39	54	<0.0026	
		0.5-2	28.9/39	12	<0.0079	
		2-10	47.6/39	84	<0.0039	
NGC 5194	3932	0.5-10	50.7/40	88	<0.0311	
		0.5-2	50.0/40	87	<0.0364	
		2-10	42.0/40	62	<0.2008	
	13813	0.5-10 (1)	58.7/40	97	<0.0568	0.0209±0.0190
		0.5-10 (2)	36.2/40	46	<0.0379	
		0.5-10 (3)	32.8/40	22	<0.0366	
		0.5-10 (4)	58.8/40	97	0.0335±0.0185	
		0.5-2 (1)	84.8/40	100	0.0572±0.0330	0.0373±0.0289
		0.5-2 (2)	36.5/40	37	<0.0454	
		0.5-2 (3)	31.8/40	18	<0.0435	
		0.5-2 (4)	60.0/40	98	0.0236±0.0217	
		2-10 (1)	28.1/40	18	<0.2318	<0.1218
		2-10 (2)	33.8/40	26	<0.2203	
		2-10 (3)	30.6/40	14	<0.2473	
		2-10 (4)	28.9/40	10	<0.2716	
	13812	0.5-10 (1)	48.9/40	84	<0.0401	<0.0227
		0.5-10 (2)	37.9/40	43	<0.0382	
		0.5-10 (3)	44.6/40	72	<0.0398	
		0.5-2 (1)	44.8/40	72	<0.0485	<0.0273
		0.5-2 (2)	40.9/40	57	<0.0459	
		0.5-2 (3)	40.5/40	55	<0.0474	
		2-10 (1)	38.1/40	45	<0.2280	<0.1423
		2-10 (2)	26.9/40	6	<0.2355	
		2-10 (3)	24.1/40	2	<0.2737	
	13814	0.5-10 (1)	54.5/40	94	<0.0440	<0.0208
		0.5-10 (2)	36.9/40	39	<0.0400	
		0.5-10 (3)	31.6/40	17	<0.0403	
		0.5-10 (4)	60.1/40	98	<0.0422	
		0.5-2 (1)	44.5/40	71	<0.0525	0.0196±0.0170
		0.5-2 (2)	49.0/40	84	<0.0497	
		0.5-2 (3)	32.7/40	21	<0.0491	
		0.5-2 (4)	70.3/40	100	0.0310±0.0222	
		2-10 (1)	23.9/40	2	<0.3524	<0.1471
		2-10 (2)	22.7/40	1	<0.2235	

Table A.6: (Cont.)

Name (1)	ObsID (2)	Energy (3)	$\chi^2/d.o.f$ (4)	Prob.(%) (5)	σ^2_{NXS} (6)	$<\sigma^2_{NXS}>$ (7)
		2-10 (3)	28.4/40	8	<0.2553	
		2-10 (4)	24.8/40	3	<0.3271	
	13815	0.5-10	27.9/40	7	<0.0351	
		0.5-2	25.1/40	3	<0.0418	
		2-10	19.4/40	1	<0.2777	
	13816	0.5-10	40.1/40	53	<0.0391	
		0.5-2	40.5/40	55	<0.0463	
		2-10	28.9/40	10	<0.2729	
MARK 273	809	0.5-10	71.8/40	100	<0.0155	
		0.5-2	49.1/40	85	<0.0287	
		2-10	60.2/40	98	<0.0337	
Circinus	9140	0.5-10	48.0/40	82	<0.0019	
		0.5-2	32.6/40	21	<0.0075	
		2-10	45.5/40	74	<0.0025	
NGC 7319	7924	0.5-10 (1)	30.3/40	13	<0.0135	<0.0093
		0.5-10 (2)	23.9/40	2	<0.0127	
		0.5-2 (1)	48.7/40	84	<0.0644	<0.0451
		0.5-2 (2)	69.6/40	99	<0.0632	
		2-10 (1)	37.2/40	40	<0.0170	<0.0116
		2-10 (2)	29.5/40	11	<0.0158	
	0021140201	0.5-10	22.8/31	16	<0.0051	
		0.5-2	24.1/31	19	<0.0121	
		2-10	17.3/31	2	<0.0089	

Notes. (Col. 1) name, (Col. 2) obsID, (Col. 3) energy band in keV, (Cols. 4 and 5) $\chi^2/d.o.f$ and the probability of being variable in the 0.5-10.0 keV energy band of the total light curve, (Col. 6) normalized excess variance, σ^2_{NXS}, and (Col. 8) the mean value of the normalized excess variance, $<\sigma^2_{NXS}>$, for each light curve and energy band.

Table A.7: Classification of Compton-thick objects.

Name (1)	ObsID (2)	Γ (3)	EW (keV) (4)	$F_x/F_{[OIII]}$ (5)	Ref.[1] $[OIII]$ (6)	CT? (7)	Classification (8)	Γ_{hard} (9)
MARK348	0067540201	$1.71\,^{1.80}_{1.64}$	$0.06^{0.07}_{0.05}$	30.00	1	✗	*Compton*-thin	
	0701180101	$1.57\,^{1.79}_{1.33}$	$0.19^{0.25}_{0.14}$	9.06		✗		
NGC424	0002942301	$1.03^{1.90}_{0.14}$	$0.99^{1.24}_{0.74}$	1.84	2	✓	*Compton*-thick	$0.54^{1.65}_{0.09}$
	0550950101	$0.16\,^{0.37}_{0.00}$	$0.87^{0.93}_{0.82}$	1.81		✓		
	3146	$0.00\,^{1.84}_{0.00}$	$0.55^{0.77}_{0.32}$	1.46		✓		
MARK573	7745	$0.18\,^{2.71}_{0.00}$	$2.17^{2.81}_{1.52}$	0.49	3	✓	*Compton*-thick	$0.50^{3.23}_{0.00}$
	13124	$0.88\,^{2.08}_{0.66}$	$2.05^{2.55}_{1.49}$	0.41		✓		
NGC788	0601740201	$1.59^{2.01}_{0.97}$	$0.43^{0.49}_{0.35}$	341.75	2	✗	*Compton*-thin	
	11680	$1.07^{2.61}_{0.17}$	$0.15^{0.22}_{0.07}$	284.26		✗		
ESO417-G06	0602560201	$1.66\,^{2.00}_{1.27}$	$0.18\,^{0.30}_{0.06}$	268.01	4	✗	*Compton*-thin	
	0602560301	$1.73^{2.17}_{1.31}$	$0.37\,^{0.53}_{0.22}$	268.01		✗		
MARK1066	0201770201	$0.46\,^{1.97}_{0.00}$	$0.60^{0.89}_{0.30}$	0.37	3	✓	*Compton*-thick	$0.31^{0.76}_{0.00}$
3C98.0	0064600101	$1.31\,^{1.67}_{0.97}$	< 0.07	10.0	5	✗	*Compton*-thin	
	0064600301	$1.41^{2.13}_{0.22}$	< 0.38	5.89		✗		
	10234	$0.67^{1.30}_{0.09}$	$0.16^{0.27}_{0.06}$	5.01		✗		
MARK3	0111220201	$0.05\,^{0.19}_{0.00}$	$0.55^{0.58}_{0.52}$	0.33	1	✓	*Compton*-thick	$0.42^{0.62}_{0.23}$
	0009220601	$0.36\,^{0.87}_{0.00}$	$0.67^{0.79}_{0.56}$	0.24		✓		
	0009220701	$0.03\,^{0.53}_{0.00}$	$0.60^{0.73}_{0.48}$	0.21		✓		

Table A.7: (Cont.)

Name	ObsID	Γ	EW (keV)	$F_x/F_{[OIII]}$	Ref.[1] $[OIII]$	CT?	Classification	Γ_{hard}
(1)	(2)	(3)	(4)	(5)	(6)	(7)	(8)	(9)
	0009220901	$0.02^{1.05}_{0.00}$	$0.49^{0.70}_{0.27}$	0.15		✓		
	0009220401	$0.01^{0.43}_{0.00}$	$0.79^{0.96}_{0.63}$	0.24		✓		
	0009220501	$0.03^{0.48}_{0.00}$	$0.63^{0.74}_{0.52}$	0.20		✓		
	0009221601	$0.01^{0.98}_{0.00}$	$1.16^{1.46}_{0.85}$	0.24		✓		
MARK1210	4875	$1.31^{1.95}_{0.74}$	$0.13^{0.20}_{0.05}$	2.97	1	✗	*Compton*-thin	
	9264	$0.89^{1.42}_{0.40}$	$0.06^{0.12}_{0.01}$	4.49		✗		
	9265	$1.41^{2.06}_{0.82}$	$0.12^{0.19}_{0.05}$	6.34		✗		
	9266	$2.03^{2.86}_{1.46}$	$0.10^{0.18}_{0.03}$	2.41		✗		
	9268	$1.24^{2.07}_{0.51}$	$0.16^{0.25}_{0.061}$	3.57		✗		
NGC3079	0110930201	$1.58^{2.47}_{0.07}$	< 0.26	0.31	1	✗	*Compton*-thin	
IC2560	0203890101	$0.22^{0.60}_{0.00}$	$1.95^{2.09}_{1.79}$	7.30	2	✓	*Compton*-thick	$0.69^{1.04}_{0.30}$
	4908	<0.77	$1.27^{1.49}_{1.04}$	4.94		✓		
NGC3393	12290	$0.55^{3.35}_{0.00}$	$1.85^{2.29}_{1.45}$	0.22	1	✓	*Compton*-thick	$0.42^{0.00}_{1.76}$
	0140950601	$0.95^{1.69}_{0.14}$	$1.41^{1.78}_{1.00}$	0.18		✓		
NGC4507	0006220201	$1.73^{1.86}_{1.59}$	$0.20^{0.22}_{0.19}$	33.08	1	✗	*Compton*-thin	
	0653870201	$1.44^{1.72}_{1.13}$	$0.44^{0.47}_{0.39}$	16.58		✗		
	0653870301	$1.34^{1.65}_{1.00}$	$0.38^{0.42}_{0.34}$	18.60		✗		
	0653870401	$0.91^{1.14}_{0.44}$	$0.46^{0.50}_{0.42}$	16.20		✗		
	0653870501	$1.01^{1.34}_{0.64}$	$0.46^{0.50}_{0.41}$	17.36		✗		
	0653870601	$0.91^{2.16}_{0.00}$	$0.43^{0.59}_{0.28}$	10.22		✗		
	12292	$0.87^{1.21}_{0.54}$	$0.36^{0.40}_{0.32}$	24.52		✗		
NGC4698	0651360401	$0.91^{1.50}_{0.49}$	< 0.46	9.23	6	✗	*Compton*-thin	
NGC5194	13812	$0.04^{2.21}_{0.00}$	$2.75^{3.26}_{2.27}$	1.47	1	✓	*Compton*-thick	$0.57^{1.74}_{0.00}$
	13813	$0.02^{2.41}_{0.00}$	$4.16^{4.88}_{3.43}$	0.13		✓		
	13814	$0.12^{3.25}_{0.00}$	$4.41^{5.14}_{3.73}$	0.17		✓		
	0112840201	$2.16^{3.19}_{1.29}$	$0.99^{1.23}_{0.75}$	0.27		✓		
MARK268	0554500701	$1.80^{3.43}_{1.11}$	< 0.17	462.73	7	✗	*Compton*-thin	
	0554501101	$1.71^{2.18}_{1.32}$	$0.26^{0.33}_{0.18}$	351.01		✗		
MARK273	0101640401	$0.01^{0.95}_{0.00}$	$0.87^{1.12}_{0.65}$	2.75	1	✓	Changing-look?	
	809	$1.69^{2.77}_{0.78}$	$0.21^{0.32}_{0.10}$	4.67		✗		
Circinus	365	$0.00^{0.28}_{0.00}$	$2.38^{2.65}_{2.11}$	0.39	1	✓	*Compton*-thick	$0.07^{0.17}_{0.00}$
	9140	$0.12^{0.33}_{0.00}$	$1.90^{1.97}_{1.83}$	0.31		✓		
	10937	$0.00^{0.10}_{0.00}$	$1.73^{1.84}_{1.63}$	0.39		✓		
	0111240101	$1.07^{1.13}_{1.01}$	$1.54^{1.56}_{1.51}$	0.35		✓		
	0656580601	$0.49^{0.60}_{0.41}$	$1.50^{1.54}_{1.47}$	0.46		✓		
NGC5643	0601420101	$0.04^{0.61}_{0.00}$	$1.37^{1.56}_{1.18}$	0.29	1	✓	*Compton*-thick	$0.84^{1.48}_{0.09}$
	0140950101	$0.01^{0.71}_{0.00}$	$1.37^{1.69}_{1.04}$	0.37		✓		
MARK477	0651100301	$0.93^{1.53}_{0.36}$	$0.32^{0.43}_{0.22}$	0.32	1	✓	*Compton*-thick	$1.02^{1.66}_{0.59}$
	0651100401	$0.88^{1.48}_{0.30}$	$0.13^{0.21}_{0.05}$	0.45		✓		
IC4518A	0401790901	$1.71^{2.16}_{1.29}$	$0.33^{0.42}_{0.25}$	-	-	✗	*Compton*-thin	
	0406410101	$1.27^{1.60}_{0.94}$	$0.45^{0.53}_{0.38}$			✗		
ESO138-G01	0405380201	$0.92^{1.33}_{0.52}$	$0.90^{1.01}_{0.78}$	23.10	2	✓	*Compton*-thick	$1.04^{1.38}_{0.73}$
	0690580101	$0.97^{1.64}_{0.58}$	$1.31^{1.48}_{1.10}$	19.67		✓		
NGC6300	10292	$0.57^{0.95}_{0.23}$	< 0.08	361.27	2	✗	*Compton*-thin	
	10293	$1.17^{1.69}_{0.90}$	< 0.08	444.46		✗		
	0059770101	$1.55^{2.11}_{1.03}$	$0.23^{0.34}_{0.13}$	12.24		✗		
NGC7172	0147920601	$1.61^{1.73}_{1.50}$	$0.12^{0.14}_{0.09}$	853.54	1	✗	*Compton*-thin	
	0202860101	$1.58^{1.67}_{1.49}$	$0.09^{0.11}_{0.07}$	834.12		✗		
	0414580101	$1.71^{1.76}_{1.66}$	$0.08^{0.09}_{0.07}$	1742.72		✗		
NGC7212	0200430201	$0.00^{0.26}_{0.00}$	$0.79^{0.99}_{0.59}$	3.83	2	✓	*Compton*-thick	$0.38^{2.19}_{0.00}$

Table A.7: (Cont.)

Name	ObsID	Γ	EW (keV)	$F_x/F_{[OIII]}$	Ref.[1] $[OIII]$	CT?	Classification	Γ_{hard}
(1)	(2)	(3)	(4)	(5)	(6)	(7)	(8)	(9)
	4078	$0.00^{2.62}_{0.00}$	$1.00^{1.39}_{0.61}$	3.04		✓		
NGC7319	789	$1.43^{2.67}_{0.84}$	$0.23^{0.34}_{0.12}$	38.69	1	✗	Changing-look?	
	7924	$1.89^{2.39}_{1.52}$	$0.23^{0.29}_{0.18}$	82.73		✗		
	0021140201	$0.23^{0.65}_{0.00}$	$0.83^{0.93}_{0.73}$	22.26		✓		

Notes. (Col. 1) name, (Col. 2) obsID, (Cols. 3 and 4) index of the power law and the equivalent width of the FeKα line from the spectral fit (PL model) in the 3–10 keV energy band, (Col. 5) ratio between the individual hard X-ray luminosity (from Table A.3) and the extinction-corrected [O III] fluxes, (Col. 6) references for the measure of $F_{[OIII]}$, (Col. 7) classification from the individual observation, (Col. 8) classification of the object, and (Col. 9) slope of the power law at hard energies for Compton-thick candidates from the simultaneous analysis (see Sect. 4.5). References: (1) Bassani et al. (1999); (2) Gu et al. (2006); (3) Bian & Gu (2007); (4) Kraemer et al. (2011); (5) Noguchi et al. (2009); (6) Panessa & Bassani (2002); and (7) Koski (1978).

Appendix B: Notes and comparisons with previous results for individual objects

In this appendix we discuss the general characteristics of the galaxies in our sample at different wavelengths, as well as comparisons with previous variability studies. We recall that long-term UV variability and short-term X-ray variations were studied only for some sources (six and ten sources, see Tables 1 and A.6, respectively), so comparisons are only made in those cases. For the remaining objects, results from other authors are mentioned, when available.

Appendix B.1: MARK 348

MARK 348, also called NGC 262, is an interacting galaxy (with NGC 266, Pogge & Eskridge 1993). It was optically classified as a Seyfert 2 (Koski 1978), while it shows broad lines in polarized light (Miller & Goodrich 1990). It shows a spiral nuclear structure (see *HST* image in Appendix C.1). *VLBI* observations showed a compact radio core and jets structure at radio frequencies and revealed variations on timescales from months to years at 6 and 21 cm (Neff & de Bruyn 1983). The *XMM*–Newton image shows that the soft X-ray emission is very weak in this object (see Appendix C.1), which was classified as a Compton-thin object (e.g., Awaki et al. 2006).

This galaxy was observed twice with *XMM*–Newton in 2002 and 2013 and once with *Chandra* in 2010. Recently, Marchese et al. (2014) have compared *XMM*–Newton and *Suzaku* data from 2002 and 2008. They fitted the data with a power law component transmitted through three absorbers (one neutral and two ionized), obtaining intrinsic luminosities of log(L(2–10 keV)) = 43.50 and 43.51, respectively. They reported variations attributed to changes in the column density of the neutral and one of the ionized absorbers, together with a variation in the ionization level of the same absorber, on timescales of months. They did not report variations in Γ and/or the continuum of the power law. Variations in the absorbing material on timescales of weeks/months were also reported by Smith et al. (2001) using *RXTE* data from 1996-97, but accompanied with continuum variations on timescales of $\sim$ 1 day. They obtained luminosities in the range log(L(2–10 keV)) = [42.90-43.53]. These results agreed with those later reported by Akylas et al. (2002), who analyzed the same observations plus 25 *RXTE* observations. Our analysis shows that variations between the two *XMM*–Newton observations are due to changes in the nuclear continuum, but variations in the absorbing material are not required. These differences may be related to the different instruments involved in the analyses.

Awaki et al. (2006) did not find short-term variations from the analysis of the *XMM*–Newton data from 2002.

In the 14–195 keV energy band, Soldi et al. (2014) estimated a variability amplitude of 25[22-28]% using data from the *Swift*/BAT 58-month survey.

Appendix B.2: NGC 424

NGC 424 was optically classified as a Seyfert 2 galaxy (Smith 1975), and broad lines have been detected in polarized light (Moran et al. 2000). At radio frequencies, it was observed with *VLA* at 6 and 20 cm, showing an extended structure (Ulvestad & Wilson 1989). A possible mid-IR variability was reported by Hönig et al. (2012) between 2007 and 2009, but it could also be due to an "observational inaccuracy". In X-rays, it is a Compton-thick source (Baloković et al. 2014).

It was observed twice with *XMM*–Newton in 2008 and 2011, and once with *Chandra* in 2002. Matt et al. (2003) studied *XMM*–Newton and *Chandra* data from 2001 and 2002. Both spectra were fitted with a model consisting on two power laws, a cold reflection component (PEXRAV), and narrow Gaussian lines. They report the same luminosity for the two spectra, log(L(2-10 keV)) = 41.68, indicating no variations. LaMassa et al. (2011) studied the same data set. They found no differences between the spectra and therefore fitted the data simultaneously with a simpler model, the 2PL. They estimated an intrinsic luminosity of log(L(2-10 keV)) = 41.56[41.39-41.75]. With the same data set, we did not find variations and obtained similar hard X-ray luminosities (41.85[41.79-41.92]).

We did not find short-term variations from the *XMM*–Newton light curve from 2008.

Appendix B.3: MARK 573

MARK 573 (also called UCG 1214) is a double-barred galaxy that shows dust lanes (Martini et al. 2001, see also Appendix C.1). It was optically classified as a Seyfert 2 galaxy (Osterbrock & Martel 1993). Observations at 6 cm with *VLA* showed a triple radio source (Ulvestad & Wilson 1984). A point-like source is observed in hard X-rays, while extended emission can be observed in soft X-rays, aligned with the bars (see Appendix C.1). It was classified as a Compton-thick candidate (Guainazzi et al. 2005b; Bianchi et al. 2010; Severgnini et al. 2012).

This galaxy was observed four times with *Chandra* between 2006 and 2010, and once with *XMM*–Newton in 2004. Bianchi et al. (2010) analyzed the *Chandra* data from 2006 and did not report flux variations when they compared their results with the analysis of Guainazzi et al. (2005b) of the *XMM*–Newton spectrum from 2004. Paggi et al. (2012) studied the four *Chandra* observations, and fitted the nuclear spectrum with a combination of a two-phased photoionized plasma plus a Compton reflection component (PEXRAV), reporting soft X-ray flux variations at 4σ of confidence level that they attributed to intrinsic variations of the source. We did not detect variations for this source, the difference most probably because we did not use two of these observations since they are affected by a pileup fraction greater than 10%.

Ramos Almeida et al. (2008) analyzed the *XMM*–Newton light curve and found variations of $\sim$ 300 s. They argue that this is an obscured narrow-line Seyfert 1 galaxy instead of a Seyfert 2, based on near-IR data. We analyzed two *Chandra* light curves but variations were not found.

Appendix B.4: NGC 788

This galaxy was optically classified as a Seyfert 2 by Huchra et al. (1982). A radio counterpart was detected with *VLA* data (Nagar et al. 1999). In X-rays, it was classified as a Compton-thin candidate using *ASCA* data (de Rosa et al. 2012), and it shows a point-like source in the 4.5-8 keV energy band (see Appendix C.1).

It was observed once with *Chandra* in 2009 and once with *XMM*–Newton in 2010. Long-term variability analyses of this source were not found in the literature. We did not find variations between the observations.

Variations in this source in the 14–195 keV energy band were studied by Soldi et al. (2014) using data from the *Swift*/BAT 58-month survey. They report an amplitude of the intrinsic variability of 15[11-19]%.

Appendix B.5: ESO 417-G06

This galaxy was optically classified as a Seyfert 2 galaxy (Maia et al. 2003). A radio counterpart was observed with *VLA* data (Nagar et al. 1999). It was classified as a Compton-thin candidate (Trippe et al. 2011).

This galaxy was observed twice with *XMM*–Newton in 2009. Long-term variability studies were not found in the literature. We found spectral variations due to changes in the absorber at hard X-ray energies.

Trippe et al. (2011) report short-term variations of a factor of about two in the count rate in the light curves from *Swift*/BAT during the 22-month survey.

Appendix B.6: MARK 1066

MARK 1066 is an early-type spiral galaxy (Afanas'ev et al. 1981) showing a double nucleus (Gimeno et al. 2004). It was optically classified as a Seyfert 2 by Goodrich & Osterbrock (1983), and broad lines were not detected in polarized light (Gu & Huang 2002). A radio counterpart showing a jet was found by Ulvestad & Wilson (1989). At X-rays, extended soft emission can be observed, aligned with a nuclear spiral structure observed at optical frequencies, also aligned with the IR emission (see Appendix C.1). Levenson et al. (2001) found this to be a heavily obscured AGN, with $N_H > 10^{24} cm^{-2}$ and an equivalent width of the Fe line ~ 3 keV using *ROSAT* and *ASCA* data; i.e., it was classified as a Compton-thick candidate.

The galaxy was observed once with *Chandra* in 2003 and once with *XMM*–Newton in 2005. Variability studies of this object were not found in the literature. We did not find any X-ray variations either.

Appendix B.7: 3C 98.0

Using the optical line measurements in Costero & Osterbrock (1977), 3C98.0 can be optically classified as a Seyfert 2 (see an optical spectrum in Appendix C.1). A nuclear core plus jet structure was observed at radio frequencies with *VLA* (Leahy et al. 1997).

It was observed twice with *XMM*–Newton in 2002 and 2003 and once with *Chandra* in 2008. Isobe et al. (2005) studied the two *XMM*–Newton data, and fitted its spectra with a thermal plus a power-law model, reporting X-ray luminosities of log(L(2–10 keV)) = 42.90[42.88-42.93] and 42.66[42.60-42.71], respectively, indicating flux variability. These measurements agree well with ours, where variations due to the nuclear continuum were found.

Awaki et al. (2006) studied short-term variations of the *XMM*–Newton observation from 2003 and calculated a normalized excess variance of $\sigma^2_{NXS} = 36[1-62] \times 10^{-3}$. We did not find short-term variations from one *Chandra* light curve, where upper limits of the σ^2_{NXS} were calculated.

We did not find any long-term UV variations in the UVW1 filter.

Appendix B.8: MARK 3

It was optically classified as a Seyfert 2 galaxy (Khachikian & Weedman 1974, see an optical spectrum in Appendix C.1). Broad lines have been found in polarized light (Miller & Goodrich 1990). A high resolution image at 2 cm with *VLA* data shows a double nucleus at radio frequencies (Ulvestad & Wilson 1984). This galaxy shows extended soft X-ray emission perpendicular to the IR emission and a point-like source at hard X-rays (see Appendix C.1). It is also a Compton-thick source (Bassani et al. 1999; Goulding et al. 2012), with a column density of $1.1 \times 10^{24} cm^{-2}$ measured with *BeppoSAX* (Cappi et al. 1999).

It was observed 11 times with *XMM*–Newton between 2000 and 2012, and once with *Chandra* in 2012. Bianchi et al. (2005b) report variations of the normalization of the absorbed power law when comparing the *XMM*–Newton from 2001 with *Chandra* and *BeppoSAX* data. Guainazzi et al. (2012) studied the X-ray variability of this nucleus during 12 years of observations with *Chandra*, *XMM*–Newton, *Suzaku*, and *Swift* satellites. Their analysis was performed in the 4-10 keV energy band. To estimate the luminosities, they fit a pure reflection model plus Gaussian lines to the spectra individually, and report a variability dynamical range greater than 70%. They also used alternative models to fit the data, variations found independently of the model used. They estimated the shortest variability timescale to be ~ 64 days from the measurement between two statistically inconsistent measures. From our analysis, variations due to the nuclear continuum were found, with an upper limit of the variability timescale of about five months, thus in agreement with the results presented by Guainazzi et al. (2012).

Short-term variations from *XMM*–Newton data were found neither by González-Martín & Vaughan (2012) nor by Cappi et al. (2006) from light curves from 2000 and 2001, respectively.

Soldi et al. (2014) reported an amplitude of the intrinic variability of 35[26-46]% in the 14–195 keV energy band using data from the *Swift*/BAT 58-month survey.

Appendix B.9: MARK 1210

This galaxy, also called the Phoenix galaxy or UGC 4203, was optically classified as a Seyfert 2 by Dessauges-Zavadsky et al. (2000). Broad lines have been observed in polarized light using spectropolarimetric data (Tran et al. 1992; Tran 1995). The *HST* image shows a nuclear spiral structure (see Appendix C.1). A very compact radio counterpart was found with *VLA* at 3.5 cm, with no evidence of a jet structure (Falcke et al. 1998). At X-rays, a point like source is observed in the 4.5-8.0 keV energy band (see Appendix C.1). It was classified as a Compton-thick candidate by Bassani et al. (1999). Furthermore, Guainazzi et al. (2002) classified this galaxy as a changing-look AGN because transitions from Compton-thick (*ASCA* data) to Compton-thin (*XMM*–Newton data) were found.

MARK 1210 was observed with *Chandra* six times between 2004 and 2008, and once with *XMM*–Newton in 2001. Matt et al. (2009) used *Suzaku* data from 2007 to study this source (caught in the Compton-thin state), and compared with previous observations from *ASCA* and *XMM*–Newton. They fit the spectra with a power law, a Compton reflection, and a thermal (MEKAL) component, and found a change in the absorber, which was about a factor of 2 higher in *Suzaku* data. They obtained intrinsic X-ray luminosities of log(L(2–10 keV)) = 42.87 and 43.04 for *Suzaku* and *XMM*–Newton data. Risaliti et al. (2010) simultaneously fit the five *Chandra* observations from 2008 using a model consisting on a doubled temperature plus power law to account for the soft energies, an absorbed power law, and a constant cold reflection component (PEXRAV). They concluded that variations are found in both the intrinsic flux and in the absorbing column density. They reported a variability time scale of ~ 15 days, whereby they estimated the physical parameters of the absorbing material, concluding that they are typical of the broad line region (BLR). Their result agrees well with ours.

Awaki et al. (2006) studied short-term variations from the *XMM*–Newton data and found $\sigma^2_{NXS} = 5.5[0.0 - 11.0] \times 10^{-3}$.

Soldi et al. (2014) used data from the *Swift*/BAT 58-month survey to account for the variability amplitude ($S_v = 24[15 - 32]$%) in the 14–195 keV energy band.

Appendix B.10: NGC 3079

This galaxy was optically classified as a Seyfert 2 (Ho et al. 1997, based on the spectra presented in Appendix C.1). Broad lines were not detected in polarized light (Gu & Huang 2002). The *HST* image shows dust lanes (Appendix C.1). A water maser and parsec-scale jets were observed at radio frequencies with *VLBI* (Trotter et al. 1998). The X-ray image in the 0.6-0.9 keV energy band shows strong diffuse emission, while a point-like source is detected in the 4.5-8.0 keV energy band (see Appendix C.1). It has been classified as a Compton-thick object with *BeppoSAX* data ($N_H = 10^{25} cm^{-2}$, Comastri 2004) and evidence was also found at lower energies (Cappi et al. 2006; Akylas & Georgantopoulos 2009; Brightman & Nandra 2011a).

It was observed once with *Chandra* and once with *XMM*–Newton, both in 2001. We did not find variability studies of this source in the literature. We did not study its variability because the extranuclear emission in *Chandra* data was too high to properly compare *XMM*–Newton and *Chandra* observations.

It is worth noting that NGC 3079 is classified as a Compton-thin candidate in this work but it has been classified as a Compton-thick candidate by Cappi et al. (2006) using the same *XMM*–Newton observation. Since these data have the lowest signal-to-noise ratio, this mismatch is most probably due to a problem related to the sensitivity of the data, because we used only data from the pn detector, while they combined pn, MOS1, and MOS2 data in their study; i.e., Cappi et al. (2006) data have a higher signal-to noise. We notice that cross-calibration uncertainties between pn and MOS cameras may add systematic to statistical uncertainties that can be misinterpreted as possible intrinsic variability due to large error bars (Kirsch et al. 2004; Ishida et al. 2011; Tsujimoto et al. 2011), thus preventing us from doing a variability analysis.

Appendix B.11: IC 2560

This galaxy was optically classified as a Seyfert 2 (Fairall 1986, see an optical spectrum in Appendix C.1). In hard X-rays it shows a point-like source (see Appendix C.1). It was classified as a Compton-thick object (Baloković et al. 2014).

IC 2560 was observed once with *XMM*–Newton in 2003 and once with *Chandra* in 2004. Variability studies were not found in the literature. We do not report X-ray variations for this source, either at short or long term.

Appendix B.12: NGC 3393

NGC 3393 was optically classified as a Seyfert 2 (Diaz et al. 1988, see an optical spectrum in Appendix C.1). A radio counterpart was found using *VLA* data, the galaxy showing a double structure (Morganti et al. 1999). The *HST* image shows a nuclear spiral structure aligned with the soft X-ray emission, where the spiral structure can also be appreciated; this emission is perpendicular to the disk emission, observed at optical wavelengths and aligned with the IR emission (see Appendix C.1). A point-like source is observed at hard X-rays (see Appendix C.1). It is a Compton–thick object observed by *BeppoSAX* ($N_H > 10^{25} cm^{-2}$, Comastri 2004).

This galaxy was observed once with *XMM*–Newton in 2003 and six times with *Chandra* between 2004 and 2012. Variability studies were not found in the literature. We did not find X-ray variations, whether on the short or the long term.

Appendix B.13: NGC 4507

The nucleus of this galaxy was optically classified as a Seyfert 2(Corbett et al. 2002, see an optical spectrum in Appendix C.1). Broad lines have been detected in polarized light (Moran et al. 2000). A radio counterpart was observed with *VLA* data (Morganti et al. 1999). In X-rays, it shows a point-like source in the hard energy band (see Appendix C.1), and it is a Compton-thin source (Bassani et al. 1999; Braito et al. 2013).

NGC 4507 was observed six times with *XMM*–Newton between 2001 and 2010, and once with *Chandra* in 2010. Matt et al. (2004) studied *Chandra* and *XMM*–Newton data from 2001. They ft the *XMM*–Newton spectrum with a composite of two power laws, a Compton reflection component (PEXRAV), plus ten Gaussian lines, and the *Chandra* spectrum with a power law plus a Gaussian line (only in the 4–8 keV spectral range). They found that the luminosity of the *Chandra* data was about twice that of *XMM*–Newton. Marinucci et al. (2013) studied five observations from *XMM*–Newton in 2010. They ft the spectra with two photoionized phases using Cloudy, a thermal component, an absorbed power law, and a reflection component. They report variations of the absorber on timescales between 1.5–4 months. Braito et al. (2013) studied *XMM*–Newton, *Suzaku*, and *BeppoSAX* data spanning around ten years to study the X-ray variability of the nucleus. They ft the spectra with the model that best represents the *Suzaku* data, composed of two power laws, a PEXRAV component, and eight Gaussian lines, and found that variations are mainly due to absorption but also due to the intensity of the continuum level. They also fit the spectra with the MYTORUS model[12] and obtained similar results, although the continuum varied less. We found variations in the absorber and the normalization of the power law, in agreement with the results by Braito et al. (2013).

We did not find short-term variations from the analysis of one *XMM*–Newton and another *Chandra* light curve.

Soldi et al. (2014) report an amplitude of the intrinsic variability of 20[16-24]% in the 14–195 keV energy band using data from the *Swift*/BAT 58-month survey.

Appendix B.14: NGC 4698

This galaxy was optically classified as a Seyfert 2 (Ho et al. 1997, see their spectra in Appendix C.1). González-Martín et al. (2009b) classified it as a LINER, but Bianchi et al. (2012) reconfirmed the Seyfert 2 classification using optical observations with the *NOT*/ALFOSC/Gr7. A radio counterpart was found by Ho & Ulvestad (2001) at 6 cm with *VLA* data. Georgantopoulos & Zezas (2003) state that this is an atypical Seyfert 2 galaxy because it showed no absoption and lacks the broad line region. The *Chandra* image revealed point-like sources around the nucleus, which can be ultraluminous X-ray sources (ULX), the closest located at $\sim 30''$ from the nucleus. In X-rays, González-Martín et al. (2009b) classified it as an AGN candidate, and Bianchi et al. (2012), based on the $\log(L_X/L_{[OIII]})$ ratio, classified it as a Compton-thick candidate.

---

[12] www.mytorus.com

This galaxy was observed twice with *XMM*–Newton in 2001 and 2010, and once with *Chandra* in 2010. Bianchi et al. (2012) compared the *XMM*–Newton spectra and did not find spectral variations, in agreement with the results reported by us.

We did not find any UV variations in the UVM2 filter.

Appendix B.15: NGC 5194

NGC 5194, also known as M 51, is interacting with NGC 5195. Optical and radio observations show extended emissions to the north and south of the nucleus, resulting from outflows generated by the nuclear activity (Ford et al. 1985). The extended emission can be observed in soft X-ray energies (top-left image in Appendix C.1). Moreover, the *HST* image shows a dusty nuclear spiral structure that can also be observed at IR frequencies (see Appendix C.1). This galaxy was optically classified as a Seyfert 2 (Ho et al. 1997, see their optical spectra in Appendix C.1). Broad lines were not detected in polarized light (Gu & Huang 2002). A point-like source is detected at hard X-ray energies (see Appendix C.1). Around the nucleus, it shows at least seven ultraluminous X-ray sources (ULX), the nearest one located at $\sim 28''$ from the nucleus (Dewangan et al. 2005). It was classified as a Compton-thick source using *BeppoSAX* data, with $N_H = 5.6 \times 10^{24} cm^{-2}$ (Comastri 2004, see also Terashima & Wilson 2001; Dewangan et al. 2005; Cappi et al. 2006).

This galaxy was observed ten times with *Chandra* between 2000 and 2012 and six times with *XMM*–Newton between 2003 and 2011. LaMassa et al. (2011) studied three *Chandra* observations between 2000 and 2003. They simultaneously fit these spectra with the ME2PL model, with spectral values in very good agreement with our SMF0 fitting and estimated a luminosity of log(L(2-10 keV))=38.95[38.42,39.45]. They did not report variability between the observations. This result agrees with ours.

Fukazawa et al. (2001) did not find any short-term variability from *BeppoSAX* data. We studied six *Chandra* light curves and did not find short-term variations either.

UV variations were not detected from the UVW2 and UVM2 filters, but variations were found in the UVW1 filter. However, since this is a Compton-thick source, variations are not expected, so it is most probable that the UV emission does not come from the nucleus. Therefore the variations might be related with, for example, circumnuclear star formation.

Appendix B.16: MARK 268

This galaxy was optically classified as a Seyfert 2 by Komossa & Schulz (1997). A radio counterpart was detected with *VLA* data at 6 cm with a weaker component 1.1 kpc away from the nucleus (Ulvestad & Wilson 1984). *XMM*-Newton data show a compact source at hard X-rays (see Appendix C.1) .

It was observed twice with *XMM*–Newton in 2008. Variability studies were not found in the literature. We did not find variations, but we notice that observations were obtained separated by only two days.

UV variations are not found from the UVM2 and the UVW1 filters.

Appendix B.17: MARK 273

Also called UGC 8696, this galaxy is an ultraluminous infrared galaxy with a double nucleus that was optically classified as a LINER (Veilleux et al. 1995), but later reclassified as a Seyfert 2 from better S/N data (Kim et al. 1998). Optical spectra are presented in Appendix C.1, together with an *HST* image which shows dust lanes. *VLBA* observations showed a radio counterpart (e.g., Carilli & Taylor 2000). Extended emission to the south is observed in soft X-rays, while it shows a point-like source at hard energies (Appendix C.1). It was classified as a Compton-thick candidate (Teng et al. 2009).

It was observed once with *Chandra* in 2000, and five times with *XMM*–Newton between 2002 and 2013. Balestra et al. (2005) fit the *Chandra* and *XMM*–Newton spectra with a composite of three thermal plus an absorbed PL components and found similar spectral parameters, except in the value of the column densities (41[35-47] and 69[50-85] $\times 10^{22} cm^{-2}$, respectively). This result is compatible with ours, with N_{H2} being responsible for the observed variations. In the same sense, Teng et al. (2009) studied *Suzaku* data from 2006 and found spectral variations when comparing with *Chandra* and *XMM*–Newton data. They attributed the changes to the covering fraction of the absorber.

We found no short-term variations from the *Chandra* light curve or UV variations from the UVW1 filter.

Appendix B.18: Circinus

It was optically classified as a Seyfert 2 galaxy (Oliva et al. 1994), and it shows broad lines in polarized light (Oliva et al. 1998). The *HST* image shows dust lanes (Appendix C.1). *ATCA* observations show a radio counterpart, a water maser, and large radio lobes (Elmouttie et al. 1998). Circinus is a Compton-thick source (Bassani et al. 1999), which in fact was observed by *BeppoSAX* ($N_H = 4.3 \times 10^{24} cm^{-2}$, Matt et al. 1999).

This galaxy was observed eight times with *Chandra* between 2000 and 2010, and twice with *XMM*–Newton in 2001 and 2014. The most comprehensive analysis of this source has recently been done by Arévalo et al. (2014), who analyzed 26 observations from *NuSTAR*, *Chandra*, *XMM*–Newton, *Swift*, *Suzaku*, and *BeppoSAX* satellites spanning 15 years and the energy range 2–79 keV. They used different models to fit the data, based on PEXMON, MyTorus, and Torus models (in XSPEC). Since different appertures were used for the analysis, they decontaminated the extranuclear emission. They conclude that the nucleus did not show variations, in agreement with our result when comparing *Chandra* data. Moreover, Arévalo et al. (2014) find that extranuclear sources included in the larger apertures showed variations (an ultraluminous X-ray source and a supernova remnant), also in agreement with our results when comparing *XMM*–Newton data, where the extranuclear sources were included, and we found variations in both the normalizations at soft and hard energies.

We analysed one *Chandra* light curves, but variations were not detected.

The analysis of light curves from the *Swift*/BAT 58-month survey by Soldi et al. (2014) showed a small variability amplitude of 11[10-12]% in the 14–195 keV energy band.

Appendix B.19: NGC 5643

This galaxy was optically classified as a Seyfert 2 (Phillips et al. 1983, see an optical spectrum in Appendix C.1), and broad lines were not detected in polarized light (Gu & Huang 2002). The *HST* image shows a nuclear spiral structure (see Appendix C.1). *VLA* data show a nuclear counterpart alongside fainter features extending to the east and west at radio frequencies (Morris et al. 1985). The *XMM*–Newton image shows a compact source at hard X-ray energies. This is a Compton-thick object observed with *BeppoSAX* ($N_H > 10^{25} cm^{-2}$, Comastri 2004).

It was observed twice with *XMM*–Newton in 2003 and 2009, and once with *Chandra* in 2004. Matt et al. (2013) analyzed the two observations from *XMM*–Newton, who found that the spectra are reproduced well by reflection from warm and cold matter. The spectral parameters were consistent with the same values for the two observations. Thus, variations are not observed. These results agree well with ours, where variations are not found.

Appendix B.20: MARK 477

This object was classified as a Seyfert 2 (Veron et al. 1997), and broad lines have been detected in polarized light (Tran et al. 1992; Tran 1995). The *HST* image reveals a structure around the nucleus, which could be a spiral or a circumnuclear ring (see Appendix C.1). A nuclear counterpart was found at 6 cm using *VLA* data (Ulvestad & Wilson 1984). It was classified as a Compton-thick candidate (Bassani et al. 1999).

The source was observed twice with *ASCA* in December 1995; variations were not found when fitting a scattered power law plus a narrow line (Levenson et al. 2001).

It was observed twice with *XMM*–Newton in 2010. We did not find variations between these observations.

Kinney et al. (1991) studied UV variability of this source with *HST*, but variations were not found. We did not find UV flux variations from the UVW1 filter.

Appendix B.21: IC 4518A

This galaxy was optically classified as a Seyfert 2 galaxy (Zaw et al. 2009). The *2MASS* image shows two interacting galaxies (see Appendix C.1). It is a Compton-thin source (Bassani et al. 1999; de Rosa et al. 2008).

It was observed twice with *XMM*–Newton in 2006. Variability analyses were not found in the literature. However, comparing the luminosities obtained by de Rosa et al. (2012) and Pereira-Santaella et al. (2011) of log(L(2-10 keV)) = 42.60 and 42.34 for the different spectra, their results are suggestive of flux variability. In fact, these luminosities agreed with our estimates. Our analysis shows that this variability is related with the nuclear continuum.

Appendix B.22: ESO 138-G01

Alloin et al. (1992) optically classified this galaxy as a Seyfert 2. It shows a jet-like morphology at radio frequencies (Morganti et al. 1999). The *XMM*–Newton image shows a compact source at hard X-ray energies (see Appendix C.1). It was classified as a Compton-thick candidate (Collinge & Brandt 2000).

This galaxy was observed three times with *XMM*–Newton in 2007 and 2013. Variability analyses were not found in the literature. We did not find any X-ray variations.

Appendix B.23: NGC 6300

NGC 6300 is a barred spiral galaxy, whose Seyfert 2 classification at optical frequencies was derived from the data reported in Phillips et al. (1983). The *HST* image shows dust lanes (see Appendix C.1). A nuclear counterpart was found at radio frequencies, without any jet structure (Ryder et al. 1996). NGC 6300 was classified as a changing-look AGN, observed in the Compton-thick state with *RXTE* in 1997 and in the Compton-thin state with *BeppoSAX* in 1999 (Guainazzi 2002).

The galaxy was observed once with *XMM*–Newton in 2001 and five times with *Chandra* during 2009. Guainazzi (2002) found variations due to a difference in the normalization of the power law when comparing *BeppoSAX* and *RXTE* data. All the observations analyzed in this work caught the object in the thin state. Variations in the normalizations at soft and hard energies were found when comparing *Chandra* and *XMM*–Newton data.

Matsumoto et al. (2004) and Awaki et al. (2005, 2006) studied the light curve from *XMM*–Newton data and found rapid variations at hard energies.

Variations in the 14–195 keV energy band were analyzed by Soldi et al. (2014) using data from the *Swift*/BAT 58-month survey, who estimated an intrinsic variability amplitude of 17[14-20]%.

Appendix B.24: NGC 7172

NGC 7172 is an early type galaxy located in the HCG 90 group, which shows dust lanes (Sharples et al. 1984, see also Appendix C.1). Optically classified as a Seyfert 2 (see an optical spectrum in Appendix C.1), no broad lines have been observed in polarized light (Lumsden et al. 2001). A radio core was detected with *VLA* data (Unger et al. 1987). At IR frequencies, Sharples et al. (1984) found variations on timescales of about three months. The nucleus of this galaxy is not detected at UV frequencies with the OM (see Table A.1). Even if *Chandra* data are available for this source, they suffer from strong pileup. The *XMM*–Newton image shows a compact source (see Appendix C.1).

Guainazzi et al. (1998) first reported X-ray flux variations in this source using *ASCA* data. They found short-term variations (hours) from the analysis of a light curve from 1996 and long-term variations when comparing the flux of these data with previous data from 1995, when it was about three times brighter. Risaliti (2002) studied two *BeppoSAX* observations taken in October 1996 and November 1997 and fit the data with an absorbed power law, a thermal component, a cold reflection, a warm reflection, and a narrow Gaussian line. They reported very similar spectral parameters for the two spectra.

This galaxy was observed once with *Chandra* in 2000 and three times with *XMM*–Newton between 2002 and 2007. LaMassa et al. (2011) analyzed the *XMM*–Newton spectra by fitting the data with the ME2PL model and needed to fit the normalization of the power law independently. They report luminosities of log(L(2-10 keV)) = 42.96±0.03 (for the spectrum from 2007) and 42.61±0.03 (for the other two spectra). These results agree well with our SMF1.

Awaki et al. (2006) analyzed the *XMM*–Newton light curve from 2002. They did not find significant variability when computing the normalized excess variance.

At higher energies, Beckmann et al. (2007) reported an intrinsic variability of $S_{Vc} = 12 \pm 9\%$ within 20 days using *Swift*/BAT data, and using data from the *Swift*/BAT 58-month survey, Soldi et al. (2014) report a variability amplitude of 28[25-31]%, both in the 14–195 keV energy band.

Appendix B.25: NGC 7212

This galaxy is interacting with a companion (see the *2MASS* image in Appendix C.1). It was optically classified as a Seyfert 2 galaxy (Veilleux & Osterbrock 1987, see an optical spectrum in Appendix C.1). Broad lines were detected in polarized light

(Tran et al. 1992). At radio wavelengths, a nuclear counterpart was found with the interacting galaxy (Falcke et al. 1998). A point-like source is detected at hard X-rays (see Appendix C.1). It was classified as a Compton-thick candidate (Severgnini et al. 2012).

It was observed once with *Chandra* in 2003 and once with *XMM*–Newton in 2004. Bianchi et al. (2006) report the same fluxes for the two spectra, also in agreement with our results.

Appendix B.26: NGC 7319

NGC 7319 is a spiral galaxy located in the Stephan's Quintet, a group composed by six galaxies including a core of three galaxies (Trinchieri et al. 2003). These three galaxies were also observed at radio wavelengths with *VLA* (Aoki et al. 1999) and later with *MERLIN* (Xanthopoulos et al. 2004), revealing a jet structure in NGC 7319. It has been optically confirmed as a Seyfert 2 (Rodríguez-Baras et al. 2014, see an optical spectrum in Appendix C.1). The nucleus of this galaxy is not detected at UV frequencies with the OM (see Table A.1). In X-rays, a point-like source is observed in the 4.5–8.0 keV energy band, and it shows extended emission at soft X-ray energies (Appendix C.1).

It was observed twice with *Chandra* in 2000 and 2007, and once with *XMM*–Newton in 2001. We did not find any variability studies in the literature. We found variations in the nuclear power of the nucleus, accompained by absorber variations at soft energies.

One *Chandra* and the *XMM*–Newton light curves were analyzed, but short-term variations were not detected.

Appendix C: Images

Appendix C.1: Optical spectra, and X-ray, 2MASS and optical HST *images*

In this appendix we present images at different wavelengths for each energy and the optical spectrum when available from NED. In X-rays we extracted *Chandra* data in four energy bands: 0.6-0.9 keV (top left), 1.6-2.0 keV (top middle), 4.5-8.0 keV (top right), and 0.5-10.0 keV (bottom left). The CSMOOTH task included in CIAO was used to adaptatively smooth the three images in the top panels (i.e., the images in the 0.5-10.0 keV energy band are not smoothed), using a fast Fourier transform algorithm and a minimum and maximum significance level of the signal-to-noise of 3 and 4, respectively. When data from *Chandra* was not available, *XMM*–Newton images were extracted in the same energy bands, and the ASMOOTH task was used to adaptatively smooth the images. At infrared frequencies, we retrieved an image from 2MASS in the K_s filter[13]. At optical frequencies we used images from the *Hubble* Space telescope (*HST*)[14], preferably in the F814W filter, but when it was not available we retrieved an image in the F606W filter. *HST* data have been processed following the sharp dividing method to show the internal structure of the galaxies (Marquez & Moles 1996). The red squares in the bottom images represent the area covered by the *HST* image (presented in the bottom right panel when available). In all images the gray levels extend from twice the value of the background dispersion to the maximum value at the center of each galaxy. We used IRAF [15] to estimate these values.

---

[13] http://irsa.ipac.caltech.edu/applications/2MASS/IM/interactive.html

[14] http://hla.stsci.edu/

[15] http://iraf.noao.edu/

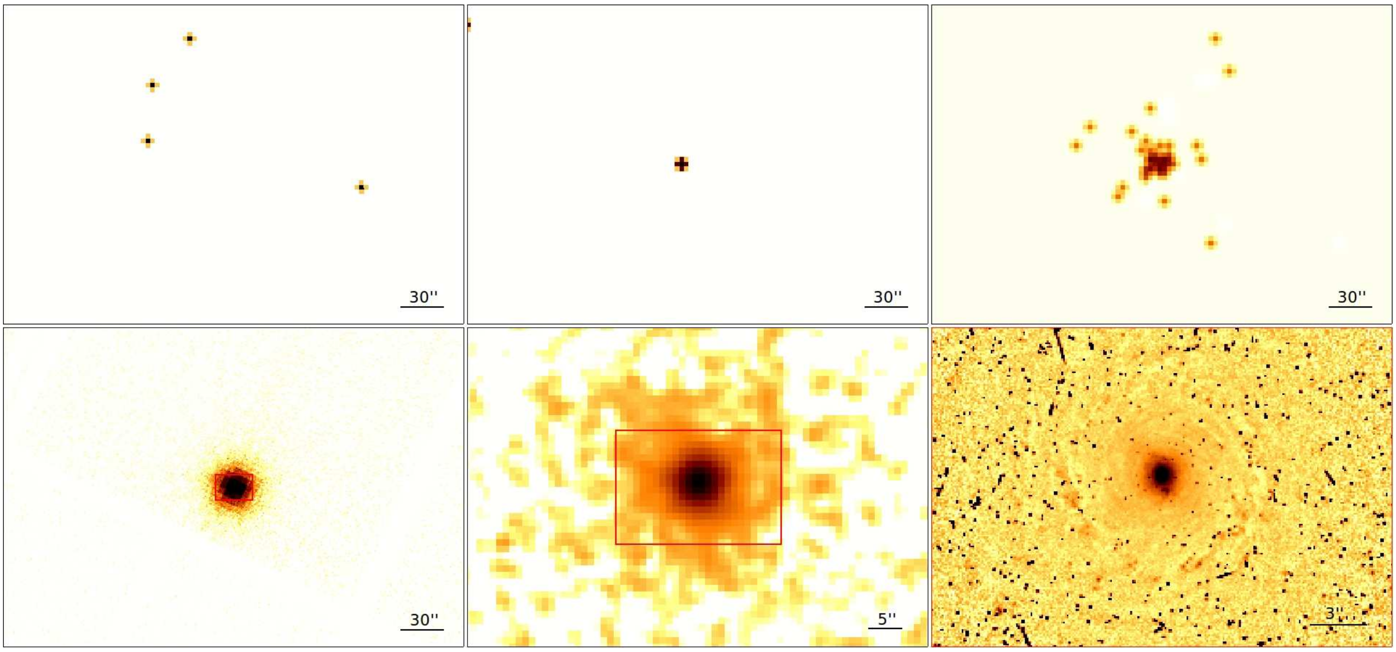

Fig. C.1: Images of MARK 348 (*XMM*–Newton data). (Top left): Smoothed X-ray 0.6-0.9 keV energy band; (top center): smoothed X-ray 1.6-2.0 keV energy band; (top right): smoothed X-ray 4.5-8.0 keV energy band; (bottom left): X-ray 0.5-10.0 keV energy band without smoothing; (bottom center): 2MASS image in the K_s band; (bottom right): Hubble image in the F606W filter.

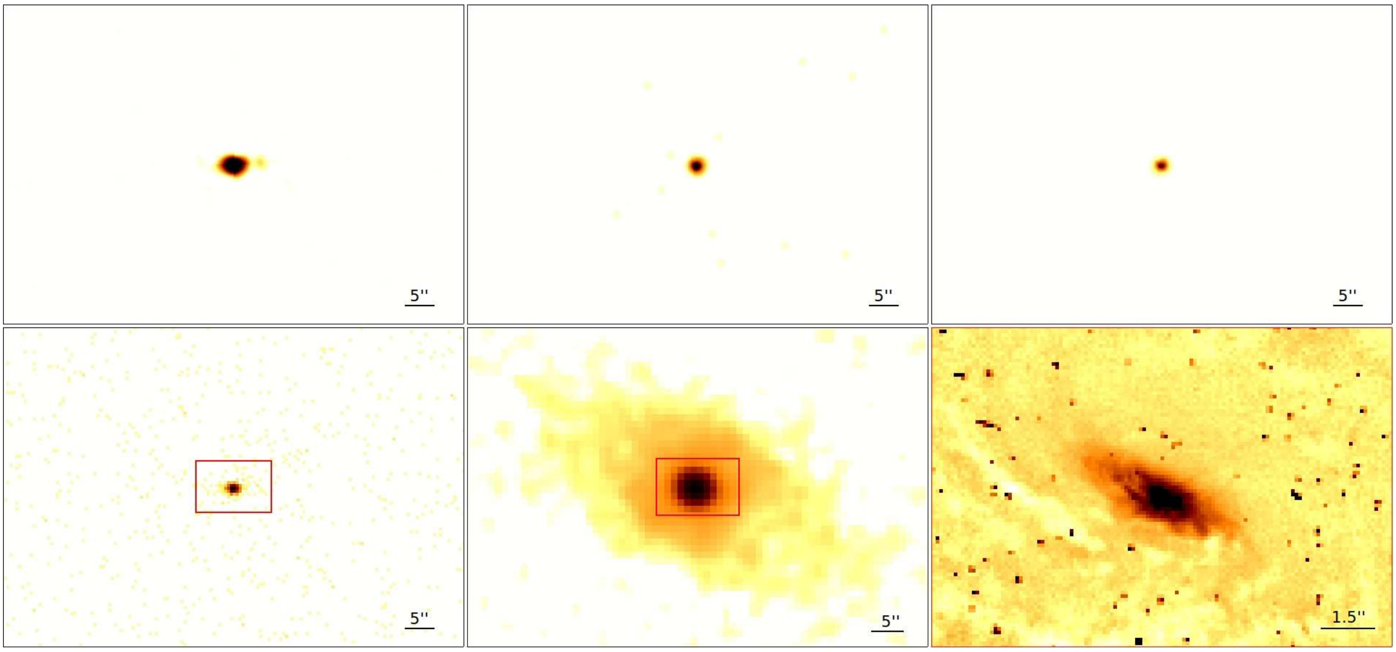

Fig. C.2: Images of NGC 424. (Top left): Smoothed X-ray 0.6-0.9 keV energy band; (top center): smoothed X-ray 1.6-2.0 keV energy band; (top right): smoothed X-ray 4.5-8.0 keV energy band; (bottom left): X-ray 0.5-10.0 keV energy band without smoothing; (bottom center): 2MASS image in the K_s band; (bottom right): Hubble image in the F606W filter.

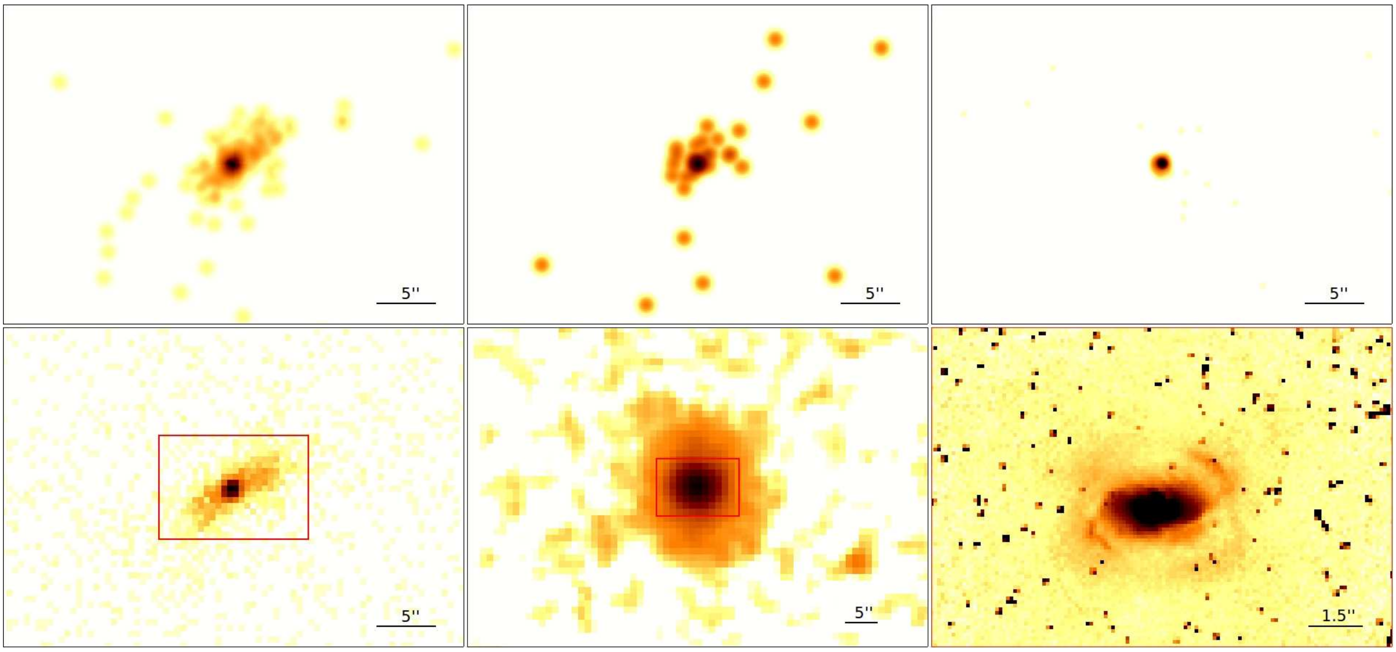

Fig. C.3: Images of MARK 573. (Top left): Smoothed X-ray 0.6-0.9 keV energy band; (top center): smoothed X-ray 1.6-2.0 keV energy band; (top right): smoothed X-ray 4.5-8.0 keV energy band; (bottom left): X-ray 0.5-10.0 keV energy band without smoothing; (bottom center): 2MASS image in the K_s band; (bottom right): Hubble image in the F814W filter.

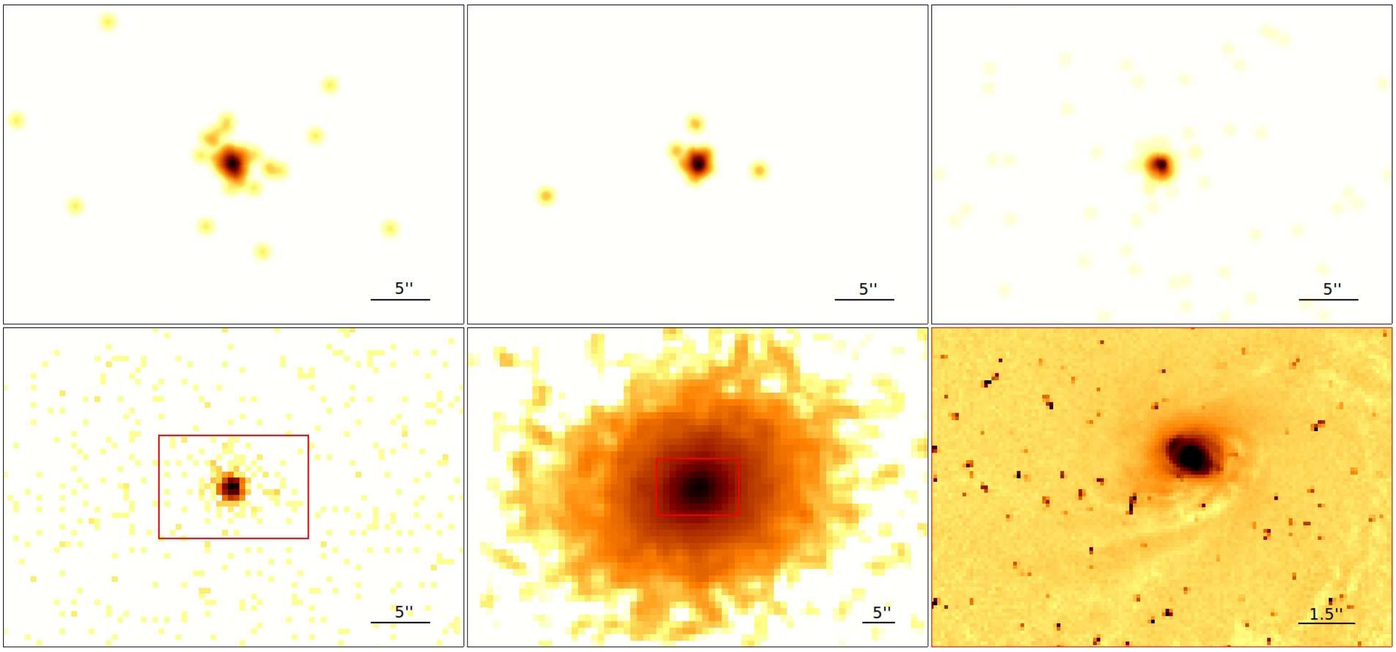

Fig. C.4: Images of NGC 788. (Top left): Smoothed X-ray 0.6-0.9 keV energy band; (top center): smoothed X-ray 1.6-2.0 keV energy band; (top right): smoothed X-ray 4.5-8.0 keV energy band; (bottom left): X-ray 0.5-10.0 keV energy band without smoothing; (bottom center): 2MASS image in the K_s band; (bottom right): Hubble image in the F606W filter.

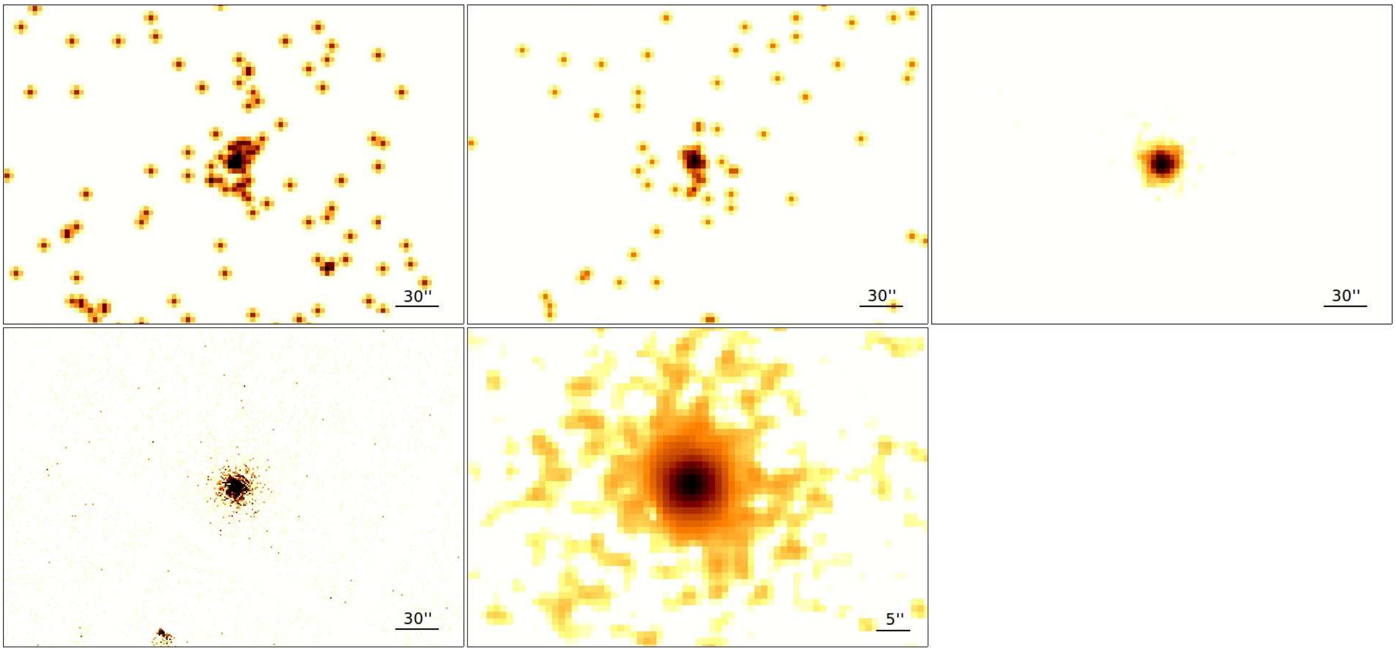

Fig. C.5: Images of ESO 417-G06 (*XMM*–Newton data). (Top left): Smoothed X-ray 0.6-0.9 keV energy band; (top center): smoothed X-ray 1.6-2.0 keV energy band; (top right): smoothed X-ray 4.5-8.0 keV energy band; (bottom left): X-ray 0.5-10.0 keV energy band without smoothing; (bottom center): 2MASS image in the K_s band.

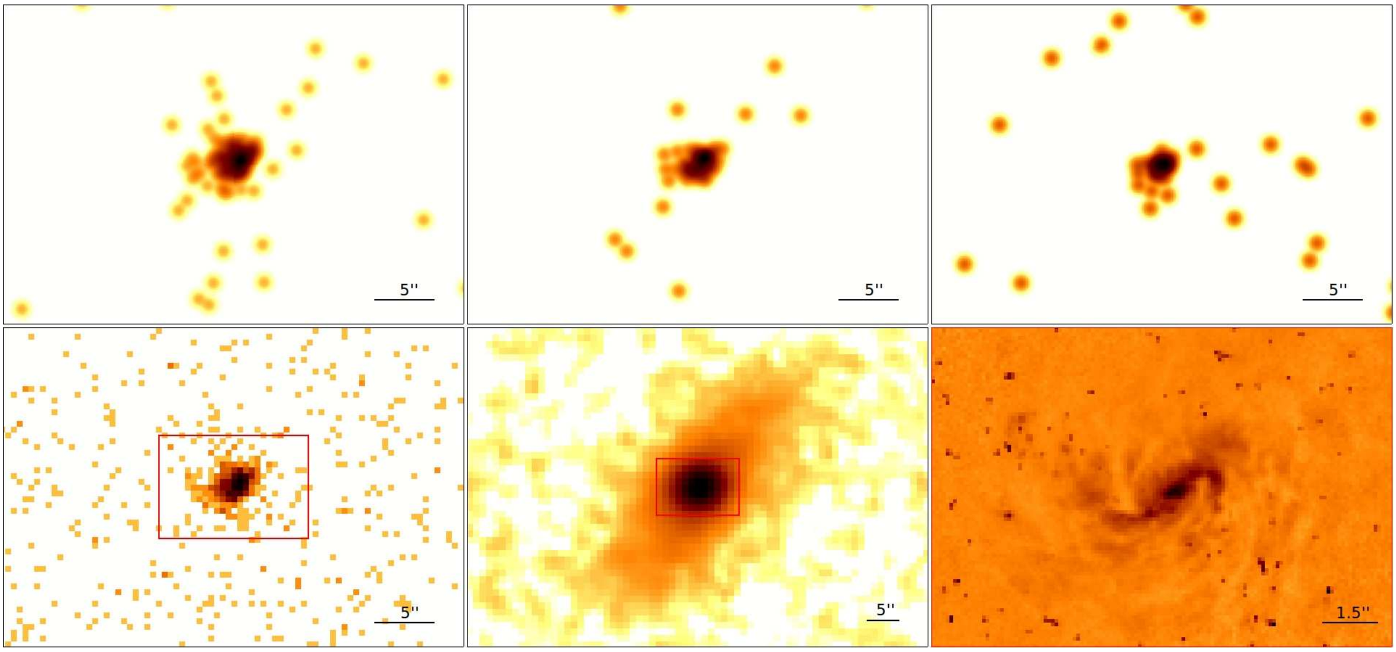

Fig. C.6: Images of MARK 1066. (Top left): Smoothed X-ray 0.6-0.9 keV energy band; (top-center): smoothed X-ray 1.6-2.0 keV energy band; (top right): smoothed X-ray 4.5-8.0 keV energy band; (bottom left): X-ray 0.5-10.0 keV energy band without smoothing; (bottom center): 2MASS image in the K_s band; (bottom right): Hubble image in the F606W filter.

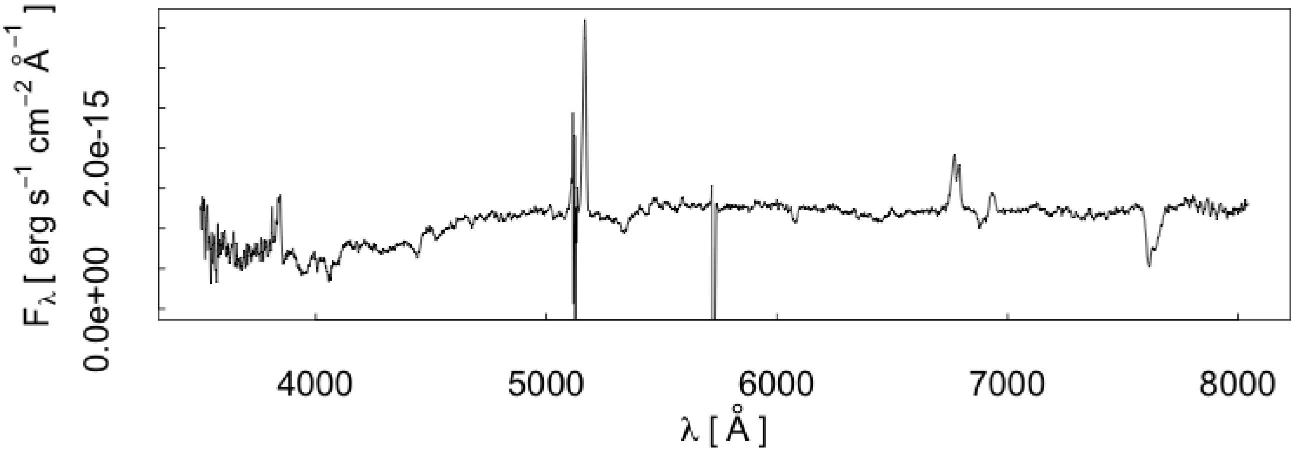

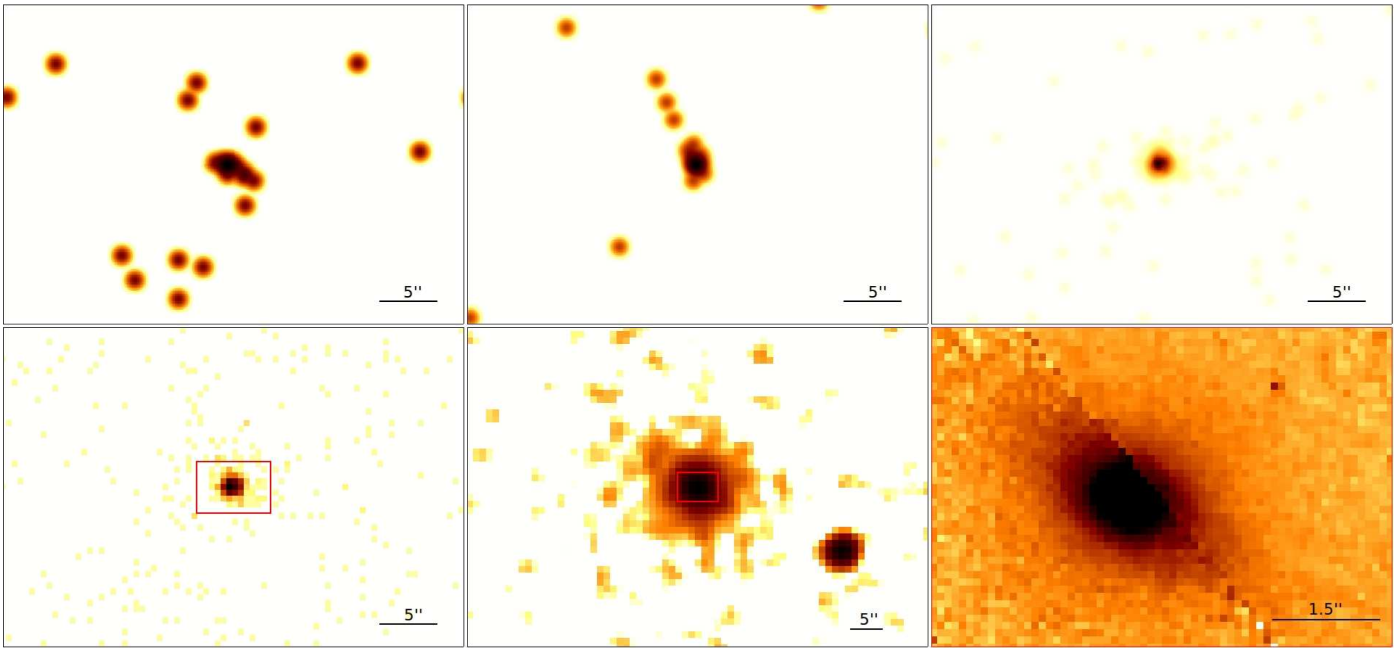

Fig. C.7: Up: Optical spectrum (from NED); bottom: images of 3C 98.0. (Top left): Smoothed X-ray 0.6-0.9 keV energy band; (top center): smoothed X-ray 1.6-2.0 keV energy band; (top right): smoothed X-ray 4.5-8.0 keV energy band; (bottom left): X-ray 0.5-10.0 keV energy band without smoothing; (bottom center): 2MASS image in the K_s band; (bottom right): Hubble image in the F606 filter.

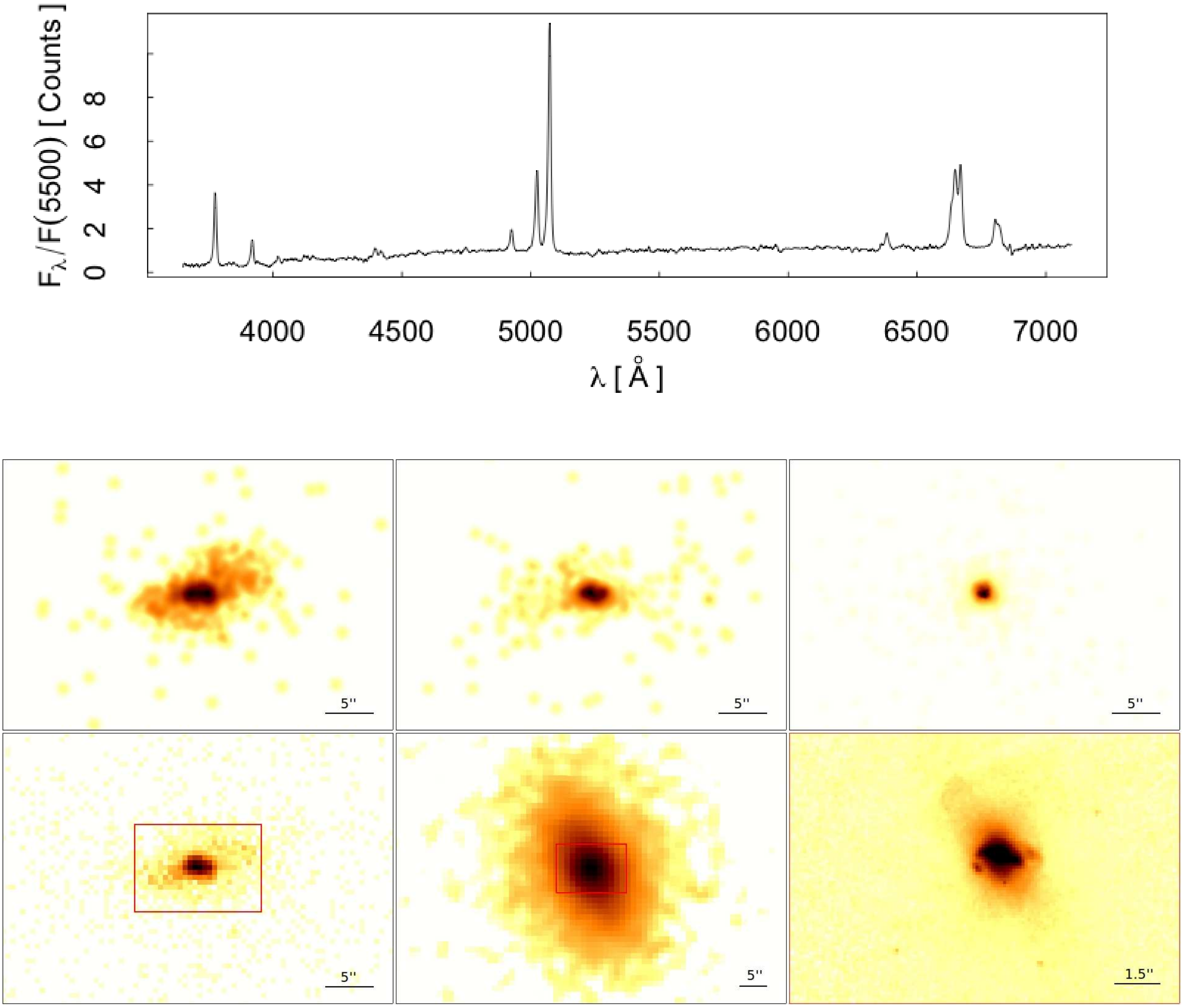

Fig. C.8: Up: Optical spectrum (from NED);bottom: images of MARK 3. (Top left): Smoothed X-ray 0.6-0.9 keV energy band; (top center): smoothed X-ray 1.6-2.0 keV energy band; (top right): smoothed X-ray 4.5-8.0 keV energy band; (bottom left): X-ray 0.5-10.0 keV energy band without smoothing; (bottom center): 2MASS image in the K_s band; (bottom right): Hubble image in the F814W filter.

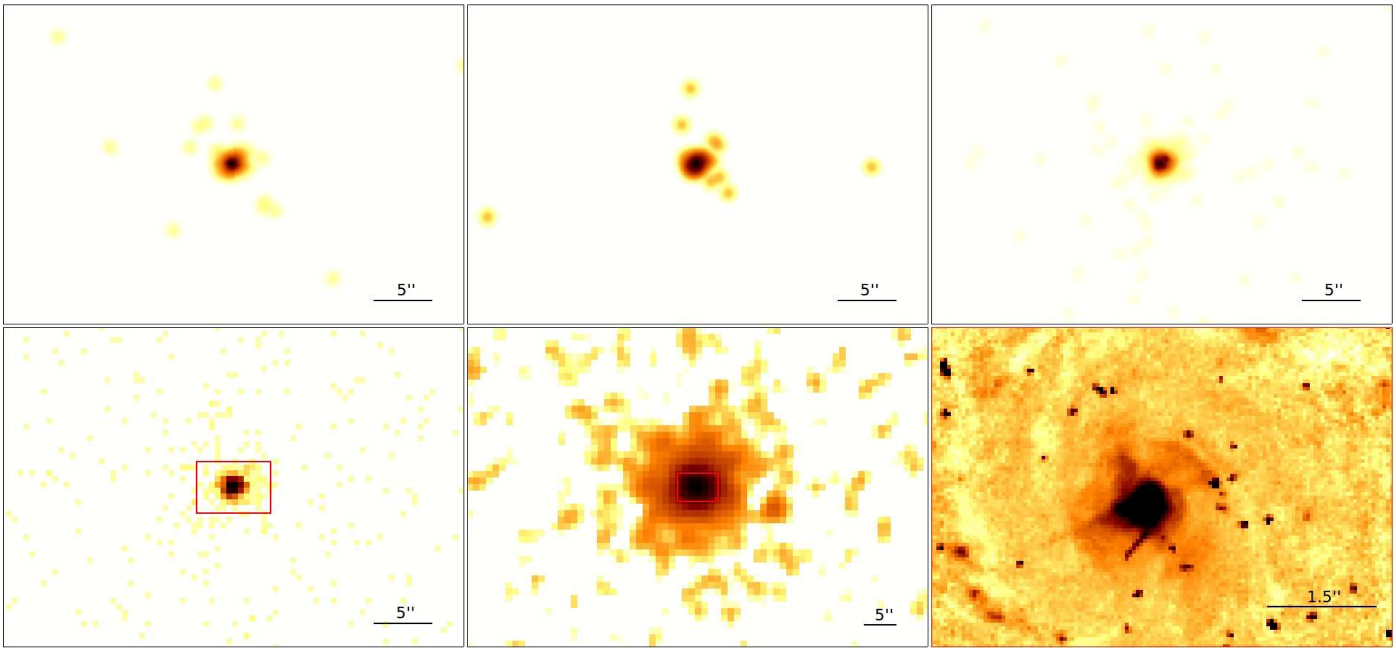

Fig. C.9: Images of MARK 1210. (Top left): Smoothed X-ray 0.6-0.9 keV energy band; (top center): smoothed X-ray 1.6-2.0 keV energy band; (top right): smoothed X-ray 4.5-8.0 keV energy band; (bottom left): X-ray 0.5-10.0 keV energy band without smoothing; (bottom center): 2MASS image in the K_s band; (bottom right): Hubble image in the F606W filter.

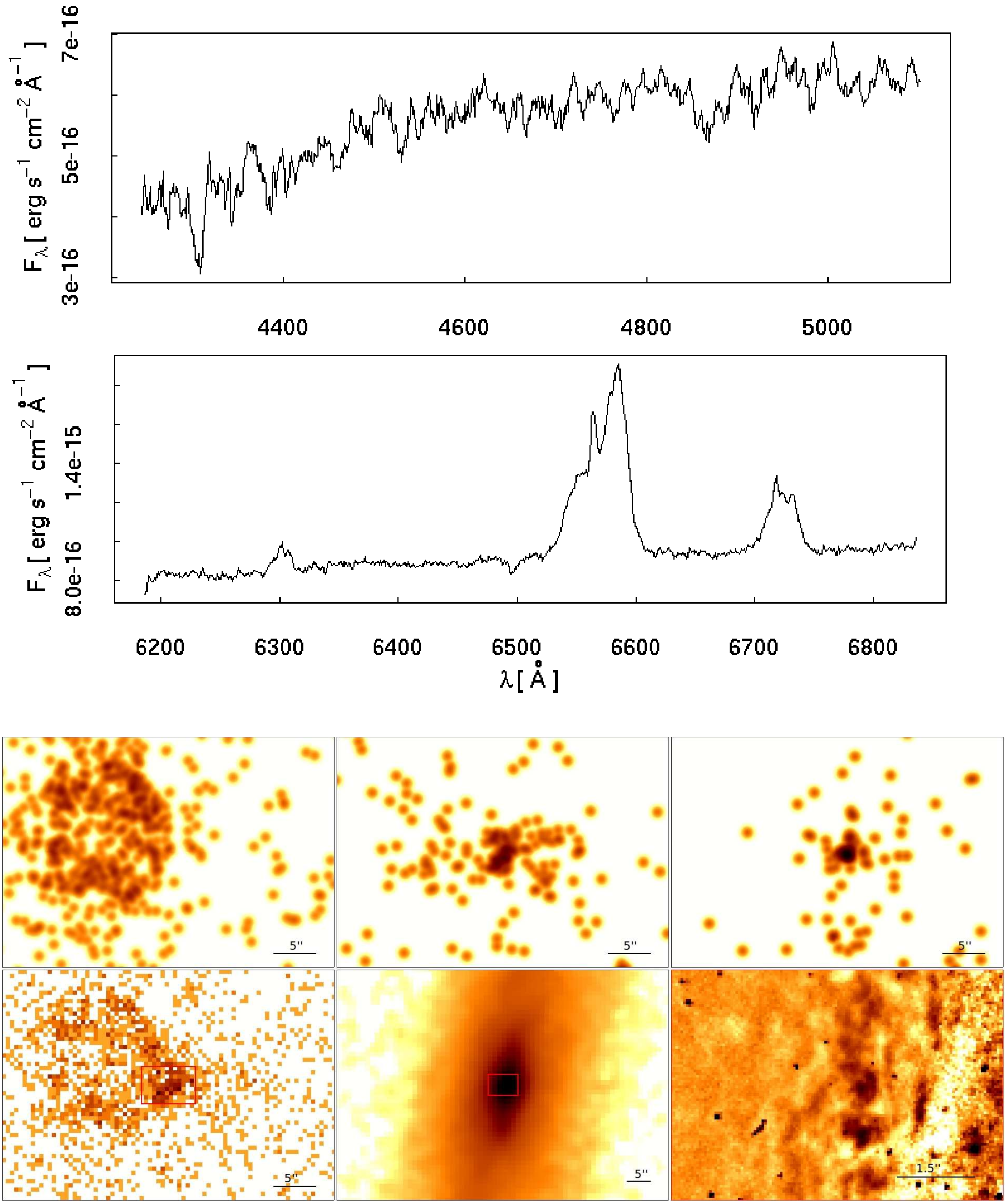

Fig. C.10: Up: Optical spectra (from NED);bottom: images of NGC 3079. (Top left): Smoothed X-ray 0.6-0.9 keV energy band; (top center): smoothed X-ray 1.6-2.0 keV energy band; (top right): smoothed X-ray 4.5-8.0 keV energy band; (bottom left): X-ray 0.5-10.0 keV energy band without smoothing; (bottom center): 2MASS image in the K_s band; (bottom right): Hubble image in the F814W filter.

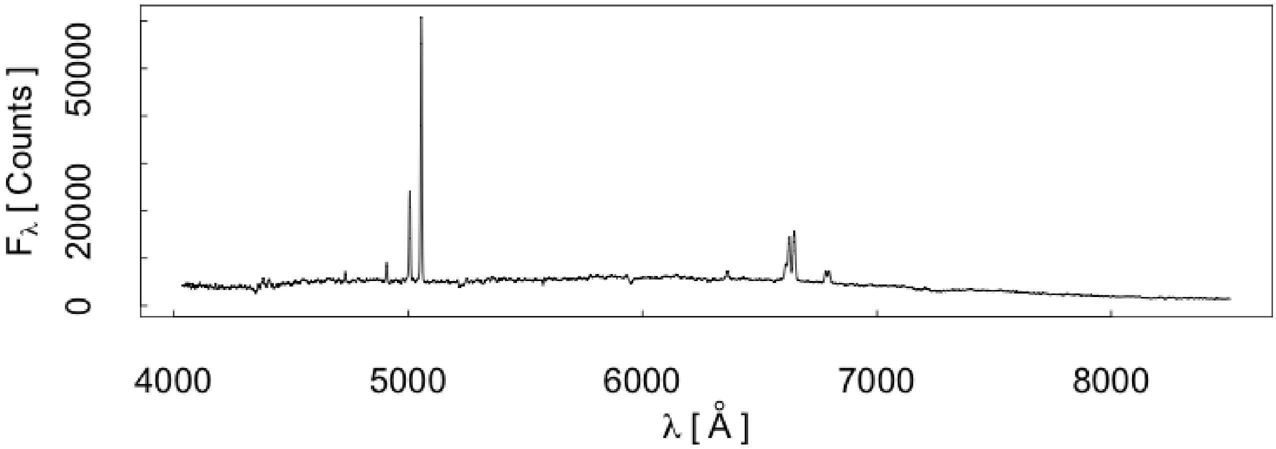

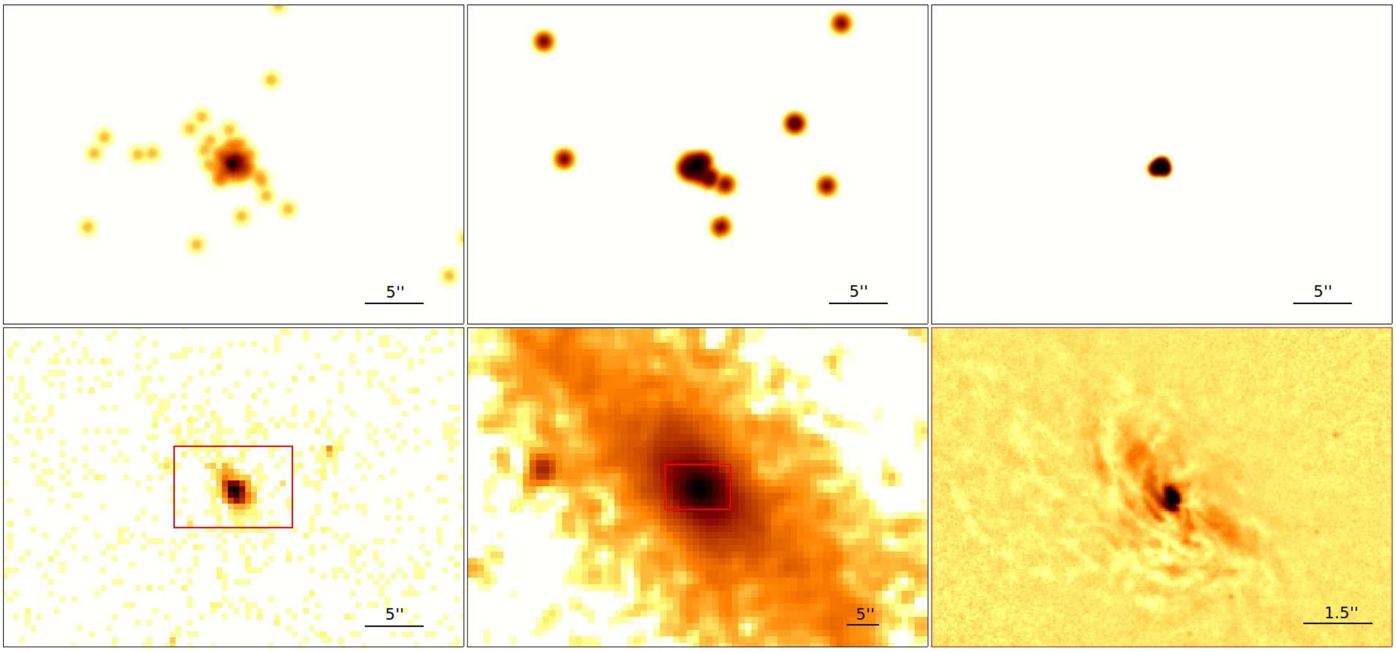

Fig. C.11: Up: Optical spectrum (from NED); bottom: images of IC 2560. (Top left): Smoothed X-ray 0.6-0.9 keV energy band; (top center): smoothed X-ray 1.6-2.0 keV energy band; (top right): smoothed X-ray 4.5-8.0 keV energy band; (bottom left): X-ray 0.5-10.0 keV energy band without smoothing; (bottom center): 2MASS image in the K_s band; (bottom right): Hubble image in the F814W filter.

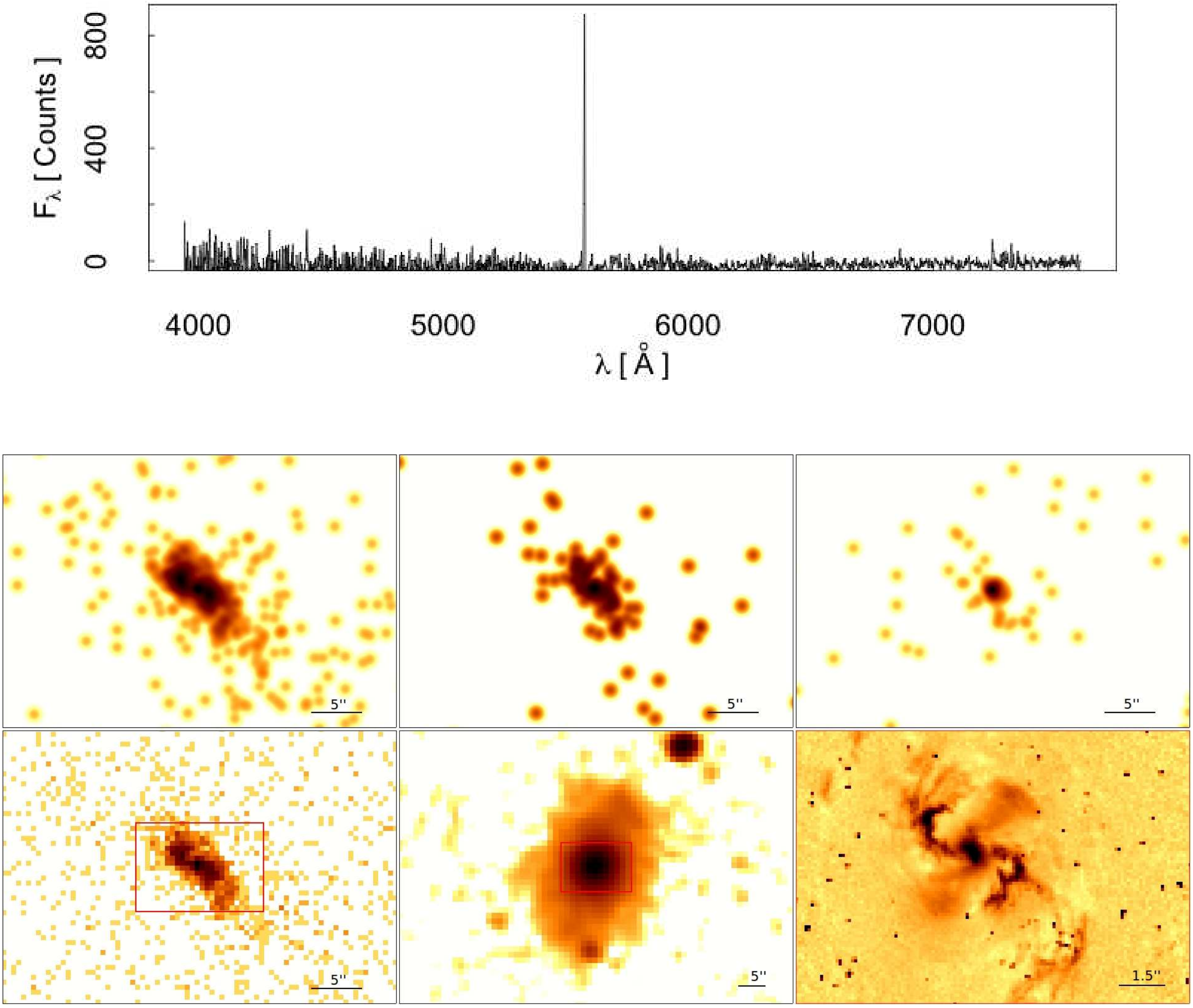

Fig. C.12: Up: Optical spectrum (from NED); bottom: images of NGC 3393. (Top left): Smoothed X-ray 0.6-0.9 keV energy band; (top center): smoothed X-ray 1.6-2.0 keV energy band; (top right): smoothed X-ray 4.5-8.0 keV energy band; (bottom left): X-ray 0.5-10.0 keV energy band without smoothing; (bottom center): 2MASS image in the K_s band; (bottom right): Hubble image in the F606W filter.

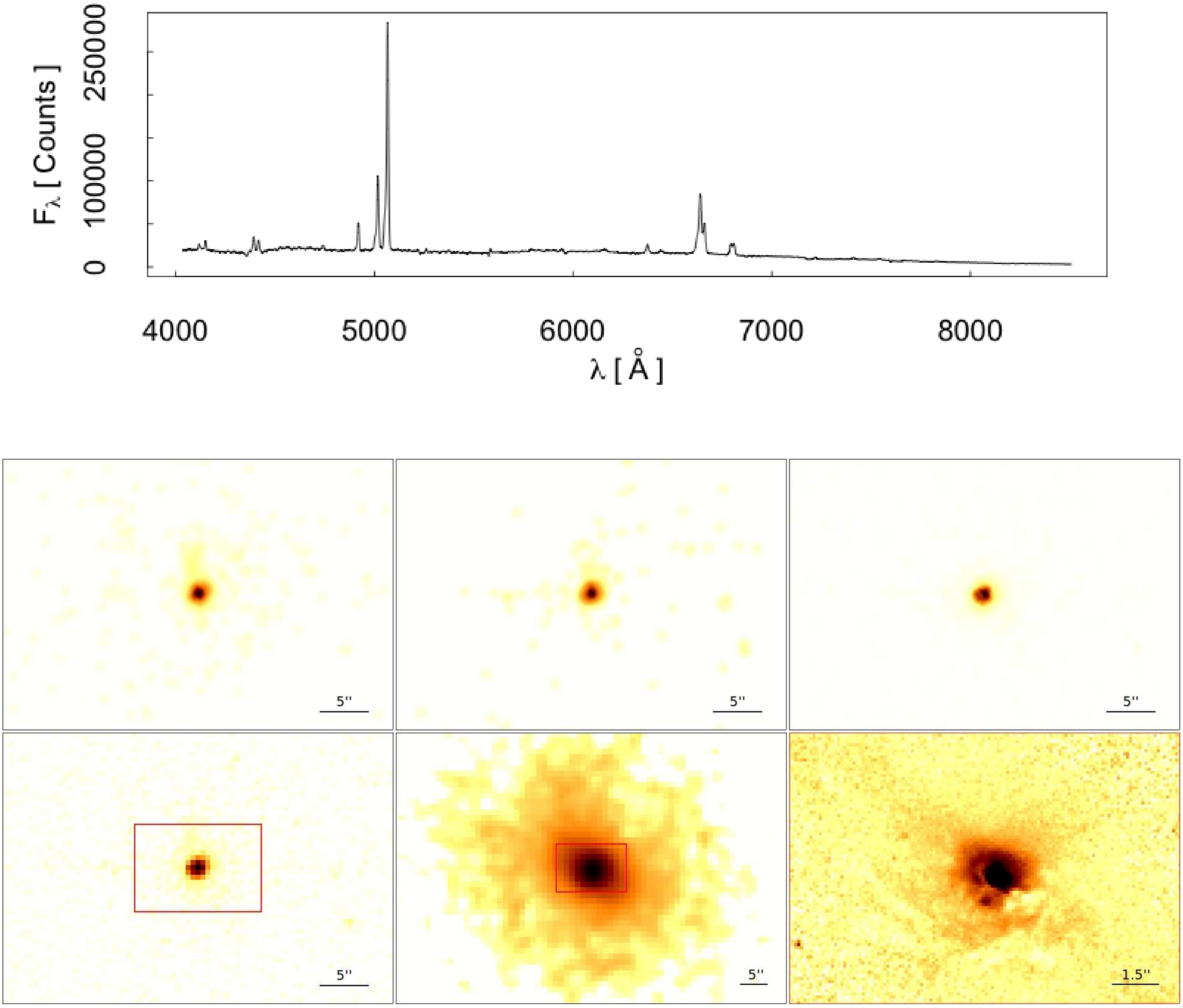

Fig. C.13: Up: Optical spectrum (from NED);bottom: images of NGC 4507. (Top left): Smoothed X-ray 0.6-0.9 keV energy band; (top center): smoothed X-ray 1.6-2.0 keV energy band; (top right): smoothed X-ray 4.5-8.0 keV energy band; (bottom left): X-ray 0.5-10.0 keV energy band without smoothing; (bottom center): 2MASS image in the K_s band; (bottom right): Hubble image in the F814W filter.

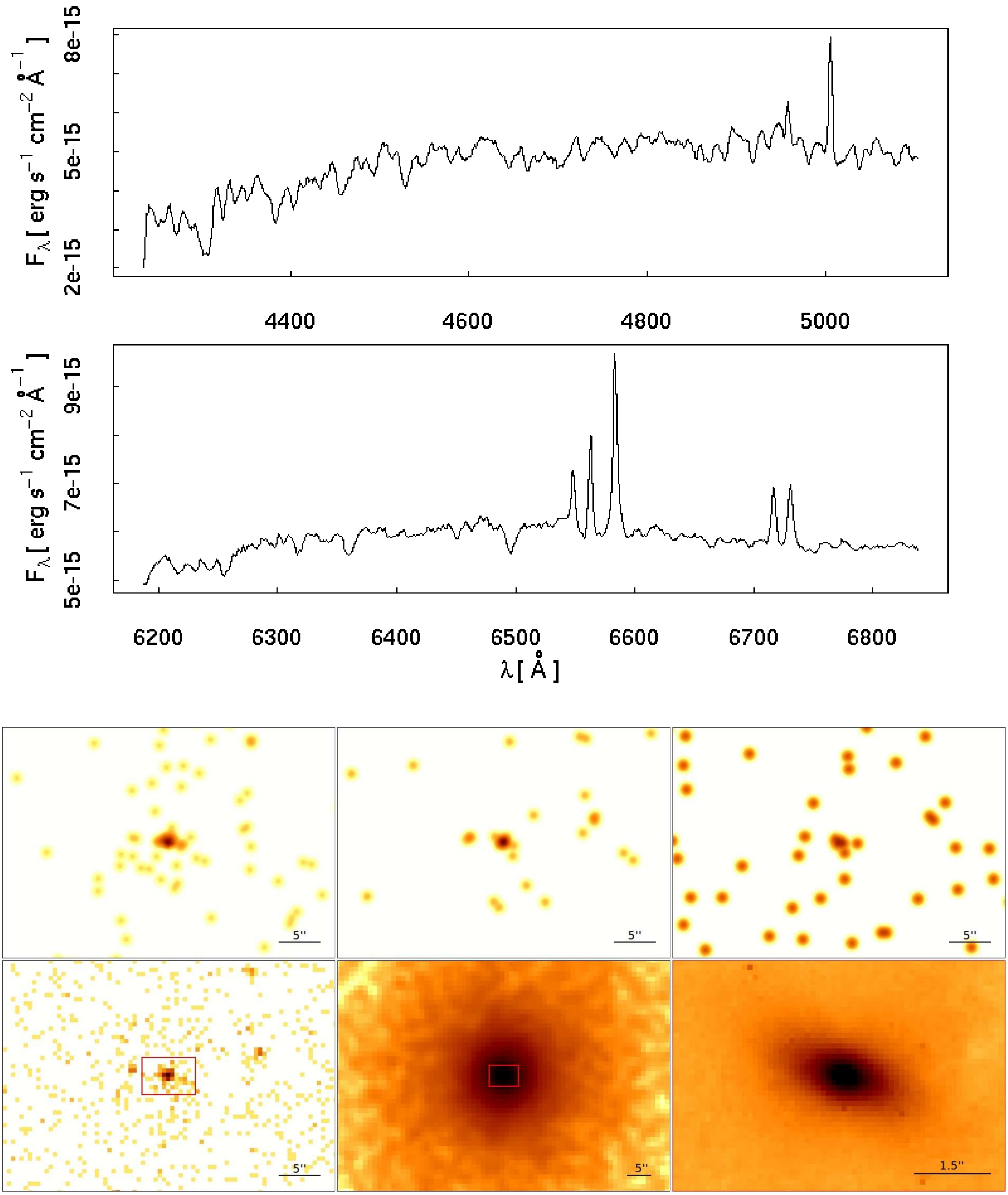

Fig. C.14: Up: Optical spectra (from NED); bottom: images of NGC 4698. (Top left): Smoothed X-ray 0.6-0.9 keV energy band; (top center): smoothed X-ray 1.6-2.0 keV energy band; (top right): smoothed X-ray 4.5-8.0 keV energy band; (bottom left): X-ray 0.5-10.0 keV energy band without smoothing; (bottom center): 2MASS image in the K_s band; (bottom right): Hubble image in the F814W filter.

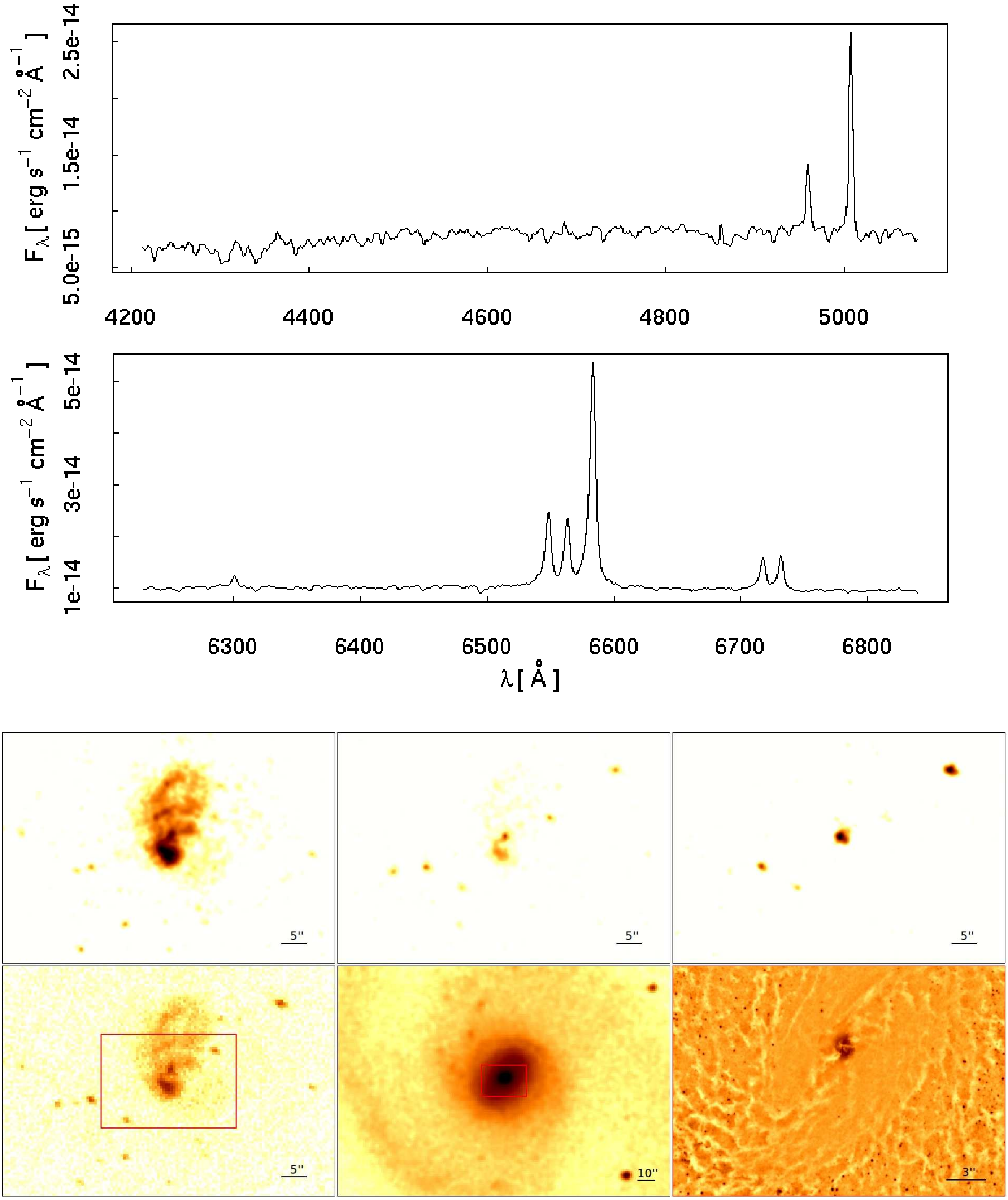

Fig. C.15: Up: Optical spectra (from NED); bottom: images of NGC 5194. (Top left): Smoothed X-ray 0.6-0.9 keV energy band; (top center): smoothed X-ray 1.6-2.0 keV energy band; (top right): smoothed X-ray 4.5-8.0 keV energy band; (bottom left): X-ray 0.5-10.0 keV energy band without smoothing; (bottom center): 2MASS image in the K_s band; (bottom right): Hubble image in the F814W filter.

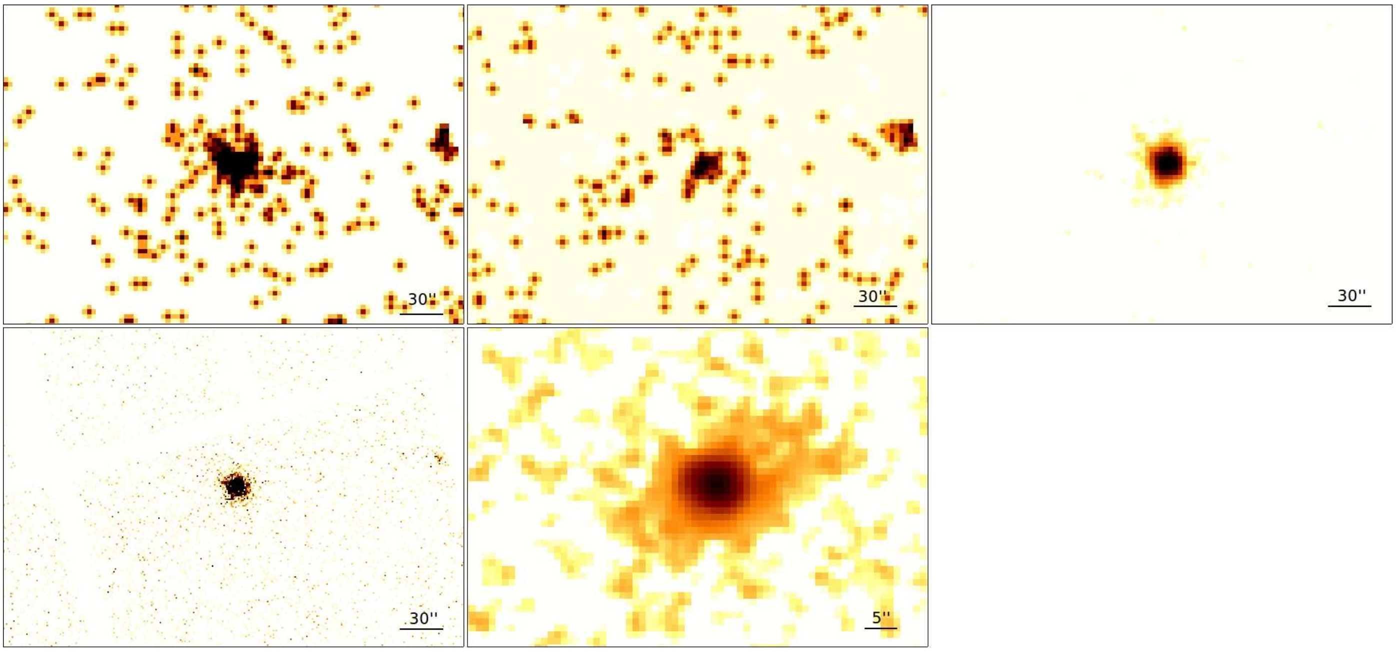

Fig. C.16: Images of MARK 268 (*XMM*–Newton data). (Top left): Smoothed X-ray 0.6-0.9 keV energy band; (top-center): smoothed X-ray 1.6-2.0 keV energy band; (top right): smoothed X-ray 4.5-8.0 keV energy band; (bottom left): X-ray 0.5-10.0 keV energy band without smoothing; (bottom center): 2MASS image in the K_s band.

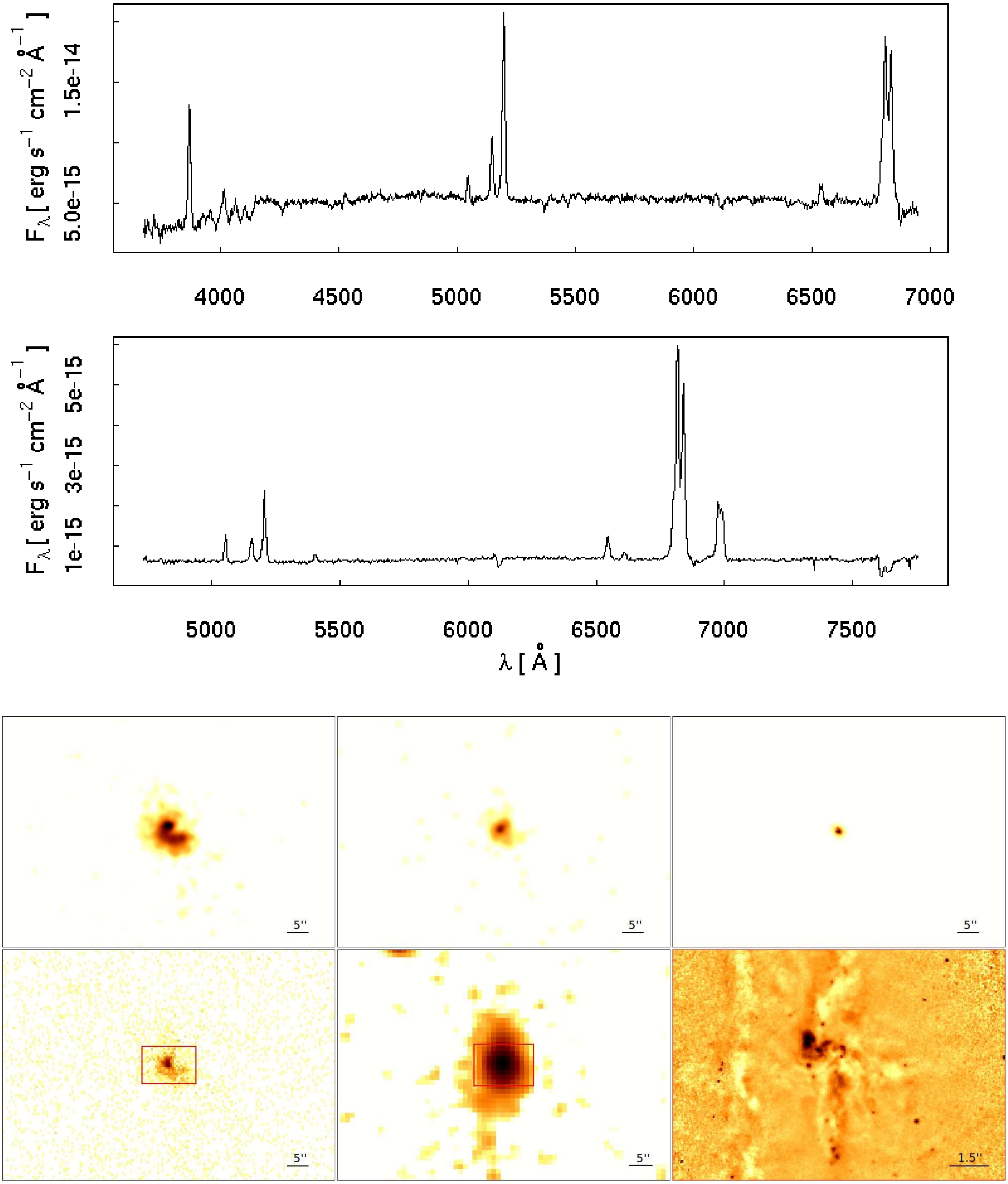

Fig. C.17: Up: Optical spectra (from NED); bottom: images of MARK 273. (Top left): Smoothed X-ray 0.6-0.9 keV energy band; (top center): smoothed X-ray 1.6-2.0 keV energy band; (top right): smoothed X-ray 4.5-8.0 keV energy band; (bottom left): X-ray 0.5-10.0 keV energy band without smoothing; (bottom center): 2MASS image in the K_s band; (bottom right): Hubble image in the F814W filter.

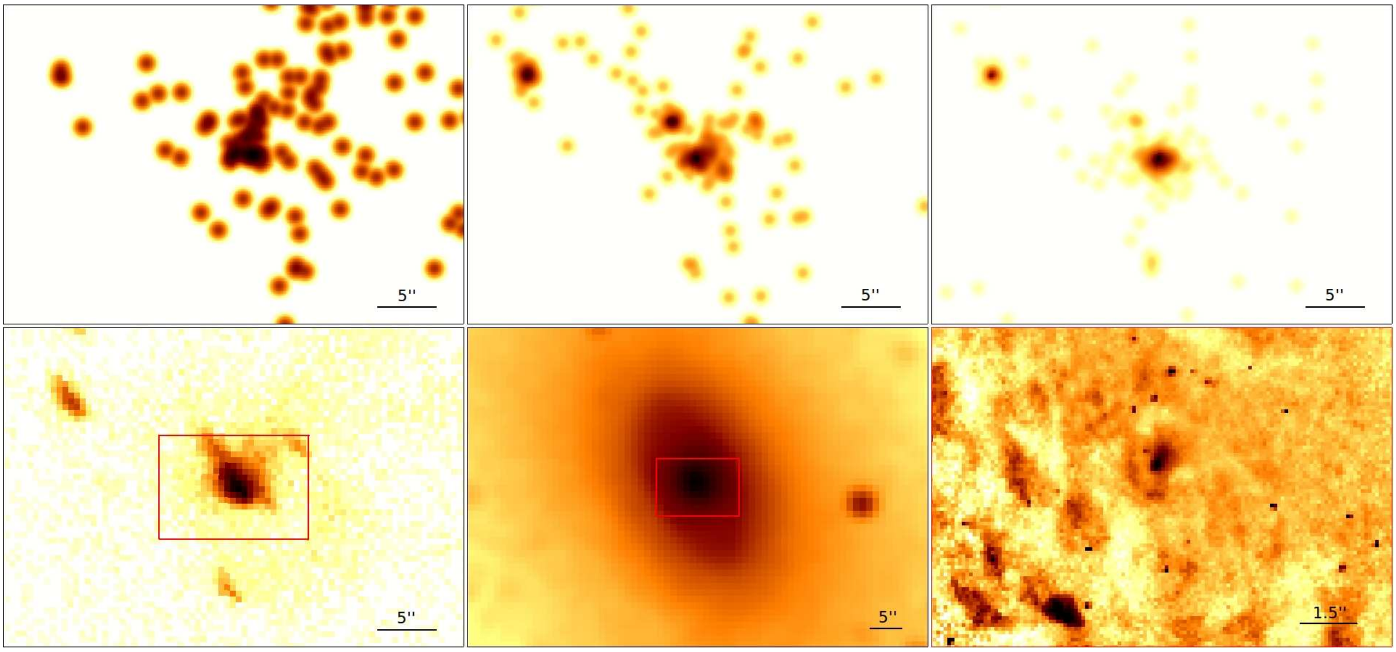

Fig. C.18: Images of Circinus. (Top left): Smoothed X-ray 0.6-0.9 keV energy band; (top center): smoothed X-ray 1.6-2.0 keV energy band; (top right): smoothed X-ray 4.5-8.0 keV energy band; (bottom left): X-ray 0.5-10.0 keV energy band without smoothing; (bottom center): 2MASS image in the K_s band; (bottom right): Hubble image in the F814W filter.

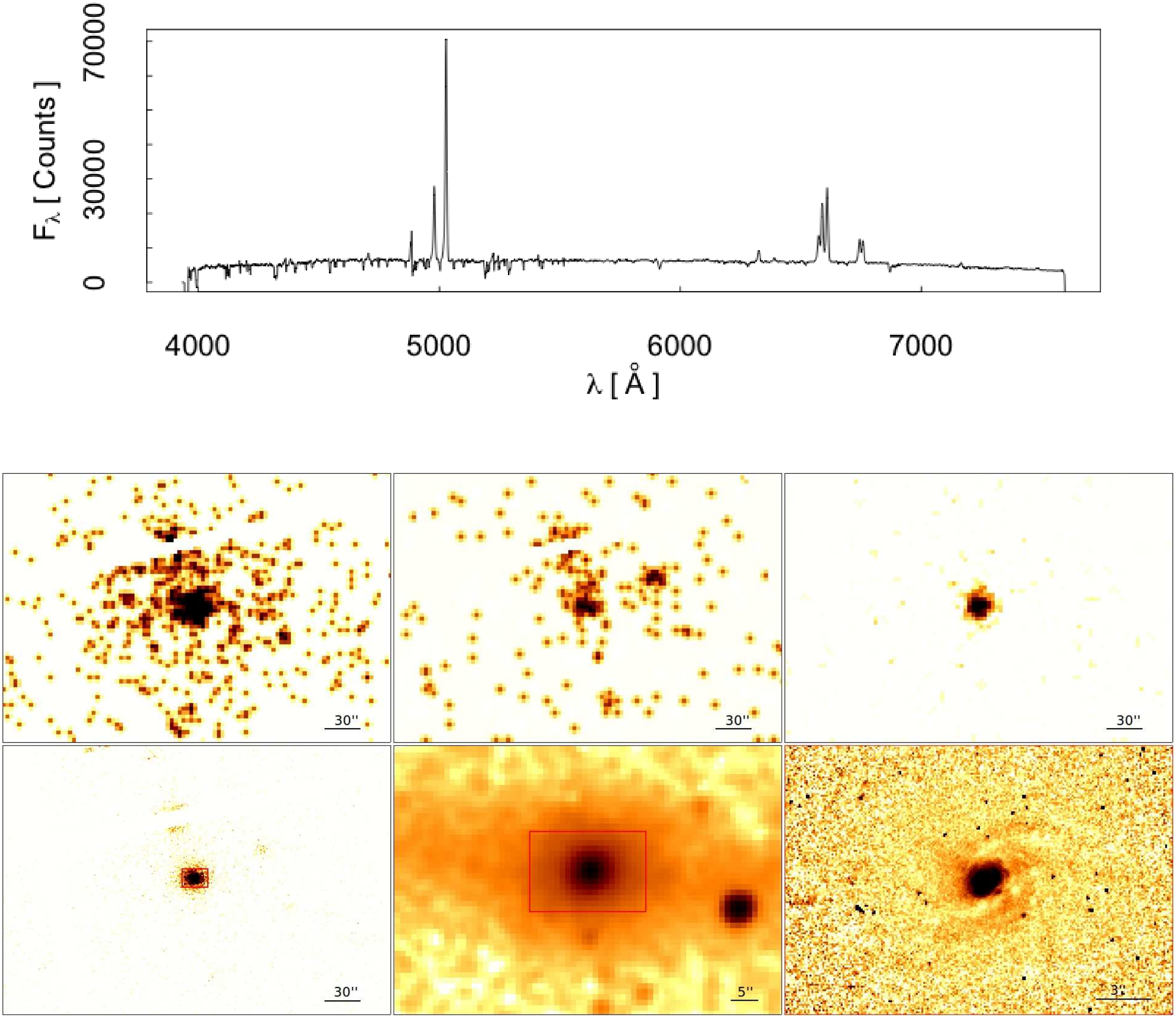

Fig. C.19: Up: Optical spectrum (from NED), and bottom: images of NGC 5643 (*XMM*–Newton data). (Top left): Smoothed X-ray 0.6-0.9 keV energy band; (top center): smoothed X-ray 1.6-2.0 keV energy band; (top right): smoothed X-ray 4.5-8.0 keV energy band; (bottom left): X-ray 0.5-10.0 keV energy band without smoothing; (bottom center): 2MASS image in the K_s band; (bottom right): Hubble image in the F814W filter.

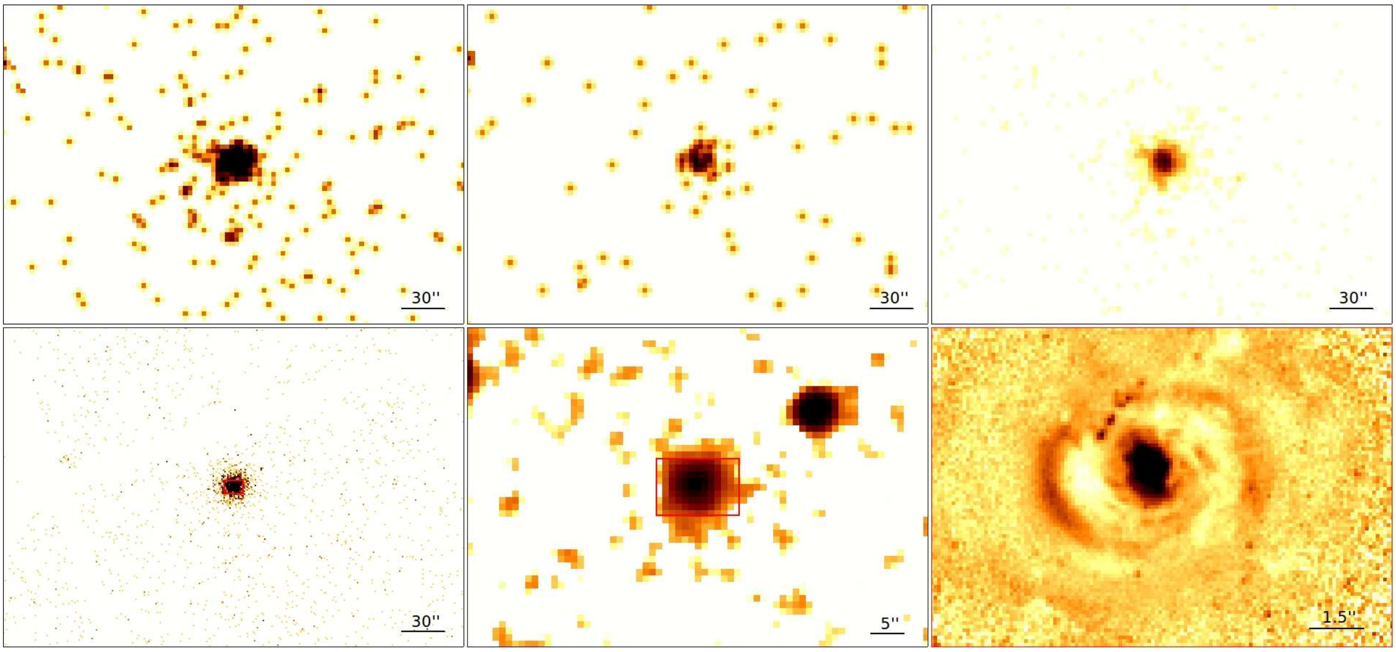

Fig. C.20: Images of MARK 477 (*XMM*–Newton data). (Top left): Smoothed X-ray 0.6-0.9 keV energy band; (top center): smoothed X-ray 1.6-2.0 keV energy band; (top right): smoothed X-ray 4.5-8.0 keV energy band; (bottom left): X-ray 0.5-10.0 keV energy band without smoothing; (bottom center): 2MASS image in the K_s band; (bottom right): Hubble image in the F606W filter.

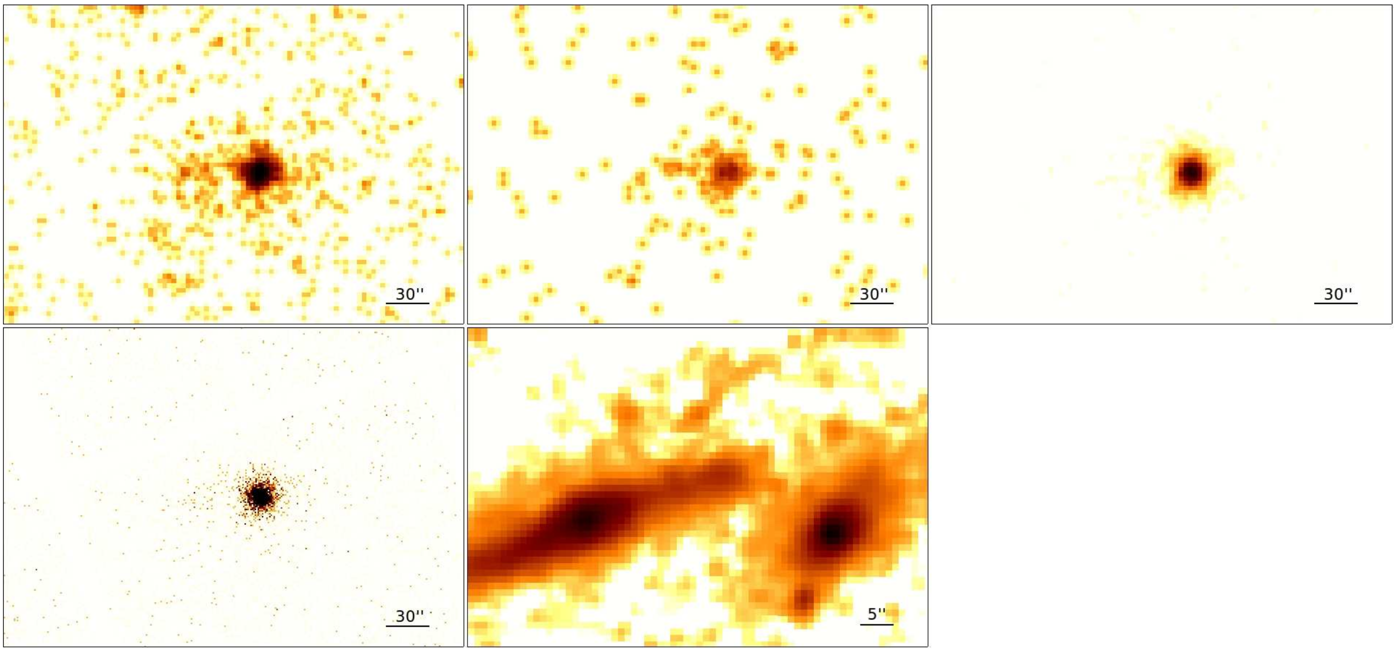

Fig. C.21: Images of IC 4518A (*XMM*–Newton data). (Top left): Smoothed X-ray 0.6-0.9 keV energy band; (top center): smoothed X-ray 1.6-2.0 keV energy band; (top right): smoothed X-ray 4.5-8.0 keV energy band; (bottom left): X-ray 0.5-10.0 keV energy band without smoothing; (bottom center): 2MASS image in the K_s band.

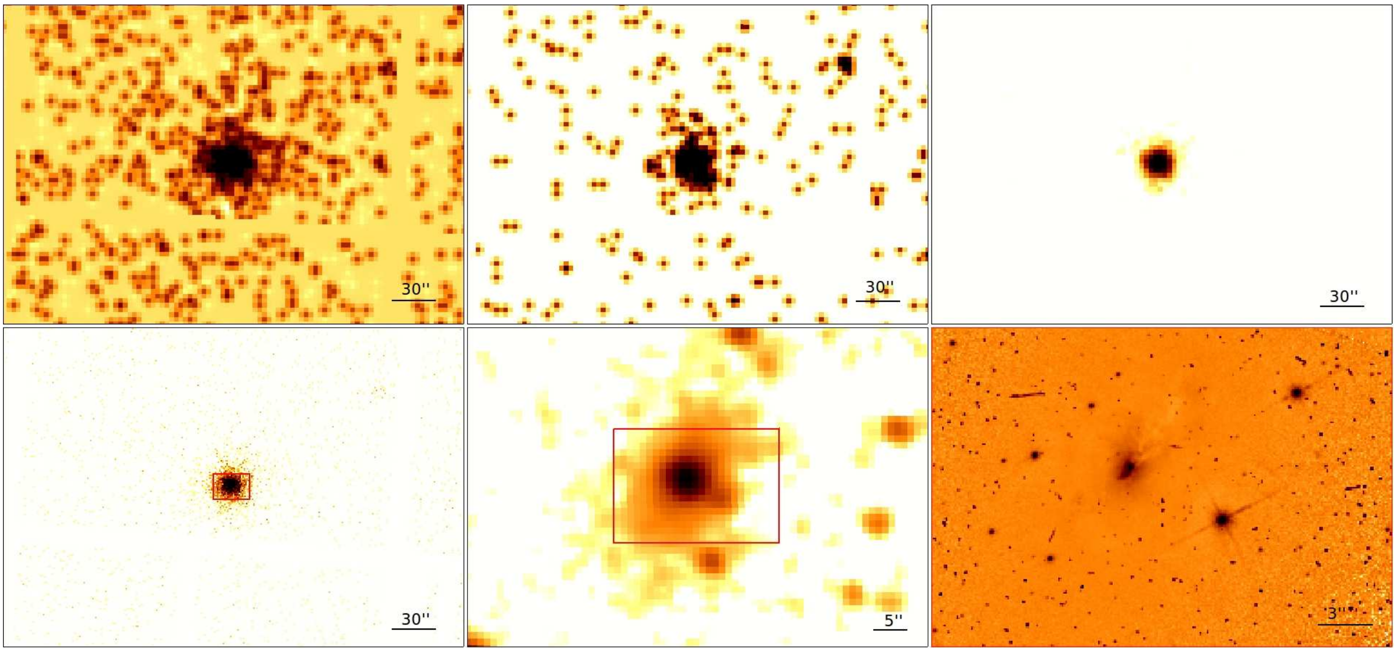

Fig. C.22: Images of ESO 138-G01 (*XMM*–Newton data). (Top left): Smoothed X-ray 0.6-0.9 keV energy band; (top center): smoothed X-ray 1.6-2.0 keV energy band; (top right): smoothed X-ray 4.5-8.0 keV energy band; (bottom left): X-ray 0.5-10.0 keV energy band without smoothing; (bottom center): 2MASS image in the K_s band; (bottom right): Hubble image in the F606W filter.

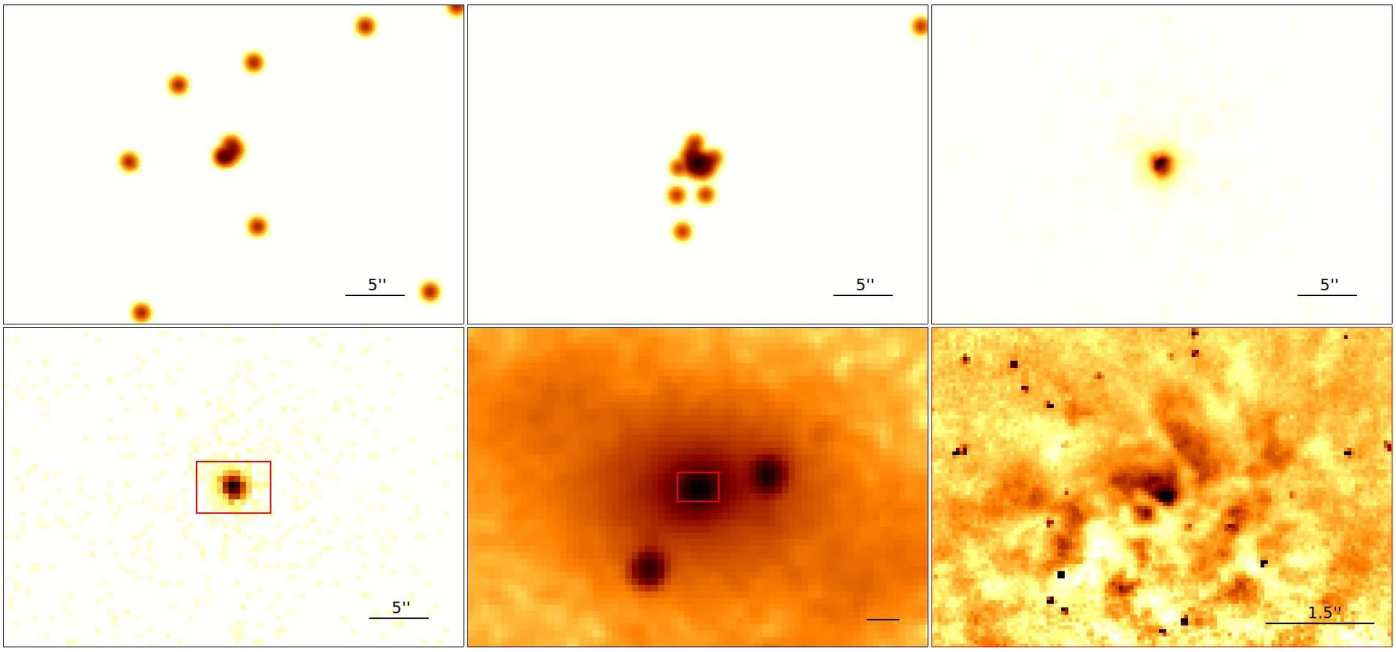

Fig. C.23: Images of NGC 6300. (Top left): Smoothed X-ray 0.6-0.9 keV energy band; (top center): smoothed X-ray 1.6-2.0 keV energy band; (top right): smoothed X-ray 4.5-8.0 keV energy band; (bottom left): X-ray 0.5-10.0 keV energy band without smoothing; (bottom center): 2MASS image in the K_s band; (bottom right): Hubble image in the F606W filter.

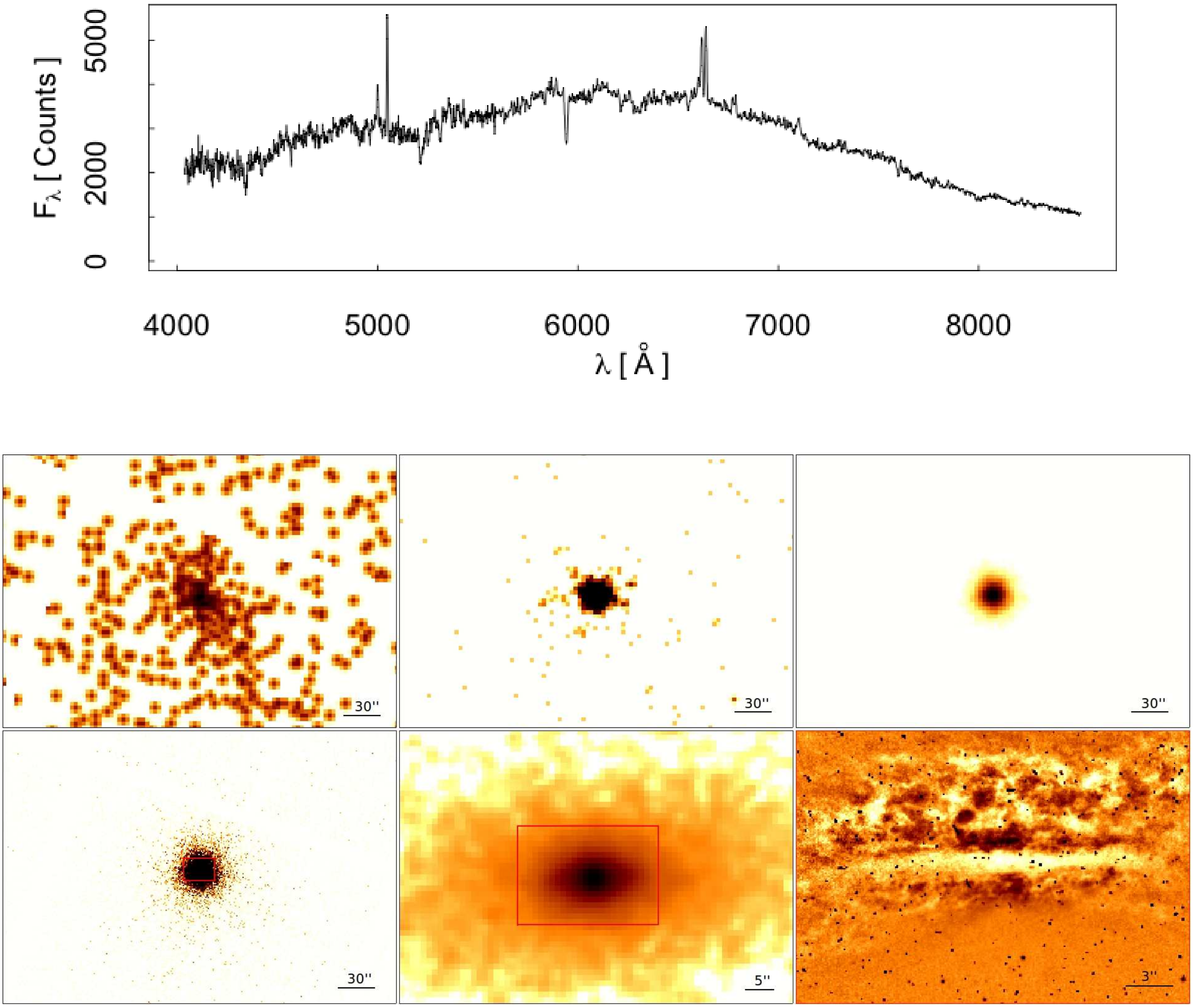

Fig. C.24: Up: Optical spectrum (from NED), and bottom: images of NGC 7172 (*XMM*–Newton data). (Top left): Smoothed X-ray 0.6-0.9 keV energy band; (top center): smoothed X-ray 1.6-2.0 keV energy band; (top right): smoothed X-ray 4.5-8.0 keV energy band; (bottom left): X-ray 0.5-10.0 keV energy band without smoothing; (bottom center): 2MASS image in the K_s band; (bottom right): Hubble image in the F606W filter.

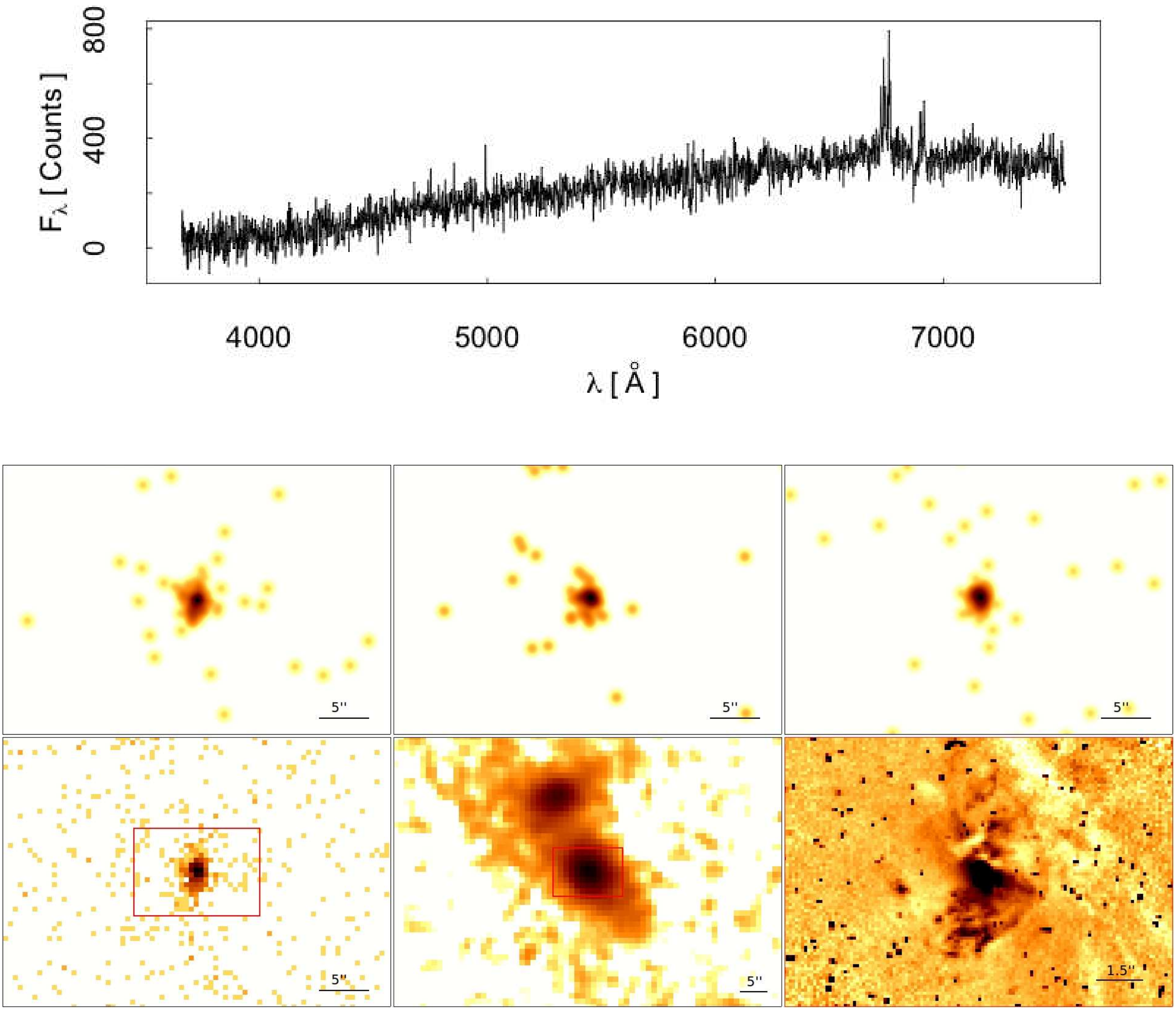

Fig. C.25: Up: Optical spectrum (from NED), and bottom: images of NGC 7212. (Top left): Smoothed X-ray 0.6-0.9 keV energy band; (top center): smoothed X-ray 1.6-2.0 keV energy band; (top right): smoothed X-ray 4.5-8.0 keV energy band; (bottom left): X-ray 0.5-10.0 keV energy band without smoothing; (bottom center): 2MASS image in the K_s band; (bottom right): Hubble image in the F606W filter.

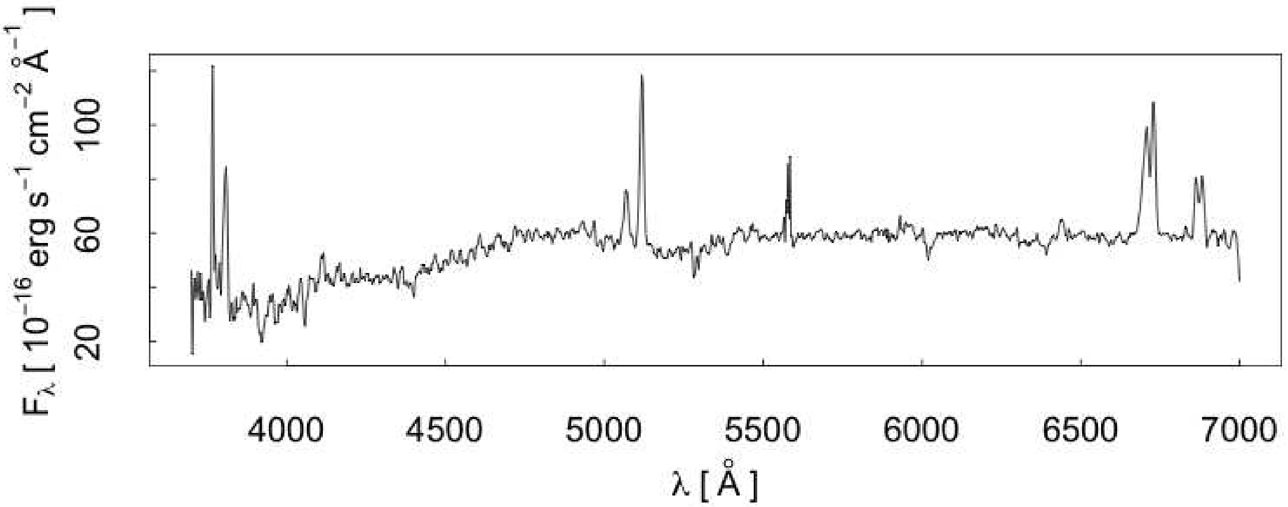

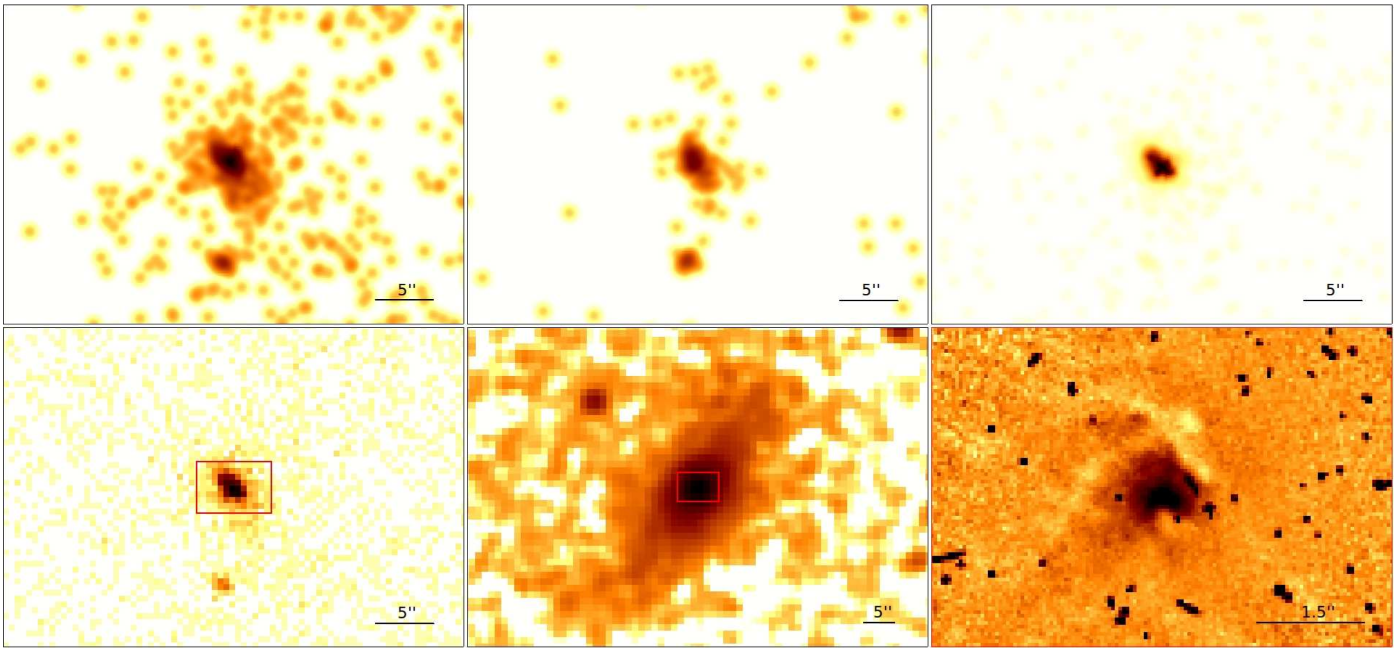

Fig. C.26: Up: Optical spectrum (from NED), and bottom: images of NGC 7319. (Top left): Smoothed X-ray 0.6-0.9 keV energy band; (top center): smoothed X-ray 1.6-2.0 keV energy band; (top right): smoothed X-ray 4.5-8.0 keV energy band; (bottom left): X-ray 0.5-10.0 keV energy band without smoothing; (bottom center): 2MASS image in the K_s band; (bottom right): Hubble image in the F814W filter.

Appendix C.2: Chandra *and* XMM–*Newton images*

In this appendix we present the images from *Chandra* (left) and *XMM*-Newton (right) that were used to compare the spectra from these two instruments in the 0.5-10 keV band. In all cases, the gray scales extend from twice the value of the background dispersion to the maximum value at the center of each galaxy.

Fig. C.27: Images for *Chandra* data (left) and *XMM*-Newton data (right) for the sources in the 0.5-10 keV band. Big circles represent *XMM*–Newton data apertures. Small circles in the figures to the left represent the nuclear extraction aperture used with *Chandra* observations (see Table A.1).

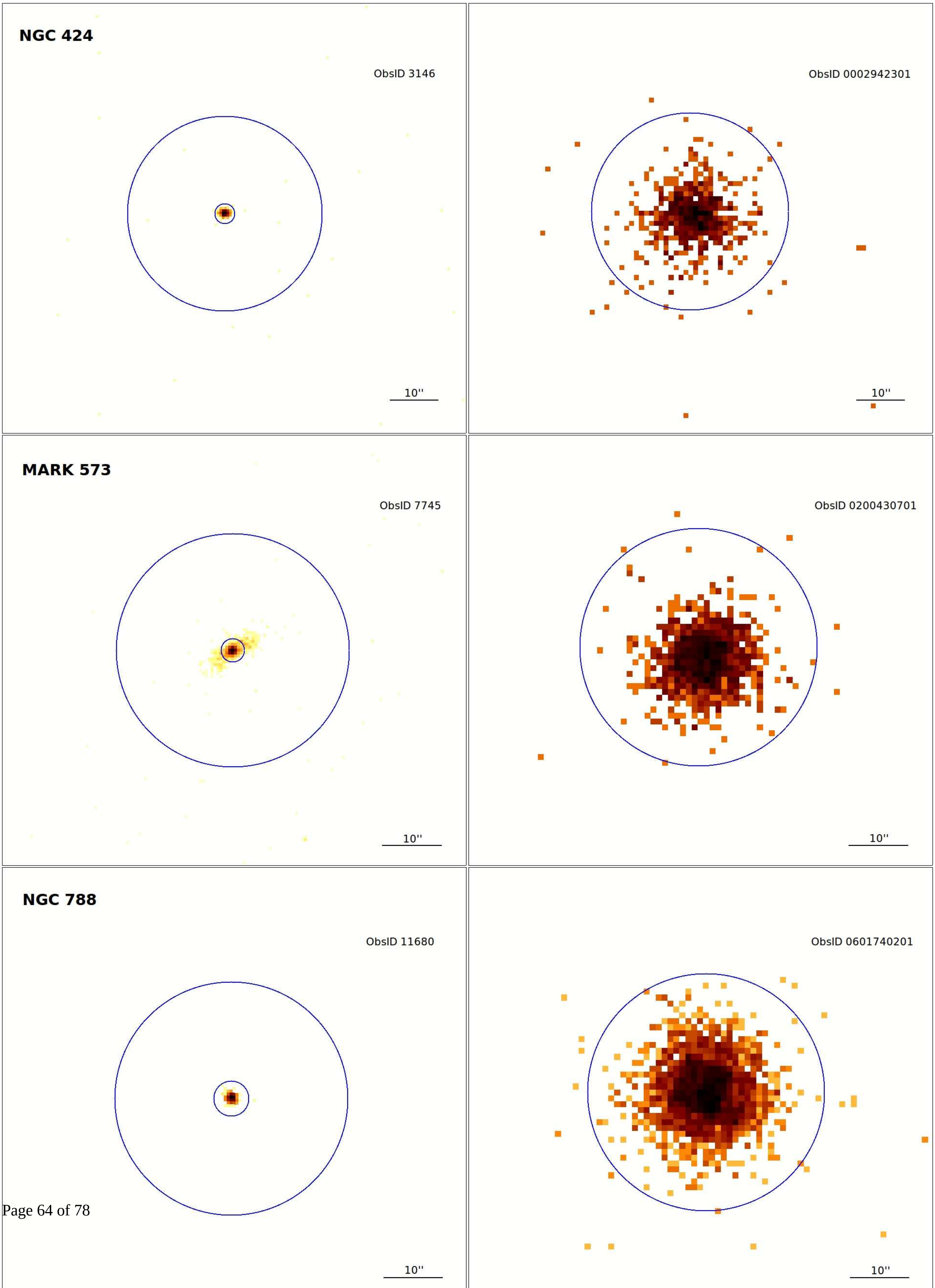

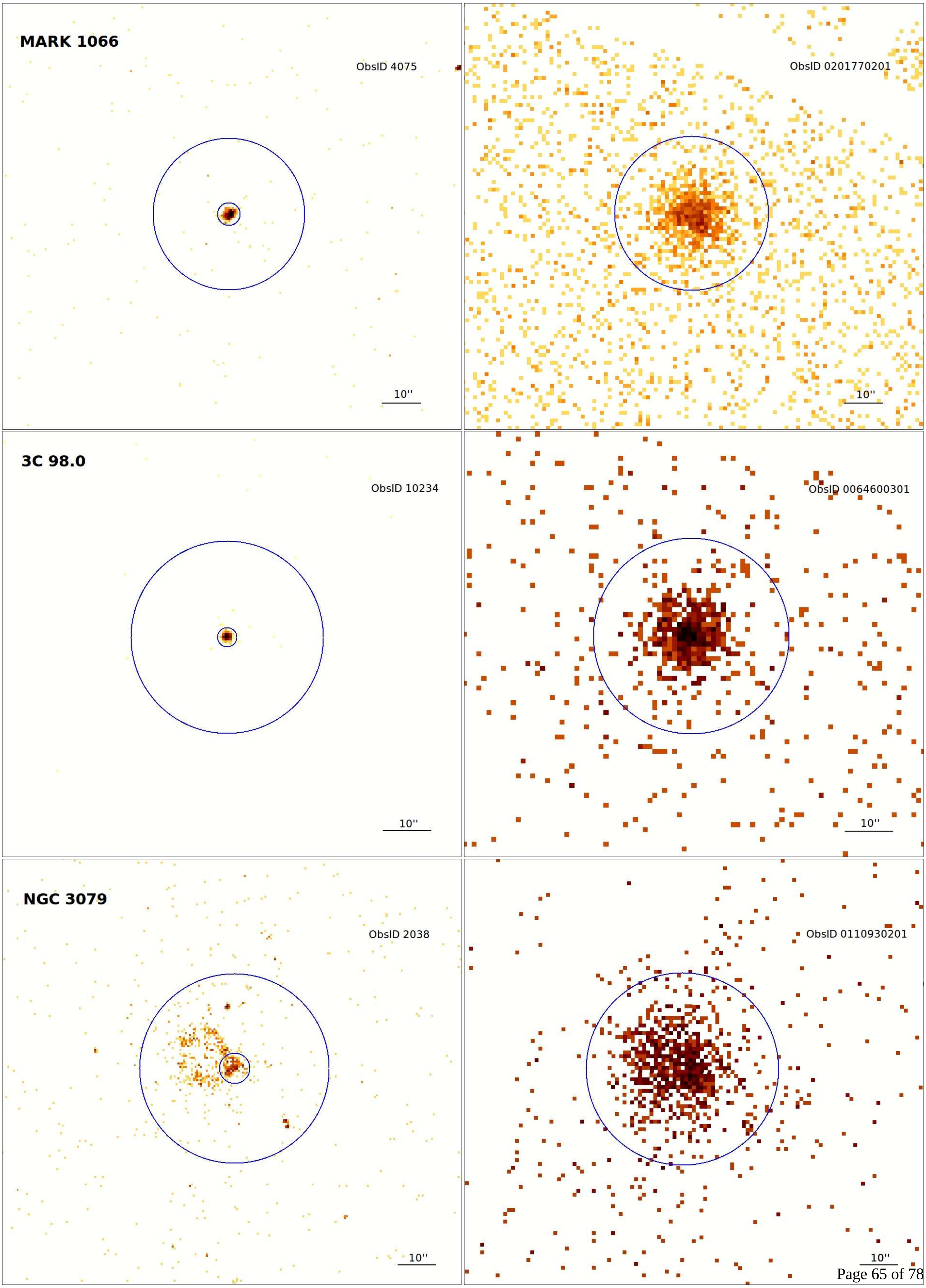
MARK 1066
ObsID 4075
10''
ObsID 0201770201
10''
3C 98.0
ObsID 10234
10''
ObsID 0064600301
10''
NGC 3079
ObsID 2038
10''
ObsID 0110930201
10''

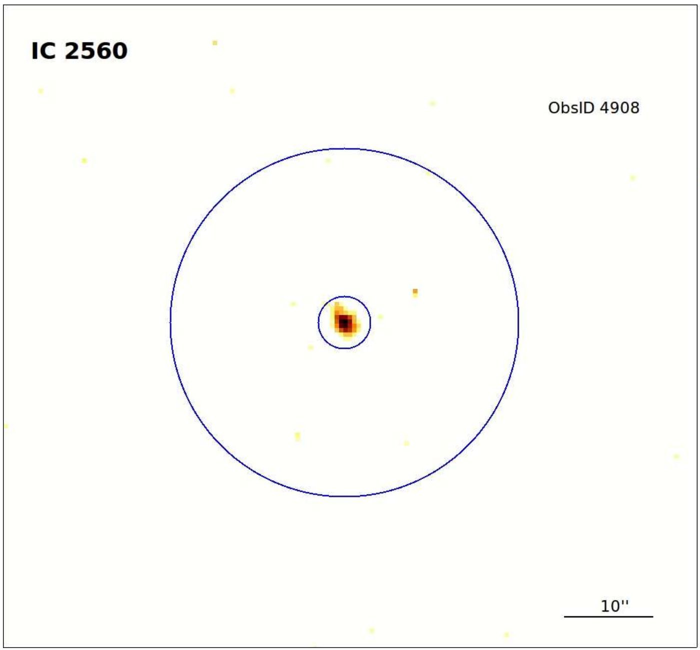
IC 2560
ObsID 4908
10''

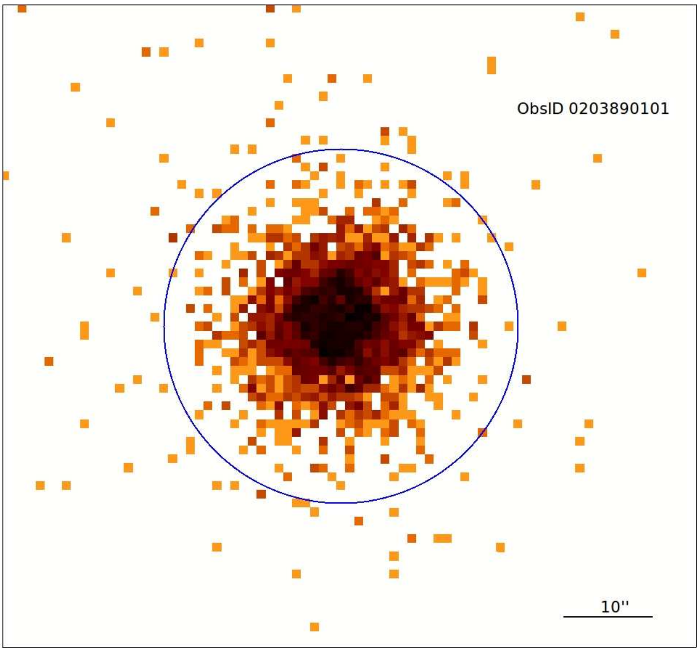
ObsID 0203890101
10''

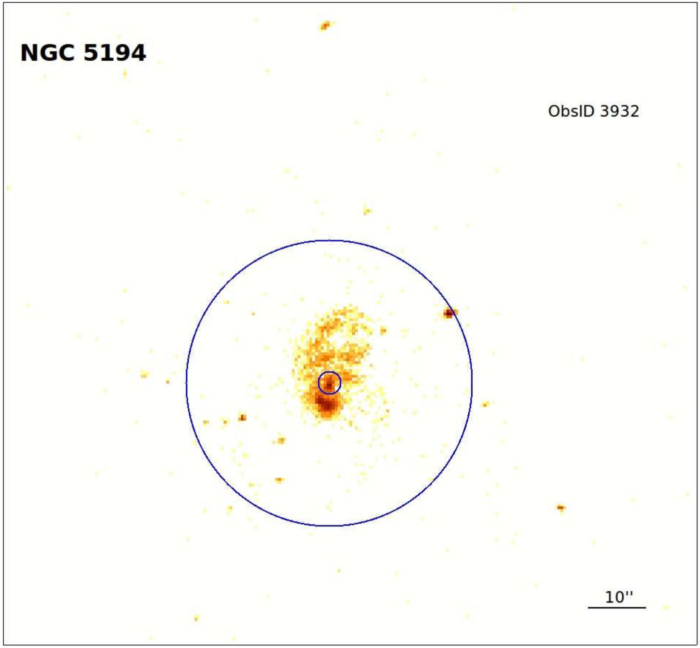
NGC 5194
ObsID 3932
10''

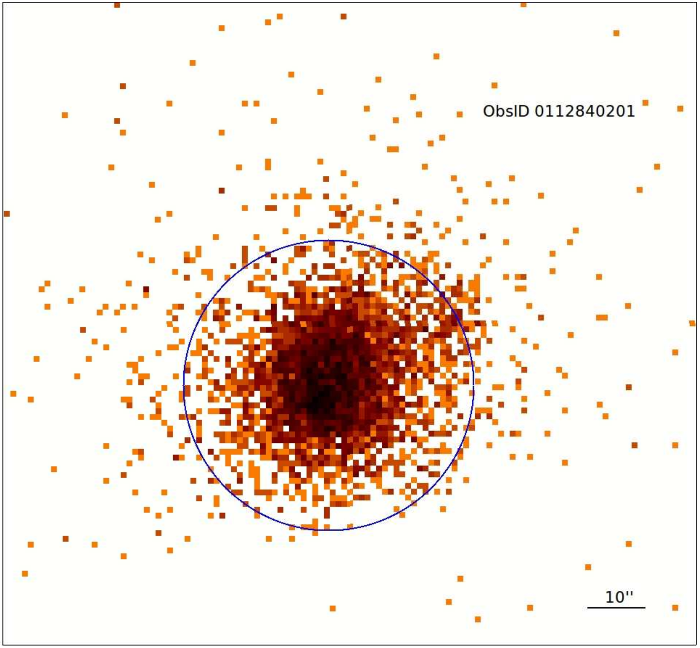
ObsID 0112840201
10''

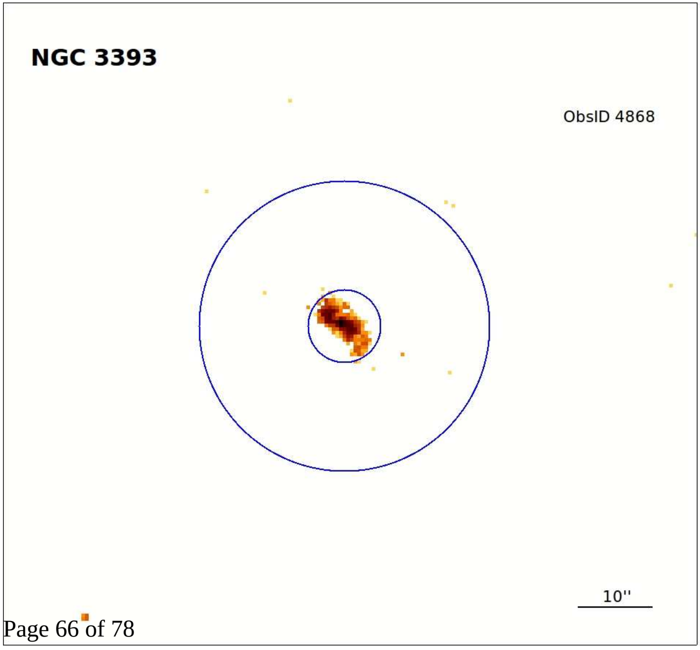
NGC 3393
ObsID 4868
10''

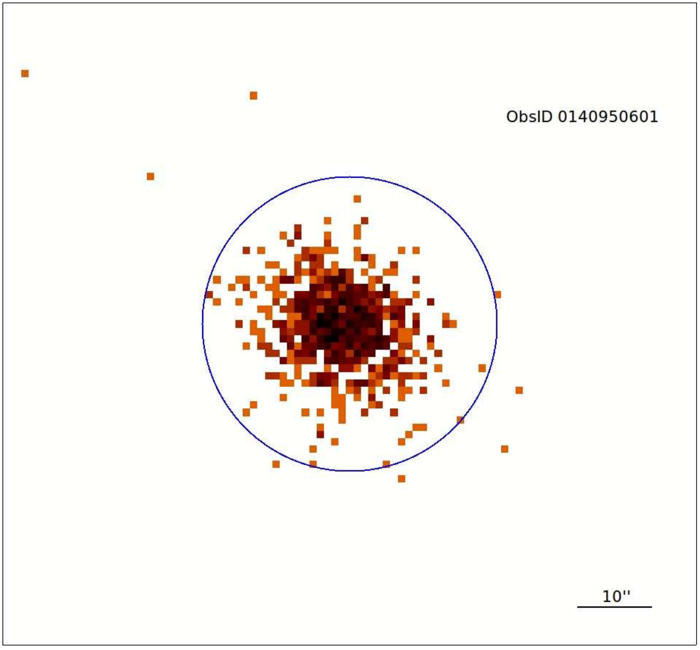
ObsID 0140950601
10''

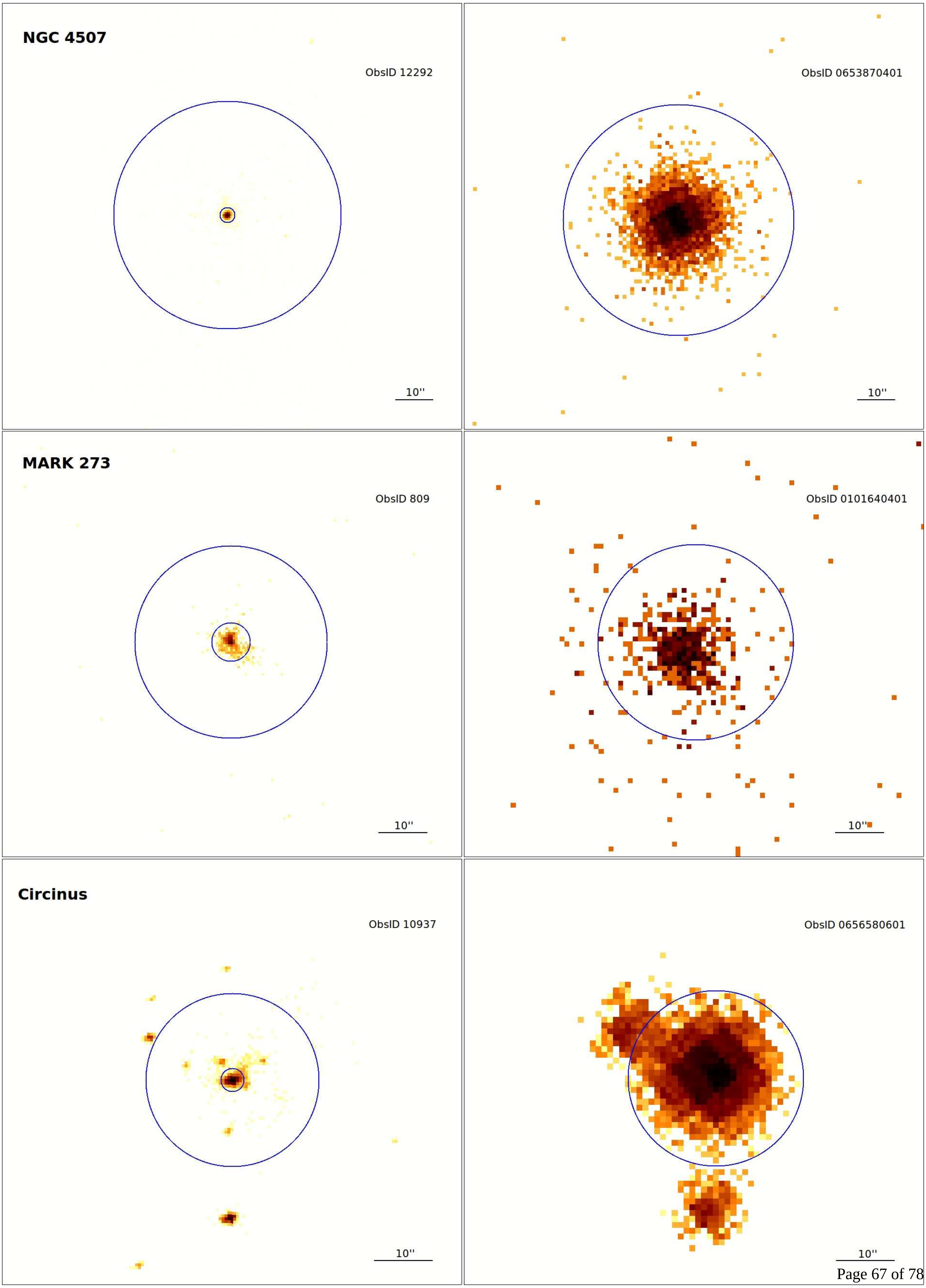
NGC 4507
ObsID 12292
10''
ObsID 0653870401
10''
MARK 273
ObsID 809
10''
ObsID 0101640401
10''
Circinus
ObsID 10937
10''
ObsID 0656580601
10''

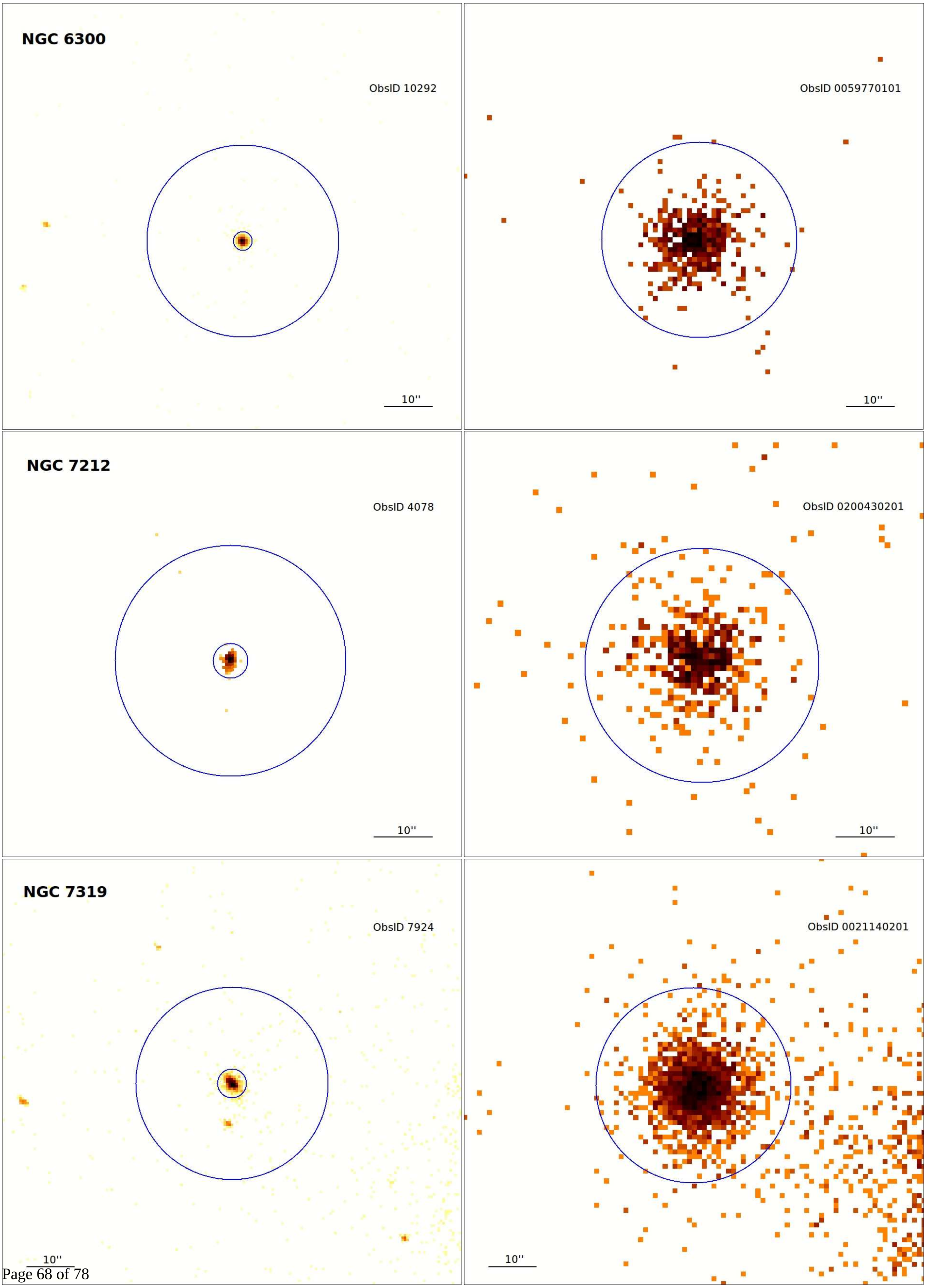
NGC 6300
ObsID 10292
10''
ObsID 0059770101
10''
NGC 7212
ObsID 4078
10''
ObsID 0200430201
10''
NGC 7319
ObsID 7924
10''
ObsID 0021140201
10''

Appendix D: Light curves

This appendix provides the plots corresponding to the light curves. Three plots per observation are presented, corresponding to soft (left), hard (middle), and total (right) energy bands. Each light curve has a minimum of 30 ksec (i.e., 8 hours) exposure time, while long light curves are divided into segments of 40 ksec (i.e., 11 hours). Each segment is enumerated in the title of the light curve. Count rates versus time continua are represented. The solid line represents the mean value, dashed lines the $\pm 1\sigma$ from the average.

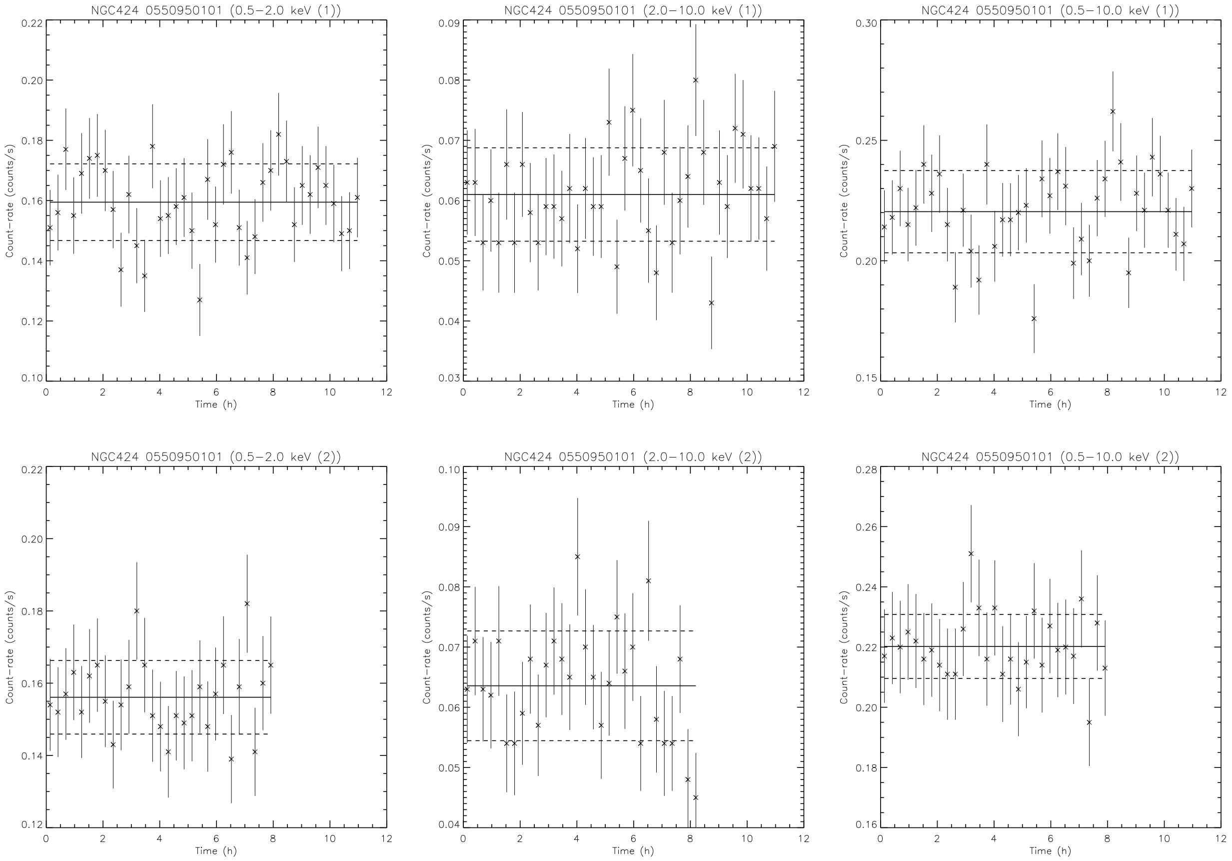
NGC424 0550950101 (0.5–2.0 keV (1))
NGC424 0550950101 (2.0–10.0 keV (1))
NGC424 0550950101 (0.5–10.0 keV (1))
NGC424 0550950101 (0.5–2.0 keV (2))
NGC424 0550950101 (2.0–10.0 keV (2))
NGC424 0550950101 (0.5–10.0 keV (2))

Fig. D.1: Light curves of NGC 424 from *XMM*–Newton data.

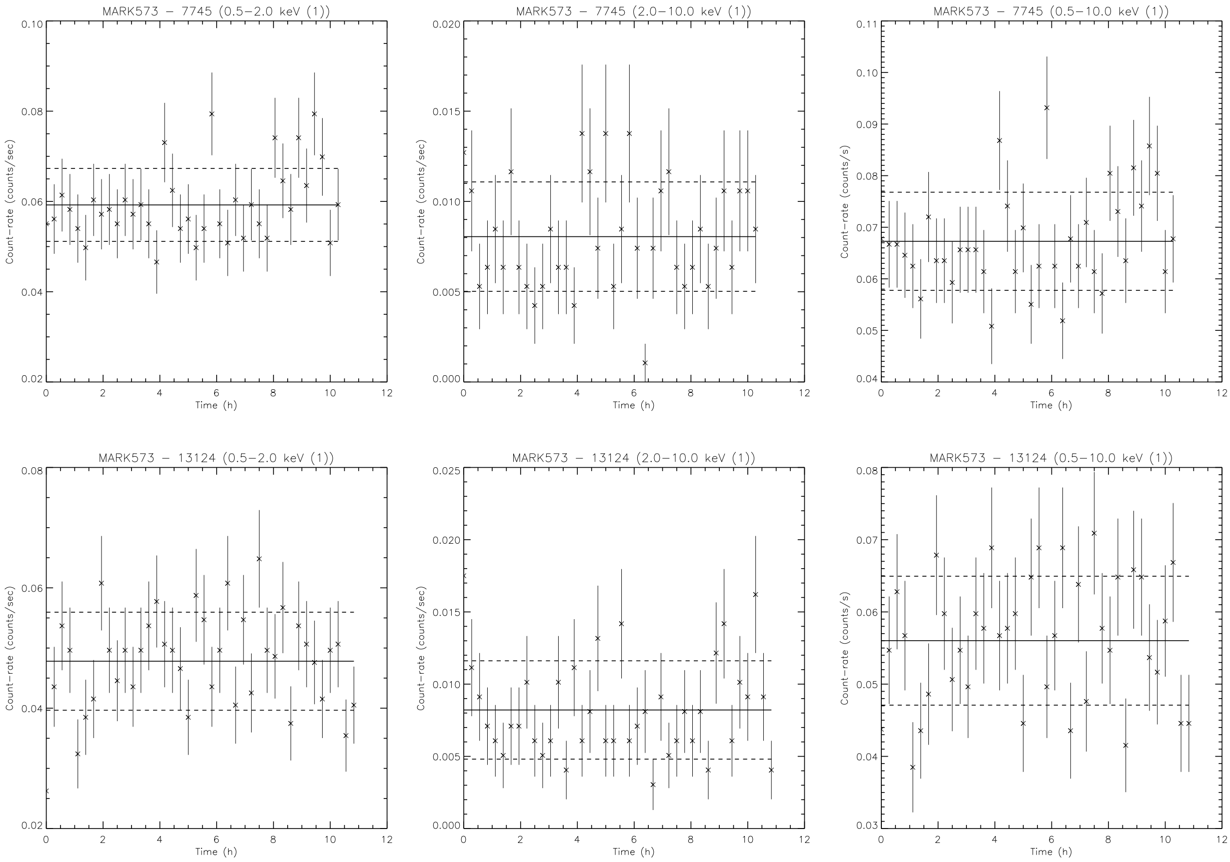

Fig. D.2: Light curves of MARK 573 from *Chandra* data.

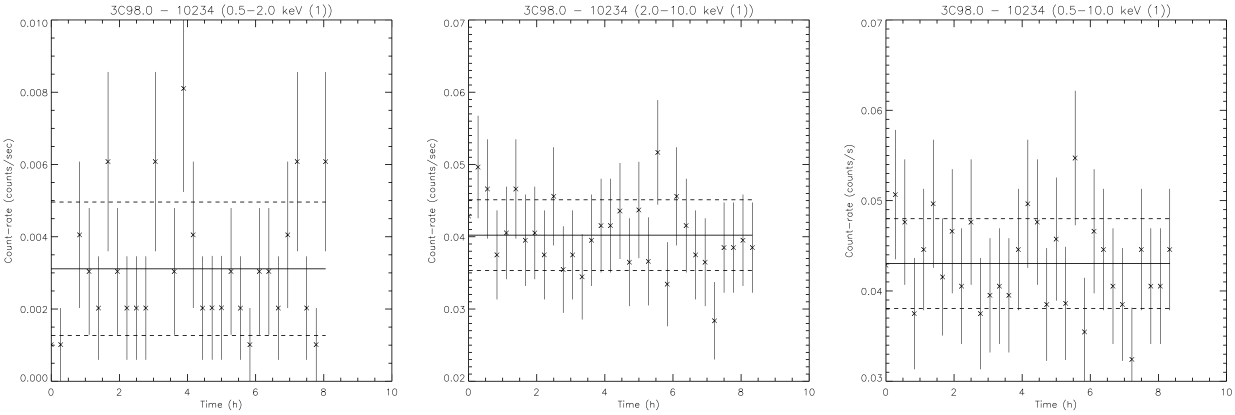

Fig. D.3: Light curves of 3C 98.0 from *Chandra* data.

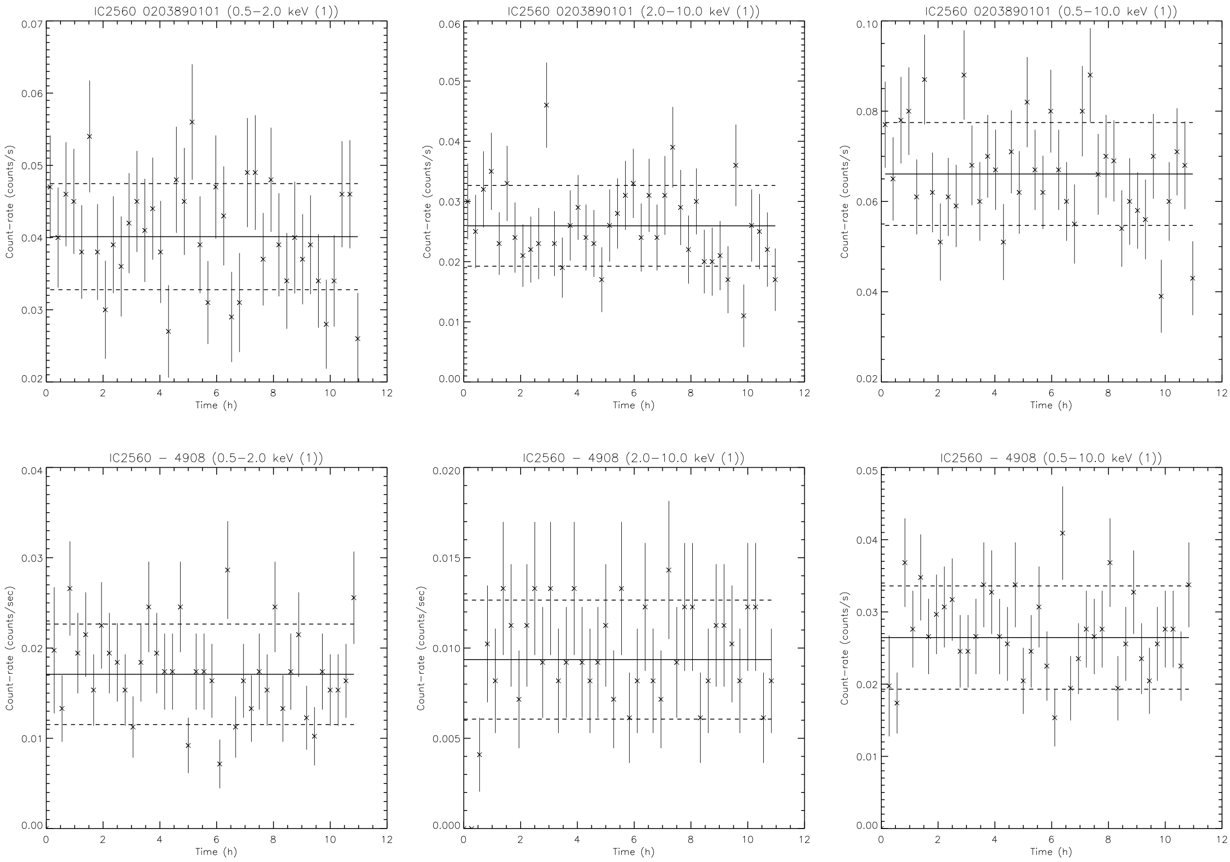

Fig. D.4: Light curves of IC 2560 from *XMM*–Newton and *Chandra* data.

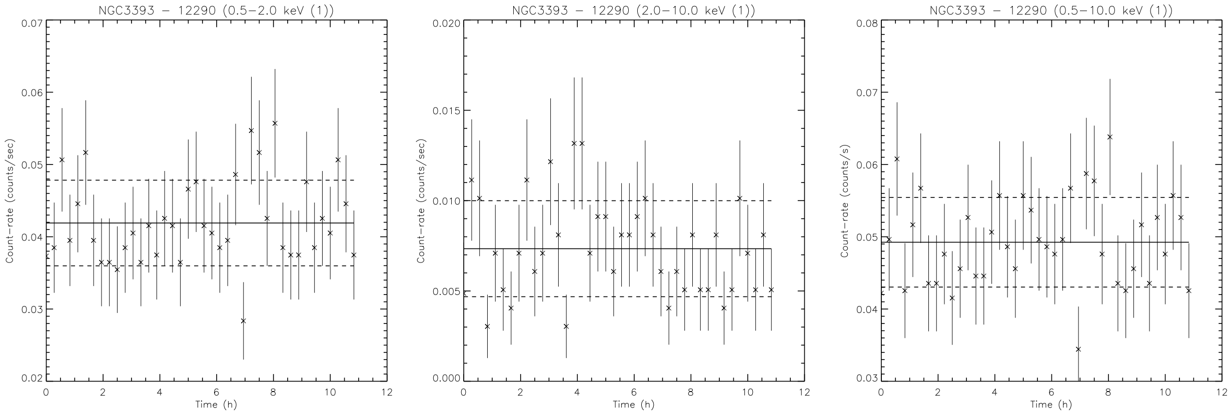

Fig. D.5: Light curves of NGC 3393 from *Chandra* data.

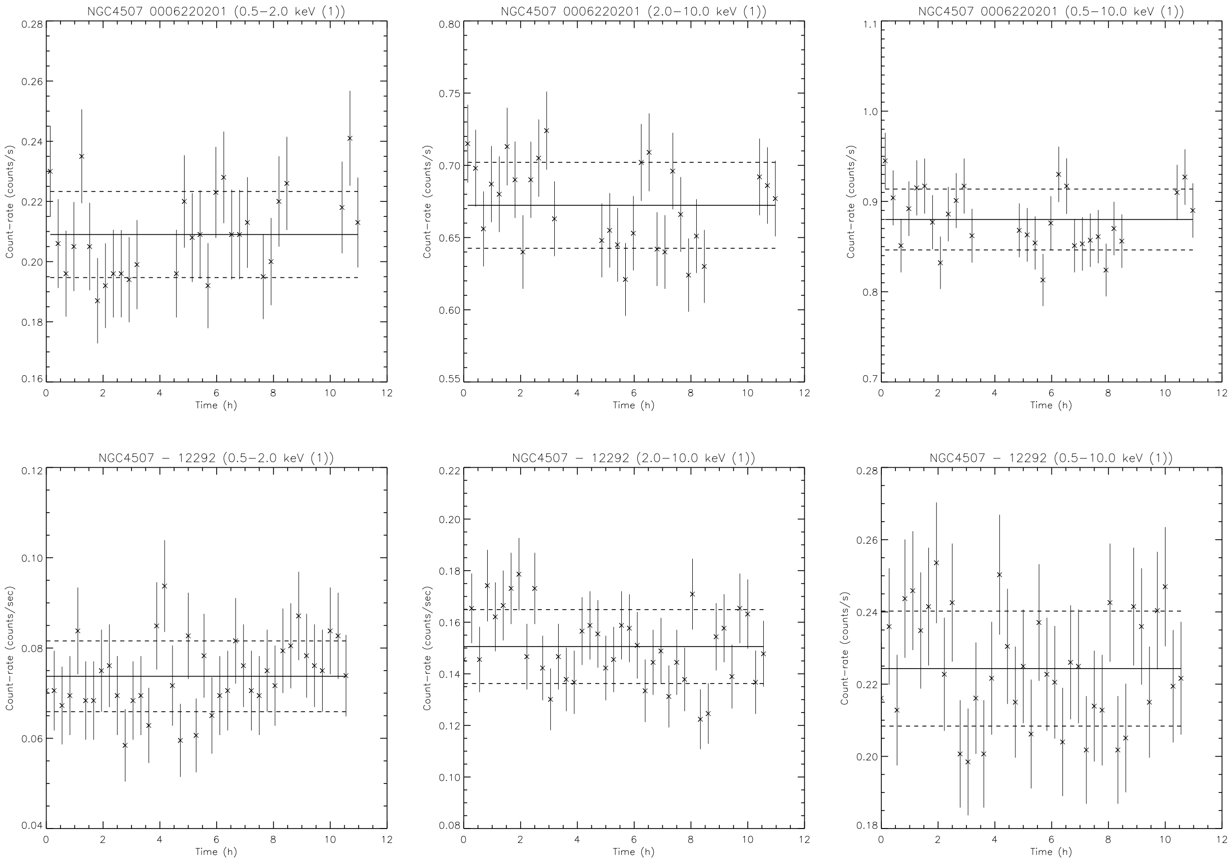

Fig. D.6: Light curves of NGC 4507 from *XMM*–Newton and *Chandra* data.

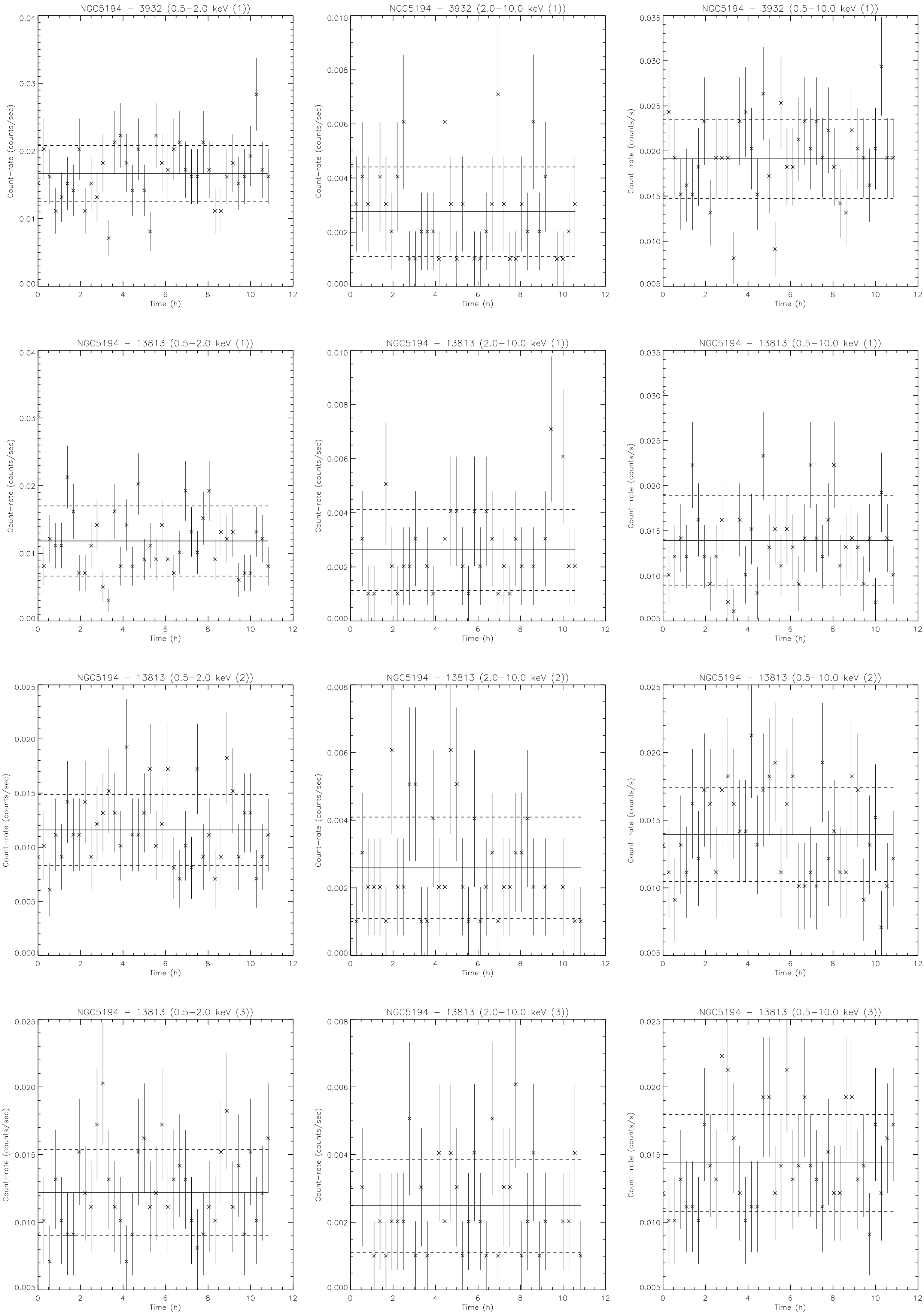

Fig. D.7: Light curves of NGC 5194 from *Chandra* data.

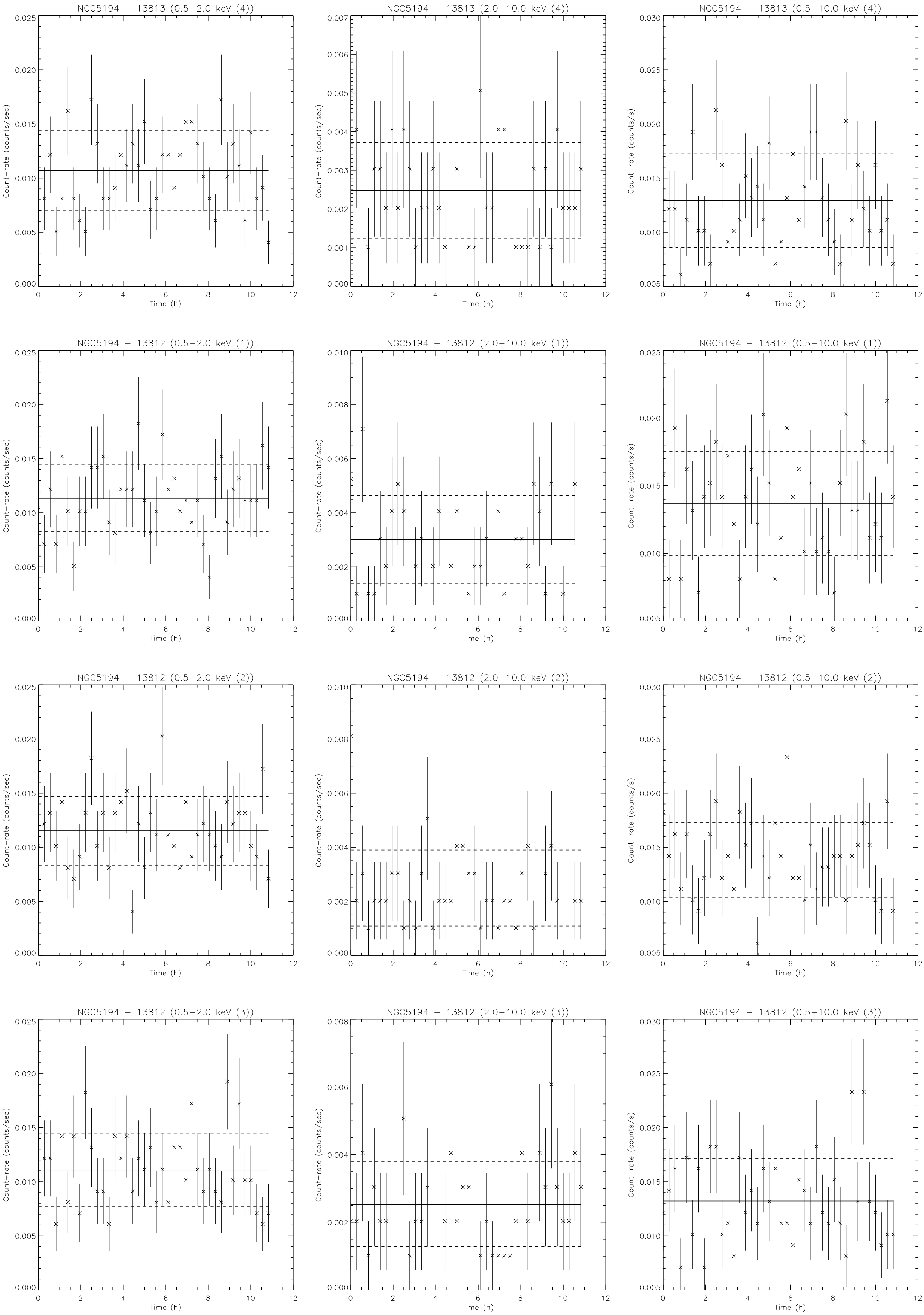
NGC5194 – 13813 (0.5–2.0 keV (4))
NGC5194 – 13813 (2.0–10.0 keV (4))
NGC5194 – 13813 (0.5–10.0 keV (4))
NGC5194 – 13812 (0.5–2.0 keV (1))
NGC5194 – 13812 (2.0–10.0 keV (1))
NGC5194 – 13812 (0.5–10.0 keV (1))
NGC5194 – 13812 (0.5–2.0 keV (2))
NGC5194 – 13812 (2.0–10.0 keV (2))
NGC5194 – 13812 (0.5–10.0 keV (2))
NGC5194 – 13812 (0.5–2.0 keV (3))
NGC5194 – 13812 (2.0–10.0 keV (3))
NGC5194 – 13812 (0.5–10.0 keV (3))
Count–rate (counts/sec)
Count–rate (counts/s)
Time (h)
0
2
4
6
8
10
12

Fig. D.7: (Cont.)

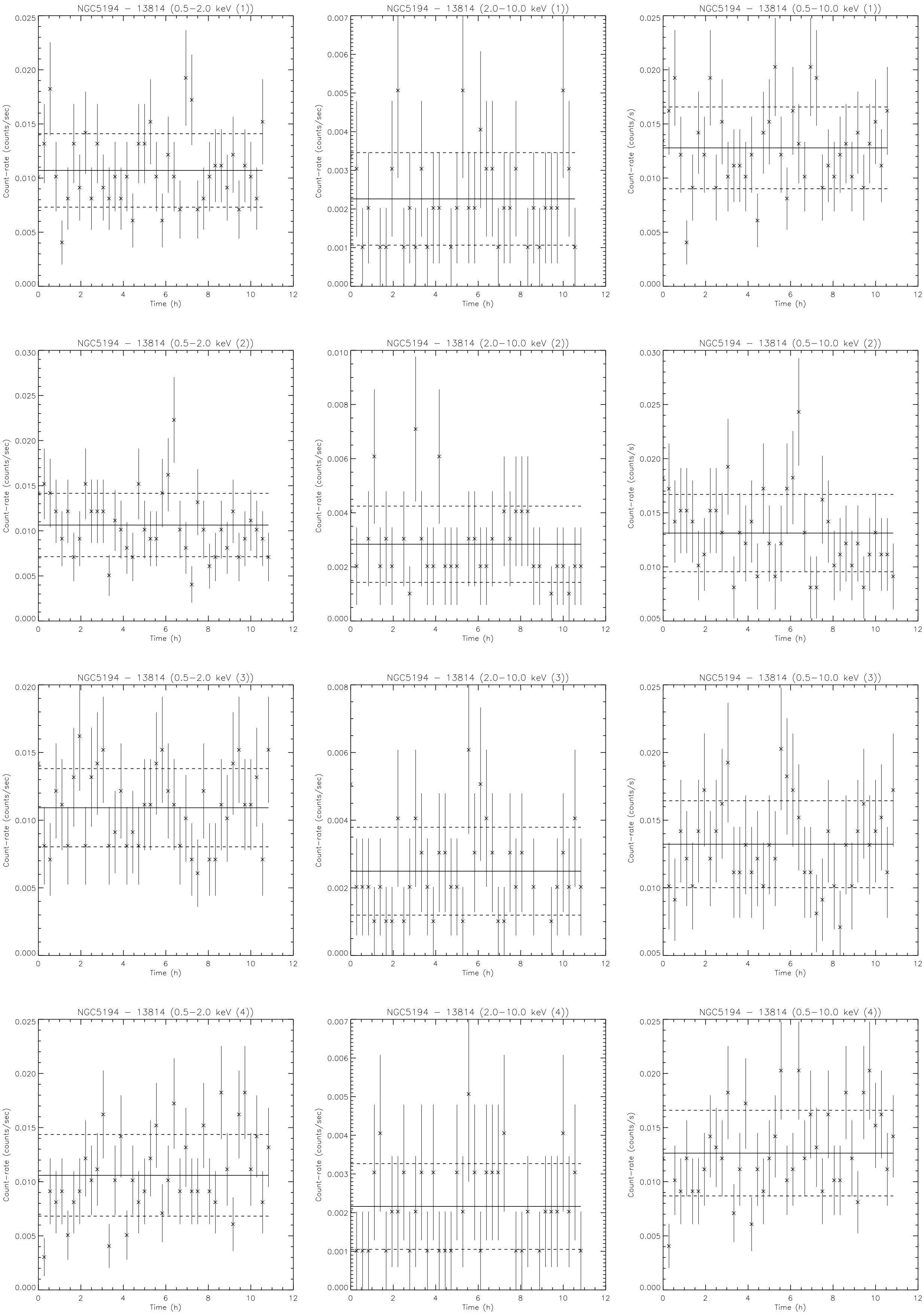
NGC5194 − 13814 (0.5−2.0 keV (1))
NGC5194 − 13814 (2.0−10.0 keV (1))
NGC5194 − 13814 (0.5−10.0 keV (1))
NGC5194 − 13814 (0.5−2.0 keV (2))
NGC5194 − 13814 (2.0−10.0 keV (2))
NGC5194 − 13814 (0.5−10.0 keV (2))
NGC5194 − 13814 (0.5−2.0 keV (3))
NGC5194 − 13814 (2.0−10.0 keV (3))
NGC5194 − 13814 (0.5−10.0 keV (3))
NGC5194 − 13814 (0.5−2.0 keV (4))
NGC5194 − 13814 (2.0−10.0 keV (4))
NGC5194 − 13814 (0.5−10.0 keV (4))
Count−rate (counts/sec)
Count−rate (counts/s)
Time (h)
0
2
4
6
8
10
12

Fig. D.7: (Cont.)

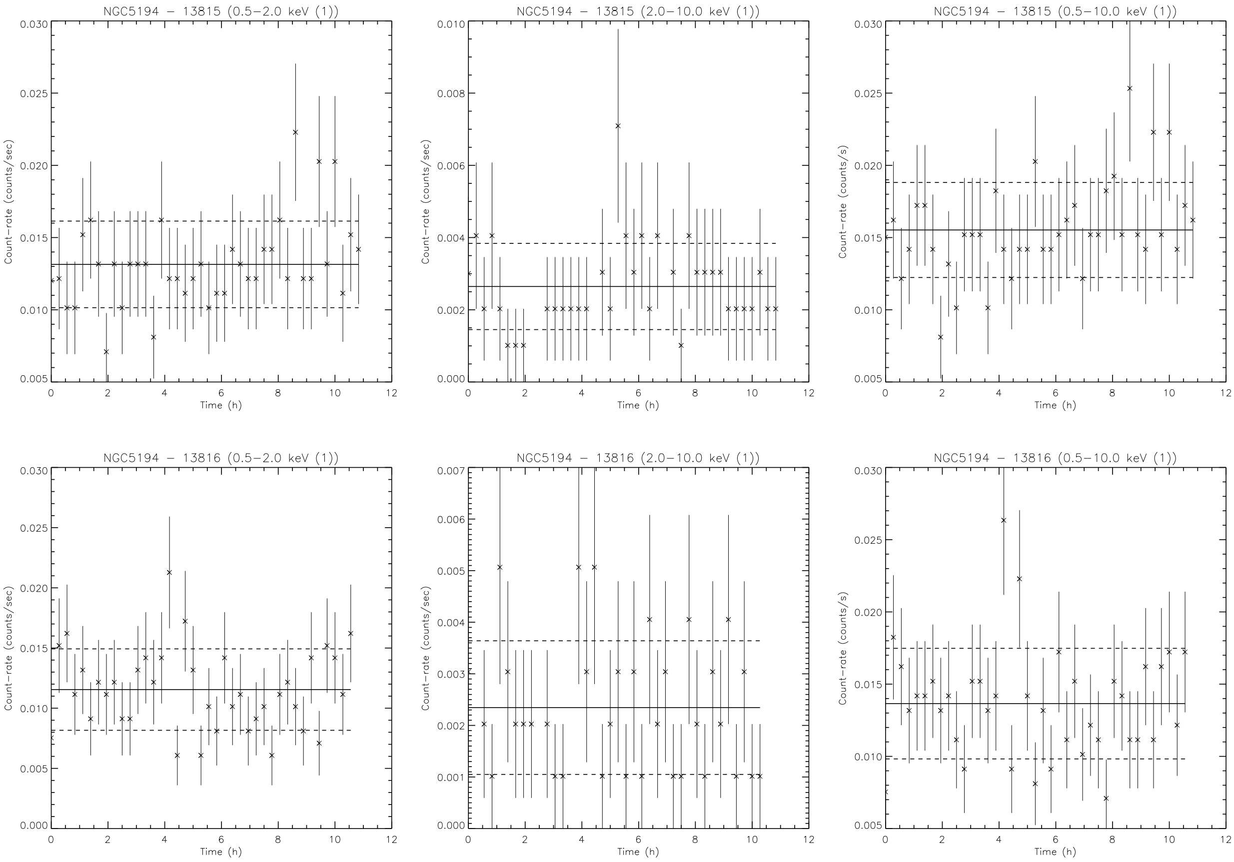

Fig. D.7: (Cont.)

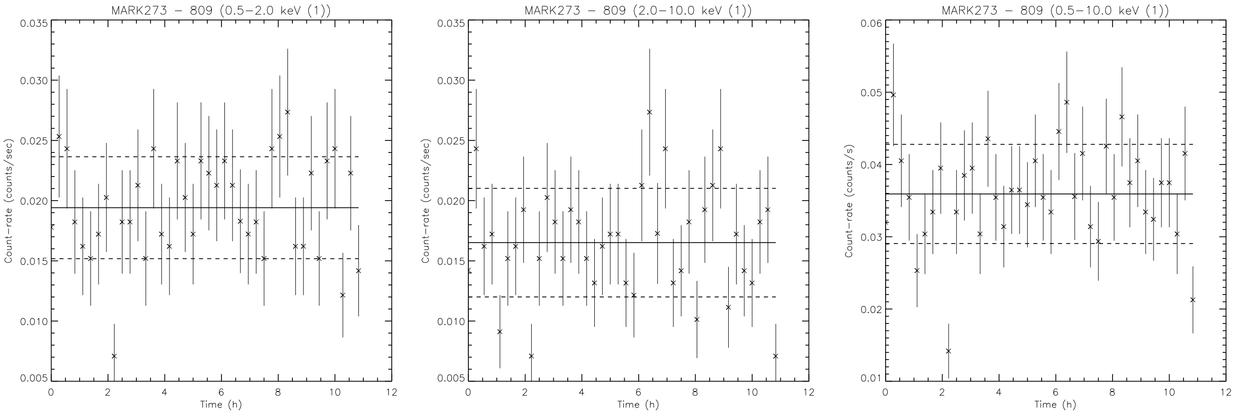

Fig. D.8: Light curves of MARK 273 from *Chandra* data.

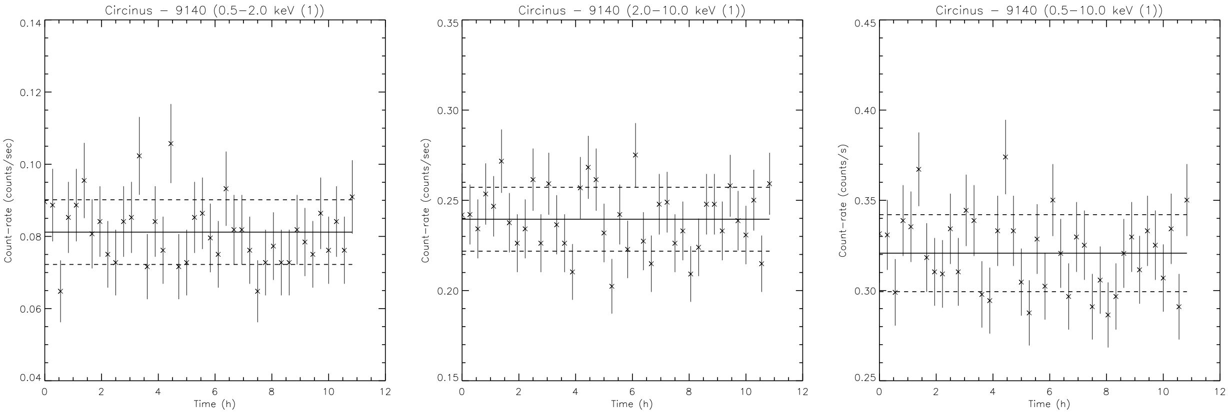

Fig. D.9: Light curves of Circinus from *Chandra* data.

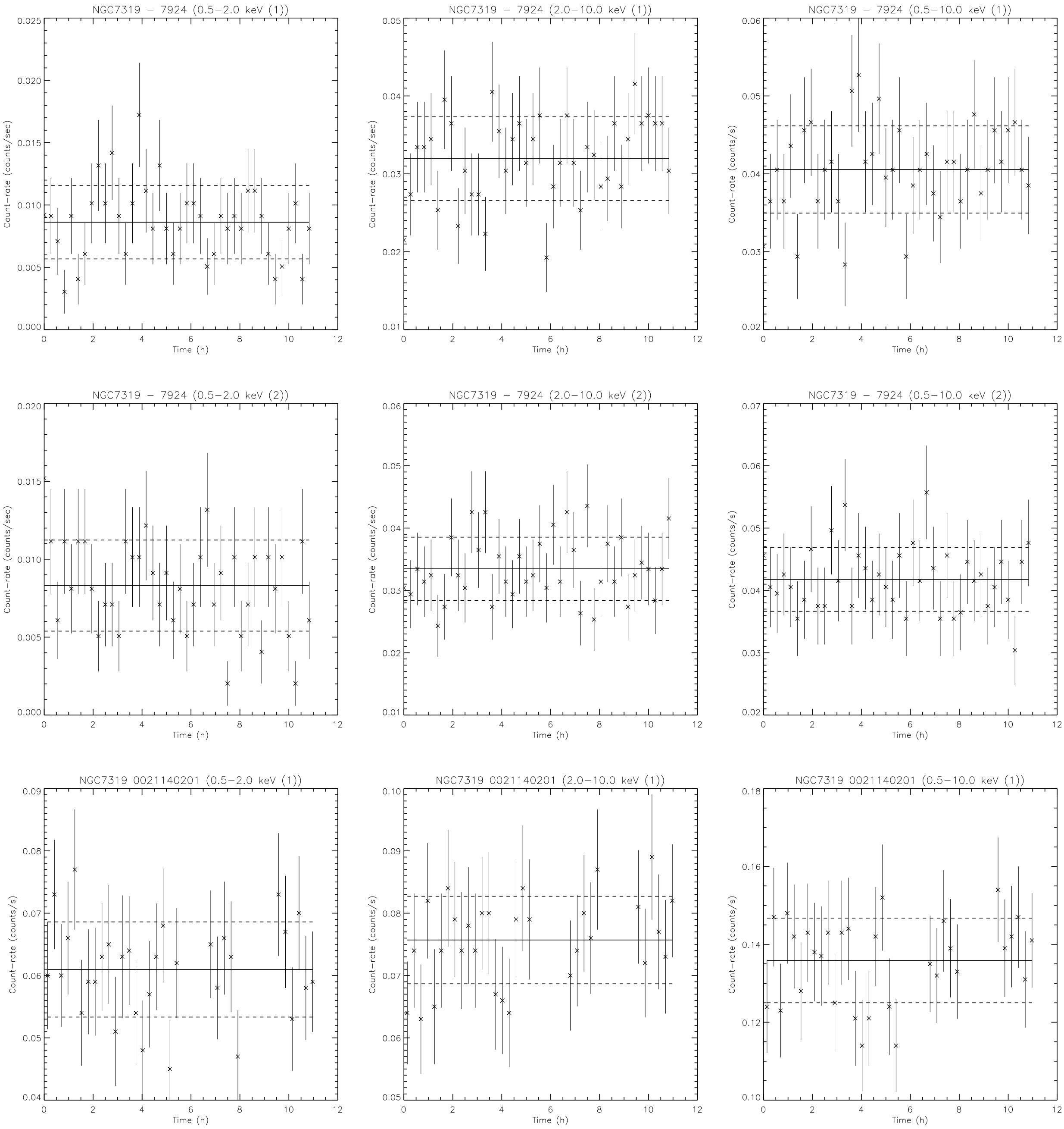

NGC7319 − 7924 (0.5−2.0 keV (1))

NGC7319 − 7924 (2.0−10.0 keV (1))

NGC7319 − 7924 (0.5−10.0 keV (1))

NGC7319 − 7924 (0.5−2.0 keV (2))

NGC7319 − 7924 (2.0−10.0 keV (2))

NGC7319 − 7924 (0.5−10.0 keV (2))

NGC7319 0021140201 (0.5−2.0 keV (1))

NGC7319 0021140201 (2.0−10.0 keV (1))

NGC7319 0021140201 (0.5−10.0 keV (1))

Fig. D.10: Light curves of NGC 7319 from *Chandra* and *XMM*–Newton data.

4

LINER vs. Seyfert 2

Once we have derived the results on the X-ray variability in LINERs and Seyfert 2s, the next natural step is to study whether these variations occur in the same way in both families of AGN. This is the main purpose of this chapter, where we have assembled the spectral properties and variability patterns of LINERs and Seyfert 2s. Taking advantage of the spectral fittings performed in Chapters 2 and 3, we can not only obtain information about the physics related to the variability occurring in these nuclei but also to infer their physical properties through the spectral components used to fit the spectra. Within this context, we discuss the nature of the accretion mechanisms and the dusty torus in AGN, which are a matter of debate within the scientific community nowadays.

The paper presented in this chapter is still work in progress that we will outline in the near future and will be submitted to Astronomy & Astrophysics.

Astronomy & Astrophysics manuscript no. LINERvsSEYFERT2
June 15, 2015

X-ray variability in AGN:

LINER vs. Seyfert 2

Hernández-García, L.[1]; Masegosa, J.[1]; González-Martín, O.[2]; Márquez, I.[1]

[1] Instituto de Astrofísica de Andalucía, CSIC, Glorieta de la Astronomía, s/n, 18008 Granada, Spain
e-mail: `lorena@iaa.es`
[2] Centro de radioastronomía y Astrofísica (CRyA-UNAM), 3-72 (Xangari), 8701, Morelia, Mexico

Received XXXX; accepted YYYY

ABSTRACT

Context. X-ray variability is very common in active galactic nuclei (AGN), but it is still unknown if these variations occur similarly in different families of AGN.
Aims. The main purpose of this work is to disentangle whether X-ray variations occur in the same way in optically selected low ionization nuclear emission line regions (LINERs) and Seyfert 2s.
Methods. We assembled the X-ray spectral properties derived from our previous analyses, as well as the X-ray variability pattern(s), which were obtained from simultaneous spectral fittings letting different parameters to vary in the model. We differentiate between *Compton*-thick and *Compton*-thin candidates as in previous works.
Results. We find that Seyfert 2s need more complex models to fit their spectra. Among the spectral parameters, major differences are observed in the soft (0.5–2 keV) and hard (2–10 keV) X-ray luminosities, and the Eddington ratios, which are higher in Seyfert 2s. Differences are observed also in the hard column densities, temperatures, and black hole masses, although less significant. Short term X-ray variations cannot be claimed, while long term variability is very common in both families. The changes are mostly related with variations in the nuclear continuum, but other patterns of variability shows that variations in the absorbers at hard energies and at soft energies can be present in a few cases. Variations at UV frequencies are observed only in LINER nuclei.
Conclusions. The X-ray variations occur in the same way in LINERs and Seyfert 2s, i.e., related to the nuclear continuum, but they might have different accretion mechanisms. As absorption variations and changing-look sources are not observed in LINERs, but UV nuclear variations are common, we speculate that the BLR and the torus might disappear in these sources.

Key words. Galaxies: active – X-rays: galaxies – Ultraviolet: galaxies

1. Introduction

Active galactic nuclei (AGN) include a number of subgroups that are thought to be represented under the same scenario, the unified model (UM) of AGN (Antonucci 1993). Under this scheme, the differences between objects are attributed only to orientation effects. Recent observations, however, suggest that the UM should be slightly modified (see Netzer 2015, for a full description), including the nature of the torus, which some authors suggest might be clumpy (e.g., Nenkova et al. 2008; Stalevski et al. 2012) and can disappear at low luminosities (e.g., Elitzur & Shlosman 2006). On the other hand, recent works suggest also a dependence of accretion on luminosity, black hole mass and galaxy evolution (e.g., Gu & Cao 2009; Schawinski et al. 2012; Yang et al. 2015).

X-ray energies provide the best way to study the physical mechanism operating in AGN since they have the power of penetrating through the dusty torus so the inner parts of the AGN can be accessed (Ho 2008; González-Martín et al. 2009b). Moreover, variability can be considered the best evidence of an AGN, and therefore its study can constrain physical properties of these sources. X-ray variability has been found in almost all AGN analyzed , from the highest luminosity regime, i.e., quasars (Schmidt 1963), through Seyferts (Risaliti et al. 2000; Evans et al. 2005; Panessa et al. 2011; Risaliti et al. 2011), to the lowest luminosity regime, i.e., LINERs (Pian et al. 2010; Younes et al. 2011; Hernández-García et al. 2014). However, it is still under debate what is the mechanism responsible for those variations, as well as whether the changes occur similarly in every AGN.

In previous works, we have studied the X-ray spectral variability of two subgroups of AGN, selected from their optical classifications: low ionisation nuclear emission line regions (LINERs, Hernández-García et al. 2013, 2014) and Seyfert 2 galaxies (Hernández-García et al. 2015). The data were obtained from the public archives of *Chandra* and/or *XMM*–Newton, and the same method was used to search for their variability pattern(s) in both subgroups. Firstly, we performed an individual spectral fit to each spectrum to select the best fit model, and then a simultaneous spectral fit was done to derive the variability pattern at long timescales (i.e., months-years) of each source. Additionally, when available, short-term (i.e., hours-days timescales) X-ray variations were studied from the analysis of the light curves, and long term UV variations were searched from the optical monitor (OM) onboard *XMM*–Newton (Hernández-García et al. 2013, 2014, 2015). These works suggest that the long-term X-ray variations are mainly related to the nuclear continuum in both subgroups, while other patterns of variability have been found in a few cases, related to changes at soft energies or to absorber variations at hard energies. On the contrary, short-term

Table 1: General properties of the sample galaxies.

Name (1)	RA (J2000) (2)	DEC (J2000) (3)	Dist.[1] (Mpc) (4)	Morph. type (5)	Optical class. (6)	*Compton*-thick candidate (7)	Variability pattern (8)
NGC 315	00 57 48.88	+00 21 08.8	59.60	E	L1.9		-
NGC 1052	02 41 04.80	+08 15 20.8	19.48	E	L1.9		$Norm_2+N_{H2}$
NGC 1961	05 42 04.6	+69 22 42	56.20	SAB(rs)c	L2		-
NGC 2681	08 53 32.73	+51 18 49.3	15.25	S0-a(s)	L1.9	✓	-
NGC 3718	11 32 34.8	+53 04 05	17.00	SB(s)a	L1.9		$Norm_2$
NGC 4261	12 19 23.22	+05 49 30.8	31.32	E	L2		-
NGC 4278	12 20 06.83	+29 16 50.7	15.83	E	L1.9		$Norm_2$
NGC 4374	12 25 03.74	+12 53 13.1	17.18	E	L2	✓	$Norm_2$
NGC 4494	12 31 24.03	+25 46 29.9	13.84	E	L2::		$Norm_2$
NGC 4552	12 35 39.81	+12 33 22.8	15.35	E	L2		$Norm_2+Norm_1$
NGC 4736	12 50 53.06	+41 07 13.6	5.02	Sab(r)	L2		-
NGC 5195	13 29 59.6	+47 15 58	7.91	IA	L2:		$Norm_2$
NGC 5982	15 38 39.8	+59 21 21	41.22	E	L2::		$Norm_2$
MARK 348	0 48 47.2	31 57 25	63.90	S0-a	S2		$Norm_2$
NGC 424	1 11 27.7	-38 5 1	47.60	S0-a	S2	✓	-
MARK 573	1 43 57.8	2 20 59	71.30	S0-a	S2	✓	-
NGC 788	2 1 6.5	- 6 48 56	56.10	S0-a	S2		-
ESO 417-G06	2 56 21.5	-32 11 6	65.60	S0-a	S2		N_{H2}
MARK 1066	2 59 58.6	36 49 14	51.70	S0-a	S2	✓	-
3C 98.0	3 58 54.5	10 26 2	124.90	E	S2		$Norm_2$
MARK 3	6 15 36.3	71 2 15	63.20	S0	S2	✓	$Norm_2$
MARK 1210	8 4 5.9	5 6 50	53.60	-	S2		$Norm_2+N_{H2}$
IC 2560	10 16 19.3	-33 33 59	34.80	SBb	S2	✓	-
NGC 3393	10 48 23.4	-25 9 44	48.70	SBa	S2	✓	-
NGC 4507	12 35 36.5	-39 54 33	46.00	Sab	S2		$Norm_2+N_{H2}$
NGC 4698	12 48 22.9	8 29 14	23.40	Sab	S2		-
NGC 5194	13 29 52.4	47 11 41	7.85	Sbc	S2	✓	-
MARK 268	13 41 11.1	30 22 41	161.50	S0-a	S2		-
MARK 273	13 44 42.1	55 53 13	156.70	Sab	S2		N_{H2}
Circinus	14 13 9.8	-65 20 17	4.21	Sb	S2	✓	-
NGC 5643	14 32 40.7	-44 10 28	16.90	Sc	S2	✓	-
MARK 477	14 40 38.1	53 30 15	156.70	E?	S2	✓	-
IC 4518A	14 57 41.2	-43 7 56	65.20	Sc	S2		$Norm_2$
ESO 138-G01	16 51 20.5	-59 14 11	36.00	E-S0	S2	✓	-
NGC 6300	17 16 59.2	-62 49 5	14.43	SBb	S2		$Norm_2+Norm_1$
NGC 7172	22 2 1.9	-31 52 8	33.90	Sa	S2		$Norm_2$
NGC 7212	22 7 2.0	10 14 0	111.80	Sb	S2	✓	-
NGC 7319	22 36 3.5	33 58 33	77.25	Sbc	S2		$Norm_2+N_{H1}$

Notes. (Col. 1) Name, (Col. 2) right ascension, (Col. 3) declination, (Col. 4) distance, (Col. 5) galaxy morphological type from González-Martín et al. (2009a) or Hyperleda, (Col. 6) optical classification, where L: LINER and S: Seyfert, (Col. 7) *Compton*-thick candidates, and (Col. 8) X-ray variability pattern (the lines mean variations are not found).

[1] All distances are taken from the NED and correspond to the average redshift-independent distance estimates.

variations are not found, and UV variations are reported only for LINER nuclei.

In this work we present the X-ray spectral properties derived from our previous analysis, as well as the X-ray variability pattern(s) obtained for LINER and Seyfert 2 galaxies, with the aim of finding similarities and/or differences within the two families of AGN. This paper is organised as follows: the sample used for the work is described in Sect. 2, the results of the comparison of the X-ray variability and spectral properties between the two families is presented in Sect. 3, which are discussed in Sect. 4. We summarize our conclusions in Sect. 5.

2. Sample and data

The sample contains 21 LINERs from the Palomar sample (Ho et al. 1997) or the sample by González-Martín et al. (2009b), and 26 Seyfert 2s from the Véron-Cetty and Véron catalogue (Véron-Cetty & Véron 2010). The data used for this work is presented in Hernández-García et al. (2013), and Hernández-García et al. (2014) for LINER nuclei, and in Hernández-García et al. (2015) for Seyfert 2s, thus we refer the reader to these papers for details on the sample selection. Some of the galaxies have been rejected from the analysis: the LINERs NGC 2787, NGC 2841, and NGC 3627 and the Seyfert 2 NGC 3079 due to the strong extranuclear emission contamination, the LINER NGC 3226 due to its contamination from the companion galaxy NGC 3227 and all

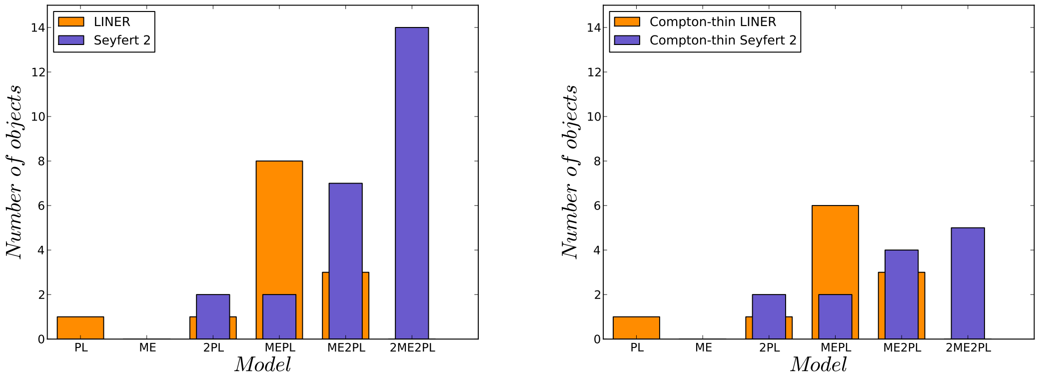

Fig. 1: Histograms of the X-ray spectral models fitted to (left): all the LINERs and Seyfert 2s in the sample, and (right): *Compton*-thin LINERs and Seyfert 2s.

the LINERs classified as non-AGN by González-Martín et al. (2009a) (NGC 3608, NGC 4636, NGC 5813, and NGC 5846).

All together, the sample contains a total of 38 sources: 13 LINERs (two *Compton*-thick candidates and 11 *Compton*-thin candidates[2]) and 25 Seyfert 2 galaxies (12 *Compton*-thick candidates and 13 *Compton*-thin candidates). Table 1 shows the sample galaxies, along with the *Compton*-thick candidates (Col. 7), and the X-ray variability pattern (Col. 8). These variability patterns are related to the normalization at soft ($Norm_1$) and high ($Norm_2$) energies, and/or the absorber at soft (N_{H1}) and hard energies (N_{H2}).

3. Results

3.1. Spectral shape and X-ray parameters

We have compared a sample of 13 LINERs and 25 Seyfert 2s. Among them, two LINERs and 12 Seyfert 2s have been classified as Compton-thick candidates (González-Martín et al. 2009b; Hernández-García et al. 2015). Observations have shown that the X-ray spectra of these objects are most probably dominated by a reflection component (Awaki et al. 1991), thus the spectral components dominating in *Compton*-thin and *Compton*-thick sources can be different. For this reason, we will treat *Compton*-thick and *Compton*-thin candidates separately.

Figs. 1 and 2 show the main spectral parameters obtained from our analysis, whose median values and 25% and 75% quartiles are presented in Table 2. In all histograms, values for the whole sample are represented in left panels, and excluding *Compton*-thick candidates (i.e., only *Compton*-thin candidates) in right panels. It can be observed in Fig. 1 that Seyfert 2s require more complex models to fit their spectra (refer to Hernández-García et al. 2015 for details on these models). There are no differences between the absorber at soft energies (N_{H1}), which is compatible with the Galactic value in most cases but Seyfert 2s appear more absorbed at high energies (N_{H2}). We notice that the N_{H2} distribution is bimodal for Seyfert 2s (with median values of $N_{H2}(low) = 9.8_{7.1}^{13.3} cm^{-2}$ and $N_{H2}(high) = 38.4_{24.0}^{46.6} cm^{-2}$) and the two changing-look candidates reported in Hernández-García et al. (2015), MARK 273, and NGC 7319, appear in $N_{H2}(high)$. The branch at $N_{H2}(low)$ is very similar to the LINER distribution. The indices of the power law representing the AGN are very similar in both families, although *Compton*-thick candidates show much flatter values, as expected (Cappi et al. 2006). When only *Compton*-thin are considered, both distributions look pretty much the same. Finally, a clear difference between the objects is observed in the temperatures, with Seyfert 2s showing a bimodal distribution with medians at kT~0.1 keV and kT~0.7 keV, whereas LINERs show only one temperature regime at kT~0.6 keV.

In Fig. 3, X-ray luminosities from the fitted models, black hole masses, M_{BH}, and Eddington ratios, R_{Edd}, are presented. M_{BH} have been calculated from the M_{BH}–σ relation (Tremaine et al. 2002, σ from HyperLeda) or taken from the literature otherwise; R_{Edd} are calculated using a bolometric correction, k, dependent on luminosity following Marconi et al. (2004). From their k–L_{bol} relation, we determined the k–$L(2-10$ keV), and fitted a fourth order polynomial to derive the relation, which was applied to each object. Seyfert 2s show lower values of M_{BH} than LINERs, although note a substantial overlap, and higher soft (0.5-2.0 keV), hard (2-10 keV) X-ray luminosities, and R_{Edd}. These differences are about an order of magnitude in all cases, except in R_{Edd} where a clear difference can be observed at 10^{-3}, with Seyfert 2s (LINERs) located above (below) this value. Notice that only one Seyfert 2, namely NGC 4698, appears in luminosity and R_{Edd} with a value characteristic of what it is found for LINERs. The optical classification of this object has been controversial in the current literature, classified as Seyfert 2 by Ho et al. (1997) and Bianchi et al. (2012), but also classified as a LINER by González-Martín et al. (2009b). However, since it is a non-variable source, its presence in any of the two families does not change our conclusions.

3.2. X-ray variability

Short-term variations cannot be claimed in any of the studied objects, as all the measurements were below the 3σ level. Regarding long term variations, it is found that LINERs and Seyfert 2s are X-ray variable objects at long timescales, i.e., from months to years, except when they are *Compton*-thick objects, where variations are not usual (one out of 12 *Compton*-thick candidate Seyfert 2s, and one out of two *Compton*-thick candidate LINERs). When transitions from *Compton*-thick to

---

[2] Classifications are obtained from González-Martín et al. (2009a). Four sources are not included in their sample and are *Compton*-thin candidates (NGC 1961, NGC 3718, NGC 5195, and NGC 5982) based on the measures of Γ and the X-ray to [O III] flux ratio (see González-Martín et al. 2009a).

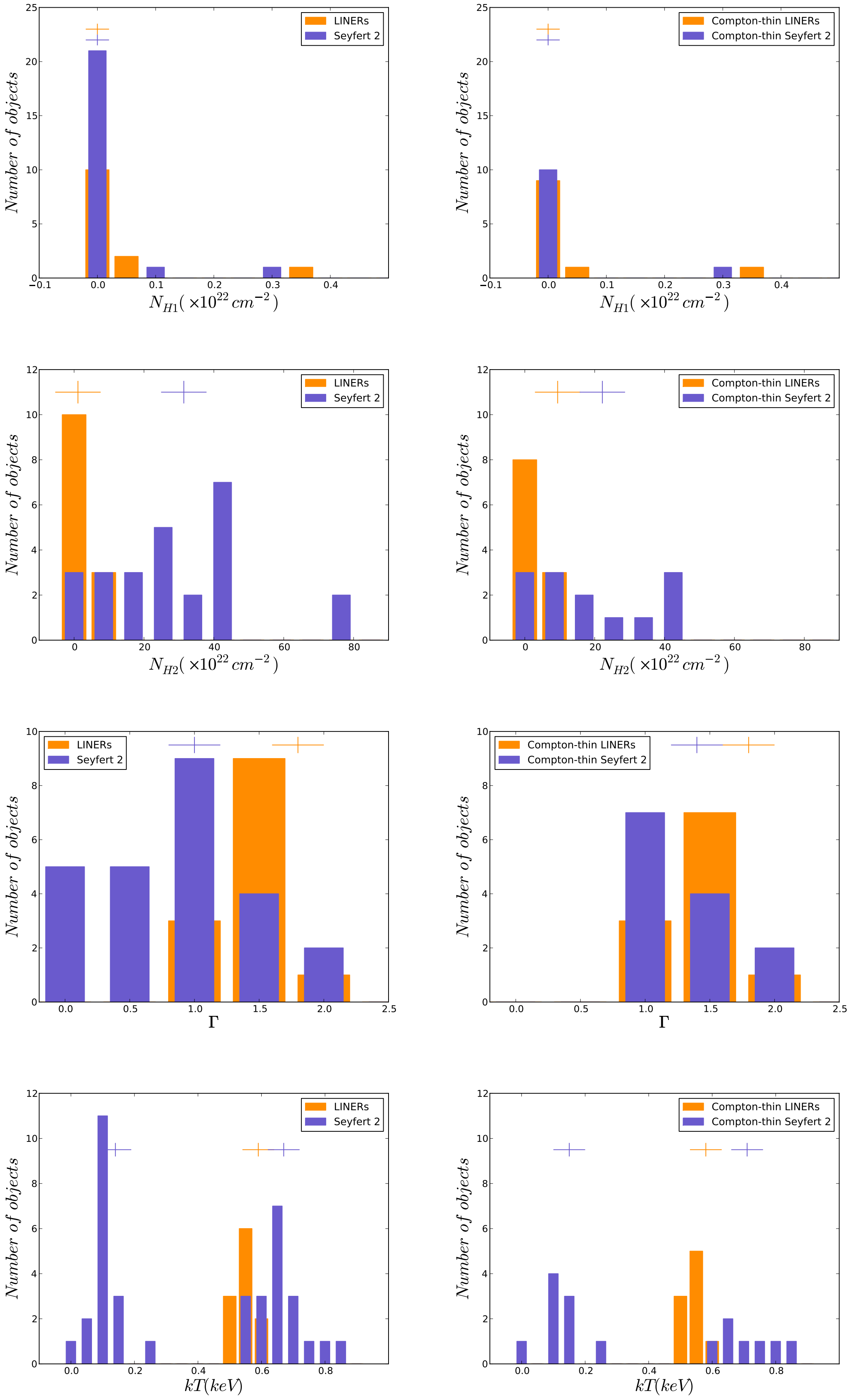

Fig. 2: Histograms of the spectral parameters obtained for: (left): all the LINERs and Seyfert 2s in the sample, and (right): *Compton*-thin LINERs, and *Compton*-thin Seyfert 2s. From up to down, the column density at soft energies, the column density at hard energies, the slope of the power law, and temperatures are presented. The crosses represent the median value reported in Table 2.

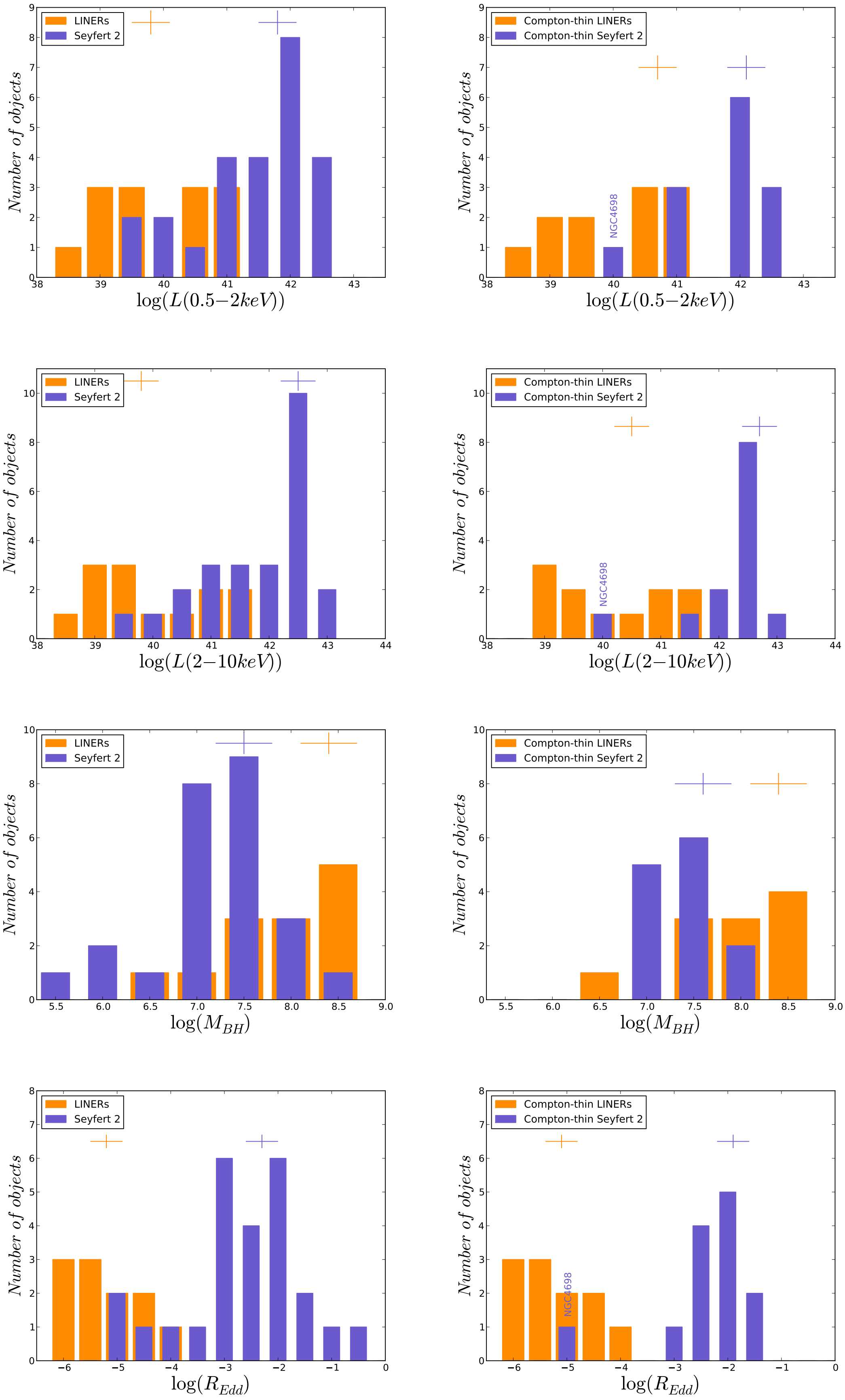

Fig. 3: From upper to lower panels, histograms of: the luminosities in the soft (0.5–2.0 keV) X-ray energy band; the luminosities in the hard (2–10 keV) X-ray energy band; the black hole masses in logarithmic scale; and the Eddington ratios in logarithmically scale. In all cases (left): all the sample of LINERs and Seyfert 2s, and (right): *Compton*-thin LINERs, and *Compton*-thin Seyfert 2s. The crosses represent the median values reported in Table 2.

Table 2: Median values and the 25% and 75% quartiles of the spectral parameters.

	LINER			Seyfert 2		
(1)	All (2)	*Compton*-thick (3)	*Compton*-thin (4)	All (5)	*Compton*-thick (6)	*Compton*-thin (7)
log(L(0.5-2 keV) [erg s^{-1}])	$39.8^{41.0}_{39.5}$	$39.6^{39.6}_{39.0}$	$40.7^{41.0}_{39.5}$	$41.8^{42.3}_{41.3}$	$41.7^{42.2}_{40.6}$	$42.1^{42.6}_{41.3}$
log(L(2-10 keV) [erg s^{-1}])	$39.8^{41.0}_{39.5}$	$39.6^{39.6}_{38.9}$	$40.5^{41.2}_{39.5}$	$42.5^{42.8}_{41.4}$	$41.5^{42.6}_{41.0}$	$42.7^{42.8}_{42.5}$
L(0.5-2 keV)/L(2-10 keV)	$0.9^{1.1}_{0.6}$	$1.2^{1.2}_{1.1}$	$0.8^{1.1}_{0.6}$	$0.4^{0.9}_{0.3}$	$0.8^{1.0}_{0.3}$	$0.4^{0.5}_{0.3}$
$\log(M_{BH}\ [M_\odot])$	$8.4^{8.7}_{7.6}$	$8.7^{8.7}_{7.1}$	$8.4^{8.7}_{7.6}$	$7.5^{7.8}_{7.2}$	$7.4^{7.8}_{6.7}$	$7.6^{7.8}_{7.4}$
$\log(R_{Edd})$	$-5.2^{-4.5}_{-5.6}$	$-5.4^{-5.4}_{-6.4}$	$-5.1^{-4.2}_{-5.6}$	$-2.3^{-1.8}_{-2.9}$	$-2.9^{-1.9}_{-3.0}$	$-1.9^{-1.8}_{-2.3}$
N_{H1} $(\times 10^{22}[cm^{-2}])$	$0.00^{0.02}_{0.00}$	$0.07^{0.07}_{0.02}$	$0.0^{0.0}_{0.0}$	$0.0^{0.0}_{0.0}$	$0.0^{0.0}_{0.0}$	$0.00^{0.02}_{0.00}$
N_{H2} $(\times 10^{22}[cm^{-2}])$	$1.1^{10.5}_{0.15}$	$0.09^{0.09}_{0.00}$	$9.4^{10.5}_{0.8}$	$31.4^{44.7}_{22.2}$	$43.3^{48.7}_{29.8}$	$22.2^{38.4}_{9.8}$
Γ	$1.8^{1.9}_{1.6}$	$2.0^{2.0}_{1.73}$	$1.8^{1.9}_{1.4}$	$1.0^{1.3}_{0.5}$	$0.5^{0.8}_{0.4}$	$1.4^{1.6}_{1.3}$
kT [keV]	$0.59^{0.60}_{0.54}$	$0.64^{0.64}_{0.59}$	$0.58^{0.60}_{0.54}$	$0.67^{0.71}_{0.63}$ $(0.14^{0.15}_{0.11})$	$0.65^{0.68}_{0.61}$ $(0.11^{0.15}_{0.10})$	$0.71^{0.81}_{0.67}(0.15^{0.18}_{0.12})$

Notes. (Col. 1) Spectral parameter, (Col. 2) all the LINERs in the sample, (Col. 3) *Compton*-thick candidate LINERs, (Col. 4) *Compton*-thin candidate LINERs, (Col. 5) all the Seyfert 2s in the sample, (Col. 6) *Compton*-thick candidate Seyfert 2s, and (Col. 7) *Compton*-thin candidate Seyfert 2s.

Compton-thin were observed in the same object, we classified them as changing-look candidates. Four changing look candidates are included in the sample of Seyfert 2s (see Hernández-García et al. 2015), from our own analysis or taken from the literature (MARK 273, MARK 1210, NGC 6300, and NGC 7319). Following the methodology in Hernández-García et al. (2015) for Seyfert 2s, i.e., by using X-ray and [O III] data to classify the objects from their individual observations as *Compton*-thin or *Compton*-thick, we did not find changing-look candidates among LINERs.

A histogram of the X-ray variability patterns is presented in Fig. 4. The most frequent long term variations observed in both families of AGN are related to the normalization at hard energies, which are observed in all the eight variable LINERs and in nine out of the 11 variable Seyfert 2s with amplitudes ranging from 20% to 80%. Variations due to absorption are less common, being more frequent in Seyfert 2s (four out of 11, i.e., 36%) than in LINERs (one out of eight, i.e., 13%). Variations at soft energies are found in only two Seyfert 2s and one LINER, in all cases accompanied with variations of the nuclear continuum.

The last result we like to report is that at UV frequencies long-term UV variations are found in most LINERs (five out of six), whereas this kind of variations are not observed in Seyfert 2s. Take notice that the presence of the nuclear UV source in Seyfert 2s is very scarce, as we have detected it only in three cases.

Therefore, the main result from our study is that long term X-ray variations at hard energies (2-10 keV) are present in these AGN with the same characteristic timescales, i.e., from months to years, and the same amplitudes, i.e., 20-80%. Since the power law represents the transmitted AGN continuum in all the models, these variations are related to the nuclear source. It seems that in principle variations have the same origin both in LINERs and Seyfert 2s.

4. Discussion

LINERs have been invoked as a scaled down version of Seyfert galaxies based in their average luminosities and R_{Edd} (Dudik et al. 2006; González-Martín et al. 2006, 2009a,b; Younes et al. 2011). González-Martín et al. (2009b) pointed to the overlap found in their properties taking the Seyfert sample from Panessa et al. (2007) as a reference. A drawback of all these works is that they also include *Compton*-thick objects. In Hernández-García et al. (2015) we found that these sources are dominated by a constant reflection component and do not vary at X-rays, in agreement with other works (e.g., LaMassa et al. 2011; Arévalo et al. 2014). Our present work separating *Compton*-thin and *Compton*-thick sources allows a more net view on the nature of these families taking variability as a selection criteria.

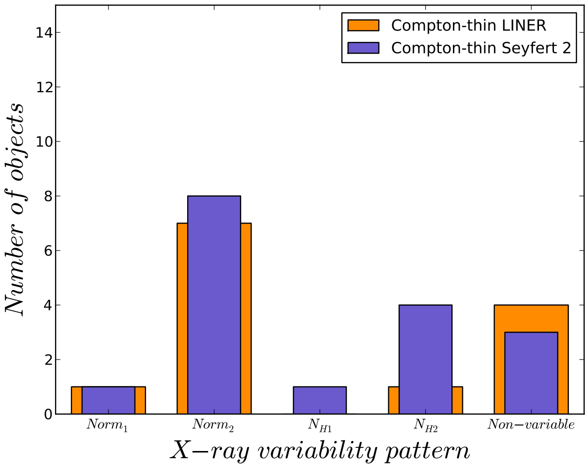

Fig. 4: Histograms of the X-ray variability patterns of the *Compton*-thin LINERs, and *Compton*-thin Seyfert 2s.

Whereas the X-ray spectral shape is indistinguishable in both Seyfert 2s and LINERs, the main difference come from the luminosity which in turn leads to a high R_{Edd} for Seyfert 2s. Several authors have studied the accretion mechanism by using the relation between the spectral slope and R_{Edd} (Γ–R_{Edd}), being a negative correlation attributed to inefficient accretion and a positive one to efficient accretion (Lu & Yu 1999; Porquet et al. 2004; Bian 2005; Shemmer et al. 2006; Gu & Cao 2009; Younes

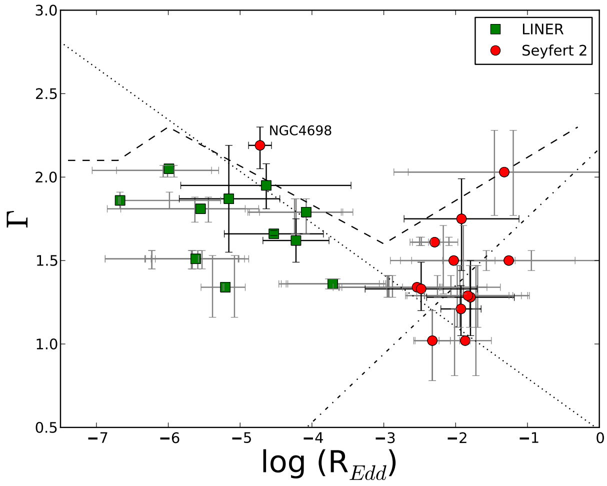

Fig. 5: Spectral index of the power law, Γ, vs Eddington ratio, R_{Edd} for *Compton*-thin LINER (green squares) and Seyfert 2 (red circles) galaxies. The error bars are black for objects where variations are not found, and grey for the individual observations of variable objects. The points represent the mean values; the dashed line represents the model of Yang et al. (2015), the dot-dashed line the results of Shemmer et al. (2006), and the dotted line the results of Younes et al. (2011).

et al. 2011; Yang et al. 2015). However, we do not find variations in the spectral index either for LINERs or for Seyferts whereas X-ray binaries (where this behaviour is well constrained for different spectral states) do present variations (e.g., Cygnus X-1, Ibragimov et al. 2005). The absence of variations in the spectral index might be attributed to the lack of studies of variability at the timescales where these spectral variations are expected. To date, the Γ–R_{Edd} has been detected only in one AGN individually (Emmanoulopoulos et al. 2012). Indeed, they used *RXTE* data monitoring the source in timescales of days, and we notice that the variations in Γ were of very short amplitude (changes from $\sim$ 1.8 to 1.9). Instead of the study of Γ variations with R_{Edd} for a single object, several studies have reported the Γ–R_{Edd} correlation variations with different objects; this produces a very high scatter instead of a clean correlation (e.g., Yang et al. 2015). In Fig. 5 we present the relation found for our *Compton*-thin candidate LINER and Seyfert 2 samples. It nearly distinguishes for the first time that at $R_{Edd} \sim 10^{-3}$ both accretion regimes are separated. Only the Seyfert 2 NGC 4698 is below that limit, although this object has also been classified as a LINER (see González-Martín et al. 2009b). However, the scatter does not allow to see a clear anti-correlation expected for LINERs.

One way to overcome this difficulty to get hints into the nature of the accretion mechanism in these objects might be studying the nature of their variability. In this work it is reported for the first time that, regardless the LINER or Seyfert nature of the source, most of the objects show variability in the continuum normalization, i.e., the transmitted continuum flux from the AGN. Moreover, the amplitudes and timescales of the variations are similar for both families. It is very suggestive that this result appear to be in agreement with that reported by Parker et al. (2015) for a sample of 26 AGN. They obtain that the variability in almost all sources is dominated by a single component, which they found correspond to the flux of the continuum. Therefore, the mechanism driving these variations should be related to fluctuations in the inner accretion disc. This might be against the idea that LINERs are in a different accretion state where the disc is partially suppressed and radiatively inefficient accretion flows (RIAF, Quataert 2004) take place for the relevant accretion mechanism. However, these kind of intrinsic continuum flux variations could be produced by both emission mechanisms (Lyubarskii 1997). It is worth noting that our spectral fits show that Seyfert 2s need two thermal components while LINERs need only the higher temperature component. It has been suggested that the lower temperature ($kT \sim 0.1$ keV) component, usually referred to as the ‘soft excess’, can be a signature of the accretion disc (e.g., Gierliński & Done 2004). The fact that this thermal component is not present in LINERs might be in agreement with RIAFs being the accretion mechanism in LINERs. Thus, we suggest that different accretion mechanisms occurring in LINERs (RIAF) and Seyfert 2s (standard accretion disc) give place to the same kind of long-term X-ray variations, which are probably related with fluctuations in the accretion flow.

The less common source of variability identified has been the absorption. It has been found in four Seyfert 2s and one LINER (NGC 1052). Using the variability timescale to obtain the location of the cloud that intersects our line of sight (following Risaliti et al. 2007), we found that these variations are related with changes in the broad line region (BLR) in two Seyfert 2s, while its location cannot be estimated in the remaining sources because the timescales between observations were too large due to the randomness of the data (Hernández-García et al. 2014, 2015). Eclipses in the BLR have been observed in type 1.8-1.9 Seyferts (Risaliti et al. 2007; Puccetti et al. 2007; Risaliti et al. 2011) and a few Seyfert 2s (Risaliti et al. 2010; Braito et al. 2013; Marinucci et al. 2013). However, the existence of the BLR and the dusty torus is still controversial for low luminosity AGN (e.g., Nenkova et al. 2008). Theoretically, (Elitzur & Shlosman 2006) have shown that at bolometric luminosities below $L_{bol} \sim 10^{42}$ $erg\ s^{-1}$ the accretion onto the SMBH cannot longer sustain the required cloud outflow rate, and the torus and the BLR might disappear. Observational works at different wavelengths in support of this scenario have been published for LINERs (which are in the luminosity regime predicted by Elitzur & Shlosman 2006) and agree with the results presented here:

The work by Maoz et al. (2005) at UV frequencies with *HST* data showed that UV variations in LINERs are common. Their work agrees well with ours, where UV variations were found for LINERs (Hernández-García et al. 2013, 2014) but not for Seyfert 2s (Hernández-García et al. 2015). This may suggest that the torus is obscured in Seyfert 2s while it is ‘naked’ in LINERs, explaining the observed variations and the disappearance of the torus and the BLR at low luminosities. At mid-IR frequencies Gonzalez-Martin et al. (2015) studied different types of AGN and found that the spectral energy distribution in faint LINERs ($\log(L(2-10keV) < 41$) are consistent with the lack of a torus. At X-rays, we searched for changing-look candidates, i.e., objects that show transitions from *Compton*-thin to *Compton*-thick, and found that they are only present among Seyfert 2s. The lack of the BLR and the torus can explain the absence of absorber variations and changing-look candidates in LINERs.

Finally, a few objects show variations at energies below 2 keV, in all cases accompanied by variations in the nuclear continuum. In two out of the three cases, these variations were obtained when comparing data from different instruments. Thus confirmation is still required. New *XMM*-Newton data at different epochs of these sources would be very helpful in order to conclude whether these variations are real or not.

5. Conclusions

In the present work we have assembled the X-ray spectral properties and variability patterns of two optically selected families of AGN: LINERs and Seyfert 2s. Since *Compton*-thick sources do not usually show variations, the work is centered in *Compton*-thin sources, including 11 LINERs and 13 Seyfert 2s. We have shown that the most frequent X-ray variability pattern occurs in timescales between months and years, and is related with changes in the nuclear continuum in both families, but other patterns of variability are also observed. Variations due to absorbers at hard X-ray energies are most frequent in Seyfert 2s than in LINERs, and variations at soft X-ray energies are rare and need to be confirmed.

We suggest that the X-ray variations occur in the same way in LINERs and Seyfert 2s and might be related with fluctuations in the accretion disc, although the accretion mechanisms can be different. Furthermore, we speculate that the BLR and the torus might disappear in LINERs, based on the scarcity of absorption variations, the lack of changing-look candidates, and the fact that UV nuclear variations are found in these sources, in contrast to what is observed in Seyfert 2s.

Acknowledgements. We thank the AGN group at the IAA for helpful comments during this work. This work was financed by MINECO grant AYA 2010-15169, AYA 2013-42227-P, and Junta de Andalucía TIC114. LHG acknowledges financial support from the Ministerio de Economía y Competitividad through the Spanish grant FPI BES-2011-043319. This research made use of data obtained from the *Chandra* Data Archive provided by the *Chandra* X-ray Center (CXC). This research made use of data obtained from the *XMM*-Newton Data Archive provided by the *XMM*-Newton Science Archive (XSA). This research made use of the NASA/IPAC extragalactic database (NED), which is operated by the Jet Propulsion Laboratory under contract with the National Aeronautics and Space Administration. We acknowledge the usage of the HyperLeda database (http://leda.univ-lyon1.fr).

References

Antonucci, R. 1993, ARA&A, 31, 473
Arévalo, P., Bauer, F. E., Puccetti, S., et al. 2014, ApJ, 791, 81
Awaki, H., Koyama, K., Inoue, H., & Halpern, J. P. 1991, PASJ, 43, 195
Bian, W.-H. 2005, Chinese Journal of Astronomy and Astrophysics Supplement, 5, 289
Bianchi, S., Panessa, F., Barcons, X., et al. 2012, MNRAS, 426, 3225
Braito, V., Ballo, L., Reeves, J. N., et al. 2013, MNRAS, 428, 2516
Cappi, M., Panessa, F., Bassani, L., et al. 2006, A&A, 446, 459
Dudik, R., Satyapal, S., Dwek, E., et al. 2006, in Bulletin of the American Astronomical Society, Vol. 38, AAS/High Energy Astrophysics Division #9, 352
Elitzur, M. & Shlosman, I. 2006, ApJ, 648, L101
Emmanoulopoulos, D., Papadakis, I. E., McHardy, I. M., et al. 2012, MNRAS, 424, 1327
Evans, D. A., Hardcastle, M. J., Croston, J. H., Worrall, D. M., & Birkinshaw, M. 2005, MNRAS, 359, 363
Gierliński, M. & Done, C. 2004, MNRAS, 349, L7
González-Martín, O., Masegosa, J., Márquez, I., & Guainazzi, M. 2009a, ApJ, 704, 1570
González-Martín, O., Masegosa, J., Márquez, I., Guainazzi, M., & Jiménez-Bailón, E. 2009b, A&A, 506, 1107
González-Martín, O., Masegosa, J., Márquez, I., Guerrero, M. A., & Dultzin-Hacyan, D. 2006, A&A, 460, 45
Gonzalez-Martin, O., Masegosa, J., Marquez, I., et al. 2015, ArXiv e-prints
Gu, M. & Cao, X. 2009, MNRAS, 399, 349
Hernández-García, L., González-Martín, O., Márquez, I., & Masegosa, J. 2013, A&A, 556, A47
Hernández-García, L., González-Martín, O., Masegosa, J., & Márquez, I. 2014, A&A, 569, A26
Hernández-García, L., Masegosa, J., González-Martín, O., & Márquez, I. 2015, ArXiv e-prints
Ho, L. C. 2008, ARA&A, 46, 475
Ho, L. C., Filippenko, A. V., Sargent, W. L. W., & Peng, C. Y. 1997, ApJS, 112, 391
Ibragimov, A., Poutanen, J., Gilfanov, M., Zdziarski, A. A., & Shrader, C. R. 2005, MNRAS, 362, 1435
LaMassa, S. M., Heckman, T. M., Ptak, A., et al. 2011, ApJ, 729, 52
Lu, Y. & Yu, Q. 1999, ApJ, 526, L5
Lyubarskii, Y. E. 1997, MNRAS, 292, 679
Maoz, D., Nagar, N. M., Falcke, H., & Wilson, A. S. 2005, ApJ, 625, 699
Marconi, A., Risaliti, G., Gilli, R., et al. 2004, MNRAS, 351, 169
Marinucci, A., Risaliti, G., Wang, J., et al. 2013, MNRAS, 429, 2581
Nenkova, M., Sirocky, M. M., Ž. Ivezić, & Elitzur, M. 2008, ApJ, 685, 147
Netzer, H. 2015, ArXiv e-prints
Panessa, F., Barcons, X., Bassani, L., et al. 2007, A&A, 467, 519
Panessa, F., de Rosa, A., Bassani, L., et al. 2011, MNRAS, 417, 2426
Parker, M. L., Fabian, A. C., Matt, G., et al. 2015, MNRAS, 447, 72
Pian, E., Romano, P., Maoz, D., et al. 2010, MNRAS, 401, 677
Porquet, D., Reeves, J. N., O'Brien, P., & Brinkmann, W. 2004, A&A, 422, 85
Puccetti, S., Fiore, F., Risaliti, G., et al. 2007, MNRAS, 377, 607
Quataert, E. 2004, in Astronomical Society of the Pacific Conference Series, Vol. 311, AGN Physics with the Sloan Digital Sky Survey, ed. G. T. Richards & P. B. Hall, 131
Risaliti, G., Elvis, M., Bianchi, S., & Matt, G. 2010, MNRAS, 406, L20
Risaliti, G., Elvis, M., Fabbiano, G., et al. 2007, ApJ, 659, L111
Risaliti, G., Maiolino, R., & Bassani, L. 2000, A&A, 356, 33
Risaliti, G., Nardini, E., Salvati, M., et al. 2011, MNRAS, 410, 1027
Schawinski, K., Simmons, B. D., Urry, C. M., Treister, E., & Glikman, E. 2012, MNRAS, 425, L61
Schmidt, M. 1963, Nature, 197, 1040
Shemmer, O., Brandt, W. N., Netzer, H., Maiolino, R., & Kaspi, S. 2006, ApJ, 646, L29
Stalevski, M., Fritz, J., Baes, M., Nakos, T., & Č. Popović, L. 2012, MNRAS, 420, 2756
Tremaine, S., Gebhardt, K., Bender, R., et al. 2002, ApJ, 574, 740
Véron-Cetty, M.-P. & Véron, P. 2010, A&A, 518, A10
Yang, Q.-X., Xie, F.-G., Yuan, F., et al. 2015, MNRAS, 447, 1692
Younes, G., Porquet, D., Sabra, B., & Reeves, J. N. 2011, A&A, 530, A149

5

AGN in clusters

Galaxies tend to gather together among them, forming bigger structures as galaxy groups and, when they are numerous enough, galaxy clusters (Kravtsov & Borgani 2012). It is usual to find AGN residing within these structures (Guennou et al. 2014). Since the cluster emission is composed by hot gas, it is of special importance to be familiar with the characteristics that group and clusters of galaxies present. We develop this chapter to the characterization of galaxy groups and clusters, using both spatial and spectral analyses. By using a sample of galaxy groups and clusters, we make a study to search for the number of AGN located within each structure.

This work was carried out during a MINECO Ph.D short-stay (three months) at the Institut d'Astrophysique de Paris (IAP) in 2013, under the supervision of Dr. Durret. This is a preliminary work that should be completed using the whole DAFT/FADA sample, and combining optical and X-ray data. The combination of these data will first allow to measure the redshifts of AGN, and, once this property is known, the characterization of AGN in galaxy clusters should be carried out.

Astronomy & Astrophysics manuscript no. Estancia_Paris_2013
June 10, 2015

Active galactic nuclei in galaxy clusters and groups

Hernández-García, L.[1]; Durret, F.[2]; Lima Neto, G.B.[3]; Guennou, L.[4]; Martinet, N.[2]; Adami C.[5]; Márquez, I.[1]; Masegosa, J.[1]; González-Martín, O.[6]

[1] Instituto de Astrofísica de Andalucía, CSIC, Glorieta de la Astronomía, s/n, 18008 Granada, Spain
e-mail: `lorena@iaa.es`
[2] Sorbonne Universités, UPMC Univ Paris 6 et CNRS, UMR 7095, Institut d'Astrophysique de Paris, 98 bis bd Arago, 75014, Paris, France
[3] Instituto de Astronomia, Geofísica e Ciências Atmosféricas, Universidade de São Paulo, R. do Matão 1226, 05508-090 São Paulo, Brazil
[4] Institut d'Astrophysique Spatiale, CNRS (UMR8617) Université Paris-Sud 11, Bâtiment 121, Orsay, France
[5] LAM, OAMP, Université Aix-Marseille & CNRS, Pôle de l'Etoile, Site de Château Gombert, 38 rue Frédéric Joliot-Curie, 13388 Marseille 13 Cedex, France
[6] Centro de radioastronomía y Astrofísica (CRyA-UNAM), 3-72 (Xangari), 8701, Morelia, Mexico

Draft: June 10, 2015

ABSTRACT

Context. Several active galactic nuclei (AGN) are located in galaxy groups and clusters, and therefore their emission might be affected by its contribution.
Aims. The main aim of this work is to search for AGN located within galaxy groups and clusters. In order to decontaminate AGN from their emission, we characterize X-ray images and spectra of galaxy groups and clusters.
Methods. We use 16 galaxy clusters (11 were studied in Guennou et al. (2013) and five are presented here for the first time) from the DAFT/FADA sample and 10 groups from Lagana et al. (in prep.) to study its properties. We extracted images in the 0.3-8.0 keV energy band and subtracted the cluster emission using a β-model, only in galaxy clusters, in order to see the residuals which are not completely part of the cluster. Spectra were extracted from the pn, MOS1, and MOS2 cameras onboard *XMM*–Newton for all the galaxy groups and clusters. Whenever possible, we searched for AGN within the groups and clusters of galaxies. Their positions were compared to optical data, and their spectra were extracted when a measurement of the redshift was available.
Results. We found three AGN in the nine studied groups of galaxies, each one located in the center of the group. We found 28 point-like sources within the 16 galaxy clusters; only nine with a measured redshift. We have identified from one to five point-like sources on each cluster.
Conclusions. A large sample of galaxy clusters and groups with optical and X-ray data is required to characterize AGN in galaxy clusters.

Key words. Galaxies: active – Galaxies: clusters: general – Galaxies: groups: general – X-rays: galaxies: clusters

1. Introduction

Observations show that almost half of the galaxies in the Universe are located in groups (Kravtsov & Borgani 2012). These groups are formed by about 50 members and bound by gravity. As our closest example, the Milky Way is located in the Local Group, which contains more than 50 galaxies. They have diameters around 0.5–2 Mpc and masses $\sim 10^{13}\ M_{\odot}$. During their evolution, galaxy groups fall into bigger structures called clusters of galaxies, which can contain several galaxy groups. It is not very clear if there is a limit between a group and a cluster, since there does not seem to be any difference, but a continuity of properties for systems of increasing mass.

Galaxy clusters are the largest and most massive well defined objects in the Universe. By using the velocity dispersions of their members, already in the thirties masses a factor ~ 200–400 larger than the luminosity of their stars were obtained (Zwicky 1937), leading to the postulation of dark matter (DM). Its existence was confirmed after the discovery of the hot intracluster medium, that emits at X-ray energies due to thermal bremsstrahlung, and provides a part of the missing mass (Cavaliere et al. 1971). DM also permits the detection of clusters at high redshifts. It is now known that clusters, which contain from hundreds to thousands of galaxies, are characterised by diameters ~ 3–4 Mpc and masses of $10^{14} - 10^{15}\ M_{\odot}$. The mass composition of galaxy clusters is 78–87% in DM, 11–14% in hot gas and 2–6% in galaxies (for $H_o = 70\ km\ s^{-1}\ Mpc^{-1}$). X-ray emission in clusters originates from hot plasma, with temperatures of kT = 2–13 keV and luminosities of $L_x = 10^{43} - 10^{45} erg\ s^{-1}$. Emission lines are also present in the X-ray spectra of clusters, implying that there are more elements than Hydrogen and Helium in the intra-cluster medium (e.g., the 6.7 keV iron emission line). The abundances of these elements correspond to about 1/3 of that seen in our Sun.

The structure formation in galaxy clusters is thought to be due to mergers and accretion from small systems. As the gas is heated it emits in X-rays, until it is dense enough to feed a process of star formation and accretion onto super massive black holes, which can result in feedback due to supernovae or active galactic nuclei (AGN), injecting heat onto the hot intracluster medium (Kravtsov & Borgani 2012).

Table 1: Properties of the clusters analysed in this work. All of them are taken from the DAFT/FADA survey.

Name (1)	RA (J2000) (2)	DEC (J2000) (3)	z (4)	Gal. Lat. (5)
CL J0152.7-1357	28.1708	-13.9625	0.8310	-70.57
BMW-HRI J052215.8-362452	80.5592	-36.4178	0.4720	-32.85
MACS J0647.7+7015	101.9413	70.2508	0.5907	+25.12
MACS J0717.5+3745*	109.3788	37.7583	0.5458	+21.05
MACS J0744.9+3927	116.2158	39.4592	0.6860	+26.65
RX J0847.1+3449	131.7971	34.8211	0.5600	+37.87
RX J0848.8+4455*	132.2050	44.9294	0.5430	+39.11
Abell 851	145.7360	46.9894	0.407	+48.29
MS 1137.5+6624	175.0970	66.1449	0.7820	+49.45
CLG J1205+4429	181.4641	44.4860	0.5915	+70.38
BMW-HRI J122657.3+333253	186.7417	33.5484	0.8900	+81.69
PDCS014S*	201.3375	30.1653	0.7200	+81.97
ZwCl 1332.8+5043	203.5833	50.5151	0.6200	+65.22
CL J1604+4314*	241.1075	43.2397	0.8652	+48.08
MACS J2129.4-0741*	322.3583	-6.3089	0.5889	-38.46
RX J2328.8+1453	352.2079	14.8867	0.4970	-43.45

Notes. Objects marked with * were not studied in Guennou et al. (2014)

One of the best ways to detect AGN is the use of X-ray data. X-ray surveys have found a high number of point-like sources in the fields of galaxy clusters (Bechtold et al. 1983; Henry & Briel 1991; Gilmour et al. 2009). Depending on the sample, the number of AGN per cluster varies significantly, as expected because this is a property related to the cluster itself. Being the main goal of this study to analyse the properties of AGN in clusters of galaxies, it will be crucial to subtract the cluster emission when extracting the X-ray spectra.

This study was done during a short stay of three months period (September-November 2013) at the Institut d'Astrophysique de Paris (IAP), and forms a preliminary study that should be completed. In this work we therefore characterize X-ray images and spectra of galaxy groups (clusters), in order to be able to decontaminate the spectra of AGN located within the group (cluster) from the group (cluster) emission. In Sect. 2 we study galaxy clusters and derive their physical properties from the study of X-ray images and spectra and also search for AGN candidates. In Sect. 3 we analyze a sample of galaxy groups in order to find evidence for AGN from their X-ray images and spectra. Finally, we discuss and summarize our results in Sect. 4.

2. Search for AGN in galaxy clusters from the DAFT/FADA survey

The main purpose of this work is to search for AGN in galaxy clusters. As explained below, 11 galaxy clusters from the DAFT/FADA sample in Guennou et al. (2014) are studied, and we add five clusters that were not studied before. Therefore, the first part of the work is focused on the characterization of galaxy clusters to infer their physical properties. The second part consists on the analysis of the point-like sources (i.e., AGN candidates).

2.1. The sample

The sample was selected from the DAFT/FADA survey[1] (PIs. M. Ulmer, C. Adami and D.Clowe). This program is producing a large survey of clusters at z=[0.4-0.9] – all with *HST* imaging data available – and calculating photometric redshifts for the field galaxies. This survey has two main goals, the first one is to determine dark energy (DE) making use of weak lensing tomography, and the second one is to create a data base of about 90 clusters (20.000 galaxies) and study their properties.

X-ray data from *XMM*-Newton public archives were obtained from the *XMM*-Newton Science Archive (XSA)[2]. Guennou et al. (2014) selected the clusters of the DAFT/FADA survey with X-ray and/or optical spectroscopic+imaging available data. From the 32 available *XMM*-Newton data where a spatial analysis was performed, we selected the 24 clusters containing AGN at optical frequencies from the bibliography in Guennou et al. (2014). We visually inspected these clusters with the *XMM*-Newton images and found that 11 of them showed point-like sources. Table 1 lists these 11 clusters, their coordinates, redshifts, and galactic latitudes. We added five clusters from the DAFT/FADA survey that were not previously studied in Guennou et al. (2014). These five clusters are marked with * in Table 1. Observational details are summarized in Table 2.

2.2. Methodology

The first part of the methodology is focused on the study of the clusters. Images from the MOS-1, MOS-2 and pn cameras are obtained, and a model representing the emission of a relaxed cluster is applied to them. The residuals show eventual substructures that may be present within the cluster. Spectral extraction of the clusters are also obtained, so we estimate their physical properties. This part of the analysis is done only for the five clusters we added to the sample, since it was already done in Guennou et al. (2014) for the 11 clusters studied in their work.

---

[1] http://cencos.oamp.fr/DAFT/

[2] http://xmm.esac.esa.int/xsa/index.shtml

Table 2: Observational details of the clusters from the DAFT/FADA survey analysed for the first time in this work.

Name (1)	Satellite (2)	ObsID (3)	Date (4)	Exptime (ksec) (5)
MACS J0717.5+3745	*XMM*-Newton	0672420101	2011-10-11	61.2
	XMM-Newton	0672420301	2011-10-15	64.1
RX J0848.8+4455	*XMM*-Newton	0085150101	2001-10-15	49.2
	XMM-Newton	0085150201	2001-10-21	51.3
	XMM-Newton	0085150301	2001-10-15	51.3
PDCS014S	*XMM*-Newton	0025740201	2001-12-12	39.5
CL J1604+4314	*XMM*-Newton	0025740101	2002-02-09	18.5
	XMM-Newton	0025740401	2002-02-10	24.3
MACS J2129.4-0741	*XMM*-Newton	0700182001	2012-05-02	36.0

The second part of the methodology is focused on the study of point-like sources within the clusters. Note here that raw data is used for the analysis, i.e., we do not use the data after the substraction of the relaxed cluster model. This is done for all the clusters studied in this work.

2.2.1. Images and subtraction of the cluster : β-model

The data were reduced using the Science Analysis Software (SAS[3]), version 13.0.0. Before extracting the images, we filtered for periods of high background, removed bad pixels and columns and made exposure map corrections (using the EEXPMAP task). The images were then extracted in the 0.3-8.0 keV energy band using the EVSELECT task.

The images were combined using IRAF[4], and specifically the IMCOMBINE task, combining the images by summing them and without rejecting any pixel.

Following Guennou et al. (2014), instead of using more complex models, we adopted a simple modeling to fit the clusters with the standard 2D β-model because they are very faint, have a small angular size and their cores are hardly resolved by *XMM*-Newton.

This model represents a relaxed cluster with a homogeneous gravitational potential. The residuals were computed as the difference between the image and the fit, allowing us to detect any perturbation from a homogeneous gravitational potential due to the presence of any eventual substructure still in the process of merging with the cluster.

The X-ray images were fitted with an azimuthally symmetric elliptical *beta*-model using the *Sherpa*[5] tool from CIAO[6]:

$$\Sigma(r) = \Sigma_0\Big[1 + \Big(\frac{r}{r_c}\Big)^2\Big]^{-3\beta+0.5} + b \tag{1}$$

where Σ(r) is the surface brightness as a function of the radius r, Σ_0 is the central surface brightness, r_c the core radius, β the shape parameter, and b accounts for the background, which is assumed to be constant throughout the image.

Whenever possible, we used data from the MOS-1 camera to fit the model, since pn and MOS-2 data are usually contaminated by bad pixels and/or have CCD gaps passing through the cluster image. This allows the analysis of the best quality data possible to search for substructures.

This part of the analysis was made for the five clusters marked with * in Table 1, since it was already made for the others by Guennou et al. (2014).

2.2.2. Spectral extraction

The data were reduced using the Science Analysis Software (SAS[7]), version 13.0.0. Before extracting the spectra, good-timing periods were selected (i.e., flares were excluded). The method used for this purpose maximizes the signal to noise ratio of the net source spectrum by applying a different constant count rate threshold on single-events, E < 10 keV field-of-view background light curve. The extraction region was determined through circles containing the source (galaxy cluster or point-like source). For galaxy clusters, the background was determined with an algorithm that selects the best circular region free of sources; when extracting the spectra of point-like sources the background was manually selected from a circular region as close as possible to the source and free of other sources, in order not to include emission from the cluster. We extracted the source and background regions with the EVSELECT task. The RMF was generated using the RMFGEN task, and the ARF was generated using the ARFGEN task. We then grouped the spectra to obtain at least 20 counts per spectral bin using the GRPPHA task, as required to use χ^2-statistics.

2.2.3. Spectral fitting of galaxy clusters

The spectral fittings were done using XSPEC[8] v.12.7.0. The model used to fit the thermal component that represents the X-ray emission from the cluster was a single MEKAL (phabs*mekal) model. The free parameters in this model are the temperature, kT, and the normalization. The Galactic absorption, N_{Gal}, was included in the model and fixed to the predicted value using the NH tool within FTOOLS (Dickey & Lockman 1990; Kalberla et al. 2005). When the spectra were of low count rate and an estimation of the temperature could not be obtained, the luminosities were estimated from a MEKAL model with a fixed kT = 5 keV.

This part of the analysis was made for the five clusters marked with * in Table 1, since it was already made for the others by Guennou et al. (2014).

---

[3] http://xmm.esa.int/sas/

[4] http://iraf.noao.edu/

[5] http://cxc.cfa.harvard.edu/sherpa4.4/ahelp/beta2d.html

[6] http://cxc.cfa.harvard.edu/ciao/

[7] http://xmm.esa.int/sas/

[8] http://heasarc.nasa.gov/xanadu/xspec/

Table 3: Spectral fittings of the clusters from the DAFT/FADA survey analysed by Guennou et al. (2014).

Name (1)	kT (keV) (2)	L_x(0.5-8.0 keV) (10^{44} erg s^{-1}) (3)	N[1] (4)
CL J0152.7-1357	7.55±0.65	7.91	3
BMW-HRI J052215.8-362452	5.64±0.66	1.70	4
MACS J0647.7+7015	7.74±0.35	16.10	2
MACS J0744.9+3927	7.87±0.28	18.70	1
RX J0847.1+3449	5*	7.11	2
Abell 851	5.17±0.16	6.13	1
MS 1137.5+6624	7.43±0.90	7.41	2
CLG J1205+4429	5*	0.68	1
BMW-HRI J122657.3+333253	8.74±0.42	20.20	5
ZwCl 1332.8+5043	5.08±0.59	2.40	3
RX J2328.8+1453	2.63±0.53	0.43	1

Notes. [1] N is the number of point-like sources on the X-ray images. A thermal model was used to fit the data in all cases. The * means that kT was fixed (see text).

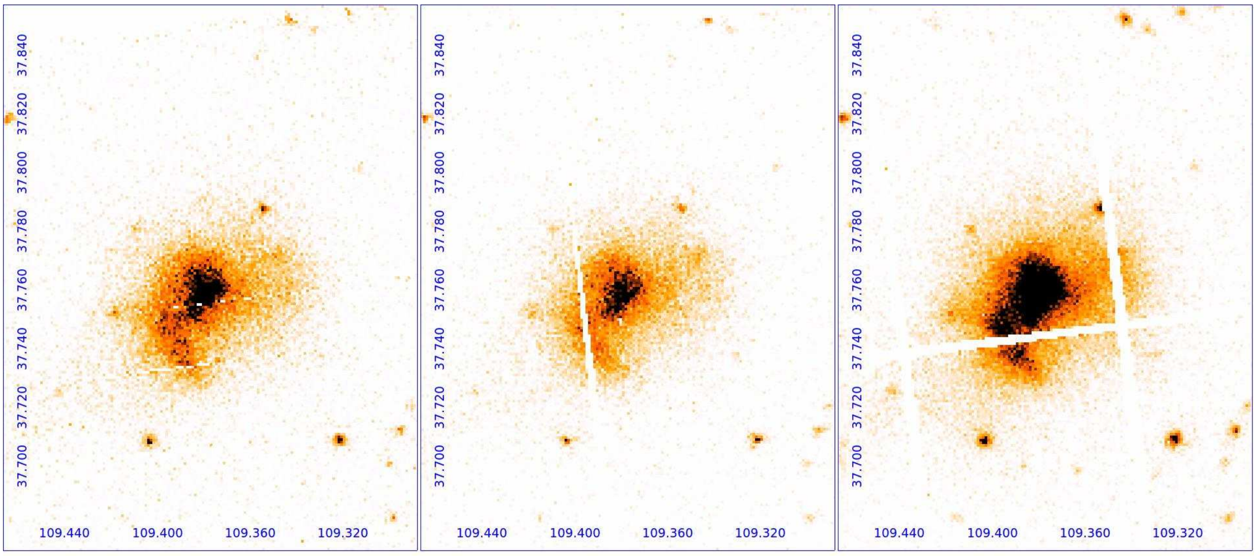

Fig. 1: From left to right, combined images from the MOS-1, MOS-2 and pn cameras of MACS J0717.5+3745. DEC and RA are represented in degrees.

2.2.4. Identification and spectral fitting of point-like sources

Whenever possible, we searched for AGN within the clusters of galaxies. We decided to search for AGN within a circular region of 2 Mpc radius from the coordinates of the galaxy cluster as provided by NED[9]. We can assess that there is an AGN candidate when a point-like source is detected in the 4.5-8.0 keV energy band (González-Martín et al. 2009). However, it is important to note that X-ray emitting objects may not be AGN but Galactic sources, as X-ray binaries (XRB) or ultraluminous X-ray sources (ULXs). The spectral shape and the luminosities of the sources will be taken into account during the discussion for considering such possibilities.

To make a proper spectral fitting, it is necessary to have a measurement of the redshift (which is not possible to obtain from the X-ray data if we are measuring only the continuum). So the next thing we did was to make a bibliographic search of the coordinates of those point-like sources. *XMM*-Newton images have the astrometry done so we obtained the coordinates from the images and searched for their near positions in NED[10], VizieR[11] and non-public catalogs from N. Martinet (private communication).

XSPEC v.12.7.0 was used for the spectral fitting. Since the objects were assumed to be AGN, the model was an absorbed power law, which corresponds to a non-thermal source. The free parameters in this model are the column density, N_H, the slope of the power law, Γ, and the normalization. The Galactic absorption was included in the model as in Sect. 2.2.3.

To make sure that the emission from the cluster was correctly subtracted, we made another spectral fitting using a combination of a thermal (emission from the cluster) plus a power law (emission from the point-like source) model to fit the data, where the

---

[9] http://ned.ipac.caltech.edu/

[10] http://ned.ipac.caltech.edu/forms/nearposn.html

[11] http://vizier.u-strasbg.fr/viz-bin/VizieR

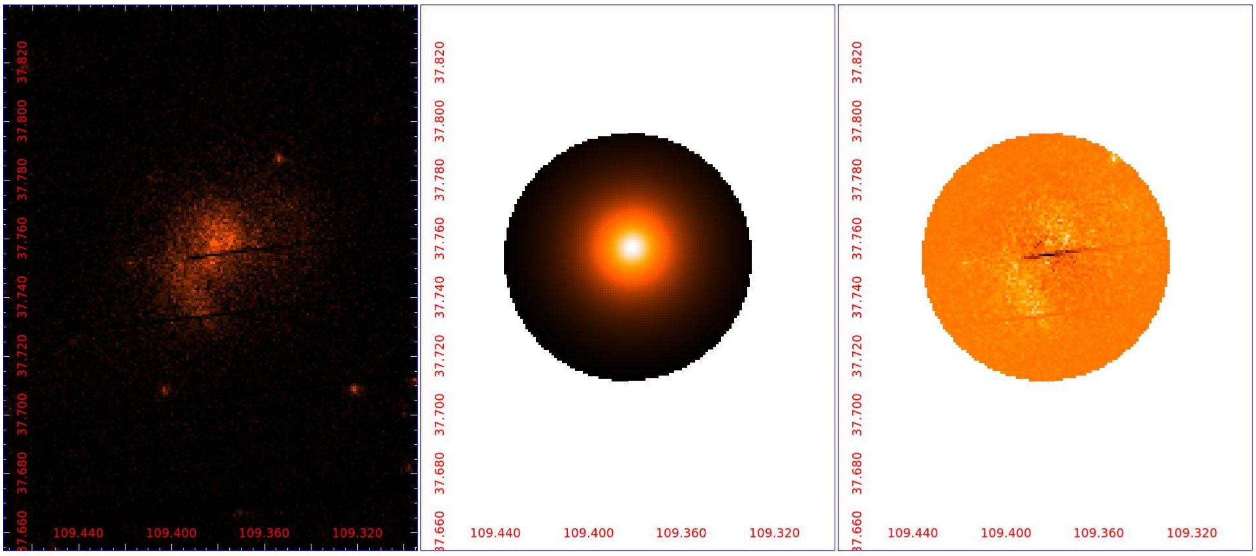

Fig. 2: β-model applied to the MOS-1 camera image of MACS J0717.5+3745. From left to right: the original image, the β-model and the residuals. The circle in the middle and right images have a 2.5' radius.

parameters of the power law were left free to vary while the parameters of the thermal model (MEKAL) were fixed to the values obtained according to Sect. 2.2.3. If this model fitted well the data, the spectrum of the point-like source was contaminated by emission coming from the cluster, and consequently, a new spectral extraction with a smaller aperture was done.

This part of the analysis was made for all the clusters in Table 1.

2.3. Results

We discuss the results obtained for the clusters (including bibliographic information) in the following.

2.3.1. Images and β-model

We refer the reader to Guennou et al. (2014) for the results on images and the application of the β-model to the 11 clusters studied in their work. Here we present the images of the galaxy clusters and the application of the β-model that were not studied in Guennou et al. (2014). The observational details are listed in Table 2.

In three cases the images from the MOS-1, MOS-2 and pn cameras were obtained and combined, but we do not present them because of the faintness of the clusters (CL J1604+4314 and PDCS014S) or because it is in the gap in the three cameras (RX J0848.8+4455). In these cases the clusters were so faint that the the β-model could not be applied.

From the three available observations of MACS J0717.5+3745, ObsID. 0672420201 was affected by radiation (as explained in the *XMM*–Newton observation log browser[12]), so we did not take it into account. For the remaining two observations (both from 2011) we obtained images in the 0.3-8.0 keV band for the MOS-1, MOS-2 and pn cameras (Figure 1).

We applied the β-model to the MOS-1 camera of MACS J0717.5+3745 image (see Figure 2). In the right panel of Figure 2 two big structures can be seen, showing two groups that might be in a merging process. We search for evidence for these substructures in the optical data (see Fig. 3) but we could not locate them.

In the case of MACS J2129.4-0741, only one observation from 2012 was available in the *XMM*-Newton archive. We obtained the images from the MOS-1, MOS-2 and pn cameras in the 0.3-8.0 keV band (Fig. 4).

We applied the β-model to the MOS-1 camera image (Fig. 5). The residuals (bottom-left) show a substructure that may be a group; a point-like source is also visible (marked with a blue circle). An optical counterpart of the point-like source was found at optical wavelengths, marked with a white circle in Fig. 6.

2.3.2. Spectra of the galaxy clusters

The spectral fittings were done as explained in Sect. 2.2.2. The results are given separately for the 11 clusters studied by Guennou et al. (2014) (Table 3) and the five clusters studied for the first time in this work (Table 4).

The results of the temperatures and luminosities in the 0.5–8 keV energy band obtained by Guennou et al. (2014) for the 11 clusters in their sample when fitting a thermal model are summarized in Table 3.

The spectra of one out of the five clusters analysed in this work were not extracted since it was on the gap (RX J0848.8+4455). The remaining four were fitted with a thermal model (i.e., MEKAL), and the results of the spectral fit are summarized in Table 4. Two clusters (CL J1604+4314 and PDCS014S) did not have enough number counts for a proper spectral fitting, so a fixed $kT = 5keV$, 0.3 solar abundance and the redshift of the cluster were used to estimate their luminosities.

In the case of CL J1604+4314, only one spectrum was extracted from a circular region of 40" (0.3 Mpc) from the pn camera from ObsID. 0025740401. From the other cameras and/or observations, the cluster was too faint or, in the case of the pn camera ObsID. 0025740101, it was on the gap. An intrinsic luminosity estimation of logL(0.5-8.0 keV) = 44.15 was obtained. Kocevski et al. (2009) studied the CL1604 supercluster (where

---

[12] http://xmm2.esac.esa.int/external/xmmobsinfo/obsviewframe.shtml

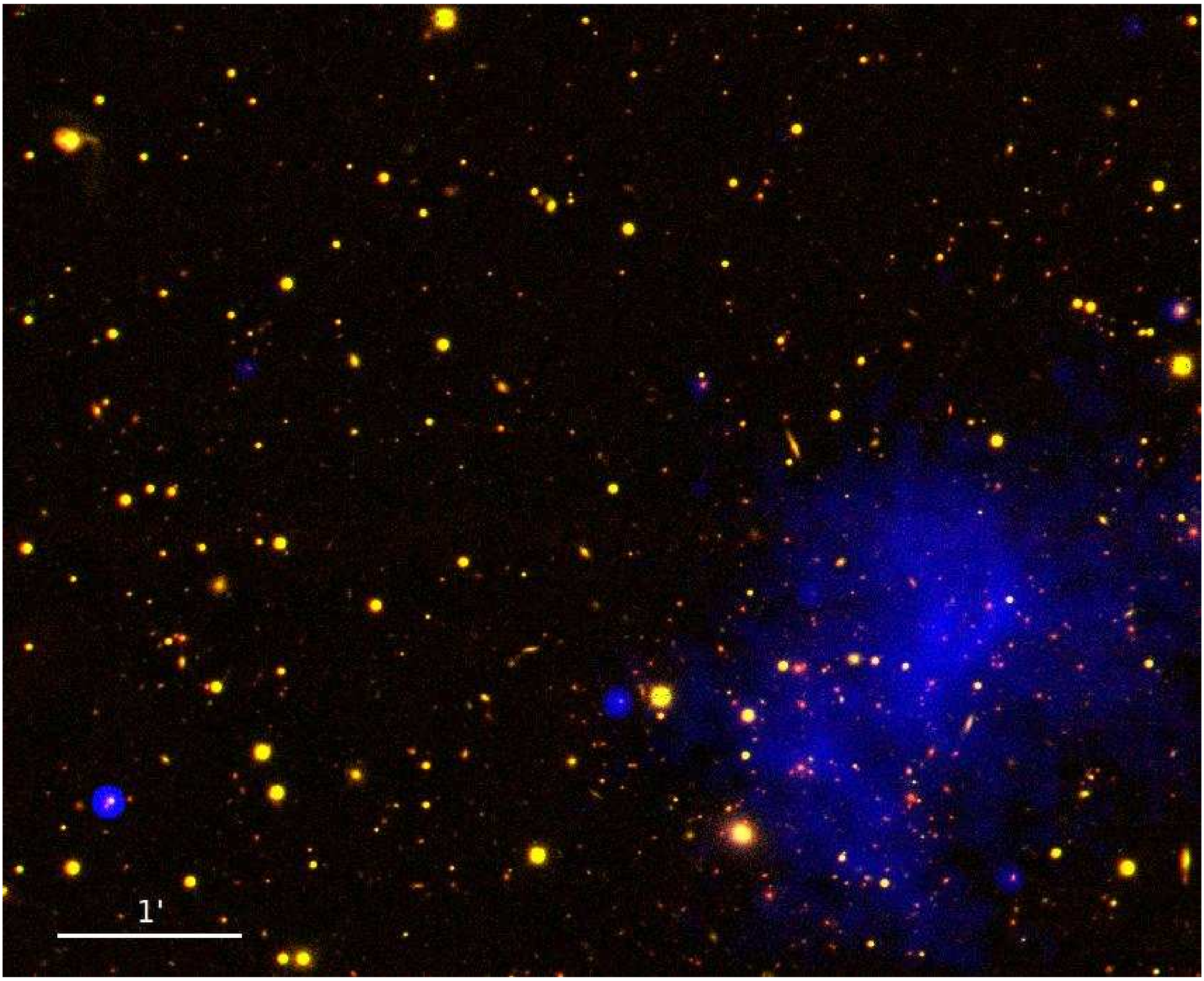

Fig. 3: Color image of MACS J0717.5+3745, combining the optical filters r (red) and v (green) from the *WYIN* telescope, and the *Chandra* 0.3–8 keV (blue).

Table 4: Spectral fittings of the clusters from the DAFT/FADA survey analysed in this work.

Object	Camera	kT	abund.	$\chi^2/d.o.f$	$logL_x$
	(radius)	keV	(Solar)		(0.5-8.0 keV)
(1)	(2)	(3)	(4)	(5)	
CL J1604+4314	pn (40”)	5*	0.3*	-	44.15
PDCS 014S	MOS-1 (60”)	5*	0.3*	-	43.76
MACS J0717.5+3745	All (1.9’)	$11.35^{11.70}_{10.94}$	$0.23^{0.28}_{0.17}$	1.03	$45.12^{45.13}_{45.11}$
MACS J2129.4-0741	All (1.0’)	$8.99^{10.28}_{8.05}$	$0.30^{0.47}_{0.12}$	1.09	$45.08^{45.07}_{45.09}$

Notes. The MEKAL model was used in all cases to fit the spectra. The * means that kT was fixed (see text).

CL J1604+4314 is located) and found a bolometric luminosity of 8.20×10^{43} h_{70}^{-2} erg s^{-1} and $kT = 1.64^{+0.65}_{-0.45}$ using *Chandra* data. They argued that this cluster is not fully relaxed and it could still be in process of formation due to galaxy and/or group mergers. The differences in the luminosities are probably due to the different temperatures used in the spectral fitting. Following the results from Kocevski et al. (2009), we obtain a lower luminosity of 44.01 when fitting a thermal model with their kT = 1.64 keV. The luminosity agree well with our estimation when fitting a thermal model with kT=5 keV. However, we notice that the temperature obtained by Kocevski et al. (2009) is very cold for a galaxy cluster; their result is most probably due to the low number count in *Chandra* data.

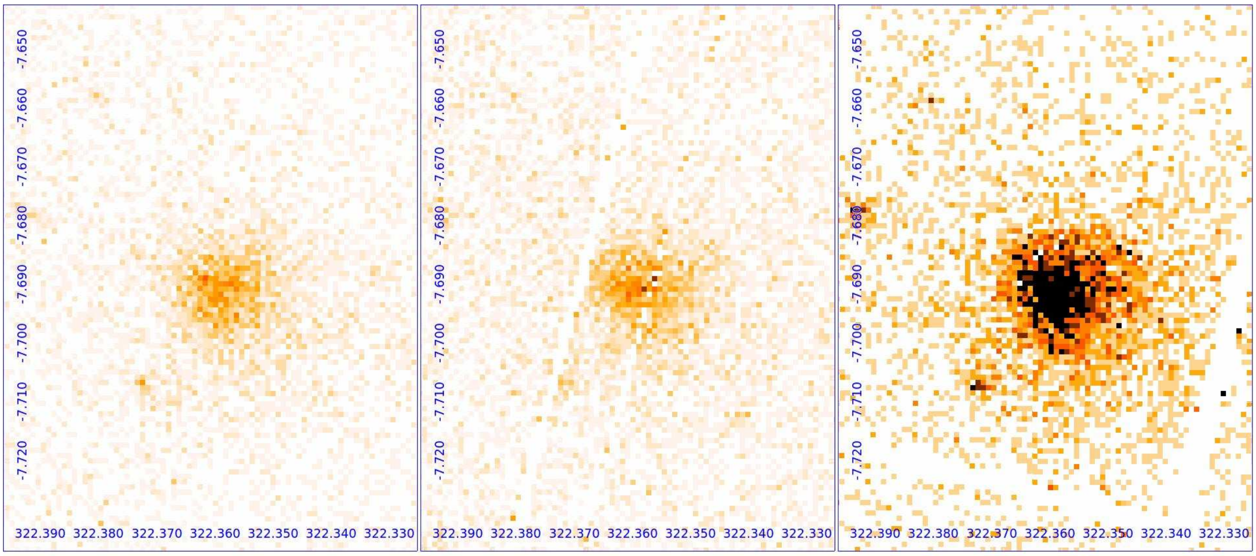

Fig. 4: From left to right, images from the MOS-1, MOS-2 and pn cameras of MACS J2129.4-0741. DEC and RA are represented in degrees.

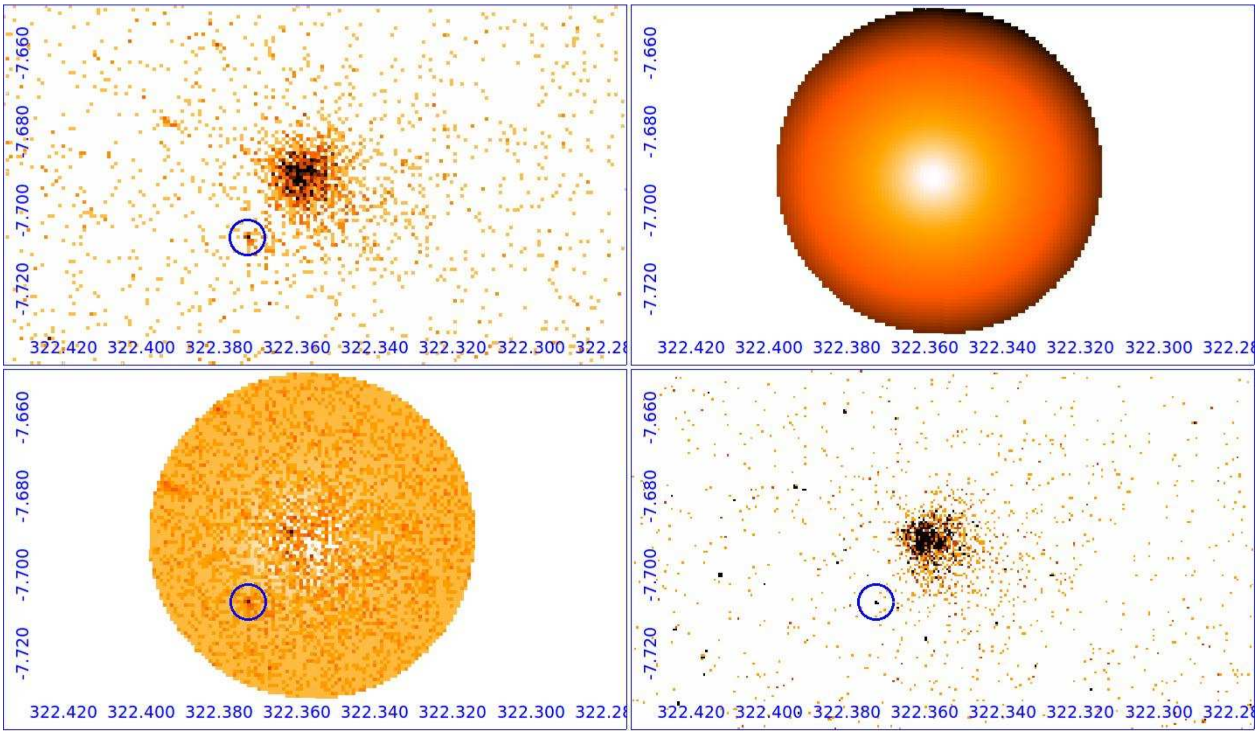

Fig. 5: β-model applied to the MOS-1 camera image of MACS J2129-0741. Top-left image: original image; top-right: β-model; botton-left: residuals; bottom-right: *Chandra* image (ObsID. 3199). The circles in the top-right and bottom-left images have a 2.5' radius. Note the point-like source located near the group (blue circle) that is much better seen after subtracting the β-model.

Only one spectrum of PDCS014S was extracted from a circular region of 60" (0.4 Mpc) from the MOS-1 camera, because the cluster was in the gap in the MOS-2 and pn cameras. An intrinsic luminosity estimation of logL(0.5-8.0 keV) = 43.76 was obtained. We did not find any bibliography in the literature for this source.

The other two clusters were well fitted with the MEKAL model. To obtain a better S/N, we fitted the spectra from the MOS1, MOS2 and pn cameras simultaneously in both cases.

The spectra of MACS J0717.5+3745 were obtained from a circular region of 1.9' (0.7 Mpc) radius, containing all the emission from the center of the cluster seen in the X-ray image. The spectral fitting was done with $N_{Gal} = 7.03 \times 10^{20}$ cm^{-2} and z = 0.5458. The best fit parameters are summarized in Table 4 and the spectra are shown in Figure 7. Stott et al. (2007) and Ebeling et al. (2007) studied *Chandra* data and obtained luminosities of logL(0.1-2.4 keV) = 45.44 and logL(0.1-2.4 keV) = 45.39 $^{+}_{-}$ 0.01 erg s^{-1}, respectively, and Ebeling et al. (2007) calculated

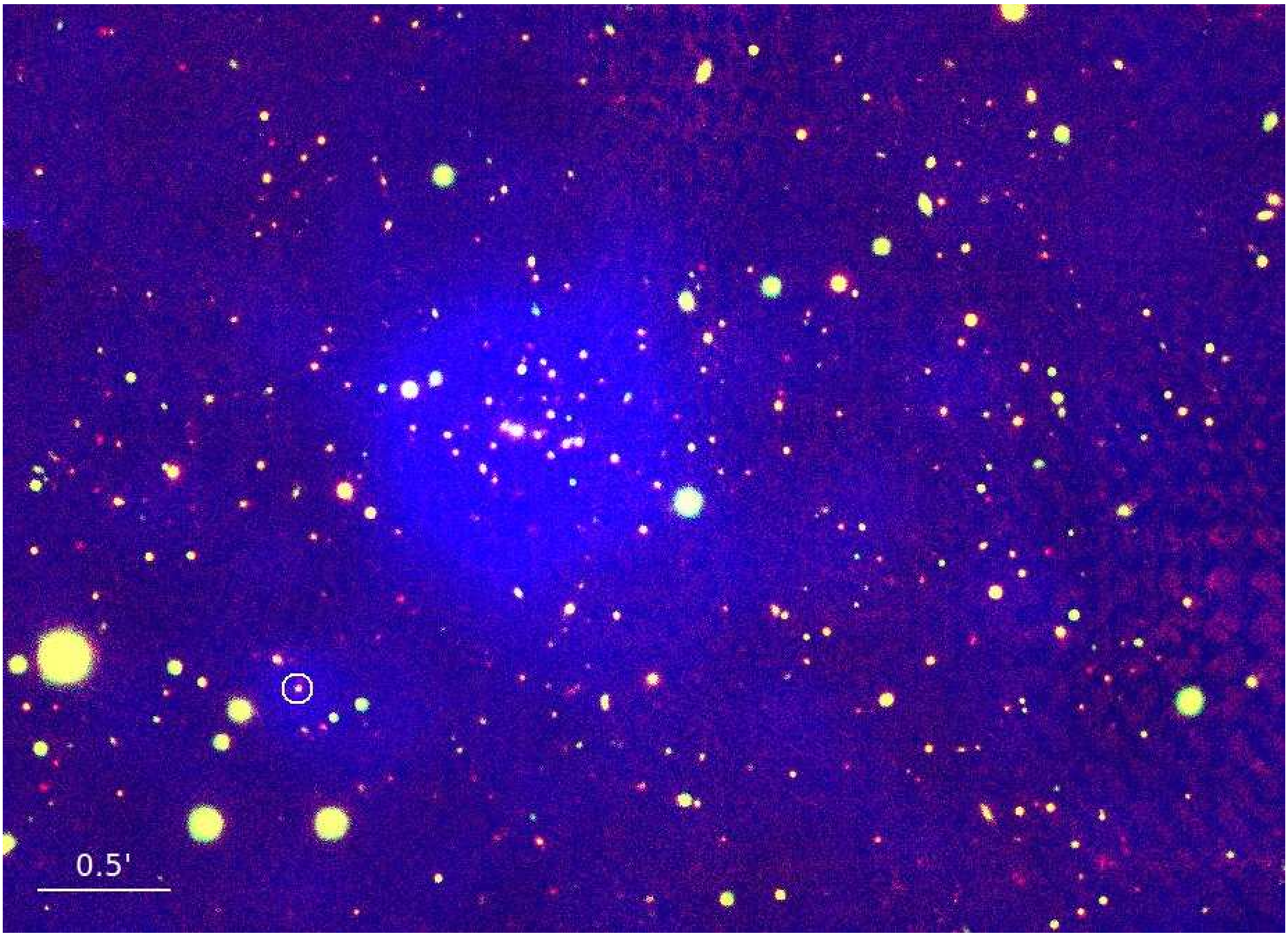

Fig. 6: Color image of MACS J2129.4-0741, combining the optical filters z (red) and r (green) from the *SOAR* telescope, and the *XMM*–Newton 0.3–8 keV (blue). The white circle contains the optical counterpart of the residual point-like source found after applying the β-model.

a temperature of kT = 11.6 ± 0.5 keV. These results agree well with the parameters obtained from our spectral fit.

The spectra of MACS J2129.4-0741 were obtained from a circular region of 1’ (0.4 Mpc). The spectral fitting was done with $N_{Gal} = 4.99 \times 10^{20}$ cm^{-2} and z = 0.5889. The best fit parameters are summarized in Table 4 and the spectra are shown in Figure 8. Stott et al. (2007) and Ebeling et al. (2007) studied *Chandra* data and obtained luminosities of logL(0.1-2.4 keV) = 45.21 and logL(0.1-2.4 keV) = 45.20 ± 0.02 erg s^{-1}, respectively, where Ebeling et al. (2007) obtained a temperature of kT = 8.1 ± 0.7 keV. These results agree well with ours.

2.3.3. Identification of AGN and spectral fitting

Here we present the results of the analysis of the point-like sources found around the 13 clusters listed in Table 1 for which the images where bright enough for our purposes (three of these clusters, namely CL J1604+4314, PDCS 014S, and RX J0848.8+4455, were not taken into account due to their faintness).

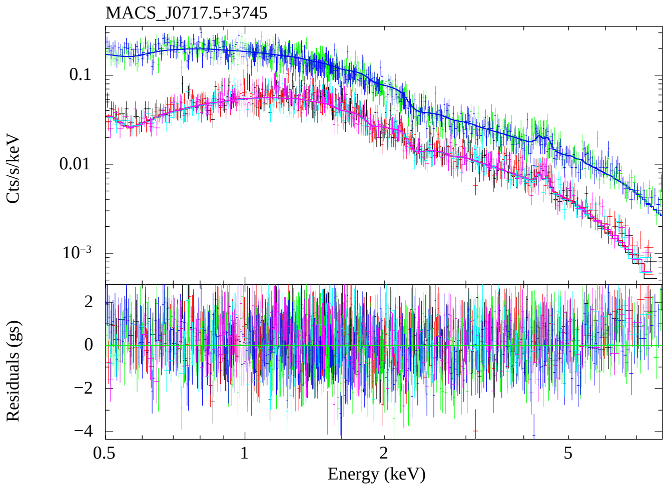

Fig. 7: Spectral fitting of MACS J0717.5+3745 using the MEKAL model, for the three cameras in two dates, and residuals in the bottom. Top: spectra from pn camera. Bottom: spectra from MOS cameras.

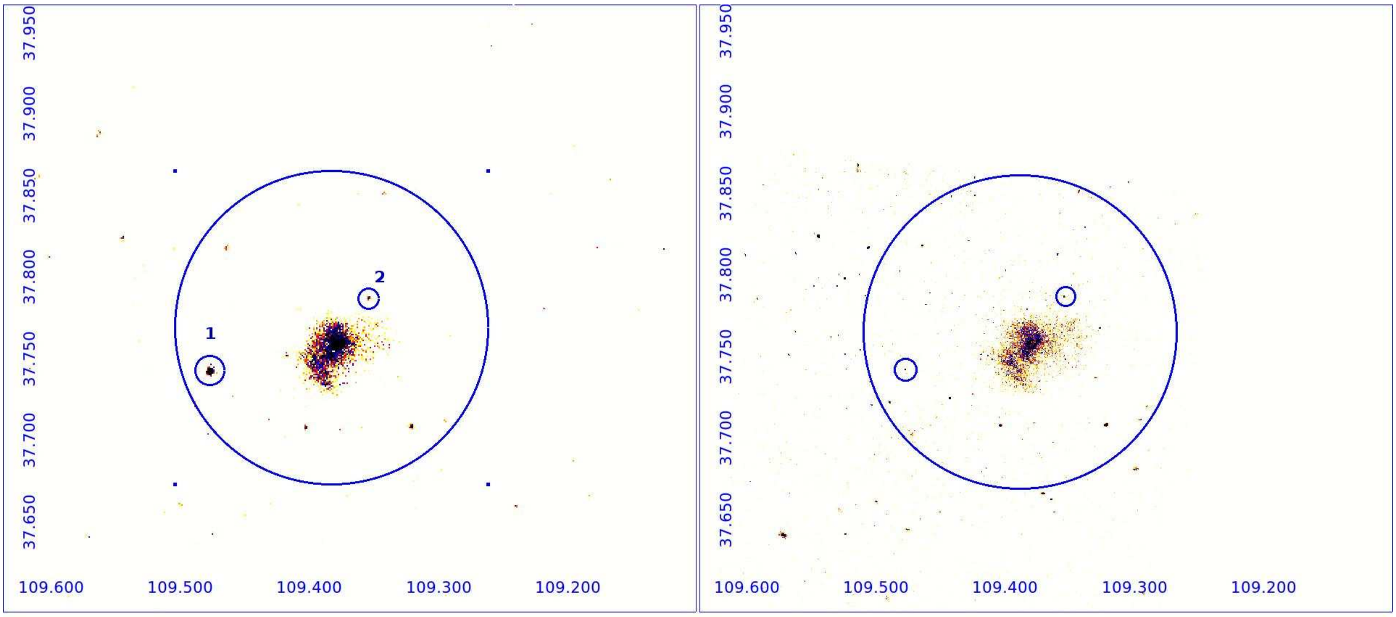

Fig. 9: Point-like sources (small circles) within a 2 Mpc radius (big circles) centered in MACS J0717.5+3745. Left: *XMM*-Newton MOS-1 camera image. Right: *Chandra* image.

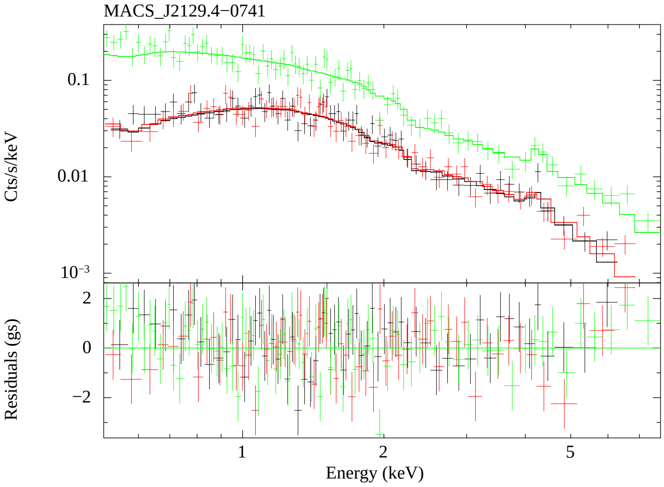

Fig. 8: Spectral fitting of MACS J2129.4-0741 using the MEKAL model, with the residuals in the bottom panel. Top: spectrum from pn camera. Bottom: spectra from MOS cameras.

The number of point-like sources found in the 11 galaxy clusters studied by Guennou et al. (2014) are numbered in Col. 4 of Table 3 (see Appendix A in Guennou et al. 2014 for details). Figures 9 and 10 show the three point like sources found in the clusters we analyse here for the first time, MACS J0717.5+3745 (two) and MACS J2129.4-0741 (one).

The *XMM*-Newton images showed from one to five point-like sources on each cluster. In total 28 point-like sources were found in 13 X-ray cluster images.

We found the redshifts for nine point-like sources, six of them located far from the redshift of the cluster. The remaining 19 point-like sources do not have an associated redshift, so it is not possible to know if they are located in the cluster or along our line of sight.

We made a test to see if we could rule out the possibility that the point-like sources were foreground Galactic objects, as for example XRB. With this purpose we considered the cluster with the Galactic latitude closer to zero, i.e., MACS J0717.5+3745 (see Table 1). Within a 2 Mpc (i.e., 5.76') radius circular region centered on its coordinates, two point-like sources were identified[13], represented with blue circles in Figure 9. Other sources were extended instead of point-like. Sources 1 (RA=+07 17 54.6, DEC=+37 44 33) and 2 (RA=+07 17 24.9, DEC=+37 47 15) were extracted from *XMM*-Newton data from circular regions of 10" and 8" apertures, respectively. The spectra are shown in Figure 11, where they were extracted from the three cameras onboard *XMM*-Newton for source number 1 and from two cameras (MOS-1 and MOS-2) for source number 2 (in the pn camera the source is in the gap). Both sources were well fitted by a non-absorbed power law, source 1 with $\Gamma = 1.58$ [1.55-1.61] and $\chi^2_r = 1.33$ and source 2 with $\Gamma = 1.52$ [1.47-1.58] and $\chi^2_r = 1.35$. We first computed the luminosities assuming that sources 1 and 2 belong to the cluster (z=0.5458), resulting in logL(2-10 keV) = 44.28 and 44.16. These values are compatible with being high luminosity AGN (Peterson 1997). To check the possibility of these objects being Galactic sources, we also computed the luminosities assuming z=0, which gives logL(2-10 keV) = 36.64 and 36.51, respectively. Hence, it cannot be excluded that these objects are close accreting Galactic binaries, with luminosities ~ 10^{35}-10^{38} $erg\ s^{-1}$ (Fabbiano 1989). Thus, both options are plausible. Since the purpose of this work is to study AGN in galaxy clusters, it is a must to measure the redshift of the point-like sources in order to perform a reliable spectral fit. For this reason we decided to consider only the spectra of point-like sources with a measured redshift.

The three point-like sources with a measured redshift within that of the corresponding cluster were located in two clusters, CL J0152.7-1357 (two, Fig. 12) and MACS J0647.7+7015 (one, Fig. 15). Thus the spectral fitting was performed for these point-like sources. The apertures for the extraction were selected de-

---

[13] Visually confirmed by four members of our team.

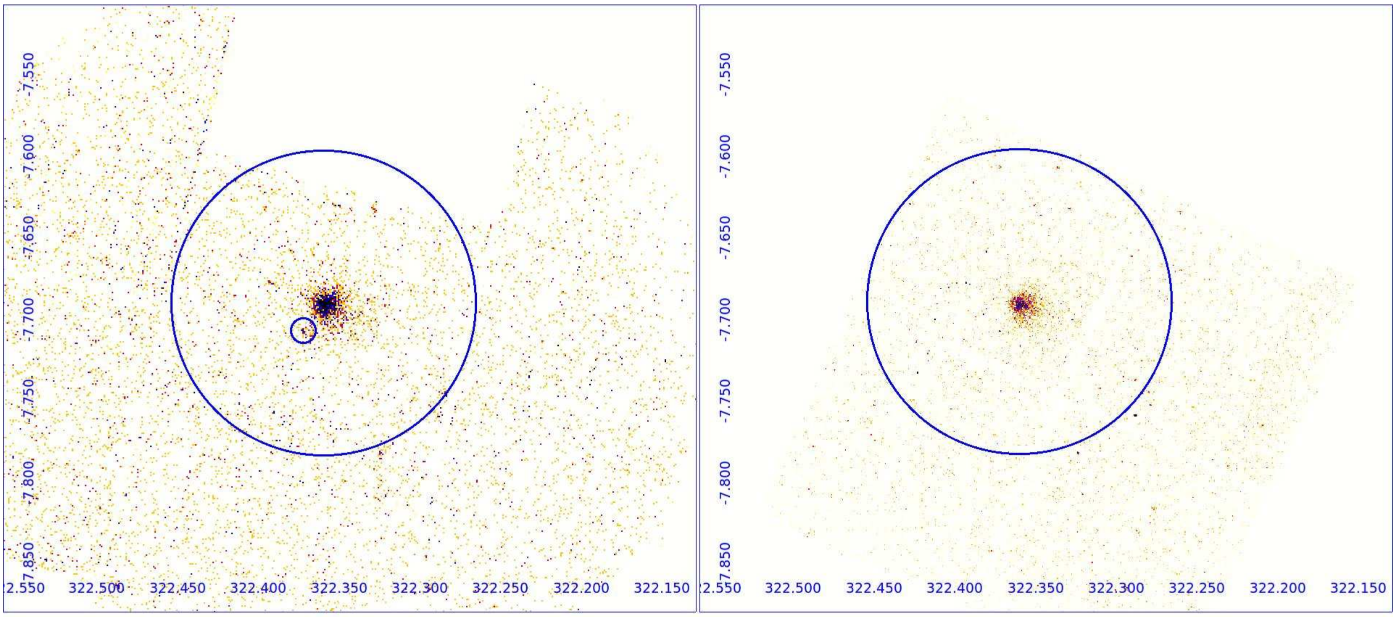

Fig. 10: Point-like source (small circle) within a 2 Mpc radius (big circles) centered in MACS J2129-0741. Left: *XMM*-Newton MOS-1 camera image. Right: *Chandra* image, where no point-like sources can be appreciated.

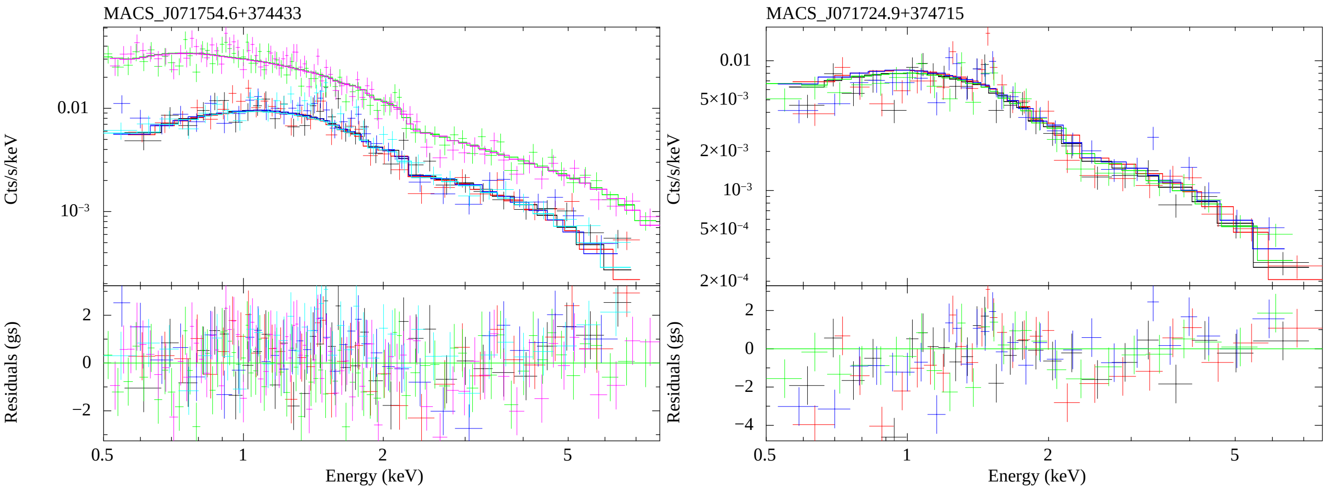

Fig. 11: Spectral fitting for the two point-like sources in MACS J0717.5+3745. Left: source number 1 extracted from a circular region of 10” from MOS-1, MOS-2 (down spectra) and pn (up spectra) cameras. Right: source number 2 extracted from circular regions of 8” from MOS-1 and MOS-2 cameras.

pending on the size of the source, from 6” to 10”. Figures 13, 14, 16 and Table 5 summarize the results obtained for these fittings, that were done using an absorbed power law model, that in all cases gave $\Gamma \sim 1.8$ and luminosities of the order of 10^{44} erg/s. Both spectral shapes and luminosities are compatible with these point-like sources being AGN.

The two point-like sources found in CL J0152.7-1357 were already reported as AGN in Demarco et al. (2005). From *Chandra* data they found luminosities L(2-10 keV) = 1.28×10^{44} erg/s and 1.96×10^{44} erg/s when fitting a power law model. These values are higher than ours, probably due to the difference in the slope of the power law, and the different instruments used for the analysis. In both AGN they found a broad MgII (λ2798) emission line, characteristic of AGN.

No reference is found in the literature for the point-like source detected in MACS J0647.7+7015, thus its AGN nature cannot be confirmed.

3. AGN in galaxy groups

3.1. The sample and the data

The sample was selected from the ten galaxy groups in Lagana et al. 2014 (in prep.). From the ten groups, we found X-ray data in the *Chandra* archives for nine of them (excluding RXCJ2315-0222). *Chandra* data were used to search for evidence of AGN in the group. We assess that there is an AGN when a point-like source is detected in the 4.5-8.0 keV energy band. Six groups did not show such point-like sources in *Chandra* images (NGC 1132, RBS 461, NGC 4104, NGC 4325, A 1991, and

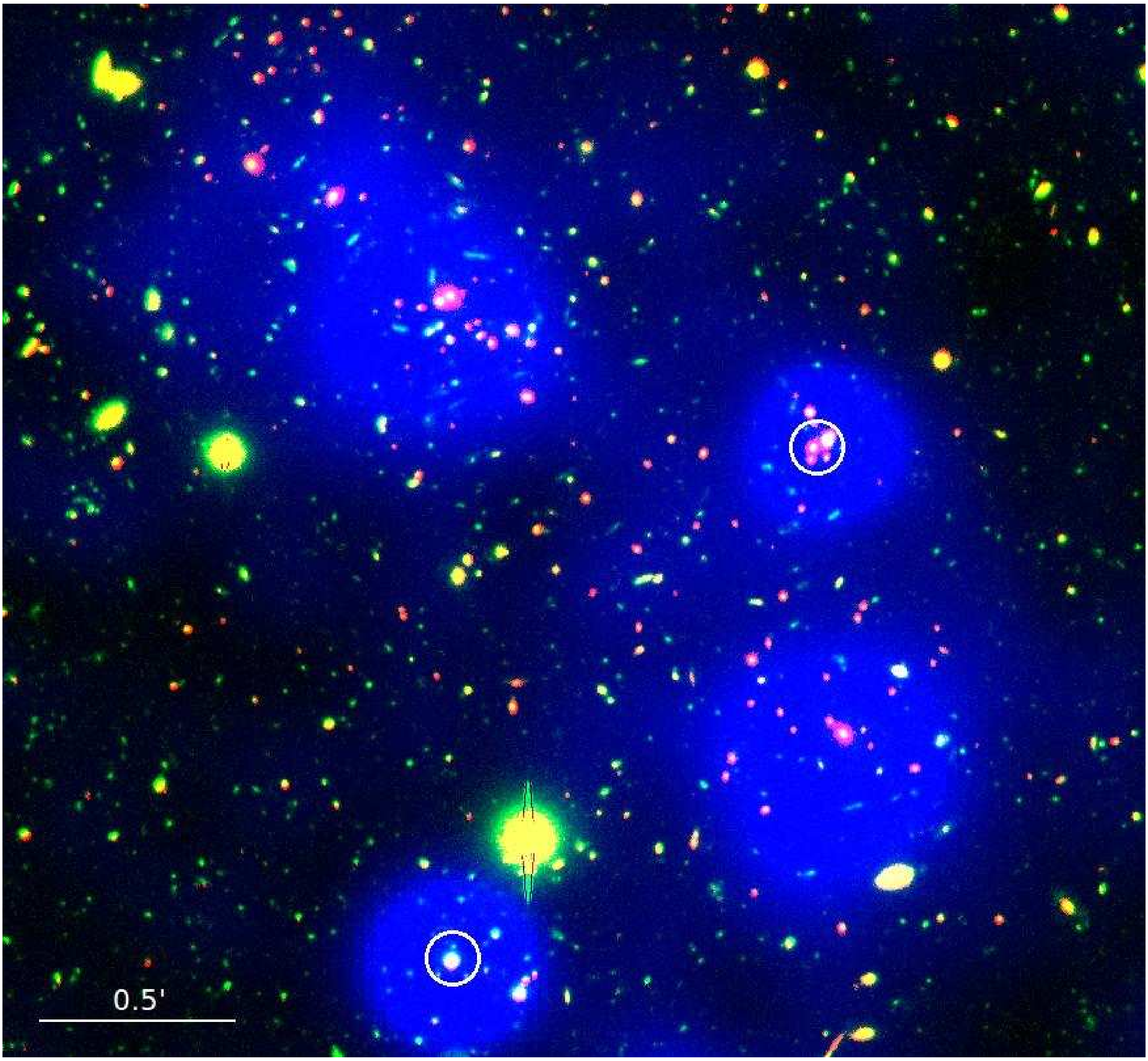

Fig. 12: Color image of CL J0152.7-1357, combining the optical filters z (red) and v (green) from *Subaru* telescope, and the *XMM*–Newton 0.3–8 keV (blue). The white circles represent the analysed AGN. North is up and East is to the left.

IC 1262), while the remaining three did (UGC 842, NGC 5098, and AWM4). The properties of the galaxies studied in this work are listed in Table 6.

3.2. Methodology

The methodology is focused on the spectral analysis (e.g., the β-model will not be applied to the images because one galaxy per group is studied and the group emission is not strong), and was made following prescriptions given in Hernández-García et al. (2013). We review the method below.

3.2.1. Chandra data

Chandra observations were obtained with the ACIS instrument (Garmire et al. 2003). The data reduction and analysis were made in a systematic, uniform way using CXC Chandra Interactive Analysis of Observations (CIAO[14]), version 4.3. Level 2 event data were extracted by using the task ACIS-PROCESS-EVENTS. We firstly cleaned the data from background flares using the LC_CLEAN.SL[15] task, that removes periods of anomalously-low (or high) count rates from light curves, from source-free background regions of the CCD. This routine calculates a mean rate from which it deduces a minimum and maximum valid count rate, and

---

[14] http://cxc.harvard.edu/ciao4.4/

[15] http://cxc.harvard.edu/ciao/ahelp/lc_clean. html

Table 5: Spectral fittings of the AGN in clusters.

AR (1)	DEC (2)	z (3)	N_H* (4)	Γ (5)	χ^2_r (6)	L_{soft}* (7)	L_{hard}* (8)
CL J0152.7-1357		0.831	0.0132				
01 52 43.7	-13 59 02	0.8201	-	$1.65^{1.72}_{1.58}$	1.42	1.00	1.97
01 52 39.9	-13 57 42	0.8672	-	$1.42^{1.45}_{1.30}$	1.35	1.30	3.61
MACS J0647.7+7015		0.591	0.0544				
06 47 38.1	70 15 27	0.6914	$0.07^{0.20}_{0}$	$1.56^{1.68}_{1.45}$	1.26	2.01	4.55

*N_H in units of $10^{22} cm^{-2}$, and luminosities in 10^{44} erg s^{-1}.

Table 6: Properties of the groups.

Name (1)	RA (2)	DEC (3)	z (4)	Gal. Lat. (5)
UGC 482	32.4617	-6.2375	0.0395	-54.42
NGC 5098	200.0675	33.1442	0.0379	+81.34
AWM4	241.2375	23.9206	0.0318	+46.49

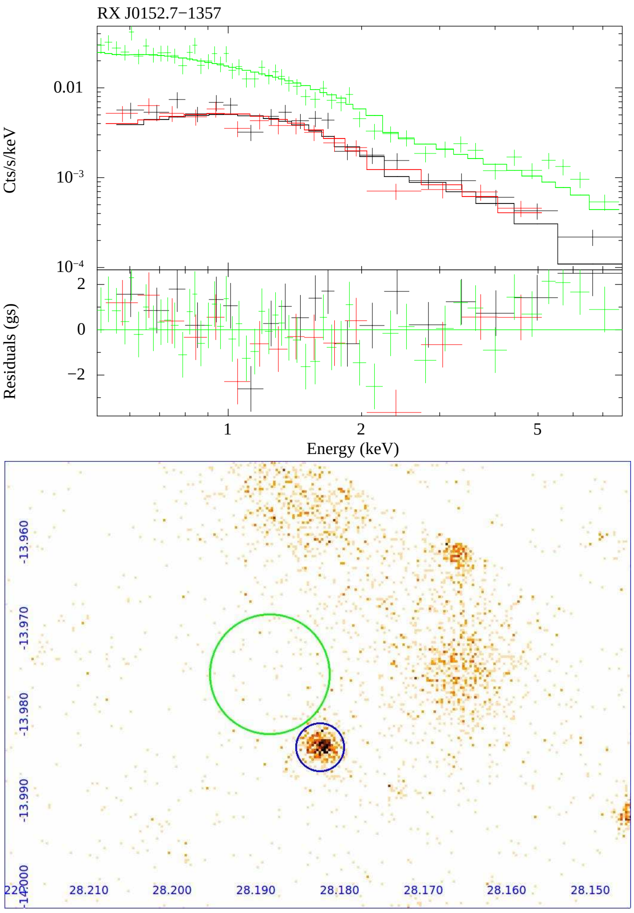

Fig. 13: Image (up) and spectrum (bottom) of one of the AGN (below in Fig. 12) from ObsID. 0109540101 of CL J0152.7-1357 (10” aperture, small blue circle). The big green circle is the background region.

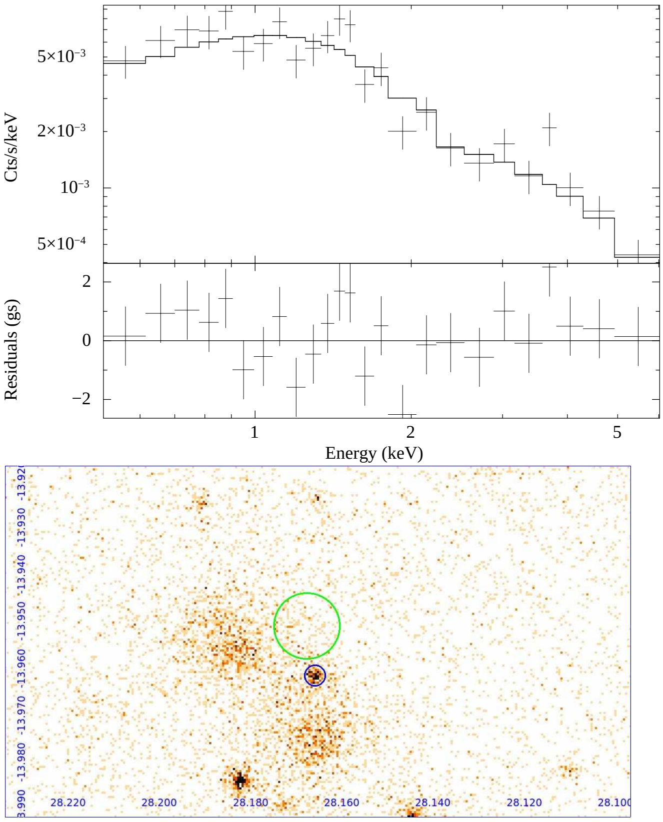

Fig. 14: Image (up) and spectrum (bottom) of one of the AGN (above in Fig. 12) from ObsID. 0109540101 of CL J0152.7-1357 (8” aperture, big blue circle). Only data from MOS2 camera was available, because the source appeared in the gap in the other cameras. The big green circle is the extracted region that accounts for the background.

creates a file with those periods which are considered to be good by the algorithm.

To extract the spectra, we used an algorithm that searches for the position of the nuclear source, by selecting the closest X-ray source to the nuclear coordinates. Nuclear spectra were extracted from 2-3” radius circular regions centered at the center of the group, trying to get all the possible photons, but not including other sources or background effects. The background selection was made taking regions free of sources, in the same chip as the target, and close to the source, to minimize effects related to the spatial variations of the CCD response.

The DMEXTRACT task was used to extract the spectra of the source and background regions. The response matrix file (RMF) and ancillary reference file (ARF) were generated for each source region using the MKACISRMF and MKWARF tasks, respectively. Before the background subtraction, the spectra were binned to have a minimum of 20 counts per spectral bin, so we are able to use the χ^2-statistics. This was made by using the GRPPHA task included in FTOOLS.

3.2.2. XMM-Newton data

The extraction of *XMM*–Newton spectra was done following prescriptions given in Sect. 2.2.2. Nuclear spectra were extracted from 20-30” radius circular regions centered at the center of the group.

3.2.3. Spectral fit

All the galaxy groups studied in Lagana et al. (2014) are located at redshifts below z <0.06, and therefore larger count rates of AGN than those found in the galaxy clusters (studied in Sect. 2) are expected. For this reason we will use single and also composite models to fit the spectra and select the one that better represent them. The spectral fitting was made using XSPEC version 12.7.0. To guarantee a proper spectral fit, only observations with at least 400 number counts will be fitted. Following the prescriptions in González-Martín et al. (2009) for the spectral fittings, six different models were used, where only VME model has been added:

1. ME: A pure thermal model (MEKAL in XSPEC). The thermal emission is responsible for the bulk of the X-ray energy distribution. The free parameters in this model are the column density, N_H, the temperature, kT, and the normalization, *Norm*.
2. VME: A MEKAL model where the abundances can vary. The free parameters in this model are the column density, N_H, the temperature, kT, the abundances and the normalization, *Norm*.
3. PL: A single power law model, which corresponds to a nonthermal source representing an AGN. The column density, N_H, is added as a free parameter, to take the absorption by matter between our galaxy and the target nucleus into account. The free parameters in this model are the column density, N_H, the slope of the power-law, Γ, and the normalization, *Norm*.
4. 2PL: A model containing two power laws with the same slope, Γ. Here the bulk of the hard X-rays is due to a primary continuum described by a power law and the soft X-rays come from a scattering component described by the other power law. The free parameters in this model are the column densities, N_{H1} and N_{H2}, the slope of the power-law, Γ, and the normalizations, $Norm_1$ and $Norm_2$.
5. MEPL: A composite of a thermal plus a single power law model. The AGN dominates the hard X-rays, but the soft X-rays require an additional thermal contribution. The free parameters in this model are the column densities, N_{H1} and N_{H2}, the temperature, kT, the slope of the power-law, Γ, and the normalizations, $Norm_1$ and $Norm_2$.

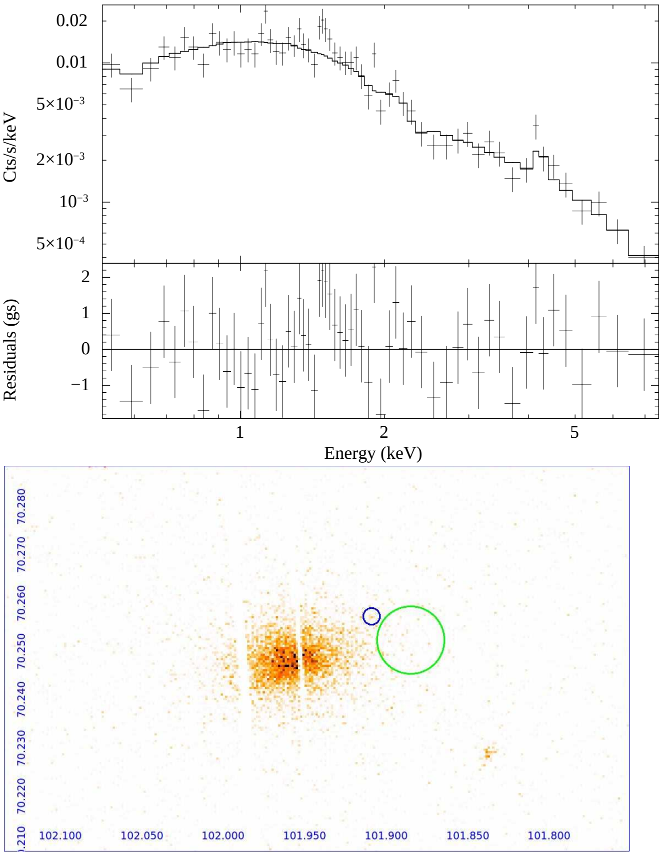

Fig. 16: Image (up) and spectrum (bottom) of our detected AGN from ObsID. 0551850401 of MACS J0647.7+7015 (6” aperture, blue circle). Only data from MOS2 camera were available, because the source appeared in the gap in the other cameras. The big green circle is the region selected for background.

6. ME2PL: A composite of a thermal plus two power laws model. This model is like MEPL but including the contribution of the thermal emission at soft X-rays. The free parameters in this model are the column densities, N_{H1} and N_{H2}, the temperature, kT, the slope of the power-law, Γ, and the normalizations, $Norm_1$ and $Norm_2$.

For models 2PL, MEPL and ME2PL we used two absorbers, N_{H1} and N_{H2}. These absorbers are included in the models as abs(N_{H1})*PL + abs(N_{H2})*PL, abs(N_{H1})*Mekal + abs(N_{H2})*PL, and abs(N_{H1})*(PL) + Mekal + abs(N_{H2})*PL. In the case of the VME model, all the abundances were left free to vary, freezing each abundance when the value was compatible with zero. Moreover, Galactic absorption has been fixed to the predicted value using the NH tool in FTOOLS (Dickey & Lockman 1990; Kalberla et al. 2005). We searched for the presence of the neutral iron fluorescence emission line, $FeK\alpha$, adding a narrow Gaussian with centroid energy fixed at the observed energy corresponding to a rest frame at 6.4 keV. Two Gaussian lines were also included to model recombination lines, FeXXV at 6.7 keV and FeXXVI at 6.95 keV. These are typical lines found in AGN.

3.3. Results

The results are discussed individually for each point-like source in the following.

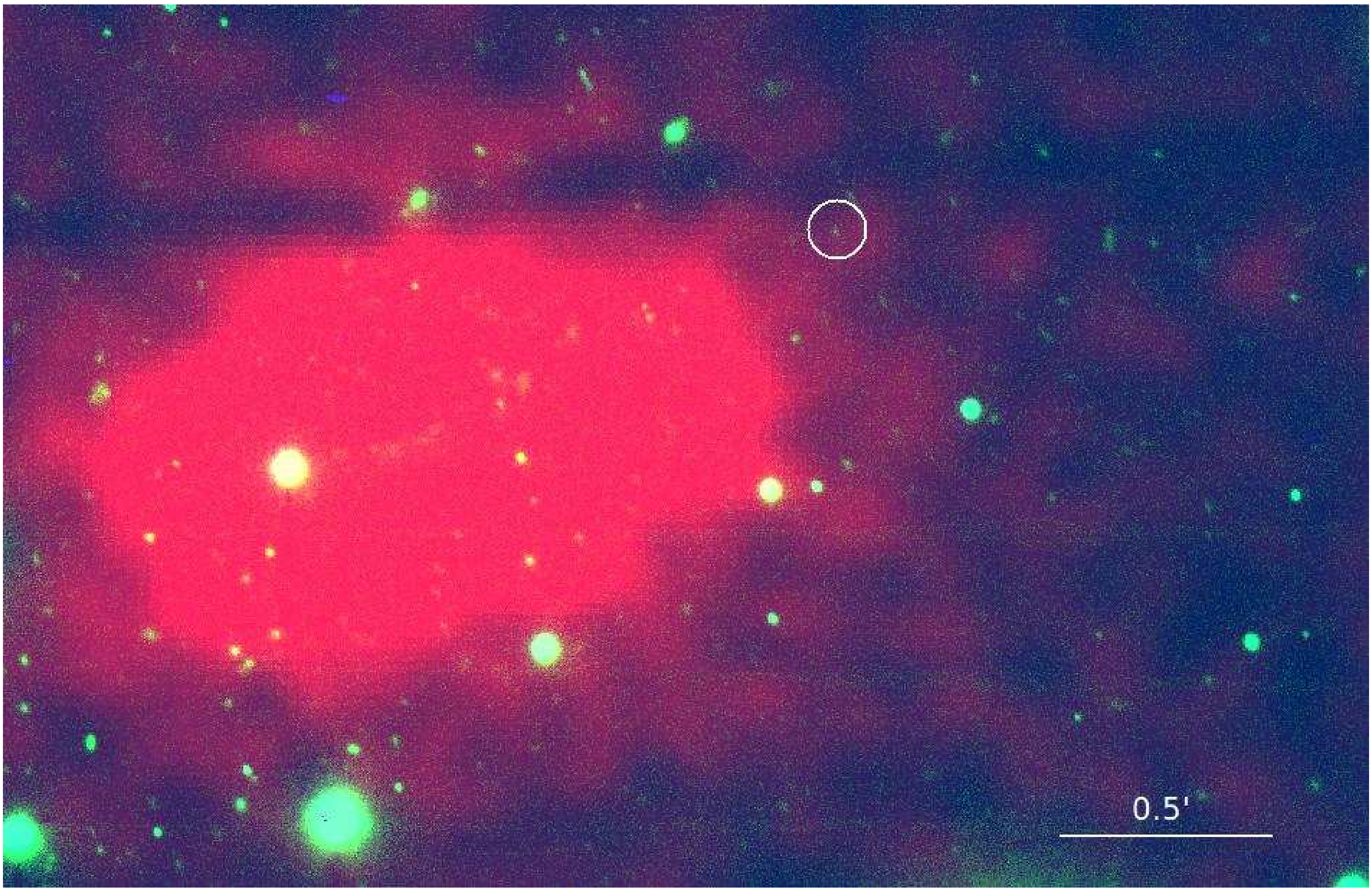

Fig. 15: Color image of MACS J0647.7+7015, combining the optical filters b (green) and v (blue) from the *WYIN* telescope, and the *XMM*–Newton 0.3–8 keV (red). The white circle represents the position of the analysed AGN.

Fig. 17: Left: *Chandra* image of UGC 842, where a point-like source can be appreciated in the 4.5-8.0 keV band. Right: Color optical image in the g and r filters of the UGC 842 group with the *CFHT* telescope. The red rectangle represents the location of the X-ray source (not to scale).

3.3.1. UGC 482

UGC 842 (z=0.045) is a bright elliptical galaxy and the group is in an extended halo with a radius of 4’ (~300 kpc) in the sky. Voevodkin et al. (2008) studied the *XMM*-Newton data and extracted the spectra of the group from a 130” radius aperture. They fitted a thermal model and obtained kT = 1.90 $\pm$ 0.30 keV, Z = 0.34 $\pm$ 0.12 $Z_\odot$ and L(0.1-20.0 keV) = 1.63 $\pm$ 0.05 $\times 10^{43} erg\ s^{-1}$. UGC 842 was classified as a BL Lac object by Brinkmann et al. (2000) using *ROSAT* data, who made a spectral analysis and obtained Γ = 1.88 [1.37-2.63].

We use one *Chandra* observation (ObsID. 4963) from 2005 with 39.8 ksec exposure time, and one *XMM*-Newton observation (ObsID. 0153170101) from 2003 with 22.2 ksec exposure time. Figure 17 (top) shows the point-like source present in the center of the group (an optical image is provided in the bottom). The results of the spectral fit are listed in Table 7.

The *Chandra* spectrum was extracted from a circular region of 3” aperture radius. This source has 212 total count number, not enough to make a proper spectral fitting. Therefore, we could not use *Chandra* data.

The *XMM*-Newton spectrum was extracted from a 20” radius circular region (Fig. 18). The spectrum has 1084 counts in the total energy band (0.5-10 keV). The best fit model is a composite of a thermal plus two power laws and two absorbers, with kT = 1.61 [1.35-2.04] keV, Γ = 2.05 [1.69-2.64] and logL(2-10 keV) = 42.04 [42.02-42.07]. In order to improve the fit (see residuals in Fig. 18), we changed the ME component for the VME, but it resulted in a similar fit (χ_r^2 = 1.40).

3.3.2. NGC 5098

NGC 5098 is located in the RGH 80 group (z=0.037). Xue et al. (2004) studied the group from the *XMM*-Newton observation from 2003 and fitted the spectrum with a two-temperature model with temperatures of kT = 0.82 and 1.51 keV and Galactic absorption, finding that the group is relatively gas rich and luminous.

Kollatschny et al. (2008) classified NGC 5098 as a low ionisation nuclear emission line region (LINER) and using *ROSAT* data found an X-ray luminosity of logL(0.1-2.4 keV) = 42.51. This galaxy has a companion which is classified as non-active and is not visible in X-rays. We have marked this galaxy with a red cross in Fig. 19 (up), and both galaxies can be seen at optical frequencies (bottom).

Randall et al. (2009) studied the *Chandra* observation from 2005 and found that NGC 5098 shows evidence for both AGN heating and gas sloshing. They extracted the spectra of the AGN with a 1.8” radius aperture, and fitted a PL model, obtaining a spectral index of Γ = 1.93 $^+_-$ 0.16 and a luminosity of $L(0.6-7keV) = 1.4 \times 10^{41} erg\ s^{-1}$.

We use one *Chandra* observation in 2005 (ObsID. 6941, 39.1 ksec), and one *XMM*-Newton observation (ObsID. 0105860101) in 2003 of 33.6 ksec of exposure time. The results of the spectral fit are listed in Table 7.

The *Chandra* spectrum was extracted from a 2” radius circular region from ObsID. 6941 (see Fig. 20 to the left). The spectrum has 404 counts, enough for a reliable spectral fitting. The best representation of the data is a combination of a mekal plus a power law model, with kT = 0.76 [0.58-0.96] keV, Γ = 1.76 [1.45-2.03] and logL(2-10 keV) = 41.74 [41.68-41.81].

The *XMM*-Newton spectrum was extracted from a 30” radius circular region centered on the source (see Fig. 20 to the right). The spectrum has 10388 counts. The best fit model resulted in a composite of a thermal plus two power laws model with two absorbers (ME2PL), with kT = 0.87 [0.86-0.88] keV, Γ = 2.27 [2.22-2.40] and logL(2-10 keV) = 41.82 [41.80-41.85].

Fig. 20 shows the *Chandra* (left) and *XMM*–Newton (right) spectra for this source.

Our results agree well with those from Randall et al. (2009). The discrepancy between the luminosity obtained by Kollatschny et al. (2008) and ours is most probably due to the different instruments and energy bands used for the analysis.

3.3.3. AWM4

AWM4 (z = 0.0317) is a poor cluster with extended and regular X-ray emission, dominated by NGC 6051 (Gastaldello et al. 2008), which is a giant galaxy of a type known as a “Cluster Dominant Elliptical". Gastaldello et al. (2008) found a bolometric luminosity of logL(0.1-100 keV) = 43.59 $^+_-$ 0.01 and a temperature of kT = 2.48 $^+_-$ 0.06 keV for the group. O’Sullivan et al. (2010) used *Chandra* and Giant Metrewave Radio Telescope data to study the interaction between the intracluster medium and the central radio source in the relaxed group AWM4. In the *Chandra* observation a small cool core or giant corona was resolved coincident with the radio core. They found emission up to 3 keV, and they suggested that the poor emission above this energy might be related to an AGN or low mass X-ray binaries (LMBX).

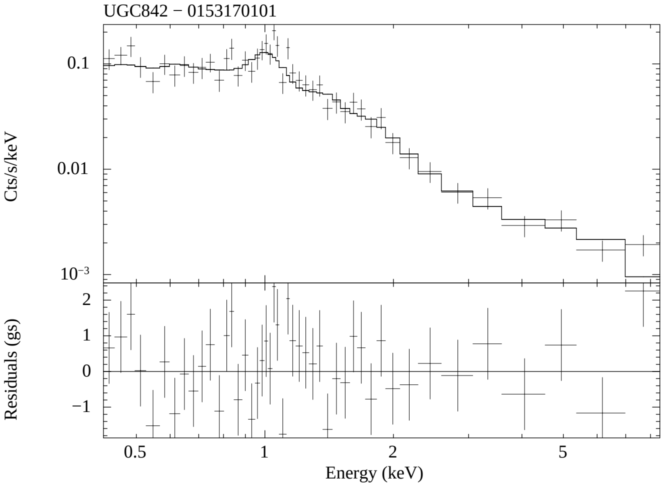

Fig. 18: The *XMM*-Newton spectrum of UGC 842. The residuals are shown in the bottom panel.

We use one *Chandra* observation from 2008 (ObsID. 9423) of 75.5 ksec exposure time, and one *XMM*-Newton observation from 2003 (ObsID. 0093060401) of 29.1 ksec exposure time. The results of the spectral fit are listed in Table 7.

The *Chandra* spectrum was extracted from a 3” radius circular region. The spectrum has 276 counts, not enough for a proper spectral fitting. Therefore we cannot use this data.

The *XMM*-Newton spectrum was extracted from a 30” radius circular region (Fig. 22). The number of counts in the total band is 6303. The best fit resulted in a pure thermal model (MEKAL), with kT = 2.73 [2.62-2.83] keV and logL(2-10 keV) = 42.27 [42.26-42.28]. The He-like iron (Fe XXV) emission line at 6.7 keV typical in galaxy clusters (e.g., Molnar et al. 2006) is present, so this means that the contribution of the group is present in the spectrum. We made a spectral extraction with a smaller aperture radius, and the presence of this line remained. We exclude the possibility of this line being the $FeK\alpha$ at 6.4 keV observed in AGN since the source is better fitted with thermal models, in contrast with the power law expected from AGN.

Thus, since the best fit model in the *XMM*–Newton spectrum is related with thermal emission and we do not find a PL component, we cannot confirm the existence of an AGN in AWM4. If there is an AGN it is contaminated by emission from the group, as can be seen in *XMM*–Newton data due to the presence of the emission line at 6.7 keV.

3.3.4. General results of galaxy groups

We have studied three point-like sources, one per galaxy group. Two of them were classified as AGN (namely UGC 842 and

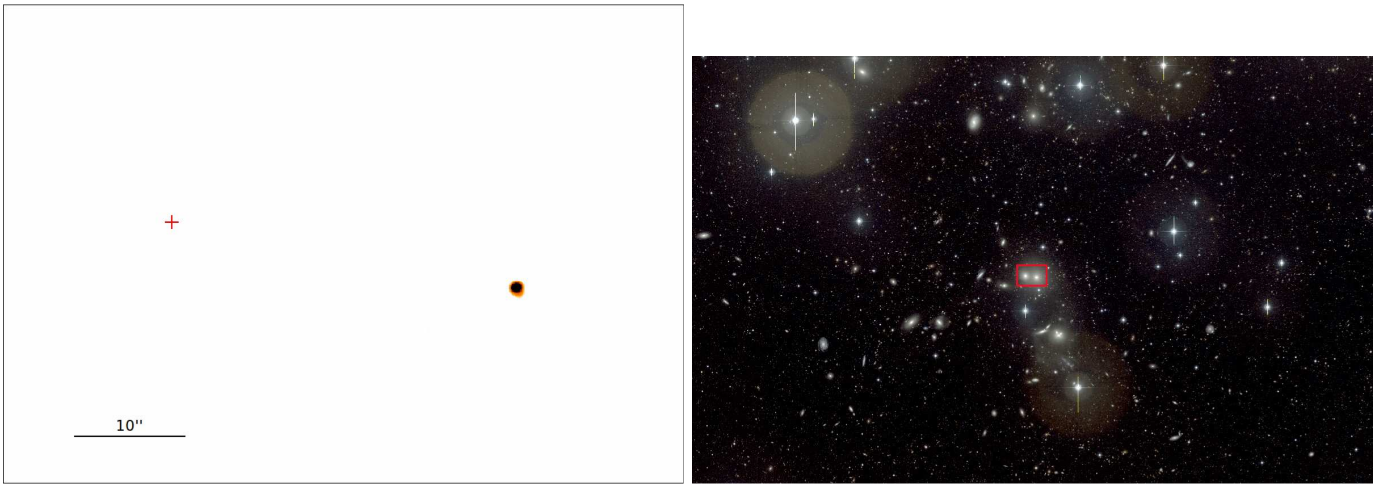

Fig. 19: Left: The *Chandra* image of NGC 5098, where a point-like source can be appreciated in the 4.5-8.0 keV band. The red cross corresponds to the companion galaxy that can be observed at optical wavelengths. Right: Color optical image in the g and r filters of the NGC5098 group with the *CFHT* telescope. The red rectangle represents the location of the X-ray source (not to scale).

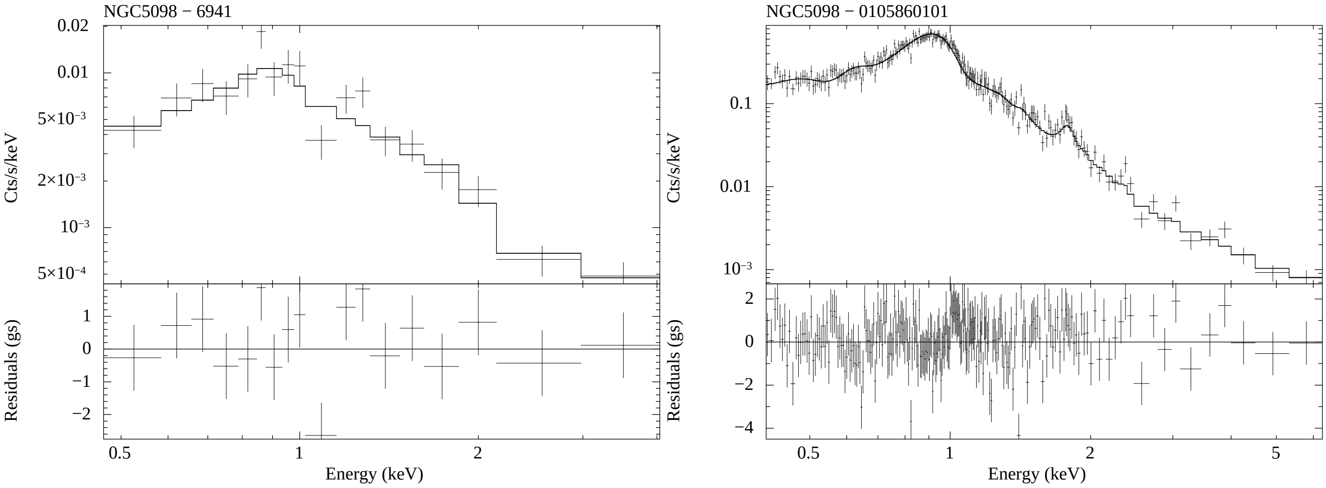

Fig. 20: Left: *Chandra* spectrum of NGC 5098. Right: *XMM*-Newton spectrum of NGC 5098. The residuals are shown in the bottom panels.

Fig. 21: Left: *Chandra* image of AWM4, where a point-like source can be appreciated in the 4.5-8.0 keV energy band. Right: Color optical image in the g and r filters of the NGC5098 group with the *CFHT* telescope. The red rectangle represents the location of the X-ray source (not to scale).

Table 7: Spectral fit models for the point-like sources in the groups.

Name (1)	Instrument (2)	Best fit (3)	N_{H1} $(10^{22} cm^{-2})$ (4)	N_{H2} $(10^{22} cm^{-2})$ (5)	kT keV (6)	Γ (7)	$\chi^2/d.o.f$ (8)	logL (2-10 keV) (9)
UGC 842	*XMM*	ME2PL	$0.04^{0.15}_{0.00}$	$46.48^{60.74}_{9.70}$	$1.61^{2.04}_{1.35}$	$2.05^{2.64}_{1.69}$	1.33	$42.04^{42.07}_{42.02}$
NGC 5098	*Chandra*	MEPL			$0.76^{0.96}_{0.58}$	$1.76^{2.03}_{1.45}$	1.49	$41.74^{41.81}_{41.68}$
	XMM	ME2PL	$0.36^{0.44}_{0.22}$	$18.68^{63.93}_{5.56}$	$0.87^{0.88}_{0.86}$	$2.27^{2.40}_{2.22}$	1.21	$41.82^{41.85}_{41.80}$
AWM4	*XMM*	MEKAL	$0.0^{0.01}_{0.0}$		$2.73^{2.83}_{2.62}$		0.98	$42.27^{42.28}_{42.26}$

NGC 5098), and we confirm their classifications in this work, since a PL component is needed to fit their spectra. We can not confirm the AGN nature of AWM4 since a thermal model was needed to fit its spectrum.

4. Preliminary conclusions and future prospects

The $L_x - T$ relation was studied by Takey et al. (2013) for a sample of ∼ 500 clusters and groups. They found the following relation:

$$log(h(z)^{-1}L) = 44.39 + 2.80 log\Big(\frac{kT}{5}\Big) \tag{2}$$

where $h(z) = [\Omega_M(1+z) + \Omega_\Lambda]^{1/2}$ is the Hubble constant normalised to its present-day value. We note that they used the luminosity in the 0.1-2.4 keV energy band. However, the emission at hard energies in clusters is not too strong so we can compare whether our estimates agree or not. The X-ray luminosities in the 0.5-8.0 keV energy band corrected for $h(z)$ against the temperatures for the galaxy groups and clusters studied in this work are represented in Fig. 23. From this we confirm that galaxy groups are less luminous and have smaller temperatures than galaxy clusters.

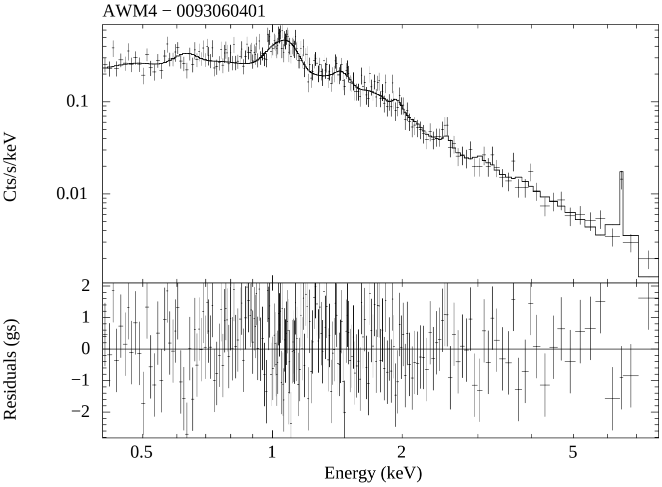

Fig. 22: The *XMM*-Newton spectrum of AWM4. The residuals are shown in the bottom panel.

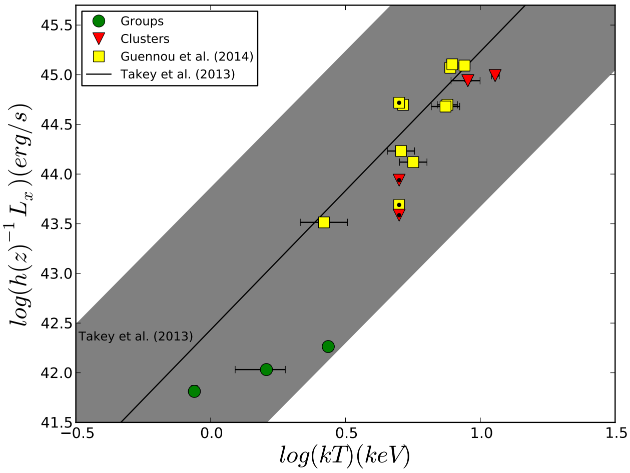

Fig. 23: X-ray luminosity in the 0.5-8.0 keV energy band corrected for h(z) against the temperatures. Galaxy groups (green circles) and clusters (red triangles) studied in this work and clusters studied in Guennou et al. (2014) (yellow squares) are presented. Points with a black dot in the center are clusters where the spectral fit was done using a MEKAL model with a fixed kT= 5 keV. The solid line is the relation given by Takey et al. (2013), while the grey area is the range of values in their sample.

From Fig. 23, we find that the X-ray luminosities and temperatures of galaxy clusters in Guennou et al. (2014) and ours agree well. We note that the temperature of one of the clusters analysed in this work (namely MACS J0717.5+3745) is higher than the rest of the clusters. Note however that our estimation of the spectral parameters is compatible with those obtained from previous works (Ebeling et al. 2007). In the same plot, the relation from Takey et al. (2013) is represented as a solid line, while the range of values presented in their work can be seen as a grey area. We find that the estimations for the galaxy clusters agree well with the relation given by Takey et al. (2013). However, the groups seems to have an excess in the temperature or the luminosity estimations. We plotted a grey area representing the range of values obtained by Takey et al. (2013), where the values obtained for the galaxy groups in our sample fit. We notice that this relation is used only to check whether our results agree with previous works and that it is out of the score of this work. Moreover, we note that the comparison between galaxy groups and clusters must be taken with caution for the following reasons: 1) galaxy groups are located at smaller redshifts (z<0.1) than clusters (z>0.4) in our sample, thus evolutionary effects that we did not take into account are probably playing a role, and 2) groups have smaller masses than clusters, and therefore they are more sensitive to non-gravitational effects such shocks, AGN or supernovae explosions.

This is an exploratory work with the main purpose of searching for AGN candidates in galaxy groups and clusters. We found three AGN out of the nine groups with X-ray data in the sample of Lagana et al. (2014). These AGN candidates were located in the center of the group, and other sources were not observed.

In the case of galaxy clusters, we found a total of 28 point-like sources in 13 clusters of the DAFT/FADA sample (from the joint analysis in Guennou et al. (2014) and in this work). Among them, 19 sources do not have a measured redshift. Based in the luminosities of the point like sources, we cannot discard the possibility of these objects being located out of the cluster, and therefore we conclude that the measure of the redshift is a must in this kind of studies. Moreover, we have identified from one to five point-like sources on each cluster, meaning that our sample is scarce and needs to be completed for a proper characterization of AGN in galaxy clusters. Thus, in order to make this kind of study, a large sample of galaxy clusters with observations at optical and X-ray wavelengths is required. This would allow the selection of AGN candidates at X-ray frequencies, and the measure of redshifts at optical frequencies.

The DAFT/FADA collaboration will allow to measure the redshifts of those 19 point-like sources, once all the optical/near infrared data for calculating photometric redshifts is available. Furthermore, the DAFT/FADA sample will contain ~ 90 clusters, so this sample should be explored in order to complete this preliminary study. From this study it should be possible to characterize AGN around galaxy clusters, and answer questions as: are they brighter or fainter than the average? how does the denser environment at the clusters outskirts affect AGN evolution?

Acknowledgements. This work has been possible thanks to Florence Durret, who has supervised my short stay at the Institut d'Astrophysique de Paris (IAP) funded by MINECO (grant EEBB-I-13-07483). We thank Gastao B. Lima Neto for helping with X–ray data, Nicolas Martinet for providing optical images and redshift catalogs of the galaxy clusters, Loic Guennou for assistance with the β-model, and Christophe Adami, Isabel Márquez, Josefa Masegosa, and Omaira González-Martín for helpful comments during this work.

References

Bechtold, J., Forman, W., Jones, C., et al. 1983, ApJ, 265, 26
Brinkmann, W., Laurent-Muehleisen, S. A., Voges, W., et al. 2000, A&A, 356, 445
Cavaliere, A. G., Gursky, H., & Tucker, W. H. 1971, Nature, 231, 437
Demarco, R., Rosati, P., Lidman, C., et al. 2005, A&A, 432, 381
Dickey, J. M. & Lockman, F. J. 1990, ARA&A, 28, 215
Ebeling, H., Barrett, E., Donovan, D., et al. 2007, ApJ, 661, L33
Fabbiano, G. 1989, ARA&A, 27, 87
Garmire, G. P., Bautz, M. W., Ford, P. G., Nousek, J. A., & Ricker, J. G. R. 2003, in Society of Photo-Optical Instrumentation Engineers (SPIE) Conference Series, Vol. 4851, Society of Photo-Optical Instrumentation Engineers (SPIE) Conference Series, ed. J. E. Truemper & H. D. Tananbaum, 28–44
Gastaldello, F., Buote, D. A., Brighenti, F., & Mathews, W. G. 2008, ApJ, 673, L17
Gilmour, R., Best, P., & Almaini, O. 2009, MNRAS, 392, 1509
González-Martín, O., Masegosa, J., Márquez, I., Guainazzi, M., & Jiménez-Bailón, E. 2009, A&A, 506, 1107
Guennou, L., Adami, C., Durret, F., et al. 2014, A&A, 561, A112
Henry, J. P. & Briel, U. G. 1991, A&A, 246, L14
Hernández-García, L., González-Martín, O., Márquez, I., & Masegosa, J. 2013, A&A, 556, A47
Kalberla, P. M. W., Burton, W. B., Hartmann, D., et al. 2005, A&A, 440, 775
Kocevski, D. D., Lubin, L. M., Gal, R., et al. 2009, ApJ, 690, 295
Kollatschny, W., Kotulla, R., Pietsch, W., Bischoff, K., & Zetzl, M. 2008, A&A, 484, 897
Kravtsov, A. V. & Borgani, S. 2012, ARA&A, 50, 353
Molnar, S. M., Birkinshaw, M., & Mushotzky, R. F. 2006, ApJ, 643, L73
O'Sullivan, E., Giacintucci, S., David, L. P., Vrtilek, J. M., & Raychaudhury, S. 2010, MNRAS, 407, 321
Peterson, B. M. 1997, An Introduction to Active Galactic Nuclei, ed. Peterson, B. M.
Randall, S. W., Jones, C., Markevitch, M., et al. 2009, ApJ, 700, 1404
Stott, J. P., Smail, I., Edge, A. C., et al. 2007, ApJ, 661, 95
Takey, A., Schwope, A., & Lamer, G. 2013, A&A, 558, A75
Voevodkin, A., Miller, C. J., Borozdin, K., et al. 2008, ApJ, 684, 204
Xue, Y.-J., Böhringer, H., & Matsushita, K. 2004, A&A, 420, 833
Zwicky, F. 1937, ApJ, 86, 217

6

Variability in ultraluminous X-ray sources

Among the variety of sources emitting at X-rays, ultraluminous X-ray sources (ULXs) are of special interest for this work, because they emit luminosities in the same range than LINERs. Nevertheless, it is well established that different emission mechanisms, i.e., different models, must be used for the spectral fits (Sutton et al. 2013). In this chapter we study the X-ray variability of ULXs using Fourier techniques. On one hand, we can obtain information about the way in which variations occur in ULXs. It is worth noting that short-term variations are observed in the ULXs studied here, and part of this chapter is devoted to those variations. Notice that the approach to search for variability, based on the determination of time delays between two energy bands, is different from that performed for LLAGN.

This work was carried out during a MINECO Ph.D short-stay (two months) at the University of Leicester (UK) in 2014, under the supervision of Dr. Vaughan. The paper presented in this chapter is nearly ready to be submitted to Monthly Notices of the Royal Astronomical Society.

Mon. Not. R. Astron. Soc. **000**, 1–**??** (2015) Printed 10 June 2015 (MN LaTeX style file v2.2)

X-ray time lags and nonlinear variability in the ultraluminous X-ray sources NGC 5408 X-1 and NGC 6946 X-1

Hernández-García, L.[1]*, Vaughan, S.[2], Roberts, T.P.[3] and Middleton, M.[4]
[1] *Instituto de Astrofísica de Andalucía, CSIC, Glorieta de la Astronomía, s/n, 18008 Granada, Spain*
[2] *X-ray & Observational Astronomy Group, Department of Physics and Astronomy, University of Leicester, Leicester LE1 7RH, UK*
[3] *Department of Physics, Durham University, South Road, Durham DH1 3LE, UK*
[4] *Institute of Astronomy, Madingley Rd, Cambridge, CB3 0HA, UK*

Draft:10 June 2015

ABSTRACT
We present our analysis of the X-ray variability of two Ultraluminous X-ray Sources (ULXs) based on multiple *XMM*–Newton observations. We show the linear rms-flux relation is present in eight observations of NGC 5408 X-1 and also in NGC 6946 X-1, but data from other ULXs is generally not sufficient to constrain any rms-flux relation. This relation was previously reported in ULXs only in two observations of NGC 5408 X-1; our results show this is a persistent property of the variability of NGC 5408 X-1 and extends to at least one other variable ULX. We speculate this is a ubiquitous property of ULXs variability, as it is for X-ray variability in other luminous accreting sources. We also recover the time delay between hard and soft bands in NGC 5408 X-1, with the soft band (<1 keV) delayed with respect to the hard band (>1 keV) by up to ~10 s (~0.2 rad) at frequencies above ~few mHz. For the first time, we extend the lag analysis to lower frequencies and find some evidence for a reversal of the lag, a hard lag of ~1 ks at frequencies of ~0.1 mHz. Our energy-resolved analysis shows the time delays may be concentrated around the 0.6–1 keV region. We argue that the lag is unlikely to be a result of reflection from an accretion disc ('reverberation') based on the lack of reflection features in the spectra, and the large size of the reflector inferred from the magnitude of the lag. We also argue that associating the soft lag with a Quasi-Periodic Oscillation (QPO) in these ULXs – and drawing an analogy between soft lags in ULXs and soft lags seen in some low-frequency QPOs of Galactic X-ray binaries – is premature.

Key words: X-rays: general – X-rays: individual: NGC 5408 X-1 – X-rays: individual: NGC 6946 X-1

1 INTRODUCTION

In recent years substantial progress has been made in understanding the nature of ultraluminous X-ray sources (ULXs). These objects are X-ray sources located within, but displaced from the nucleus of, nearby galaxies, that display observed X-ray luminosities in excess of 10^{39} erg s^{-1} (see Feng & Soria 2011, for the most recent review). In particular, there is strong evidence for three relatively nearby ULXs containing stellar-mass black holes ($M_{\rm BH} \sim 10 M_{\odot}$), and so accreting at super-Eddington rates (Middleton et al. 2013; Liu et al. 2013; Motch et al. 2014). The last of these objects is particularly important as it directly links super-Eddington emission to the peculiar X-ray spectrum displayed by many bright ULXs (see e.g., Stobbart et al. 2006; Bachetti et al. 2013), and so supports the notion of some ULXs accreting in a new, super-Eddington *ultraluminous state* (Gladstone et al. 2009; Sutton et al. 2013). The physics of this state are only just emerging, but it appears that the variety of X-ray spectra and the coarse variability properties of individual objects may be consistent with a model in which massive, radiatively-driven winds are launched from a geometrically thick accretion disc, bloated by the advection of its hot inner regions towards the black hole, and a combination of the collimation of the X-radiation emerging from the innermost regions of the accretion flow by the optically thick wind and the viewing angle of the observer dictates what is seen (Poutanen et al. 2007; King 2009; Sutton et al. 2013; Middleton et al. 2015). However, this may not explain all ULXs, which we now are certain to be a heterogeneous population after the discovery of pulsations from a luminous ULX in M 82, demonstrating that it hosts a neutron star (Bachetti et al. 2014). Additionally, there is evidence that at least some of the brightest ULXs may still harbour the long-sought intermediate-mass black holes ($M_{\rm BH} \sim 100 - 10000 M_{\odot}$, e.g. Farrell et al. 2009; Sutton et al. 2012; Mezcua et al. 2015). So, much work still remains to be done to understand both the composition and the accretion physics of the ULX population.

X-ray variability can be a powerful tool for investigating lu-

---

* E-mail: lorena@iaa.es

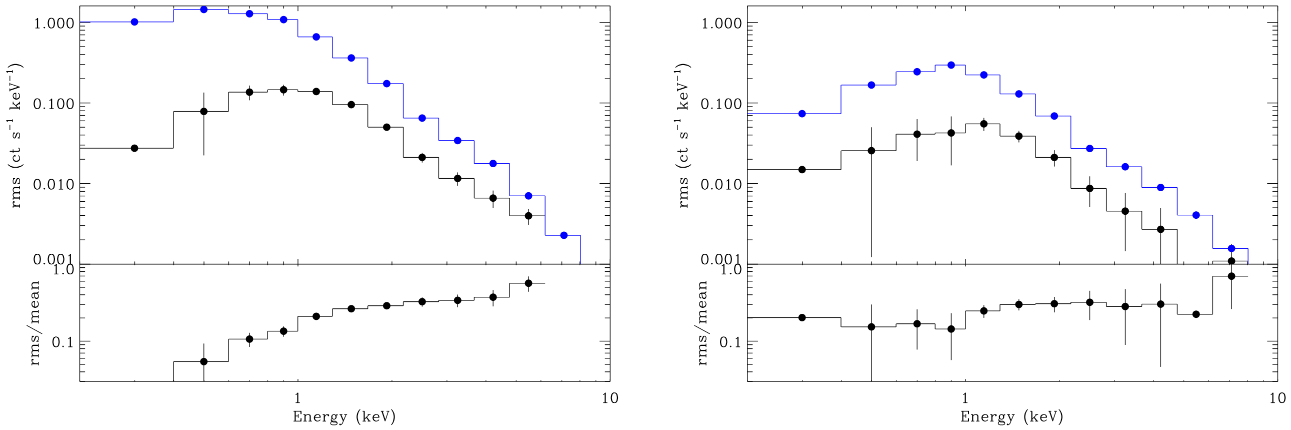

Figure 1. rms spectrum (black) and mean spectrum (blue) of (left): NGC 5408 X-1 using the 2010 and 2011 observations, and (right): NGC 6946 X-1 using the 2007 and 2012 observations. The lower panels show the raton between the rms and the mean spectrum. We used segments of constant length of 10.4 s respecting the “good” time interval list, and segments of 10 ksec duration for the estimation of the rms.

minous, accreting black-hole binaries (BHB, Remillard & McClintock 2006) or active galactic nuclei (AGN, Vaughan et al. 2003b). The study of X-ray variability has been made for a few ULXs using different approaches, from changes in their light curves (Sutton et al. 2013), the study of quasi-periodic oscillations (QPO, e.g., Dheeraj & Strohmayer 2012; Caballero-García et al. 2013), the rms-flux relation or time delays between different energy bands (Heil et al. 2009; De Marco et al. 2013b). However, the study of variability in ULXs is hampered by their relatively low count rates, and usually requires long exposures in order to recover the statistical properties of the ULXs variability. For example, the rms-flux relation or time lags have to date been detected in only one ULX, NGC 5408 X-1. Heil & Vaughan (2010) first showed that this source follows the rms-flux relation from two *XMM*–Newton observations. This property of the X-ray variability seems to be ubiquitous among Galactic black hole X-ray binaries (XRB) and also AGN (Uttley & McHardy 2001; Uttley et al. 2005; Heil et al. 2012). The discovery in NGC 5408 X-1 demonstrates a strong connection between at least this ULXs and the better-understood accreting black hole systems in XRBs and AGN. Heil & Vaughan (2010) also studied time delays between the soft and hard X-ray energy bands in NGC 5408 X-1 and found a soft lag, i.e., variations in the soft photons lag those in hard photons at mHz frequencies also in NGC 5408 X-1. This result was later confirmed by De Marco et al. (2013b), who studied six *XMM*–Newton observations to study the QPO and the soft time lag.

Here we revisit the *XMM*–Newton observations of ULXs, concentrating on NGC 5408 X-1 and NGC 6946 X-1. Our focus is on the frequency dependent time lags (extending to lower frequencies than previously published) and confirming and extending the one published example of the rms-flux relation in a ULX. This paper is organised as follows: in Sect. 2 we describe the data used for the analysis and the data reduction, in Sect. 3 we present the rms-flux relation for the two ULX, and in Sect. 4 the cross-spectrum analysis and the results of the coherence, time and phase delay, and the phase lag spectrum. Finally, the results derived from this study are discussed in Sect. 5.

Table 1. Observational details.

Object	ObsID	Date	T^a (ksec)	T^b (ksec)
NGC 5408 X-1	0302900101	2006-01-13	130	99
	0500750101	2008-01-13	113	47
	0653380201	2010-07-17	104	60
	0653380301	2010-07-19	128	111
	0653380401	2011-01-26	119	90
	0653380501	2011-01-28	124	95
	0723130301	2014-02-11	35	34
	0723130401	2014-02-13	33	32
NGC 6946 X-1	0500730201	2007-11-02	28	25
	0500730101	2007-11-08	33	31
	0691570101	2012-10-21	114	99

^{a} Exposure time before the flares correction.
^{b} Duration after the flares correction (see text).

2 DATA REDUCTION

In this paper we focus on the multiple *XMM*–Newton observations of NGC 5408 X-1 and NGC 6946 X-1. These are among the brightest and most variable known ULXs and have some of the longest publically available *XMM*–Newton observations. We have in fact performed much of our analysis on all 20 ULXs in the sample discussed by Sutton et al. (2013), but for the other 18 sources the data were not sufficient to obtain meaningful constraints from the time lag and rms-flux analyses. We used *XMM*–Newton archival data up to March 2015. The log of the used observations is given in Table 1.

For these objects we rejected the observations with exposure times shorter than 10 ksec because the analysis was performed using continuous segments of this length in order to reach low frequencies. To obtain a high signal-to-noise ratio (S/N) we combined data from EPIC pn, MOS1, and MOS2 detectors. We forced MOS and pn light curves to have the same TSTART and TSTOP. The event files for the source were extracted from circular regions (aperture

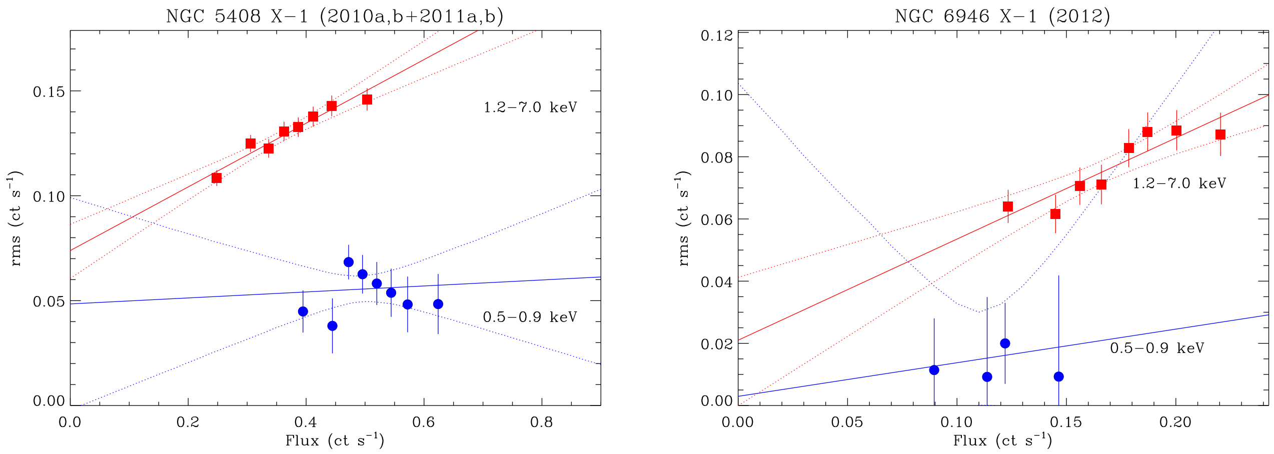

Figure 2. rms-flux relation in the soft (0.5-0.9 keV) and hard (1.2-7 keV) energy bands for (left): the four observations from 2010 and 2011 of NGC 5408 X-1, and (right): the 2012 observation of NGC 6946 X-1. The rms is measured over the 4–50 mHz frequency range from segments of length 150 s (NGC 5408 X-1) and 250 s (NGC 6946 X-1). The dashed lines show the 95% "confidence bands" around the best-fitting linear model.

radius of $40''$ and $25''$ for NGC 5408 X-1 and NGC 6946 X-1[1]) and for the background from rectangular regions using the Science Analysis Software (SAS[2]), version 13.0.0. Standard event patterns (PATTERN $\leqslant 4$ for the pn detector, PATTERN $\leqslant 12$ for the MOS detectors) and filter (FLAG = 0) were used.

The subsequent analysis was carried out using IDL software[3]. The ULXs are relatively weak sources (in some cases < 0.1 ct/s in the 2–10 keV band), and so may be overwhelmed by the background during periods of high and flaring background. Strong background flares may introduce spurious variability and time lags into the data (the spectrum of a background flare evolves with time) if not properly excluded from the data. In order to mitigate against this, we carefully filtered each observation for background flares as follows. A light curve of the background was extracted in the 1-12 keV energy band using 2.6 s bins and smoothed using a 500 s width boxcar filter to improve the S/N. We manually selected a suitable background threshold for each observation, above which data were considered to be affected by background flares, and excluded from further analysis. The background thresholds were in the range 0.028–0.036 ct/s for the NGC 5408 X-1 observations, and in the range 0.010–0.015 ct/s for the NGC 6946 X-1 observations.

Col. 5 in Table 1 shows the total amount of "good" exposure time after these high background periods have been excluded. We notice that the rms-flux analysis (Sect. 3) and the cross spectral analysis (Sect. 4) were each carried out using equal length segments of continuous good data, but the lengths of the segments used for each analysis were different. This is because the rms-flux analysis concentrates on the higher frequency (i.e., shorter timescale) variations (the "red noise" part of the PSD) while for the cross spectrum analysis we are interested in the variability properties to lower frequencies (i.e., longer timescales). Requiring fixed length segments of uninterrupted good time means some small intervals of good time were not used; the amount of "good" data used for each analysis is therefore slightly different (lower) for each observation than the "good" duration given in Table 1.

Finally, we obtained an rms spectrum (defined as the square root of the normalised excess variance; see Vaughan et al. 2003b, for details) of the source (see Fig. 1), and checked at which energies variability is found in order to select the energy bands. The spectral analysis performed by Middleton et al. (2011) showed the need of two spectral components to fit the spectrum of NGC 5408 X-1, which are separated at ~ 1 keV. Therefore, we will take 1 keV as the separation point for the energy band selection. From this analysis we selected the soft and hard energy bands as 0.5–0.9 keV and 1.2–7.0 keV as these were the bands where the strongest variations were found.

3 RMS-FLUX RELATION

In this section we describe our analysis of the rms-flux relation in these two ULXs. The analysis follows closely the analysis of Heil & Vaughan (2010) and we refer the interested reader to this paper (and that of Heil et al. 2011) for specific details. Briefly, we divided each observation into continuous 150 s and 250 s segments of "good" data, for NGC 5408 X-1 and NGC 6946 X-1, and from each segment computed a periodogram and the mean count rate. The periodograms were then averaged in eight groups according to the mean count rate, and the rms estimated from each. The rms is the square root of the Poisson noise-subtracted variance, itself computed by integrating the average periodograms over the $\sim$ 4–50 mHz range. The analysis was performed for a soft and a hard band. Linear models of the form $\sigma = k(\langle F \rangle - C)$, where F is the flux and k (i.e., $d\sigma/d\langle F \rangle$) and C are constants, were fitted to the rms-flux data using weighted least squares (min χ^2). We also estimated the 95% "confidence bands" around the best-fitting linear model. We randomly generated 500 models, each one from the distribution of parameters (specified by the best-fit values and covariance matrix), and extracted the 2.5% and 97.5% y values at each x value, and within these we estimated the 95% confidence band.

Heil & Vaughan (2010) demonstrated a positive, linear rms-flux relation for the harder band data during the 2006 and 2008 observations of NGC 5408 X-1. Appendix A shows the rms-flux relations for the 2010, 2011 and 2014 observations (the best fitting linear model parameters were consistent between the two 2010 observations, between the two 2011 observations, and between the two

---

[1] PN data of obsID 0200670301 and 0200670401 were extracted from elliptical regions to avoid the gaps of the detector.

[2] http://xmm.esac.esa.int/sas/

[3] Available from http://www.star.le.ac.uk/sav2/idl.html

2014 observations, and so the closely spaced pairs of observations were combined). In agreement with the results for 2006 and 2008 obtained by Heil & Vaughan (2010), the 2010, 2011 and 2014 observations also show the rms-flux relation in the harder band data, that are well fitted by a linear model (p > 0.05 in all cases), although the parameters are slightly different between the three years. These detections (in the sense that the gradient k > 0) are significant at the 4.8σ, 7.8σ and 6.6σ levels, respectively. We notice that the gradients and intercepts between the 2010 and 2011 observations are consistent within the 2σ level, so we have combined the four observations. Fig. 2 (left) shows the rms-flux relation for these observations of NGC 5408 X-1, whose detection is significant at the 7.2σ level in the hard energy band.

The soft band appears significantly different (see left panel in Fig. 2, and Appendix A); the gradient *k* is much smaller. The gradient *k* gives the fractional rms after subtracting any constant flux or rms components; the much lower gradient in the soft band indicates that, even after removing any constant component, the fractional amplitude of the variability is greatly suppressed. A linear model fits well the data (p > 0.05), although all the detections are below the 3σ level, so the rms-flux relation cannot be confirmed in the soft energy band of NGC 5408 X-1.

We also show the rms-flux relation for NGC 6946 X-1 for the first time (Fig. 2, right panel for the 2012 observation). Data from 2007 were used together because the linear fit was consistent between the observations (see Appendix A), and the 2012 data was treated separately. The rms-flux relation is clearly detected in the hard band at the 4.5σ and 4.4σ level for the 2007 and 2012 data, respectively. In the soft band the detections are below 3σ, although again we obtain p > 0.05 in every fit.

Therefore, the rms-flux relation is clearly detected in the hard energy band of both ULXs, but we cannot claim this relation for the soft energy band in any of the ULXs.

4 CROSS-SPECTRUM

Here we report our cross-spectrum analysis, which was made following standard procedures (see e.g., Nowak et al. 1999). We extracted the background-subtracted source light curves in the soft (0.5-0.9 keV) and hard (1.2-7.0 keV) energy bands using time bins of 10.4 s (four times the MOS frame time) respecting the “good” time interval list. We used segments of 10 ks duration, and from these we estimated the power spectra (PSD), coherence, phase and time lags in the Fourier frequency domain in the standard way (see e.g., Vaughan & Nowak 1997; Nowak et al. 1999; Vaughan et al. 2003b). The fractional normalisation was adopted and we rebinned over logarithmic frequency bins, each spanning a factor ~1.7 in frequency.

A soft lag in NGC 5408 X-1 was first reported by Heil & Vaughan (2010) from the *XMM*–Newton data from 2006, and later confirmed by De Marco et al. (2013b) using six *XMM*–Newton observations between 2006 and 2011. They combined data from the same year as stationarity was observed. Since the PSDs differ between epochs, as previously noted by De Marco et al. (2013b), we first made the analysis separately for each year, as in Sect. 3. We found that the variability is stronger in 2010 and 2011 (four observations in total) and the phase lag spectra appear consistent, and thus we combined these data in order to obtain a higher S/N. The results of the cross spectrum for NGC 5408 X-1 are shown in Fig. 3, including the coherence, phase, and time lag between the energy bands. The soft lag is detected at the 4.2σ level. In Fig. 3 it can be appreciated that at lower frequencies the sign of the time lag changes and becomes positive. However, we cannot claim a hard lag because this measurement is at the 2.9σ level.

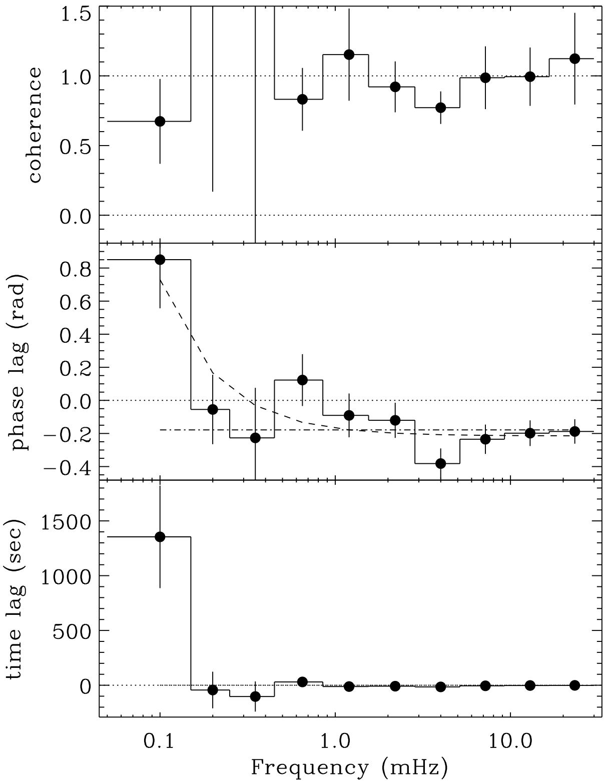

Figure 3. Results of the cross-spectrum analysis between the soft (0.5-0.9 keV) and hard (1.2-7.0 keV) energy bands for NGC 5408 X-1 showing, from upper to lower panels: the coherence; phase-lag; and time lag between the energy bands. The phase lag above ~1 mHz is is significantly negative, at around -0.2, corresponding to a time lag of ~10 s at ~4 mHz. At lower frequencies the lag becomes consistent with zero or even positive lag in the lowest frequency band. Middle panel shows a constant model (dot-dashed line) and a power law plus a constant model (dashed line) we fitted to the phase lag (see text).

Although a similar time lag behaviour is observed in NGC 6946 X-1 (see Appendix B), the S/N of the data is not enough to confirm the lags, whose detections are significant at the 2.3σ (soft lag) and 1.3σ (hard lag) level at high and low frequencies, respectively.

We fitted two different models to the phase lag (see middle panels in Fig. 3 and Appendix B). The first one is a constant model (dot-dashed line), and the second one consists on a power law plus a constant (dashed line) as phase lag $\Delta\phi = Af^{-\alpha} + B$, where A and B are constants. The second model fits both sources better, with $A = 0.05 \pm 0.07$, $B = -0.21 \pm 0.04$, $\alpha = 1.3 \pm 0.7$, $\chi^2/d.o.f = 9.2/7$ and $p = 0.24$ for NGC 5408 X-1, and $A = 0.7 \pm 0.7$, $B = -0.6 \pm 0.6$, $\alpha = 0.4 \pm 0.4$, $\chi^2/d.o.f = 1.9/7$, and $p = 0.97$ for NGC 6946 X-1. With this model the hard lag at low frequencies has a $\Delta\phi \propto f^{-1}$ dependence at low frequencies, and a constant phase soft lag of -

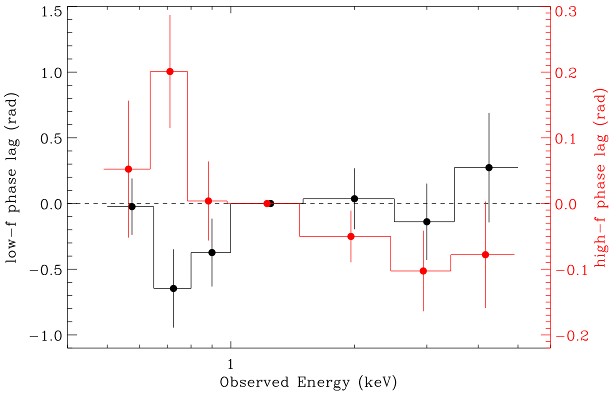

Figure 4. Phase lag spectrum of NGC 5408 X-1 at low (black; 0.1–0.3 mHz) and high (red; 1–20 mHz) frequencies. These show the average lag between a given band and the 1–1.5 keV reference band. The high frequency lag-energy spectrum decreases with energy, indicating the phase lag becomes more negative for widely separated energy bands. The y-axis are different for low (left) and high (right) frequencies.

0.2 rad at high frequencies. Therefore the phase lag is not constant with frequency, nor is the time lag.

For NGC 5408 X-1 we also computed the phase lag vs. energy spectrum from the cross-spectra, averaging over the frequency bands, i.e., plotting the phase lag vs. energy. Fig. 4 shows the phase lag spectrum from the 2010 and 2011 observations of NGC 5408 X-1 at low (0.1-0.3 mHz, in black) and high (1-20 mHz, in red) frequencies, corresponding with the hard and soft lags for NGC 5408 X-1. The 1.0-1.5 keV energy band was used as the reference band because this is where the signal is highest. The lags have not been shifted, so zero-lag means that there is no time delay between that bin and the reference band. Similarly, a negative lag means that the bin leads to the reference band, and positive lags mean that the bin lags behind the reference band. At low frequencies (i.e., hard lag) the phase lag increases with energy, from ∼ -0.6 at 0.8 keV to ∼ 0.3 at 3 keV. On the contrary, at high frequencies (i.e., soft lag) the phase lag spectrum decreases with energy, from ∼ 0.2 at 0.8 keV down to ∼ -0.1 at 3 keV. Note that the y-axis is different for low (left y-axis) and high (right y-axis) frequencies. The same behaviour was reported by De Marco et al. (2013b) for the time lag vs. energy spectrum of the soft lag.

5 DISCUSSION

We have shown that a linear rms-flux relation is present in the hard energy band of the two ULXs studied here, NGC 5408 X-1 and NGC 6946 X-1, and that it is persistent across multiple observations spanning ∼8 years. The limitations of the soft band data are such that we are unable to place any interesting constraints on the rms-flux relation in the soft band (this is due to the relatively low total count rate of these sources, $\lesssim 1$ ct s^{-1}, and low fractional rms amplitude below 1 keV, which means the intrinsic rms is low, the Poisson noise is relatively high and the flux range is small). We also examined the frequency-dependent X-ray time lags, extending the analysis to lower frequencies than previous studies. We find the coherence between soft (<0.9 keV) and hard (>1.2 keV) bands is high, consistent with ≈ 1 at all frequencies. The soft phase lag can be recovered for most observations of NGC 5408 X-1 at frequencies above ∼few mHz, but the phase lag is not constant down to the lowest frequencies we probe (∼0.1 mHz) and get less negative at lower frequencies. We find tentative evidence for a hard lag (positive phase lag) at the lowest frequencies.

5.1 The rms-flux relation

Heil & Vaughan (2010) used the 2006 and 2008 observations to show that NGC 5408 X-1 exhibits a linear rms-flux relation. We show the relation persists through further observations in 2010, 2011 and 2014. The parameters of the best-fitting linear models differ between observations, presumably due to modest changes in mean flux and PSD shape. We also detected a linear rms-flux relation in the 2012 observation of NGC 6946 X-1, demonstrating that NGC 5408 X-1 is not unique among ULXs. We were unable to obtain useful constraints on the possible rms-flux relations in other ULXs from the sample of Sutton et al. (2013). As NGC 5408 X-1 and NGC 6496 X-1 are among the brightest and best-observed of the variable ULXs, we speculate that the rms-flux relation is a common property of ULX variability.

The rms-flux relation appears to be ubiquitous in luminous, accreting objects, such as active galactic nuclei (AGN, Vaughan et al. 2003b,a), Galactic X-ray binaries (XRB) with black hole or neutron star accretors (Uttley & McHardy 2001; Uttley 2004) and cataclysmic variables (Scaringi et al. 2012; Van de Sande et al. 2015). The simplest conclusion is that a common physical mechanism explains the strong, aperiodic variability, following a linear rms-flux relation, in all these sources. Currently the favoured explanation is in terms of propagating accretion rate fluctuations (Lyubarskii 1997; Arévalo & Uttley 2006), although any similar scheme for multiplicative modulation of random fluctuations will produce a linear rms-flux relation (Uttley et al. 2005). In this model, random fluctuations in the viscosity occurring on all spatial scales in the accretion flow modulate the accretion rate further in, but high frequency variations occurring on large scales are damped as they move inwards. Irrespective of this, the presence of the linear rms-flux relation in more than one ULX suggests the same underlying variability mechanism is at work in ULXs as in the sub-Eddington XRB and AGN.

5.2 Interband X-ray time delays

The soft lag in NGC 5408 X-1 was first detected by Heil & Vaughan (2010), based mainly on the 2006 *XMM*–Newton observation of NGC 5408 X-1. De Marco et al. (2013b) subsequently used six *XMM*–Newton observations (2006, 2008, 2010a,b and 2011a,b) and recovered similar soft X-ray lags in each, above frequencies of ∼few mHz. We extended the lag-frequency analysis to lower frequencies (∼ 0.1 mHz) and find that the soft lag extends down to ∼ 1 mHz with an amplitude of tens of seconds, but neither the phase lag nor time lag is constant with frequency, with the phase lag constant at ∼ −0.2 rad (soft lag) above ∼1 mHz but increasing at lower frequencies. A similar lag-frequency spectrum is found for NGC 6946 X-1.

The soft vs. hard band coherence is high, indicating the variations in each band are linearly correlated, and probably driven by the same process. Any additional source of uncorrelated variations adding to one band must be weak. The lags may then be imposed by the action of linear filters (“impulse response functions”) acting on the driving variations in one or both bands.

The interpretation of these lags remains challenging. In the following, we discuss possible implications and comparison with other accreting sources.

5.2.1 Comparison with AGN scaling relations

Soft X-ray time lags are now well established in AGN (see Uttley et al. 2014, for a review), where they are observed typically at frequencies above ~ 0.1 mHz, below which a hard lag dominates. The most accepted scenario for AGN assumes that the hard lag is produced by accretion rate fluctuations moving inwards through the accretion disc and energising a radial extended corona (e.g., Kotov et al. 2001; Arévalo & Uttley 2006). The soft lags are thought to be produced by a separate process – "reverberation", i.e. light-travel time delays as the primary coronal emission is reprocessed in the inner regions of an ionised disc (see Fabian et al. 2009, and the review by Uttley et al. 2014). Typically the reverberation is thought to be generated by the inner disc, within $\sim 10r_g$ of the central black hole.

De Marco et al. (2013a) studied a sample of 32 AGN and found a scaling relation between the black hole mass and the soft time lag using the 15 objects where a soft time delay was detected. If their scaling relation extends to ULXs, we would expect the soft lag to be located at frequencies in the range $20 - 200$ mHz with amplitudes of $0.03 - 0.4$ s for black hole masses of $10 - 1000 M_{\odot}$, as expected for stellar-mass to intermediate-mass black holes (see e.g. Fig. 9 of De Marco et al. 2013b). As shown in Fig. 3, the soft lag in NGC 5408 X-1 occurs at frequencies of the order of mHz with amplitudes of tens of seconds, much larger than expected for a stellar mass black hole binary and more typical of a low-mass AGN. However, NGC 5408 X-1 is clearly identified with a stellar object on the outskirts of a dwarf galaxy and is therefore not an AGN (e.g., Pakull & Mirioni 2003; Cseh et al. 2013). If the soft lag in NGC 5408 X-1 is a reverberation signal from the accretion disc, as is proposed to explain the AGN lags (e.g., Fabian et al. 2009; Uttley et al. 2014), the size and distance of the reflecting medium are large. If the observed maximum soft time lag of ~ 10 s is not "diluted" (due to the contribution of direct emission to both bands), such that the delay corresponds to a path length of $\sim 3 \times 10^9$ m, this corresponds to $\sim 10^4 (M_{BH}/100 M_{\odot}) r_g$.

Indeed, ULX spectra lack the obvious signs of strong reflection (such as iron emissions lines and the "Compton hump") commonly seen in Seyfert 1s.

5.2.2 Association with XRB QPOs

Another suggestion discussed by De Marco et al. (2013b) is that the soft lag is associated with a QPO, as sometimes occurs in BH XRBs. There are some problems with this interpretation. Foremost is that the QPOs claimed for NGC 5408 X-1 are generally not clear and distinct features like QPOs in BH XRBs (of the "type-C" variety). We will discuss this further in a companion paper (Vaughan et al., in prep.), but even if we take the PSD fits of Dheeraj & Strohmayer (2012), De Marco et al. (2013b) or Caballero-García et al. (2013) at face value, the soft lags extend over a much broader range of frequencies than the QPO-like features, indicating the lags are associated with the noise PSD. It is also not clear that lags in ULXs, e.g., between the 0.5–0.9 keV and 1.2–7 keV bands at ~1 mHz QPOs, can be compared to those in XRBs usually observed between hard bands (e.g., 3–5 keV and 5–13 keV) for ~1 Hz QPOs (Remillard et al. 2002; Casella et al. 2004).

5.2.3 Possible origins for the soft lag

The spectrum of these "soft ultraluminous" sources (Gladstone et al. 2009; Sutton et al. 2013; Middleton et al. 2015) are often described in terms of two components. The softer component, dominating below ~ 1 keV has a quasi-thermal spectrum and shows little, if any, short timescale variability. The latter fact is inferred from the lack of "soft excess" in the rms and covariance spectra (see Fig. 1 and also Middleton et al. 2015). The harder component, dominating over $\sim 1 - 10$ keV, resembles a cut-off power law (see also Walton et al. 2013, 2014), and produces most or all of the rapid variability. In the context of the supercritical accretion model (Shakura & Sunyaev 1973; King et al. 2001; Poutanen et al. 2007; Middleton et al. 2015) the hard component represents emission from the inner accretion flow (either inverse-Compton emission from a moderately optically thick corona or the thermal emission from a slim disc), while the soft component is thermal emission from the base of an optically thick, massive wind driven off the disc at larger radii (as expected for super-Eddington accretion flows).

The lack of variability of the softer component suggests it plays no role in generating the soft lags. Further, the high coherence between soft and hard bands is most simply explained if there is a single "driver" of the variability. Together, these are consistent with the soft lag being intrinsic to the harder component and not a delay between the two spectral components. In other words, it is only the hard component that varies rapidly, and its variations on timescales shorter than ~ 1 ks occur at higher energies first, with the softer emission (from the same spectral component) taking up to few seconds to respond. These delays may be intrinsic to the emission mechanism (from the inner accretion flow) or imposed by processes intercepting and delaying some fraction of this emission.

One explanation for X-ray time lags is in terms of scattering in an intervening medium. A soft lag could be produced as hard X-ray photons from the primary X-ray source pass through and are down-scattered to lower energies. Low energy photons typically have undergone more scatterings and so escape the scattering medium after a longer delay. The lag-frequency spectrum for NGC 5408 X-1 shows clear frequency dependence, being constant in neither phase lag nor time lag. Such lags are difficult to reproduce in a simple scattering scenario which would more naturally produce an approximately constant time lag (at frequencies below the wrap around frequency; Miller et al. 2010; Zoghbi et al. 2011; Uttley et al. 2014).

A further possibility is that the soft lag somehow results from the propagation of photons through an optically thin shroud of material, likely to result from an expanded wind (a prediction of the super-critical ULX model). Should the absorption opacity of this material be low in the hard band and high in the soft band (perhaps as a result of high abundances of Oxygen and Neon but relatively low abundances of Iron, Middleton et al. 2014), the hard photons will arrive to the observer scattered (with the exact scattered fraction dependent on the Thompson optical depth) whilst the soft photons will be absorbed and re-emitted. There are indeed strong indications that residuals at soft energies in the time-averaged spectra are associated with absorption and emission features associated with a strong outflow (Middleton et al. 2014; Middleton et al. in prep) and, should this provide an origin for the soft lag, the magnitude of the lag should provide constraints on the extent of the wind. However, such models incorporating outflows are by their very nature "messy" with the impact of reverberation and absorption heavily dependent on inclination angle and structure of the wind.

A final possibility is that the lags are intrinsic to the X-ray source itself, i.e., that the part of the inner accretion flow that first responds to inward moving accretion rate variations has a harder spectrum than the later responding parts of the flow. This is in the opposite sense to the models used to explain hard lags in XRB (e.g., Kotov et al. 2001; Arévalo & Uttley 2006). But this should perhaps not rule out this idea, as the structure of the hard X-ray emitting inner regions of ULXs may be quite different from the corona or jet-base thought to produce the thermal/non-thermal, variable hard X-ray spectrum in sub-Eddington XRB and AGN.

5.2.4 Low frequency lags

At frequencies below $\sim$ 1 mHz the sign of the time lag estimate changes and becomes a hard (or positive) lag. We do caution that, even with multiple observations of one of the brightest ULXs, the lag at $\sim$ 0.1 mHz has large uncertainties, with the lag exceeding zero only at the $2-3\sigma$ level.

Hard lags at low frequency, along with soft lags at higher frequencies, have been observed in many AGN (Fabian et al. 2009; Zoghbi et al. 2011; Emmanoulopoulos et al. 2011; Kara et al. 2013; De Marco et al. 2013a). The best studied source is the narrow line Seyfert 1 1H0707-495 (e.g., Fabian et al. 2009; Zoghbi et al. 2011). Kara et al. (2013) argued that the different energy dependence of the high and low frequency lags (soft and hard, respectively) in this object revealed that different emission processes are involved. Interestingly, the lag-energy spectra for NGC 5408 X-1 at low and high frequencies (Fig. 4) look like very similar (after a change of sign and scaling). But given the low significance of the low frequency hard lag it would perhaps be premature to place much weight on this.

The limited spectral-timing data for ULXs leave a few clues about the origin of the lags. Longer observations with higher S/N would be able to access both lower and higher frequencies, and allow us to better estimate the frequency and energy dependence of the lags. Such constraints will be crucial for ruling out lag models, but may require future, larger X-ray missions.

ACKNOWLEDGMENTS

This paper is based on observations obtained with *XMM*–Newton, an ESA science mission with instruments and contributions directly funded by ESA Member States and the USA (NASA). This research has made use of NASA's Astrophysics Data System and of data, software and web tools obtained from NASA's High Energy Astrophysics Science Archive Research Center (HEASARC), a service of Goddard Space Flight Center and the Smithsonian Astrophysical Observatory. This work was financed by MINECO grant AYA 2010-15169 and AYA 2013-42227-P. SV, TPR are supported in part by STFC consolidated grants, MJM appreciates support via ERC grant 340442, and LHG acknowledges financial support from the Ministerio de Economía y Competitividad through the Spanish grants FPI BES-2011-043319 and EEBB-I-14-07885.

REFERENCES

Arévalo P., Uttley P., 2006, MNRAS, 367, 801
Bachetti M., et al., 2013, ApJ, 778, 163
Bachetti M., et al., 2014, Nature, 514, 202
Caballero-García M. D., Belloni T. M., Wolter A., 2013, MNRAS, 435, 2665
Casella P., Belloni T., Homan J., Stella L., 2004, A&A, 426, 587
Cseh D., Grisé F., Kaaret P., Corbel S., Scaringi S., Groot P., Falcke H., Körding E., 2013, MNRAS, 435, 2896
De Marco B., Ponti G., Cappi M., Dadina M., Uttley P., Cackett E. M., Fabian A. C., Miniutti G., 2013a, MNRAS, 431, 2441
De Marco B., Ponti G., Miniutti G., Belloni T., Cappi M., Dadina M., Muñoz-Darias T., 2013b, MNRAS, 436, 3782
Dheeraj P. R., Strohmayer T. E., 2012, ApJ, 753, 139
Emmanoulopoulos D., McHardy I. M., Papadakis I. E., 2011, MNRAS, 416, L94
Fabian A. C., et al., 2009, Nature, 459, 540
Farrell S. A., Webb N. A., Barret D., Godet O., Rodrigues J. M., 2009, Nature, 460, 73
Feng H., Soria R., 2011, New A Rev., 55, 166
Gladstone J. C., Roberts T. P., Done C., 2009, MNRAS, 397, 1836
Heil L. M., Vaughan S., 2010, MNRAS, 405, L86
Heil L. M., Vaughan S., Roberts T. P., 2009, MNRAS, 397, 1061
Heil L. M., Vaughan S., Uttley P., 2011, MNRAS, 411, L66
Heil L. M., Vaughan S., Uttley P., 2012, MNRAS, 422, 2620
Kara E., Fabian A. C., Cackett E. M., Steiner J. F., Uttley P., Wilkins D. R., Zoghbi A., 2013, MNRAS, 428, 2795
King A. R., 2009, MNRAS, 393, L41
King A. R., Davies M. B., Ward M. J., Fabbiano G., Elvis M., 2001, ApJ, 552, L109
Kotov O., Churazov E., Gilfanov M., 2001, MNRAS, 327, 799
Liu J.-F., Bregman J. N., Bai Y., Justham S., Crowther P., 2013, Nature, 503, 500
Lyubarskii Y. E., 1997, MNRAS, 292, 679
Mezcua M., Roberts T. P., Lobanov A. P., Sutton A. D., 2015, MNRAS, 448, 1893
Middleton M. J., Roberts T. P., Done C., Jackson F. E., 2011, MNRAS, 411, 644
Middleton M. J., et al., 2013, Nature, 493, 187
Middleton M. J., Walton D. J., Roberts T. P., Heil L., 2014, MNRAS, 438, L51
Middleton M. J., Heil L., Pintore F., Walton D. J., Roberts T. P., 2015, MNRAS, 447, 3243
Miller L., Turner T. J., Reeves J. N., Braito V., 2010, MNRAS, 408, 1928
Motch C., Pakull M. W., Soria R., Grisé F., Pietrzyński G., 2014, Nature, 514, 198
Nowak M. A., Vaughan B. A., Wilms J., Dove J. B., Begelman M. C., 1999, ApJ, 510, 874
Pakull M. W., Mirioni L., 2003, in Arthur J., Henney W. J., eds, Revista Mexicana de Astronomia y Astrofisica Conference Series Vol. 15, Revista Mexicana de Astronomia y Astrofisica Conference Series. pp 197–199
Poutanen J., Lipunova G., Fabrika S., Butkevich A. G., Abolmasov P., 2007, MNRAS, 377, 1187
Remillard R. A., McClintock J. E., 2006, ARA&A, 44, 49
Remillard R. A., Sobczak G. J., Muno M. P., McClintock J. E., 2002, ApJ, 564, 962
Scaringi S., Körding E., Uttley P., Knigge C., Groot P. J., Still M., 2012, MNRAS, 421, 2854
Shakura N. I., Sunyaev R. A., 1973, A&A, 24, 337
Stobbart A.-M., Roberts T. P., Wilms J., 2006, MNRAS, 368, 397
Sutton A. D., Roberts T. P., Walton D. J., Gladstone J. C., Scott A. E., 2012, MNRAS, 423, 1154
Sutton A. D., Roberts T. P., Middleton M. J., 2013, MNRAS, 435, 1758

Uttley P., McHardy I. M., 2001, MNRAS, 323, L26
Uttley P., 2004, MNRAS, 347, L61
Uttley P., McHardy I. M., Vaughan S., 2005, MNRAS, 359, 345
Uttley P., Cackett E. M., Fabian A. C., Kara E., Wilkins D. R., 2014, A&A Rev., 22, 72
Van de Sande M., Scaringi S., Knigge C., 2015, MNRAS, 448, 2430
Vaughan B. A., Nowak M. A., 1997, ApJ, 474, L43
Vaughan S., Fabian A. C., Nandra K., 2003a, MNRAS, 339, 1237
Vaughan S., Edelson R., Warwick R. S., Uttley P., 2003b, MNRAS, 345, 1271
Walton D. J., et al., 2013, ApJ, 779, 148
Walton D. J., et al., 2014, ApJ, 793, 21
Zoghbi A., Uttley P., Fabian A. C., 2011, MNRAS, 412, 59

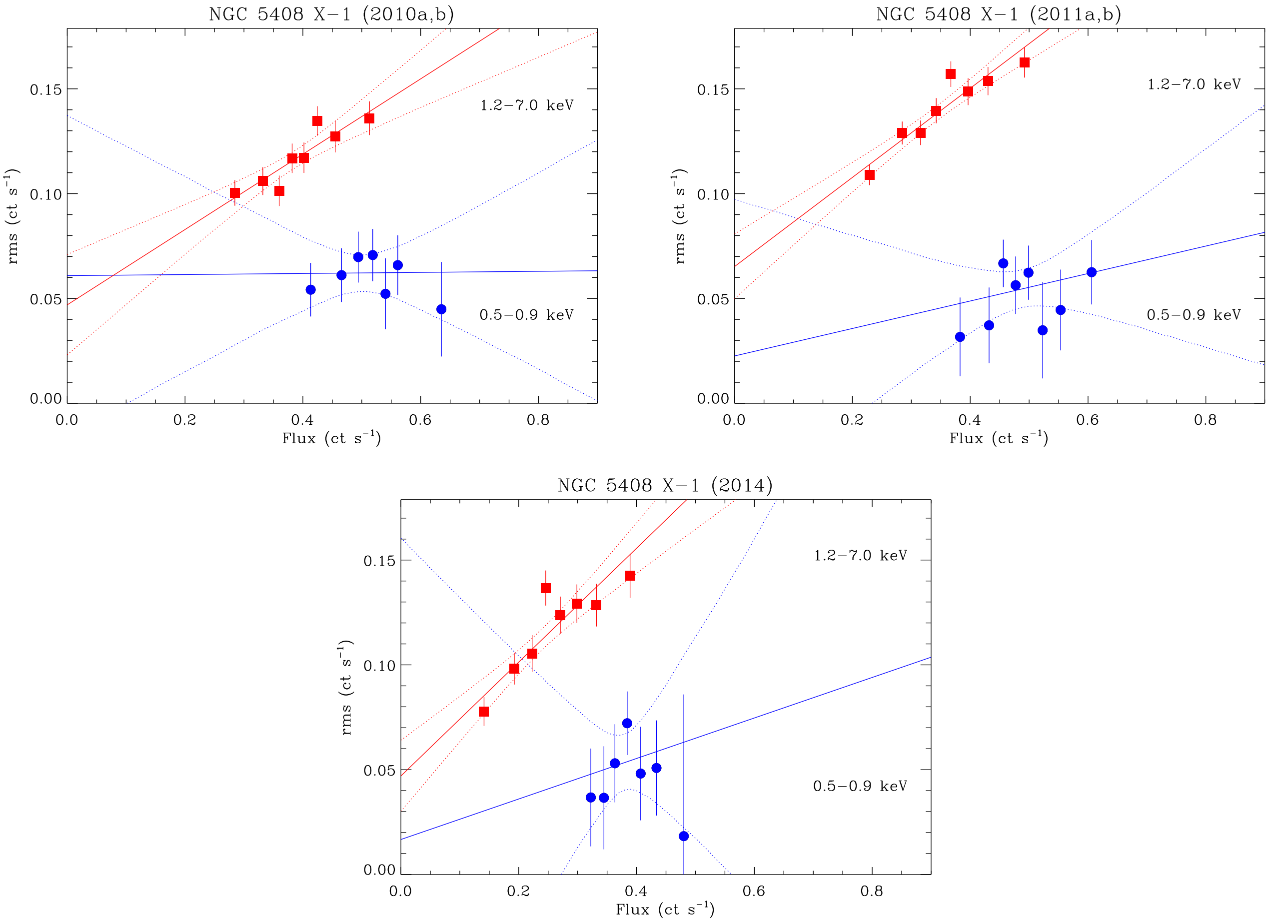

Figure A1. rms-flux relation for NGC 5408 X-1 in the soft (0.5–0.9 keV) and hard (1.2–7 keV) energy bands, for observations from 2010, 2011, and 2014. The rms is measured over the 4–50 mHz frequency range from segments of length 150 s. The dashed lines show the 95% “confidence bands” around the best-fitting linear model.

APPENDIX A: RMS-FLUX RELATION

In this appendix we provide the plots of the rms-flux relation for NGC 5408 X-1 and NGC 6946 X-1 for each year separately. The results are presented in Sect. 3

APPENDIX B: CROSS-SPECTRUM

In this appendix we present the cross-spectrum analysis for NGC 6946 X-1, including the coherence, phase lag, and time lag between the soft and hard energy bands. The trend of the lag is similar to that observed in NGC 5408 X-1, although the coherence is badly constrained, and both the soft and hard lag are below the 3σ level. Therefore, we cannot confirm the lags in this ULX.

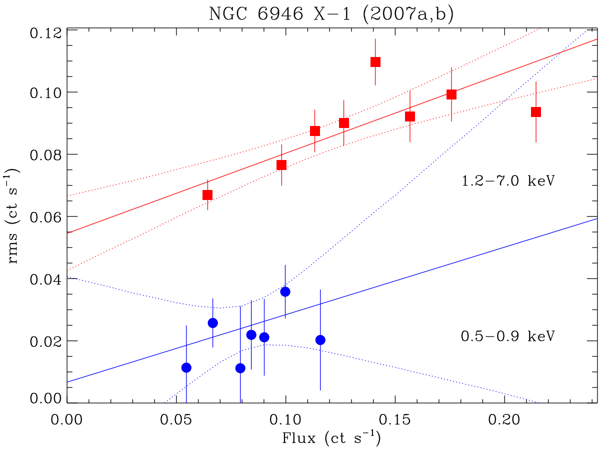

Figure A2. rms-flux relation for NGC 6946 X-1 in the soft (0.5–0.9 keV) and hard (1.2–7 keV) energy bands, for observations from 2007. The rms is measured over the 4–50 mHz frequency range from segments of length 250 s. The dashed lines show the 95% "confidence bands" around the best-fitting linear model.

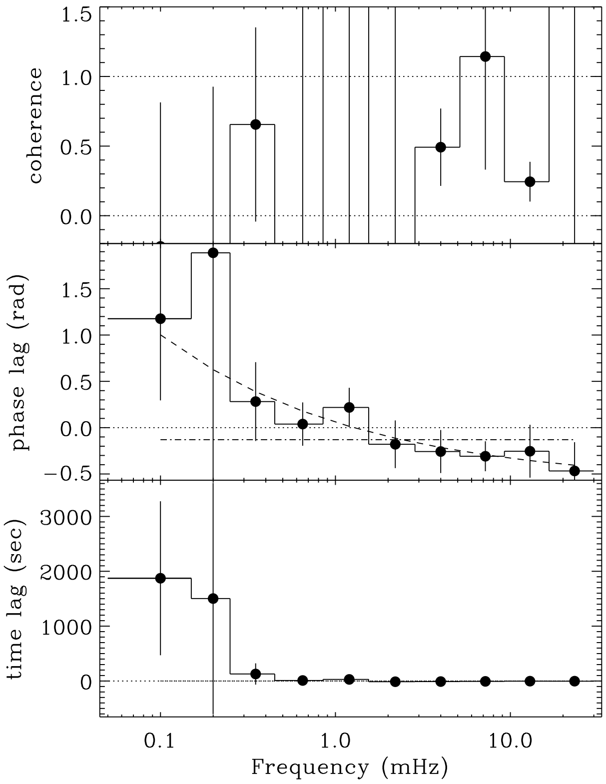

Figure B1. Results of the cross-spectrum analysis between the soft (0.5-0.9 keV) and hard (1.2-7.0 keV) energy bands for NGC 6946 X-1 showing, from upper to lower panels: the coherence; phase-lag; and time lag. Middle panel shows a constant model (dot-dashed line) and a power law plus constant model (dashed line) we fitted to the phase lag (see text).

7

Conclusions

Throughout this thesis, I have presented a study on the variability of low luminosity active galactic nuclei (LLAGN), including optically selected low ionisation nuclear emission line region (LINER) and Seyfert 2 nuclei, which constitutes the core of the thesis work. The data were retrieved from the *XMM*–Newton and *Chandra* satellites, which provide information at X-ray and UV frequencies. The **long-term X-ray variations**, i.e., with timescales ranging from months to years, as well as the pattern of variability, were obtained from a **simultaneous spectral fitting** of the spectra of the same source at different dates, by leaving different parameters to vary in the model. Additionally, **short-term X-ray variations**, i.e., with timescales in the range from hours to days, from the analysis of the light curves, and **long-term UV flux variations** were searched for. The main conclusions obtained from this study are summarized in the following:

- The sample of **21 LINERs** is divided in AGN (17 sources, among them two are *Compton*-thick candidates) and non-AGN (four sources, all *Compton*-thick) candidates.
    - ▷ **Short-term X-ray variations are not found** in any of the sources.
    - ▷ The **non-AGN candidates do not show X-ray variations**, but two of them are variable at UV frequencies, consistent with the work by Maoz et al. (2005), who claimed UV variations in most of the LINERs in their sample. This might suggest

  that they should be AGN because variations would not be expected in case of multiple stellar sources.

  - ▷ X-ray variations have been analysed in 13 out of 17 **AGN candidates**; eight of them show variations in timescales from months to years. Variations are also observed at UV frequencies in five out of the six sources. It is therefore found that **variability at hard energies is a common property of LINERs**, which is observed in at least one energy band, **X-rays and/or UV, in 11 out of the 14 studied sources**. Only one of the *Compton*-thick candidates shows variations. This is expected because variations in sources dominated by the reflection component are not common, because this component is located far from the nuclear source.
  - ▷ The **X-ray variability pattern** observed in all the variable LINERs is related with the **nuclear continuum**, in one source accompanied by absorption variations (NGC 1052), and in another source accompanied by variations at soft energies (NGC 4552).
  - ▷ The timescales of the variability observed in LINERs is consistent with the variability plane which relates the black hole masses, accretion rates and variability timescales, as more powerful AGN do. Since LINERs have the highest black hole masses and lower Eddington rates, their variability timescales are between months and years, fully consistent with our results.

- The sample of **26 Seyfert 2s** is divided in *Compton*-thick (12 sources), *Compton*-thin (12 sources), and changing-look candidates (two sources).

  - ▷ **Short-term X-ray variations are not found** in any of the sources.
  - ▷ **UV nuclear variability is not found** in any of the sources. In fact, the nuclear source is observed only in three Seyfert 2s, while the remaining sources are undetected. This is consistent with the obstructed view of the nucleus due to the dusty torus, explained within the unified model of AGN.
  - ▷ **Long-term X-ray variability** has been observed in 11 out of the 25 analysed sources, only one of them being a *Compton*-thick candidate (MARK 3). Therefore, X-ray variability is **common in Seyfert 2s**. We explain our results in a scenario where there are a constant reflection component located far from the nucleus and a variable nuclear continuum. *Compton*-thick sources are dominated by reflection and do not show variations, whereas *Compton*-thin and changing-look objects are dominated by the nuclear continuum and thus show variations. Moreover, we confirm that low luminosity Seyfert 2s are due to a decrease of luminosity in *Compton*-thick sources.

  - ▷ The main **X-ray variability pattern** observed in these nuclei is related to changes in the **nuclear continuum**, but **absorption variations** have been found **in four sources** (in two of them accompanied with variations in the nuclear continuum), and at soft energies in two cases (both accompanied with variations in the nuclear continuum).

- Taking advantage of the X-ray spectral analyses performed for **LINER and Seyfert 2s**, we have assembled their spectral properties. We have differentiated between *Compton*-thin and *Compton*-thick candidates because they seem to be dominated by different spectral components. The sample includes a total of 38 sources, 13 LINERs (two *Compton*-thick candidates) and 25 Seyfert 2s (12 *Compton*-thick candidates).

  - ▷ **Major differences** in the spectral parameters are related to the **X-ray luminosities**, which in turn leads to higher **accretion rates** in Seyfert 2s. Minor differences are observed in the absorbing column densities, temperatures or black hole masses. The spectral indices of the power law representing the AGN are very similar for both.
  - ▷ The X-ray variability show the **same timescales and amplitudes** both in LINERs and Seyfert 2s, and are mainly related to **changes in the nuclear continuum**.
  - ▷ Although variations occur in a similar way, the relation between the spectral index and the Eddington ratio shows that **different accretion mechanisms** take place. This behaviour has been explained as a different accretion mechanism, being efficient for Seyfert 2s and inefficient for LINERs.
  - ▷ Variations of the absorber, as well as objects changing from/to *Compton*-thin to/from *Compton*-thick, although scarce, are more common in Seyfert 2s, suggesting the presence of an obscuring material close enough to the accretion disc to produce variations in scales between months and years. Furthermore, UV nuclear variations are only observed in LINERs, indicating a naked view of the inner parts of the AGN in these cases. All together suggest that **the broad line region and/or the torus**, where the obscured material is producing the absorber variations seen in Seyfert 2s, **might disappeared in LINERs at least in some sources**, as suggested from theoretical arguments.

In addition to the research explained above, we have performed a study of **AGN located in galaxy groups and clusters**, and a variability study on **ultraluminous X-ray sources** (ULX). The main conclusions of these studies are summarized in the following:

- We have searched for AGN in 16 galaxy clusters and 10 galaxy groups by identifying the number of AGN within each structure. We found three AGN in the nine studied groups of galaxies, each one located in the center of the group. We found 28 point-like sources within the 16 galaxy clusters; only nine with a measured redshift. We have identified **from one to five point-like sources on each cluster**. This was an exploratory work that can be completed in a large sample of galaxy groups and clusters.

- We have analysed the X-ray variability of two ULXs based on multiple *XMM*–Newton observations. We have shown that the **rms-flux relation** is present in both sources, as it is for other luminous accreting objects. We have computed the time delay between hard and soft energy bands in NGC 5408 X-1, with the **soft band delayed with respect to the hard band at frequencies above a few mHz**. For the first time, we have extended the lag analysis to lower frequencies and find some evidence for a **reversal of the lag at frequencies of about 0.1 mHz**. The methodology used in this work can eventually be applied to a sample of LLAGN in order to obtain information about the physical processes happening in their nuclei.

8

Future prospects

The work presented in this thesis paves the way for new open questions. In the following, we present topics of interest related with this thesis that will be addressed in the near future:

- **X-ray variability in type 1 Seyferts**: In this thesis we have focused in Seyfert 2 objects, i.e., AGN that are observed through the dusty torus from the point of view of the unified model. It would therefore be interesting to apply the same methodology to a sample of optically selected type 1-1.9 sources. From the literature, we know that type 1 sources show X-ray variations, in many cases related to absorptions at soft and/or hard energies. However, we note that a systematic study of these sources has not been performed yet. Indeed, the individual variability analyses of many of the most studied cases refer to objects classified as NLSy1s, whose properties might be different to those of Seyfert 1s in various respects. Thus it is also crucial to distinguish for the different subgroups considering their optical classifications in order to clarify whether these kind of variations are common in Seyfert 1s.
- **X-ray variability in nearby AGN**: Joining the spectral properties and variability patterns of Seyfert 1s with the ones presented in this thesis for LINERs and Seyfert 2s, we will produce a panoramic view of the X-ray variability in nearby AGN. This study will be made in analogy to the one presented in Chapter 4 of this thesis. Some

of the possible questions to address will be: to find whether the X-ray variations occur in the same way in every AGN, and to understand the physical origin of such variations; to find for similarities and/or discrepancies in the spectral parameters, as for example if there exist Seyfert 1s with high column densities; to study the accretion mechanisms; or to compare the UV variations that we expect to observe in Seyfert 1s with those observed in LINERs.

Moreover, some other works related to the results presented in this thesis that can be done in the future are summarized in the following:

- **Variability at soft X-ray energies**: Within our study, three sources revealed variability at energies below 2 keV. However, in two of these objects the variations were found when comparing data from different instruments. These kind of variations are rare, so more data are required in order to confirm the variations. The analysis must be done with X-ray instruments which covers the 0.5–2.0 keV energy band. Due to its high spatial resolution, imaging from *Chandra* is necessary in order to resolve the sources, to be sure that extranuclear sources are not responsible for the variations. For bright enough sources, *Chandra* data at different epochs would be useful for the study. Fainter sources with low count rates at these energies would require *XMM*–Newton data along with *Chandra* imaging; in case of multiple sources within the *XMM*–Newton aperture it will be necessary to assure that the variability comes from the nucleus, what can only be done using at least two *Chandra* observations or by decontaminating the extranuclear emission in *XMM*–Newton data (e.g., following the procedure explained in the methodology of this thesis).
- **X-ray variability in a complete sample of LLAGN**: The work presented here is composed by samples of AGN selected for having observations at different epochs separated by times ranging from months to years. First, the number of objects included in the sample is not big enough to statistically quantify the X-ray variability issue in LLAGN. Second, the various samples are by no means complete or statistically representative in a broad sense. The same analysis should be performed on a complete sample of LINERs and Seyferts in order to establish the fraction of variable LINER and Seyfert nuclei. This should be done by the selection of a complete sample and the monitoring of the sources at different dates. The *XMM*–Newton spectral-fit database (XMMFITCAT, Corral et al. 2015, A&A 576 A61) might be useful for this purpose, as is a catalogue of spectral fitting results for about 78000 sources selected from the latest version of the 3XMM Data Release 4 (3XMM-DR4), containing at least 50 net (background-subtracted) counts per detector in the 0.5–10 keV energy band. We

first should select the sources with multiple observations and search for their optical classifications, in order to assess if the sample is complete.

- **Fourier techniques applied to LLAGN**: In the last years, Fourier techniques have been applied to powerful AGN as Seyfert 1s to search for time lags between different energy bands. The study of these time lags can be used to understand the origin of the variations. The application of Fourier techniques to LLAGN has not been done yet mainly due to the low count rates of their spectra. In this work we searched for time lags in ULXs, whose luminosities are in the same range of LLAGN. Although long timescale coverages are required in order to measure the time delays, and thus it is not possible to make this study in a large sample of LLAGN, some of the sources can have enough exposure times to be able to use these techniques. We note that, because of the experience obtained during this work, the selection of the sample is not straightforward, as it does not depend on the exposure time and/or the count rate alone, but to a combination of both. The samples of LINERs and Seyfert 2s presented in this thesis can be used for a exploratory work. The methodology should be applied to the whole sample, combining all the available observations, to determine whether the coherence between the energy bands is high.
- **UV variability**: Two types of Seyfert 2s have been identified in the current literature: “truly obscured” and “naked” AGN. The first ones are characterized by large amounts of dust and gas along our line of sight so that the nucleus cannot be observed at optical or UV frequencies. The “naked” AGN, on the contrary, do not show high column densities so that their nuclei are expected to be observed at UV wavelengths. In our study, three Seyfert 2s with nuclear UV emission have been observed, i.e., they might be candidates to be “naked” AGN. A systematic study of UV emission in Seyfert 2s needs to be undertaken and a follow up variability of naked AGN deserve further analysis. Objects showing discordant classifications at X-rays and optical frequencies are ideal for the study. In the work by Merloni et al. (2014, MNRAS 437 3550), they found 21 sources optically classified as type 2 objects but with small column densities at X-rays, so this subsample could be used for the analysis. Data from the *HST* public archive at different epochs would be required in order to search for variations at UV frequencies.
- **Dusty torus**: We find that absorption variations and changing-look candidates (where these variations are expected) are scarce among LINERs; on the other hand, the nuclei of LINERs can be observed, and in fact are variable, at UV frequencies, while the UV nuclei are obscured for Seyfert 2s. These results might suggest the disappearance of the torus in LINERs. Therefore, the question is: what is the nature

of the obscuration and *Compton*-thickness in LINERs? To resolve this enigma, it is needed to study LINERs at high energies, with satellites such as *Suzaku* or *NuSTAR*. We note that the use of *Suzaku* might not be the best choice as it is not sensitive enough for faint sources. Our group is currently working in a project using *CanariCam* data to study a sample of seven *Compton*-thick candidate LINERs at mid infrared (mid-IR) frequencies, where the obscuring material is expected to produce a huge amount of thermal re-emission of the intercepted optical-UV nuclear radiation. We searched in the public archives, and found that three of these sources (NGC 835, UGC 05101, and NGC 3690B) have been observed with *NuSTAR*. It would therefore be interesting to apply for telescope time to observe the remaining four sources so that X-ray and mid-IR could be used together to study the obscuration in LINERs.

9

Other works

Finally, I would like to report other works in which I have participated but do not constitute the core of my main research. I was invited to collaborate in these studies because they are related to the work I have been carrying out during the development of this thesis.

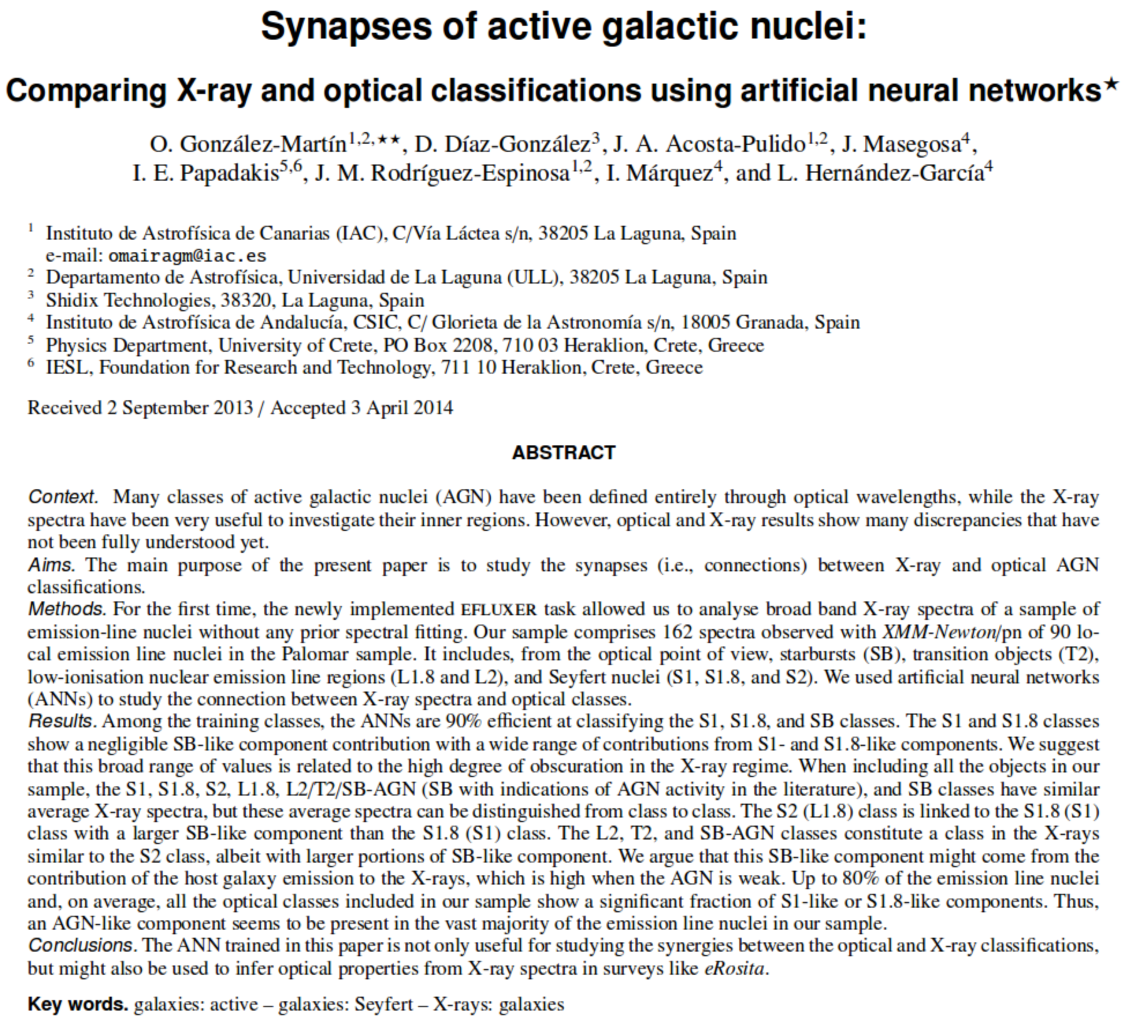

Synapses of active galactic nuclei:

Comparing X-ray and optical classifications using artificial neural networks★

O. González-Martín[1,2,★★], D. Díaz-González[3], J. A. Acosta-Pulido[1,2], J. Masegosa[4],
I. E. Papadakis[5,6], J. M. Rodríguez-Espinosa[1,2], I. Márquez[4], and L. Hernández-García[4]

[1] Instituto de Astrofísica de Canarias (IAC), C/Vía Láctea s/n, 38205 La Laguna, Spain
e-mail: `omairagm@iac.es`
[2] Departamento de Astrofísica, Universidad de La Laguna (ULL), 38205 La Laguna, Spain
[3] Shidix Technologies, 38320, La Laguna, Spain
[4] Instituto de Astrofísica de Andalucía, CSIC, C/ Glorieta de la Astronomía s/n, 18005 Granada, Spain
[5] Physics Department, University of Crete, PO Box 2208, 710 03 Heraklion, Crete, Greece
[6] IESL, Foundation for Research and Technology, 711 10 Heraklion, Crete, Greece

Received 2 September 2013 / Accepted 3 April 2014

ABSTRACT

Context. Many classes of active galactic nuclei (AGN) have been defined entirely through optical wavelengths, while the X-ray spectra have been very useful to investigate their inner regions. However, optical and X-ray results show many discrepancies that have not been fully understood yet.

Aims. The main purpose of the present paper is to study the synapses (i.e., connections) between X-ray and optical AGN classifications.

Methods. For the first time, the newly implemented EFLUXER task allowed us to analyse broad band X-ray spectra of a sample of emission-line nuclei without any prior spectral fitting. Our sample comprises 162 spectra observed with *XMM-Newton*/pn of 90 local emission line nuclei in the Palomar sample. It includes, from the optical point of view, starbursts (SB), transition objects (T2), low-ionisation nuclear emission line regions (L1.8 and L2), and Seyfert nuclei (S1, S1.8, and S2). We used artificial neural networks (ANNs) to study the connection between X-ray spectra and optical classes.

Results. Among the training classes, the ANNs are 90% efficient at classifying the S1, S1.8, and SB classes. The S1 and S1.8 classes show a negligible SB-like component contribution with a wide range of contributions from S1- and S1.8-like components. We suggest that this broad range of values is related to the high degree of obscuration in the X-ray regime. When including all the objects in our sample, the S1, S1.8, S2, L1.8, L2/T2/SB-AGN (SB with indications of AGN activity in the literature), and SB classes have similar average X-ray spectra, but these average spectra can be distinguished from class to class. The S2 (L1.8) class is linked to the S1.8 (S1) class with a larger SB-like component than the S1.8 (S1) class. The L2, T2, and SB-AGN classes constitute a class in the X-rays similar to the S2 class, albeit with larger portions of SB-like component. We argue that this SB-like component might come from the contribution of the host galaxy emission to the X-rays, which is high when the AGN is weak. Up to 80% of the emission line nuclei and, on average, all the optical classes included in our sample show a significant fraction of S1-like or S1.8-like components. Thus, an AGN-like component seems to be present in the vast majority of the emission line nuclei in our sample.

Conclusions. The ANN trained in this paper is not only useful for studying the synergies between the optical and X-ray classifications, but might also be used to infer optical properties from X-ray spectra in surveys like *eRosita*.

Key words. galaxies: active – galaxies: Seyfert – X-rays: galaxies

Reference: González-Martín et al. (2014), A&A, 567, A92

My contribution to this paper was to check that the observations which compose the sample met our requirements. I also actively participated in the discussion of the paper.

A MULTI-WAVELENGTH VIEW OF THE CENTRAL KILOPARSEC REGION IN THE LUMINOUS INFRARED GALAXY NGC 1614

Rubén Herrero-Illana[1], Miguel Á. Pérez-Torres[1,2,3], Almudena Alonso-Herrero[4,13], Antxon Alberdi[1],
Luis Colina[5], Andreas Efstathiou[6], Lorena Hernández-García[1], Daniel Miralles-Caballero[7],
Petri Väisänen[8,9], Christopher C. Packham[10], Vinesh Rajpaul[11], and Albert A. Zijlstra[12]
[1] Instituto de Astrofísica de Andalucía-CSIC, P.O. Box 3004, E-18008 Granada, Spain
[2] Centro de Estudios de Física del Cosmos de Aragón (CEFCA), E-44001 Teruel, Spain
[3] Dpto. de Física Teórica, Universidad de Zaragoza, E-50009 Zaragoza, Spain
[4] Instituto de Física de Cantabria, CSIC-Universidad de Cantabria, E-39005 Santander, Spain
[5] Centro de Astrobiología (INTA-CSIC), Ctra. de Torrejón a Ajalvir, km 4, E-28850 Torrejón de Ardoz, Madrid, Spain
[6] School of Sciencies, European University Cyprus, Diogenes Street, Engomi, 1516 Nicosia, Cyprus
[7] Instituto de Física Teórica, Universidad Autónoma de Madrid, E-28049 Madrid, Spain
[8] South African Astronomical Observatory, P.O. Box 9, Observatory 7935 Cape Town, South Africa
[9] Southern African Large Telescope, P.O. Box 9, Observatory 7935 Cape Town, South Africa
[10] Department of Physics and Astronomy, University of Texas at San Antonio, One UTSA Circle, San Antonio, TX 78249, USA
[11] Department of Physics, University of Oxford, Denys Wilkinson Building, Keble Road, Oxford OX1 3RH, UK
[12] Jodrell Bank Centre for Astrophysics, University of Manchester, Manchester M13 9PL, UK

Received 2013 November 15; accepted 2014 March 26; published 2014 April 25

ABSTRACT

The Luminous Infrared Galaxy NGC 1614 hosts a prominent circumnuclear ring of star formation. However, the nature of the dominant emitting mechanism in its central ∼100 pc is still under debate. We present sub-arcsecond angular resolution radio, mid-infrared, Paα, optical, and X-ray observations of NGC 1614, aimed at studying in detail both the circumnuclear ring and the nuclear region. The 8.4 GHz continuum emission traced by the Very Large Array and the Gemini/T-ReCS 8.7 μm emission, as well as the Paα line emission, show remarkable morphological similarities within the star-forming ring, suggesting that the underlying emission mechanisms are tightly related. We used a *Hubble Space Telescope*/NICMOS Paα map of similar resolution to our radio maps to disentangle the thermal free–free and non-thermal synchrotron radio emission, from which we obtained the intrinsic synchrotron power law for each individual region within the central kiloparsec of NGC 1614. The radio ring surrounds a relatively faint, steep-spectrum source at the very center of the galaxy, suggesting that the central source is not powered by an active galactic nucleus (AGN), but rather by a compact ($r \lesssim 90$ pc) starburst (SB). *Chandra* X-ray data also show that the central kiloparsec region is dominated by SB activity, without requiring the existence of an AGN. We also used publicly available infrared data to model-fit the spectral energy distribution of both the SB ring and a putative AGN in NGC 1614. In summary, we conclude that there is no need to invoke an AGN to explain the observed bolometric properties of the galaxy.

Key words: galaxies: individual (NGC 1614) – galaxies: nuclei – galaxies: starburst – infrared: galaxies – radio continuum: galaxies – supernovae: general

Online-only material: color figures

Reference: Herrero-Illana et al. (2014), ApJ, 786, 156.

My contribution to this work was the analysis of the X-ray data of NGC 1614, including the spatial and spectral analyses. Closely following the methodology used in this thesis for LINERs and Seyferts, the spectral analysis was performed by fitting different models to the spectrum to obtain the model which best fits the data. Moreover, I actively participated in the discussion of the paper.

On the LINER nuclear obscuration, Compton-thickness and the existence of the dusty torus

Clues from *Spitzer*/IRS spectra

O. González-Martín[1,2,3★], J. Masegosa[4], I. Márquez[4], J.M. Rodríguez-Espinosa[1,2], J. A. Acosta-Pulido[1,2], C. Ramos Almeida[1,2], D. Dultzin[5], L. Hernández-García[4], D. Ruschel-Dutra[1,2,6], and A. Alonso-Herrero[7,8]

[1] Instituto de Astrofísica de Canarias (IAC), C/Vía Láctea, s/n, E-38205 La Laguna, Spain
[2] Departamento de Astrofísica, Universidad de La Laguna (ULL), E-38205 La Laguna, Spain
[3] Centro de Radioastronomía y Astrofísica (CRyA-UNAM), 3-72 (Xangari), 8701, Morelia, Mexico
[4] Instituto de Astrofísica de Andalucía, CSIC, Glorieta de la Astronomía s/n 18008, Granada, Spain
[5] Instituto de Astronomía, Universidad Nacional Autónoma de México, Apartado Postal 70-264, 04510 México DF, Mexico
[6] Departamento de Astronomia, Universidade Federal do Rio Grande do Sul, 9500 Bento Goncalves, Porto Alegre, 91501-970, Brazil
[7] Instituto de Física de Cantabria, CSIC-UC, E-39005 Santander, Spain
[8] Department of Physics and Astronomy, University of Texas at San Antonio, San Antonio, TX 78249, USA

Received 31st October 2014; accepted 15th January 2015

ABSTRACT

Context. Most of the optically classified low ionisation narrow emission-line regions (LINERs) nuclei host an active galactic nuclei (AGN). However, how they fit into the unified model (UM) of AGN is still an open question.
Aims. The aims of this work are to study at mid-infrared (mid-IR) (1) the Compton-thick nature of LINERs (i.e hydrogen column densities of $N_H > 1.5 \times 10^{24} cm^{-2}$); and (2) the disappearance of the dusty torus in LINERs predicted from theoretical arguments.
Methods. We have compiled all the available low spectral resolution mid-IR spectra of LINERs from the InfraRed Spectrograph (IRS) onboard *Spitzer*. The sample contains 40 LINERs. We have complemented the LINER sample with *Spitzer*/IRS spectra of PG QSOs, Type-1 Seyferts (S1s), Type-2 Seyferts (S2s), and Starburst (SBs) nuclei. We have studied the AGN versus the starburst content in our sample using different indicators: the equivalent width (EW) of the polycyclic aromatic hydrocarbon (PAH) at 6.2μm, the strength of the silicate feature at 9.7μm, and the steepness of the mid-IR spectra. We have classified the spectra as SB-dominated and AGN-dominated, according to these diagnostics. We have compared the average mid-IR spectra of the various classes. Moreover, we have studied the correlation between the 12μm luminosity, $\nu L_\nu(12\mu m)$, and the 2-10 keV energy band X-ray luminosity, $L_X(2-10\ keV)$.
Results. In 25 out of the 40 LINERs (i.e., 62.5%) the mid-IR spectra are not SB-dominated, similar to the comparison S2 sample (67.7%). The average spectra of both SB-dominated LINERs and S2s are very similar to the average spectrum of the SB class. The average spectrum of AGN-dominated LINERs is different from the average spectra of the other optical classes, showing a rather flat spectrum at $6-28\mu m$. We have found that the average spectrum of AGN-dominated LINERs with X-ray luminosities $L_X(2-10\ keV) > 10^{41} erg/s$ is similar to the average mid-IR spectrum of AGN-dominated S2s. However, faint LINERs (i.e. $L_X(2-10\ keV) < 10^{41} erg/s$) show flat spectra different from any of the other optical classes. The correlation between $\nu L_\nu(12\mu m)$ and $L_X(2-10\ keV)$ for AGN nicely extends toward low luminosities only if SB-dominated LINERs are excluded and the 2-10 keV band X-ray luminosity is corrected in Compton-thick LINER candidates.
Conclusions. We have found that LINERs proposed as Compton-thick candidates at X-ray wavelengths may be confirmed according to the X-ray to mid-IR luminosity relation. We show evidence in favour of the dusty-torus disappearance when their bolometric luminosity is below $L_{bol} \simeq 10^{42} erg/s$. We suggest that the dominant emission at mid-IR of faint LINERs might be a combination of an elliptical galaxy host (characterised by the lack of gas), a starburst, a jet, and/or ADAF emission. Alternatively, the mid-IR emission of some of these faint LINERs could be a combination of elliptical galaxy plus carbon-rich planetary nebulae. In order to reconcile the Compton-thick nature of a large fraction of LINERs with the lack of dusty-torus signatures, we suggest that the material producing the Compton-thick X-ray obscuration is free of dust.

Key words. Galaxies:active - Galaxies:nuclei - infrared:galaxies

Reference: González-Martín et al. (2015), accepted for publication in A&A.

I have been a co-investigator of the GTC/CanariCam proposals of LINERs GTC42-12B and GTC35-13A, and I contributed to this paper by being an active member of the discussion.

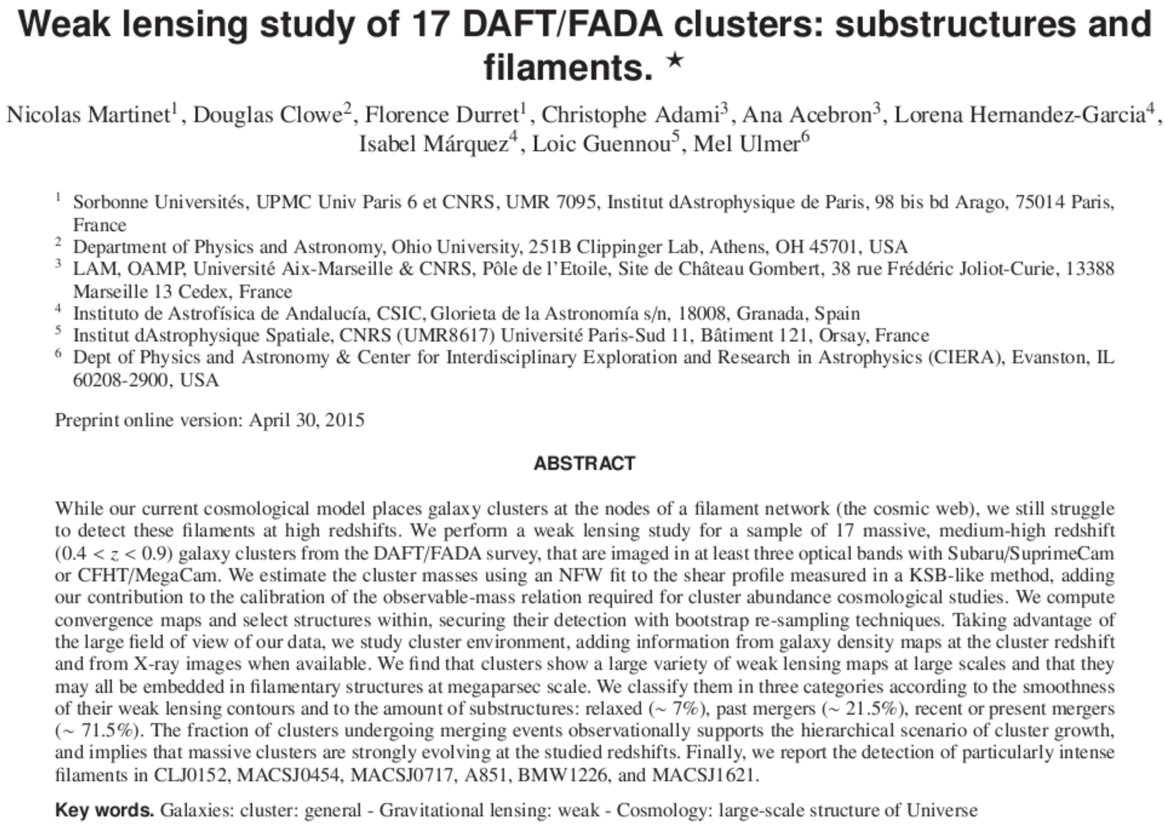

Weak lensing study of 17 DAFT/FADA clusters: substructures and filaments. ⋆

Nicolas Martinet[1], Douglas Clowe[2], Florence Durret[1], Christophe Adami[3], Ana Acebron[3], Lorena Hernandez-Garcia[4], Isabel Márquez[4], Loic Guennou[5], Mel Ulmer[6]

[1] Sorbonne Universités, UPMC Univ Paris 6 et CNRS, UMR 7095, Institut dAstrophysique de Paris, 98 bis bd Arago, 75014 Paris, France
[2] Department of Physics and Astronomy, Ohio University, 251B Clippinger Lab, Athens, OH 45701, USA
[3] LAM, OAMP, Université Aix-Marseille & CNRS, Pôle de l'Etoile, Site de Château Gombert, 38 rue Frédéric Joliot-Curie, 13388 Marseille 13 Cedex, France
[4] Instituto de Astrofísica de Andalucía, CSIC, Glorieta de la Astronomía s/n, 18008, Granada, Spain
[5] Institut dAstrophysique Spatiale, CNRS (UMR8617) Université Paris-Sud 11, Bâtiment 121, Orsay, France
[6] Dept of Physics and Astronomy & Center for Interdisciplinary Exploration and Research in Astrophysics (CIERA), Evanston, IL 60208-2900, USA

Preprint online version: April 30, 2015

ABSTRACT

While our current cosmological model places galaxy clusters at the nodes of a filament network (the cosmic web), we still struggle to detect these filaments at high redshifts. We perform a weak lensing study for a sample of 17 massive, medium-high redshift ($0.4 < z < 0.9$) galaxy clusters from the DAFT/FADA survey, that are imaged in at least three optical bands with Subaru/SuprimeCam or CFHT/MegaCam. We estimate the cluster masses using an NFW fit to the shear profile measured in a KSB-like method, adding our contribution to the calibration of the observable-mass relation required for cluster abundance cosmological studies. We compute convergence maps and select structures within, securing their detection with bootstrap re-sampling techniques. Taking advantage of the large field of view of our data, we study cluster environment, adding information from galaxy density maps at the cluster redshift and from X-ray images when available. We find that clusters show a large variety of weak lensing maps at large scales and that they may all be embedded in filamentary structures at megaparsec scale. We classify them in three categories according to the smoothness of their weak lensing contours and to the amount of substructures: relaxed (~ 7%), past mergers (~ 21.5%), recent or present mergers (~ 71.5%). The fraction of clusters undergoing merging events observationally supports the hierarchical scenario of cluster growth, and implies that massive clusters are strongly evolving at the studied redshifts. Finally, we report the detection of particularly intense filaments in CLJ0152, MACSJ0454, MACSJ0717, A851, BMW1226, and MACSJ1621.

Key words. Galaxies: cluster: general - Gravitational lensing: weak - Cosmology: large-scale structure of Universe

Reference: Martinet et al. (2015), submitted to A&A.

My contribution to this work was to extract and analyse the X-ray images used to compare with optical data and to search for filaments. Part of the work was developed during my short-stay in Paris in 2013 and is related to Chapter 5. Furthermore, I actively participated in the discussion of the paper.

Glossary

$\odot$	solar symbol: widely used to refer to solar mass ($M_\odot$) or luminosity ($L_\odot$).
ACIS	Advanced Charged couple Imaging Spectrometer: an X-ray detector on board *Chandra*.
ADAF	Advection-Dominated Accretion Flow: a model of sub-Eddington accretion disc.
AGN	Active Galactic Nucleus: a compact region in the center of the galaxy with high luminosity that cannot be explained by stellar processes.
ARF	Auxiliary Response File: a file containing the combined telescope/filter/detector areas and the quantum efficiency as a function of energy averaged over time.
BHB	Black Hole Binary: a system of two black holes in close orbit around each other.
BLR	Broad Line Region: a gaseous region with typical velocities of 3000 $km\ s^{-1}$.
CCD	Charge-Coupled Device: an integrated circuit etched onto a silicon surface forming pixels.
CIAO	Chandra Interactive Analysis of Observations: a software developed by the *Chandra* team to reduce data.
CT	Compton-Thick: Objects with column densities higher than $1.5 \times 10^{24} cm^{-2}$ at X-rays.
DM	Dark Matter: a kind of matter that cannot be seen.
EPIC	European Photon Imaging Camera: an X-ray detector on board *XMM*–Newton.
EW	Equivalent Width: measure of the area of a spectral line.
FWHM	Full Width at Half Maximum: distance between points on a curve at which the function reaches half its maximum value.
HBLR	Hidden Broad Line Region: an AGN that shows a BLR in polarized light.
HR	Hardness Ratio: the equivalent of a photometric color index in X-rays, calculated as a normalized difference of the exposure corrected counts in two energy bands.
HST	*Hubble Space Telescope*: an international 2.4 m mirror space telescope.
LINER	Low Ionization Nuclear Emission line Region: a type of AGN characterized by strong low ionization lines.
LLAGN	Low Luminosity Active Galactic Nuclei: AGN with bolometric luminosities lower than $\sim 10^{43} erg\ s^{-1}$.
NHBLR	Non-Hidden Broad Line Region: an AGN that do not show a BLR in polarized light.
NLR	Narrow Line Region: a gaseous region with typical velocities of 500 $km\ s^{-1}$.
NLSy1	Narrow Line Seyfert 1: a type of AGN characterized by being similar to Seyferts but lacking the broad lines.
NS	Neutron Star: a type of stellar remnant resulting from the gravitational collapse of a massive star after a supernova.
OM	Optical Monitor: a detector on board *XMM*–Newton covering between 170 nm and 650 nm.
PSD	Power Spectral Density: the product of the Fourier transform of a function and its complex conjugate.

PSF	Point Spread Function: the response of an imaging system to a point source or point object.
QPO	Quasi-Periodic Oscillations: flickering in a light curve at certain frequencies.
QSO	Quasi-Stellar Object or quasar: an AGN type characterized by an extreme luminosity.
RIAF	Radiative Inefficient Accretion Flow: a model of sub-Eddington accretion disc.
RMF	Redistribution Matrix File: a file containing maps from energy space into detector pulse height (or position) space.
S/N	Signal-to-Noise-ratio: a measure of a signal to the level of background noise.
SAS	Science Analysis Software: a software developed by the *XMM*–Newton team to reduce data.
SMBH	Super Massive Black Hole: a black hole with a mass $\gtrsim 10^6 M_\odot$.
Sy	Seyfert: a type of AGN characterized by high ionization lines.
ULIRG	Ultra Luminous InfraRed Galaxy: a galaxy with an infrared luminosity higher than $10^{12} L_\odot$.
ULX	Ultraluminous X-ray Source: an astronomical source of X-rays.
UM	Unified Model: a model with the aim of accommodate every type of AGN.
UV	UltraViolet: an electromagnetic radiation with a wavelength from 400 nm to 100 nm.
VLA	Very Large Array: a 27 identical 25 m antennas interferometer.
XRB	X-Ray Binary: a class of binary stars that are luminous in X-rays.